DOCTOR OF PHILOSOPHY

Flexible Supercapacitors Utilising the Multifunctional Rôle of Ionic Liquids

Lorenzo Fernandez, Marta

Award date:
2018

Awarding institution:
Queen's University Belfast

DOCTOR OF PHILOSOPHY

Flexible Supercapacitors Utilising the Multifunctional Rôle of Ionic Liquids

Lorenzo Fernandez, Marta

Award date:
2018

Awarding institution:
Queen's University Belfast

Flexible Supercapacitors Utilising the Multifunctional *Rôle* of Ionic Liquids

By

Marta Lorenzo Fernández, BSc, MSc

Being the Thesis submitted for the degree of

Doctor of Philosophy

to the

School of Chemistry and Chemical Engineering

Based on the research carried out under the supervision of

Dr Geetha Srinivasan

Dr Cristina Lagunas Castedo

School of Chemistry and Chemical Engineering,

The Queen's University of Belfast

May 2018

To my family

To K. R. Seddon, in memoriam

"Science is not only a discipline
Of a reason but, also, one of
Romance and passion"

Stephen Hawking

"To see a world in a grain of sand,
And a heaven in a wild flower,
Hold infinity in the palm of your hand,
And eternity in an hour"

William Blake, Auguries of Innocence

Acknowledgements

I would like to dedicate this thesis to **Prof Kenneth R. Seddon**, one of the greatest scientists and specialists in the ionic liquids field. He was one of the two mentors that gave me the opportunity to start this PhD at QUILL. He showed me how to think in every angle and to question everything. He was an excellent guide and I thank him for all the knowledge and support shared. TA Ken!

The other person who made this PhD and thesis possible is **Dr Geetha Srinivasan**, she is the driving force who was supporting and encouraging me all this time. I grew as a person and scientist thanks to her. I cannot thank her enough, just to say that she is more than a supervisor, she is like family, thanks for everything!

I would like to thank **Dr Cristina Lagunas** for her input and supervision. Also, I would like to express my gratitude to all the QUILLians, **Dr Natalia Plechkova**, **Dr Nimal Gunaratne**, **Dr Manuela Gilea** and **Ms Deborah Poland** that were part of this journey making every day easier and funnier.

Part of the results obtained in this PhD were possible due to the help of the School of Chemistry and Chemical Engineering technicians, **Ms Angela Brownlie**, **Dr Susanne Huq**, **Mr Richard Murphy**, **Mr Conor McGrann**, **Mr Darren Baskerville** and **Dr Bronagh Millar** from the Polymer Processing Research centre. Thanks to all of them!

I remember when I first arrived in Belfast, I was like a little Bambi and the first people who helped and gave me a bed for a few days were Pedro and Isabel. **Pedro**, I am so grateful for your friendship, you rock! And **Isabel**, from the beginning you helped me and tried to make me laugh all the time, I hope that our friendship is forever because people like you are worthy! During my first day in the School, I met **Darius**, my new PhD mate and now good friend, thanks for all the funny videos during these three years. After two months, a little *bambino* called **Fede** arrived and he showed us the party! I will never forget all the moments we spent together because you are unique. **Albert** & **Ana,** my favourite couple, who always helped me during the good and bad times. Albert thanks for all our conversations and Ana thanks for all the shopping and Patisserie Valerie days. **Fabio** (*el tío de moda*)

thanks for all the chatting and cooking. **Floriana**, my darling, what can I say? Just, I love you so much and I hope to visit you in Palermo and enjoy some amazing holidays. **Nati** & **Laura**, it was a pleasure getting to know you, I had a lot of fun with both of you shopping, cooking, moving…, so many adventures, thanks for your friendship. During these three and a half years, more people made this journey very special, I would like to mention **Yoan**, **Kike**, **Joaquín**, **Eva**, **Stratos**, **Magda**, **Alex**, **Eris**, **Kasia**, **Eunice**, **Anne**, **Rawan**, **Fergal**, **Eoghain**, **Rachel**, **Luci**, **James**, **Marcos** and **Rosana**. I will never forget our Friday Pub evenings at Eglantine, thanks people!

Ahora me gustaría darle las gracias a mi familia por toda la ayuda, comprensión y oportunidad de llevar a cabo esta experiencia tan gratificante. ¡Gracias **mamá**, **papá** y **hermanita**! ¡Os quiero muchísimo! También, me gustaría nombrar a mi **madrina**, **tíos**, y **primos**, gracias por apoyarme siempre.

También tengo que incluir en esta tesis a mis amigas y amigos, a los cuales he echado tanto de menos durante mi estancia en Belfast. Gracias por esperarme y soportarme durante los meses que he pasado en Vigo acabando de escribir esta tesis. **Zara**, **Amanay**, **Fla**, **Isma**, **Ovenza**, **Luci**, **Billy** y sin olvidarme de mi ahijado **Lucas**, ¡os quiero!

Y de último y más importante, **Daniel**, tú has hecho que mi experiencia en Belfast fuera perfecta. Sin tener ni idea de inglés decidiste acompañarme en esta aventura y con ello, hacerme la persona más feliz del mundo. Me ayudaste y soportaste en mis malos momentos, me hiciste reír y llorar de alegría y eso me ha hecho quererte cada día más. Por todo eso y por todo lo que ya hemos vivido juntos, mi contestación del 11 de marzo de 2017 fue ¡Sí, quiero! Gracias por todo lo que haces por mí, ¡te quiero!

Publications

Peer review journal articles

- **Lorenzo, M.**, Zhu, B. and Srinivasan, G., "Intrinsically flexible electronic materials for smart device applications", *Green Chem.* **18** (12), 3513-3517 (2016).
- **Lorenzo, M**. and Srinivasan, G., "Durable Flexible Supercapacitors Utilizing the Multifunctional Role of Ionic Liquids", *Energy Technology* **6** (1), 196-204 (2018).

Conference contributions

- **Conference poster**: "Flexible Supercapacitors for Biomedical Applications", Faraday Discussions conference (2017) Cambridge. (Poster Prize)
- **Competitive Mobility Scholarship**: granted by Santander Universities UK to go to Tuft's University (Boston, US) for 5 weeks during summer 2016.
- **Flash oral presentation and conference poster**: "Flexible Supercapacitors", RSC Energy Sector Early Careers Symposium 2016, London.
- **Oral and poster presentation at the "QUILL meeting"**. Presentation of the results to the industrial members of the QUILL research centre, every 6 months, Belfast. (Oral presentation second prize in March 2017)

Abstract

The study on flexible, ultrathin and safe energy storage devices such as supercapacitors or batteries is an emerging area to "power-up" the next-generation of portable and flexible electronics such as mobile phones, computers, displays, wearable and implantable biomedical devices. In general, a supercapacitor is composed of two electrodes, electrolyte, separator and current collectors and it can store and deliver charge at relatively high rates. The challenge to design such supercapacitors to be flexible lies in the development of flexible electrodes and leak-proof electrolytes, as well as, the retention of the electrochemical characteristics of high power density, long cycle life and high efficiency under considerable physical deformation.

An innovative one-pot synthesis to fabricate electronically conducting polymer-biopolymer composites films such as polypyrrole-cellulose composites that are intrinsically conducting and flexible is presented. The method consisted of an *in situ* polymerisation of pyrrole in a solution of cellulose in the ionic liquid, 1-butyl-3-methylimidazolium chloride. The resulting polypyrrole-cellulose composite film was chemically blended, and it showed flexible polymer properties while retaining the electronic properties of the polypyrrole. Addition of a hydrophobic ionic liquid, trihexyl(tetradecyl)phosphonium bis{(trifluoromethyl) sulfonyl}amide and graphite powder enhanced the flexibility and conductivity of the composite films, respectively.

The composites films obtained were applied as electrodes in flexible supercapacitors using a simple scalable method to design flexible, ultrathin and safe supercapacitors. Three devices were fabricated, (i) electrical double-layer supercapacitors, (ii) electrochemical supercapacitors and (iii) hybrid supercapacitors. The multifunctional *rôle* of ionic liquids as solvent, electrolyte and plasticiser was exploited to fabricate these novel flexible supercapacitors which showed an excellent cycle life of 15000 cycles with nearly 100 % of capacitance retention, an operational voltage between 1.6 V and 3.2 V and a maximum energy and power density of 0.008 μW h cm^{-2} and 1.78 μW cm^{-2}, respectively. Moreover, the design nature of these electrodes, chemical stability and feasibility to use

biocompatible components will enable the fabrication of task-specific flexible supercapacitors with durable cycle life and chemical stability.

Table of Contents

List of figures

List of tables

List of abbreviations

A	Area
A (unit)	Ampere
A^-	Anion
AC	Activated carbon
APS	Ammonium persulfate
ATR	Attenuated total reflectance
BS	Benzenesulfonate
BSA	Benzenesulfonic acid
BDM	Bockris-Devanthan-Müller
C	Capacitance
C	Concentration
C (unit)	Coulomb
C^+	Cation
C_{Areal}	Areal capacitance
CE	Counter electrode
Cellfib	Fibrous cellulose
cP (unit)	Centipoise
CS	Camphor sulfonate
CSA	Camphor sulfonic acid
C_{Spec}	Specific capacitance
CV	Cyclic voltammetry
d	Distance
D	Diffusion coefficiency
DBSA	*p*-dodecylbenzene sulfonic acid
DMF	Dimethylformamide
DMSO	Dimethyl sulfoxide
E	Energy
E_{AL}	Anodic limit potential
E_{CL}	Cathodic limit potential
E_{AP}	Anodic peak potential
E_{CP}	Cathodic peak potential
EC	Electrochemical capacitor
ECP(s)	Electronically conducting polymer(s)
$E_{Density}$	Energy density
EDLC	Electrical double-layer capacitor
EDLS	Electrical double-layer supercapacitor
EIS	Electrochemical impedance spectroscopy
ES	Electrochemical Supercapacitor
E_{Spec}	Specific energy
ESD(s)	Energy storage device(s)

ESR	Equivalent series resistance
EW	Electrochemical window (three electrodes)
	Operational voltage (two electrodes)
	Potential (equations)
E_ω	Frequency response-potential
F (unit)	Farads
FESD(s)	Flexible energy storage device(s)
FSC(s)	Flexible supercapacitors
FRA	Frequency response analyser
FT-IR	Fourier transform infrared
G (unit)	Grams
GENE Lab	Green Energy and Nanostructured Electronics Laboratory
GCD	Galvanostatic charge-discharge
GPES	General purpose electrochemical system
HOMPP	2-hydroxy-2-methylpropiophenone
HS	Hybrid supercapacitor
i	Current
I	Discharge current
I_{Const}	Constant discharge current
i_p	Peak maximum current
IHP	Inner Helmholtz plane
IL(s)	Ionic liquids
IR	Infrared
IR_{drop}	Potential drop
IUPAC	The International Union of Pure and Applied Chemistry
I_ω	Frequency response-current
k	Temperature dependant constant
LIC	Lithium ion capacitor
m	Electrode mass
min	Minutes
NEC	Nippon Electric Company
NMR	Nuclear magnetic resonance
NMMO	*N*-methyl-morpholine-*N*-oxide
OCP	Open circuit potential
OHP	Outer Helmholtz plane
P	Power
PCl	$[P_{6\,6\,6\,14}]Cl$ (trihexyl(tetradecyl)phosphonium chloride)
$P_{Density}$	Density power
PEGDA	Poly(ethylene glycol) diacrylate

$PNTf_2$	$[P_{6\,6\,6\,14}][NTf_2]$ (trihexyl(tetradecyl)phosphonium bis{(trifluoromethyl)sulfonyl}amide)
PPy	Polypyrrole
PRI	Pinnacle Research Institute
P_{Spec}	Specific power
PVA	Polyvinyl alcohol
Q	Electric charge
RE	Reference electrode
r.t.	Room temperature
RTIL(s)	Room temperature ionic liquid(s)
s	Seconds
S	Surface area
SC(s)	Supercapacitor(s)
SEM	Scanning electron microscopy
SSA	Specific surface area
TBAP	Tetrabutylammonium perchlorate
t_{dis}	Discharge time
$TEABF_4$	Tetraethylammonium tetrafluoroborate
TGA	Thermogravimetric analysis
T_{on}	Temperature Onset
TSIL(s)	Task-Specific Ionic Liquid(s)
V_f	Final operational voltage limit
V_i	Initial operational voltage limit
V (unit)	Volts
VOCs	Volatile organic solvents
WE	Working electrode
wt %	Weight percent
Z	Impedance
Z′	Real impedance
Z′′	Imaginary impedance
ΔE	Peaks separation potential
[BETI]	Bis{(perfluoroethyl)sulfonyl}amide

Symbols

ß	Hydrogen bond acceptor
n	Number of electrons transferred
ε	Permittivity
Ω (unit)	Ohms
Λ	Molar conductivity
η	Viscosity
ν	Scan rate

Ionic liquids

$[C_2mim]Cl$	1-ethyl-3-methylimidazolium chloride
$[C_2mim][C_1COO]$	1-ethyl-3-methylimidazolium ethanoate
$[C_2mim][FAP]$	1-ethyl-3-methylimidazolium tris(pentafluoroethyl)trifluoro phosphate
$[C_2mim][NTf_2]$	1-ethyl-3-methylimidazolium bis{(trifluoromethyl)sulfonyl}amide
$[C_4mim]Cl$	1-butyl-3-methylimidazolium chloride
$[C_4mim][C_1COO]$	1-butyl-3-methylimidazolium ethanoate
$[C_4mim][NTf_2]$	1-butyl-3-methylimidazolium bis{(trifluoromethyl)sulfonyl}amide
$[P_{6\,6\,6\,14}]Cl$	Trihexyl(tetradecyl)phosphonium chloride
$[P_{6\,6\,6\,14}][NTf_2]$	Trihexyl(tetradecyl)phosphonium bis{(trifluoromethyl)sulfonyl}amide

Chapter 1

Introduction to Supercapacitors

1.1. Energy Storage Devices

During the past decades, the massive demand for electrical energy to power up portable electronic devices such as smartphones, laptops or tablets, as well as, the emerging fabrication of electric or hybrid vehicles has increased leading to the need for new energy storage technologies [1]. Although the energy consumption from these devices seems individually rather small, the overall energy required for electric and electronic devices is huge, just as an example, there are more than three billion people in the world that own a mobile phone [2].

For this reason, energy storage devices (ESDs) are starting to play an important *rôle* [3]. ESDs are systems able to store electric charge and release it when requires [4]. The most common energy storage devices are fuel cells [5], batteries [6], dielectric capacitors [7] and supercapacitors (SCs) [8].

Supercapacitors are considered promising candidates for energy storage applications. They are power devices able to store and deliver charge at relatively high rates, in other words, can be fully charged and discharged within seconds. Similar to other energy devices, SCs are composed of two electrodes (anode and cathode), an electrolyte, a separator (to electrically isolate the two electrodes), and two current collectors, as shown in Figure 1.1 (a).

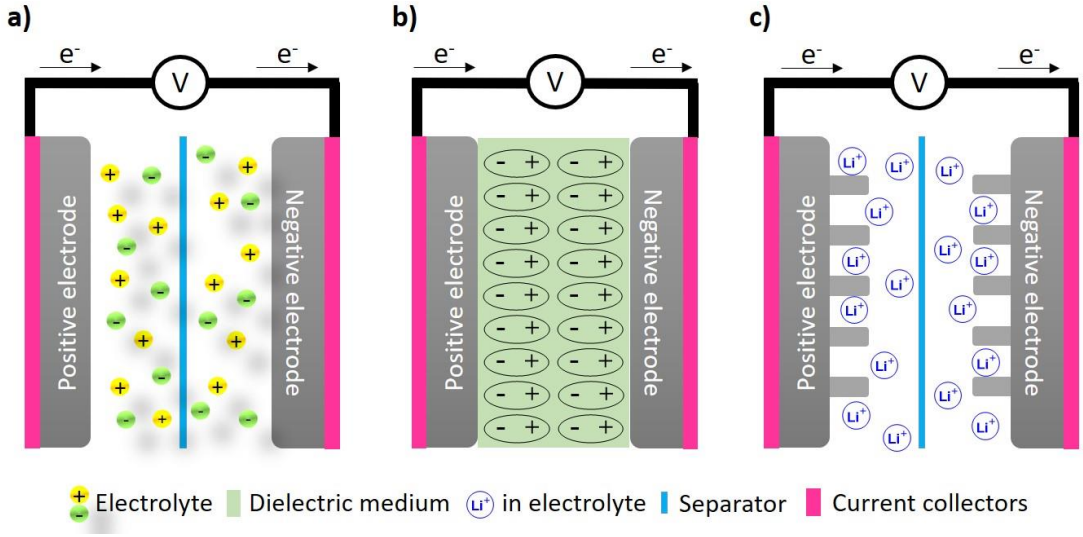

Figure 1.1 Fundamental structure model of a) supercapacitor, b) conventional capacitor and c) Li-ion battery

SCs have attracted great research and industrial curiosity due to their characteristics such as high specific power (10-55 kW kg^{-1}), great rate efficiency (0.85-0.98), fast charge-discharge time (seconds), long cycle life (10^6 cycles) with excellent

stability and low maintenance cost. Commonly, SCs show around 20-200 times more capacitance per unit mass than conventional capacitors [3,9]. The properties of supercapacitors can be better explained by comparing them to conventional capacitors and batteries that are widely used in electronic devices.

Conventional capacitors are composed of two conductive plates with different electrical potential (positive and negative) separated by a non-conducting dielectric layer with a very high dielectric constant and low leakage current characteristics as it can be seen in Figure 1.1 (b) [10]. Commonly, the dielectric materials are oxide layers such as SiO_2, paper, mica or ceramic. In capacitors, the charge storage mechanism relies on this dielectric material that is able to accumulate electric charge at the interface between the electrode plate and itself, due to the dipoles polarisation [11].

In contrast to conventional capacitors, batteries use the conversion of chemical energy into electrical energy *via* reversible Faradaic reactions at both electrodes *e.g.*, lithium ion intercalation into graphite [5]. Figure 1.1 (c) shows the structure of a Li-ion battery where insertion reactions take place to store the charge [12]. Li-ion batteries are energy storage devices with a high specific energy (120-200 Wh kg^{-1}) but low specific power (0.4-3 kW kg^{-1}) and low cycle life (~1000 cycles) [13].

The comparison amongst conventional capacitors, supercapacitors and batteries are often represented using the Ragone plot (Figure 1.2) to show how quickly the charge can be stored or delivered and the amount of charge that can be stored in the devices. A Ragone plot is a graph that relates the energy and power of different devices which allows comparing the performance of the devices under study [14]. For example, if a supercapacitor is used in an electric elevator, the specific power will define how fast the elevator can travel, and the specific energy will determine how many lifts can be carried out on a single charge. Time shown in the graph is the time constants of the devices, obtained by dividing the specific energy by the power. Figure 1.2 shows the main difference between energy storage devices in terms of specific power and energy. In the case of dielectric capacitors, they have a very high specific power and an almost null specific energy, however, batteries are the opposite; they have a large specific energy and a small specific power. Supercapacitors are considered devices able to fill the gap between conventional capacitors and batteries

due to their ability to obtain higher specific power than batteries and much higher specific energy than capacitors.

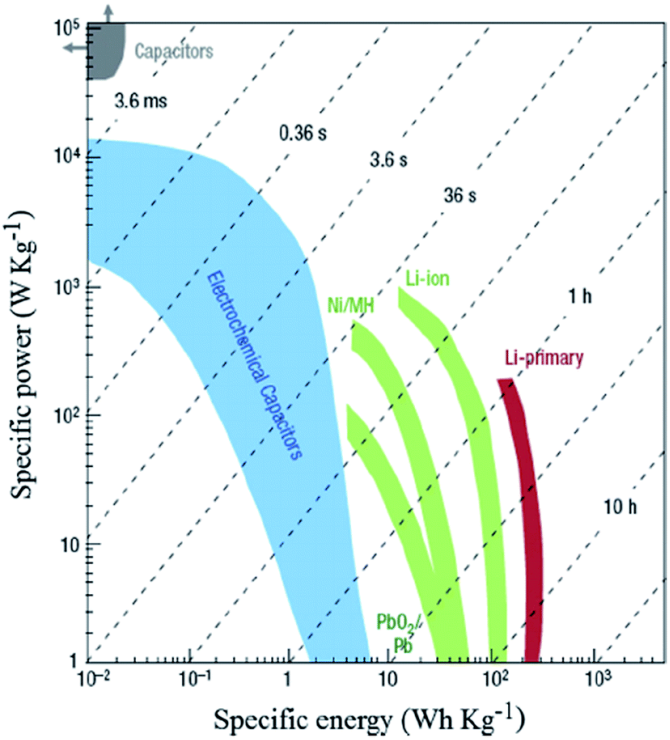

Figure 1.2 Ragone plot showing, specific power *vs*. specific energy for various electrical energy storage devices. Figure adapted from reference [3]

1.2. Background - Supercapacitors

In 1853, Hermann von Helmholtz described for the first time the concept of "double-layer capacitance" which corresponds to the charge accumulation between the electrode-electrolyte interface (see Figure 1.4 in section 1.4) [15]. However, in that period, there was not an application for this discovery [16]. It was not until 1957 when Becker patented the first electric double-layer capacitor (EDLC), using carbon electrodes and an aqueous electrolyte [17]. The Sohio Corporation (Cleveland), in 1962, granted a patent of an EDLC using carbon electrodes and a nonaqueous solvent containing a tetraalkylammonium salt electrolyte. In 1971, the Nippon Electric Company (NEC) introduced the first electrochemical capacitor (EC) product in the market under the name of "Supercapacitor" as a memory backup device in computers [18]. Between 1975 and 1983 Conway *et al.* carried out extensive work on ruthenium oxide-based electrochemical capacitors, bringing a new concept called "pseudocapacitance" that involves fast and reversible Faradaic processes (redox reactions) on the surface of the electrodes (see section 1.4.2) [19].

By the 1980s, several companies produced double-layer capacitors such as the "Goldcaps" brand developed by Panasonic or the first supercapacitor under the name of "PRI Ultracapacitor" by Pinnacle Research Institute (PRI) [20]. In 1992, Maxwell Laboratories (currently Maxwell Technologies) took over PRI development and changed the name to "Boost Caps". Nowadays, universities, research centres and companies are working to improve the characteristics of supercapacitors such as specific energy, specific power and cycle life.

1.3. Supercapacitors Classification

Supercapacitors can be categorised depending on (i) the charge storage mechanisms or (ii) the active material used as electrodes. Both classifications can be merged into one because they are interrelated, *i.e.* depending on the electrode material chosen the energy storage mechanism can be different.

Therefore, SCs can be further classified into three categories depending on the charge storage and release mechanism, *viz.* (i) electrical double-layer supercapacitor (EDLS), (ii) pseudocapacitor or electrochemical supercapacitor (ES) and (iii) hybrid supercapacitor (HS) [21]. Each category can be subdivided into the active materials used as it can be seen in Figure 1.3.

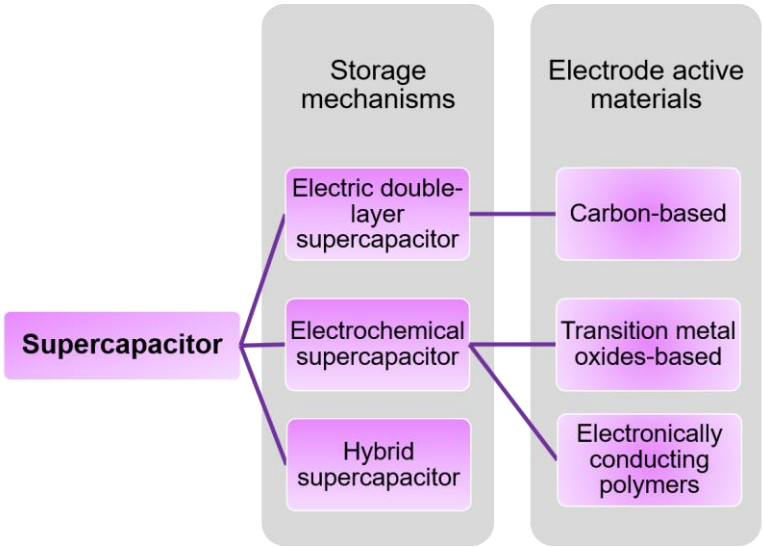

Figure 1.3 Scheme representing the classification of supercapacitors depending on the storage mechanisms and the electrode active materials

EDLS stores the electrical charge electrostatically by a reversible adsorption of ions at the electrode-electrolyte interface using carbon-based electrodes. ES based on electronically conducting polymers or transition metal oxides can store the charge on the electrode surface *via* fast and reversible Faradaic reactions. In the case of the

hybrid supercapacitors, both EDLS and ES mechanisms work together in a single device; *i.e.* the charge is stored electrostatically and electrochemically [22a,19c,22b-22d,9].

Apart from the classification explained above, supercapacitors can be symmetric or asymmetric depending on the electrodes used for assembly [23], *i.e* the assembly of two electrodes with the same composition as positive and negative electrodes originate a symmetric supercapacitor and, whereas the assembly of two electrodes with different composition as positive and negative electrodes make an asymmetric supercapacitor for example, a battery type electrode as the energy source and a capacitor type electrode as the power source [24], *e.g*. lithium-ion capacitor (LIC) that is an asymmetric hybrid device [25] due to the combination of a battery mechanism in the negative electrode (lithium titanate) and an electric double-layer supercapacitor mechanism of in the positive electrode (activated carbon) [26].

1.4. Energy Storage Mechanisms in Supercapacitors

As mentioned in the previous section the storage of electrical charge in a supercapacitor can be carried out electrostatically and/or electrochemically. When the charge is stored electrostatically it is known as electrical double-layer capacitance mechanism and when the charge is stored electrochemically it is known as pseudocapacitance mechanism. Both mechanisms will be explained in the next sections.

1.4.1. Electrical Double-layer Capacitance Mechanism

The ability of a system to store electrical charge when a potential difference exists is known as capacitance; the best system where capacitance is produced is a capacitor [20a]. In a capacitor, the electrical charge is stored through the electrical double-layer formed between the electrode and electrolyte interface, which can be explained using the theory of the electrical double-layer from Helmholtz in 1879. This description is the simplest models to understand the operating principles of an EDLS [19c]. According to the Helmholtz model, when an electrode (electronic conductor) is in contact with an electrolyte (ionic conductor) the charges organise at the electrode-electrolyte surface forming the "electrical double-layer", as shown in Figure 1.4 [27,5].

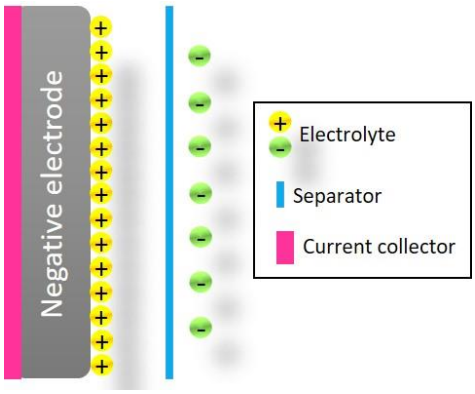

Figure 1.4 Scheme of the compact electrical double-layer described by the Helmholtz model

Following the Helmholtz model (compact layer), other models have been introduced which describe in more detail the possible formation of the "electrical double-layer" including diffusion in the solution or the interaction of the solvent with the electrode surface. The most important ones are the Gouy-Chapman model (involving a diffuse double-layer) [28], the Stern model (combines the compact and the diffuse double-layer) and the Bockris-Devanathan-Müller (BDM) model that includes the solvent action in the electrode interface and the previous models [29]. The BDM model is the most detailed one and it states that there is a first layer formed at the electrode surface called inner Helmholtz plane (IHP) referring to the monolayer of the polarised solvent molecules and a second layer corresponding to the charge layer in the electrolyte that is known as outer Helmholtz plane (OHP) as it can be seen in Figure 1.5 [30]. This model further describes that the orientation and permittivity of the solvent molecules strongly depend on the electric field.

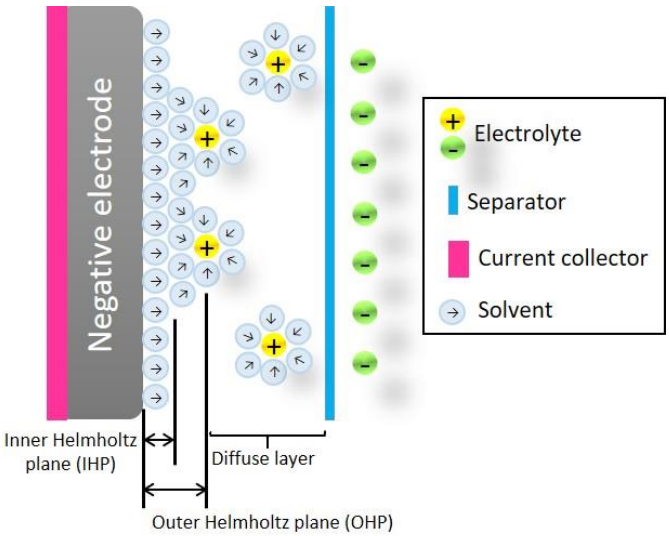

Figure 1.5 Schematic view of a double-layer between a negative electrode surface and an electrolyte by the BDM model [30]

It must be taken into account that a supercapacitor is still a capacitor and should be governed by all the equations that described a dielectric capacitor. In an ideal dielectric capacitor, the capacitance, *C*, is defined by Equation 1.1 and it is measured in farads (F), as the ratio of the electric charge on each electrode, *Q* (C), to the operational voltage, *EW* (V), of the capacitor. In other words, the potential is proportional to the charge stored in the capacitor ($C \cdot EW = Q$) [31].

$$C = \frac{Q}{EW} = \varepsilon \frac{S}{d} \qquad \text{Equation 1.1}$$

For conventional capacitors, C is directly proportional to the surface area, S, of one of the electrodes and inversely proportional to the distance, d, between electrodes; ε is the permittivity of the medium between the electrodes.

Two main characteristics of a capacitor are its energy and power density, and both can be expressed as a quantity per unit area (energy or power density) or per unit weight (specific energy or power). The energy, *E*, stored is directly proportional to its capacitance, *C* (F), because it is related to the charge, *Q* (C), that can be accumulated at each electrode-electrolyte interface and the operational voltage of the supercapacitor, *EW* (V), as can be seen in Equation 1.2.

$$E = 1/2 \cdot C \cdot EW^2 \qquad \text{Equation 1.2}$$

Power, *P*, is usually the rate of energy delivered per unit time and it is calculated using Equation 1.3. In order to determine *P* in a supercapacitor, the device operational voltage, *EW* (V), and all the resistances existing in the supercapacitor assembly have to be taken into account. The resistances that can be found in a supercapacitor are the resistances of the electrodes, electrolyte, separators and current collectors. All these resistances can be aggregated under the name of equivalent series resistance, ESR (Ω), thus, ESR is how the resistance of the device itself is determined [32].

$$P = \frac{EW^2}{4 \cdot ESR} \qquad \text{Equation 1.3}$$

From Equation 1.2 and Equation 1.3, it can be seen that an increase of the capacitor operational voltage, *V*, causes a significant enhancement in the power, *P*, and energy, *E*.

Another important characteristic of a supercapacitor is the time needed to charge and discharge that is usually in seconds. The charge-discharge in a supercapacitor (EDLS) usually consists of the movement of the ions from the

electrolyte as shown in Figure 1.6. In the case of the charging state, the ions move to the electrode surface to form the double-layer, *i.e.* cations move to the negative electrode and the anions move to the positive electrode [33].

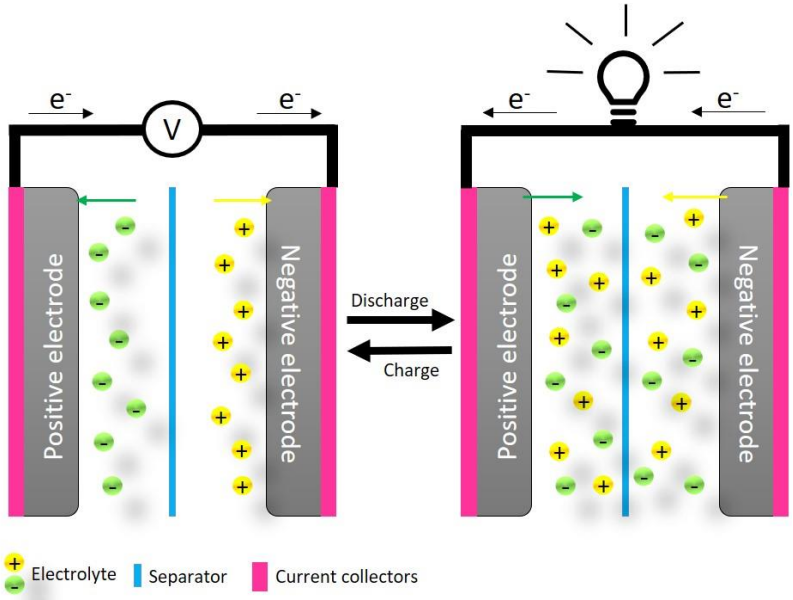

Figure 1.6 Two electrodes EDLS scheme, showing the charges distribution when it is charged (left) and discharged (right)

1.4.2. Pseudocapacitance (or Electrochemical) Mechanism

As it was explained previously, the performance of an EDLS is based on electrostatic adsorption of ions at the electrode/electrolyte interface obtaining capacitance based on the electrode surface source and the electrolyte medium used.

Another source to enhance this capacitance is by reversible and fast faradaic reactions (associated with electron transfer) on the active material's surface. This effect is known as pseudocapacitance and it is induced in the electrodes when active materials such as electronically conducting polymers (ECPs) or transition metal oxides are utilised as electrodes [34]. Figure 1.7 shows a schematic view of a positive electrode formed by an electronically conducting polymer in which fast electron transfer reactions take place in the polymer chain due to the ECP reduction and oxidation, that provokes the passage of charge across the double layer, like the charging and discharging processes in a battery [35]. Possible Faradaic processes going on in a pseudocapacitive material *viz.* reversible doping-dedoping in an electronically conducting polymer [36], reversible adsorption-desorption of *e.g.* hydrogen in Pt [37] and redox reactions of a transition metal oxides based electrodes [38].

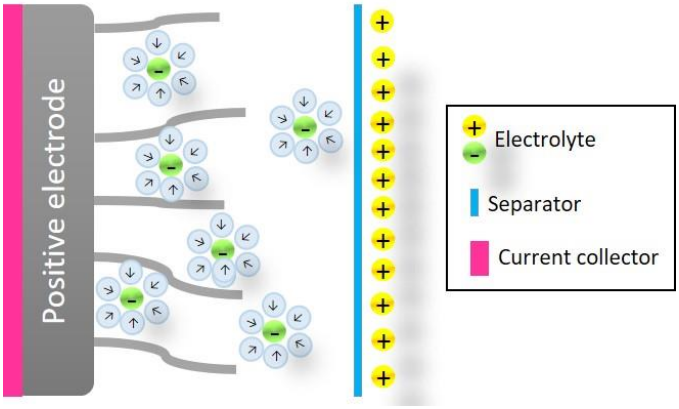

Figure 1.7 Schematic view of the positive electrode of a pseudocapacitor or electrochemical supercapacitor formed by an electronically conducting polymer

For a better understanding, the main difference between an electrochemical supercapacitor and a battery lies in the place where the charge is stored; in the case of an ES the charge is stored at the electrode surface and in a battery, the entire electrode is involved [9]. For an ES or pseudocapacitor, the charge transferred during these fast and reversible Faradaic processes is proportional to the voltage, as it happens in an EDLS, and due to these rapid redox processes the power density increases, therefore, an ES normally shows much higher power density than batteries [39].

1.5. Supercapacitor Components

As it was shown in Figure 1.1 (a), a supercapacitor is composed of two electrodes (anode and cathode), an electrolyte, a separator and two current collectors.

1.5.1. Electrodes

The design and control of the electrode materials play an important *rôle* in the performance of the SCs including the capacitance, rate capability and the cycle life stability [40].

In general, one of the most important characteristics of the electrode in a supercapacitor is to have a high surface area because the double-layer storage and the pseudocapacitance mechanisms are surface-based processes; the surface features of the electrode greatly influence the capacitance of the cell *e.g.* in a porous electroactive electrode the increase of the porosity will enhance the ion penetration of the electrolyte into the electrode surface [32,31,20b,3,41]. Other features that electrodes should have are high electric conductivity, good corrosion resistance, high-temperature stability, controlled pore structure and relatively low cost [22d]. As

mentioned in section 1.3, the classification of supercapacitors is determined by the storage mechanism and also depending on the electrodes compositions. In the next subsections, different electrode materials used in SCs will be explained.

1.5.1.1. Carbon-based Electrodes

For a good electric double-layer supercapacitor performance, materials with high surface area and pores adapted to the size of the ions from the electrolyte are needed [42]. The porosity of the electrode material will be crucial for the EDLS performance, *e.g.* the surface area can be increased by the development of porosity in the carbon materials showing an enhancement in the capacitance [30]. The International Union of Pure and Applied Chemistry (IUPAC) defined pores by their size as follows: macropores (larger than 50 nm), mesopores (between 2 and 50 nm) and micropores (smaller than 2 nm) [43].

Carbon-based electrodes such as activated carbon (AC), nanotubes, nanofibers, graphite or graphene have been investigated as electrodes for SCs because of their accessibility, non-toxicity, high thermal and chemical stability, their large specific surface area (SSA), high electrical conductivity, and wide temperature range stability [44].

Activated carbons are currently the most widely used materials due to their high SSA and moderate cost. From these materials, it has been possible to obtain capacitance values of 100-120 F g^{-1} in organic electrolytes and around 150-300 F g^{-1} in aqueous electrolytes. However, in the latter, a lower operational voltage is observed due to water decomposition which limits the operational voltage [3].

Supercapacitors are power supply devices so, there is a tremendous research effort to improve their energy density without losing their high power delivery and cycle life. The challenge of increasing the energy without losing power density can be solved by adding other materials with pseudocapacitive behaviour (fast surface redox reactions) such as transition metal oxides or electronically conducting polymers to the carbon [44].

1.5.1.2. Transition Metal Oxides-based Electrodes

Metal oxides such as RuO_2, Fe_3O_4 or MnO_2 have been extensively studied in the past decades for their application in supercapacitors as electrodes [3]. RuO_2 is the

most promising electrode material because of its high rate capability, good electrochemical reversibility, long cycle life, high specific capacitance and high conductivity. It has, however, some drawbacks due to lack of abundance and cost of the precious metal Ru [9]. Hence, other metal oxides such as the manganese oxide have been studied, especially because of its environmentally friendly character and low cost [45].

Despite metal oxides being considered as promising pseudocapacitive materials, they usually have low power density due to their poor electric conductivity limiting the electron transfer rates, and poor cycle life stability because of the morphology damage caused by the swelling and shrinkage of the electrode material during the charge and discharge process (redox reaction of the metal oxide) [46].

1.5.1.3. Electronically Conducting Polymer-based Electrodes

Polymers are materials containing long-chain molecular structures which are normally insulators, flexible and they are obtained by a straightforward synthesis. However, electronically conducting polymers, a type of semiconducting polymers also known as "synthetic metals" [47] started to be developed in 1977 when Shirakawa *et al.* [48] synthesised and characterised them showing that they can have excellent electrical and optical properties. This discovery received the Novel Prize in Chemistry in 2000 (*i.e.* "for the discovery and development of metal-like conducting polymers") [49].

These polymers possess electronically conducting properties due to the delocalisation of electrons along the *p*-orbitals of their conjugated polymer backbone. These unusual properties allow conjugated polymers to be used for many applications replacing metals, including in sensing devices, actuators and energy storage devices such as supercapacitors or batteries. However, most of the ECPs are intractable (*i.e.* insoluble or brittle) due to the backbone rigidity that is intrinsically associated with the delocalised conjugated structure. Table 1.1 shows the most common electronically conducting polymers used as electrodes in energy storage devices [50].

Table 1.1 The most commonly used electronically conducting polymers for energy storage devices

ECP	Structure	Date conductivity was discovered	Conductivity (S cm^{-1})	Reference
Polyacetylene		1977	103 - 105	[48]
Polypyrrole	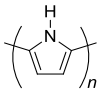	1979	102 - 103	[51]
Polyaniline	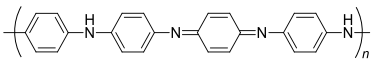	1980	30 - 200	[52]
Polythiophene	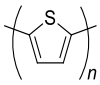	1981	10 - 103	[53]

1.5.1.3.1. Polymerisation Process

ECPs can be synthesised chemically or electrochemically, and the advantages and inconveniences of each method are presented in Table 1.2. The chemical polymerisation can be carried out using methods such as condensation or addition polymerisation [54]. Condensation polymerisation consists of the loss of small molecules, such as water or hydrochloric acid; whereas, in the case of the addition polymerisation, radical, cation and anion polymerisation can be carried out, depending on the respective radical, cation or anion intermediates that control the reactivity of the polymer chain [55]. Electrochemical polymerisation, proposed by Diaz *et al.* [51] in 1979, is the most commonly employed method for making conducting polymer films; it is a straightforward electrochemical synthesis using a three-electrode system (working, reference and counter electrode) in an electrolyte composed of a solution of the monomer and dopant in a suitable solvent [56]. This method consists of the electrodeposition of the conducting polymer at the working electrode (anode) when a current/voltage is applied through the system [55,57].

Table 1.2 Advantages and challenges of chemical and electrochemical polymerisation of conducting polymers

Polymerisation nature	Advantages	Challenges
Chemical polymerisation	Multiple routes of synthesis	Complicated synthesis
	Novel ECPs can be synthesised with new monomers	Cannot make very thin films
	Scale-up	Difficult homogeneity and uniformity in films; processing difficulties
Electrochemical polymerisation	Straightforward synthesis	Difficult to remove films from the electrode surface
	Very thin films can be made (20 nm)	Scale-up is difficult due to film breaking in large scale
	Simultaneous ECPs doping	

The electrochemical polymerisation of conducting polymers starts with the oxidation of the monomers at the working electrode to form radical cations and, follows with the reaction among these radical cations, forming insoluble polymer chains at the electrode surface. The mechanism of the electrochemical polymerisation of ECPs is shown in Figure 1.8.

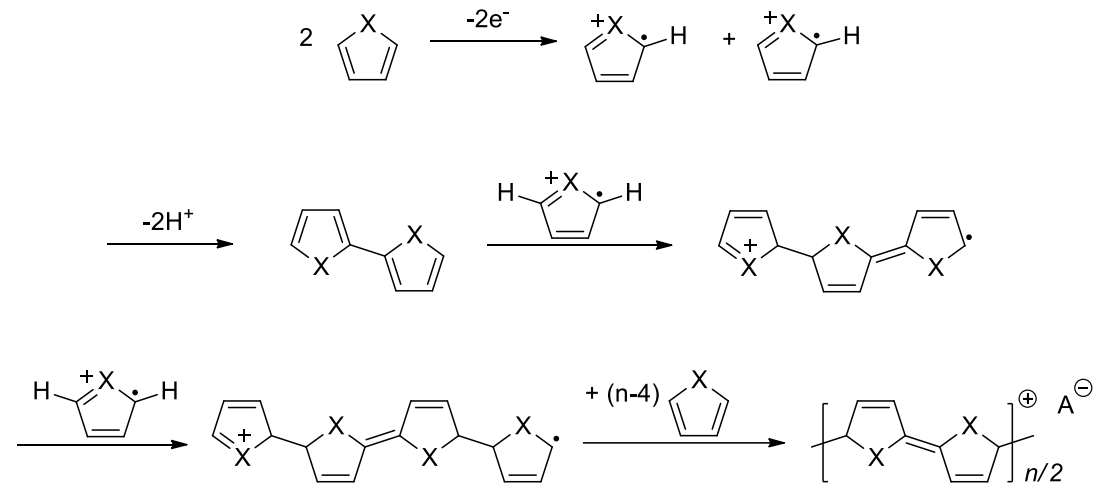

Figure 1.8 Electrochemical polymerisation mechanism of a heterocycle. X = NH, S or O. A^- corresponds to the counterion from the dopant [58,55]

1.5.1.3.2. Conduction Mechanism

The conductivity of electronically conducting polymers consists of electron transportations which can be intra-chain, inter-chain or inter-domain, and it is influenced by orientation, crystallinity and purity. However, the full details for each

transportation processes are still not fully understood. The most obvious factor which influences conductivity is the doping process of ECPs.

Different types of doping process exist such as chemical, electrochemical, photo or non-redox doping. Chemical doping is the most common process, and it consists of the partial oxidation (*p*-doping) or partial reduction (*n*-doping) of the polymer chain in a solution containing a dopant as shown in Figure 1.9. *P*-doping is achieved using oxidants such as I_2, $FeCl_3$ or ammonium persulfate, and in the case of *n*-doping, is necessary to use reductants such as Na or K [58].

$$ECP \rightleftharpoons ECP^{n+}(A^-)^n + ne^- \ (p\text{-doping})$$

$$ECP + ne^- \rightleftharpoons ECP^{n-}(C^+)^n \ (n\text{-doping})$$

Figure 1.9 Reversible redox reaction of electronically conducting polymers that can be *p*-doped with anions (A^-) or *n*-doped with cations (C^+) demonstrating that they can be utilised for the charging/discharging process in SCs

The most common type of doping is the *p*-doping which oxidises the ECPs chain. The dopant has to be negatively charged to act as the counterion and maintain the charge balance within the polymer (*i.e.* positive charges are developed along the polymer backbone as shown in Figure 1.10). Firstly, a *polaron* is formed (neutral and charged *soliton* (one charge defect) in the same chain), which is essentially a singly charged cation radical at the polymer chain coupled with local deformations and then, a *bipolaron* can be formed if two charged defects form a pair [59].

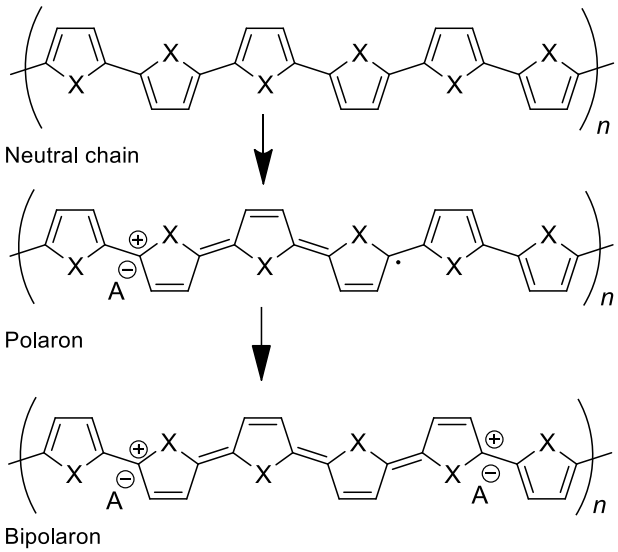

Figure 1.10 Doping process for ECPs with a heterocycle monomer. X = NH, S or O and anion (A^-) required to maintain electroneutrality

Different dopants precursors can be incorporated to carry out the doping of ECPs such as p-dodecylbenzene sulfonic acid (DBSA), camphor sulfonic acid (CSA) or β-naphthalene, being the most commonly used those containing a sulfonic acid group in the structure. Several articles reported that the use of sulfonic acid as a dopant precursor of ECPs resulted in a better thermal stability and in an increment of the conductivity of the ECPs [57,60].

To sum up, the doping process is considered as the introduction of charge defects in the polymer chains but, it is not general for all the ECPs, the doping process is still a matter of discussion [59]. Nevertheless, the band theory (Figure 1.11) developed by Harrison [61] in 1979 (well-established for solid materials) could explain the changes in the electronic structure induced by the doping process. Metallic conductors (a) are characterised by a partially filled valence band or an overlap between the valence and the conduction bands. Insulators (b) and semiconductors (c) possess a band gap between the top of the valence band and the bottom of the conduction band, being the gap energy rather large for an insulator and, in contrast, relatively small for a semiconductor. The application of this theory to the electronically conducting polymers consists of the assumption that the neutral ECP (reduced and undoped) is considered as an insulator because it has a full valence band and an empty conduction band separated by a bandgap. In the case of the *polaron* and the *bipolaron*, the ECPs are considered semiconductors or even metals, depending on the grade of doping (oxidation and incorporation of counterions) [62]. Another case in which an ECP can be considered an insulator is when it has been overoxidised; the overoxidation process is an irreversible oxidative degradation of a ECP under an anodic applied potential or a strong oxidant agent [63].

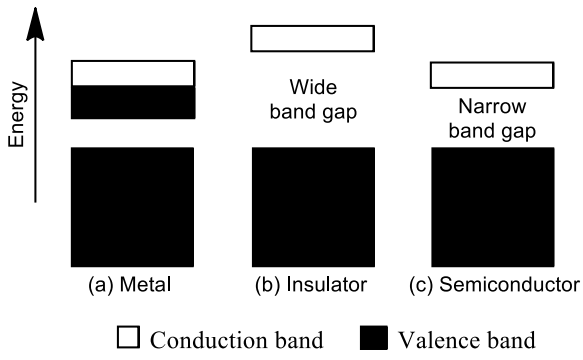

Figure 1.11 A schematic representation of energy gaps according to the band theory for solid materials [50]

ECPs can be easily altered between conducting and insulating states depending on their electrochemically or chemically oxidation and reduction processes. During this unique situation, other ECPs properties can be altered such as their conductivity [54].

ECPs have been tested in supercapacitors as pseudocapacitive materials and have shown high capacitance and low ESR [64]. However, supercapacitors based on ECPs face problems such as capacitance fade, incomplete electro-wetting, restrictions on the thickness of electrodes, mechanical stability, and use of environmentally toxic chemicals [65,3].

1.5.2. Electrolyte

Generally, the selection of the electrolyte material depends on the electrode type, but in principle, any ionic conductor can be used as an electrolyte in an energy storage device such as a supercapacitor. The main characteristics that are required for the electrolyte materials are high double-layer capacitance, wide electrochemical window, high ionic conductivity, wide operating temperature, as well as to be highly safe including low volatility and flammability and to be environmentally friendly [27].

The nature of the electrolyte has an influence on the supercapacitor performance, in other words, the capacitance, the energy/power densities and the cycle life can be affected by the electrolyte chosen. This is because the electrochemical window of the electrolyte directly determines the supercapacitor operational voltage, through which energy and power densities are affected, as shown in Equation 1.2 and Equation 1.3 [66].

Common electrolytes used in commercial energy storage devices are sulfuric acid, potassium hydroxide or potassium chloride in water and $TEABF_4$ in acetonitrile or in propylene carbonate [67]. The major limitation of commonly used electrolytes is their decomposition when a voltage is applied. Moving from aqueous to organic electrolytes the operational voltage changes from 0.9 V to 2.5-2.7 V for EDLSs [68].

Accordingly, stable electrolytes with a wider electrochemical window are needed. In the past decade, ionic liquids (ILs) have been identified as “greener” and better electrolytes candidates. ILs are defined as organic salts that possess melting points below 100 ºC and they are composed entirely of ions [69]. They have unique features such as high chemical and thermal stability [70], wide electrochemical

windows (EW) with values up to 6.5 V [71], high ionic conductivity [72], negligible vapour pressure [73], non-flammable nature [74], and recyclability [75]. A further review of ionic liquids will be discussed in section 2.1.

1.5.3. Separator

A separator allows the transfer of the charged ions but forbids the electronic contact between electrodes. The separator should have a high ionic conductance, a high electronic separator resistance and low thickness to obtain a competitive supercapacitor [76]. There are different separators that can be used depending on the electrolytes. In organic electrolytes, polymers *e.g*. polyvinyl chloride, Teflon®, polypropylene or paper separators are used and; with aqueous electrolytes, glass fibre or ceramic separators are applied [20b].

Nowadays, one of the major aims is to replace the components of the supercapacitors with more biodegradable and recyclable materials, and therefore, the use of paper separators has increased in the last years. Paper-based separators are low-cost, non-toxic and safe materials, thus representing a green alternative to conventional materials such as the polymer separators [77].

1.6. Applications of Supercapacitors

Supercapacitors allow new opportunities for power electronics because of their high-power capability. There are numerous articles highlighting the applications of supercapacitors. Some of them are listed in Table 1.3.

Currently, there is an emerging field of work involving the use of energy storage devices to "power-up" applications that require flexible, ultrathin and safe designs due to the demand for the next-generation of portable and flexible electronics such as wearable devices [78], roll-up displays or biomedical implants [22c]. Hence, the research on flexible energy storage devices (FESDs) is being developed to meet the rapidly growing demand for these flexible electronics.

Table 1.3 Possible applications of supercapacitors

Applications of supercapacitors	Brief description	References
Hybrid vehicles	Supercapacitors may supply the power to the electric vehicle. For start-stop and regenerative energy needed	[79]
Uninterruptible power supplies	An uninterruptible power supply is made up of rectifier, inverter, electrical energy storage unit and switches, for applications in healthcare, emergencies, and in operating computing applications	[80]
Memory back-up	SCs can be used for memory back-up in toys, cameras or mobile phones due to fast charge/discharge in less than 2 minutes	[3]
Portable power supplies	For portable electronic equipment with moderate energy demands, SCs are well suited to act as rechargeable stand-alone power sources	[81]
Power quality	To improve the reliability and quality of power distribution avoiding harmonics and spikes, SCs can be a good option as an energy storage device	[82]
Biomedical applications	Supercapacitors can be used as a replacement for batteries for implantable medical devices that just need fast power-up systems in emergencies	[83]

1.7. Flexible Energy Storage Devices

The need for smart materials that can function on external activation for their use in modern electronic devices has increased tremendously over the last decades, with a market size of $34.3 billion that is expected to grow to $80.2 billion by 2020 [84]. In the meantime, there is a growing need for developing electronic materials from natural resources such as bio-waste, specifically for energy storage device applications. This urge for using bio-renewable sources for electronic materials fabrication is due in order to avoid the large electronic waste generated nowadays, for example, the Environmental Protection Agency reported that 3,140,000 tonnes of electronic waste was generated until 2013 [85].

Flexible energy storage devices are energy conversion systems that can operate (store and release electric charge) under considerable physical deformation [86]. They have recently attracted a lot of interest for their potential applications in various flexible electronic systems including [31], microfluidic devices, portable devices, organic electronics, wearable personal multi-media and roll-up and bendable displays [87].

As in the case of energy storage devices, there are different FESDs such as lithium rechargeable batteries [88], flexible fuel cells [89] and flexible supercapacitors [90]. This thesis will be focussed on flexible supercapacitors due to their application as power devices in wearable or portable electronics that need to be bendable while demonstrating an excellent performance [91].

1.7.1. Flexible Supercapacitors

Research articles on flexible supercapacitors (FSCs) started to appear around 2000 as shown in Figure 1.12 (b). However, it was not until 2013 when there were more than 203 publications per year about flexible supercapacitors.

Figure 1.12 shows how emerging is the field of the study on flexible supercapacitors in comparison to the general field of supercapacitors. As it can be seen in Figure 1.12 (a) the supercapacitors investigation started in 1986 and, in 2010 there were more than 1000 publications containing the term supercapacitor in the title.

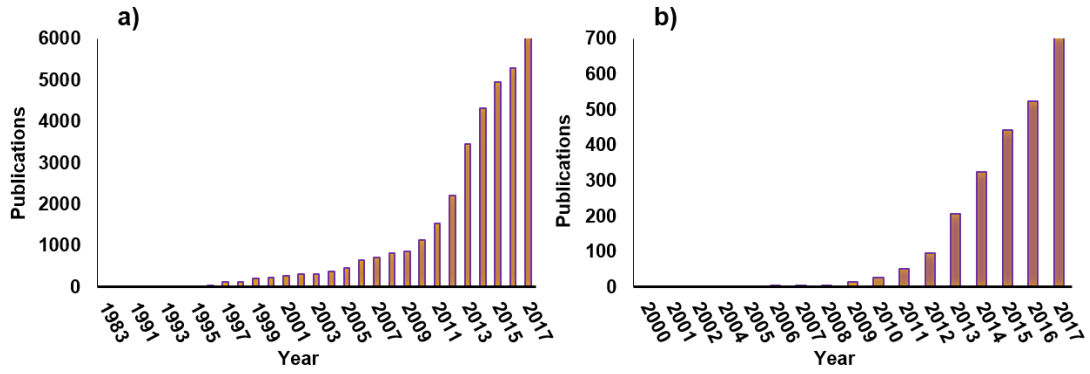

Figure 1.12 (a) Supercapacitors publications from 1986 until 2017, (b) Flexible Supercapacitors publications from 2000 to 2017. Data obtained from SciFinder CAS

Flexible supercapacitors development started to be important due to the boost of flexible and bendable consumer electronics which require "next generation" supercapacitors with flexible, bendable and lightweight characteristics [92]. Therefore, they are being investigated to determine if they are suitable power sources for the new consumer electronics.

Figure 1.13 General flexible supercapacitor design based on a sandwich type design, composed of sealer (yellow), current collectors (grey), flexible electrodes (black) and a separator (blue) soaked in electrolyte

Flexible supercapacitors are composed of flexible active materials/films as electrodes, solid-state or encapsulating electrolytes, separator and current collectors as all the other energy storage devices, but also, there are new prerequisites needed for the accommodation of flexible supercapacitors under a wide range of bending and pressure conditions [22c]. Different designs have been attempted, however, the most commonly used is known as "sandwich-type" that consists of the assembly of electrode-electrolyte-separator-electrolyte-electrode as it is shown in Figure 1.13 [86]. A further review on the flexible electrodes used in flexible supercapacitors will be shown in section 2.5.1.

1.8. Aim of this Thesis

The aim of this PhD is to design, fabricate and characterise a flexible supercapacitor using new flexible electrodes based on biopolymer-conducting polymer composites as electrodes and ionic liquids as the electrolyte. Therefore, the objectives will be divided into two sections; the first part focuses on the design, fabrication and characterisation of the new composite materials as electrodes and, the second part will be dedicated to the application of these composite materials as flexible electrodes in flexible supercapacitors which will be assembled and electrochemically characterised by cyclic voltammetry (CV), galvanostatic charge-discharge (GCD) and electrochemical impedance spectroscopy (EIS).

The first step consists of preparing the flexible cellulose-based composite electrodes using the ionic liquid technology to process the cellulose. To induce electronic conductivity to these cellulose-based electrodes the addition of a conducting polymer such as polypyrrole is proposed. The addition of an ionic liquid as a plasticiser and graphite powder as a conducting material is proposed to improve the flexibility and the conductivity of the composites, respectively. The full characterisation of the new composites will be carried out by solid-state characterisation techniques such as Fourier Transform-Infrared (FT-IR) and Raman spectroscopies and thermogravimetric analysis (TGA). The morphology of the materials and elemental analysis will be studied using scanning electron microscopy (SEM) and energy dispersive X-Ray (EDX); mechanical properties will be analysed by tensile strength measurements, and electroactivity will be evaluated by cyclic

voltammetry. Figure 1.14 shows a scheme that summarises the cellulose-based composite development and characterisation.

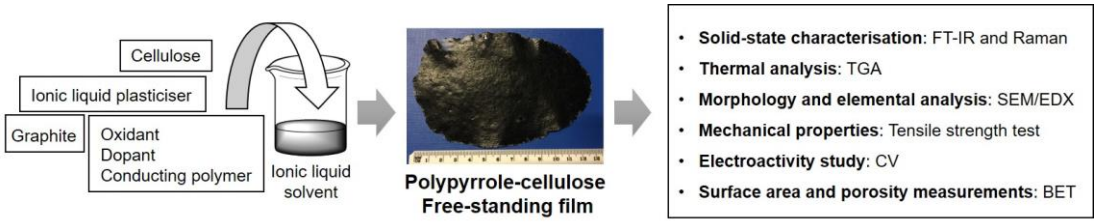

Figure 1.14 Scheme of the cellulose-based composites development and the characterisation proposed

In summary, the aim of this PhD *i.e.,* the fabrication of a supercapacitor which is flexible while retaining the superior properties of a supercapacitor such as high power density, long cycle life and good rate capability (as shown in Figure 1.15) will be carried out using the cellulose-based composite electrodes developed and an ionic liquid as the electrolyte.

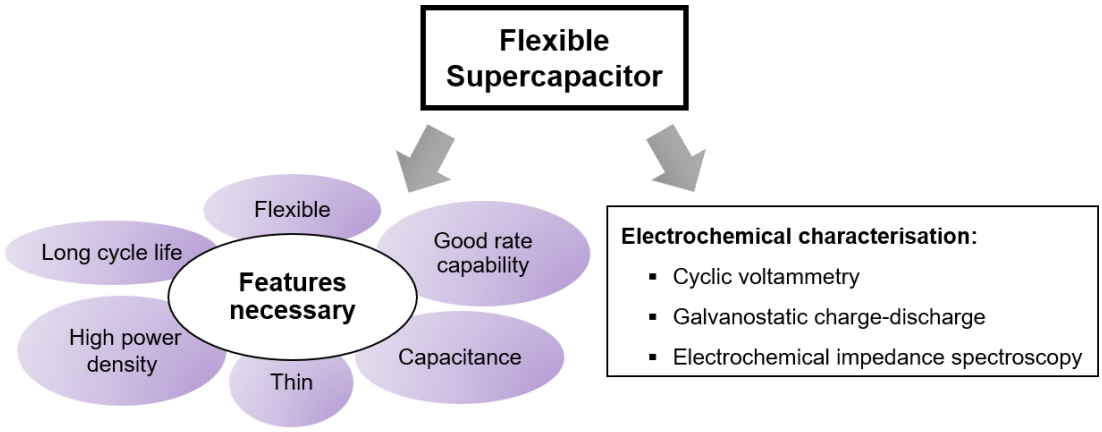

Figure 1.15 Scheme showing the aim of this PhD

Chapter 2

Literature Review

Chapter 2 will be dedicated to the review of all the components used throughout this PhD research for the fabrication of flexible electrodes for flexible supercapacitors. A literature review of ionic liquids, cellulose and electronically conducting polymers will be presented followed by a review of flexible supercapacitors as shown in Figure 2.1.

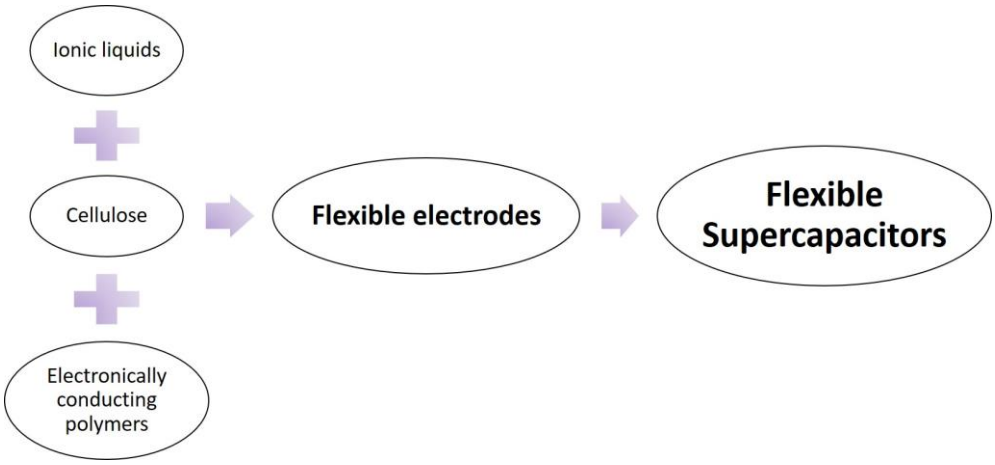

Figure 2.1 Scheme summarising the topics involved in Chapter 2

2.1. Ionic Liquids

Ionic Liquids are known since 1888 when Gabriel and Weiner [93] synthesised the first ionic liquid reported, ethanolammonium nitrate, with a melting point of 52-55 ºC. In 1914, Walden synthesised ethylammonium nitrate, a salt with a melting point of 12 ºC, being the first room temperature ionic liquid (RTIL) known [94]. But was not until 1950, when the interest in ILs gathered momentum and the first so-called ionic liquids were obtained by the mixture of aluminium(III) chloride and 1-ethylpyridinium bromide, to use them for the electrodeposition of aluminium [95]. From 1975 the group of Osteryoung [96] and Wilkes [97] studied the electrolyte application of ILs in batteries. The major increase in the study of ionic liquids took place at the beginning of the 90s when their great diversity and ability to be tuned was discovered [98]. From this period, the research interest in ILs experienced an exponential increase, as it can be seen in Figure 2.2; also, the comparison with other three top topics showed how high was the research in ionic liquids and it is still nowadays.

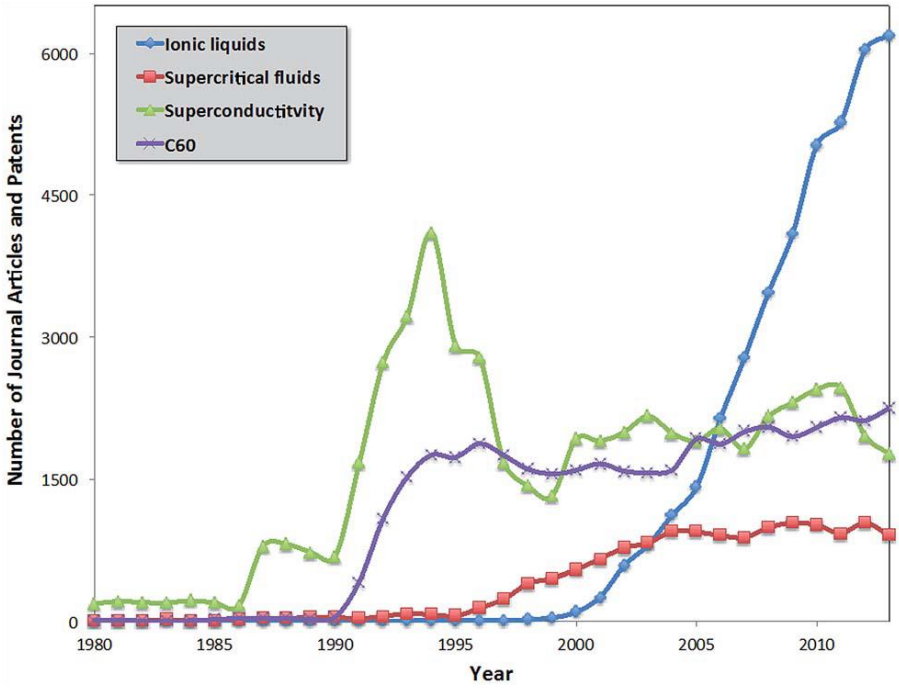

Figure 2.2 Ionic liquids articles and patents from 1980 until the end of 2013. Graph published by Deetlefs *et al.* [99] in 2014

As shown in Figure 2.3, ILs are generally formed by an organic cation based on heterocyclic nitrogen, quaternary nitrogen or phosphorous, and an anion which may be either inorganic or organic [100].

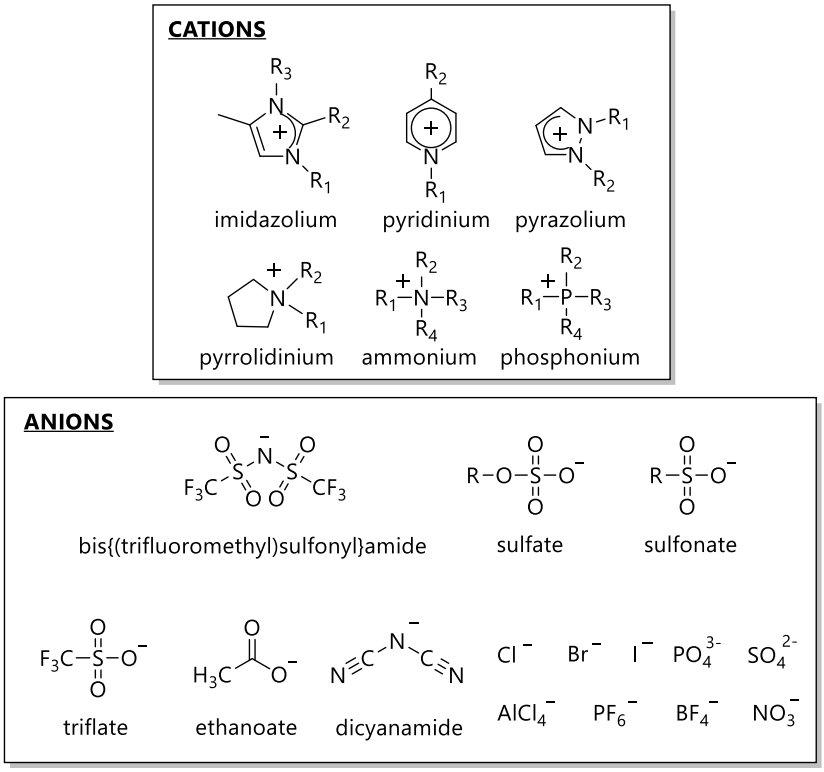

Figure 2.3 Common cations and anions used to form ILs. Figure adapted picture from reference [101]

2.1.1. Synthesis of Ionic Liquids

The synthesis of simple ILs is generally carried out in one or two steps as shown in Figure 2.4 [102]. The first step is known as the quaternisation reaction and involves the alkylation or protonation of a starting material (amine, phosphine or sulphide) to generate the cation-anion ion pair [103]. The second step is known as metathesis and involves an anion exchange reaction to change the previous anion for a new one, this reaction is not always necessary [104].

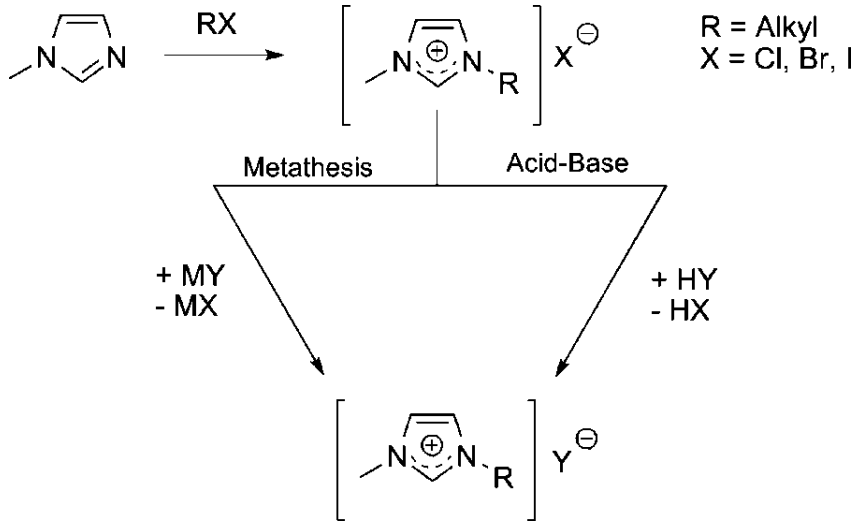

Figure 2.4 General synthesis paths for ionic liquid preparation. Figure adapted from reference [35]

In some cases, however, to modify the properties of an IL for a specific application, needs the incorporation of various functional groups to the structure of the cation, anion or both is needed [105]. For the preparation of these more complex ILs, called "Task-Specific Ionic Liquids" (TSILs) [106], it is necessary to apply organic synthesis methods that comprise several steps. There are many books, reviews and research articles describing the application of TSILs in physical chemistry [73], electrochemistry [107], designing ability of structure [108], metal extraction [109] and catalytic or solvent ability in organic reactions [110].

The application of TSILs in catalysis can be considered one of the most common examples. For example, the phosphonium sulfonate synthesised by Cole *et al.* [111] in 2002 was used as a catalyst in organic reactions such as esterification or dehydration reactions. Another application for TSILs is in electrochemistry, more specifically, the design of electrolytes. In 2009, Devarajan *et al.* [112] developed a novel oxygen-containing spiro ammonium salt, for its use as an electrolyte in electrical double-layer

supercapacitors, this IL, oxazolidine-3-spiro-1′-pyrrolidinium tetrafluoroborate, shows higher potential window (~ 5 V) and capacitance in comparison to the commercial and standard electrolyte, $TEABF_4$.

Hence, the ionic liquid ion structures can be designed and tuned with the objective of changing their properties and, consequently, their interesting characteristics.

2.1.2. Properties of Ionic Liquids

In this section, the description of the ionic liquids' properties such as their melting point, decomposition temperature, viscosity, density and conductivity will be discussed.

2.1.2.1. Melting Point

In contrast to traditional ionic salts with strong ionic bonds, in ILs the cation and anion areas, sizes and symmetries are very different, providing little efficient packaging and weaker Coulombic forces (attraction forces between cation-anion) than in traditional salts as it can be seen in Figure 2.5 (b). In this, the IL, $[C_4mim][PF_6]$, is represented by different colours *i.e.* the charge parts of the cation and anion (*i.e.*, imidazolium rig of the cation and the entire PF_6^- anion) are red and the nonpolar parts (*i.e.*, side chains of the cation) are green [113]. For comparison, an example of an ionic salt, sodium chloride (NaCl), showing a cubic and well-packed crystal lattice structure is included in Figure 2.5 (a). In this, each ion is surrounded by six ions of the opposite charge.

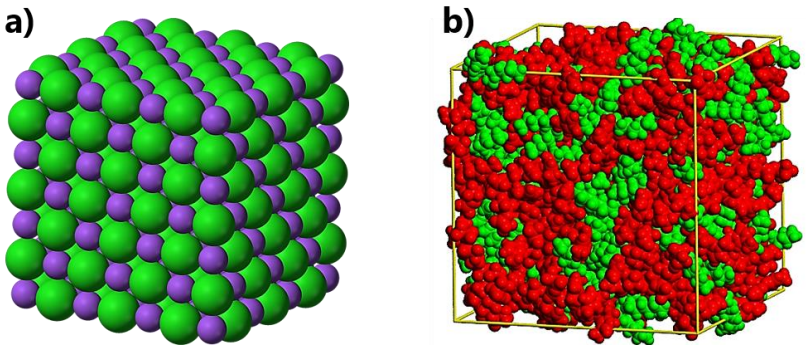

Figure 2.5 a) Sodium chloride cubic crystal system where the chloride (green) and the sodium (purple) are close-packed and, b) snapshots of the pure ionic liquid, $[C_4mim][PF_6]$, in a simulation box where the charged parts of the cation and anion are colored in red and the nonpolar parts were in green. Figure adapted from reference [114]

The difference in the cations and anions interaction and packing provides one of the most peculiar properties of ionic liquids which is their lower melting point. Ionic liquids usually have low melting points (close to room temperature) but they can reach, in some cases, -100 °C [115]. The melting point and the decomposition temperature of a fluid determine its liquid range which, in the case of ionic liquids, can be as large as 200-300 °C [116].

Melting points of ionic liquids depend on the structure of the cation and anion, with the main factors being the size and symmetry of the ions and the length and shape of the alkyl chains from the ions [117]. In general, an increase in the size of the ions causes that the Coulombic interactions become weaker, and consequently the melting points decrease [117]. Other factors that can also affect the melting point of ILs include, π-π aromatic interactions, Van der Waals forces between the alkyl chains or the formation of hydrogen bonds [116,118].

The influence on the melting point by the length and shape of the alkyl chains of the ions can be seen, for example, in ILs containing 1-alkyl-3-methylimidazolium cations, $[C_nmim]^+$. In these, a melting point drop is observed as the aliphatic chain increases from 1 to 6-8 carbon atoms; however, from 8 carbon atoms, the melting point increases due to the formation of van der Waals forces between the aliphatic chains (Figure 2.6) [117,119]. In the case of the pyrrolidinium salts, the lowest melting point is obtained with alkyl chain lengths of n= 3 or 4 [120].

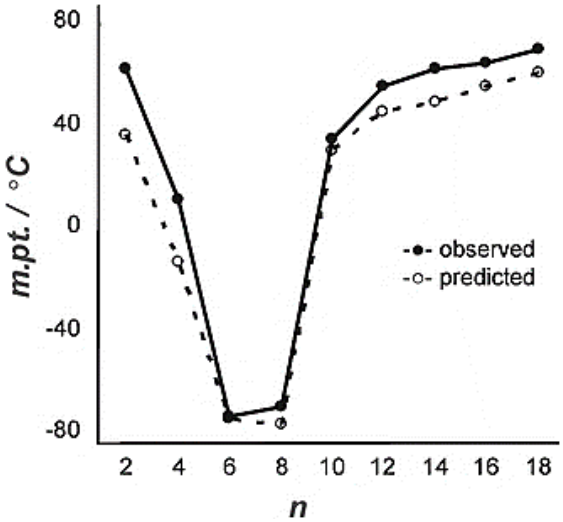

Figure 2.6 Predicted and observed melting points of a series of 1-alkyl-3-methylimidazolium hexafluorophosphate, $[C_nmim][PF_6]$, ionic liquids with increasing carbon chain length on the cation, n= 2-18. Graph adapted from reference [121]

2.1.2.2. Decomposition Temperature

The decomposition temperature of an ionic liquid is known as thermal stability and is obtained by thermogravimetric analysis [122]. ILs generally have high thermal stabilities, being able to rise above 400 °C. In general, the thermal stability of ILs notably depends on the type of anion, being lower the effect of the cation [123]. Thermal stability increases with the size of the anion and decreases with the increase of its hydrophilicity [124]. Among the most common anions, the decomposition temperature decreases in the series: $[BETI]^-$ > $[NTF_2]^-$ > $[CF_3SO_3]^-$ > $[BF_4]^-$ > $[PF_6]^-$ >> Br^- > Cl^- [125,115].

2.1.2.3. Viscosity

Transport properties such as viscosity, diffusion coefficient and ionic conductivity, have a crucial *rôle* in chemical and engineering processes. Fundamentally, the transport properties of the ILs depend on the nature of the cation and anion, as well as the temperature and pressure conditions [116,126]. In the case of the viscosity, which describes the resistance of a fluid to flow, ILs generally display high viscosities from 10 to 105 cP, *i.e.*, much higher values than in the case of water which shows 1 cP [127].

For the most common cations, it has been found that the lowest viscosity corresponds to the anion $[NTf_2]^-$. The viscosity of ILs increases with the type of anion as follows: $[NTF_2]^-$ < $[FAP]^-$ < $[BETI]^-$ < $[CF_3SO_3]^-$ <$[BF_4]^-$ < $[C_2SO_4]$<$[C_1SO_4]$< $[PF_6]^-$ < $[C_1COO]^-$ < Cl^- < Br^- [127,115]. According to the cation, the viscosity increases following the trend: *n*-alkylimidazolium < *n*-alkylpyridinium < *n*-alkylpyrrolidinium [116].

2.1.2.4. Density

The density is dependent on temperature, decreasing when the temperature increases [128]. It also, depends on the structure of the IL, with the density decreasing when the volume of the cation or the anion (molecular weight) increases; for example, when the size of the alkyl chains increases. The addition of CH_2 groups to the alkyl chain in the imidazolium cation decreases the density because the CH_2 is less dense than the imidazolium ring [119]. Another factor to consider is the presence of heavy

atoms. Heavy atoms in the structure increase the density because the density depends on the molecular mass of the compound [129].

2.1.2.5. Ionic Conductivity

Ionic liquids are composed entirely of ions; hence, they have relatively high ionic conductivities, *i.e.* the ions can move easily without restriction from solvent molecules. The conductivity (ion-mobility) of ILs increases significantly with temperature and is related to the viscosity; the conductivity of the ILs decreases when the viscosity increases and *vice versa*. It is, also, affected by the molecular weight, density and ions size [130,124,126]. In the case of the ions size, the conductivity decreases with the anion volume, *e.g.* with imidazolium cations, the conductivity follow the trend: $[C_2mim][BF_4] > [C_2mim][PF_6] > [C_2mim][BETI]$ [131].

There are different rules that correlate viscosity with the conductivity. The most suitable for pure ionic liquids is the Walden rule (Equation 2.1) where Λ is the molar conductivity, η corresponds to the viscosity and k is the temperature dependant constant.

$$\Lambda \cdot \eta = k \qquad \text{Equation 2.1}$$

A typical Walden plot is shown in Figure 2.7 [27]. A Walden plot of log(molar conductivity, Λ) *vs.* log(reciprocal viscosity, η^{-1}) is a convenient and versatile method that provides a qualitative measurement and treatment of the ionic conductivity of an electrolyte [132]. The calibration line is obtained from a standard solution of 0.01 M KCl that allows the calculation of k which is placed in the Walden plot as the reference line passing through the origin and, the classification of ionic liquids as poor, good and superionic liquids can be done *i.e.* the ionicity of the ionic liquids is determined (the ionicity is the measurement of adherence to the Nernst-Einstein equation for the conductivity calculation) [133].

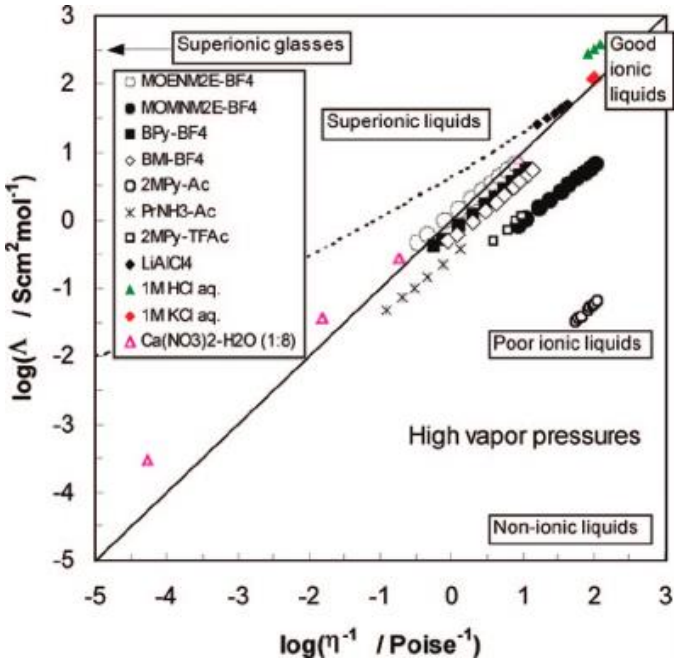

Figure 2.7 Walden plot for different ILs and salts. This graph may serve to indicate ionicity of ionic liquids compared with a standard electrolyte. Graph adapted from reference [27]

2.1.3. Characteristics and Applications of Ionic Liquids

Due to their unique properties as described above, ILs have been explored in a plethora of applications. The most important characteristics of ILs are listed in Table 2.1.

Table 2.1 Main characteristics of ionic liquids

Characteristics	Brief description	References
Very low volatility	It has a negligible vapour pressure. Therefore, they are considered an alternative to the traditional volatile organic solvents	[134]
High thermal stability	The upper temperature limit is given by their thermal degradation point normally between 200 and 400 °C	[135]
Non-flammability	"Green" character, presenting many advantages for its application in industry	[135]
Electrochemical stability	Because of its high electrochemical stability and good ionic conductivity, one of its main applications is in electrochemistry	[136]

Figure 2.8 shows different applications where the ILs can be utilised. The most common applications are as solvents and catalysts in synthesis or biomass processing [137], electrolytes in electrochemistry [72], as plasticiser or lubricants in engineering [138], or their application in medicine or pharmaceutics due to their biological activity [139].

Figure 2.8 Ionic liquids applications. Figure adapted from reference [121]

In the following subsections, four ionic liquids' applications are described in detail due to their use in this thesis *e.g.* ILs have been applied as electrolytes, as ionic liquid gels, as plasticisers and as solvent media to fabricate flexible composite electrodes.

2.1.3.1. Ionic Liquids as Electrolytes

In chapter 1 (section 1.5.2.) the *rôle* and the different types of electrolytes were described. Here, a further review about ILs as electrolyte will be presented.

Typically, the operational voltage of an electrochemical device is mainly limited by the electrochemical stability or electrochemical window (EW) of the electrolyte used, which is a term that indicates the potential range and the potential difference; it is calculated by subtracting the reduction potential limit from the oxidation potential limit obtained from a CV (the calculation of the EW is explained in section 4.2.1) [27]. Aqueous electrolytes can display up to 1.23 V as the maximum electrochemical window because of the limiting factors from hydrogen and oxygen evolution, as it is

displayed in Figure 2.9 [140,66], and in the case of the non-aqueous electrolytes the electrochemical window can reach over 2.7 V thanks to the use of organic solvents such as acetonitrile or propylene carbonate, however, non-aqueous electrolytes have limitations due to their volatility and toxicity [67,136a].

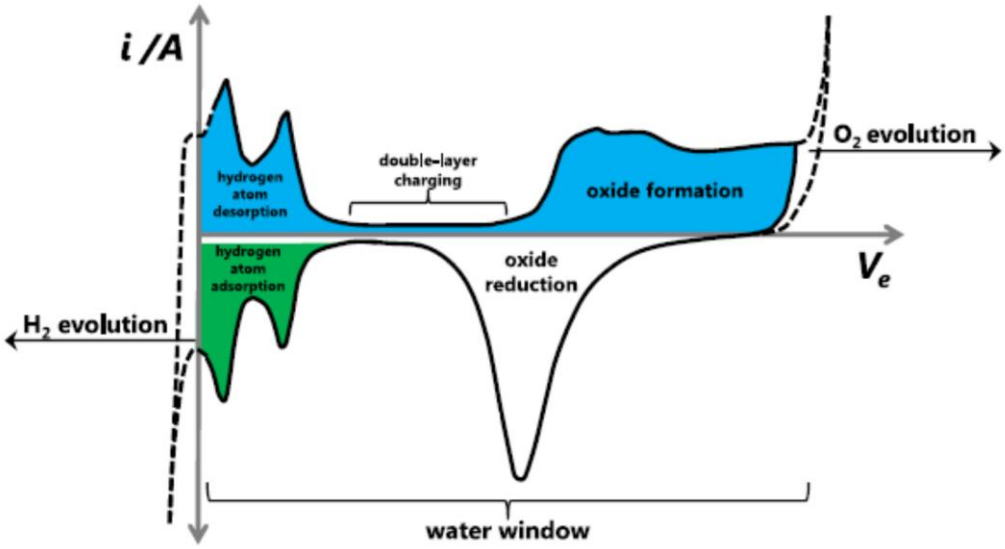

Figure 2.9 The potential window of Pt in 0.5 M H_2SO_4, demonstrating the H_2/O_2 evolution reactions at 1.0 atm and at room temperature. Figure adapted from reference [140]

The use of RTILs as electrolytes was one of the pioneering applications of ILs resulting in electrolyte systems composed of ions and their combinations and, therefore, free of any molecular solvent [141]. ILs as electrolytes for supercapacitors and batteries have been studied to improve the performance of these devices avoiding the disadvantages of organic or aqueous electrolytes such as their decomposition or flammability [27,142]. The main reasons to propose ionic liquids as electrolytes are for the development of novel, safer and greener electrochemical devices, owing to their unique properties such as high electrochemical stability, since they present large electrochemical window owing to their ionic nature, good ionic conductivity, low volatility (avoiding leakage due to evaporation), non-flammability, high thermal and chemical stability, and recyclability [143,66].

The most investigated classes of ionic liquids for electrochemical applications are those with imidazolium and pyrrolidinium cations. Imidazolium-based ILs usually show higher conductivities and pyrrolidinium-based ILs display higher electrochemical stabilities [144,66].

In the case of batteries, researchers started to be very interested in the ILs with quaternary ammonium and phosphonium as cations and $[NTf_2]^-$ as anion because the lithium electrochemistry was stable within the electrochemical window of these ILs and the ion transport and charge transfer was high [145]. Cyclic pyrrolidinium and piperidinium bis{(trifluoromethyl)sulfonyl}amide ILs offered more cathodic stability and less viscosity than the aliphatic cations [146].

The IL electrolytes for supercapacitors are often aprotic ILs based on pyrrolidinium [147] and imidazolium cations [148]. EDLS using pyrrolidinium-based ILs can reach an operational voltage of 3.5-3.7 V and in the case of imidazolium-based ILs, the operational voltage can be in the order of 3-3.2 V [66]. Because of this higher operational voltage, supercapacitors using pyrrolidinium electrolytes displays higher energy than using imidazolium-based ILs. In contrast, imidazolium-based ILs show higher power due to their lower viscosity and higher conductivity [149].

2.1.3.2. Ionic Liquids as Gels

A gel is known as a substance composed of a liquid phase dispersed in a continuous solid phase, known as colloid and it is a type of soft matter [150]. In the case of an ionic liquid gel, the ionic liquid is the liquid dispersed in a continuous solid phase, for example, a polymer, as it can be seen in Figure 2.10 [151]. The supported ionic liquid-based composite obtained offers many benefits of ILs in an immobilised and flexible form [152]. Ionic liquid gels can be fabricated using a variety of structural support materials, including polymers [153], colloidal particles [151], carbon nanotubes [154] and small organic gelators [155].

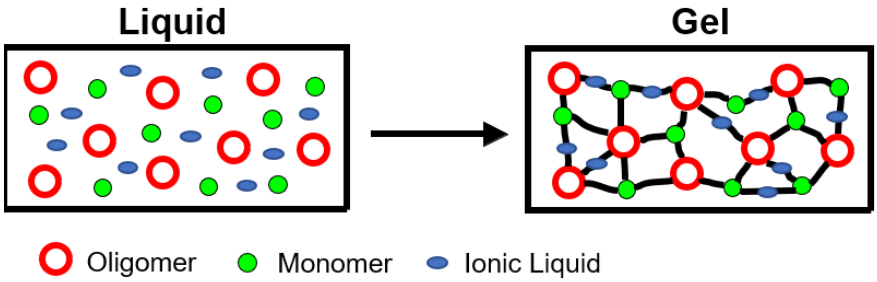

Figure 2.10 Ionic liquid gel preparation by the polymerisation of monomers/oligomers in an ionic liquid. Figure adapted from reference [152]

Ionic liquid gels have numerous advantages, including high ionic liquid content, good electrical performance, wide electrochemical window, thin-film forming ability, transparency and mechanical elasticity [151]. In addition, they are relatively easy to

synthesise and process, which makes them convenient materials for electrochemical applications *e.g.* in electrocatalysis [156] or biosensors [157] and, in energy devices such as solar cells [158], fuel cells [159] or supercapacitors [160].

Kang *et al.* [161] in 2012 reported an all-solid-state flexible supercapacitor based on papers coated with carbon nanotubes and an ionic liquid-based gel as an electrolyte. The gel electrolyte was made of silica nanopowder mixed with the IL $[C_2mim][NTf_2]$. The solid-state supercapacitor showed a comparable performance to the one with neat ionic liquid electrolyte; it showed excellent stability for 4000 cycles with a specific capacitance retention of 97 % and the energy and power density was stable for 100 bending cycles with a radius of 4.5 mm.

Another example of an ionic liquid gel as electrolyte in solid-state supercapacitors was published by Pandey *et al.* [162], who fabricated a flexible and free-standing gel polymer electrolyte based on plastic crystalline succinonitrile and the ionic liquid, $[C_4mim][BF_4]$, entrapped in a copolymer for their application in solvent-free solid-state EDLS. The device fabricated using activated carbon as electrodes showed good cycle life stability for 10000 cycles with a ~ 80 % of capacitance retention.

2.1.3.3. Ionic Liquids as Plasticisers

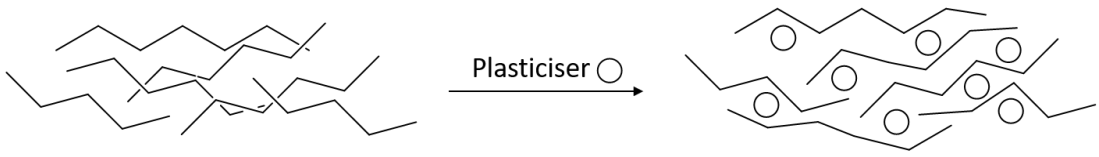

Figure 2.11 Polymer chains without plasticiser (on the left) which cannot move in relation to each other. The picture on the right corresponds to polymer chains with a plasticiser that helps to the movement of the polymer chains

In 1951, the International Union of Pure and Applied Chemistry (IUPAC) stated "a plasticiser is a substance or material incorporated in a material (usually a plastic or an elastomer) to increase its flexibility, workability or extensibility. A plasticiser may reduce the melt viscosity, lower temperature of a second order transition, or lower the elastic modulus of the product", in other words, a plasticiser will affect the reorganisation of the material preventing its rigid state [43]. For example, in a polymer, the use of a plasticiser will separate the polymer chains and will help the mobility of the chains allowing that they slide past to each other, as it is shown in Figure 2.11 [163]. The use of a plasticiser improves the mechanical properties of a polymer such

as Young's modulus, % elongation and ultimate tensile strength which can be visualised in a stress-strain curve (Figure 2.12).

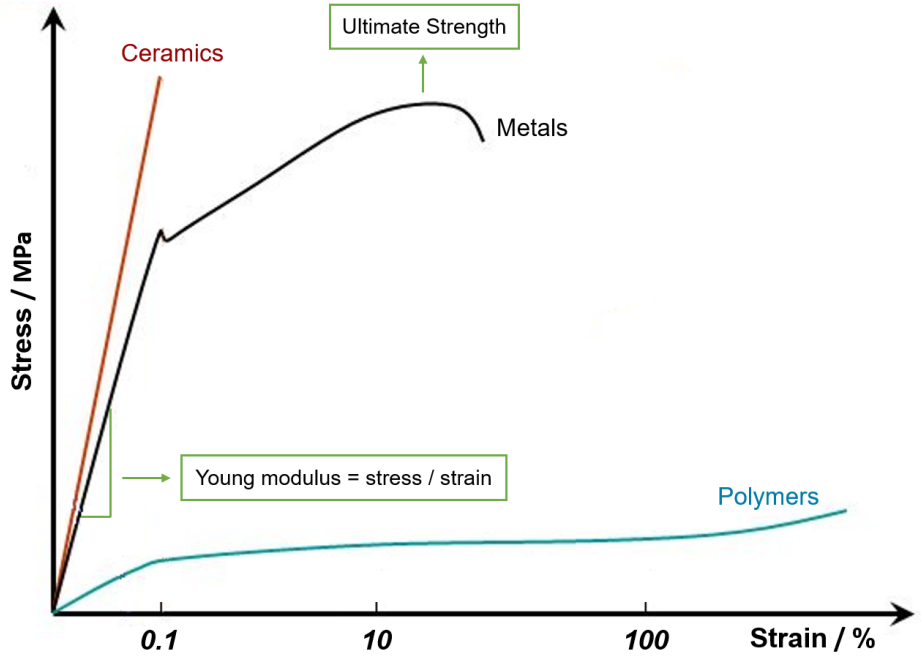

Figure 2.12 Stress-strain curve of polymers, metals and ceramics. Graph adapted from reference [164]

Figure 2.12 shows the stress and strain curves of three different materials such as ceramics, metals and polymers. Ceramics are the stiffest or the most rigid materials (the straightness of the line provides the stiffness of a material). The length of the lines in reference to the stress axis indicates the strength of a material and in reference to the strain axis, the ductility of a material. Therefore, ceramics and metals are stronger than polymers and, in contrast, polymers are more ductile than metals or ceramics.

Generally, plasticisers such as dioctyl phthalate, diisodecyl phthalate or fatty acid esters [165] are used to increase the flexibility of polymers and composites, however, in the current work application of ionic liquids as plasticisers for conducting polymer composites was explored due to their low melting point, negligible vapour pressure and their ability to form hydrogen bonds which should result in better mechanical properties [138a].

As reported by Scott *et al.* [166] in 2002, ionic liquids can be used as plasticisers. The author found that the RTIL, 1-butyl-3-methylimidazolium hexafluorophosphate, $[C_4mim][PF_6]$, was an efficient plasticiser for poly(methyl methacrylate), in comparison

to traditional plasticisers, with promising results for the development of flexible polymeric materials.

In 2009, Ning *et al.* [35] studied the ionic liquid 1-allyl-3-methylimidazolium chloride, [Amim]Cl, as a novel plasticiser for corn-starch. Due to the strong hydrogen bond forming abilities of this IL with starch, thermoplastic starch can be formed. One year later, Sankri *et al.* [167] used 1-butyl-3-methylimidazolium chloride, [C_4mim]Cl, as a plasticiser for thermoplastic starch and they found out that this IL decreased the elastic Young's modulus of thermoplastic starch, from 8 MPa to 0.5 MPa, in comparison to classical glycerol plasticised thermoplastic starch. In contrast, the elongation at break increased from 100 % to 400 %. Both data demonstrated that the starch became less rigid and less resistant to elongation and stretching using the IL, [C_4mim]Cl, as the plasticiser.

In 2010, Lunstroot *et al.* [168] reported the use of [C_6mim][NTf_2] as a plasticiser in a new type of luminescent hybrid material, which was prepared by doping europium(III) complexes in a matrix of a blend of poly(methyl methacrylate) in the IL, [C_6mim][NTf_2]. They demonstrated the plasticity effect of the IL, as well as an improvement of the europium solubility in the poly(methyl methacrylate) resulting in a flexible and luminescence coloured film.

Further work on ILs as plasticisers has been published in the last years [169]. For example, in 2016, Colomines *et al.* [170] published their research about starch plastification including the use of bio-friendly ionic liquids such as ILs with cholinium cation with different low toxicity and/or biocompatible anions *e.g.* lactate, tricitrate, fluorate or salicylate.

2.1.3.4. Ionic Liquids as Solvents Media

As described above, ionic liquids are also described as "designer" solvents because they can be modified to suit the requirements of a particular chemical reaction or process [171]; as they are obtained by the combination of large organic cations with a variety of anions resulting in above 10^{18} different possibilities of ILs. Ionic liquids have also gained the popularity as "green" alternatives to volatile organic solvents (VOCs) to be applied in electrochemical, synthetic and separation processes due to their negligible vapour pressure, nonflammability and recyclability [134,137a]. It is worth to mention that ILs are not intrinsically green, however, they can be

designed to be green; nonetheless, in comparison to VOCs, they are safer because they are not flammable [171].

As Seddon [69] explained in a review published in 1997, ILs are worthy to use as neoteric solvent in, for example, catalysis instead of volatile organic solvents due to their following characteristics: they have negligible vapour pressure, they are thermally stable with decomposition temperatures above 200 ^{0}C, they are able to dissolve a wide range of compounds (organic and inorganic compounds or biomass such as, cellulose), they have a wide liquid range and often, they can be recycled leading to a reduction of the costs of the processes.

In 1999, Welton [102] published a review showing different synthesis and catalytic procedures using ionic liquids as solvents to demonstrate their potential. Twelve years later, the same author published the second part of this review discussing the extraordinary advances in the understanding of how ionic liquids can affect chemical syntheses such as non-stoichiometric chemical reactions or transition-metal-catalysed reactions [100a]. All over that decade, around 6000 papers were published containing the phrase "ionic liquid(s)" in the title, being over the half of these about applications in chemical synthesis or catalysis [172,100a]. Currently, the number of publications using the same search terms increased to ~ 90000, demonstrating the wide scope of ionic liquids in multiple applications [173].

The dissolution of cellulose in ILs was another significant application using ILs as solvents, and the pioneering work was published in 2002 by Swatloski *et al.* [174] After this publication, the exploitation of ILs for the dissolution of biomass became one of the most important applications of ILs [175]. Currently, there are almost 2000 publications with the topic dissolution of cellulose using ionic liquids (searched by SciFinder CAS), showing that every year, from 2008, nearly 200 publications about this topic are issued demonstrating the importance of the area.

2.2. Cellulose

Biomass is the most consumed resource of renewable energy material on the earth with a 53 % of consumption, followed by the hydroelectric power with a 31 % as reported by the Independent Statistics & Analysis U.S. Energy Information Administration in 2012 [176]. One of the major components of biomass is cellulose, an available and renewable biopolymer typically combined with lignin and

hemicelluloses in the cell wall of upper parts of plants [177]. Cellulose, since was discovered by Payen in 1838 [178], has been considered a source of advanced materials for the next generation devices; for example, it has been utilised for flexible energy storage devices [86], as smart paper [179], paper transistor and in biomimetic actuators [180].

Cellulose, which is biodegradable, hydrophilic, odourless and water-insoluble, consists of a linear carbohydrate polymer of repeating D-glucopyranose monomers held together by 1,4-ß-glycose bonds as it can be seen in Figure 2.13. Owing to its extensive network of inter- and intramolecular hydrogen bonds and van der Waals interactions between cellulose fibres, it is very difficult to dissolve cellulose in common solvents. Therefore, the highly stable chemical nature of cellulose presents a big challenge for the reuse of this abundant resource and its utilisation in useful applications [181,77].

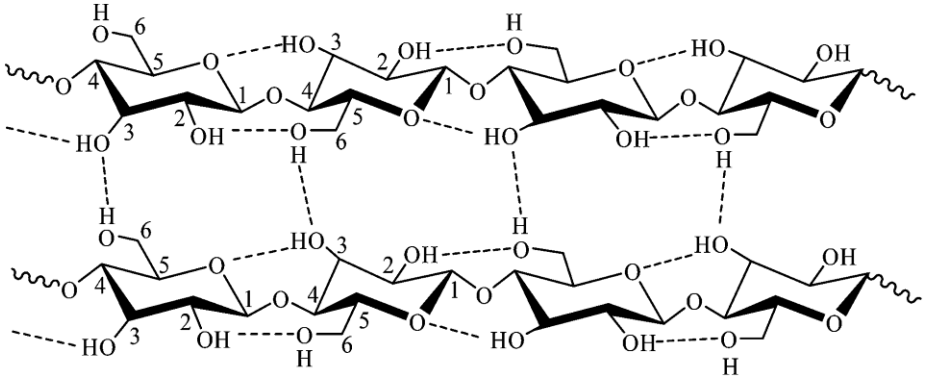

Figure 2.13 Structure of cellulose, showing the linear nature formed by ß(1→4) linkages and intra- and intermolecular hydrogen bonding. Figure adapted from reference [182]

There are several reasons for dissolving cellulose, but most of them are related to its reutilisation [183]. Cellulose can be reutilised when regenerated and utilised to produce innovative materials in the form of films or fibres [184]; or valuable cellulose derivatives [185]; as well as to degrade cellulose more efficiently [186].

The conventional method to dissolve cellulose is known as the "*Viscose process*" that entails the chemical functionalisation of hydroxyl residues along the cellulose backbone with carbon disulphide to form xanthate esters, greatly to improving the solubility [187]. Carbon disulphide is an environmentally harmful solvent and the "*Viscose process*" generates two kilogrammes of this hazardous waste along with heavy metals per kilogramme of cellulose obtained [188], so since 1970s novel

solvents for cellulose dissolution have been developed such as a LiCl solvent system, dimethyl sulfoxide (DMSO)/paraformaldehyde and *N*-methyl-morpholine-*N*-oxide (NMMO) in the "*Lyocell process*". The chemicals used in these processes are not harmless as they are often volatile, toxic, expensive and, difficult to recover [181,189].

In 1934, Graenacher [190] affirmed that molten *N*-ethylpyridinium chloride could be used to dissolve cellulose in the presence of nitrogen-containing bases, but the work did not attract enough attention at that time. It was not until 2002 when Swatloski *et al.* [174] published an article about using the ionic liquid 1-butyl-3-methylimidazolium chloride, $[C_4mim]Cl$, as a solvent for the dissolution of cellulose. Since then, an enormous number of publications and patents appeared in this context, which demonstrates the huge potential of ionic liquids to dissolve biomass [191a,189,191b,191c].

A variety of ionic liquid cations are available today that are able to dissolve cellulose such as ammonium, pyridinium, imidazolium and phosphonium when paired with strongly basic and hydrogen bond accepting anions [192a,192b,137b,192c].

Zhang *et al.* [193] demonstrated that 1-allyl-3-methylimidazolium chloride, [Amim]Cl, has a higher capability (14.5 wt % of cellulose at 80 ºC) to dissolve cellulose than $[C_4mim]Cl$ (10.0 wt % of cellulose at 100 ºC) due to the allyl group which can form H-bonds with the -OH groups of cellulose. Afterwards, Fukaya *et al.* [194] reported that ILs with strong hydrogen bond acceptability such as *N,N'*-dialkylimidazolium formates and 1-methyl-3-ethylimidazolium dimethylphosphate are good candidates to dissolve cellulose. In 2010, Xu *et al.* [182] synthesised some ILs with Brønsted basic anions, such as $[C_1COO]^-$, $[HSC_1COO]^-$, $[HCOO]^-$ and $[C_1C_2OHCOO]^-$ and 1-butyl-3-methylimidazolium as a cation. These authors found that an increment in the number of hydrogen bond accepting ability of the anions in the ILs increases the solubility of cellulose [195]. Several studies showed that a wide variety of ILs can be used to dissolve cellulose but the most commonly used ILs are $[C_4mim]Cl$, [Amim]Cl and $[C_2mim][C_1COO]$ [196,193].

There are other compounds known to facilitate the dissolution of cellulose such as lithium salts (LiCl, $LiNO_3$ or LiBr); interaction with the hydroxyl oxygen by the Li^+ disrupts the intermolecular hydrogen bonds in cellulose [197]. Also, it is common to use co-solvents, such as dimethylformamide (DMF) or DMSO, that can influence the

solubility of cellulose in ILs; the reason for this could be that these solvents facilitate the mass transport by decreasing the viscosity of the mixture [196a,198].

2.2.1. Mechanism of Cellulose Dissolution in Ionic Liquids

Although the mechanism of the dissolution of cellulose in ionic liquids is not yet completely clear there are several hypotheses about it [183].

It is known that the formation of hydrogen bonds between ILs and cellulose hydroxyl groups is the key factor in breaking the inter- and intramolecular hydrogen bonds of cellulose as shown in Figure 2.14 [195]. As the dissolution depends on the formation of hydrogen bonds, the hydrogen bond basicity of the IL is crucial [181], whereby ß (hydrogen bond accepting scale) is an important parameter to quantify solvent's solvation effects by the Kamlet-Taft equation [199]. The values of ß for ionic liquids should be higher than 0.8 to dissolve cellulose as it is the case for [C_4mim]Cl and [Amim]Cl with values of 0.84 and 0.83, respectively [194,189].

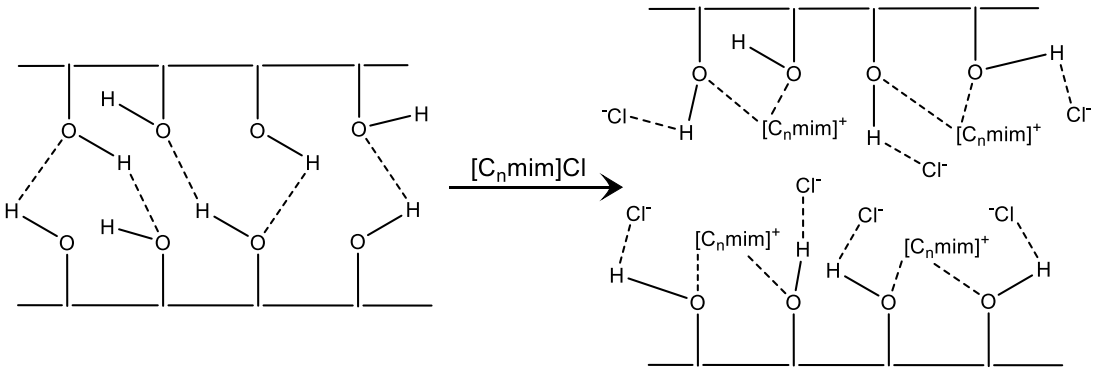

Figure 2.14 Possible mechanism of the dissolution of cellulose using ionic liquids, *e.g.* the IL *N,N'*-dialkylimidazolium chloride. Adapted from reference [193]

Swatloski *et al.* [200] using ^{13}C and $^{35/37}$Cl NMR relaxation measurements and molecular dynamics studies for the IL, [C_4mim]Cl, proposed that the strong hydrogen bond between chloride anions and the hydroxyl groups of cellulose is the decisive factor of dissolution. There are several theories about the influence of the IL cation on the dissolution of cellulose, but all of them have in common that the cation should have a conjugated group, such as the conjugated ring of the imidazolium cation. It is known by molecular dynamic studies that the conjugated ring has close contact with sugar rings through van der Waals interactions [201].

In summary, in order to dissolve cellulose, the IL should satisfy at least two features [202]: (i) anions must be good hydrogen bond acceptors, so having high

electron density to form hydrogen bonds with cellulose hydroxyl groups, *e.g.*, Cl^- or $[C_1COO]^-$ anions and; (ii) cations should be conjugated, moderate hydrogen bond donors and preferably be small and polarising, *e.g.* without long alkyl chains increasing the steric hindrance effect.

2.2.2. Regeneration of Cellulose

As already mentioned, the interest of dissolving cellulose stems from the need to process it and regenerate it for the fabrication of cellulose fibres or cellulose films [203]. Cellulose regeneration is known as the precipitation of cellulose when it is in contact with an anti-solvent or a coagulation bath such as water, methanol, propanone, *etc.* [183].

The mechanism of the regeneration of cellulose is different depending on the solvent used for the previous dissolution of the cellulose. Herein, the focus will be on the regeneration of cellulose after using ionic liquids as the solvent. The process consists of the exchange of the solvent that is dissolving the cellulose *e.g.* ionic liquid, with an anti-solvent. This exchange leads to a desolvation of the cellulose molecules from the ionic liquid and to their reformation of intra- and inter-molecular hydrogen bonds, *i.e.* the interactions between cellulose-IL are broken when an anti-solvent is added, following with the restructuring of the cellulose and the dissolution of the ionic liquid in the anti-solvent [189,192c].

The reconstructed cellulose from ILs shows lower degrees of crystallinity than the crystalline cellulose before being dissolved. The crystallinity of the cellulose is usually measured using XRD (for example, Zhang *et al.* [193]) or by FT-IR as shown by Zhao *et al.* [204] in 2009. Both techniques showed that the crystallinity of the regenerated cellulose is different depending on the IL used for its dissolution, demonstrating that regeneration of the cellulose depends on the choice of the solvent for the dissolution of the cellulose. The same case was found for the anti-solvent used for the regeneration of the cellulose due to its purpose, that consist of the extraction of the ionic liquid used to dissolve the cellulose [205].

A recent review published by Aleman *et al.* [77] shows how the dissolution and regeneration of cellulose can be applied in supercapacitors, for example, they stated that it can be used as a lightweight mechanical substrate to improve flexibility and strength to active materials (carbon nanotubes or conducting polymers); a natural

template for the coating of an active material for electrode applications; a separator between supercapacitors electrodes and; a material with good wettability, improving the adsorption of the electrolyte in the electrode. Therefore, the use of a conducting material is needed if the cellulose is chosen as part of an electrode. The conducting materials chosen in this PhD were the electronically conducting polymers.

2.3. Electronically Conducting Polymers

As it was introduced in section 1.5.1.3, ECPs are organic polymers that exhibit electrical, magnetic and optical properties usually associated with metals, whilst also retaining many advantageous mechanical properties of a polymer.

ECPs are classified as 'smart materials' due to their inherent property to accept a counter ion for charge balance when oxidised/reduced and to expel the counter ion when reduced/oxidised through their conjugated bond system along the polymer backbone. They are generally synthesised through chemical oxidation or electrochemical oxidation of the monomer [64].

Polypyrrole is one of the most promising ECPs for the fabrication of pseudocapacitors (or electrochemical supercapacitors) as part of the electrodes due to its unique features such as high conductivity, good thermal stability, low cost, fast charge-discharge mechanism and high energy density [65]. It is one of the most studied electronically conducting polymers for energy storage devices [64].

2.3.1. Polypyrrole

Polypyrrole (PPy) is an electronically conducting polymer with a polyheterocycle structure that possesses a high nitrogen content as shown above, in Table 1.1. PPy holds a unique position due to its high electrical conductivity [206], low environmental toxicity and biocompatibility [58] and, at the same time, being a relatively stable and a low-cost material in comparison with metal oxides [207].

The electronically conducting polymer, polypyrrole, can be synthesised electrochemically or chemically. Diaz *et al.* [51] reported for the first time the electrochemical polymerisation of pyrrole as mentioned in section 1.5.1.3.1. The use of ILs as solvent for the electrochemical synthesis of pyrrole was first developed in 1984 by Pickup and Osteryoung [208] but, it was not until 2002 when Sekigushi *et al.* [209] reported an electropolymerisation of pyrrole in the air stable ionic liquid,

[C_2mim][NTf_2], showing the electrochemical capacity improvements that the polypyrrole films obtained can have in comparison to the films obtained using conventional solvent systems. The first example of chemical polymerisation of pyrrole was published in 1916 by Angeli and Alessandri [210] where the authors described a method to obtain polypyrrole as a black powder, named "pyrrole black" using hydrogen peroxide and acetic acid as oxidant and solvent, respectively. Other oxidising agents can also be used, for example, nitrous acid, lead dioxide, ferric chloride, quinones and ozone [211]. The mechanism to obtain polypyrrole by chemical polymerisation is controversial, but the most accepted mechanism involves the coupling between radical cations as shown in Figure 2.15 [212].

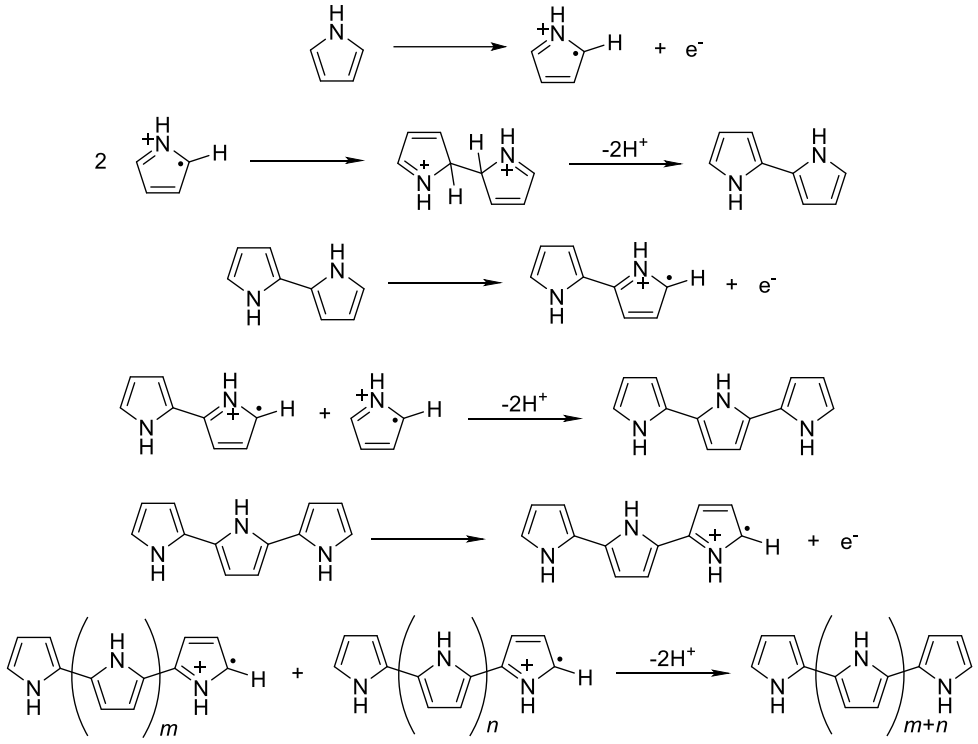

Figure 2.15 Polypyrrole chemical polymerisation mechanism [54]

Pyrrole chemical oxidation in ionic liquids was first reported by Pringle *et al.* [56] in 2006. The authors synthesised different ECPs using the IL, [C_2mim][NTf_2], as the solvent in combination with a range of oxidants. They concluded that ILs are an excellent new solvent media for the synthesis of ECPs nanoparticles, due to their chemical stability that makes the ILs very stable when the oxidation of the monomer is carried out.

Electronically conducting polymers, for example, polypyrrole, have a poor processability because they are intractable, insoluble and non-thermoformable,

making them not suitable for their application in many fields, for example, when flexible materials are needed [65]. Therefore, different methods were developed in order to improve their properties such as polypyrrole grafting over another material [213] or the mixture, *via* chemical synthesis, of polypyrrole with another polymer with better mechanical properties giving, as a result, a polypyrrole-polymer composite (*e.g.*, polypyrrole-cellulose composites) [214].

2.4. Composite Materials

According to IUPAC, a composite material is "a multicomponent material comprising multiple, different (non-gaseous) phase domains in which at least one type or phase domain is a continues phase" [43].

There are different types of composites for multiple applications, for example, electronically conducting polymer-polymer composite [215], polymer-carbon composite [216], polymer-cellulose composite [217], polymer-metal oxides composite [218] *etc.* Composites materials suitable for electrodes in electrochemical devices will be the topic reviewed herein.

Electronically conducting polymer-polymer composites materials were developed due to the poor processability and stability of ECPs and, the need for improving the mechanical properties as it was discussed in sections 1.5.1.3. and 2.3. For example, in 1983, three electrically conductive thermoplastic elastomer/polyacetylene composites were fabricated by Lee and Jopson [219] using blending techniques such as acetylene gas polymerised over a thermoplastic elastomer film.

Ojio and Miyata [220], in 1986, published an article in which an electronically conducting polymer-polymer composite consisting of polypyrrole and a polymeric matrix (poly(vinyl alcohol)) was developed. The method consisted of exposing the polymeric matrix film containing ferric chloride to pyrrole vapour resulting in transparent composite films.

The first article on the use of cellulose in composites for their application in flexible energy storage devices was published in 2007 by Pushparaj *et al.* [86]. The authors fabricated a nanocomposite paper composed of embedded carbon nanotubes in cellulose and the ionic liquid, $[C_4mim]Cl$. Since then, paper or cellulose were used as a new component for flexible supercapacitors due to the advantages

that stemmed from the use of the cellulose matrix such as its biodegradability and recyclability [221].

A lightweight, ultrathin and flexible graphene-based supercapacitor was reported in 2013 by He *et al.* [222]. The flexible electrode consisted of a three-dimensional graphene- MnO_2 composite; the synthesis method consisted of an electrochemical deposition of MnO_2 materials on 3D graphene networks resulting in a free-standing composite that was applied as an electrode in a FSC with a specific capacitance retention of 93 % for 500 cycles.

Fabrication of composites can overcome the drawbacks from individual substances and combine all the advantages of the composite components *e.g.* enhancing the specific surface area, inducing porosity, protecting active materials from mechanical degradation and improving cycle life stability [39].

2.5. Flexible Supercapacitors

As it was introduced in section 1.7.1, the development of supercapacitors has become an important task due to their advantageous characteristics of high power density, long cycle life and high efficiency [223,22c] while able to perform under deformation conditions. Flexible supercapacitors for future applications (*e.g.*, wearable electronics such as implantable medical devices) have their own specific requirements, such as small dimensions, flexibility, stretchability, lightweight and biocompatibility [13].

The first article published about the fabrication of flexible electrodes and their application in electrochemical capacitors was in 2006 by Sugimoto *et al.* [224]. This article described the fabrication of a thin, flexible and transparent film electrode composed by ruthenic acid nanosheets prepared by electrophoretic deposition over ITO-coated poly(ethylene terephthalate).

Conventional supercapacitors based on flexible or rigid materials that are folded or rolled into a rectangular or cylindrical shape which is stacked in a rectangular or cylindrical rigid container can be found in the industrial market. Although these materials are folded and assembled, they do not perform when they are physically bent as a device [222]. Therefore, the fabrication and testing of novel flexible supercapacitors using flexible materials as electrodes started to be the new objective for researchers.

In section 1.7.1 the device configuration of flexible supercapacitors was explained. As expected, the electrode materials have a significant influence on the performance of flexible supercapacitors making them an indispensable component of the devices. These electrodes should have not only good electrochemical properties but also, high mechanical flexibility upon folding or bending, compact design and lightweight properties [225].

2.5.1. Flexible Electrodes

The most common materials used as flexible electrodes in a flexible supercapacitor are the following: carbon-based (activated carbon, graphene and carbon nanotubes) [226], transition metal oxides-based (ruthenium, copper, nickel cobalt and manganese) [46], conducting polymer-based (polypyrrole and polyaniline) [65] or composites such as paper-based electrodes [227].

2.5.1.1. Carbon-based Flexible Electrodes

Carbon materials can have different functions inside a flexible supercapacitor such as acting as a conductive path for electron transport due to their good electrical conductivity or supplying a good flexible matrix because of their good mechanical properties. They can contribute to a high capacitance of the composites electrodes providing multiple pathways of ion transport for full electrolyte accessibility due to their porous structure [226]. Up to the present time, carbon-based flexible electrodes are being developed continuously due to the variety of available carbon materials including, activated carbon [87], carbon nanotubes [228], graphene [223] or templated carbon such as carbon cloth [229].

The most common method for the fabrication of carbon-based electrodes is the coating method that consists of coating the carbon materials onto any flexible template/substrate [87,230].

Graphene, as well as carbon nanotubes, is the material with more potential for flexible energy storage devices, as demonstrated, for example, by Yoo *et al.* [231] who fabricated an ultrathin flexible supercapacitor using multilayer graphene with a specific capacitance of 394 μF cm^{-2}.

In some cases, a final step is needed in order to obtain the required flexible electrodes. This consists of the functionalisation of the carbon material with other

compounds such as transition metal oxides or electronically conducting polymers. For example, Jiang *et al.* [232] functionalised cotton textile with carbon nanotubes and subsequently, hierarchical MnO_2 nanoflakes were coated electrochemically to obtain flexible supercapacitors with a specific capacitance of 247 F g^{-1} at a specific current of 1 A g^{-1}.

2.5.1.2. Transition Metal Oxides-based Flexible Electrodes

Metal oxides are considered suitable materials for supercapacitors because they can provide higher energy density than carbon materials. They have two different ways of storing charge. Like the carbon materials, metal oxides can store the charge electrostatically and also, they are capable to store charge through electrochemical Faradaic reactions at the electrode surface. The most studied metal oxides in supercapacitors are RuO_x, albeit it is a very expensive and rare oxide and MnO_x which is cheaper, more abundant and has a low toxicity [46].

Metal oxides have been incorporated into flexible supercapacitors as part of flexible composites used as electrodes. For example, the combination of titanium oxide and multiwalled carbon nanotubes using a chemical method was published by Amitha *et al.* [233] in 2009; and in 2010, Chen *et al.* [234] reported the fabrication and characterisation of flexible asymmetric supercapacitors using flexible thin-film composite electrodes made of manganese oxide and indium oxide nanowires together with single-walled carbon nanotubes. Although these and other articles have dealt with the use of metal oxides as the main component of flexible composite electrodes, these are still associated with challenges on cost-effectiveness [46].

2.5.1.3. Electronically Conducting Polymers-based Flexible Electrodes

Electronically conducting polymers can improve the performance of a supercapacitor as they undertake a redox reaction to store charge in the bulk of the electrode and thereby increase the energy stored and reduce self-discharge. ECPs are very attractive due to their low cost in comparison to the metal oxides, intrinsic flexibility and high charge density, resulting in supercapacitors with low equivalent series resistance and high energy and power. The main drawback of ECPs is their low cycle life compared to those based on carbon, which is due to the volume change of the ECPs induced by the doping and de-doping in the conducting polymer electrode.

This does not happen in the carbon-based electrodes which involve only simple ion sorption and desorption [64]. The volume change is known also as the electromechanical action when the redox state changes, and it can be related to the intrinsic change in the bond lengths and conformation of the polymer backbone and the osmotic expansion of the polymer phase [235].

The most used method to obtain conducting polymer-based electrodes is by the electropolymerisation technique; for example, Horng *et al.* [236] in 2010 were the first to demonstrate the use of this technique using polyaniline nanowires on carbon cloth to fabricate a flexible supercapacitor with high capacitance and a cycle life of 2100 cycles.

Nowadays, conducting polymer-based flexible electrodes are composed of other components apart from the ECPs to improve flexibility. The procedures used for the fabrication of these composites are chemical polymerisation of the monomer using a template that becomes the other component of the electrodes, or coating or depositing the polymer already synthesised over other conducting materials such as carbon cloth. For example, Zhu *et al*. [237] in 2012 published a method to deposit polyaniline onto vertically aligned carbon nanotubes for preparing supercapacitors with high capacitance. Later, Zhang *et al*. [238] fabricated a flexible composite membrane composed of polypyrrole nanowires and reduced graphene oxide *via in situ* reductions of the graphene oxide in the presence of polypyrrole nanowires.

Recently, Peng *et al.* [239] published the fabrication and electrochemical characterisation of a flexible composite electrode composed of polypyrrole, copper sulphide and bacterial cellulose nanofibrous material with good characteristics as flexible supercapacitor electrodes. Their method consisted of the deposition of polypyrrole and copper sulphide on commercial bacterial cellulose membranes to obtain nanofibrous composite electrodes of PPy/CuS/BC.

2.5.1.4. Paper-based Flexible Electrodes

As it was described in section 2.4, paper-based or cellulose-based flexible electrodes for energy storage devices were first introduced in 2007 by Pushparaj *et al.* [86], who presented a flexible energy storage device based on nanocomposite paper, more specifically, the electrodes comprised the IL $[C_4mim]Cl$ and multiwalled nanotubes embedded inside cellulose paper. Nevertheless, it was not until 2011 when

most of the interest in this field started *i.e.* after Nyholm *et al.* [240] published a progress report about the development of different paper-based flexible energy storage devices composed of electronically conducting polymers. The authors focused on the advantages and disadvantages of using ECPs and cellulose-based electrodes in flexible energy devices such as supercapacitors and batteries. For example, the use of ECPs in a composite improved the cycle life and rate performances compared to devices based on ECPs alone. The power delivery also improved significantly due to the ability to control the thickness and morphology of the ECPs' layers. However, additional work is still needed for understanding the overoxidation of ECPs, and an improvement in the devices' designs is needed for new applications where flexibility while retaining good energy device performance is required.

Paper-based flexible supercapacitors are based on conducting materials within a cellulose matrix. Cellulose can form strong inter- and intra-molecular hydrogen bonds, making it perfect structurally as a matrix or template material, in conjunction with conducting materials such as carbon nanotubes, graphene and conducting polymers such as polypyrrole [241,184b]. Additionally, cellulose networks can also provide pathways for ion transport [242,221b]. All these characteristics and the fact that cellulose is the most abundant biopolymer on the earth, makes it a good candidate for its use in paper-based flexible supercapacitors with low cost while being sustainable and eco-friendly energy storage devices.

In 2011, Weng *et al.* [243] reported a simple and scalable method to fabricate graphene-cellulose paper membranes which exhibited great advantages as flexible electrodes for flexible supercapacitors. Their method consisted of filtering a suspension of graphene nanosheets through a filter paper sheet; the graphene nanosheets were attached, by electrostatic interaction, to the cellulose fibres in the filter paper, resulting in a graphene-cellulose paper flexible electrode. The stability of the graphene-cellulose paper was confirmed by SEM after peeling off a part of the film.

A review published by Zhang *et al.* [221b] in 2015 summarised all the methods used, up to then, to fabricate paper-based flexible electrodes for flexible electronics such as pencil drawing [244], chemical and physical deposition [245], dip coating and

(vacuum) filtration [246], printing [247], paper-making technique [248] or molecular mixing [184b].

Chapter 3

Development and Characterisation of Flexible Composite Electrodes

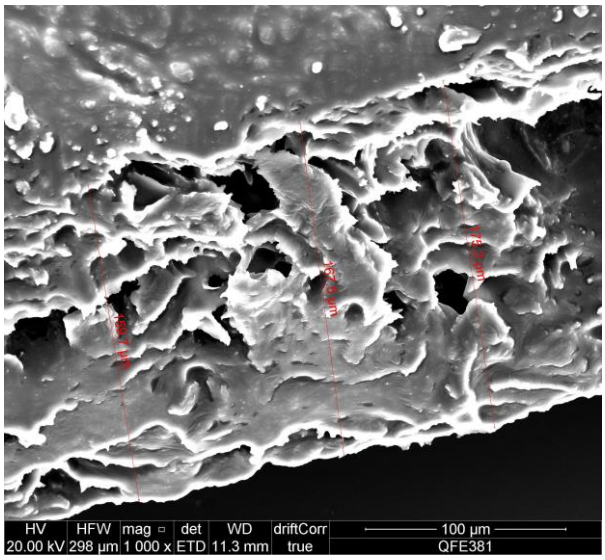

The need for flexible, ultrathin and biocompatible electronic materials for energy storage devices such as supercapacitors or medical implant applications including electrochemical targeted drug delivery and biosensing has dramatically increased over the last decade [249]. Electronically conducting polymers (ECPs) have been identified to be one of the ideal candidates as functional electrode materials for such applications because of their electrical and optical properties that are usually associated with metals, whilst retaining many of the beneficial mechanical properties of organic polymers [31,48]. They are often described as 'synthetic metals/smart materials' due to their inherent property of accepting a counter ion for charge balance when oxidised and expelling the counter ion when reduced and they can be used for the drug loading and release mechanism in controlled release applications [47]. Even though these materials are promising candidates for such biomedical purposes, there are a few disadvantages associated to ECPs; they are intractable, insoluble and not thermoformable which restrict their usage in practical applications. Alternatively, ECPs can be made flexible by grafting them on flexible materials like paper [250], fabric [251] *etc.* and also by modifying carbon electrodes using ECPs [252]. However, the grafted polymers suffer from poor adherence to the surface of their host materials and inhomogeneity leading to non-uniform surfaces. Therefore, they may not be suitable for sustainable flexible electronic device applications.

In this chapter, a method to fabricate chemically blended electronically conducting polymer–biopolymer-ionic liquid composites that are intrinsically flexible for functional electrode applications is presented. The electronically conducting polymer chosen was polypyrrole and as biopolymer, cellulose was selected. Polypyrrole was polymerised *in situ* after the cellulose dissolution process using the IL 1-butyl-3-methylimidazolium chloride, [C_4mim]Cl, as the solvent medium. The obtained polypyrrole–cellulose composite was chemically linked and showed flexible polymer properties while retaining the electronic properties of an ECP. The addition of a hydrophobic ionic liquid such as trihexyl(tetradecyl)phosphonium bis{(trifluoromethyl)sulfonyl}amide, enhanced the flexibility of the composites. This strategy opens up a new design for a wide spectrum of materials for smart electronic device applications wherein the functionality of doping and de-doping of

electronically conducting polymers is retained and their processability issue is addressed by exploiting the ionic liquid technology [253].

3.1. Materials and Instruments

Starting materials used in this chapter are shown in Appendix A.1 and the instrumental techniques used are described in Appendix A.2. The synthesis and characterisation of the following ILs: 1-butyl-3-methylimidazolium chloride [C_4mim]Cl, 1-butyl-3-methylimidazolium ethanoate [C_4mim][C_1COO] and trihexyl(tetradecyl)phosphonium bis{(trifluoromethyl)sulfonyl}amide [$P_{6\,6\,6\,14}$][NTf_2] are reported in Appendix C.

3.2. Dissolution and Regeneration of Cellulose Using Ionic Liquids

The objective of this chapter consists of the development of electronically conducting polymer-biopolymer-based composite electrodes; therefore, the first step was related to the understanding of the biopolymer processing method. The dissolution of the biopolymer was carried out using ionic liquid technology to obtain biopolymer-based films necessary for the next step, which involved the addition of an electronically conducting polymer. The biopolymer chosen was cellulose because is a renewable, sustainable, cheap and scalable material that can originate flexible and lightweight energy devices as it was explained in section 2.2 [77].

3.2.1. Methodology to Obtain Cellulose Films

The first stage consisted of selecting the best ionic liquid for the dissolution of cellulose. The ionic liquids chosen were [C_4mim]Cl, [C_2mim]Cl, [C_4mim][C_1COO] and [C_2mim][C_1COO]. These ILs were chosen as solvents because they are the most commonly used in the literature for the dissolution of cellulose due to their anions ability to form hydrogen bonds as it was explained in section 2.2 [254].

The ionic liquids [C_4mim][C_1COO] and [C_2mim][C_1COO] were dried under high vacuum at 50 ºC and, [C_4mim]Cl and [C_2mim]Cl ILs were dried at 75 ± 2 ºC for 24 hours previous to their use, in order to remove water and volatile impurities; the purity of the ionic liquids was checked by ^{1}H and ^{13}C NMR spectroscopies, TGA and DSC (see "Synthesis and characterisation of ILs" in Appendix C). After drying, the ILs were weighed, powder cellulose (10 wt % of the IL weight) was then added over the ILs, and the mixtures stirred and heated at 100 ± 2 ºC for 3 hours as reported by Swatloski *et*

al. in 2002 [174]. In the case of $[C_4mim]Cl$ and $[C_2mim]Cl$, the ILs were melted at 70 ± 2 ºC and 80 ± 2 ºC, respectively, prior to the addition of the cellulose. The dissolution of cellulose in the ILs was carried out under a nitrogen flow using a Schlenk line, to minimise the contact with water because, as it has been reported, the water decreases the solubility of cellulose in ILs [255]. Previously, the dissolution of the cellulose in the same ionic liquids was carried out inside a glovebox, however, the same results were obtained than using the nitrogen flow in a fume hood. Therefore, it was decided that the dissolution of the cellulose would be developed outside the glovebox to facilitate the posterior sample treatment.

Table 3.1 Ionic liquids used, the quantity of powder cellulose experimentally used, the procedure and the dissolution results, as well as the anti-solvent used for the regeneration of the cellulose

Ionic liquids	Powder cellulose / wt %	Dissolution conditions	Mixture aspect	Regeneration: anti-solvent
$[C_4mim]Cl$	10.1	100 ± 2 ºC for 3 hours	Viscous and colourless	Deionised water
$[C_2mim]Cl$	9.7		Semi-solid and colourless	
$[C_4mim][C_1COO]$	10.2	100 ± 2 ºC for 2 hours	Slightly viscous and light yellow	
$[C_2mim][C_1COO]$	10.5		Slightly viscous and light yellow	

Table 3.1 shows the ionic liquids used for dissolving ~ 10 wt % of powder cellulose at the same temperature (100 ± 2 ºC) for comparison reasons, and the aspects of the mixture obtained after the dissolution. In terms of colour, the mixtures from the ILs with Cl^- anion were colourless, in contrast to the mixtures from the ILs with $[C_1COO]^-$ anions that were slightly yellow as Figure 3.1 (a) and (b) show.

Even though the ILs containing $[C_1COO]^-$ as anion showed a faster dissolution of cellulose and the solutions obtained were much less viscous than with the chloride-containing ILs, the chloride ILs were preferred due to possible undesirable reactions of the cation in $[C_4mim][C_1COO]$ and $[C_2mim][C_1COO]$ with cellulose. *I.e.*, in 2015, Clough *et al.* [181] reported decomposition pathways of cellulose and other carbohydrates when they were dissolved in carboxylate ILs, due to the reaction of the C^2 carbon of the imidazolium ring with the sugar part of the carbohydrates.

After dissolving the powder cellulose in the IL, the regeneration of cellulose was carried out; the mixtures were cast in a petri-dish and they were immersed into the anti-solvent (re-precipitating solvent), distilled water. The anti-solvent has two interrelated *rôles*, one is to dissolve the IL used for the dissolution of the cellulose and the other is to precipitate the cellulose as explained in section 2.2.2. A film was formed in the anti-solvent after five minutes and, in 2 hours, the film was peeled off from the petri-dish and the anti-solvent was removed and stored. The cellulosepowder films obtained were dried at room temperature for 24 hours.

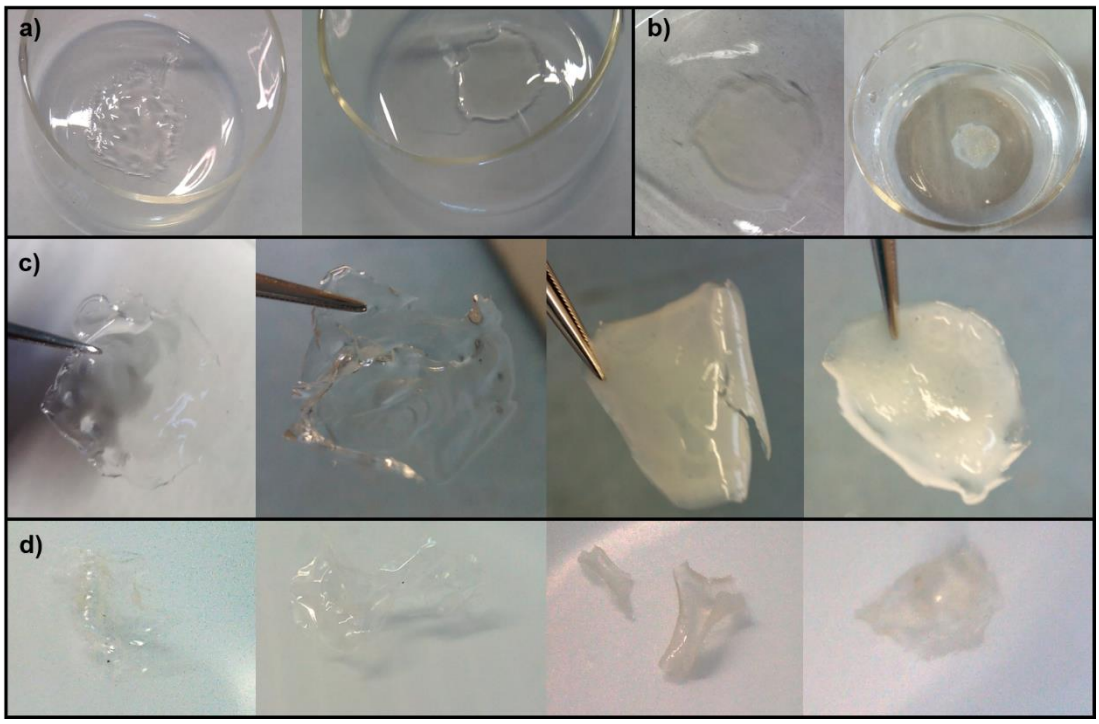

Figure 3.1 a) Cellulose-IL solvent mixtures cast in a petri-dish, b) cellulose-IL solvent mixtures after 5 minutes in water (anti-solvent), c) four fresh cellulosepowder films obtained from each IL dissolution (from left to right, films obtained from the ILs: $[C_4mim]Cl$, $[C_2mim]Cl$, $[C_4mim][C_1COO]$ and $[C_2mim][C_1COO]$) and d) cellulosepowder films after 24 hours drying

Figure 3.1 (a, b) shows the wet films before and after the regeneration process and Figure 3.1 (c) shows the regenerated films obtained. As shown in the first two pictures, on the left, the films obtained using the chloride-based ILs for the cellulose dissolution were colourless, whereas off-white cellulose films resulted when using the carboxylate-ILs (shown in the two pictures on the right). These four cellulosepowder films were dried at room temperature for 24 hours and, as it can be seen in Figure 3.1 (d) all of them suffered shrinkage during the drying process, although this was less significant for the films obtained using the chloride-ILs. It is worth to mention that at

this early stage, there was no control for casting the cellulosepowder films; the method consisted of pouring the mixture on a petri-dish using a spatula, resulting in films with different shape and thickness (Figure 3.1 (d)).

In summary, from this initial study, [C_2mim]Cl and [C_4mim]Cl were selected as convenient IL solvents due to their ability to dissolve the cellulose and because the regenerated cellulosepowder films obtained experienced less shrinkage after drying than the films using the $[C_1COO]^-$ containing ILs. It has been reported in the literature [256,193] that chloride-containing ionic liquids are effective solvents for cellulose because hydrogen bonds form between the non-hydrated chloride ions of the IL and the sugar hydroxyl protons. These interactions disrupt the hydrogen bonding network of the cellulose polymer and lead to its dissolution, as it was explained in section 2.2.1 and showed in Figure 2.14 [174]. Of the two chloride ILs used, [C_4mim]Cl was ultimately chosen for further studies due to its lower melting point (65 ºC) in comparison to [C_2mim]Cl (87 ºC) [257]; [C_4mim]Cl was easier to melt and this facilitated the addition and mixture of cellulose.

Additionally, a study of two different cellulose types: powder cellulose (fine powder) and fibrous cellulose (fibers aspect) from Sigma-Aldrich was developed to find the most suitable cellulose for the films as it is displayed in Table 3.2. After dissolving the two different types of cellulose in the IL, the regeneration was carried out as it will be explained in page 57. The regenerated cellulosepowder films and cellulosefibrous films obtained were dried at room temperature for 24 hours.

Table 3.2 Dissolution conditions and regeneration process for two types of cellulose (powder and fibrous) dissolved in the IL [C_4mim]Cl

Ionic liquid	Cellulose type	Dissolution conditions	Regeneration: anti-solvent
[C_4mim]Cl	11 wt % powder cellulose	100 ± 2 ºC for 3 hours	Deionised water
	13 wt % fibrous cellulose	100 ± 2 ºC for 2 hours	

During the dissolution of both types of cellulose, it was observed that the fibrous cellulose dissolved faster than the powder cellulose, *i.e.*, the fibrous cellulose could not be detected in the mixture after stirring for 2 hours at 100 ºC, whereas 3 hours were needed for the dissolution of powder cellulose at the same temperature. Henceforth, the fibrous cellulose it was the cellulose type chosen to prepare the films.

The ionic liquid [C_4mim][Cl], and the fibrous cellulose were therefore selected as the solvent and the biopolymer, respectively, to follow-up with the development of the flexible electronic composite electrodes.

In addition, in order to improve the film-making process, a coating machine was used to cast the films (Figure 3.2). In particular, a control coater (model K control 101 from RK Printcoat Instruments) was used to cast wet films with a thickness of ~ 100 μm between two proofing papers at room temperature (glossy paper that cannot interfere with the films was used, as there is no abrasion effect from the smooth paper surface due to its hydrophobic additive). This automatic machine uses standard wire wound bars to produce a uniform and repeatable coating [258]. The wire wound bar used was number 8 (wire diameter 1.27 mm).

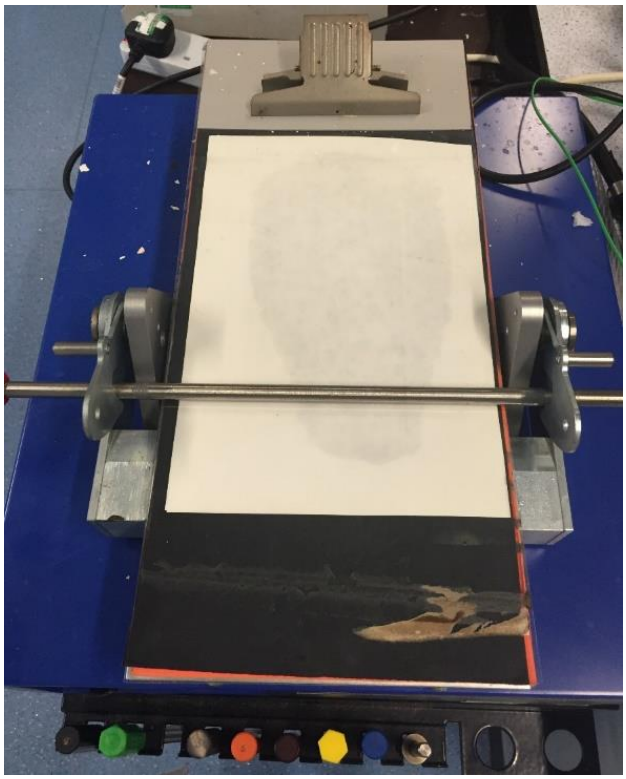

Figure 3.2 Coating machine used for casting the films

After casting the wet film between the proofing papers, the wet film together with the papers was immersed into the anti-solvent bath to regenerate the cellulose (re-precipitation process of the cellulose). When the regeneration was completed, both papers could be peeled off and a free-standing film was obtained as it can be seen in Figure 3.3 (a). After 24 hours air drying at room temperature the film obtained

(Figure 3.3 (b)) was reduced in size almost 4 cm and its thickness was ~ 200 µm. It is likely that the shrinkage increased the thickness of the cellulosefibrous film.

In conclusion, the use of the coating machine facilitates the casting of the films and provides control in the size and thickness of the free-standing films cast.

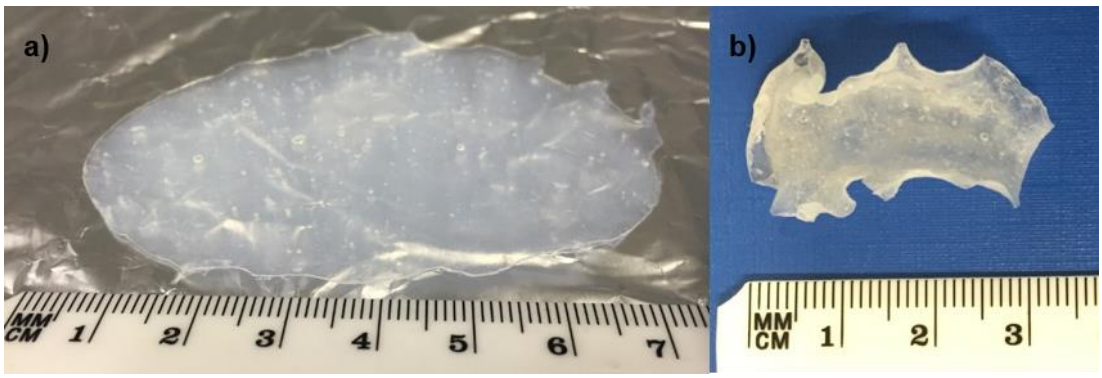

Figure 3.3 a) Wet cellulosefibrous film cast using the coating machine and b) the same cellulosefibrous film after 24 hours drying

3.2.2. Characterisation of the Cellulosefibrous Films

The solid-state characterisation of the obtained cellulosefibrous film was carried out using a Fourier transform infrared (FTIR) spectrometer equipped with an attenuated total reflectance (ATR) accessory and, as well as by using a Raman spectrometer. The thermal analysis was carried out using a thermogravimetric analyser (TGA) and the morphology and elemental composition were analysed by scanning electronic microscopy (SEM) and energy dispersive X-Ray (EDX).

Figure 3.4 shows the infrared spectra of fibrous cellulose (starting material), IL solvent ([C_4mim]Cl), cellulosefibrous-[C_4mim]Cl mixture and the regenerated cellulosefibrous film obtained. From these, the main peaks from the cellulose and from [C_4mim]Cl can be identified and compared to those of the cellulose-IL mixture and the regenerated film. The infrared spectrum of the cellulose-[C_4mim]Cl mixture was recorded after 2 hours stirring at 100 ºC, and the cellulosefibrous film was obtained using water as anti-solvent.

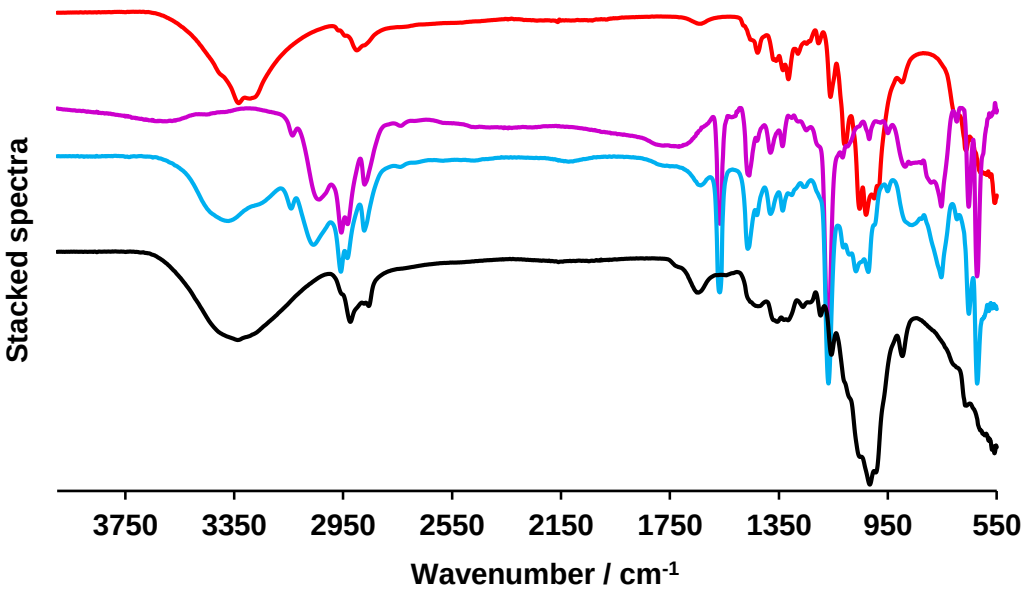

Figure 3.4 Stacked infrared spectra of fibrous cellulose (red), [C_4mim]Cl (purple), cellulosefibrous-[C_4mim]Cl mixture (blue) and the regenerated cellulosefibrous film (black)

The peaks assignment from the spectra (Figure 3.4) is shown in Table 3.3 [259]. It is interesting to note that in the regenerated cellulosefibrous film (black), the peaks corresponding to [C_4mim]Cl (3129, 3056, 1556, 1486, 1170 and 735 cm^{-1}) are not present, indicating that no IL solvent remained in the cellulosefibrous film [260]; this will be further corroborated by EDX analysis. The spectrum of fibrous cellulose shows some differences with the regenerated cellulosefibrous film, reflecting a change in the cellulose after the re-precipitation, from cellulose I (crystalline cellulose) to cellulose II (amorphous cellulose). For example, the peak corresponding to the cellulose asymmetric in phase-ring stretching at 897 cm^{-1} is sharper in the regenerated cellulose than in the fibrous cellulose and, the peak assigned to the cellulose CH_2 symmetric bending at 1427 cm^{-1} is weakened in the regenerated cellulose. The peak around 897 cm^{-1} corresponds to amorphous cellulose and, in contrast, the 1427 cm^{-1} peak is related to the crystalline form [176b]. Therefore, it can be said that during the regeneration process there is a transformation from cellulose I to cellulose II.

Table 3.3 Infrared peak assignments of the fibrous cellulose (starting material), $[C_4mim]Cl$, cellulose-$[C_4mim]Cl$ mixture and the cellulosefibrous film obtained

Fibrous cellulose/ cm^{-1}	$[C_4mim]Cl$/ cm^{-1}	Mixture cellulose-$[C_4mim]Cl$/ cm^{-1}	Cellulosefibrous film / cm^{-1}	Bonds
3336,3293		3387	3346	OH stretching
	3129	3150		Asymmetric/Symmetric stretching C-H imidazolium ring
	3056, 2975	3070, 2982		Asymmetric stretching CH_2
2889	2917, 2867	2935, 2870	2919, 2853	Asymmetric and symmetric C-H stretching
	1556	1573		C=C stretching
	1486	1458		C-N stretching
1428			1427	CH_2 symmetric bending
1361			1356	C-H bending
1326			1325	Ring stretching
	1170	1166		-C-C-N stretching
1045	1016	1020	1011	C-OH, C-C, C-H ring and side group vibrations (cellulose)
892			897	Asymmetric in phase-ring stretching (cellulose)
	735	756		Out-of-plane C-H imidazolium ring

Both Raman and infrared spectroscopies can be used for the characterisation of cellulose because all its vibrational modes are potentially active in both techniques. Raman spectroscopy has the advantage that the water does not interfere with the cellulose spectra because the water has weak Raman bands [261]. The Raman spectra of the fibrous cellulose (starting commercial material) and the cellulosefibrous film are shown in Figure 3.5. Fibrous cellulose well-defined peaks are fairly typical of the spectrum of cellulose with relatively high crystallinity [262]. In the case of the cellulosefibrous film, the broader Raman peaks indicate that the cellulose crystallinity is lost after dissolving it and regenerating it as a film, in agreement with that observed by IR spectroscopy.

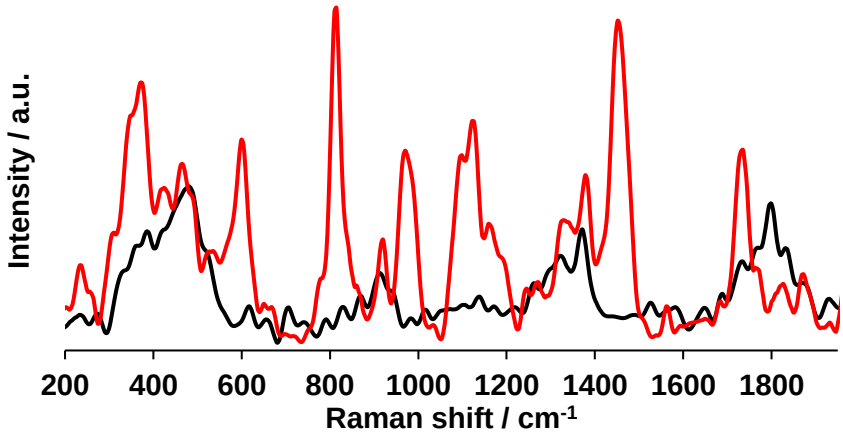

Figure 3.5 Raman spectra of fibrous cellulose (red) and regenerated cellulosefibrous film (black). Spectra normalised and re-plotted using Spectrogryph

Table 3.4 Raman shift assignment of fibrous cellulose (starting material) and the cellulosefibrous film obtained

Fibrous cellulose / cm^{-1}	Cellulosefibrous film / cm^{-1}	Bonds
1735	1799	C-C bending
1452	-	C-O and C-C-O stretching (CH_2OH part)
1380	1372	H-C-C and C-O-H bending (CH_2OH part)
975 915	906	H-C-C and C-O-H bending (CH_2OH part)
812	812	Out-of-plane bending vibrations of hydrogen-bonded OH groups
608	-	C-C-C of ring and glycoside bond
488	492	C-O bending
376		C-C-C vibrations of glucose rings

Table 3.4 shows the Raman peak assignments of the fibrous cellulose and cellulosefibrous film, which have been done by comparison with available literature data [263,261]. The most significant change that supports the loss of crystallinity in the cellulose (after dissolved it in the IL and then regenerated it) can be found in the Raman signals at 1452 and 1380 cm^{-1}, that correspond to methylene stretching and bending modes of two CH_2OH groups stereochemically non-equivalents of the crystalline cellulose, and which merge into one much broader peak around 1400 cm^{-1} (*i.e.*, 1372 cm^{-1}) in the case of amorphous cellulose [263b,263d,261].

The thermal stability of the cellulosefibrous film obtained was studied using a thermogravimetric analyser (TGA) which measures the changes in the physical and chemical properties of the material as a function of loss of mass while the temperature increases gradually. TGA gives the decomposition temperature or onset temperature (T_{on}) of the samples [264].

Figure 3.6 shows the thermogram of the fibrous cellulose (starting commercial material) with a decomposition temperature of 316 ºC and the cellulosefibrous film which is thermally stable until 239 ºC, being both values comparable to those in the literature [174]. In the case of the cellulosefibrous film, a slow mass loss (6.00 wt %) was observed around 125 ºC which may be attributed to the loss of intermolecularly bonded water molecules.

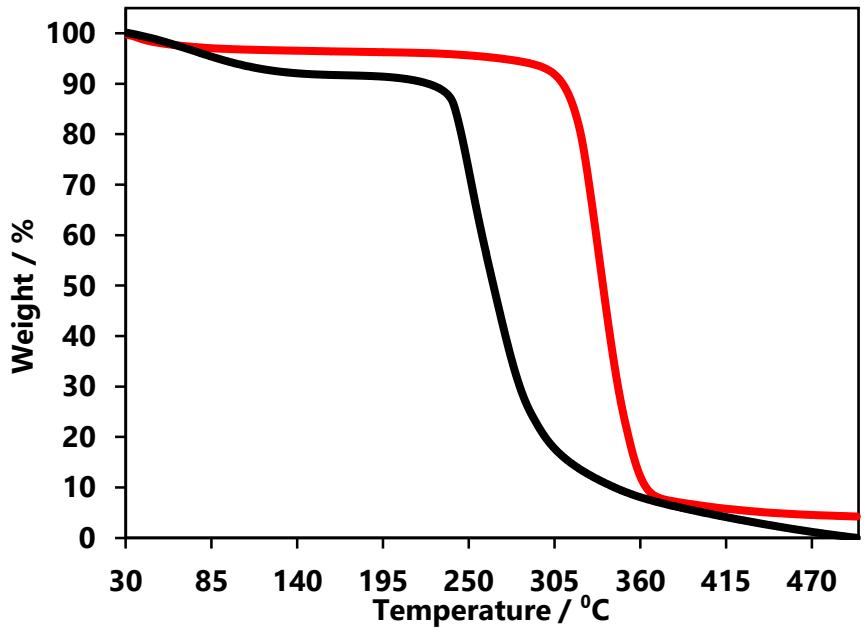

Figure 3.6 Thermogram of fibrous cellulose (red) and cellulosefibrous film (black)

The topography and morphology of the materials were studied using scanning electron microscopy (SEM) attached with energy dispersive X-ray (EDX) spectrometer and an Everhart-Thornley detector (ETD). The films were sputtered with gold prior to the examination due to the non-conductive polymeric matrix (cellulose) and to avoid the charging effect during measurement because of the surface accumulation of electrostatic negative charges from the electron beam of the SEM. The sputter coating for SEM is the process of applying a thin coating of an electrically conducting metal

such as gold (Au) to earth down the accumulated charge and provide a clear image of the surface.

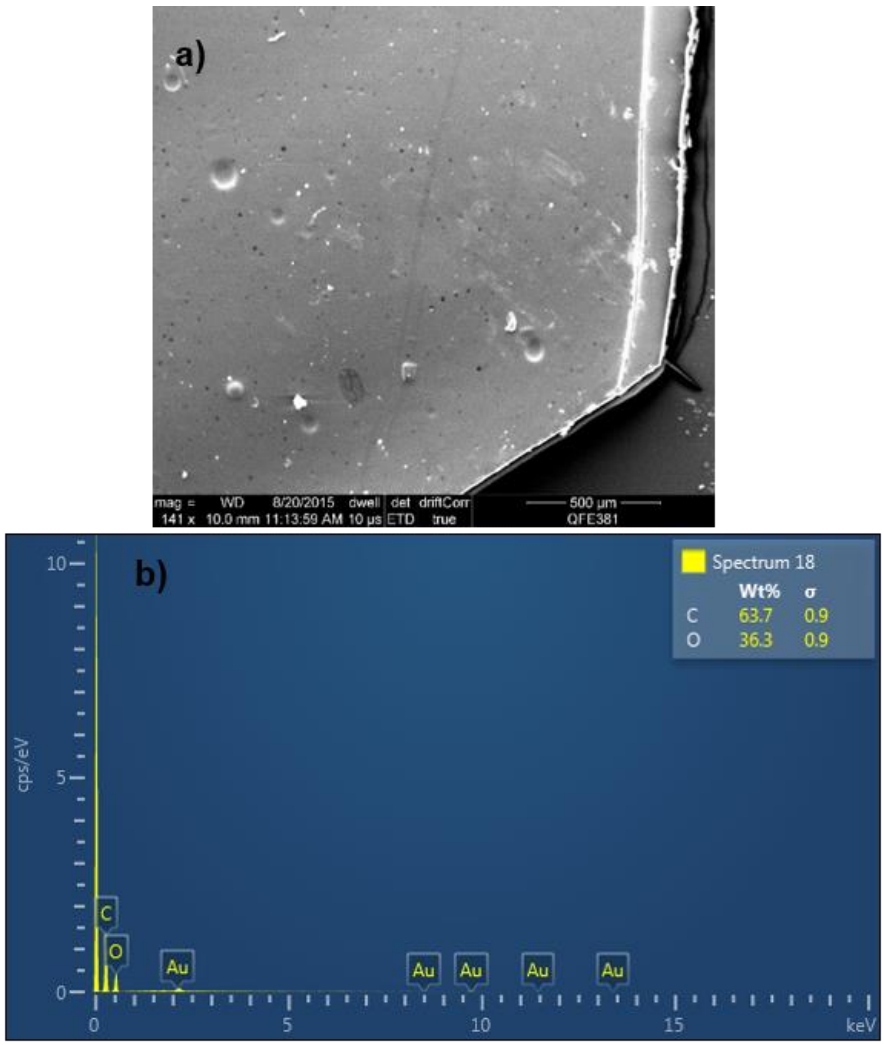

Figure 3.7 a) SEM picture of cellulosefibrous film and b) EDX spectra of cellulosefibrous film (presence of Au from sputtering)

The SEM image of the cellulosefibrous film, provided in Figure 3.7 (a), had a smooth morphology with no electronically conducting regions, as indicated by the absence of bright regions on the SEM image. Moreover, longer exposures (> 30 s) caused the film to break under the electron beam which is expected when the thin paper film is heated by the beam current. Elemental analysis using EDX confirmed the presence of the elements carbon and oxygen that constituted the cellulosefibrous film. The absence of chlorine and nitrogen in the film indicates that any residual [C_4mim]Cl remaining in the composite film was below the detection limit of EDX analysis *e.g.* 1 wt %.

3.3. Addition of Ionic Liquids as Plasticisers

Ionic liquids can be applied as plasticisers as it was explained in section 2.1.3.3. The addition of a plasticiser is needed to improve the flexibility of the polymer composites. The decision was to use a hydrophobic ionic liquid as plasticiser to prevent its dissolution when the regeneration of the cellulose in water is carrying out. The ILs chosen were phosphonium based ILs, specifically with the cation $[P_{6\,6\,6\,14}]^+$, because their chemical structures, with long alkyl chains, are similar to the conventional plasticiser structures (*e.g.*, phthalates), which also have apolar and polar elements [265]. Other advantaged include their commercial availability and relative cheapness [266], high chemical and thermal stability [267], and low toxicity in comparison to the phthalates plasticisers that are potentially toxic [265].

3.3.1. Methodology to Obtain Cellulosefibrous Films Containing IL plasticisers

The first IL tested was trihexyl(tetradecyl)phosphonium chloride, $[P_{6\,6\,6\,14}]Cl$ (PCl), but the use of chloride was avoided in further work to construct electrodes. Chloride ILs are also often moisture sensitive and corrosive [141]. Therefore, the use of trihexyl(tetradecyl)phosphonium bis{(trifluoromethyl)sulfonyl}amide, $[P_{6\,6\,6\,14}][NTf_2]$ ($PNTf_2$), as the plasticiser was proposed as a better option due to its higher thermal stability, hydrophobicity and ionic conductivity, as well as lower viscosity, compared to $[P_{6\,6\,6\,14}]Cl$. Results with both ILs are presented below [143a,268].

For the addition of the IL plasticiser, the cellulose fibrous-$[C_4mim]Cl$ mixture, previously prepared (see section 3.2.1), was set at 90 ºC and the IL plasticiser was added and stirred until a homogeneous mixture was obtained. When the IL plasticiser was added to the colourless mixture and stirred, the solution turned white and the colour did not change after the regeneration of the cellulose. The free-standing films obtained were also white as it can be seen in Figure 3.8.

After trying different quantities of IL plasticiser (5, 10 and 15 wt %) the maximum quantity that could be added to the mixture was 10 wt % of the $[C_4mim]Cl$ weight. When more than 10 wt % of IL plasticiser was added to the mixture, it was possible to see drops of the IL over the anti-solvent (water) while the regeneration of the cellulose was taking place, indicating that there was too much IL plasticiser in the mixture.

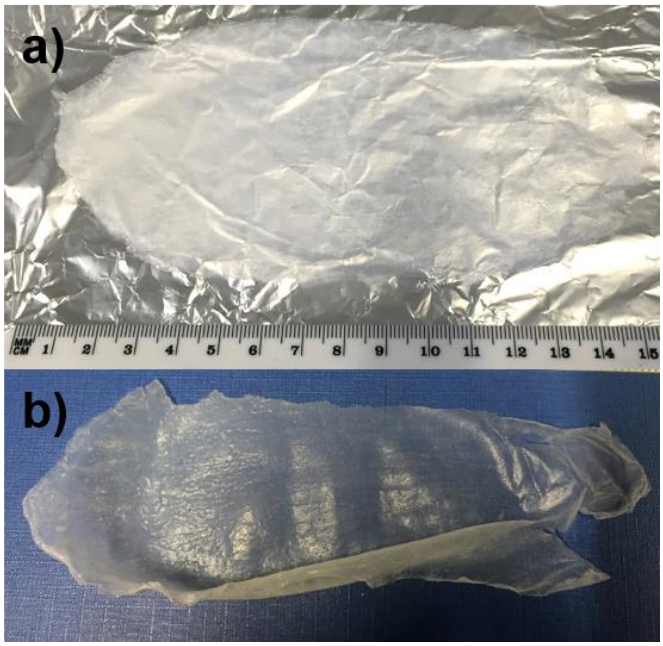

Figure 3.8 Pictures of a) wet cellulosefibrous-$PNTf_2$ film after using the coating machine and b) the same film after drying using a weight

The casting of the films was carried out using the coating machine as explained previously and, it was immersed into a water bath to obtain two different free-standing films: a cellulosefibrous-PCl film when $[P_{6\,6\,6\,14}]Cl$ was the plasticiser and, a cellulosefibrous-$PNTf_2$ film when $[P_{6\,6\,6\,14}][NTf_2]$ was used. The drying process was improved by adding a weight over the films when they were drying, and also, by protecting the films with papers while drying. With these improvements, it was possible to avoid the shrinkage of the films as shown in Figure 3.8 (b).

3.3.2. Characterisation of the Cellulosefibrous Films Containing IL plasticisers

Figure 3.9 shows the infrared spectra associated with the cellulosefibrous-PCl film, the starting materials used for its synthesis and the mixture of the cellulosefibrous-$[C_4mim]Cl$-$[P_{6\,6\,6\,14}]Cl$. The assignment of the peaks from the fibrous cellulose and $[C_4mim]Cl$ was discussed in section 3.2.2. Peaks for the new compound added, *e.g.* IL plasticiser $[P_{6\,6\,6\,14}]Cl$, could be found which were retained in the cellulosefibrous-PCl film such as the two sharp peaks at 2926 and 2856 cm^{-1}, which correspond to C-H stretching modes and are sharper than those in cellulose due to the large number of methylene groups in the plasticiser cation, $[P_{6\,6\,6\,14}]^+$. The two peaks at 1373 and 1318 cm^{-1} corresponding to the C-H bending of the alkyl chain of the plasticiser cation are also retained in the spectrum of the film [269]. More importantly, the elimination of $[C_4mim]Cl$ (IL solvent) from the cellulosefibrous film

was confirmed with this technique, in agreement with the results presented in section 3.2.2.

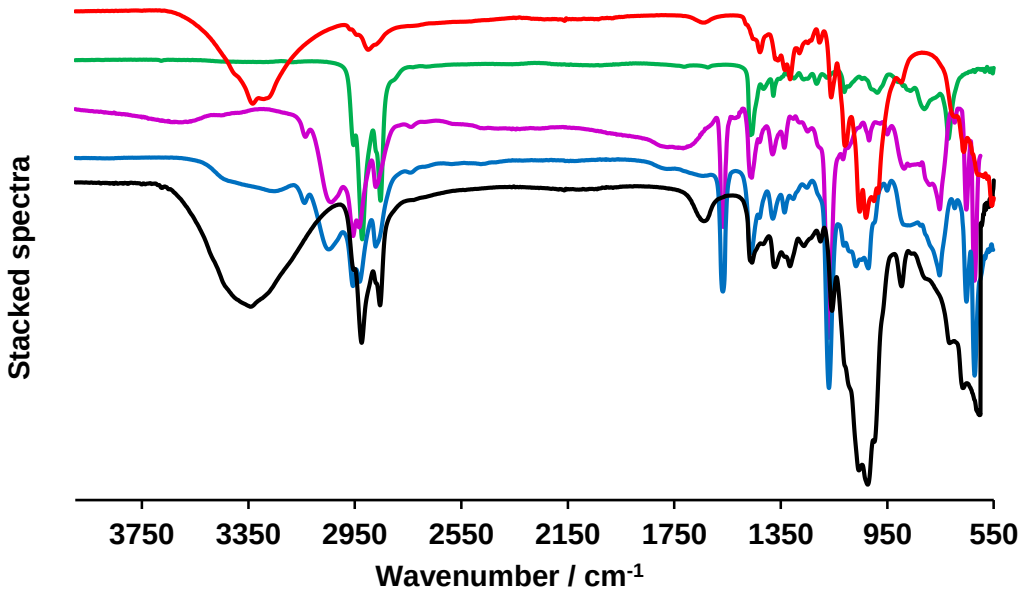

Figure 3.9 Infrared spectra of fibrous cellulose (red), [C_4mim]Cl (purple), [$P_{6\,6\,6\,14}$]Cl (green), cellulosefibrous-[C_4mim]Cl-[$P_{6\,6\,6\,14}$]Cl mixture (blue) and cellulosefibrous-PCl film (black)

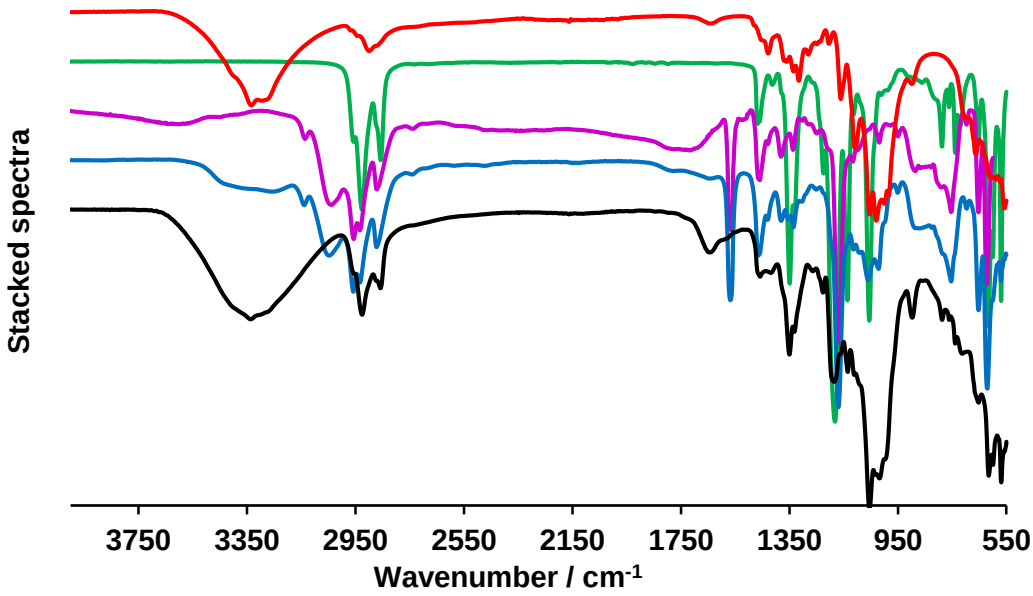

Figure 3.10 Infrared spectra of fibrous cellulose (red), [C_4mim]Cl (purple), [$P_{6\,6\,6\,14}$][NTf_2] (green), cellulosefibrous-[C_4mim]Cl-[$P_{6\,6\,6\,14}$][NTf_2] mixture (blue) and cellulosefibrous-$PNTf_2$ film (black)

In the case of the cellulosefibrous-$PNTf_2$ film, Figure 3.10, it was found that four different peaks from the IL plasticiser were retained in the film. The peaks at 2927 and 2860 cm^{-1} corresponding to the methylene groups from the cation, $[P_{6\,6\,6\,14}]^+$; and

the peaks at 1350 and 1181 cm^{-1}, assigned to the S=O asymmetric and symmetric stretching of the $[NTf_2]^-$ anion, respectively [269].

Figure 3.11 and Figure 3.12 display the Raman spectra of the cellulosefibrous-PCl film and cellulosefibrous-$PNTf_2$ film, respectively. The Raman spectra of the IL plasticisers used and the cellulosefibrous film previously characterised were also added for comparison.

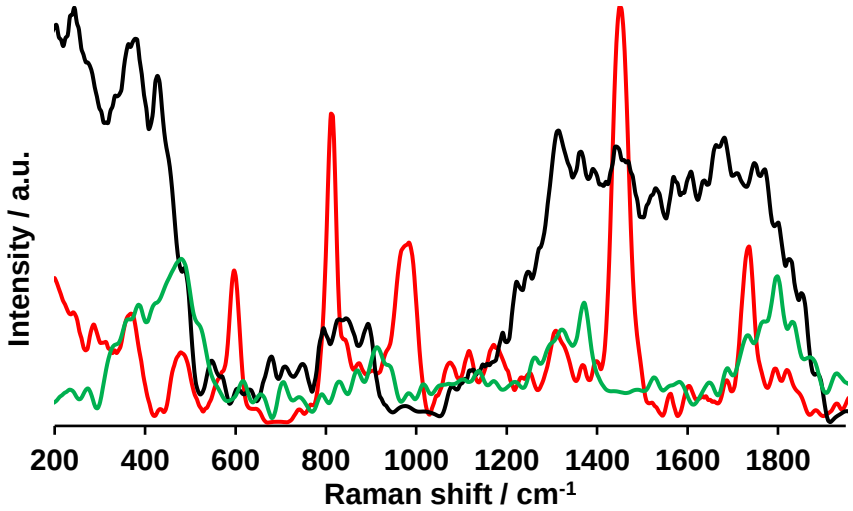

Figure 3.11 Raman spectra of $[P_{6\,6\,6\,14}]Cl$ (red), cellulosefibrous film (green) and cellulosefibrous-PCl film (black). Spectra normalised and re-plotted using Spectrogryph

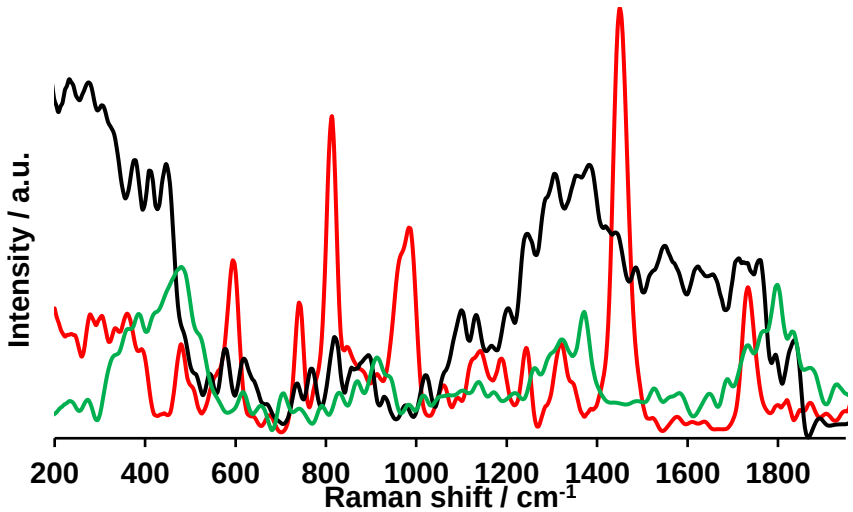

Figure 3.12 Raman spectra of $[P_{6\,6\,6\,14}][NTf_2]$ (red), cellulosefibrous film (green) and cellulosefibrous-$PNTf_2$ film (black). Spectra normalised and re-plotted using Spectrogryph

Table 3.5 shows the Raman shift assignments [270] for the spectra included in Figure 3.11 and Figure 3.12 where it can be seen that most of all the Raman peaks from the ionic liquid plasticisers cannot be found in the cellulosefibrous-IL plasticiser films. One possible reason could be that the peaks for the plasticiser are overlapped

with the cellulose peaks. In the case of the plasticiser $[P_{6\,6\,6\,14}][NTf_2]$, there is a peak at 1207 cm^{-1} corresponding to the CF_3 stretching of the anion that could be identified in the cellulosefibrous-$PNTf_2$ film at 1236 cm^{-1} as a broad peak. In both cellulosefibrous-IL plasticiser films there is a big broad peak from 1300 to 1800 cm^{-1} that did not appear in the cellulosefibrous film, and therefore, could be considered as a characteristic feature of the plasticiser-containing films. As the common part of the plasticiser is the cation, $[P_{6\,6\,6\,14}]^+$, it can be speculated that the broad peak is related to the cation.

Table 3.5 Raman shift assignments of cellulosefibrous-IL plasticiser films in comparison to the IL plasticisers and a cellulosefibrous film

$[P_{6\,6\,6\,14}]Cl$ / cm^{-1}	$[P_{6\,6\,6\,14}][NTf_2]$ / cm^{-1}	Cellulose fibrous film / cm^{-1}	Cellulose fibrous-PCl film / cm^{-1}	Cellulose fibrous-$PNTf_2$ film / cm^{-1}	Bonds
1732	1695	1799	1687	1723	C-C bending
1409	1417		1448	1385	H-C-H bending plasticiser
1304	1320	1372	1312	1352	H-C-C (CH_2 plasticiser) and C-O-H bending (CH_2OH part) cellulose
	1207			1236	CF_3 symmetric stretching
984	988	944			H-C-C (CH_2 plasticiser) and C-O-H bending (CH_2OH part) cellulose
816	816	829	812	848	Out-of-plane bending of OH groups cellulose and C-C stretching CH_2 plasticiser
	744				CF_3 symmetric deformation
592	596				C-C-C bending plasticiser
480	505	492	424	444	C-O bending cellulose, C-C bending plasticiser cation and C-N-C deformation plasticiser anion

The thermal stabilities of the cellulose films containing ILs plasticisers are presented in Figure 3.13 and Figure 3.14. The decomposition temperature of the IL $[P_{6\,6\,6\,14}]Cl$ was 301 ºC and for the cellulosefibrous-PCl film, this onset temperature decreased to 250 ºC. The thermogram corresponding to the IL plasticiser, $[P_{6\,6\,6\,14}][NTf_2]$, shows a higher thermal stability as expected due to the higher stability of the anion [271], with a decomposition temperature of 329 ºC. In the case of the

cellulosefibrous-$PNTf_2$ film, the decomposition temperature was 251 ºC. Both films obtained show a higher onset temperature that in the case of the cellulosefibrous film (green plot); hence, the IL plasticisers enhance the thermal stabilities of the cellulosefibrous films due to a possible interaction with the cellulose in the film [272].

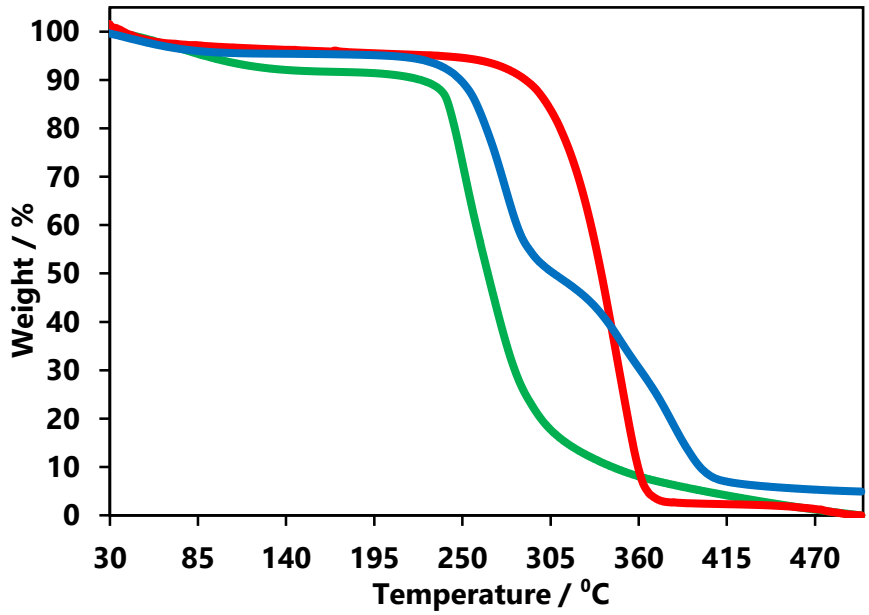

Figure 3.13 Thermogram of $[P_{6\,6\,6\,14}]Cl$ (red), cellulosefibrous film (green) and cellulosefibrous-PCl film (blue)

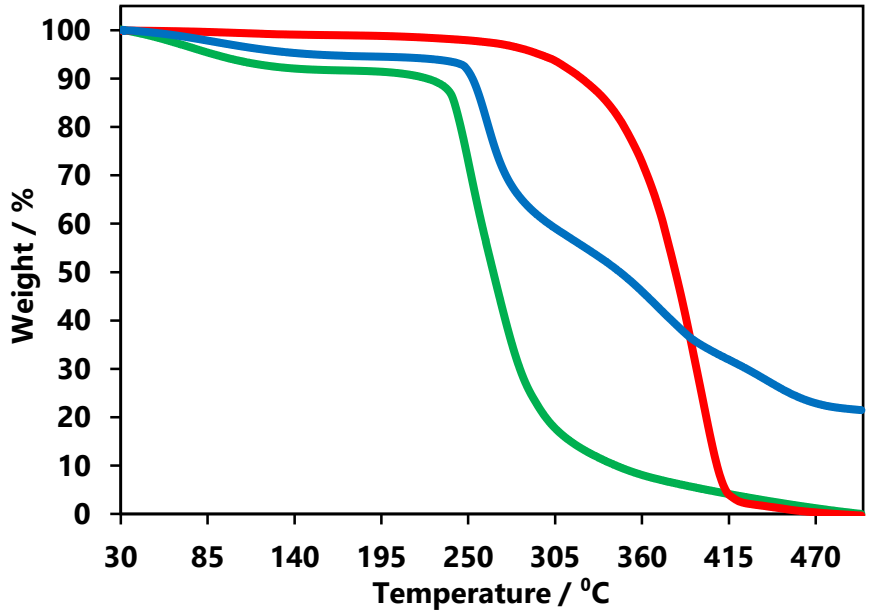

Figure 3.14 Thermogram of $[P_{6\,6\,6\,14}][NTf_2]$ (red), cellulosefibrous film (green) and cellulosefibrous-$PNTf_2$ film (blue)

The quantity of water found in these two cellulosefibrous-IL plasticiser films were 4.2 wt % for the cellulosefibrous-PCl film and 4.0 wt % for the cellulosefibrous-

$PNTf_2$ film. Both films showed a second decomposition temperature around 333 ºC for the cellulosefibrous-PCl film and around 341 ºC for the cellulosefibrous-$PNTf_2$ film. This second decomposition temperature could be linked to free IL plasticiser retained inside the films [272].

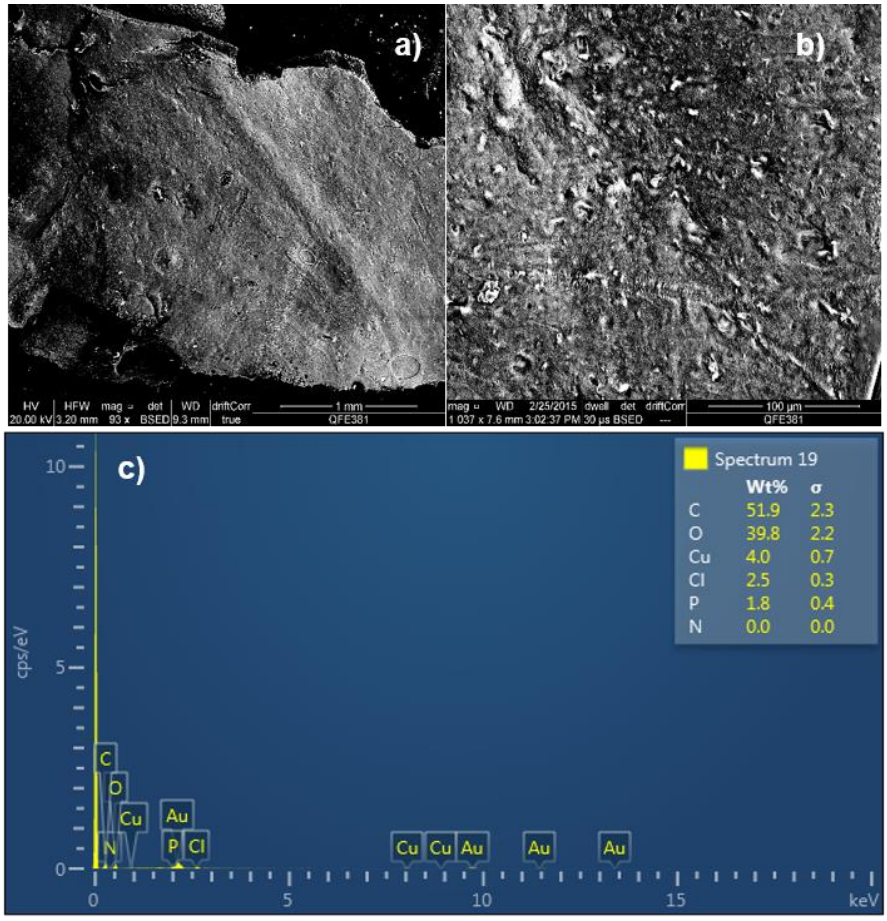

Figure 3.15 SEM picture of cellulosefibrous-PCl film showing a) magnification 100 and b) magnification 1K. EDX spectra showing c) the composition of the cellulosefibrous-PCl film (presence of Au from sputtering and Cu from the copper tape)

SEM/EDX data for the cellulosefibrous-PCl and cellulosefibrous-$PNTf_2$ films are shown in Figure 3.15 and Figure 3.16, respectively. The cellulosefibrous film showed in section 3.3.1 was very thin (*i.e.* as a piece of paper), but when the plasticiser, $[P_{6\,6\,6\,14}]Cl$, was added the cellulosefibrous-PCl film obtained was thicker with porosity created throughout as it can be seen in the cross-section showed in Figure 3.15 (a). The elemental analysis carried out using EDX (Figure 3.15 (c)) show the presence of elements from the cellulose (C and O) and from the plasticiser (P and Cl).

Similarly to the cellulosefibrous-PCl film, the cellulosefibrous-$PNTf_2$ film shows porosity that can be seen in Figure 3.16 (a). Elements from the cellulose (C and O) and

from the IL plasticiser (P, S and F) were also identified by EDX, as shown in Figure 3.16 (b).

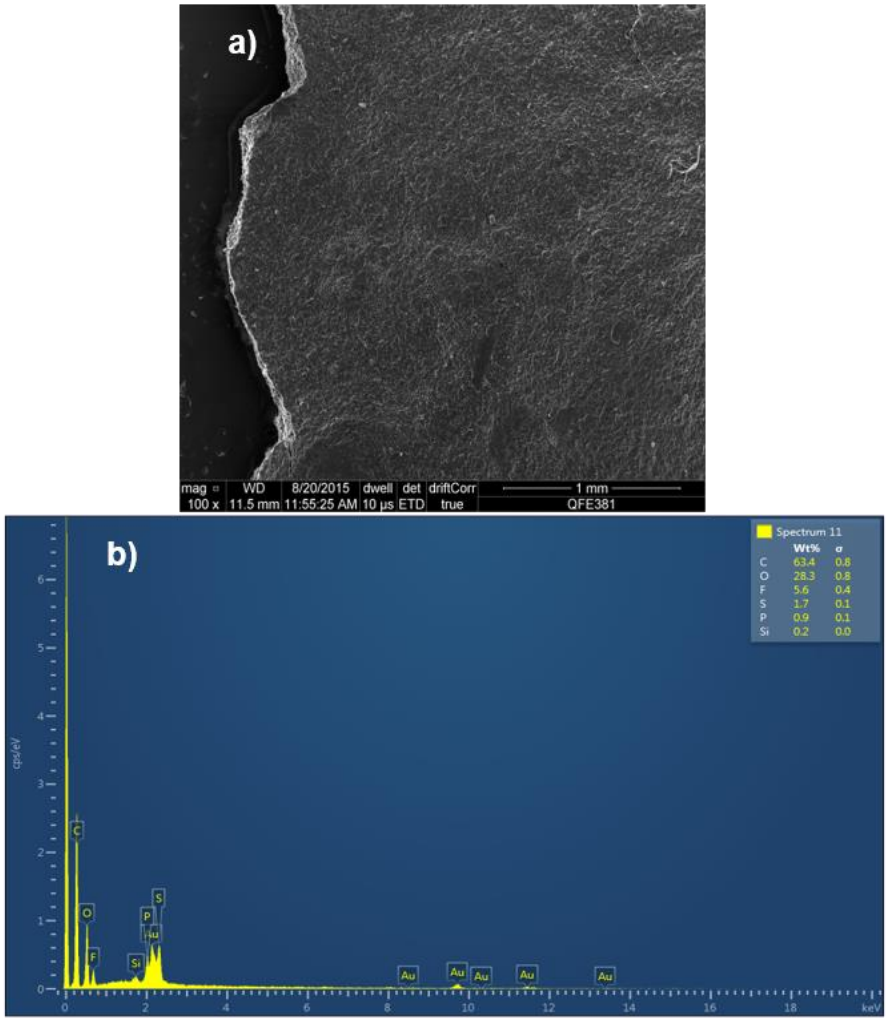

Figure 3.16 SEM picture of the cellulosefibrous-NTf_2 film a) showing magnification 100. EDX spectra showing b) the composition of the cellulosefibrous-$PNTf_2$ film (presence of Au from sputtering)

The elemental composition from the EDX is tabulated in Table 3.6 where the main differences between the films can be identified. The amount of carbon increased from the film with the plasticiser $[P_{6\,6\,6\,14}]Cl$ to the film with $[P_{6\,6\,6\,14}][NTf_2]$ due to the anion $[NTf_2]$ which has carbon. Also, this anion has sulfur and fluorine which appeared in the analysis of the cellulosefibrous-NTf_2 film. Phosphorous appears in both films due to the plasticiser cation, $[P_{6\,6\,6\,14}]^+$. Chlorine was found in the cellulosefibrous-PCl film due to the plasticiser anion, Cl^-, but in the cellulosefibrous-$PNTf_2$ film, this element was not found. As explained in section 3.2.2, the absence of chlorine shows that significant amounts of $[C_4mim]Cl$, used for cellulose dissolution, do not remain in the film.

Table 3.6 Elemental composition of the cellfib-IL plastisicer films using EDX

Films	C / %	O / %	P / %	S / %	F / %	Cl / %
cellulosefibrous-PCl film	51.9	39.8	1.8	-	-	2.5
cellulosefibrous-NTf_2 film	63.4	28.3	0.9	1.7	5.6	-

3.4. NMR Study of the Cellulose-Ionic liquids Mixtures

In this section, nuclear magnetic resonance (NMR) studies were carried out to evaluate the interactions of the cellulose with the IL solvent ([C_4mim]Cl), and with the ILs plasticisers ([$P_{6\,6\,6\,14}$]Cl and [$P_{6\,6\,6\,14}$][NTf_2]). In the case of the cellulose-IL solvent interaction a ^{35}Cl NMR study was carried out and in the case of the cellulose-IL solvent-IL plasticiser ^{35}Cl NMR and ^{31}P NMR studies were developed.

In the literature, studies on the mechanism using ^{13}C and $^{35/37}$Cl NMR relaxation measurements and molecular dynamics studies can be found, as introduced in section 2.2.1 [200]. The reason for choosing ^{35}Cl NMR for the analysis of chloride in ILs are the natural abundance of ^{35}Cl (75.5 %) and its short relaxation time caused by its quadrupole nucleus (I=3/2) [273]. In the case of ^{31}P NMR, its isotopic abundance is about 100 % and its nucleus spin is ½, making spectra rather easy to understand [274].

The study of the interaction of cellulose with the IL solvent, [C_4mim]Cl, and with two different IL plasticisers, [$P_{6\,6\,6\,14}$]Cl and [$P_{6\,6\,6\,14}$][NTf_2], was carried out using Bruker NMR (600 and 400 Hz) instruments. ^{35}Cl NMR and ^{31}P NMR experiments were completed with frequencies of 59 MHz and 162 MHz, respectively.

Solutions of powder cellulose (5 and 10 wt %) and fibrous cellulose (5 and 10 wt %) in [C_4mim]Cl were prepared by mixing the cellulose-IL solvent at 100 ºC with constant stirring for 3 hours for the powder cellulose and for 2 hours for the fibrous cellulose. In the case of the solution including the ILs plasticisers, [$P_{6\,6\,6\,14}$]Cl and [$P_{6\,6\,6\,14}$][NTf_2], the cellulose was dissolved as explained previously (*i.e.*, a 10 wt % of IL plasticiser was added to the cellulose-[C_4mim]Cl mixture at 90 ºC, which was then stirred until a homogeneous mixture was obtained).

Neat ILs and completed dissolutions were transferred to 5 mm NMR tubes that were subsequently fitted with a 50 µL co-axial external reference containing a solution of 0.1 M NaCl in D_2O for the ^{35}Cl NMR experiments and another 50 µL co-axial external reference containing trimethylphosphate for the ^{31}P NMR spectra. The transfer of the

neat ILs and the cellulose dissolutions was carried out very carefully using a heat gun and a syringe.

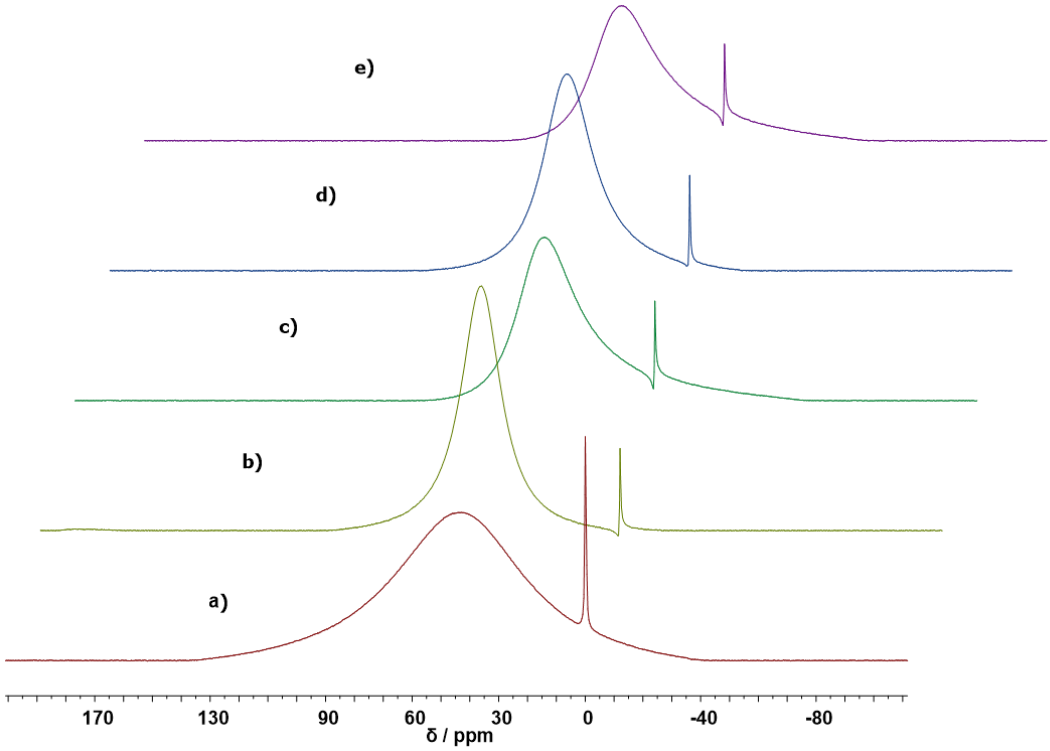

Figure 3.17 Stacked ^{35}Cl NMR spectra of a) IL solvent [C_4mim]Cl, b) 5 wt % powder cellulose in [C_4mim]Cl, c) 5 wt % fibrous cellulose in [C_4mim]Cl, d) 10 wt % powder cellulose in [C_4mim]Cl and e) 10 wt % fibrous cellulose in [C_4mim]Cl

Figure 3.17 shows the ^{35}Cl NMR spectra obtained for the neat IL solvent, [C_4mim]Cl, and its mixture with powder cellulose and fibrous cellulose in different quantities. The peak followed in the spectra is the one corresponding to the chloride from the IL solvent, [C_4mim]Cl, which is the peak that is in more concentration in comparison to the other components of the mixtures.

In Table 3.7 the chemical shift and line width of the chloride peaks obtained for the neat [C_4mim]Cl and its mixtures with cellulose are summarised. From these values and based on related work in the literature [275], it was possible to analyse the behaviour of the chloride anion with different cellulose types and quantities added.

The chemical shift and line width of the chloride peak in each of the mixtures are compared to those in the spectrum of neat [C_4mim]Cl. Thus, upon addition of powder cellulose, the chemical shift of the chloride changed downfield, whereas for the fibrous cellulose, the chemical shift moved upfield. This result was unexpected because, in principle, the same field change was expected for both types of cellulose.

Avent *et al.* [275a] related an upfield chemical shift to the cation-anion interactions in an IL (*e.g.*, $[C_2mim]Cl$) being broken due to the dissociation of the IL in a solvent (*e.g.*, acetonitrile). This theory could be applied for the dissolution of cellulose in the IL, $[C_4mim]Cl$, since, as cellulose is dissolved in the IL, new hydrogen bonds are created between cellulose and IL and the cation-anion association in the IL is broken. Therefore, the upfield chemical shift of the fibrous cellulose could relate to the fact that this type of cellulose is easier to dissolve than the powder cellulose, that seemed not completely dissolved. In the case of the quantity added for both cellulose types, when 10 wt % of the cellulose was added the chemical shift moved upfield for both cellulose, so it may be established that with this quantity of cellulose the behaviour is more pronounced due to the increase in the concentration of the biopolymer-ionic liquid interactions.

After the cellulose was dissolved in the IL solvent, $[C_4mim]Cl$, changes in the line width were also observed, which are related to a physical change (*e.g.* viscosity or mobility), rather than chemical. The nuclear relaxation becomes slower (smaller linewidth) as the solution becomes less viscous [200]. Accordingly, when both cellulose types were added the resultant mixture seemed to be less viscous because the line width is smaller than in the case of the neat $[C_4mim]Cl$.

Table 3.7 Chemical shift and line width of the chloride peaks by ^{35}Cl NMR spectroscopy obtained from the samples of neat $[C_4mim]Cl$ and its mixture with cellulose. The peak under study corresponded to the chloride in the IL solvent $[C_4mim]Cl$. The chemical shift of the peak was chosen as the highest point of the peak and, in the case of the line width, it was the difference in the frequency width of the peak

Sample	^{35}Cl NMR chemical shift δ / ppm	Line width / kHz
Neat $[C_4mim]Cl$	42.86	10.23
$[C_4mim]Cl$ + 5 wt % powder cellulose	47.96	6.17
$[C_4mim]Cl$ + 10 wt % powder cellulose	42.76	6.41
$[C_4mim]Cl$ + 5 wt % fibrous cellulose	38.01	7.74
$[C_4mim]Cl$ + 10 wt % fibrous cellulose	35.74	7.34

Figure 3.18 shows the ^{35}Cl NMR spectra of different IL solvent-fibrous cellulose-IL plasticiser mixtures. Changes in the chloride peak position of the $[C_4mim]Cl$, used as a solvent, were monitored when the hydrophobic IL plasticisers were added to the mixture. From the spectra, there are several changes in the chemical shift and in the line width of the chloride peak in the different samples.

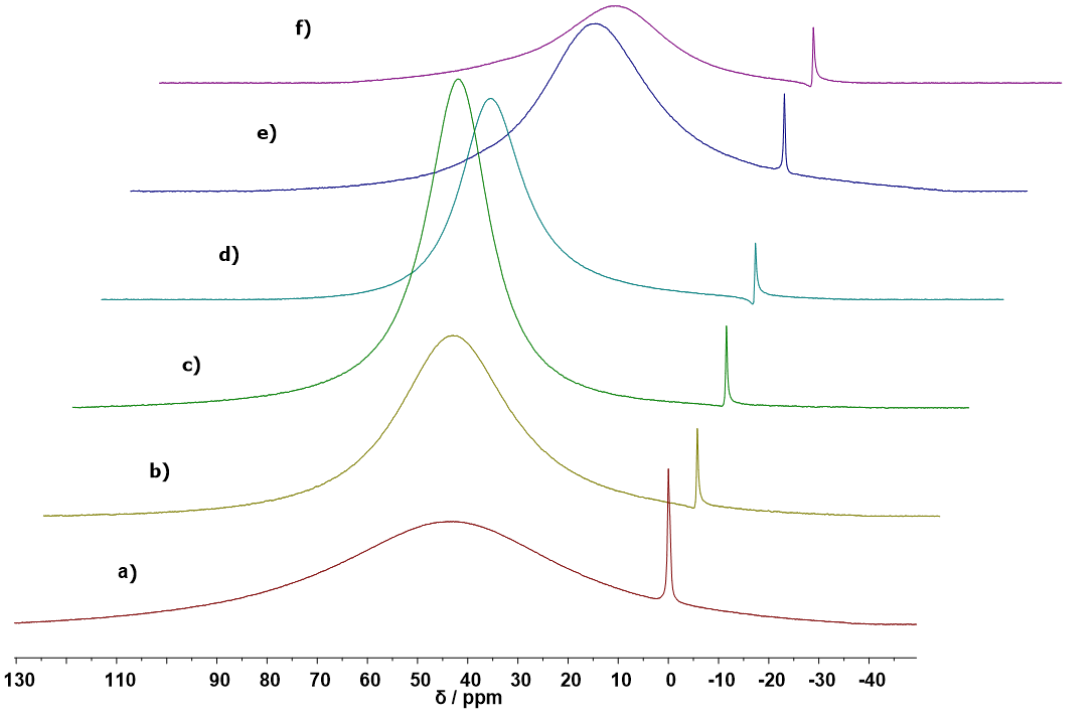

Figure 3.18 Stacked ^{35}Cl NMR spectra of a) IL solvent $[C_4mim]Cl$, b) IL plasticiser $[P_{6\,6\,6\,14}]Cl$, c) 10 wt % of $[P_{6\,6\,6\,14}]Cl$ in $[C_4mim]Cl$, d) 10 wt % of $[P_{6\,6\,6\,14}][NTf_2]$ in $[C_4mim]Cl$ e) 10 wt % of fibrous cellulose and 10 wt % of $[P_{6\,6\,6\,14}]Cl$ in $[C_4mim]Cl$ and f) 10 wt % of fibrous cellulose and 10 wt % of $[P_{6\,6\,6\,14}][NTf_2]$ in $[C_4mim]Cl$

The chemical shift and line width values of the samples from Figure 3.18 are summarised in Table 3.8. For a better understanding Figure 3.19 compares the ^{35}Cl NMR spectra of the $[C_4mim]Cl$ + 10 wt % fibrous cellulose mixture and the two plasticiser mixtures of: $[C_4mim]Cl$ + 10 wt % fibrous cellulose + 10 wt % $[P_{6\,6\,6\,14}]Cl$ and $[C_4mim]Cl$ + 10 wt % fibrous cellulose + 10 wt % $[P_{6\,6\,6\,14}][NTf_2]$. As it can be seen, the peak in the plasticiser mixtures (blue and red plots) moved downfield in comparison to the $[C_4mim]Cl$ + 10 wt % fibrous cellulose mixture (green). In the view of this downfield movement of the Cl^- peak, from the $[C_4mim]Cl$, in comparison to the fibrous cellulose-IL solvent mixture, it can be said that the IL plasticiser had a chemical influence in the Cl^- of the under study. The environment of the Cl^-, from the $[C_4mim]Cl$, changed because the other ILs, $[P_{6\,6\,6\,14}]Cl$ and $[P_{6\,6\,6\,14}][NTf_2]$, were part of the cellulose matrix. This downfield movement indicates that an interaction between the IL plasticiser and the cellulose takes place that makes the cation-anion interaction in the $[C_4mim]Cl$ stronger because it is less bonded to the cellulose. As it was explained in section 3.3.2 when the thermal analysis of the cellulose films containing IL plasticiser

was carried out, there was an interaction between IL plasticiser and cellulose which increased the decomposition temperature of the composite films obtained.

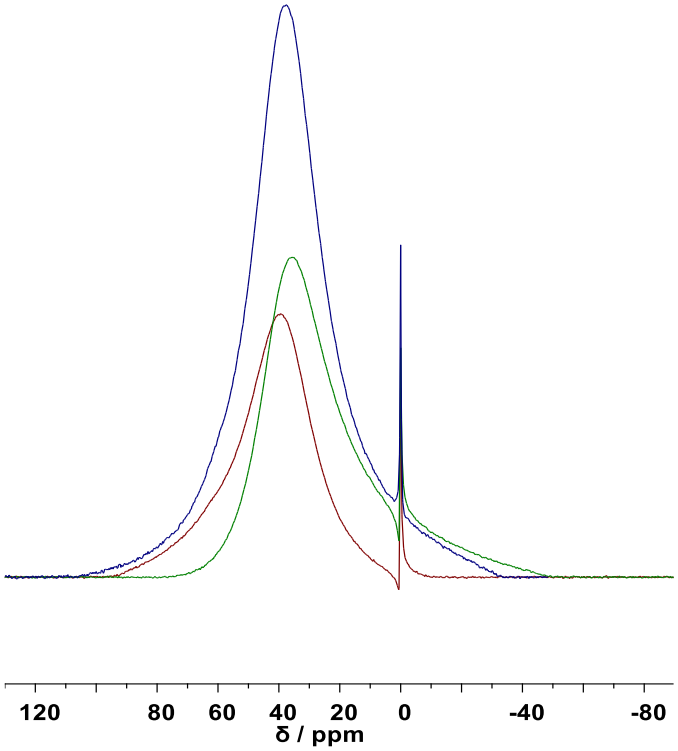

Figure 3.19 Overlaid ^{35}Cl NMR spectra of 10 wt % fibrous cellulose in [C_4mim]Cl (green); 10 wt % of fibrous cellulose and 10 wt % of [$P_{6\,6\,6\,14}$]Cl in [C_4mim]Cl (blue) and, 10 wt % of fibrous cellulose and 10 wt % of [$P_{6\,6\,6\,14}$][NTf_2] in [C_4mim]Cl (red)

Table 3.8 Chemical shift and line width of the chloride peaks by ^{35}Cl NMR spectroscopy obtained from the samples of neat [C_4mim]Cl and its mixture with cellulose and IL plasticisers. The reference peak was corresponding to the chloride in the IL solvent [C_4mim]Cl

Sample	^{35}Cl NMR chemical shift δ / ppm	Line width / kHz
Neat [C_4mim]Cl	42.86	10.23
Neat [$P_{6\,6\,6\,14}$]Cl	47.34	9.73
[C_4mim]Cl + 10 wt % [$P_{6\,6\,6\,14}$]Cl	53.40	8.19
[C_4mim]Cl + 10 wt % [$P_{6\,6\,6\,14}$][NTf_2]	52.77	6.56
[C_4mim]Cl + 10 wt % fibrous cellulose	35.74	7.34
[C_4mim]Cl + 10 wt % fibrous cellulose + 10 wt % [$P_{6\,6\,6\,14}$]Cl	37.68	8.37
[C_4mim]Cl + 10 wt % fibrous cellulose + 10 wt % [$P_{6\,6\,6\,14}$][NTf_2]	39.50	6.23

Another important point is related to the line width of the peaks. If both, [C_4mim]Cl-10 wt % fibrous cellulose-10 wt % [$P_{6\,6\,6\,14}$]Cl and [C_4mim]Cl-10 wt % fibrous cellulose-10 wt % [$P_{6\,6\,6\,14}$][NTf_2], mixtures are compared it can be seen that

the line width value of the mixture using 10 wt % $[P_{6\,6\,6\,14}][NTf_2]$ as plasticiser is smaller in comparison with the mixture using 10 wt % $[P_{6\,6\,6\,14}]Cl$. The reason of this can be attributed to a decrease in the viscosity of the mixture when $[P_{6\,6\,6\,14}][NTf_2]$ was added due to its lower viscosity (453.64 mPa s at 25 ºC) [276] in comparison to $[P_{6\,6\,6\,14}]Cl$ (1683 mPa s at 25 ºC) [277].

As it was pointed out above, there was a change in the ^{35}Cl NMR peak when the IL plasticiser was added to the $[C_4mim]Cl$-10 wt % fibrous cellulose mixture. To determine which, the cation or anion from the plasticisers, were interacting with the cellulose, another experiment was carried out. As the cation, $[P_{6\,6\,6\,14}]^+$, was the same for both plasticisers, ^{31}P NMR spectroscopy was chosen to study any interaction involving the cations, as it is shown in Figure 3.20. The singlets for the neat IL, $[P_{6\,6\,6\,14}]Cl$ and $[P_{6\,6\,6\,14}][NTf_2]$, corresponded to the phosphorous from $[P_{6\,6\,6\,14}]^+$ and were accompanied by minor satellites (36.50 ppm) as a result of ^{13}C-^{31}P coupling to the α-carbon [266].

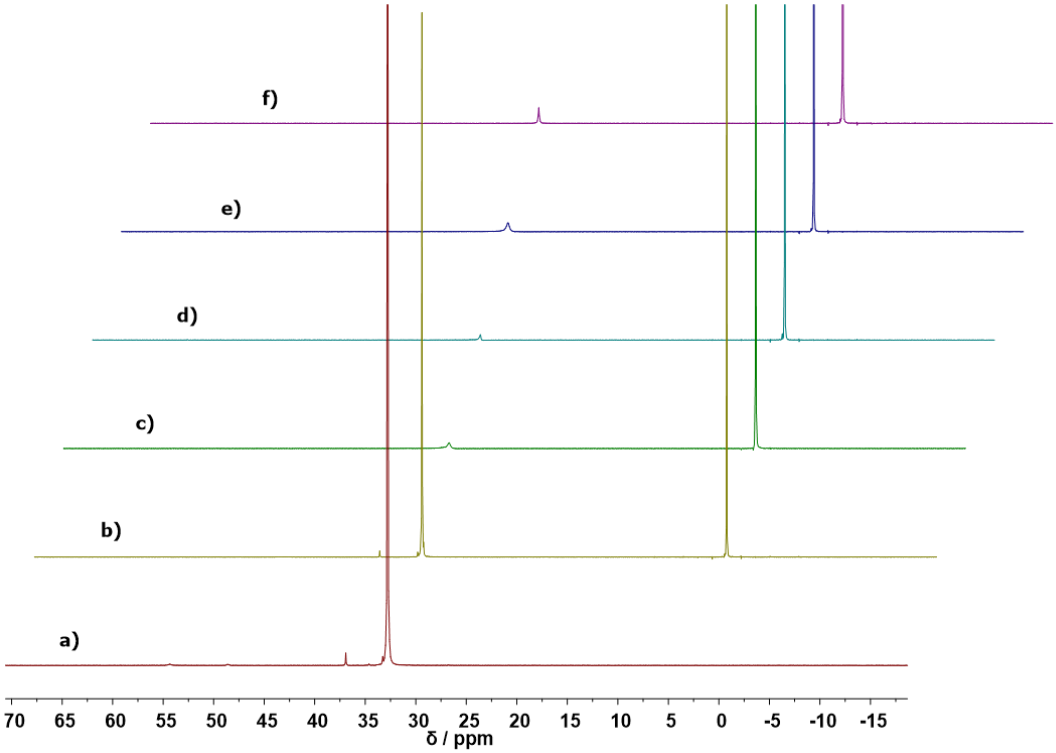

Figure 3.20 Stacked ^{31}P NMR spectra of a) IL plasticiser $[P_{6\,6\,6\,14}]Cl$, b) IL plasticiser $[P_{6\,6\,6\,14}][NTf_2]$, c) 10 wt % of $[P_{6\,6\,6\,14}]Cl$ in $[C_4mim]Cl$, d) 10 wt % of $[P_{6\,6\,6\,14}][NTf_2]$ in $[C_4mim]Cl$, e) 10 wt % of fibrous cellulose and $[P_{6\,6\,6\,14}]Cl$ in $[C_4mim]Cl$ and f) 10 wt % of fibrous cellulose and $[P_{6\,6\,6\,14}][NTf_2]$ in $[C_4mim]Cl$

From Table 3.9 it can be assumed that the cation, $[P_{6\,6\,6\,14}]^+$, is not interacting with the cellulose or $[C_4mim]Cl$ due to the fact that the phosphorous chemical shift of

the plasticisers did not change from the neat ILs to the mixtures. Therefore, if there is any interaction among the ILs plasticisers and the other compounds may be due to the interaction of the plasticisers anions, Cl^- or $[NTf_2]^-$.

Table 3.9 ^{31}P NMR chemical shift obtained for the IL plasticisers and their mixtures with $[C_4mim]Cl$ and fibrous cellulose

Sample	^{31}P NMR chemical shift δ / ppm
Neat $[P_{6\,6\,6\,14}]Cl$	32.78
Neat $[P_{6\,6\,6\,14}][NTf_2]$	32.26
$[C_4mim]Cl$ + 10 wt % $[P_{6\,6\,6\,14}]Cl$	32.45
$[C_4mim]Cl$ + 10 wt % $[P_{6\,6\,6\,14}][NTf_2]$	32.22
$[C_4mim]Cl$ + 10 wt % fibrous cellulose + 10 wt % $[P_{6\,6\,6\,14}]Cl$	32.35
$[C_4mim]Cl$ + 10 wt % fibrous cellulose + 10 wt % $[P_{6\,6\,6\,14}][NTf_2]$	32.18

To summarise, ^{35}Cl NMR data indicated that the fibrous cellulose was easier to dissolve in $[C_4mim]Cl$ than the powder cellulose. In terms of interaction among the three components in the mixture, it can be said that the IL plasticiser interacts with the cellulose, competing with the $[C_4mim]Cl$.

3.5. Chemical Polymerisation of Pyrrole

Polypyrrole was chosen as the electronically conducting polymer, because of its high electrical conductivity [206], low toxicity, biocompatibility [58] and relatively low cost [207], as it was described in section 2.3.1. Polypyrrole was synthesised by chemical polymerisation, based on the coupling between radical cations, as explained in section 2.3.1.

The chemical polymerisation of pyrrole in methanol with different oxidants was carried out first in order to understand the behaviour of the electronically conducting polymer before synthesising it using ionic liquids as solvents. The two oxidants chosen were anhydrous iron (III) chloride and ammonium persulfate.

3.5.1. Methodology to Obtain Powder Polypyrrole Using Iron (III) Chloride as the Oxidant

To carry out the polymerisation of pyrrole using anhydrous iron (III) chloride as the oxidant, three methods were followed; all of them are described in the literature [278]. The different conditions used for each procedure are shown in Table 3.10.

Table 3.10 Procedures followed to synthesise the ECP polypyrrole showing the quantities and conditions utilised

Procedure name	Pyrrole / mL	Oxidant iron (III) chloride / g	Solvent	Temperature / ºC	Time of reaction / h
A	0.45	0.06	methanol (5 mL)	25	17
B	1	0.046	H_2O pH 3-4 (10.5 mL)	25	48
C	1	5.728	methanol (15 mL)	0-5	1

The general procedure followed for these syntheses consisted of dissolving the monomer pyrrole in methanol. Then, anhydrous iron (III) chloride was added to the mixture stirred at the required temperature during the time shown in Table 3.10. In all the cases, the solution turned to a dark green colour immediately, which can be due to oligomerisation taking place prior to the final polymerisation when PPy turned to a black precipitate [279]. The black precipitate formed was filtered and washed with 15 mL of methanol and 15 mL of water until the washed solution was colourless, which was interpreted as an indication that all the oxidant had been eliminated. However, EDX results (see section 3.5.3) showed that there were traces of oxidant still remaining in the powder polypyrrole. The black powder (Figure 3.21) was dried in an oven (75 ºC) for 4 hours.

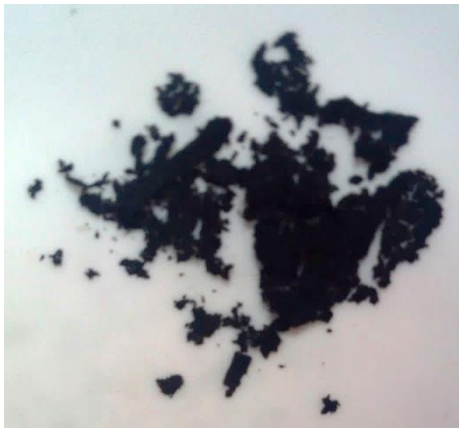

Figure 3.21 Picture of the powder polypyrrole obtained using anhydrous iron (III) chloride as the oxidant

3.5.2. Methodology to Obtain Powder Polypyrrole Using Ammonium Persulfate as the Oxidant

The procedure followed earlier for the chemical polymerisation of pyrrole consisted of using anhydrous iron (III) chloride as the oxidant. To avoid the use of

corrosive chemicals, like iron (III) chloride anhydrous, in the films, a common organic and milder oxidant was chosen: ammonium persulfate (APS), $(NH_4)_2S_2O_8$. To obtain a doped polypyrrole a radical coupling mechanism showed in Figure 3.22 is proposed. As dopant precursor, benzenesulfonic acid (BSA), was used so that the dopant will be benzenesulfonate (BS) (structure shown in Figure 3.33) [207].

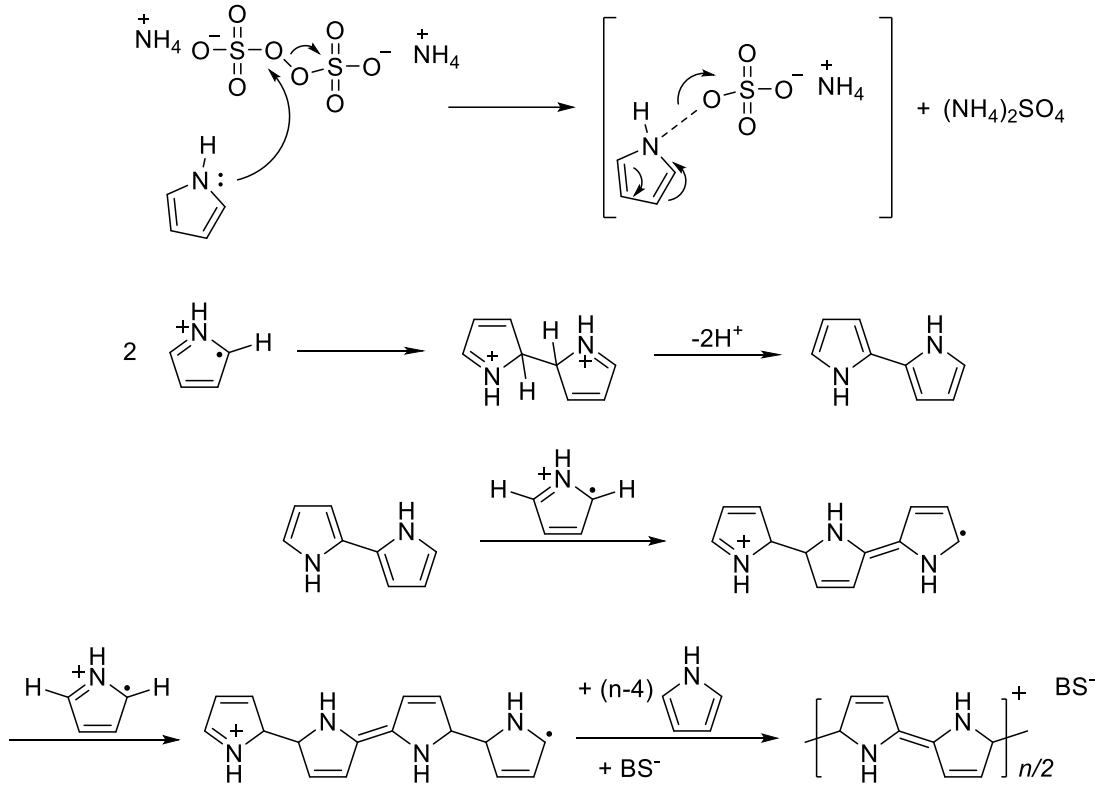

Figure 3.22 Radical coupling mechanism proposed for the chemical polymerisation of pyrrole using APS as the oxidant and BS as the dopant

The procedure followed consisted of adding 0.1065 g (0.047 mmol) of APS and 0.2280 g (1.44 mmol) of benzenesulfonic acid over 5 mL of methanol that was previously immersed in an ice bath, and the mixture was stirred for 30 minutes. Water (1 mL) was added to help the oxidant dissolution. After the oxidant was completely dissolved, 1 mL of pyrrole was added. The solution was stirred slowly for 1 hour in an ice bath and for another hour at room temperature. When pyrrole was added, the solution turned from colourless to green and finally to black obtaining a black powder that was filtered and washed with methanol and water. Finally, the polypyrrole obtained was dried in air and then stored in a vacuum desiccator with phosphorous pentoxide as the desiccant.

When pyrrole was added to the oxidant/dopant precursor solution, it was possible to observe that the polymerisation was slower than in the case of using iron (III) chloride, the solution turned from colourless to green in 20 min and in about 1 hour the solution turned black.

Figure 3.23 Picture of the powder polypyrrole obtained using ammonium persulfate as the oxidant and benzenesulfonate as the dopant

3.5.3. Characterisation of Powder Polypyrrole

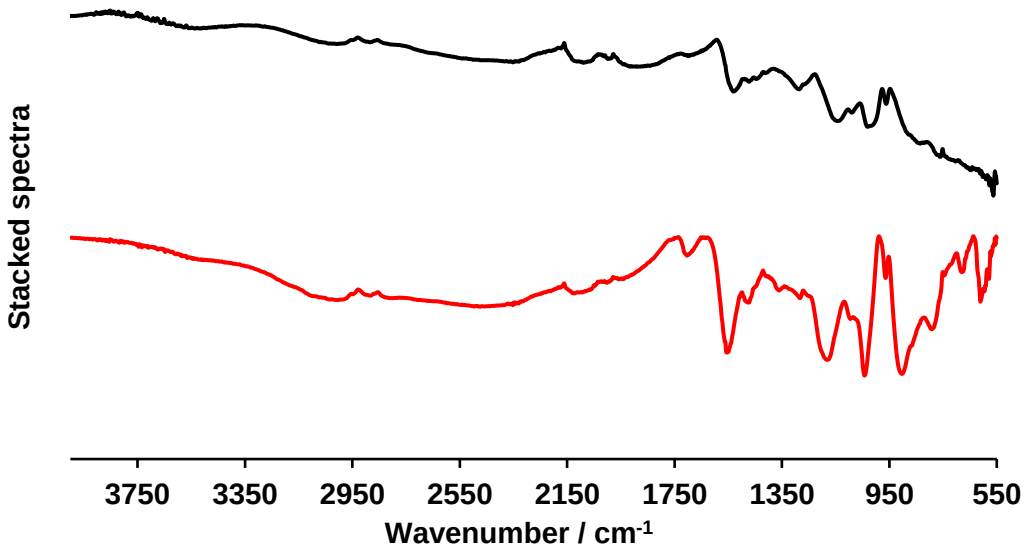

Figure 3.24 Infrared spectra of powder polypyrrole using anhydrous iron (III) chloride as the oxidant (black) and powder polypyrrole using APS as the oxidant and BS as the dopant (red)

Infrared spectroscopy was used to characterise the molecular structure of the polypyrrole synthesised in the previous section.

Figure 3.24 shows the infrared spectra of the polypyrrole powder obtained from each of the two methods described above. The black plot corresponds to the polypyrrole using anhydrous iron (III) chloride as the oxidant and the red plot

corresponds to the polypyrrole using ammonium persulfate as oxidant and benzenesulfonic acid as the dopant precursor.

The assignments of the polypyrrole peaks are reported in Table 3.11. Mainly the infrared spectra exhibited strong peaks in the region 1750 – 800 cm^{-1} where the pyrrole ring stretching and bending vibrations can be found. In the case of the polypyrrole doped with benzenesulfonate (BS) (red plot), it was possible to identify the characteristic O=S=O stretching band at 914 cm^{-1} due to the phenyl ring attached with a sulfonate group. As expected, this band does not appear in the infrared spectrum corresponded to the polypyrrole (black plot) [207,237]. Another important peak related to the oxidised state of the polypyrrole can be found around 1700 cm^{-1}. This peak is assigned to the C=O stretching, and results from an overoxidation of polypyrrole during the polymerisation, as it is shown in Figure 3.25 [280]. This peak suggests the overoxidation of the polypyrrole chain that could lead to a decrease in the conductivity of the ECP as it was discussed in section 1.5.1.3.2 [280b].

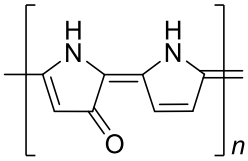

Figure 3.25 α, β-unsaturated ketones formed in the polypyrrole chain as a result of oxidation at the β'-position of the pyrrole

Table 3.11 Infrared peak assignments of the powder polypyrrole

Polypyrrole using APS as oxidant and BS as dopant / cm^{-1}	Polypyrrole using anhydrous iron (III) chloride as oxidant / cm^{-1}	Bonds vibrations
3000	3000	CH_2 asymmetric and symmetric stretching
1705		Oxidised state polypyrrole (C=O stretching)
1550	1532	C=C stretching ring
1475	1437	C-N stretching ring
1199	1161	C-N in-plane ring deformation and bending
1037	1000	C-H and N-H deformation
914		O=S=O stretching phenyl group substituted by a sulfonic acid group

The Raman spectra of the polypyrrole were also carried out (Figure 3.26). The most important peaks for the characterisation of PPy were found in the range between 800 – 1800 cm^{-1}. Table 3.12 displays the Raman shift assignments for PPy done by comparison to that found in the literature [281].

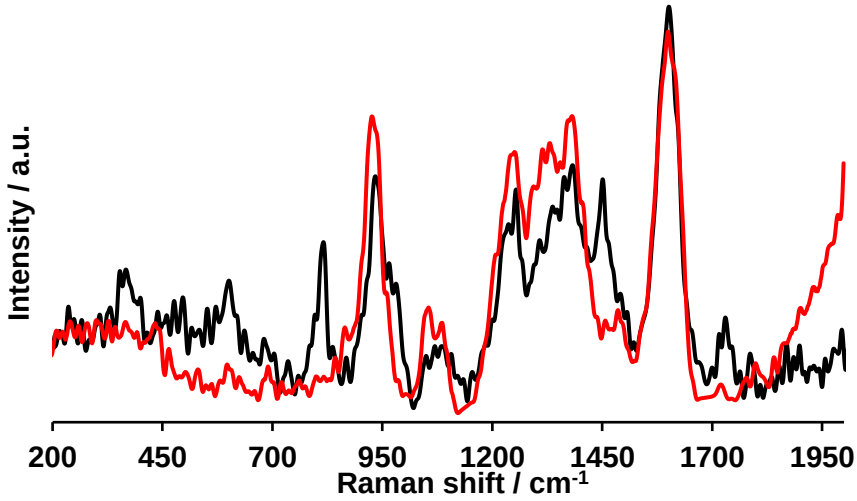

Figure 3.26 Raman of PPy using APS as the oxidant and BS as the dopant (red) and PPy using anhydrous iron (III) chloride as the oxidant (black); Spectra normalised and re-plotted using Spectrogryph

According to the literature [281a], the position of the C=C backbone stretching band was found in PPy can be used to differentiate between PPy in oxidised and reduced state; when the peak is located at approximately 1560 cm^{-1} the PPy is in its reduced state (de-doped) and when the peak is at 1650 cm^{-1} the PPy is oxidised (doped). In the case of the PPy synthesised with both methods, the peak appeared at 1599 cm^{-1} using APS as the oxidant and BS as the dopant, and at 1606 cm^{-1} using anhydrous iron (III) chloride as the oxidant. Hence, it seems that both PPy were oxidised; PPy (red plot) had benzenesulfonate as the dopant, whereas and in the case of the other PPy (black plot), it seems that the chloride ion from the oxidant is acting as dopant. It has been reported that in PPy obtained using anhydrous iron (III) chloride as the oxidant, the Cl^- ion can be retained in the polymer backbone as dopant [207]. A further elemental characterisation was carried out using SEM/EDX techniques.

Table 3.12 Raman shift assignments for the powder polypyrrole

Polypyrrole using APS as the oxidant and BS as the dopant / cm^{-1}	Polypyrrole using anhydrous iron (III) chloride as the oxidant / cm^{-1}	Bonds
-	1733	C-C bending
1599	1606	C=C backbone stretching
1333, 1379	1376,1453	Ring stretching
1255	1253	N-H in-plane deformation
1087	1081	C-H in-plane deformation
1059	1093	Ring deformation
929	943	C-H out-of-plane deformation
-	818	C-C stretching

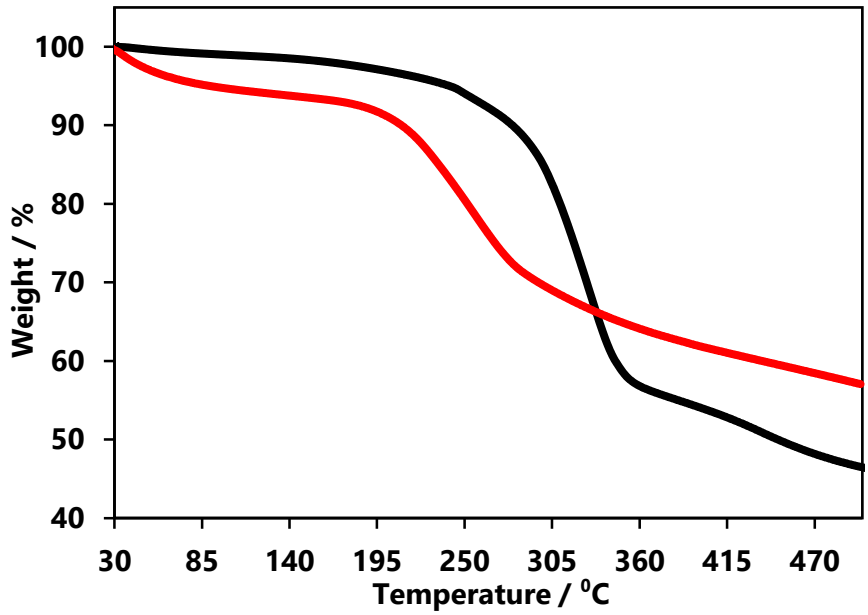

Figure 3.27 Thermogram of PPy using anhydrous iron (III) chloride as the oxidant (black) and PPy using APS as the oxidant and BS as the dopant (red)

Figure 3.27 shows the thermogram of both synthesised polypyrrole compounds. The polypyrrole obtained using iron (III) chloride as oxidant is more stable, with a decomposition temperature of 285 ºC, compared to the polypyrrole using APS as the oxidant, which decomposes at 208 ºC. These values were in agreement with the literature and the difference in the decomposition temperatures may be due to the cross-link between chain segments in the PPy using anhydrous iron (III) chloride as the oxidant [207,60b,282]. Both PPy show slow thermal degradation, but the residual mass at 500 ºC was different for each polypyrrole. In the case of the polypyrrole using APS as oxidant, the residual mass was almost 60 %, whereas the

polypyrrole using iron (III) chloride had the residual mass of about 45 %. The higher residue mass obtained for the PPy using APS as the oxidant may be due to longer chains obtained during the polymerisation process.

Figure 3.28 shows the SEM images and EDX analysis of the polypyrrole synthesised Both polypyrrole SEM pictures (Figure 3.28 (a) and (b)) showed a cauliflower structure [283], with the individual particles being nano-sized (see higher magnification pictures in the insets).

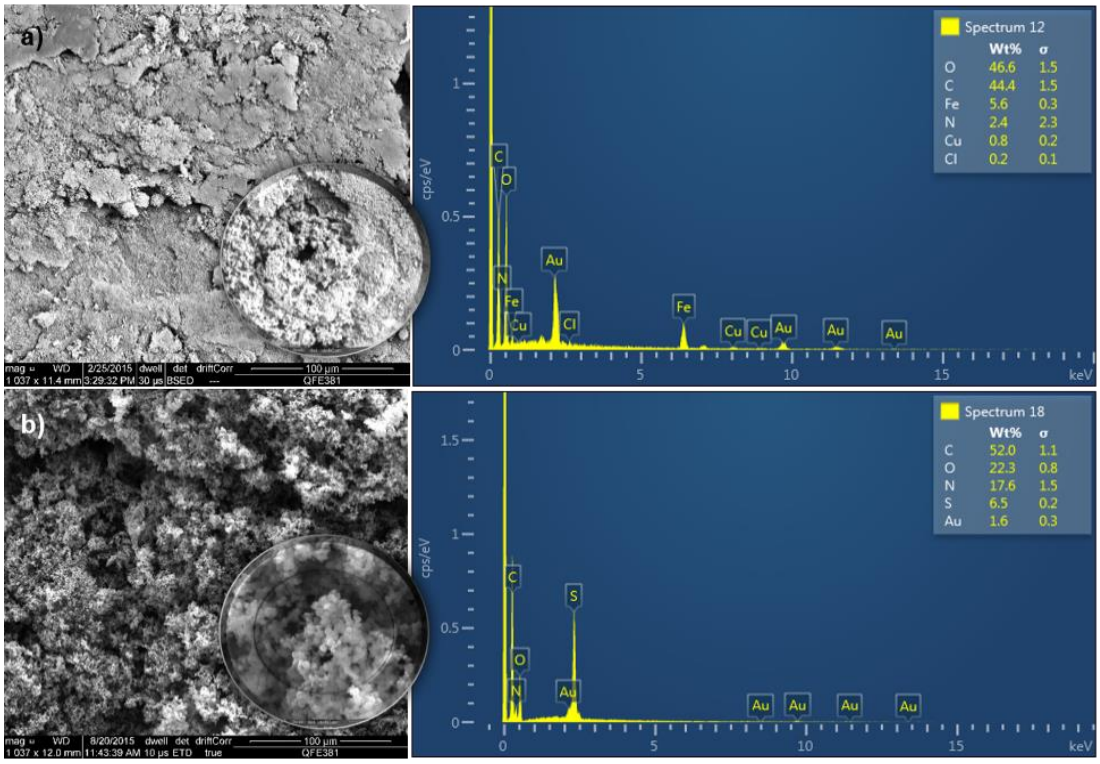

Figure 3.28 SEM pictures with magnification 1K and, EDX spectra of a) PPy using anhydrous iron (III) chloride as the oxidant and b) PPy using APS as the oxidant and BS as the dopant. (Presence of Au from sputtering and Cu from the copper tape). Higher magnification 10K SEM images are shown in the insets.

The EDX analysis shows the presence of the elements expected from the polypyrrole backbone (C and N) as well as O, Fe and Cl (Figure 3.28 (a)), which may be due to contaminants remaining, such as water and oxidant (iron (III) chloride). It seems that the elimination of water and oxidant, in this case, was more difficult than using the ammonium persulfate as the oxidant. As shown in the EDX elemental analysis in Figure 3.28 (b), elements from the oxidant, APS, seemed not to be present. The elements that can be identified are the ones corresponding to the polypyrrole (C, N) and dopant, benzenesulfonate (C, O and S).

Table 3.13 Elemental composition of the powder polypyrrole obtained using EDX

Films	C / %	O / %	N / %	S / %
PPy using anhydrous iron (III) chloride	44.4	46.6	2.4	-
PPy using APS and BS	52.0	22.3	17.6	6.5

3.6. *In situ* Polymerisation of Pyrrole in a Cellulose-IL Mixture – Evolution of Flexible Electronic Composites

3.6.1. Methodology to Obtain Cellulosefibrous Films Containing Polypyrrole

After the study of the behaviour of the cellulose in the ionic liquids and its dissolution and regeneration as free-standing films, the addition of the electronically conducting polymer chosen, polypyrrole, to convert the cellulose matrix in an electronically conducting material by binding it to an electronically conducting polymer matrix was carried out. The development of an *in situ* polymerisation of pyrrole in a cellulose-IL solvent mixture was carried out using different oxidants and dopants and variating their compositions in order to optimise the development of flexible composite electrodes.

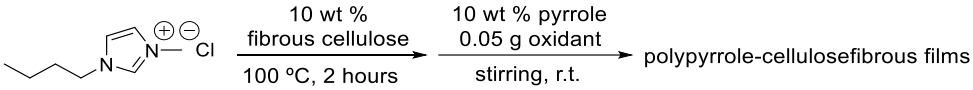

Figure 3.29 Procedure used to obtain a polypyrrole-cellulosefibrous film

Using the method described in Figure 3.29, three polypyrrole-cellulosefibrous films (PPy-cellfib films) were obtained varying the anti-solvent used to regenerate them. Therefore, after dissolving the cellulose in the IL, $[C_4mim]Cl$, as it was explained in section 3.2.1, the addition of a catalytic amount (~ 0.05 g) of the oxidant ammonium persulfate was carried out. After obtaining a homogeneous mixture, 10 wt % of pyrrole was added and mixed. The mixture changed from colourless to dark green and finally to black in approximately 30 minutes. When the mixture was totally black, three films were cast to investigate how the anti-solvent affects the regenerated films. The anti-solvents used were methanol, water and propanone. Figure 3.30 (a) shows the PPy-cellfib film using methanol as the anti-solvent and (b) the PPy-cellfib film using water and (c) the PPy-cellfib film using propanone. The use of different anti-solvents influenced the colour and flexibility of the films. From the literature, it is known that

the anti-solvent affects the precipitation of the cellulose due to its contribution to the formation of the intramolecular hydrogen bonds of the cellulose, therefore, changes in the morphology of the cellulose films obtained were expected [176b].

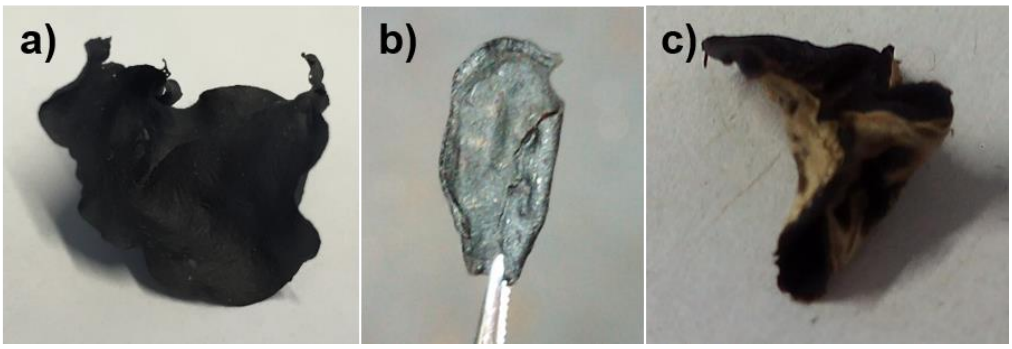

Figure 3.30 Pictures of polypyrrole-cellulosefibrous films a) using methanol, b) using water and c) using propanone as the anti-solvents

In order to improve the flexibility of the composite films, an IL plasticiser was added as it is shown in Figure 3.31. The addition of the plasticiser was carried out as explained in section 3.3.1. Two IL plasticisers were utilised, *i.e.* $[P_{6\,6\,6\,14}]Cl$ and $[P_{6\,6\,6\,14}][NTf_2]$ to check the differences between them. As shown in Figure 3.32, the addition of the IL plasticiser resulted in an increment in the flexibility of the films, which could be detected visually. Since the plasticisers used are hydrophobic compounds, the anti-solvent chosen for the regeneration of the polypyrrole-cellulosefibrous-IL plasticiser films (PPy-cellfib-PCl and PPy-cellfib-$PNTf_2$ films) was water, to avoid the dissolution of the IL plasticiser.

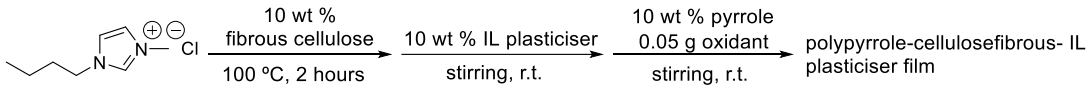

Figure 3.31 Procedure used to obtain a polypyrrole-cellulosefibrous-IL plasticiser film

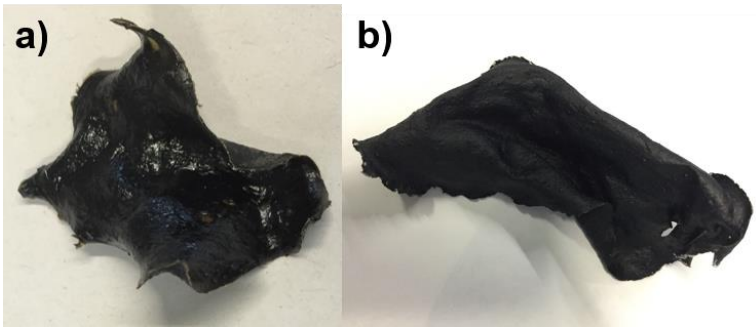

Figure 3.32 Pictures of polypyrrole-cellulosefibrous-IL plasticiser films a) using $[P_{6\,6\,6\,14}]Cl$ and b) using $[P_{6\,6\,6\,14}][NTf_2]$ as IL plasticisers

The introduction of a dopant to the polypyrrole-cellulosefibrous-IL plasticiser composite films should impart electronic conductivity along the PPy coplanar π-

conjugated system [60b]. Therefore, the addition of the dopants, (+)-camphor-10-sulfonate (ß) and benzenesulfonate was carried out as explained in the paragraph below. Figure 3.33 (a) shows the structure of the dopant (+)-camphor-10-sulfonate and Figure 3.33 (b) benzenesulfonate.

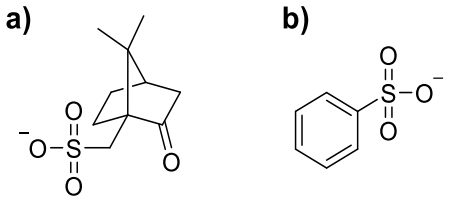

Figure 3.33 Structures of the dopant a) (+)-camphor-10-sulfonate and b) benzenesulfonate

The dissolution of cellulose in [C_4mim]Cl and the addition of the IL plasticiser was carried out as explained in section 3.3.1. After this mixture was homogeneous, at room temperature, ammonium persulfate and dopant precursor were added. The optimal dopant quantity was 0.1 mol relative to pyrrole and the oxidant was between 0.05 - 0.1 g. The mixture was stirred to homogeneity and then, 10 wt % of pyrrole was added and stirred vigorously with an overhead and ringed stirrer. The mixture was cast as described previously on page 57, using the coating machine. The regenerated film was washed several times with water and air dried at room temperature for 24 hours (Figure 3.34).

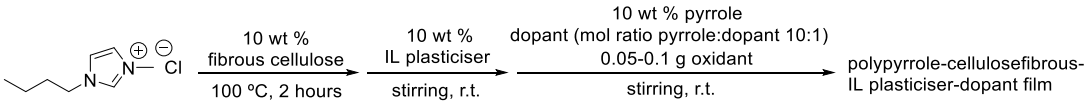

Figure 3.34 Procedure used to obtain a polypyrrole-cellulosefibrous-IL plasticiser-dopant film

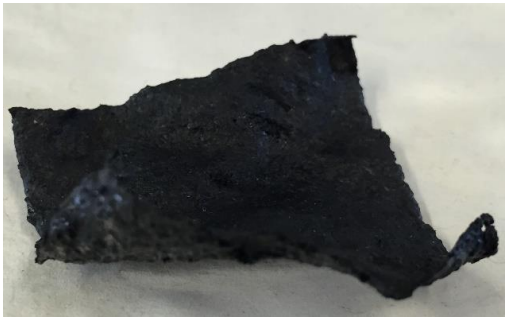

Figure 3.35 Picture of a PPy-cellfib-PCl-CS film using [$P_{6\,6\,6\,14}$]Cl (PCl) as the IL plasticiser and (+)-camphor-10-sulfonate (CS) as the dopant

Figure 3.35 shows a PPy-cellfib-IL plasticiser-dopant film in which the IL plasticiser was [$P_{6\,6\,6\,14}$]Cl (PCl) and the dopant (+)-camphor-10-sulfonate (CS). When this dopant precursor, which is a solid at r.t., was added, the mixture became very viscous and it was not possible to dissolve it in the cellulose-IL plasticiser mixture.

Therefore, the use of another dopant that can be dissolved in this mixture was required.

The other dopant precursor used was the benzenesulfonic acid (BSA). With this dopant precursor, the stirring of the mixture was much easier due to its higher solubility (visual test) in the cellulose-IL plasticiser mixture in comparison to the CSA.

Figure 3.36 shows the final process in the polymerisation of pyrrole using ammonium persulfate as the oxidant and benzenesulfonic acid (BSA) as the dopant precursor, as the film is treated in water (after casting, the film was added to the antisolvent and the regeneration process started, in less than 5 min the film was regenerated, and the polymerisation of pyrrole was just starting). Figure 3.36 (a) shows the regenerated film and the pyrrole polymerisation 10 min after immersing it in water. Figure 3.36 (b) and (c) show the last stages of the polymerisation which took place in less than 1 hour. The film was left immersed in the water for 2 hours in total to ensure that the polymerisation had finished, and all the IL solvent was washed from the film. Finally, Figure 3.36 (d) shows the PPy-cellfib-IL plasticiser-dopant film after being dried in a vacuum desiccator overnight.

To summarise, pyrrole was polymerised *in situ* in a solution of 10 wt % fibrous cellulose in the IL 1-butyl-3-methylimidazolium chloride, [C_4mim]Cl and 10 wt % of IL plasticiser [$P_{6\,6\,6\,14}$][NTf_2], ($PNTf_2$), at room temperature using ammonium persulfate as the oxidant and benzenesulfonate anion (BS) as the dopant. The solution turned dark green within two minutes of stirring and transformed to black in less than 1 hour, as it was observed when powder PPy was synthesised *i.e.* oligomerisation followed by polymerisation of pyrrole [279]. The mixture was cast into wet films of ~ 100 µm thickness using a coating machine and washed with water to remove the [C_4mim]Cl ionic liquid solvent. Shiny black flexible films were obtained, washed with water several times to remove any residual ammonium persulfate, dried in air followed by drying in a vacuum desiccator overnight to obtain a PPy-cellfib-$PNTf_2$-BS film.

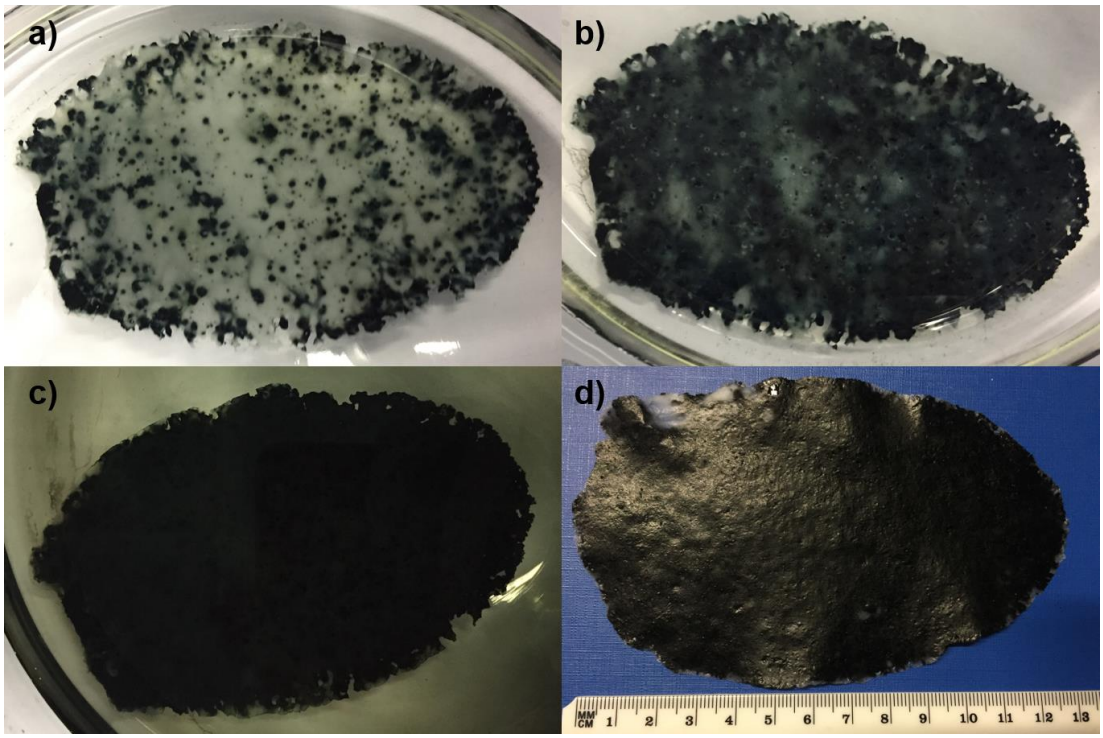

Figure 3.36 Pictures of a PPy-cellfib-IL plasticiser-dopant film using $[P_{6\,6\,6\,14}][NTf_2]$, ($PNTf_2$) as the IL plasticiser and) benzenesulfonate (BS) as the dopant, a) after 10 min immersed in water (anti-solvent), b) after 1 hour in the water, c) after 2 hours in the water and d) after overnight drying process in a vacuum desiccator

3.6.2. Characterisation of Cellulosefibrous Films Containing Polypyrrole

The first characterisation test carried out to the PPy-cellfib films was an "Adhesion by Tape Test" (ASTM D3359). Polypyrrole impregnated onto a flexible material like paper, fails this "Adhesion by Tape Test", as the film peels off, indicating that it is a non-homogeneous material, as it is shown in Figure 3.37 (a). In the films prepared herein, as polypyrrole and cellulose are chemically blended to each other during the preparation process, chemically homogeneous films were produced. When tested using the "Adhesion by Tape Test" the composites films did not stick to the tape as it is shown in Figure 3.37 (b). This indicated that polypyrrole was naturally bound to the cellulose matrix and, therefore, the surface was homogeneous and uniform.

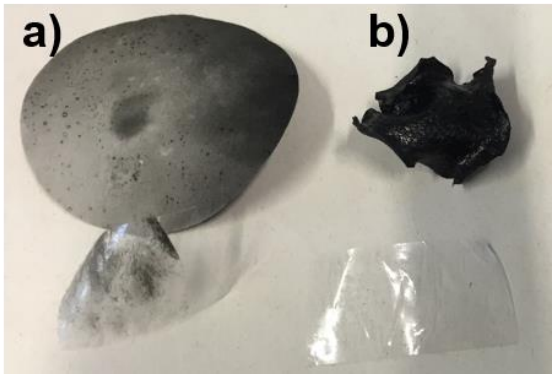

Figure 3.37 Adhesion by Tape Test a) polypyrrole-grafted on a laboratory filter paper and b) a polypyrrole-cellulosefibrous film

Figure 3.38 shows the spectra of five different composite films obtained comprising of different components to study the main differences among them: (a) PPy-cellfib film, (b) PPy-cellfib-PCl film, (c) PPy-cellfib-$PNTf_2$ film, (d) PPy-cellfib-PCl-CS film and (e) PPy-cellfib-$PNTf_2$-BS film.

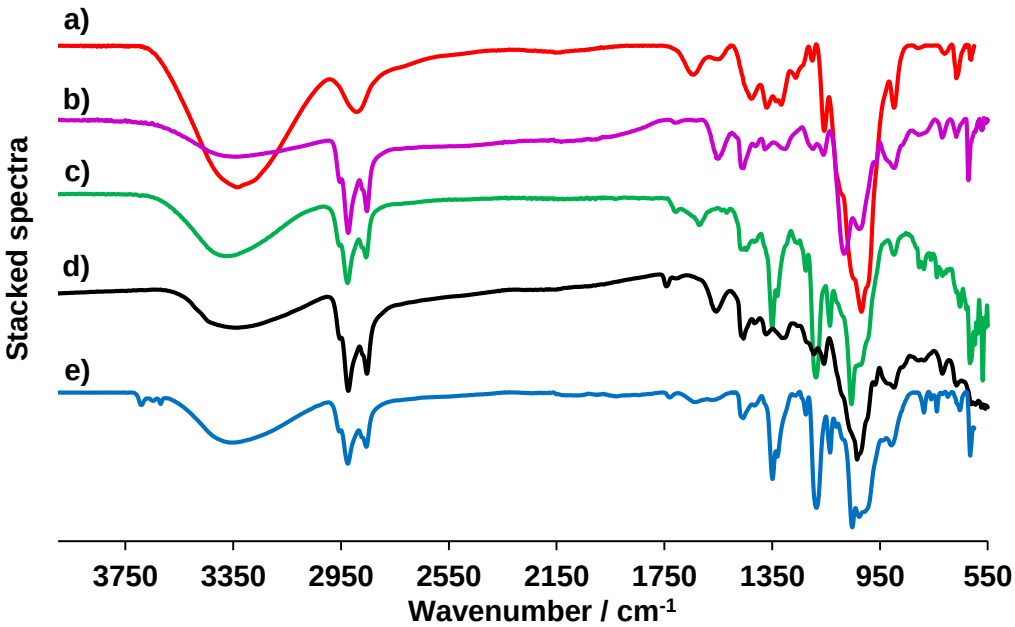

Figure 3.38 Infrared spectra of a) PPy-cellfib film (red), b) PPy-cellfib-PCl film (purple), c) PPy-cellfib-$PNTf_2$ film (green), d) PPy-cellfib-PCl-CS film (black) and e) PPy-cellfib-$PNTf_2$-BS film (blue)

The infrared spectra of the cellulosefibrous composite films containing polypyrrole, Figure 3.38, were analysed by comparison with the IR spectra previously assigned for the cellulosefibrous films in section 3.2.2, cellulosefibrous-IL plasticiser films in section 3.3.2 and powder polypyrrole in section 3.5.3, as well as with literature data. The peaks values and their assignment are shown in Table 3.14

[280a,259,207,280b,269,237]. It was possible to identify the main peaks corresponding to the cellulose, IL plasticisers ([$P_{6\,6\,6\,14}$]Cl and [$P_{6\,6\,6\,14}$][NTf_2]), polypyrrole and dopants.

The peak corresponding to the C=C stretching of the polypyrrole ring showed a blue shift in the cellulosefibrous composite films containing polypyrrole (1566, 1556, 1613, 1562 and 1575 cm^{-1}) in comparison to the powder polypyrrole (1551 cm^{-1}, Table 3.11). This blue shift may be due to the hydrogen bond interaction between the N-H of the pyrrole ring and the O-H of the cellulose moiety [184b,284].

Other important peaks identified were the ones corresponding to the dopants (+)-camphor-10-sulfonate and benzenesulfonate. The sulfonate functional group, present in both dopants, gives rise to an O=S=O stretching band at 921 and 932 cm^{-1} for PPy-cellfib-PCl-CS film (black plot) and PPy-cellfib-$PNTf_2$-BS film (blue plot), respectively. In the case of the PPy-cellfib-$PNTf_2$-BS film, there are three peaks at 3686, 3641 and 3617 cm^{-1}. These peaks were seen just in this film, when the dopant benzenesulfonate was combined with the polypyrrole, the ionic liquid plasticiser, [$P_{6\,6\,6\,14}$][NTf_2], and the cellulose. Several IR spectra with the same three peaks were found in the literature, but none of the articles commented on them [285]. The IR spectrum of benzenesulfonate was found in the literature, but it showed no peaks around 3600 cm^{-1} [286]. Therefore, the assignment of these three peaks was not quite clear. Given their high wavenumber, it is hypothesised that they may be related to hydrogen bond interactions between this specific dopant and the water absorbed by the composite film; this unusual hydrogen bonding has been described between water and single-walled carbon nanotubes by Byl *et al.* [287] in 2006.

Table 3.14 Infrared peak assignments of the cellulosefibrous films containing polypyrrole

a) / cm^{-1}	b) / cm^{-1}	c) / cm^{-1}	d) / cm^{-1}	e) / cm^{-1}	Bonds
3321	3339	3378	3339	3347	OH stretching (cellulose) and N-H stretching (polypyrrole)
2881	2920, 2831	2921, 2854	2919, 2851	2922, 2855	Asymmetric and symmetric C-H stretching
	1710	1701	1738	1731	Oxidised state polypyrrole (C=O stretching)
1566	1556	1613	1562	1575	C=C stretching ring (polypyrrole)
1421	1453	1462	1457	1454	CH_2 symmetric bending
		1341		1351	S=O asymmetric stretching ($[P_{6\,6\,6\,14}][NTf_2]$)
		1183		1181	S=O symmetric stretching ($[P_{6\,6\,6\,14}][NTf_2]$)
1137	1156	1134	1160	1138	C-N in-plane ring deformation and bending (polypyrrole)
1096	1076	1077	1039	1054	C-H and N-H deformation (polypyrrole)
1023	1019	1019	1039	1000	C-OH, C-C, C-H ring and side group vibrations (cellulose)
			921	932	O=S=O stretching of a sulfonic acid group (dopant)
894	893	894	894	901	Asymmetric in-phase ring stretching (cellulose)

Raman spectroscopy revealed peaks related to the cellulose, IL plasticisers and polypyrrole as it can be seen in Figure 3.39 and Figure 3.40. In both graphs, the same characteristic three peaks from 1200 to 1800 cm^{-1} were obtained for all the cellulose composite films containing polypyrrole. These three peaks at 1350 cm^{-1}, 1600 cm^{-1} and 1730 cm^{-1} are related to the PPy ring stretching, the C=C backbone stretching and the PPy, cellulose and IL plasticiser C-C bending, respectively. The shape of these three peaks was different in comparison to the powder polypyrrole shown in section 3.5.3. This change can be related to the chemical blending between the polypyrrole and the cellulose which was also visualised in the infrared spectra (Figure 3.38).

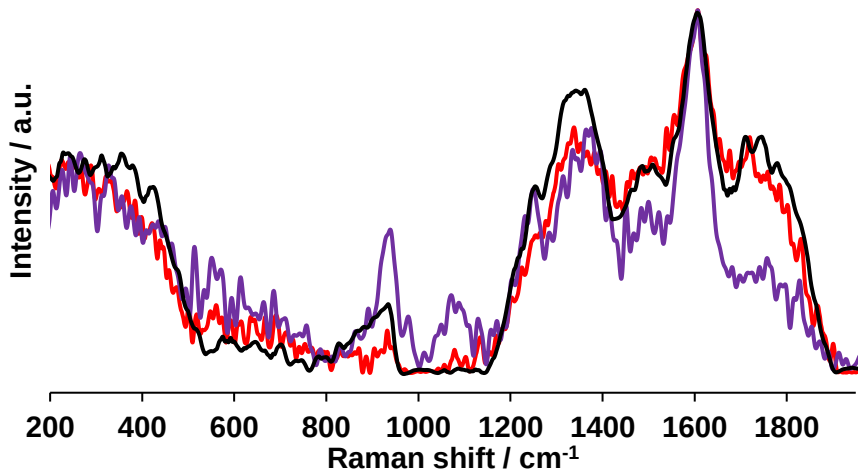

Figure 3.39 Raman spectra of PPy-cellfib film (red), PPy-cellfib-PCl film (purple) and PPy-cellfib-PCl-CS film (black)

In the case of the dopants added to the PPy-cellfib-PCl-CS film (black plot, Figure 3.39) and PPy-cellfib-$PNTf_2$-BS film (blue plot, Figure 3.40), no peaks related to them were found. Most of the Raman peaks from these dopants could have been hidden by the cellulose, polypyrrole and IL plasticiser peaks *e.g.* at 600 cm^{-1} SO_3 bending, at 990 cm^{-1} the C-C aromatic ring BS and at 1600 cm^{-1} the C-CH ring stretching from BS or the C=O from CS [288].

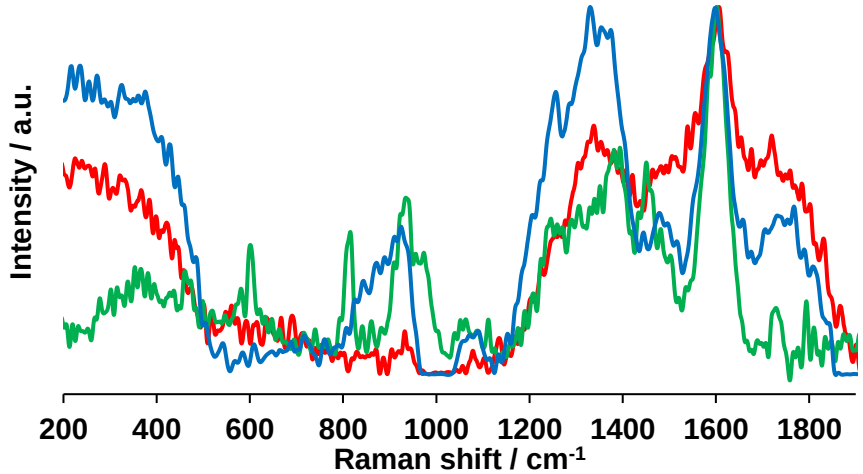

Figure 3.40 Raman spectra of PPy-cellfib film (red), PPy-cellfib-$PNTf_2$ film (green) and PPy-cellfib-$PNTf_2$-BS film (blue)

Decomposition temperatures of these cellulose films containing polypyrrole films were between 210 ºC and 279 ºC, demonstrating that the addition of polypyrrole without or with dopant provided thermally stable films. Figure 3.41 shows thermograms for the PPy-cellfib-PCl film and PPy-cellfib-PCl-CS films and Figure 3.42

displays those for the PPy-cellfib-$PNTf_2$ and PPy-cellfib-$PNTf_2$-BS films. In both figures, the thermograms for the PPy-cellfib film it is also included for comparison. The thermal degradation among the films is different. The PPy-cellfib film showed the lowest decomposition temperature, in contrast, it showed the highest residual mass left at 500 ºC, with a gradual degradation that suggests decomposition of the polypyrrole backbone, which decomposes around 800 ºC [289].

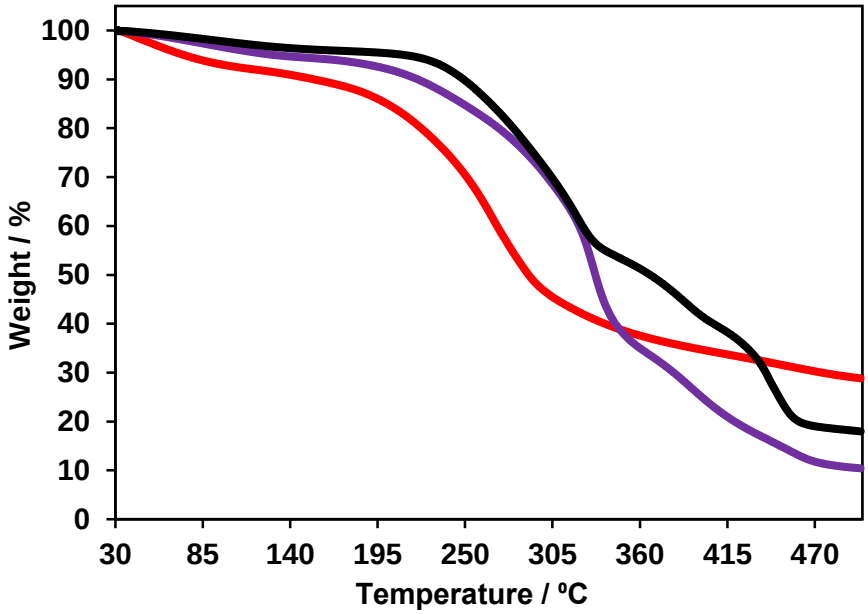

Figure 3.41 Thermogram of PPy-cellfib film (red), PPy-cellfib-PCl film (purple) and PPy-cellfib-PCl-CS film (black)

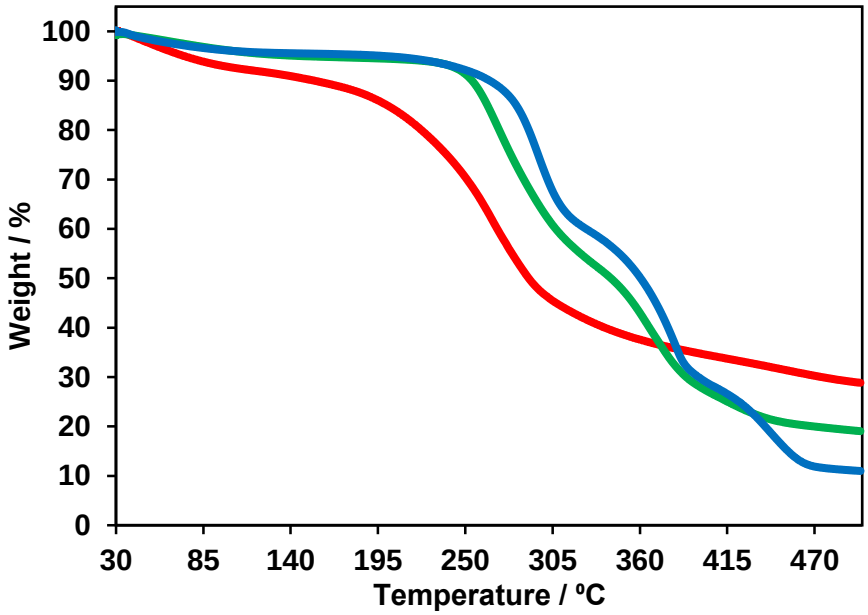

Figure 3.42 Thermogram of PPy-cellfib film (red), PPy-cellfib-$PNTf_2$ film (green) and PPy-cellfib-$PNTf_2$-BS film (blue)

Table 3.15 displays the values of the decomposition temperatures and the water content of each film calculated by TGA from Figure 3.41 and Figure 3.42. The PPy-cellfib film was less thermally stable than the cellulosefibrous film; this decrease in the thermal stability of the PPy-cellfib film in comparison to the cellulosefibrous film may be due to the loss of intramolecular hydrogen bonding within the cellulose moiety and substitution by interaction with polypyrrole units *via* intermolecular hydrogen bonding [284]. The PPy-cellfib film presented an increase in the decomposition temperature when the IL plasticisers were added which could be explained as an interaction of the cellulose matrix with the IL plasticiser (increasing the T_{on}), and also, part of the IL plasticiser could have been entrapped in the composite film as free IL plasticiser within the cellulose matrix (2^{nd} T_{on}) as it was explained in section 3.3.2 [272]. In the case of the 3^{rd} decomposition temperature, it can be associated with the degradation of the dopants.

Table 3.15 Decomposition temperatures and water content obtained from TGA of the cellulosefibrous films containing polypyrrole and the cellulosefibrous film for comparison

Name of the composite films	T_{on} / ^{0}C	2^{nd} T_{on} / ^{0}C	3^{rd} T_{on} / ^{0}C	Water content / wt %
Cellulosefibrous film	239	-	-	6.00
PPy-cellfib film	210	-	-	7.52
PPy-cellfib-PCl film	245	368	-	5.45
PPy-cellfib-$PNTf_2$ film	261	351	-	4.02
PPy-cellfib-PCl-CS film	237	367	431	2.96
PPy-cellfib-$PNTf_2$-BS film	279	354	425	4.27

Scanning electron microscopy was used to study the morphology of the polypyrrole-cellulosefibrous films. Figure 3.43 shows the morphology of the PPy-cellulosefibrous composite, presenting a smooth surface that after exposition to the electron beam from the SEM started to crack (picture in the right).

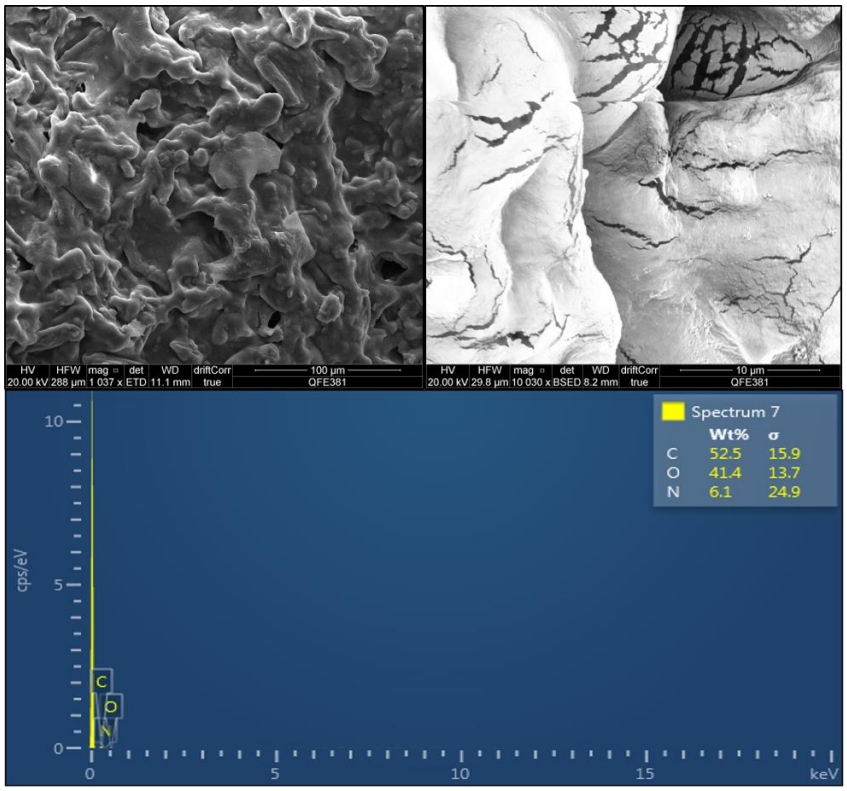

Figure 3.43 SEM images with magnification 1K and 10K and EDX spectra of PPy-cellfib film

Addition of the ionic liquids plasticisers, $[P_{6\,6\,6\,14}]Cl$ and $[P_{6\,6\,6\,14}][NTf_2]$, produced films with a porous interior, as shown in Figure 3.44 (a) and (b), respectively

Figure 3.45 displays the SEM images and EDX analysis of the PPy-cellfib-IL plasticiser films with the dopant. As it was explained previously (section 3.6.1) the dopant was added to *p*-doped the polypyrrole, and it was possible to see that the films with dopant show a different surface. SEM images show a rough surface with cauliflower shape, attributed to the polypyrrole, in comparison to the SEM images in Figure 3.43 that shows a smooth surface.

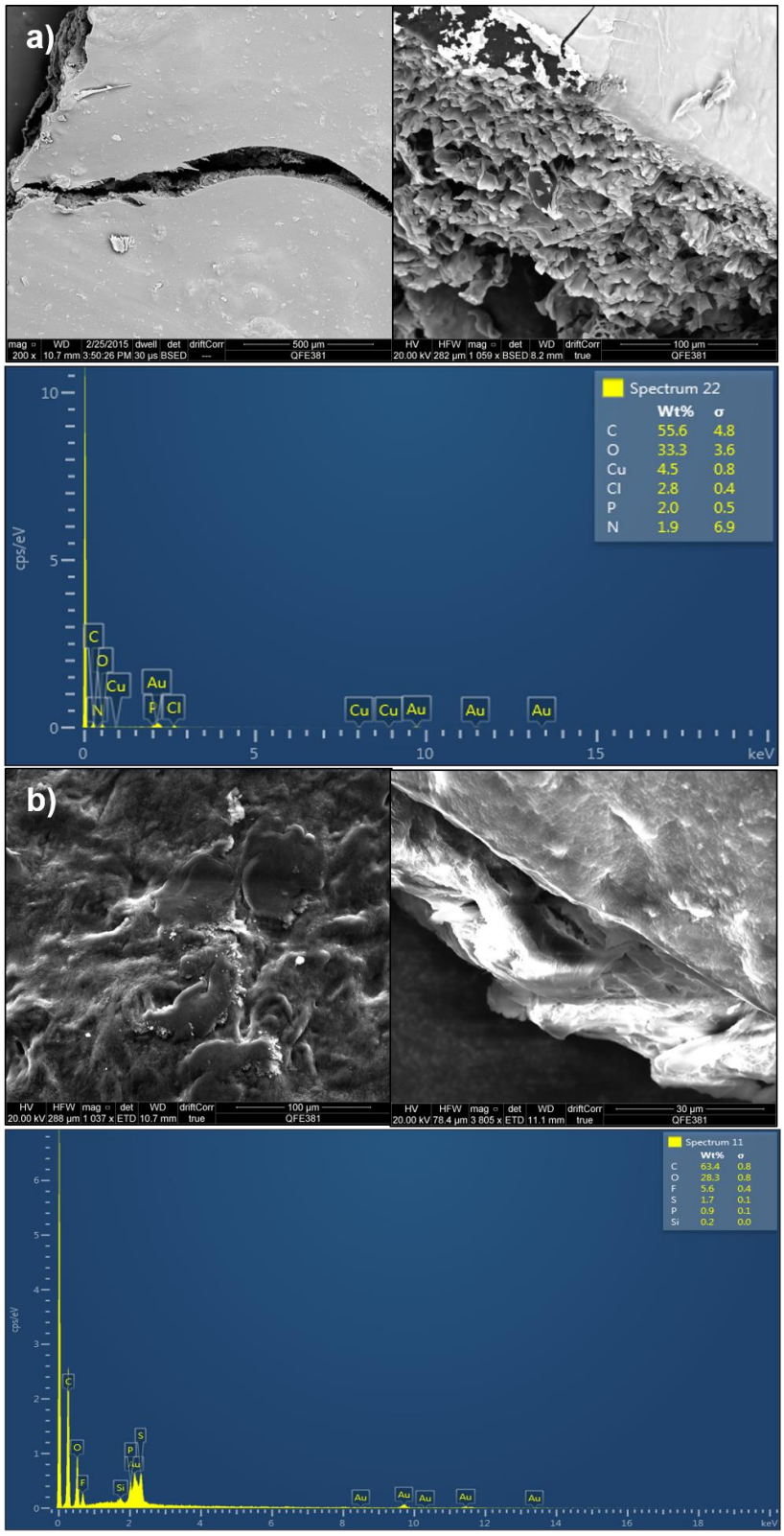

Figure 3.44 a) SEM images with magnification 200, 1K and, EDX spectra of PPy-cellfib-PCl film and, b) SEM images with magnification 1K, 4K-cross-section and EDX spectra of the PPy-cellfib-$PNTf_2$ film (presence of Au from sputtering and Cu for the copper tape)

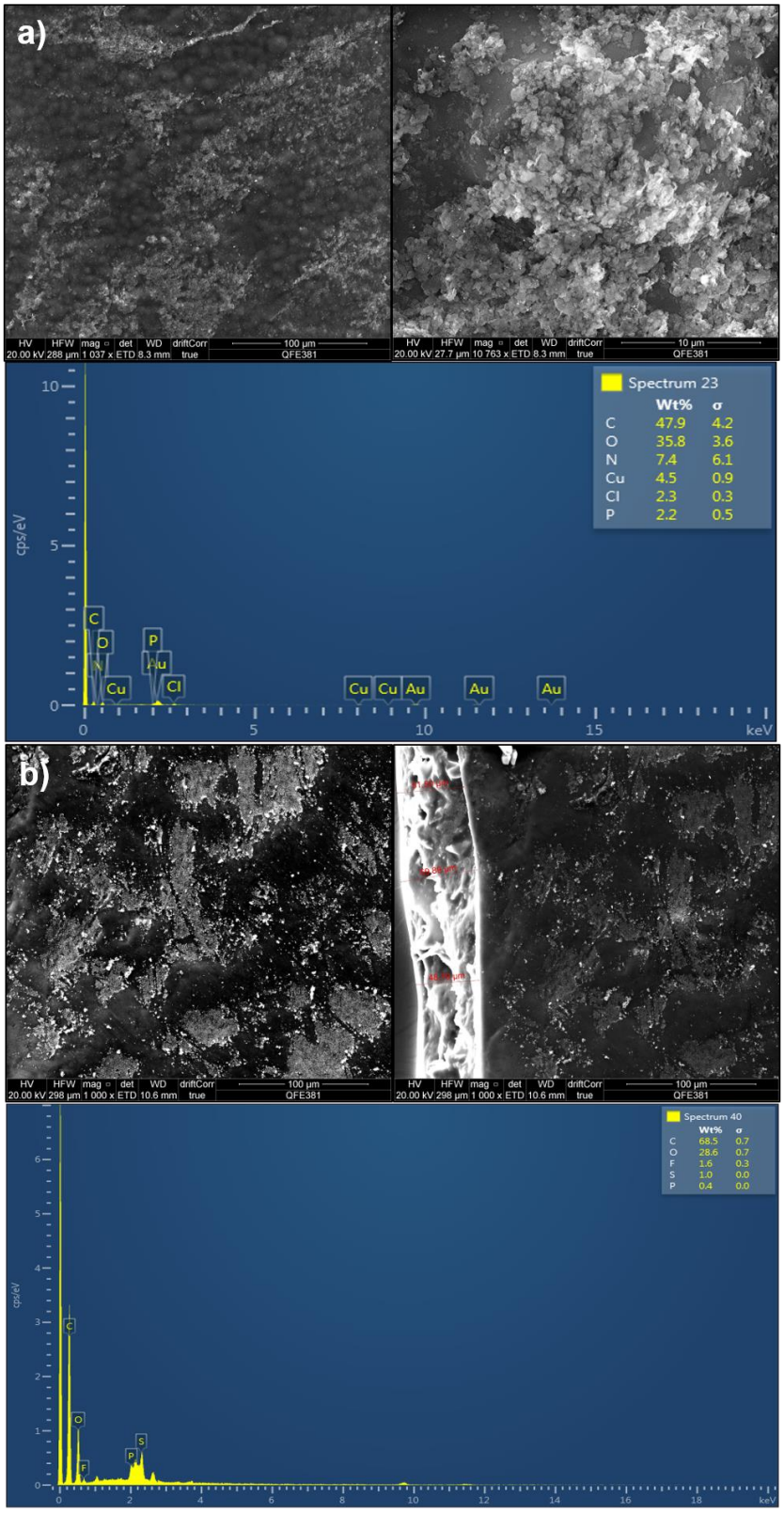

Figure 3.45 a) SEM images with magnification 1K and 10K and EDX spectra of PPy-cellfib-PCl-CS film and b) SEM images with magnification 1K and 1K cross-section and EDX spectra of PPy-cellfib-$PNTf_2$-BS film (presence of Au from sputtering and Cu for the copper tape)

Table 3.16 shows the elemental analysis of the cellulosefibrous films containing polypyrrole. The PPy-cellfib film contained the three elements (C, O and N) found in cellulose and polypyrrole. The incorporation of the IL plasticisers in the PPy-cellfib-PCl and PPy-cellfib-$PNTf_2$ films was confirmed by the presence of the elements P and Cl for $[P_{6\,6\,6\,14}]Cl$, and P, S and F for $[P_{6\,6\,6\,14}][NTf_2]$. In the case of the dopant-containing films, a sulfur (S) peak would be expected for the PPy-cellfib-PCl-CS film, but this peak did not appear; in contrast to the PPy-cellfib-$PNTf_2$-BS film which showed a S peak corresponding to the dopant and/or the IL plasticiser. The reason why the dopant CS did not appear in the EDX analysis can be due to the inhomogeneous nature of the composite film, as it was explained in section 3.6.1 (the CS was not soluble in the cellulose-IL solvent mixture and another dopant was chosen to avoid this problem).

Table 3.16 Elemental composition of the cellulosefibrous film and the cellulosefibrous films containing polypyrrole using EDX

Films	C / %	O / %	N / %	P / %	S / %	F / %	Cl / %
Cellulosefibrous film	63.7	36.3					
PPy-cellfib film	52.5	41.4	6.1				
PPy-cellfib-PCl film	55.6	33.3	1.9	2.0			2.8
PPy-cellfib-$PNTf_2$ film	66.3	28.3		0.9	1.7	5.6	
PPy-cellfib-PCl-CS film	47.9	35.8	7.4	2.2			0.3
PPy-cellfib-$PNTf_2$-BS film	68.5	28.6		0.4	1.0	1.6	

3.7. Addition of Graphite

The graphite is an allotrope of carbon and is a non-metallic conductor showing high electrical conductivity [250,290]. Graphite was added as a binder in the composite films; it was dispersed in the film without interacting with the other components. Graphite is expected to reinforce the composite improving its mechanical properties, as well as increasing its conductivity [291].

3.7.1. Methodology to Obtain Cellulosefibrous Films Containing Graphite

The addition of graphite consisted of weighing 10 wt % of graphite in reference to $[C_4mim]Cl$ and adding it to the cellulose-$[C_4mim]Cl$ mixture which was then, stirred until a homogeneous black mixture was obtained. This addition was carried out right after the dissolution of the cellulose was completed and a graphite-cellfib film was obtained (Figure 3.46 (a)). In the case of the graphite-cellfib-$PNTf_2$ film, Figure 3.46 (b),

the addition of the graphite was carried out after the addition of the IL plasticiser, that was $[P_{6\,6\,6\,14}][NTf_2]$.

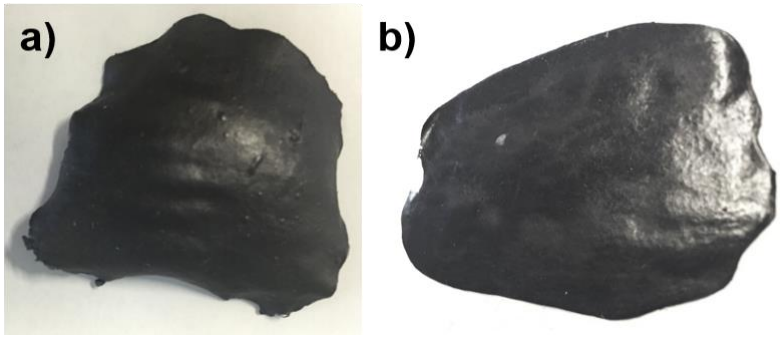

Figure 3.46 a) Picture of the graphite-cellfib film and b) picture of a graphite-cellfib-$PNTf_2$ film

Finally, in the case of the PPy-cellfib-$PNTf_2$-graphite film (Figure 3.47), there were two possibilities for the addition of graphite: (i) after the cellulose was dissolved or (ii) after all the other components were added. Both options were carried out, and the best results were obtained by adding the graphite at the end of the synthesis (option ii). The amount added was optimised to be 10 wt %. This option was chosen because it allowed a better monitoring of the colour changes produced in the solution when polypyrrole was polymerising.

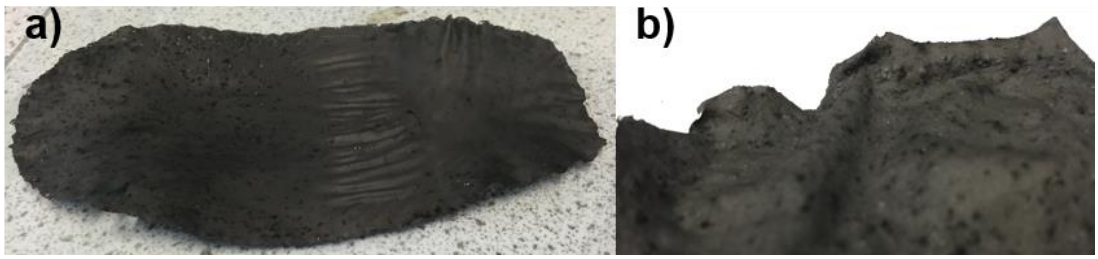

Figure 3.47 a) Picture of the PPy-cellfib-$PNTf_2$-BS-graphite film and b) zoomed in a photograph of the same film

3.7.2. Characterisation of Cellulosefibrous Films Containing Graphite

The three films synthesised with graphite (graphite-cellfib film, graphite-cellfib-$PNTf_2$ film and PPy-cellfib-$PNTf_2$-BS-graphite film) were studied using infrared spectroscopy. The peaks from the cellulose, polypyrrole and IL plasticiser could be seen in the three films, as shown in Figure 3.48. No peaks from graphite appear because it does not contain any functional group [292], and its spectrum is featureless, as it can be seen in the figure (black plot).

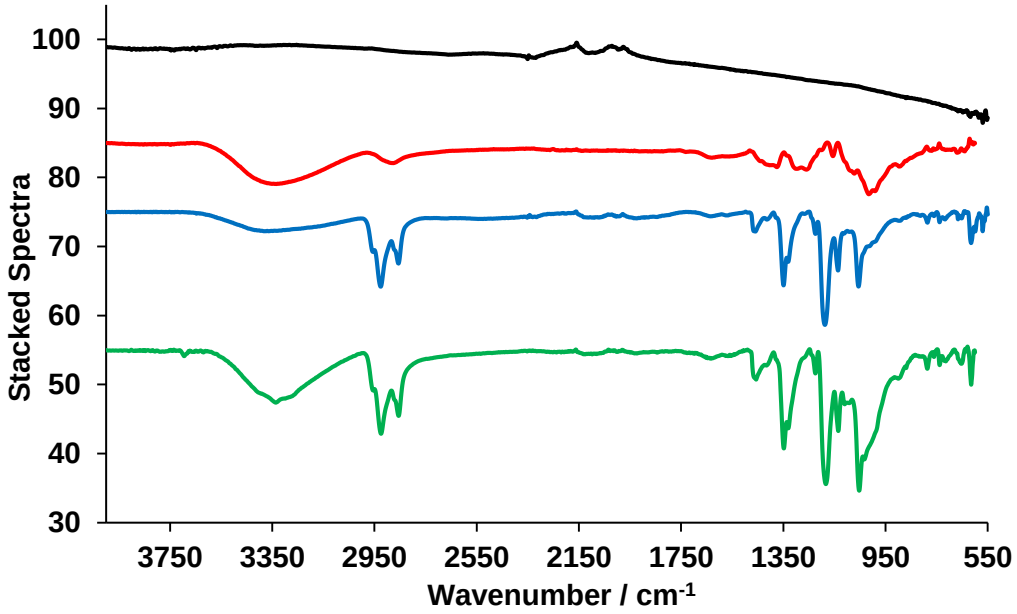

Figure 3.48 Infrared stacked spectra of the graphite powder (black), graphite-cellfib film (red), graphite-cellfib-$PNTf_2$ film (blue) and PPy-cellfib-$PNTf_2$-BS-graphite film (green)

Figure 3.49 shows the Raman spectra of the three films containing graphite (graphite-cellfib film, graphite-cellfib-$PNTf_2$ film and PPy-cellfib-$PNTf_2$-BS-graphite film), compared with the spectrum of graphite powder (starting material). With this technique, it was not possible to observe the two peaks that graphite usually shows at 1550 and 1350 cm^{-1}, known as the *G* and *D* band, respectively [293]. The *G* band is due to the bond stretching of all pairs of sp^2 atoms in both rings and chains and the *D* band corresponds to the bending modes of sp^2 atoms in rings [294]. The only film that showed any peaks was the PPy-cellfib-$PNTf_2$-BS-graphite film which, shows the peaks corresponding to the cellulose and polypyrrole. A possible reason for the absence of the graphite peaks can be that the graphite used is presented as amorphous carbon which does not show these two peaks [295].

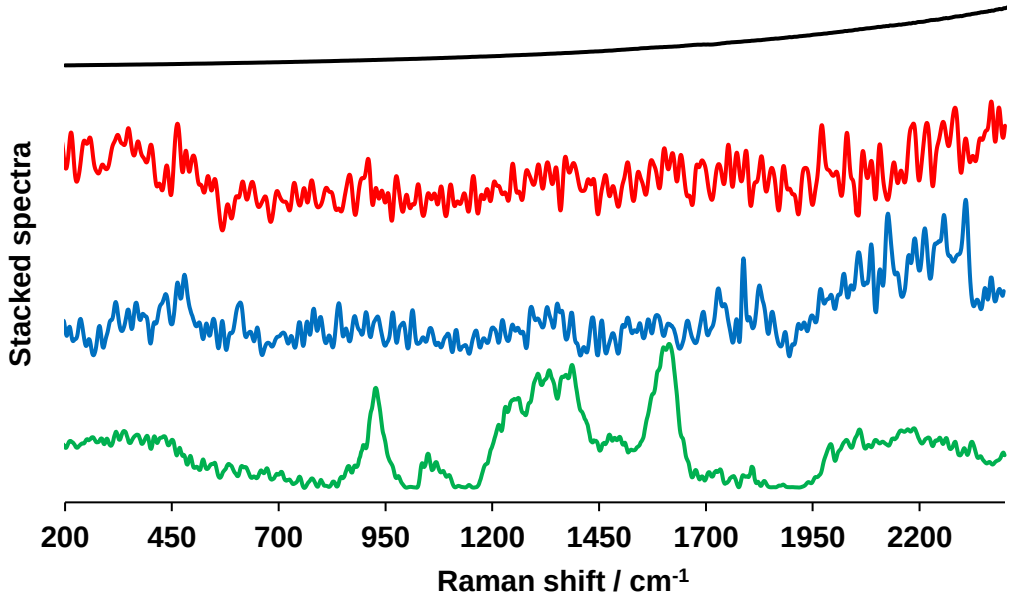

Figure 3.49 Raman stacked spectra of the graphite powder (black), graphite-cellfib film (red), graphite-cellfib-$PNTf_2$ film (blue) and PPy-cellfib-$PNTf_2$-BS-graphite film (green). Spectra normalised and re-plotted using Spectrogryph

Figure 3.50 shows the thermograms of the three films obtained after the addition of graphite. In the case of the graphite-cellfib film (red plot), the decomposition temperature obtained was 235 ºC, similar to that of the cellulosefibrous film. When the IL plasticiser was added to form a graphite-cellfib-$PNTf_2$ film the temperature raised to 263 ºC and, in the case of the PPy-cellfib-$PNTf_2$-BS-graphite film the onset temperature was 283 ºC. The same behaviour was observed when the polypyrrole-cellulosefibrous films were studied (section 3.6.2), where the addition of the IL plasticiser $[P_{6\,6\,6\,14}][NTf_2]$ and the dopant benzenesulfonate, resulted in an increase of the thermal stability.

A larger amount of residue can be observed in thermograms of the graphite-cellfib and graphite-cellfib-$PNTf_2$ films, due to the existence of graphite which has a higher thermal stability [296]. In the case of the PPy-cellfib-$PNTf_2$-BS-graphite film, the residue was reduced considerably, very similar to the polypyrrole-cellulosefibrous films showed in the section 3.6.2.

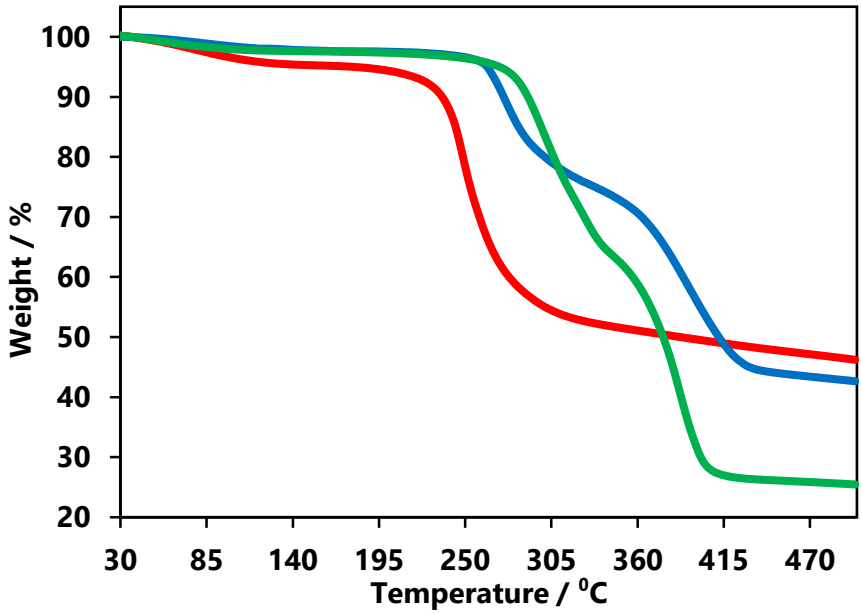

Figure 3.50 Thermogram of the graphite-cellfib film (red), graphite-cellfib-$PNTf_2$ film (blue) and PPy-cellfib-$PNTf_2$-BS-graphite film (green)

SEM images of these three composite films containing graphite are shown in Figure 3.51 with a magnification of 1K. All of them showed a rough surface and better physical uniformity than in the other films prepared.

Each image from Figure 3.51 contains the EDX spectra that shows the elemental analysis carried out for each film. All of them show an increase in the wt % of the carbon in comparison to a cellulosefibrous film which can be attributed to the graphite addition, therefore, indicating the existence of graphite in the films.

Table 3.17 Elemental composition of the cellulosefibrous film and the cellulosefibrous films containing graphite using EDX

Films	C / %	O / %	N / %	P / %	S / %	F / %	Cl / %
Cellulosefibrous film	63.7	36.3					-
graphite-cellfib film	86.2	13.8					-
graphite-cellfib-$PNTf_2$ film	91.5	8.3		0.1			-
PPy-cellfib-$PNTf_2$-BS-graphite	70.1	14.4		1.2	2.8	11.5	-

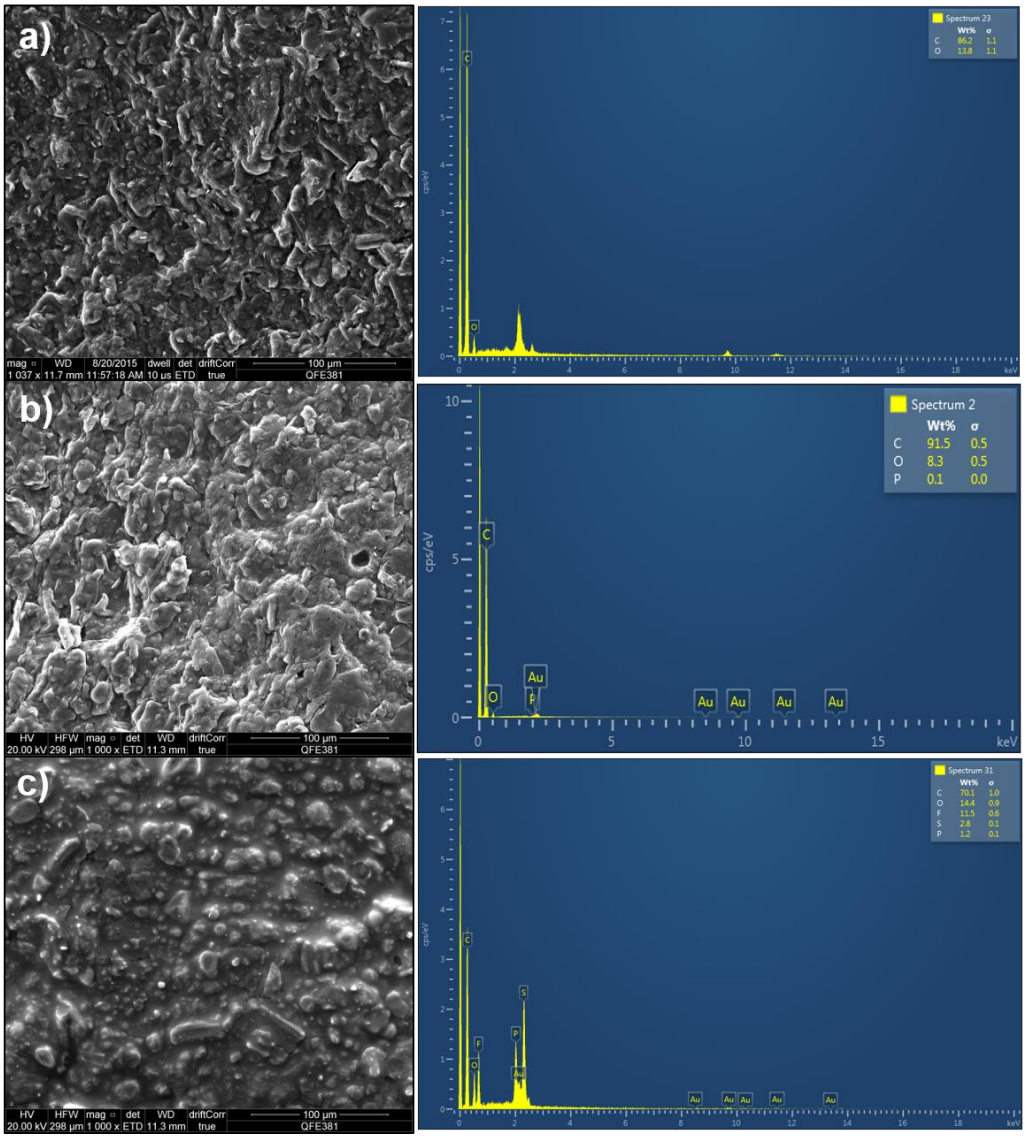

Figure 3.51 a) SEM image with magnification 1K and EDX spectra of graphite-cellfib film, b) SEM image with magnification 1K and EDX spectra of graphite-cellfib-$PNTf_2$ film and c) SEM image with magnification 1K and EDX spectra PPy-cellfib-$PNTf_2$-BS-graphite film (presence of Au from sputtering)

3.8. Flexible Composite Electrodes Fabrication and Characterisation

The development of the composite films described in sections 3.6 and 3.7 facilitated the fabrication and optimisation of three different composite electrodes. Table 3.18 shows the composite films obtained with this optimised procedure, together with their names and wt % compositions. These three flexible composites were shortlisted to be used for the fabrication of three types of supercapacitor devices that will be discussed in the upcoming chapters. Henceforth, the names displayed in Table 3.18 will be the names used for the flexible electrodes in the remaining chapters of this thesis.

Table 3.18 Composite electrode names and their composition

Composite electrode names	Composition and % by weight of [C_4mim]Cl (solvent IL)
graphite-cellfib-IL plasticiser	10 wt % graphite, 10 wt % fibrous cellulose and 10 wt % [$P_{6\,6\,6\,14}$][NTf_2] IL plasticiser
PPy-cellfib-IL plasticiser	10 wt % of pyrrole, 10 wt % fibrous cellulose, 10 wt % [$P_{6\,6\,6\,14}$][NTf_2] IL plasticiser and benzenesulfonate
PPy-cellfib-IL plasticiser-graphite	10 wt % of pyrrole, 10 wt % fibrous cellulose, 10 wt % [$P_{6\,6\,6\,14}$][NTf_2] IL plasticiser, benzenesulfonate and 10 wt % graphite

3.8.1. Fabrication of Flexible Composite Electrodes

The preparation of the flexible electrodes started by adding 3.235 g of [C_4mim]Cl in a 100 mL round bottom flask equipped with a mechanical stirrer and heated under nitrogen at 100 ºC until it was melted and the fluidity increased. 10 wt % of fibrous cellulose was added, stirred and heated at 100 ºC for 2 hours, as previously described in section 3.2.1. 10 wt % [$P_{6\,6\,6\,14}$][NTf_2] IL plasticiser (0.355 g, 0.05 mmol) was added to the mixture. The mixture was stirred until it became homogeneous.

Graphite-cellfib-IL was prepared by adding 10 wt % graphite (0.358 g) to the cellulosefibrous-IL mixture obtained previously and stirred until a homogeneous mixture was obtained. In the case of the PPy-cellfib-IL plasticiser, the cellulose-IL mixture was cooled to r.t., the oxidant ammonium persulfate (0.113 g, 0.50 mmol), and dopant precursor, benzenesulfonic acid (0.211 g, 1.33 mmol), were added. The dopant quantity was 0.3 ± 0.1 mol relative to pyrrole. The mixture was stirred to homogeneity and then, 10 wt % of pyrrole (0.37 mL, 5.00 mmol) was added and stirred further to obtain a homogeneous solution. The PPy-cellfib-IL plasticiser-graphite composite film was prepared similarly to PPy-cellfib-IL plasticiser film followed by adding 10 wt % graphite (0.3938 g) to the mixture and stirred until a homogeneous mixture was obtained. When all the components were dissolved in [C_4mim]Cl, the mixture was cast into a film between two proofing papers and using the bar No. 8 (wet film thickness 100 μm) in a coating machine (K control coater model 101 from RK Printcoat Instruments). Subsequently, the wet film cast was immersed in a water bath (anti-solvent) to regenerate the cellulose by removing the [C_4mim]Cl IL. After being washed several times with deionised water, the films formed (Figure 3.52). They were then dried at r.t. in air for 24 hours and stored in a vacuum desiccator.

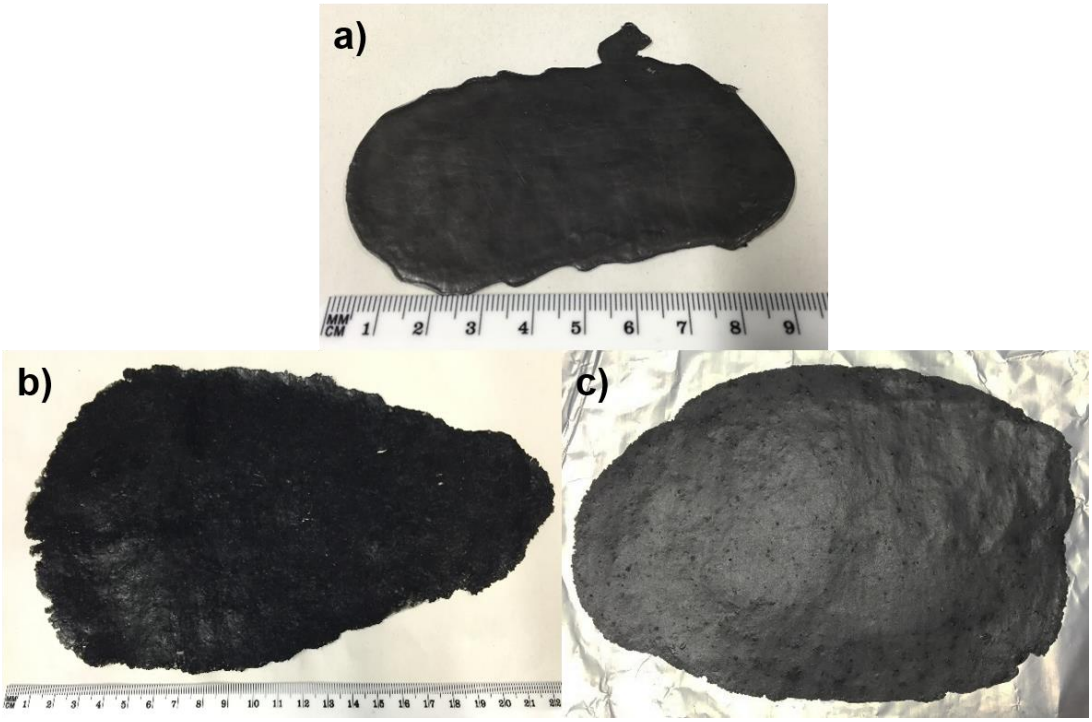

Figure 3.52 Pictures of the flexible composite electrodes a) graphite-cellfib-IL plasticiser film, b) PPy-cellfib-IL plasticiser film and c) PPy-cellfib-IL plasticiser-graphite film

The chemical stability of one of the composite films in water and in phosphoric acid was studied; these two liquids were chosen because they are commonly used as electrolytes in electrochemical devices *e.g*. phosphoric acid could be a good candidate for solid-state electrolyte as it is reported in the literature [297]. The composite chosen was the PPy-cellfib-IL plasticiser-graphite film and it was soaked in water at room temperature for two years without any change observed visually (Figure 3.53 (a)), demonstrating the high stability of these composites in water. In the case of the phosphoric acid, the film disintegrated in less than 24 hours, as shown in Figure 3.53 (b). Therefore, with this study, it can be said that the composites can be used as electrodes using non-acidic aqueous electrolytes.

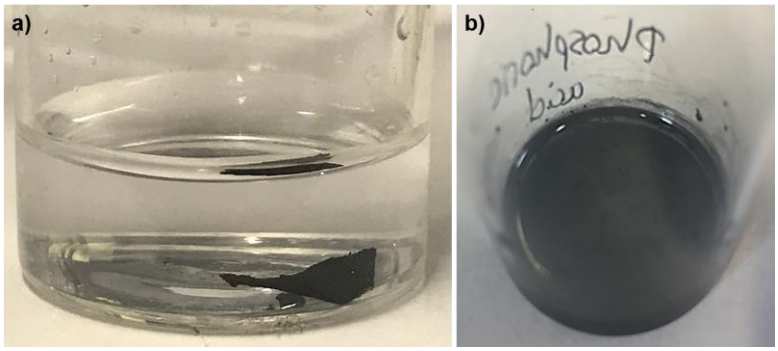

Figure 3.53 Picture of the PPy-cellfib-IL plasticiser-graphite film a) after two years soaked in water and b) after 24 h soaked in phosphoric acid where the film disintegrated

3.8.2. Characterisation of Flexible Composite Electrodes

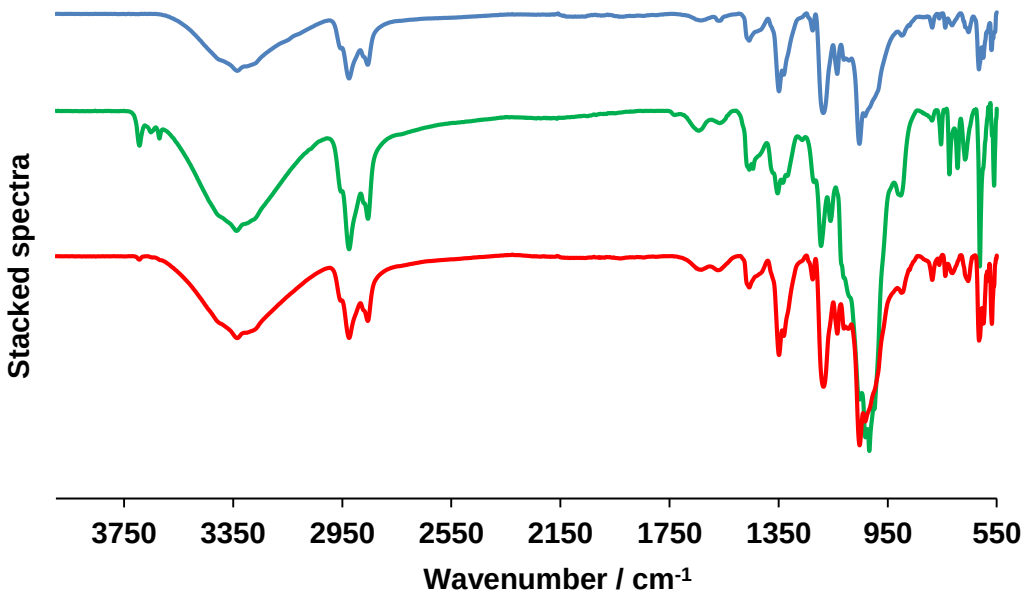

Figure 3.54 Infrared spectra of graphite-cellfib-IL plasticiser film (blue), PPy-cellfib-IL plasticiser film (green) and PPy-cellfib-IL plasticiser-graphite film (red)

Using infrared and Raman spectroscopy the identification of the compounds that composed the composite films was attempted. Figure 3.54 compares the infrared spectra obtained for the graphite-cellfib-IL plasticiser film (blue plot), PPy-cellfib-IL plasticiser film (green plot) and PPy-cellfib-IL plasticiser-graphite film (red plot). The most relevant peaks corresponding to the cellulose, IL plasticiser and polypyrrole were successfully identified using this technique, *i.e.*, the broad peak around 3336 cm^{-1} corresponded to the overlapped -OH and -NH stretching bands of the cellulose and polypyrrole, respectively. PPy-cellfib-IL plasticiser film (green) and PPy-cellfib-IL plasticiser-graphite film (red) showed the C=C stretching band from the pyrrole ring at 1567 cm^{-1} and the C-N stretching of the pyrrole at 1460 cm^{-1}. In the three composite films, two peaks at 1350 and 1181 cm^{-1} can be observed, which corresponded to the S=O asymmetric and symmetric stretching, respectively. These two peaks belong to the anion, $[NTf_2]$, of the IL plasticiser, $[P_{6\,6\,6\,14}][NTf_2]$.

In the case of the Raman spectroscopy, the spectra provided less information than with the infrared technique (Figure 3.55). The spectrum of the graphite-cellfib-IL plasticiser film (blue plot) showed only a flat baseline, whereas those of the PPy-cellfib-IL plasticiser film (green plot) and PPy-cellfib-IL plasticiser-graphite film (red plot), gave peaks which can be attributed to the cellulose and polypyrrole, *i.e.*, the

C=C backbone stretching from the polypyrrole can be found at 1610 cm^{-1}, and the peak at 1340 cm^{-1} corresponds to the pyrrole ring stretching, S=O asymmetric stretching of the plasticiser and dopant (benzenesulfonate) and the H-C-O bending of the cellulose. The last peak to be discussed is the one at 930 cm^{-1} that is assigned to the C-H out-of-plane deformation of the pyrrole and the H-C-C of the cellulose and IL plasticiser.

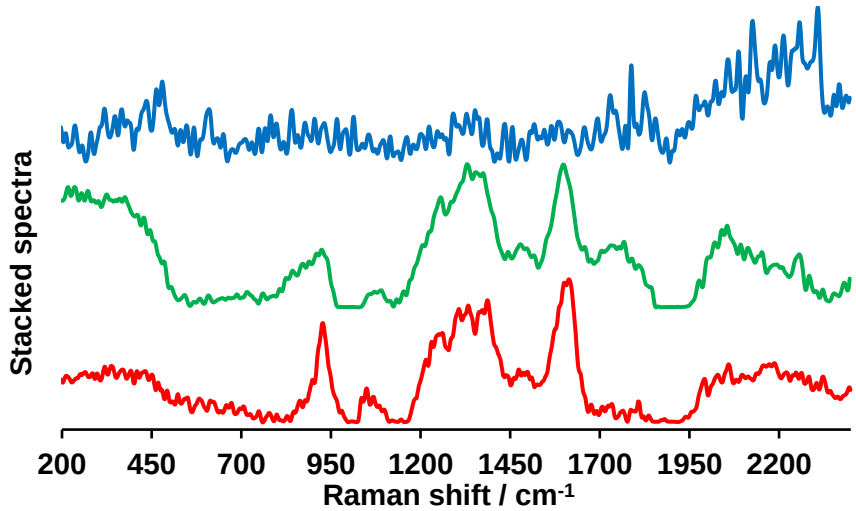

Figure 3.55 Raman spectra of graphite-cellfib-IL plasticiser film (blue), PPy-cellfib-IL plasticiser film (green) and PPy-cellfib-IL plasticiser-graphite film (red). Spectra normalised and re-plotted using Spectrogryph

Figure 3.56 compares the thermal stability of the three composite films. Their decomposition temperatures follow the trend *viz.* PPy-cellfib-IL plasticiser-graphite film> PPy-cellfib-IL plasticiser film > graphite-cellfib-IL plasticiser film with values for the decomposition temperature of 283 ºC, 279 ºC and 263 ºC, respectively. These composite materials with thermal stabilities over 200 ºC cover most of the real world electronic device operational temperatures [184b].

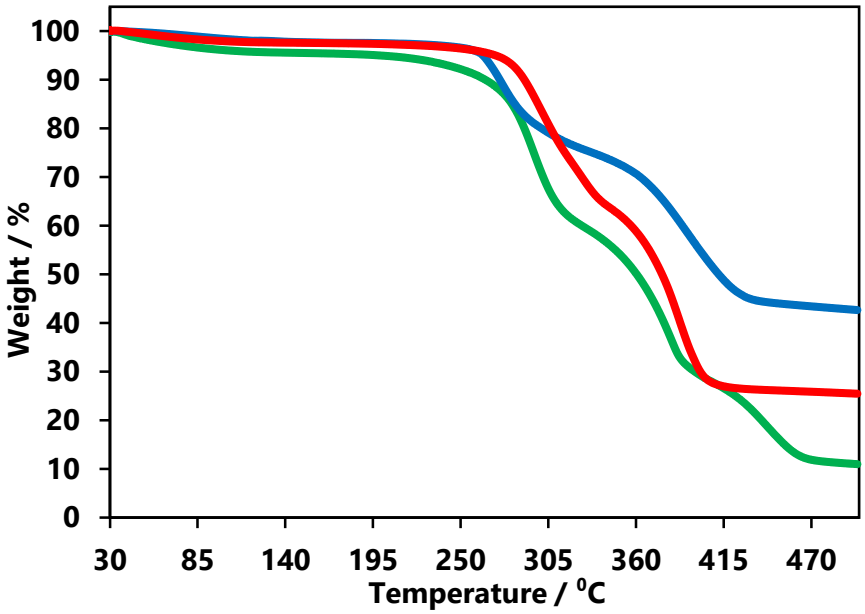

Figure 3.56 Thermogram of graphite-cellfib-IL plasticiser (blue), PPy-cellfib-IL plasticiser (green) and PPy-cellfib-IL plasticiser-graphite (red)

Figure 3.57 shows the SEM images of the three composite film electrodes with a magnification of 1K. As it can be seen, their surfaces were rough which could be attributed to the porosity induced in the film due to IL plasticiser and polypyrrole as it was explained in the previous sections. In Figure 3.57 (b), corresponding to the PPy-cellfib-IL plasticiser film, bright parts were observed and were accounted for integrated polypyrrole portions. From Figure 3.58 with a magnification of 10K, the different surface obtained for each composite film is displayed. Figure 3.58 (a) and (c) corresponds to the composite films which contain graphite and as it can be seen, the surface shows a layered profile. In the case of Figure 3.58 (c), which corresponds to the PPy-cellfib-IL plasticiser film, the surface presents a cauliflower shape over the cellulose matrix confirming the integration of polypyrrole over the cellulose matrix.

Elemental analysis using EDX confirmed the presence of most of the elements that constituted the respective composite films, as it can be seen in Table 3.19. However, it was not possible to calculate the exact ratio between polypyrrole and cellulose as the molecular weight of the polymerised pyrrole was difficult to determine. For example, the graphite-cellfib-IL plasticiser film showed the presence of carbon, oxygen, fluorine, sulfur and phosphorous. In the case of the PPy-cellfib-IL plasticiser film, the presence of phosphorous and fluorine from the IL plasticiser and sulfur from IL plasticiser and dopant can be seen. PPy-cellfib-IL plasticiser-graphite

film showed all the elements contained in the composite and, in comparison to the PPy-cellfib-IL plasticiser film, the quantity of carbon is higher due to the addition of graphite.

For the three films, there was no evidence of chlorine from the IL, $[C_4mim]Cl$, used for the dissolution of the cellulose. Therefore, it can be said that any residual $[C_4mim]Cl$ remaining in the composite films was below the detection limit of EDX analysis (1 wt %).

Table 3.19 Elemental composition of the flexible composite electrodes using EDX

Composite film name	C / wt %	O / wt %	F / wt %	S / wt %	P / wt %	Cl / wt %
Graphite-cellfib-IL plasticiser film	63.1	32.9	2.4	0.8	0.3	-
PPy-cellfib-IL plasticiser film	62.3	35.1	-	1.3	1.0	-
PPy-cellfib-IL plasticiser-graphite film	70.1	14.4	11.5	2.8	1.2	-

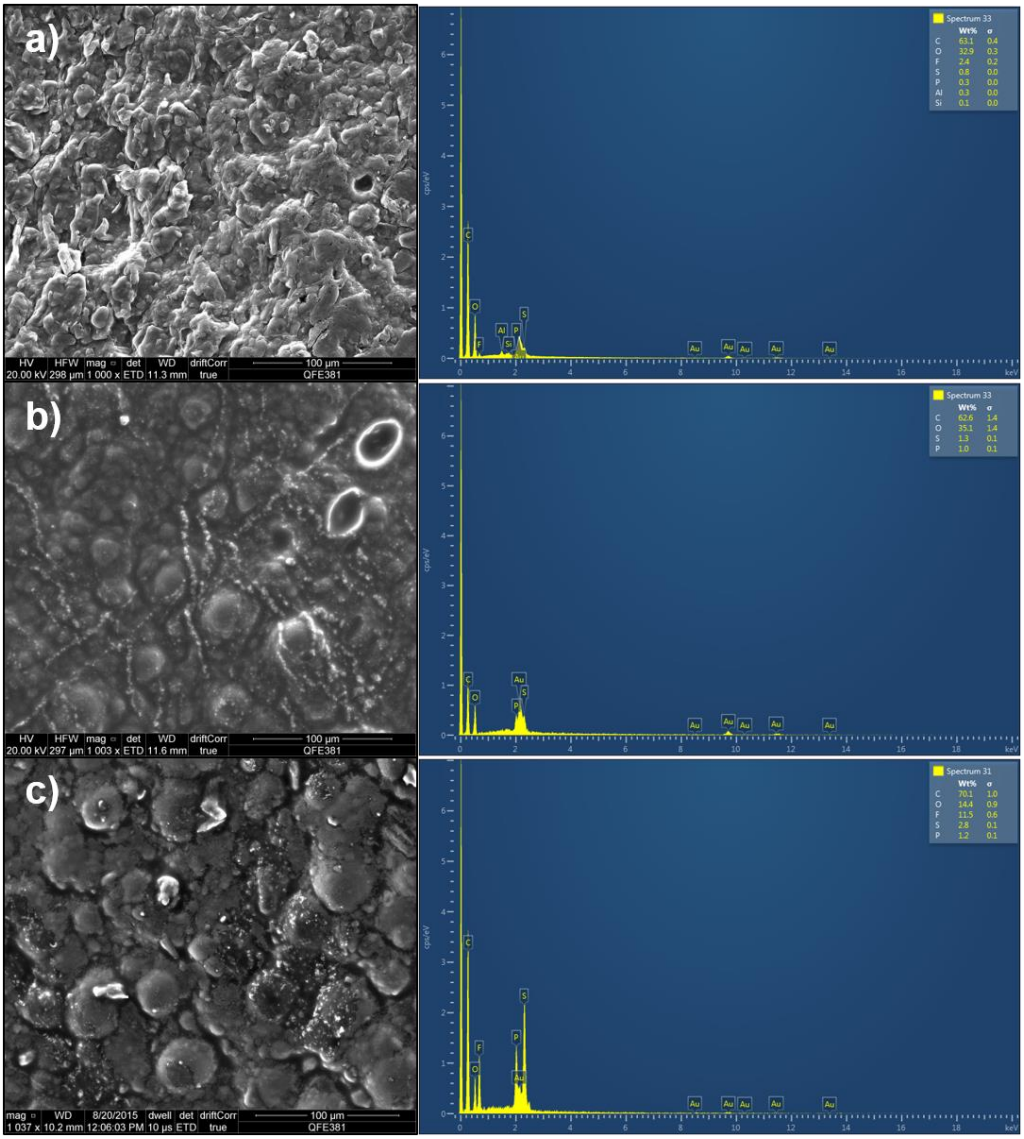

Figure 3.57 a) SEM picture with magnification 1K and EDX spectrum of a) graphite-cellfib-IL plasticiser film, b) PPy-cellfib-IL plasticiser film and c) PPy-cellfib-IL plasticiser-graphite film (presence of Au from sputtering)

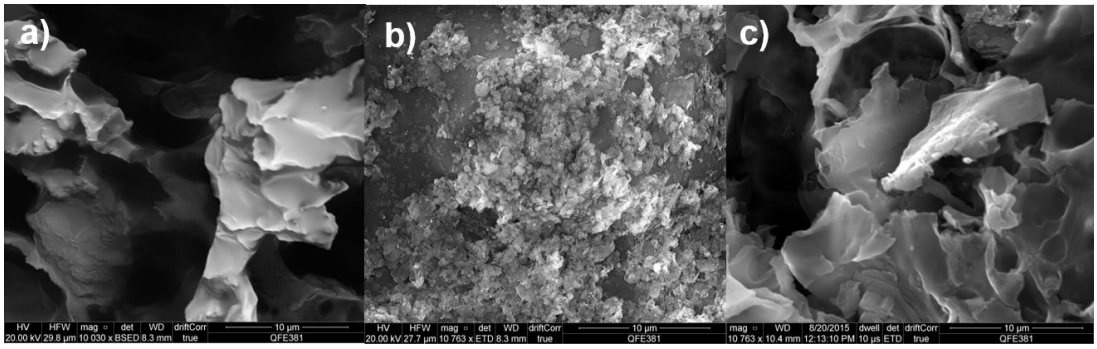

Figure 3.58 SEM pictures with magnification 10K of a) graphite-cellfib-IL plasticiser film, b) PPy-cellfib-IL plasticiser film and c) PPy-cellfib-IL plasticiser-graphite film (presence of Au from sputtering)

Electronically conducting polymers such as polypyrrole have poor mechanical integrity and generally form as powder or dispersions as was shown in section 3.5 [50]. This inherent brittle nature of the polymer limits its usage in practical implementation in devices. The mechanical properties of polypyrrole may be improved by templating on cellulose but they can be poorly adherent to the cellulose matrix leading to attrition as shown in section 3.6.2 [184b]. The composites developed in this thesis, however, as cellulose and polypyrrole are chemically blended homogeneously *via* hydrogen bonding, as it was demonstrated by infrared spectroscopy in section 3.6.2 [184b], were more stable to attrition.

The mechanical properties of the composite films were measured through the tensile strength test method in collaboration with Dr Bronagh Millar from the Polymer Processing Research Centre at the Queen's University of Belfast and Ms Claire Anderson, MEng student in Mechanical and Aerospace Engineering. The chemical synthetic work and tensile strength testing of the composite films were carried out by myself.

The tensile strength test measures the force required to break a material when an elongation or stretching of the material is applied until its breaking point [298]. The results obtained can be used to determine Young's Modulus, tensile strength, strain and elongation at the yield and break points. For this measurement, there are several factors that must be taken into account such as the material thickness, speed of testing or type of grips used to obtain precise and comparable results [299].

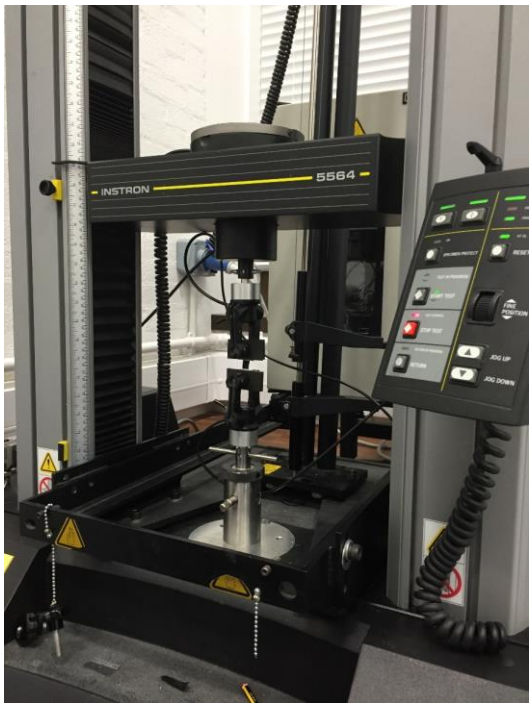

Figure 3.59 Instron instrument used to measure the polymer properties of the films obtained

The Instron instrument used for the tensile strength test is shown in Figure 3.59 and it is capable to measure Young's Modulus or, in other words, the modulus of elasticity that is the index of the stiffness of the material under study [299]. Other properties measured using this instrument are the values of stress and strain that are used to plot a stress-strain curve which, gives the ultimate strength, yield point and elastic limit of a material, as it was explained in section 2.1.3.3.

The experimental procedure consisted of cutting the samples in a rectangular shape and size of 10 x 15 mm and measure their thickness (using a Micrometre Screw Gauge) that is required for the program calculations. For this measurement, three samples of each film were tested. After preparing the samples, they were inserted, one by one, between the hydraulic grips, covered by a paper to protect the samples. In the Instron instrument, the load was balanced, and the test was started, which consisted of elongating the materials using a speed of 5 mm min^{-1}, until failure. After fracture, the program recorded the stress-strain curve (Figure 3.60) from where the break stress and strain values and from which the software could calculate Young's Modulus using Equation 3.1 [300].

$$Young's\ Modulus\ (MPa) = \frac{Tensile\ Stress\ (MPa)}{Tensile\ Strain\ (\%)} \qquad \text{Equation 3.1}$$

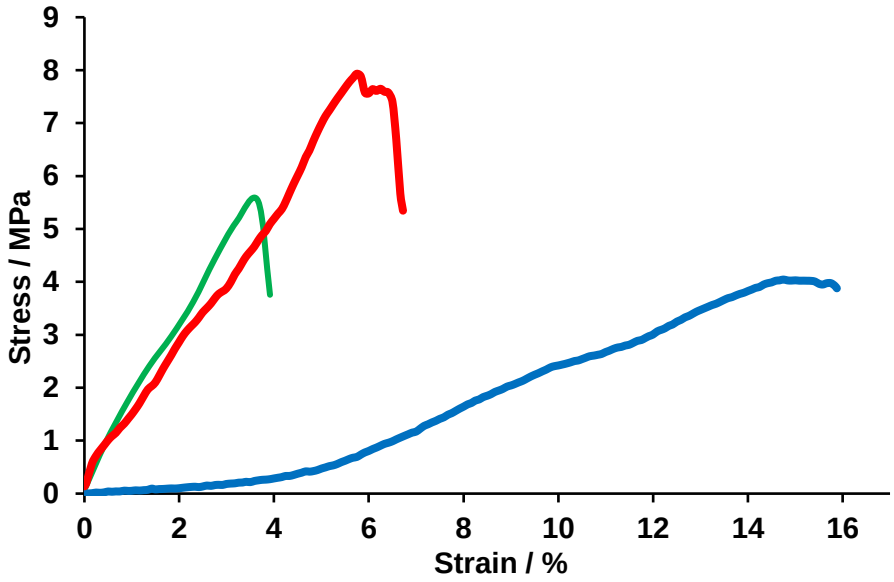

Figure 3.60 Stress-strain curve of the three films obtained: graphite-cellfib-IL plasticiser film (blue), PPy-cellfib-IL plasticiser film (green) and PPy-cellfib-IL plasticiser-graphite film (red)

From Figure 3.60 the stress-strain curve of the three composite films fabricated is displayed, where it can be seen how these three materials behave when a load is applied to them. The length of the curves in references to the stress axis indicates the strength of a material and in reference to the strain axis the materials' ductility as t was explained in section 2.1.3.3. Therefore, among these three materials the graphite-cellfib-IL plasticiser film (blue plot) is the most ductile and the PPy-cellfib-IL plasticiser-graphite film (red plot) is the strongest film.

The Young's Modulus of the three films are compared in Figure 3.61, where the modulus values decrease following the trend PPy-cellfib-IL plasticiser film (green) > PPy-cellfib-IL plasticiser-graphite film (red) > graphite-cellfib-IL plasticiser film (blue). Therefore, the PPy-cellfib-IL plasticiser film has the highest Young's Modulus value amongst the three composite films. The three films were tested, and the measurements' standard deviation was determined. Both films containing polypyrrole show the smallest standard deviation in comparison to the graphite-cellfib-IL plasticiser film that showed much larger variances. This could be due to a non-homogeneous dispersion of the graphite in the films. The Young's Modulus measures the resistance of a material to elastic deformation under load and, therefore, a high value means that the material is more rigid because it requires a higher load to elastically deform it, whereas, a low value means that the material is more flexible [300]. Given these points, the composite films with graphite show less rigidity (*i.e.* the

flexibility of the films increases, therefore, their stiffness decreases) in comparison with the PPy-cellfib-IL plasticiser because the graphite was added as a binder which is dispersed in the composite film, instead of chemically blended to the other components as happened to polypyrrole and cellulose [291].

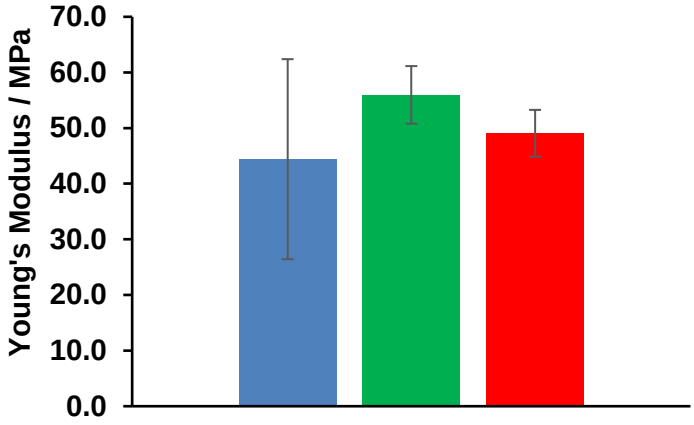

Figure 3.61 Young's Modulus chart corresponding to graphite-cellfib-IL plasticiser (blue), PPy-cellfib-IL plasticiser (green) and PPy-cellfib-IL plasticiser-graphite (red). The standard deviation of the average is shown for each film

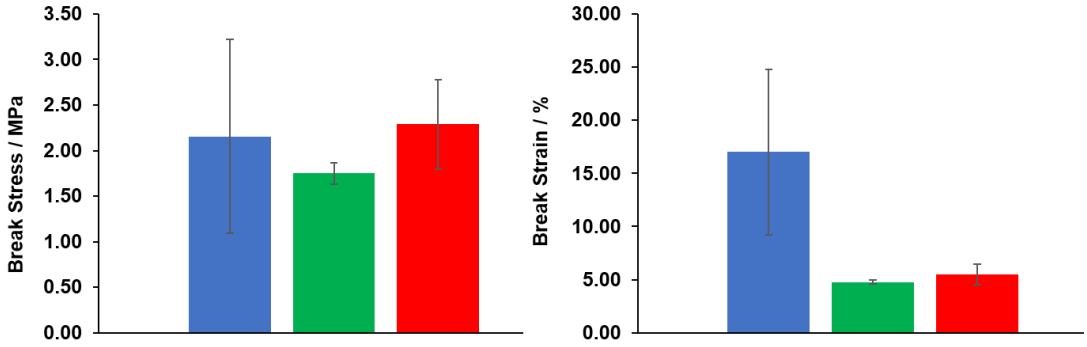

Figure 3.62 Break stress and strain average values corresponding to graphite-cellfib-IL plasticiser (blue), PPy-cellfib-IL plasticiser (green) and PPy-cellfib-IL plasticiser-graphite (red). The standard deviation of the average is shown for each film

The results of the break stress and break strain are shown in Figure 3.62. In the case of the break stress or ultimate tensile stress, the PPy-cellfib-IL plasticiser film showed the lowest average value which means that this film broke more quickly than the ones containing graphite. The break strain values reveal the elongation that the films can stand before they break. The values showed differences among the films, showing a much higher break strain value for the graphite-cellfib-IL plasticiser film than in the case of the other two films containing polypyrrole. Therefore, the graphite-cellfib-IL plasticiser film elongated more before the breaking point in comparison the other two films. This result agreed with Young's Modulus value obtained for the

graphite-cellfib-IL plasticiser film that revealed that it was the most flexible of the three films.

The Young's Modulus and ultimate tensile strength values obtained for these three composite films were comparable to those reported in the literature for regenerated cellulose films from ionic liquids [252,301], and also, for polypyrrole composite films; *e.g*. for a conducting composite film based on crosslinked poly(styrene-butyl acrylate-hydroxyethyl acrylate) and PPy developed by Yin *et al.* [302], the tensile strength and Young's Modulus were 4.2 MPa and 46.8 MPa, respectively. In addition, the results obtained for these three composites films were very similar to the results obtained by Ms Claire using composite films with different components such as poly(3,4-ethylenedioxythiophene) showing Young's Modulus values between 50 and 150 MPa, ultimate tensile strength values between 2 and 6 MPa, and break strain around ~ 5 % [303].

The last technique applied for the characterisation of the composite films was the cyclic voltammetry (CV), *i.e.,* the electrochemical investigation of the composites using them directly as working electrodes, with an area of 1 cm^2, was carried out. The CV experiment involved the application of a potential to the working electrode (composite films synthesised) and monitoring the variation in current with time.

To perform the CV experiment, a three-electrode set-up was used with working, reference and counter electrodes. A current-potential curve was recorded using a potentiostat for controlling the voltage between the working and the reference electrodes and for measuring the current flow between the working and the counter electrodes. The potentiostat is an amplifier that can control the potential drop between the working electrode and the electrolyte solution [304].

Figure 3.63 shows the cyclic voltammogram obtained from the three composite films and a cellulosefibrous film synthesised previously to compare their electrochemical performance. As it can be seen, the films graphite-cellfib-IL plasticiser, PPy-cellfib-IL plasticiser and PPy-cellfib-IL plasticiser-graphite showed electroactivity, related to a capacitive response, unlike the cellulosefibrous film which exhibits a resistor response indicating, as expected, that it is not a conducting material.

The graphite-cellfib-IL plasticiser film (blue) showed electroactivity, indicating that this film is a conducting material due to the addition of graphite. In the case of

PPy-cellfib-IL plasticiser film (red) and PPy-Cellfib-IL plasticiser-graphite film (green), a well-defined faradaic response with a cathodic peak around -0.3 V, corresponding to the reduction of the polypyrrole, and an anodic shoulder around 0.2 V, from the oxidation of the polypyrrole, was observed [305]. These peaks are related to the doping state of the PPy (see section 1.5.1.3.2), *i.e.*, when the PPy is reducing is also de-doping and when the PPy is oxidising is doping. This electrochemical behaviour is related to the fast and reversible redox reactions in the PPy, as shown Equation 3.2.

$$ECP \rightleftharpoons ECP^{n+}(A^-)^n + ne^- \qquad \text{Equation 3.2}$$

Among the three composite films, there is a difference in current density *i.e.* the graphite-cellfib-IL plasticiser film showed a higher current density response in comparison to the other composite films containing PPy. This can be due to a dissimilar size of the working electrode (composite film), the conductivity of the films or different scan rate applied. As it was discussed previously, the size of the composite films was the same (1 cm^2) and the scan rate was 20 mV s^{-1} for the three films, therefore, a difference in the conductivity of the film may be the reason for the increase in the current density. The conductivity change may be due to the hydrogen bonding between cellulose and PPy within the PPy-cellfib-IL plasticiser-graphite film which can decrease the conductivity in comparison to the graphite-cellfib-IL plasticiser film, where graphite is dispersed over the cellulose matrix.

The electrochemical responses obtained for the composite films were tested using a standard electrolyte (0.1 M KCl aqueous solution) indicating that they could be used as electrodes in, for example, energy storage devices such as supercapacitors. The three films are expected to have different storage behaviour if they are used as electrodes in a supercapacitor; in the case of graphite-cellfib-IL plasticiser film an electrostatic mechanism (double-layer capacitance) is expected and for the PPy-cellfib-IL plasticiser film and PPy-cellfib-IL plasticiser-graphite film, an electrochemical mechanism (pseudocapacitance) is likely, because of the polypyrrole oxidation and reduction.

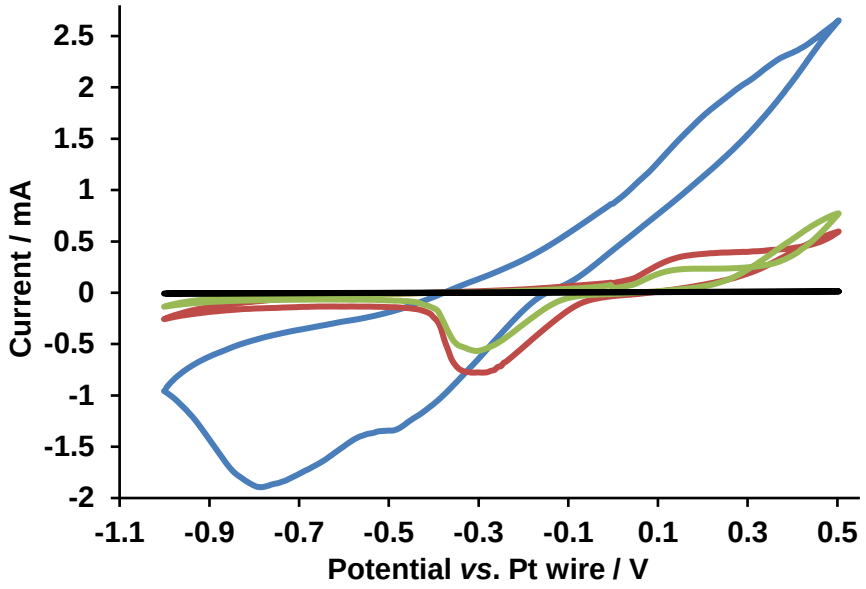

Figure 3.63 Cyclic voltammogram of the films synthesised as working electrodes: graphite-cellfib-IL plasticiser film (blue), PPy-cellfib-IL plasticiser film (red) and PPy-cellfib-IL plasticiser-graphite film (green) and a previous cellulosefibrous film (black). The potential range chosen was from −1.0 to +0.5 V *vs*. Pt wire at the scan rate of 20 mV s^{-1} in 0.1 M KCl aqueous solution and at 25 ± 2ºC

3.9. Summary and Conclusions

In this Chapter, the fabrication of novel and flexible cellulose-based composites was discussed.

Ionic liquid technology was employed to dissolve cellulose using, $[C_4mim]Cl$, and to obtain free-standing cellulose-based films through the cellulose regeneration process using an anti-solvent (water). The one-pot synthesis proposed was an *in situ* polymerisation of an electronically conducting polymer (polypyrrole) over a solution of an oxidant and dopant mixed in the cellulose-IL solvent mixture. The addition of polypyrrole had the purpose to induce electroactivity to the cellulose-based composites. Other components *i.e.* IL as plasticisers and graphite were added to induce flexibility and more conductivity to the composite films, respectively. The hydrophobic IL, $[P_{6\,6\,6\,14}][NTf_2]$, was incorporated successfully in the cellulose matrix to induce plasticity and also, to facilitate electro-wetting if they are used as electrodes. In the case of the graphite powder, it remained as a dispersion in the cellulose matrix and it improved the fluidity and conductivity of the films.

In summary, an effective method for fabricating thin, lightweight and flexible free-standing cellulose-based composites was presented. They were analysed and characterised using infrared and Raman spectroscopy. Their thermal stability was

analysed by thermal gravimetric analysis, showing that the film with the highest decomposition temperature of 283 ºC was the PPy-cellfib-IL plasticiser-graphite film. The morphology of the composite films surface was studied using scanning electron microscopy and using the energy dispersive X-Ray attachment the components of the composite films were further analysed.

These electronically conducting polymer-biopolymer-IL plasticiser composites that are chemically blended can be a novel class of electronically active materials that can be used as electrodes in different applications such as energy storage devices.

The chemical interaction between polypyrrole and cellulose was corroborated by infrared spectroscopy and thermal analysis. As the flexibility of the composites was confirmed by tensile strength test with Young's Modulus around 50 MPa, and their electroactivity by cyclic voltammetry, these films can be applied as flexible electrodes in flexible supercapacitors.

These materials have the potential to be tuned in terms of physicochemical properties; they could also be used in flexible electronic devices such as actuators, antistatic coatings when designed accordingly by carefully choosing the appropriate components needed for the specific application.

Chapter 4

Flexible Electrical Double-Layer Supercapacitors (EDLS)

Flexible energy storage devices (FEDs) are systems that can store and release electric charge under physical deformation, as it was discussed in section 1.7. FESDs can be used in portable electronic devices that are utilised in our daily life, such as laptops, smartphones and tablets and also, they are promising devices for biomedical applications which supply the necessary power for health monitoring and treatment purposes [306]. Currently, the use of harmful organic solvents, electrolyte leakages, potential explosion, and high internal resistance are hazards associated with using lithium batteries to power-up medical implants. These rigid energy devices are also implanted under the skin, wired to a medical device, and this can cause patient discomfort who must adapt their body shapes to fit these rigid batteries. Replacement of lithium batteries with flexible supercapacitors composed of biocompatible organic composites and green electrolytes would, therefore, be highly advantageous for biomedical applications [249].

From the procedure developed in Chapter 3, three different flexible composite electrodes were obtained, and were used to fabricate three different flexible supercapacitors: (a) electrical double-layer supercapacitor (EDLS), (b) electrochemical supercapacitor (ES) and (c) hybrid supercapacitor (HS). This chapter will be dedicated to the fabrication, chemical characterisation and electrochemical testing of an electrical double-layer supercapacitor (EDLS). The electrochemical supercapacitor (ES) and the hybrid supercapacitor (HS) will be discussed in chapter 5 and 6, respectively. Table 4.1 correlates the composite electrodes obtained with the corresponding flexible supercapacitors fabricated and subsequently, the chapter where they are discussed. The composition of each composite film was displayed in Table 3.18.

Table 4.1 Correlation among the composite electrodes and the flexible supercapacitors fabricated from them. Also, the chapter where they are explained is displayed

Composite electrodes	Flexible supercapacitors	Explained in…
Graphite-cellfib-IL plasticiser	Electrical double-layer supercapacitor (EDLS)	Chapter 4 (current one)
PPy-cellfib-IL plasticiser	Electrochemical supercapacitor (ES)	Chapter 5
PPy-cellfib-IL plasticiser-graphite	Hybrid supercapacitor (HS)	Chapter 6

The flexible supercapacitors described in this chapter were symmetric EDLSs using graphite-cellfib-IL plasticiser composite films as both electrodes. In these electrodes, an electrical double-layer mechanism (see section 1.4.1) was established due to the graphite component. $[C_2mim][NTf_2]$ and $[C_2mim][FAP]$ ILs were chosen as electrolytes to be used in the devices. These inherently homogeneous and flexible composite electrodes [184b] constitute more durable electrodes and, ionic liquids are considered safe replacements for organic solvent/aqueous based electrolytes as they are non-flammable, they impart longer cycle life, have wide operational voltage (EW) and could be incorporated into biopolymer membranes such as cellulose to provide solid-state electrolytes with no leakage issues and low internal resistance [72].

Different electrochemical techniques were used in this chapter to carry out the EDLSs characterisation. Cyclic voltammetry was utilised for the study of the electrochemical window of the ionic liquids (electrolytes), as well as, for the operational voltage of the devices and the calculation of the specific and areal capacitance of the supercapacitor during the cycle life and the bending study. Galvanostatic charge-discharge (GCD) was applied to study the rate capability of the supercapacitors and, electrochemical impedance spectroscopy (EIS) was employed to study the charge transfer and ion diffusion properties of the electrodes in the SCs during the cycle life. A brief introduction of these three techniques and their theory is discussed in Appendix B. Also, the chemical nature, thermal stability and morphology of the composite films, as fresh films and after using them as electrodes for 15000 charge-discharge cycles in the flexible supercapacitor, were analysed.

4.1. Experimental Part

In this section, the experimental part related to the electrochemical study of two ILs as electrolytes using different working electrodes and temperatures is shown. In addition, the fabrication of a set of electrical double-layer supercapacitors using the two ILs, previously studied as the electrolytes, is presented, as well as, their electrochemical characterisation.

4.1.1. Electrochemical Study of Ionic Liquids as Electrolytes

The electrochemical window of the electrolytes was studied using cyclic voltammetry. The ionic liquids studied were 1-ethyl-3-methylimidazolium

bis{(trifluoromethyl)sulfonyl}amide, [C_2mim][NTf_2], and 1-ethyl-3-methylimidazolium tris(pentafluoroethyl)trifluoro phosphate, [C_2mim][FAP]. Both ILs were donated by Merck and used without any further purification. The purity of both ILs was checked by ^{1}H and ^{13}C NMR (see Appendix A.1) and the water content of both ILs was determined using the Karl Fischer titration method. The water content for [C_2mim][NTf_2] was 150 ppm and for [C_2mim][FAP] was 130 ppm.

The three electrodes cell set-up showed in Figure 4.1 was used. The measurements were carried out by degassing the electrolyte (*i.e.*, bubbling Argon into the IL to remove the existing O_2 and water) and during all the experiments an Argon current was passed through using the inlet of the cell (yellow inlet showed in Figure 4.1). The experiments were performed at two different temperatures, 25 ± 2 ºC and 70 ± 2 ºC (controlled by a thermometer and a temperature control probe) using three different working electrodes: platinum (Pt), gold (Au) and glassy carbon (GC). A platinum wire was used as the counter electrode and an Ag|Ag^+ electrode (Ag|10 mM $AgNTf_2$ in [C_2mim][NTf_2]) as the reference electrode (the reference electrode was fabricated and calibrated as is explained in Appendix D). The reference electrode was placed as close as possible to the working electrode (0.5 mm) to minimise the cell resistance. An IL-based reference electrode was used to avoid the contamination from the water and in order to obtain highly accurate and reproducible electrochemical measurements [307]. The ionic liquids were tested both as neat electrolytes an also containing an internal standard (10 mM of ferrocene dissolved in the electrolyte).

The electrochemical cell was connected to a potentiostat Autolab PGSTAT302N from Eco Chemie with GPES software to conduct the cyclic voltammetry. The electrochemical characteristics were determined at different scan rates (50, 100 and 500 mV s^{-1}), starting from the open circuit potential and from cathodic to anodic potentials and reversing back. The anodic and cathodic limits were established at the potential at which current reached higher than 0.05 mA which was selected as the cut-off current to calculate the EWs [266].

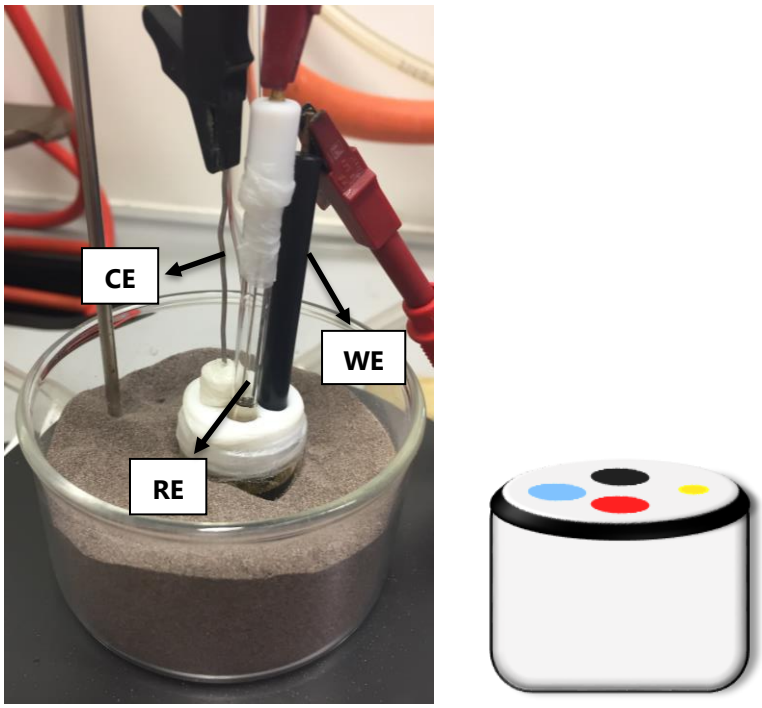

Figure 4.1 Photograph of the three-electrode set-up used for measuring the EW of the ILs under an Argon blanket; the metal probe controlled the temperature of the sand bath. The picture on the right shows the schematic representation of the electrochemical cell with the colour code assignation for the electrodes: working (red), reference (blue) and counter (black) electrodes and an inlet for the Argon current (yellow)

4.1.2. Fabrication of the Flexible EDLS

The preparation of the graphite-biopolymer-ionic liquid plasticiser (graphite-cellfib-IL plasticiser film) composite electrode used in the electrochemical double-layer supercapacitors was carried out using the procedure reported in section 3.8 [184b]. All composite films used as electrodes were dried prior to assembly in a vacuum desiccator for 48 h.

The fabrication of the flexible and symmetrical supercapacitors was carried out by punch-cutting 1 cm^2 size sheets of the composite electrodes, sandwiched with a 1.5 cm^2 paper sheet separator (lab tissue paper) dip-coated with the IL electrolytes 1-ethyl-3-methylimidazolium bis{(trifluoromethyl)sulfonyl}amide ($[C_2mim][NTf_2]$) or 1-ethyl-3-methylimidazolium tris(pentafluoroethyl)trifluorophosphate, ($[C_2mim][FAP]$) as shown in Figure 4.2. Conventional kitchen aluminium foil (surface activation by methanol polishing) was used as current collectors and waterproof polyester self-adhesive sheets from Labelplanet were used for packaging. Total device thickness of this supercapacitor (excluding current collectors) was around ~ 250 μm (measured by a digital ruler with an error of 10 μm) leading to an ultrathin flexible assembly [308].

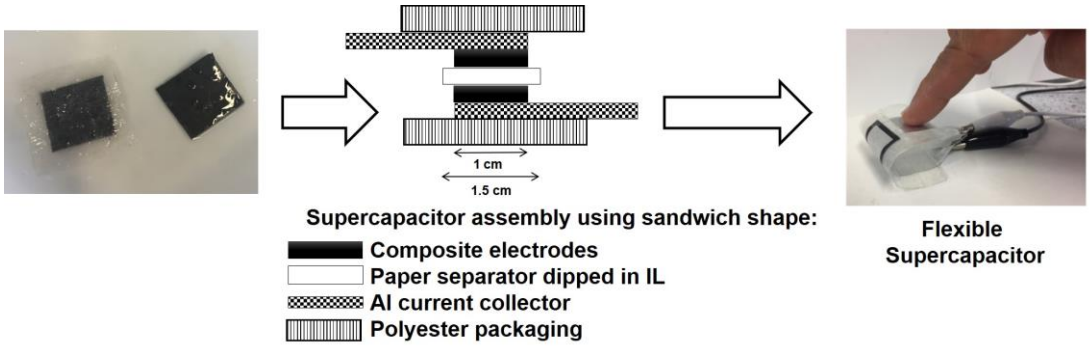

Figure 4.2 Scheme of the fabrication process of the flexible supercapacitor using the composite electrodes fabricated and the dip-coated paper separator for the final assembly of the flexible supercapacitor

4.1.3. Electrochemical Study of the EDLS Fabricated

The performance of the flexible supercapacitors was characterised using a Potentiostat/Galvanostat with GPES software by cyclic voltammetry (CV) measurements and galvanostatic charge-discharge (GCD) studies. Electrochemical impedance spectroscopy (EIS) was measured using the same potentiostat with a built-in frequency response analyser (FRA) by a frequency logarithmically swept from 100 KHz to 10 mHz with an AC perturbation of 10 mV at the open-circuit potential. All the electrochemical characterisations were carried out using a two electrodes system at room temperature (25 ºC ± 2 ºC) *i.e.* using the fabricated supercapacitors directly for the study. The composite films as electrodes were the positive and negative electrodes of the device and they were connected, through the aluminium current collectors, to the terminal ports: one was the working electrode and the other was the reference and counter electrodes together.

The procedure to characterise the devices was carried out as follows: After the assembly of the supercapacitors, they were stored in a vacuum desiccator to settle down for 24 hours. The first technique used was EIS at the open-circuit potential (OCP), followed by the CV and GCD experiments that were carried out after the equilibration time for each supercapacitor was achieved to obtain the stable OCP of the supercapacitor. The OCP is the potential of the system at which there is no external current applied, it is known also as the equilibrium potential which in the case of symmetric supercapacitors should be zero or near zero due to the same electrodes composition [309].

Figure 4.3 (a) shows the experimental set-up used to carry out the electrochemical study of the devices and Figure 4.3 (b) shows the experimental set-up for the bending study with an angle of 120 degrees using a glass sample bottle as a guide. In both cases, a sand bath was used to keep the temperature of the devices at 25 ºC ± 2 ºC. The bending study was carried out for 10 cycles at the bending angle of 120 degrees, and the 10th cyclic voltammogram was used for analysis (after the system stabilised).

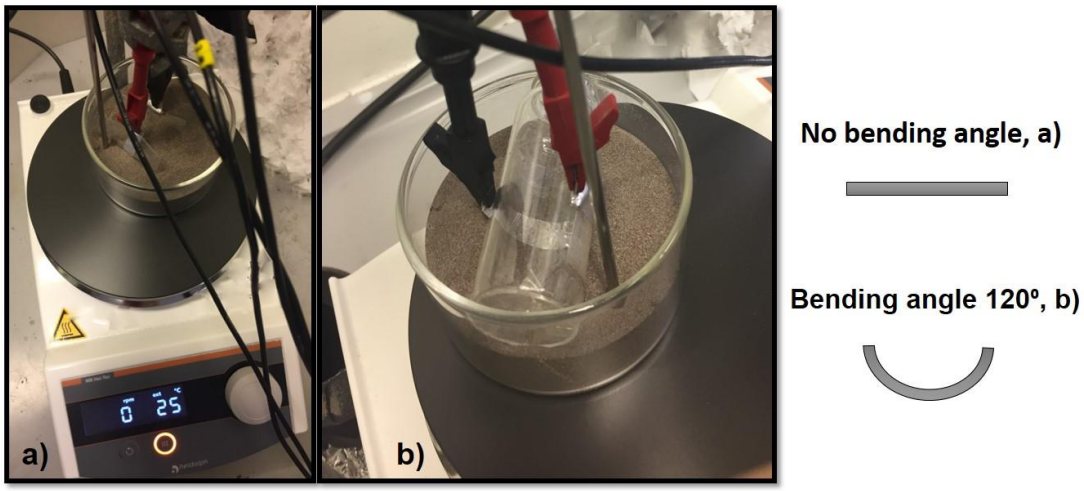

Figure 4.3 Two-electrodes device system (set-up) used for the electrochemical measurements with temperature control using a sand bath at 25 ± 2 ºC a) no bending angle applied and b) 120 degrees bending angle applied

4.2. Results and Discussion

4.2.1. Measurement of the Electrochemical Window of Ionic Liquids Electrolytes

The electrochemical study of two ILs was carried out to obtain their electrochemical window, that will be later compared to the supercapacitors' EWs using the same two ILs as the electrolytes. The electrochemical window refers to the chemical stability between the anodic and cathodic limits of the electrolyte with a given electrode, *i.e.* the potential range where the electrolyte does not suffer either an oxidation or reduction on a given electrode and normally noble metals such as Pt, Au and glassy carbon (non-metals) are used for standard measurements [27]. These electrodes are chosen on the merit that they are more stable in general and do not participate in Faradaic reactions with the electrolyte. Therefore, for a general study on electrochemical windows non-reactive electrodes are used to make sure that the EW

best describes the inherent nature of the electrolyte. Figure 4.4 shows the typical cyclic voltammogram of an IL and how to extract the EW from the difference values between the anodic (E_{AL}) and cathodic limits (E_{CL}) obtained at certain current or current density which is called cut-off current, as shown in Equation 4.1.

$$EW = E_{AL} - E_{CL} \qquad \text{Equation 4.1}$$

The choice of the cut-off current is arbitrary, there is not an established value. Different values are reported in the literature due to the strong dependence in the mass transport of the electrolyte and also the working electrode and scan rate utilised, making very difficult to compare definitively the EW values of ILs [310]. From the literature, general cut-off current values are between 0.01 and 5.0 mA. For this thesis, the cut-off value chosen was 0.05 mA. It is also worth mentioning that the small peaks, shoulders or plateaus observed in the CVs were neglected for the EW calculation if their currents were below the limit of the cut-off current (due to their very low current density); nevertheless, they will be analysed in this chapter.

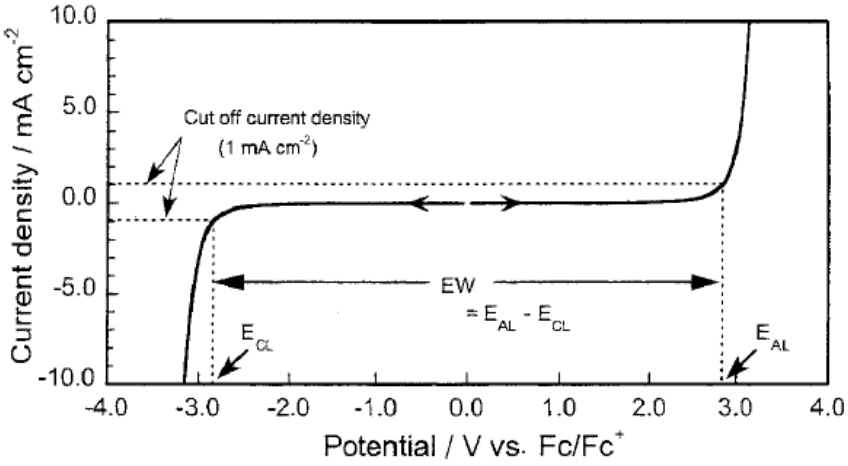

Figure 4.4 Typical cyclic voltammogram of ILs, showing the anodic and cathodic limits and how the extraction of the EW is carried out [27]

The first ionic liquid studied was 1-ethyl-3-methylimidazolium bis{(trifluoro methyl)sulfonyl}amide, [C_2mim][NTf_2], and its structure is shown in Figure 4.5. This IL is well known for its good characteristics such as high thermal and electrochemical stability, low viscosity, and, non-volatile and non-combustible nature [311,27]. Due to its known electrolyte characteristics and because it is important to use a known electrolyte to validate the new electrodes fabricated, it was chosen to be used as an electrolyte in the supercapacitors fabricated.

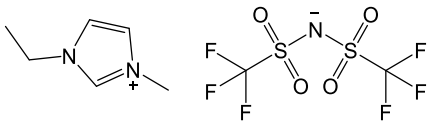

Figure 4.5 Structure of IL 1-ethyl-3-methylimidazolium bis{(trifluoromethyl)sulfonyl}amide, [C_2mim][NTf_2]

The evaluation of the EW of the neat ILs was carried out obtaining their anodic and cathodic limits *vs*. a reference electrode, in this case, Ag|$AgNTf_2$ in [C_2mim][NTf_2] (Ag|Ag^+). These limits related to the degradation of the electrolyte on the application of over potential. It is well known that the cathodic limit corresponds to the cation reduction and the anodic limit is the anion oxidation [27]. In the case of the [C_2mim][NTf_2], the cation imidazolium can be reduced to a carbene [312] and the anion bis{(trifluoromethyl)sulfonyl}amide can be oxidised losing one electron, although it is not clear what compounds are obtained from the oxidation of the IL anion [313].

Figure 4.6 shows three graphs in which three different working electrodes Pt, Au and GC were used and at different scan rates (50, 100 and 500 mV s^{-1}). Figure 4.6 (a) shows the voltammogram obtained using Pt as the working electrode at different scan rates where an anodic peak around -0.35 V and a cathodic peak around -0.5 V were found which can be related to the reversible reactions of the hydrogen adsorption and desorption over the platinum electrode surface due to the existence of water in the system [140]. These peaks showed an increment of the current when faster scan rates were applied. This may occur due to the increase of the concentration gradient as it is established in Randles-Sevcik (Equation 4.2) at 25 ^{0}C, where i_p (A) is the peak maximum current, n is the number of electrons transferred in the redox reaction, A (cm^2) electrode area, D (cm^2 s^{-1}) diffusion coefficient, C (mol cm^{-3}) is the concentration and ν (V s^{-1}) corresponded to the scan rate.

$$i_p = 268600\, n^{3/2} \cdot A \cdot D^{1/2} \cdot C \cdot \nu^{1/2} \qquad \text{Equation 4.2}$$

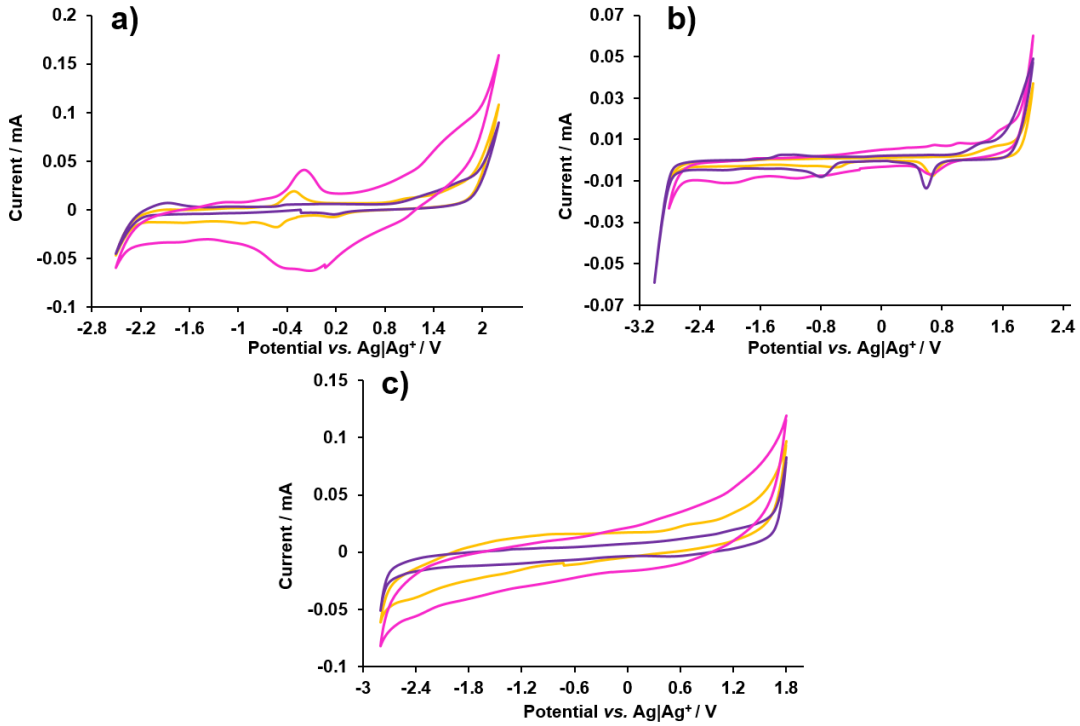

Figure 4.6 Cyclic voltammograms of $[C_2mim][NTf_2]$ at 25 ± 2 ºC using different scan rates 50 (purple), 100 (yellow) and 500 mV s^{-1} (pink) and different working electrodes a) Pt, b) Au and c) GC

The voltammograms obtained using gold as working electrode (Figure 4.6 (b)) show an anodic peak around 1.7 V related to the formation of gold oxides (*e.g.* Au_2O_3) at the electrode surface in presence of water in the system through the electrooxidation of the gold electrode itself [314]. The gold oxide formed at positive potentials can be reduced back to elemental gold when the direction of the scan becomes negative, as it can be seen there is cathodic peak around 0.7 V that corresponds to the reduction of gold (III) oxide to metallic gold.

The voltammogram obtained using glassy carbon as the working electrode, Figure 4.6 (c), showed capacitive behaviour due to the bigger surface area of the GC electrode. As in the other voltammograms, the current increased at faster scan rates and also, the water impurity can be deduced from the voltammogram due to a little hump at the cathodic current around 0.8 V. The EW values obtained from the voltammograms of Figure 4.6 are displayed in Table 4.2.

Figure 4.7 shows the voltammograms obtained at 70 ± 2 ºC for the same three electrodes (Pt, Au and GC), and at different scan rates (50, 100 and 500 mV s^{-1}). As it can be seen, the same peaks related to water appeared, and similar values of electrochemical windows were found, as it is shown in Table 4.2.

As it was expected, the current density, generated in the cyclic voltammogram, increased when the experiment was recorded at high temperatures due to the drop in the viscosity of the electrolyte. Lower viscosities provoke to increase the mobility of the ions and therefore, the conductivity increases [130].

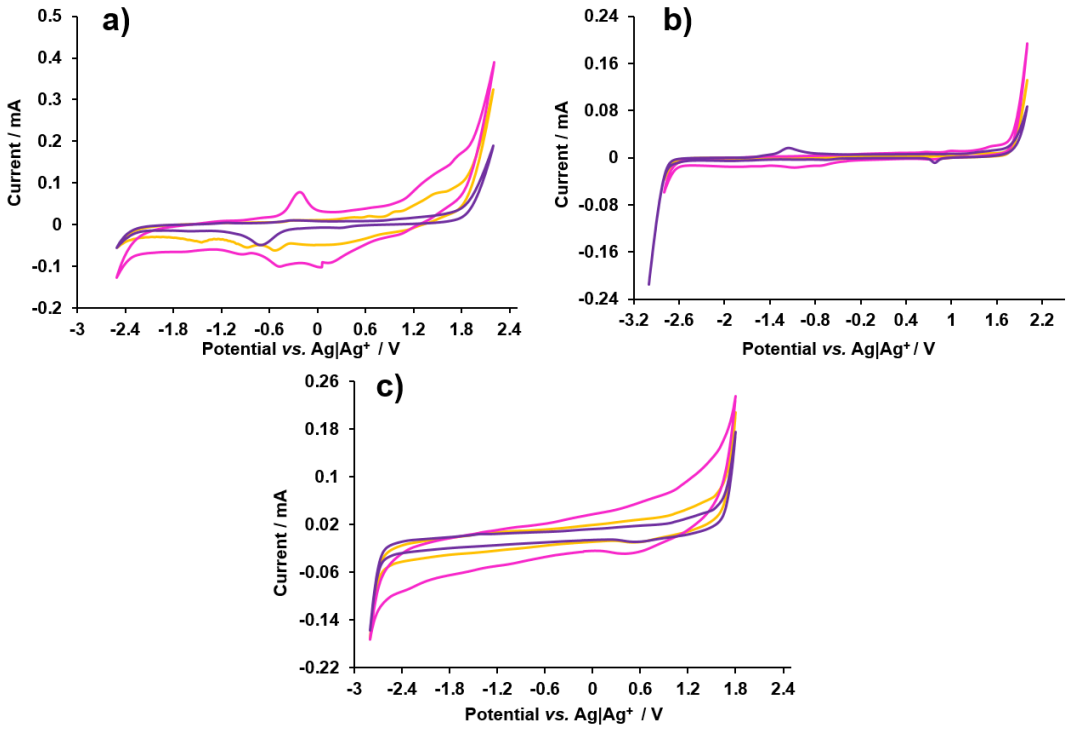

Figure 4.7 Cyclic voltammograms of $[C_2mim][NTf_2]$ at 70 ± 2 ºC using different scan rates 50 (purple), 100 (yellow) and 500 mV s^{-1} (pink) and different working electrodes a) Pt, b) Au and c) GC

Table 4.2 shows the EW values at the scan rate of 50 mV s^{-1} for the three electrodes and at 25 ± 2 ºC and 70 ± 2 ºC. As it can be seen, for both temperatures, the widest EW was obtained using the Au electrode. For this study, depending on the electrode used, the EW decrease at 25 ± 2 ºC as follows, Au > GC ~ Pt and, in the case of 70 ± 2 ºC, the sequence changed as follows, Au > Pt ~ GC. The EW values obtained for $[C_2mim][NTf_2]$ agreed with the values found in the literature [315]; the maximum EW value obtained for $[C_2mim][NTf_2]$ was 4.98 V at 25 ± 2 ºC using gold as the working electrode. A possible reason for the smaller EW using Pt and GC could be due to the greater reactivity of the Pt with the water and, in the case of the GC could be due to the double-layer charging effect.

Table 4.2 EW, anodic and cathodic potentials *vs.* $Ag|Ag^+$ of the IL $[C_2mim][NTf_2]$ at the scan rate of 50 mV s^{-1} and at the cut-off current of 0.05 mA using Pt, Au and GC as the working electrodes at 25 ± 2 ºC and 70 ± 2 ºC

25 ± 2 ºC (scan rate 50 mV s^{-1})			
Electrode	E_{AL} / V	E_{CL} / V	EW / V
Pt	2.02	-2.50	4.52
Au	2.00	-2.98	4.98
GC	1.73	-2.80	4.53
70 ± 2 ºC (scan rate 50 mV s^{-1})			
Electrode	E_{AL} / V	E_{CL} / V	EW / V
Pt	1.86	-2.48	4.34
Au	1.91	-2.83	4.74
GC	1.55	-2.68	4.23

Apart from the calculation of the EW of the neat electrolyte, the measurement of the EW using ferrocene as an internal standard was carried out, as displayed in Figure 4.8, allowing the comparison of the potential limits. An internal standard for electrochemical processes is a compound which can be used as a reference because it does not interact with the electrolyte species and has a well-defined reversible redox couple [316]. This criterion is adequately filled by ferrocene, but other compounds can be used as internal standard in ionic liquids *e.g.* cobaltocenium/cobaltocene redox couple [317].

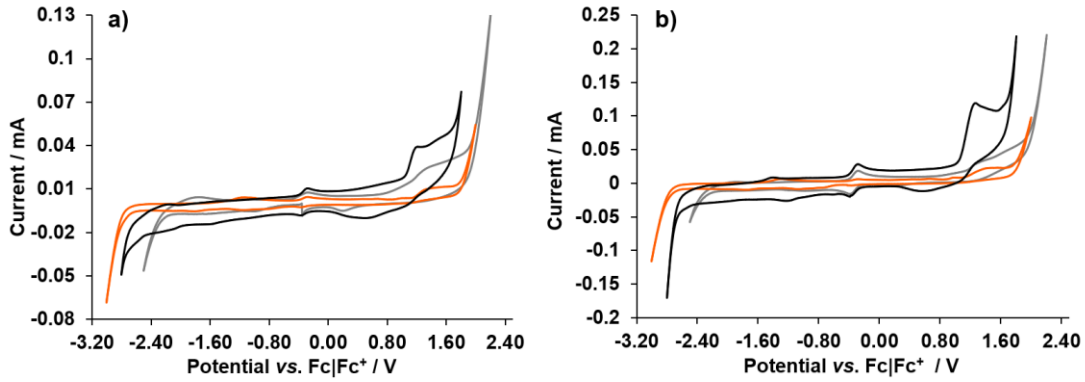

Figure 4.8 Cyclic voltammograms of $[C_2mim][NTf_2]$ at the scan rate of 50 mV s^{-1} using ferrocene as internal standard and different working electrodes: Pt (grey), Au (orange) and GC (black) at a) 25 ± 2 ºC and b) 70 ± 2 ºC

The electrochemical window was calculated taking into account the ferrocene redox couple peaks as an internal standard. Generally, the ferrocene|ferrocenium couple ($Fc|Fc^+$) undergoes a reversible oxidation/reduction, as shown Equation 4.3.

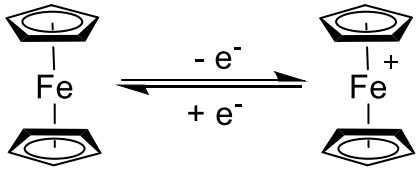

Equation 4.3

As the ferrocene|ferrocenium couple is a one-electron reaction it exhibits a ferrocene peaks separation potential ($\Delta E_{Fc|Fc+}$) of 0.059 V, as shown in Equation 4.4, where $E_{AP} - E_{CP}$ (V) corresponds to the separation between the peak potentials (E_{AP} for me anodic peaks and E_{CP} for the cathodic peak) and n is the number of electrons transferred [318].

$$\Delta E = E_{AP} - E_{CP} \cong \frac{0.059}{n} \quad \text{Equation 4.4}$$

$\Delta E_{Fc|Fc+}$ values obtained for this IL were higher in comparison to the typical or reversible processes as it can be seen in Table 4.3. Nevertheless, it was found in the literature that the values expected from the ferrocene couple in ILs are approximately 0.081 V showing a quasi-reversible process [319]. It is reported that in non-aqueous solvents, a high solution resistance can exist which can be translated in large peak separations; in fact, the values obtained in this case agreed with the values found in the literature [316].

Equation 4.5 describes the EW calculation of the ILs considering the internal standard redox couple $Fc|Fc^+$, where E_{AL} and E_{CL} are the anodic cathodic limits of the IL, respectively and, E_{AP} and E_{CP} corresponds to the anodic and cathodic peaks of the $Fc|Fc^+$ redox couple. The EW values obtained *vs.* $Fc|Fc^+$, using Equation 4.5, were very similar than in the case of the neat electrolytes, following the trend Au > Pt > GC at 25 ± 2 ºC and Au > Pt > GC at 70 ± 2 ºC. Table 4.3 summarises the EW values at the scan rate of 50 mV s^{-1}, using different working electrodes and at two different temperatures.

$$EW = (E_{AL} - E_{AP}) - (E_{CL} - E_{CP}) \quad \text{Equation 4.5}$$

The main difference was found for the EW using GC as the working electrode at 70 ± 2 ºC. The EW was reduced 0.85 V from the neat IL to the IL *vs.* $Fc|Fc^+$, due to the

presence of a shoulder before the anodic limit, which reduced the EW substantially. This peak at 1.32 V may be attributed to chloride oxidation (Equation 4.6) and the little shoulder at 0.70 V found in the reverse scan may be the chloride reduction peak [320]. The oxidation of chloride at a glassy carbon electrode can be assigned to Equation 4.6. The origin of this impurity is not known due to the absence of chloride in the IL under study.

$$2Cl^- \longrightarrow Cl_2 + 2e^- \qquad \text{Equation 4.6}$$

Table 4.3 EW, $\Delta E_{Fc|Fc+}$, anodic and cathodic potentials *vs.* $Fc|Fc^+$ of the IL $[C_2mim][NTf_2]$ at the scan rate of 50 mV s^{-1} and at the cut-off current of 0.05 mA using Pt, Au and GC as the working electrodes at 25 ± 2 ºC and 70 ± 2 ºC

25 ± 2 ºC (scan rate 50 mV s^{-1})				
Electrodes	E_{AL} / V	E_{CL} / V	$\Delta E_{Fc\|Fc+}$ / V	EW / V
Pt	1.98	-2.50	0.078	4.40
Au	1.98	-2.96	0.073	4.87
GC	1.65	-2.80	0.073	4.38
70 ± 2 ºC (scan rate 50 mV s^{-1})				
Electrodes	E_{AL} / V	E_{CL} / V	$\Delta E_{Fc\|Fc+}$ / V	EW / V
Pt	1.69	-2.47	0.078	4.08
Au	1.88	-2.88	0.068	4.69
GC	1.10	-2.66	0.078	3.68

The other IL studied was 1-ethyl-3-methylimidazolium tris(pentafluoroethyl) trifluoro phosphate, $[C_2mim][FAP]$, the structure of which is shown in Figure 4.9. This IL was chosen because of it is an attractive candidate for electrochemical applications as *e.g.* electrolyte due to its hydrophobicity, low viscosity and high electrochemical and thermal stabilities [321].

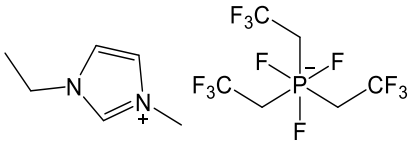

Figure 4.9 Structure of the IL 1-ethyl-3-methylimidazolium tris(pentafluoroethyl) trifluoro phosphate, $[C_2mim][FAP]$

The same peaks seen above, from water impurities, were also found when using the Pt and Au working electrodes at 25 ± 2 ºC (Figure 4.10). In comparison to the

previous IL, [C_2mim][NTf_2], the electrochemical windows were wider, demonstrating that [C_2mim][FAP] is more stable electrochemically.

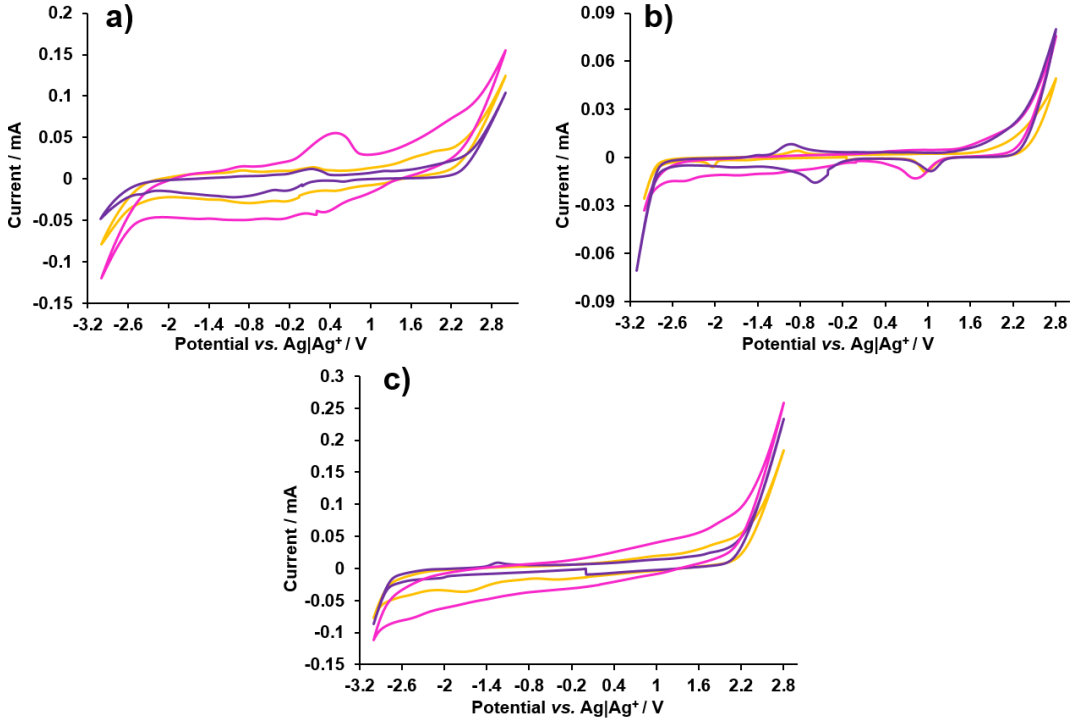

Figure 4.10 Cyclic voltammograms of [C_2mim][FAP] at 25 ± 2 ºC using different scan rates 50 (purple), 100 (yellow) and 500 mV s^{-1} (pink) and different working electrodes a) Pt, b) Au and c) GC

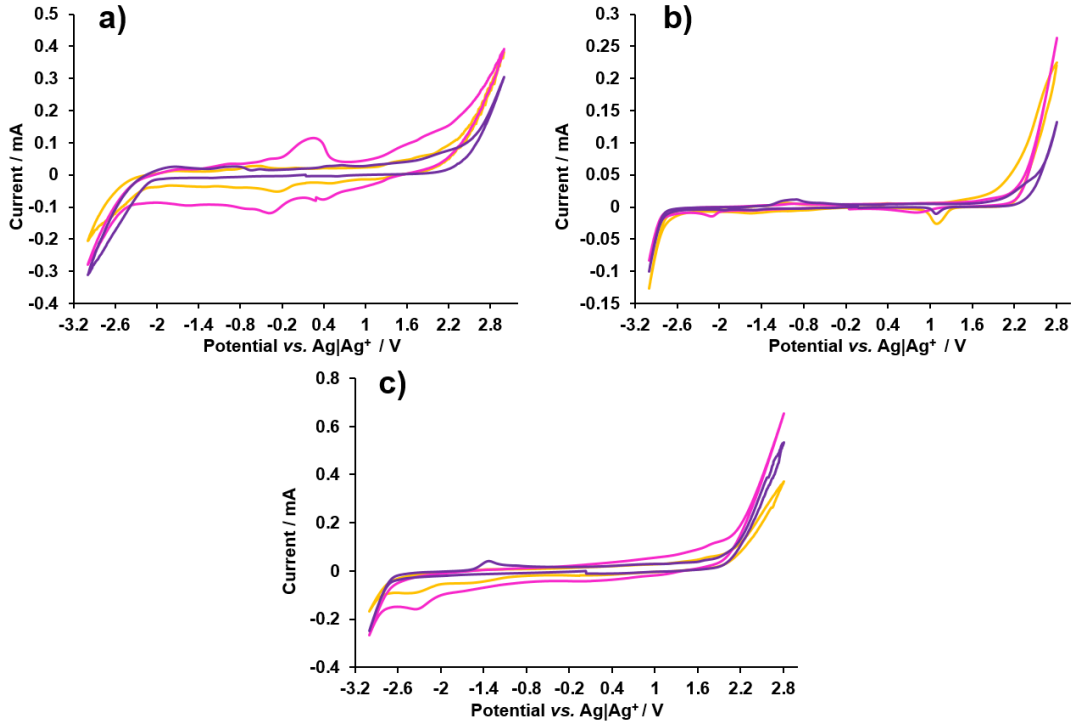

Figure 4.11 Cyclic voltammograms of [C_2mim][FAP] at 70 ± 2 ºC using different scan rates 50 (purple), 100 (yellow) and 500 mV s^{-1} (pink) and different working electrodes a) Pt, b) Au and c) GC

The cyclic voltammograms of [C_2mim][FAP] using three different working electrodes (Pt, Au and GC) *vs.* $Ag|Ag^+$ at the temperature of 70 ± 2 ºC and at different scan rates 50, 100 and 500 mV s^{-1}, are shown in Figure 4.11.

The EWs for [C_2mim][FAP] were wider than in the case of [C_2mim][NTf_2], as it can be seen in Table 4.4, with a maximum value of 5.65 V at 25 ± 2 ºC for the Pt electrode. The EW trend found, depending on the electrode used, was Pt > Au > GC at 25 ± 2 ºC, and in the case of 70 ± 2 ºC, the trend was Au > GC > Pt. The most relevant changes between both temperatures were found for the Pt and GC electrodes, with a decrease of their EW of ~ 1.6 V and ~ 0.59 V, respectively. This reduction in the EW was due to the decrease of both cathodic and anodic limits, and the reason could be that at 70 ± 2 ºC there is a higher reactivity of the Pt with water and, in the case of the GC it could be due to the double-layer charging effect, as it was reported for [C_2mim][NTf_2] (page 129).

Table 4.4 EW, anodic and cathodic potentials *vs.* $Ag|Ag^+$ of the IL [C_2mim][FAP] at the scan rate of 50 mV s^{-1} and at the cut-off current of 0.05 mA using Pt, Au and GC as the working electrodes at 25 ± 2 ºC and 70 ± 2 ºC

25 ± 2 ºC (scan rate 50 mV s^{-1})			
Electrode	E_{AL} / V	E_{CL} / V	EW / V
Pt	2.64	-3.01	5.65
Au	2.57	-3.02	5.59
GC	2.21	-2.89	5.10
70 ± 2 ºC (scan rate 50 mV s^{-1})			
Electrode	E_{AL} / V	E_{CL} / V	EW / V
Pt	1.81	-2.24	4.05
Au	2.50	-2.91	5.41
GC	1.80	-2.71	4.51

Figure 4.12 shows the cyclic voltammograms of [C_2mim][FAP] using ferrocene as the internal standard for the three electrodes at the scan rate of 50 mV s^{-1} and two different temperatures 25 ± 2 ºC and 70 ± 2 ºC, where the ferrocene couple can be found at potentials around -0.3 V.

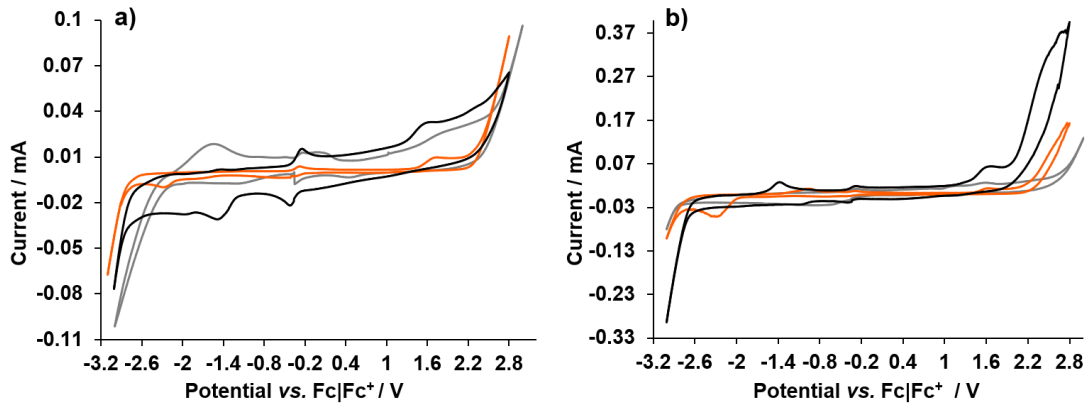

Figure 4.12 Cyclic voltammograms of [C_2mim][FAP] at the scan rate of 50 mV s^{-1} using ferrocene as internal standard and different working electrodes: Pt (grey), Au (orange) and GC (black) at a) 25 ± 2 ºC and b) 70 ± 2 ºC

From the voltammograms, the EW values of the IL were calculated with respect to the ferrocene couple peak potentials (Equation 4.5) as is shown in Table 4.5. The maximum EW value obtained *vs.* $Fc|Fc^+$ was 5.57 V using the Au electrode at 25 ± 2 ºC, being 80 mV smaller than the one obtained for the neat IL (5.65 V at 25 ± 2 ºC for the Pt electrode). The sequence for the stability of this IL *vs.* $Fc|Fc^+$ at 25 ± 2 ºC, depending on the electrode, was Au > Pt ~ GC and, in the case of 70 ± 2 ºC, the sequence was Pt > Au > GC. All the EW values *vs.* $Fc|Fc^+$ found for [C_2mim][FAP] were greater than 5 V except for the GC electrode at 70 ± 2 ºC (4.05 V), showing a decrease of 1.25 V in comparison of the EW *vs.* $Fc|Fc^+$ at 25 ± 2 ºC.

Table 4.5 EW, $\Delta E_{Fc|Fc+}$, anodic and cathodic potentials *vs.* $Fc|Fc^+$ of the IL [C_2mim][FAP] at the scan rate of 50 mV s^{-1} and at the cut-off current of 0.05 mA using Pt, Au and GC as the working electrodes at 25 ± 2 ºC and 70 ± 2 ºC

25 ± 2 ºC (scan rate 50 mV s^{-1})				
Electrodes	E_{AL} / V	E_{CL} / V	$\Delta E_{Fc\|Fc+}$ / V	EW / V
Pt	2.73	-2.66	0.079	5.31
Au	2.59	-3.04	0.064	5.57
GC	2.53	-2.90	0.122	5.31
70 ± 2 ºC (scan rate 50 mV s^{-1})				
Electrodes	E_{AL} / V	E_{CL} / V	$\Delta E_{Fc\|Fc+}$ / V	EW / V
Pt	2.67	-2.93	0.087	5.51
Au	2.47	-2.89	0.074	5.29
GC	1.50	-2.67	0.122	4.05

Comparing the electrochemical test results for these two ILs it can be said that the IL [C_2mim][FAP] is more electrochemically stable than [C_2mim][NTf_2], and shows an increment in the EW of at least ~ 0.3 V. The maximum difference in the EW is of 1.1 V, found for the Pt electrode at 25 ºC. This increase in the EW was driven by both the anion and cation. The anion oxidation corresponds to the anodic limit and shows a maximum rise of ~ 0.6 V for [C_2mim][FAP] in comparison to [C_2mim][NTf_2]. In the case of the cathodic limits, which is related to the cation reduction, [C_2mim]$^+$, the maximum difference in the potential values was ~ 0.5 V. The cathodic limit variation could be related to the water content in the ILs, as the same cation, [C_2mim]$^+$ is used in both systems [322].

These two ILs showed that the EW values decreased ~ 100 mV when the experiment was carried out at 70 ± 2 ºC in comparison to the EWs at 25 ± 2 ºC. The drop in EW was rather small, therefore, it can be said that these two ILs are stable electrochemically at higher temperatures on standard electrodes.

The electrode that procured the widest EW for these ILs was Au for [C_2mim][NTf_2] at 25 ± 2 ºC (4.98 V) and 70 ± 2 ºC (4.74 V) and, in the case of [C_2mim][FAP] the larger EW was obtained with different electrodes depending on the temperature *i.e.* the maximum EW was found 5.65 V with the Pt electrode at 25 ± 2 ºC and, at 70 ± 2 ºC the Au electrode showed the widest EW (5.41 V).

In the case of the EWs trends depending on the electrode used and at different temperatures, differences between neat ILs were found. In the case of [C_2mim][NTf_2] the EW trend was Au > Pt > GC at both temperatures and, for [C_2mim][FAP] the trend at 25 ± 2 ºC was Pt > Au > GC and Au> GC > Pt at 70 ± 2 ºC. From these results, it can be said that [C_2mim][NTf_2] is more electrochemically stable using gold as the working electrode at different temperatures and, in the case of [C_2mim][FAP], the highest electrochemical stability was obtained using platinum and gold as working electrodes at 25 ± 2 ºC and 70 ± 2 ºC, respectively.

4.2.2. Electrochemical Study of the EDLS Fabricated Using [C_2mim][NTf_2] as the Electrolyte

The electrochemical study of a set of three EDLSs with graphite-cellfib-IL plasticiser composite films as electrodes, and using [C_2mim][NTf_2] as the electrolyte

was carried out to establish their energy storage device capabilities. All the electrochemical measurements were performed as a two-electrode system at 25 ± 2 ºC, to make it similar to that used in practical applications (Figure 4.2).

An EDLS is an energy storage device with an electrostatic storage mechanism which means that no redox reactions are involved. The active material was the graphite from the graphite-cellfib-IL plasticiser composite film, compromising a 33.3 wt % of the total weight at each electrode. The total mass of the active material was 5.0 ± 1.0 mg, the area 1 cm^2 and the thickness of the electrodes 130 ± 30 µm.

For the set of three EDLS devices using $[C_2mim][NTf_2]$ as the electrolyte, the open-circuit potential (OCP) found was 0.06 ± 0.02 V, which is near zero as it was expected (see section 4.1.3).

4.2.2.1. Cyclic Voltammetry

The first feature to consider in a new device is its operational voltage (EW). The EW procurement consists of a CV test that applies a linearly changed electric potential between positive and negative electrodes for two-electrode systems using a speed potential change in V s^{-1} named as scan rate (ν) [323].

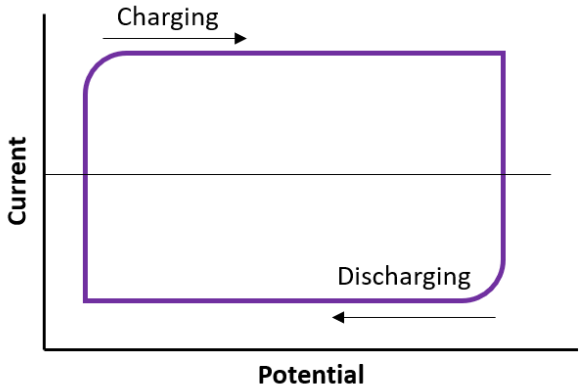

Figure 4.13 Ideal cyclic voltammogram for a double-layer supercapacitor

An ideal double-layer supercapacitor gives a rectangular cyclic voltammogram (Figure 4.13), governed by Equation 1.1 ($C = \frac{Q}{EW}$). The rectangular voltammogram is a qualitative criterion to judge the capacitive behaviour of a device or an electrode material that is governed by Equation 4.8, where i (A) is the current flowing through the device, C (F) is the capacitance and ν (V s^{-1}) correspond to the scan rate.

Equation 4.8 is obtained differentiating Equation 1.1 against time, considering the capacitance (C) as constant and assuming that the potential varies linearly with

the time, then $dEW/dt = v$. Equation 4.7 was simplified more considering $dQ/dt = i$ (current) giving as a result Equation 4.8.

$$\frac{dQ}{dt} = C\frac{dEW}{dt} + V\frac{dC}{dt} = C\frac{dEW}{dt} \qquad \text{Equation 4.7}$$

$$i = C \cdot v \qquad \text{Equation 4.8}$$

Figure 4.14 shows the cyclic voltammogram obtained for the EDLS fabricated with an operational voltage of 2.1 V from -1.0 V to 1.1 V. From this EDLS a nearly rectangular shape and symmetric voltammogram was obtained, demonstrating an almost ideal capacitive behaviour for this energy storage device.

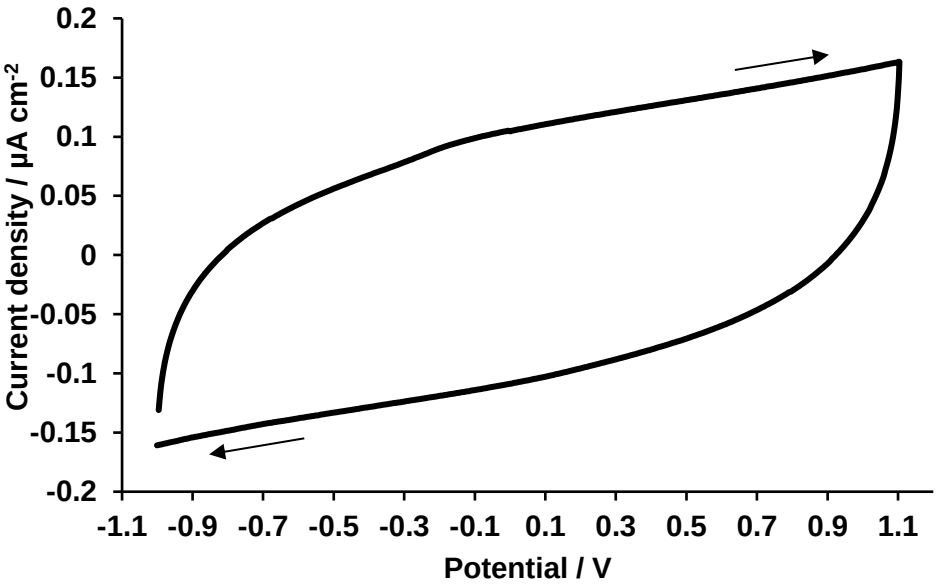

Figure 4.14 Cyclic voltammogram of one of the EDLS fabricated using $[C_2mim][NTf_2]$ as the electrolyte at 50 mV s^{-1} at 25 ± 2 ^{0}C. Arrows show the potential direction of the cyclic voltammogram

The comparison of this operational voltage (2.1 V) with the electrochemical window of the neat electrolyte, $[C_2mim][NTf_2]$, (4.53 V *vs*. $Ag|Ag^+$ using glassy carbon as the working electrode) shows a drop in the potential value of 2.43 V. The main reason for the potential variation in the EW is the different set-up used. In the case of the EW of the neat electrolyte, $[C_2mim][NTf_2]$, a three-electrode system was utilised (see section 4.1.1) and for the EDLS measurements a two-electrode system was used (see section 4.1.3). The three-electrode experiment is used to analyse the working electrode isolated *i.e.* this set-up measures only one half of the cell (the counter

electrode is the one that completes the current path), whereas, the two-electrode system measures the whole cell, the positive electrode *vs*. the negative electrode [324].

From the CV curves, the specific capacitance (C_{Spec}) of the supercapacitor can be obtained using Equation 4.10, which was obtained from Equation 1.1. For the calculation of Q (C), the integral of the discharge current obtained from the CV was used, as it is shown in Equation 4.9 and assuming that $dt = {dV}/{v}$.

$$\mathrm{Q} = \int_{t_i}^{t_f} I(t)dt = \frac{1}{v}\int_{V_i}^{V_f} I(V)dV \qquad \text{Equation 4.9}$$

$$C_{spec} = \frac{1}{m \cdot v\,(V_f - V_i)}\int_{V_i}^{V_f} I(V)dV \qquad \text{Equation 4.10}$$

Therefore, the specific capacitance was calculated using Equation 4.10 where m (g) is the mass of the active material in the electrodes v (V s^{-1}) is the scan rate, V_f and V_i (V) corresponds to the operational voltage limits (with *i* and *f* referring to initial and final) and $\int_{V_i}^{V_f} I(V)dV$ (A) refers to the integral of the discharge current I (A) in the voltammogram.

In the case of the areal capacitance (C_{Areal}) the same Equation 4.10 was used but, instead of dividing by the mass of the active material, the capacitance was divided by the area of the electrodes (1 cm^2).

The same operational voltage (2.1 V) was obtained for the three EDLS fabricated, as it is shown in Figure 4.15. It can be seen that two of the EDLS showed an identical cyclic voltammogram and the third device differed a little, showing a thinner cycle. In the case of the capacitance values, the specific capacitance obtained was 6.6 ± 1.2 mF g^{-1} and 34.2 ± 3.3 μF cm^{-2} for the areal capacitance at the scan rate of 50 mV s^{-1}. The EW and capacitance values, for this EDLS using [C_2mim][NTf_2], were found to be very similar to those reported by Horowitz *et al.* [160] who found an EW of 2.5 V and an areal capacitance of 7.7 ± 0.4 μF cm^{-2}, using the same IL, [C_2mim][NTf_2], as electrolyte, over glassy carbon.

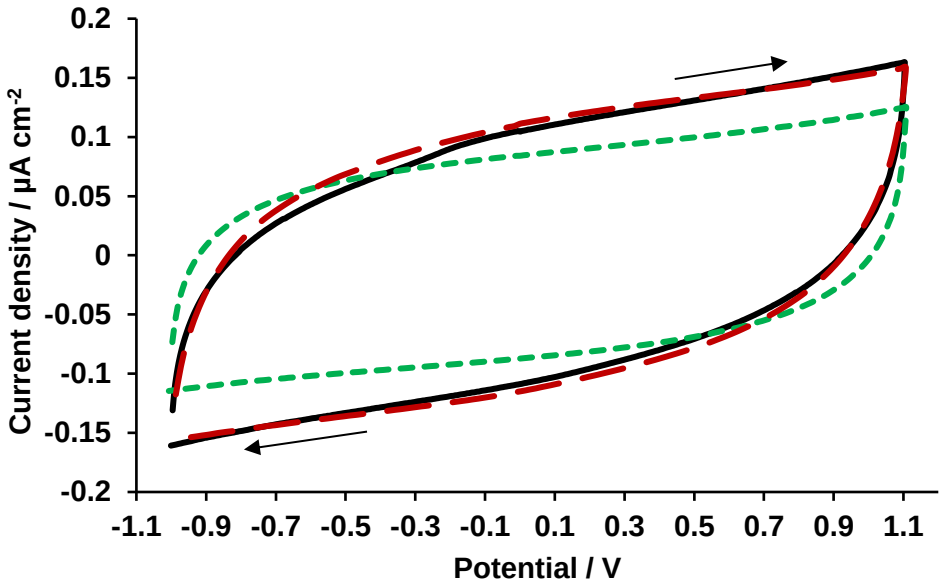

Figure 4.15 Cyclic voltammograms of the three EDLS fabricated using [C_2mim][NTf_2] as the electrolyte at 50 mV s^{-1} and at 25 ± 2 ^{0}C. Arrows show the potential direction of the cyclic voltammogram

To evaluate the power capability of the EDLS, cyclic voltammetry experiments were performed at scan rates ranging from 20 to 1000 mV s^{-1} (Figure 4.16). From low to high scan rates, the CV curves showed more of a resistive behaviour due to the decrease in the ionic transport of the electrolyte into the porous electrode, *i.e.,* at faster scan rates there is minimal time to form the double-layer [325]. This fact means that the capacitance decreases at higher scan rates, as it is illustrated in Table 4.6.

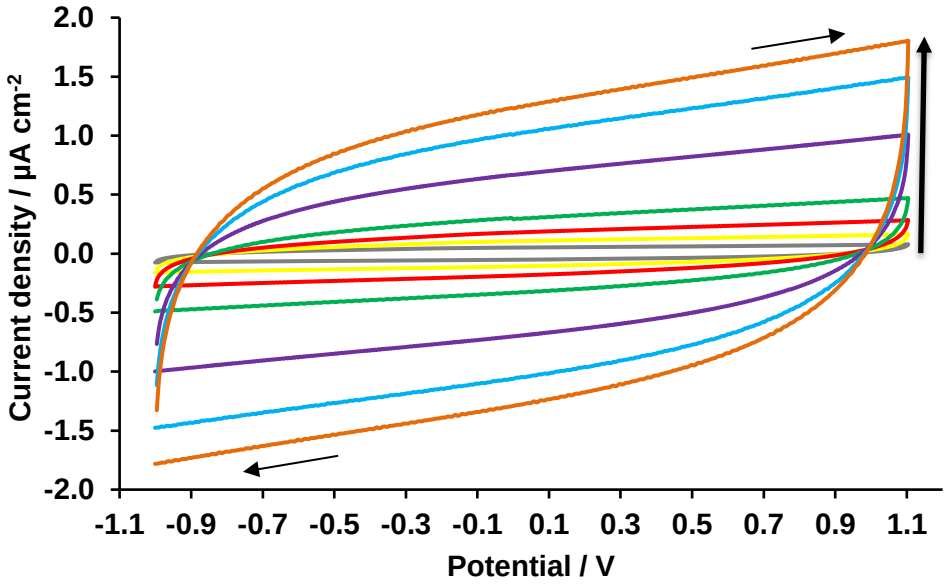

Figure 4.16 Cyclic voltammogram of one of the EDLS using [C_2mim][NTf_2] as the electrolyte at various scan rates: 1000 (orange), 800 (light blue), 500 (purple), 200 (green), 100 (red), 50 (yellow), 20 (grey) mV s^{-1} and at 25 ± 2 ^{0}C. Arrows show the potential direction of the cyclic voltammogram and the vertical arrow indicates the faster scan rates applied

The capacitance values (Table 4.6) dropped rapidly at slow scan rates from 20 to 50 mV s^{-1}, in contrast to that found at higher scan rates, for which the capacitance dropped slowly. From these results, the maximum capacitance values obtained was at the smallest scan rate (20 mV s^{-1}): 18.8 ± 5.8 mF g^{-1} for the specific capacitance, and 97.8 ± 24.0 µF cm^{-2} for the areal capacitance. The maximum areal capacitance value obtained was found to be comparable to the areal capacitance value reported by Yoo *et al.* [231] using pristine graphene (80 µF cm^{-2}) or multilayer graphene films (140 µF cm^{-2}) on copper foil, and gold sputtering on the external edges of both electrodes as the current collectors, using a sandwich shape supercapacitor with polyvinyl alcohol-phosphoric acid (PVA-H_3PO_4) as gel electrolyte.

Table 4.6 Specific and areal capacitance average values of the EDLS using [C_2mim][NTf_2] as the electrolyte calculated from the CV at various scan rates

Scan rate / mV s^{-1}	$C_{Spec.}$ / mF g^{-1}	C_{Areal} / µF cm^{-2}
20	18.8 ± 5.8	97.8 ± 24.0
50	6.6 ± 1.2	34.2 ± 3.3
100	3.0 ± 0.6	15.4 ± 0.2
200	1.3 ± 0.4	6.8 ± 0.6
500	0.4 ± 0.2	2.2 ± 0.4
800	0.3 ± 0.1	1.3 ± 0.4
1000	0.18 ± 0.08	0.9 ± 0.3

Since one of the purposes of this thesis is to obtain a flexible supercapacitor, a bending study (set-up showed in Figure 4.3) on these EDLS was carried out by recording their cyclic voltammograms at a bending angle of 120 degrees. Figure 4.17 (a) shows the tests for the first EDLS prior, during and after bending, which exhibited a slight distortion in the discharge cycle. This may be attributed to an electrical disconnection between graphite particles dispersed in the cellulose matrix during bending, which could be recovered after the bending finished, as shown in last voltammogram (black plot). In the other two EDLS fabricated (Figure 4.17 (b)), more stability during the bending study was found, with no distortion in the voltammograms observed.

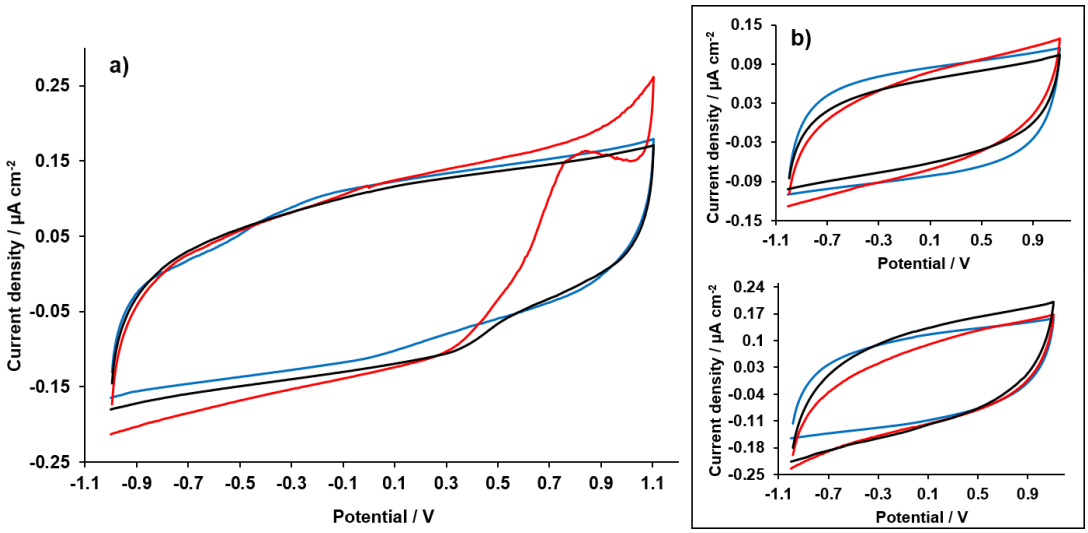

Figure 4.17 Bending study at an angle 120 degrees of a) one of the EDLS and b) the other two EDLS fabricated using $[C_2mim][NTf_2]$ as the electrolyte at the scan rate of 50 mV s^{-1} and at 25 ± 2 ^{0}C. Cyclic voltammogram before (blue), during (red) and after (black) bending

During the bending study the capacitance values of the three EDLS were recorded (Table 4.7) showing a slight change in the values before, during and after bending. The capacitance decreased during the bending state in comparison to the capacitance before bending due to higher resistor behaviour (red plot), whilst, the capacitance was retrieved after bending the supercapacitor.

Table 4.7 Specific and areal capacitance average values of the EDLS using $[C_2mim][NTf_2]$ as the electrolyte during the bending study

Bending state	$C_{Spec.}$ / mF g^{-1}	C_{Areal} / µF cm^{-2}
Prior to bending	6.5 ± 1.1	33.9 ± 4.4
120 degrees angle	6.1 ± 0.7	32.6 ± 10.1
After bending	6.5 ± 2.0	34.6 ± 11.1

Good long-term cycle stability is required for supercapacitor applications so, the cycle life of one of the EDLS was studied by cyclic voltammetry (it was possible to study only one supercapacitor out of the three, due to time restrictions). At a scan rate of 50 mV s^{-1} up to 15000 cycles was recorded, as shown in Figure 4.18 (a). During and after 15000 cycles, the EDLS retained almost 100 % of its initial capacitance with a fluctuation of ± 6 %; Figure 4.18 (b) shows the capacitance retention during the 15000 cycles, demonstrating its high cycle life stability in comparison to flexible graphene-cellulose supercapacitors that showed a cycle life of 5000 cycles [243].

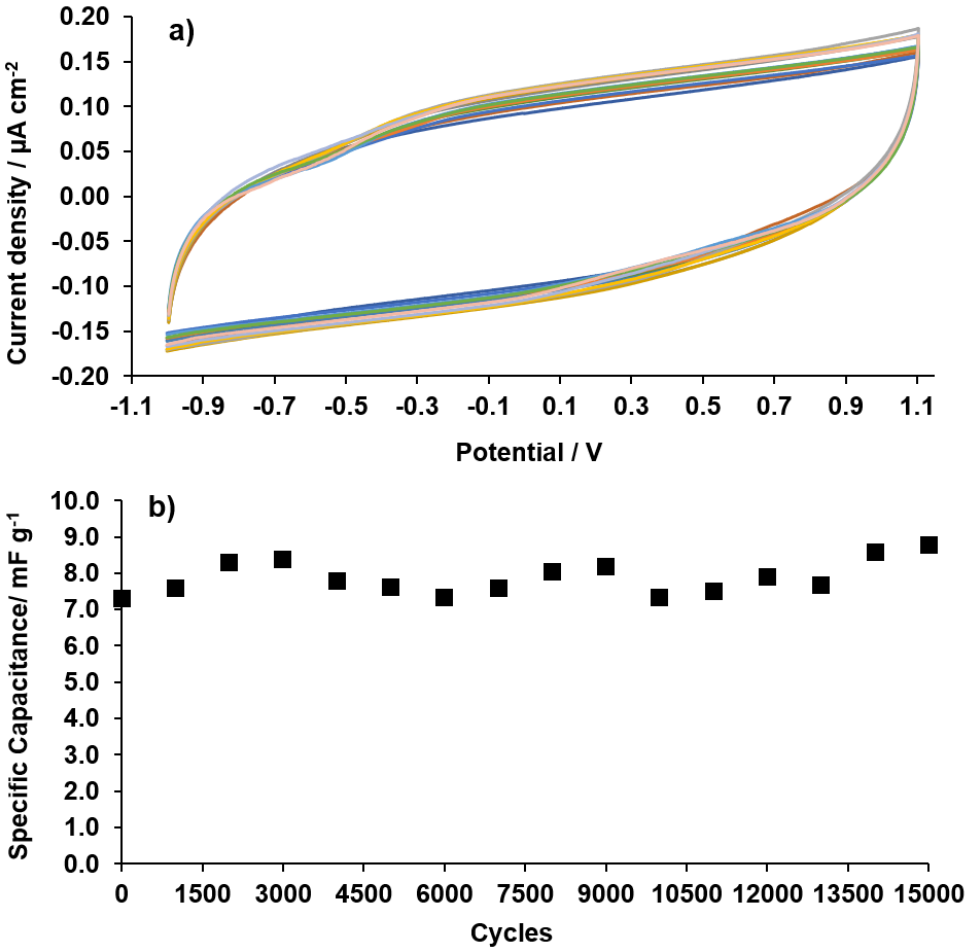

Figure 4.18 a) Cyclic voltammograms of one of the EDLS fabricated using [C_2mim][NTf_2] as the electrolyte at every 1000th scan from 2 to 15000 cycles at the scan rate of 50 mV s^{-1} and at 25 ± 2 ^{0}C and; b) specific capacitance during 15000 cycles

Table 4.8 shows the specific and areal capacitance values of the second and 15000-cycle, where an increase of the capacitance can be appreciated. The average values during the 15000 cycles were 7.9 ± 0.5 mF g^{-1} and 36.3 ± 2.1 µF cm^{-2} for the specific and areal capacitance, respectively. These values showed that this device had good cycle life stability for over 15000 cycles.

The increase of the capacitance during the cycle life could be related to a raise in the temperature during the charge-discharge process that has as consequence a capacitance increase. This behaviour is known as thermocapacitance [326]. The factors that could have changed if there is an increase of the temperature during charge-discharge could be related to the IL electrolytes [327]: (i) the viscosity (higher temperatures decrease the viscosity) and (ii) the ionic conductivity (higher temperatures increase the ionic conductivity). Both properties were described in section 2.1.2. Therefore, the thermal mechanism originated inside the supercapacitor

may be accounted to the heat generated during the charge-discharge process at the electrode/electrolyte surface, and then, this heat is carried away by conduction through the electrodes to the current collectors and finally dissipated by convection outside the device [328].

Table 4.8 Specific and areal capacitance of the second cycle and the 15000 cycle of one of the EDLS fabricated using $[C_2mim][NTf_2]$ as the electrolyte

Cycle 2		Cycle 15000	
C_{Spec} / mF g^{-1}	C_{Areal} / µF cm^{-2}	C_{Spec} / mF g^{-1}	C_{Areal} / µF cm^{-2}
7.3	33.71	8.8	40.4

4.2.2.2. Galvanostatic charge-discharge

Galvanostatic charge-discharge experiments were carried out to determine the rate capability of the device by applying constant currents densities between 0.02 and 1 µA cm^{-2} within a potential window ranging from -1.0 V to 1.1 V (chosen from the operational voltage of the device obtained by CV experiment). In galvanostatic experiments, a constant current is applied to charge (positive current) or discharge (negative current) the supercapacitor, as it is shown in Figure 4.19.

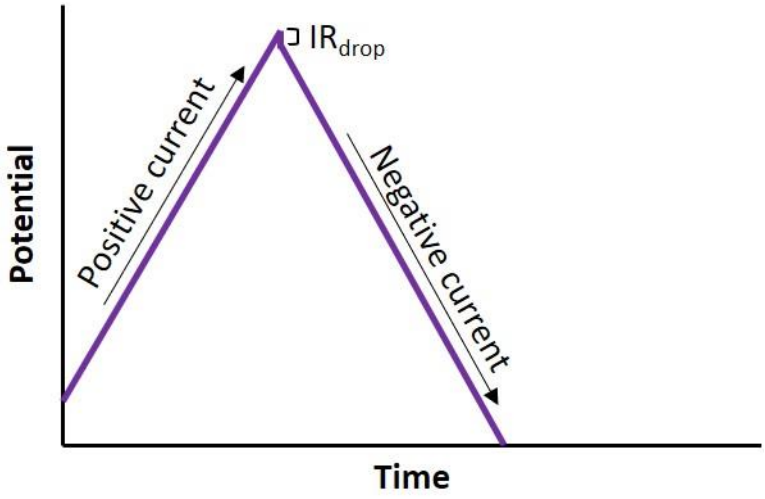

Figure 4.19 Ideal charge-discharge curve for a double-layer supercapacitor. The positive current was used for charge and the negative current for discharge the supercapacitor. In the positive limit, the IR_{drop} (V) is revealed

The potential of the supercapacitor is plotted against the time during a cycle of constant current for charging and discharging, giving as result a nearly symmetric triangular curve due to the voltage change almost linearly as time increases, as is shown in Figure 4.20. From this plot various information can be obtained *e.g.* the

discharge time needed for the EDLS that is altered when different current densities were applied; *i.e.*, when the smallest current density (0.02 μA cm^{-2}) was applied, this device needed 312 s to discharge and at the highest current density applied, the EDLS just needed 4 s to discharge. This demonstrates, as expected, that at high currents faster discharge times are obtained suggesting a decrease in the charge storage [329].

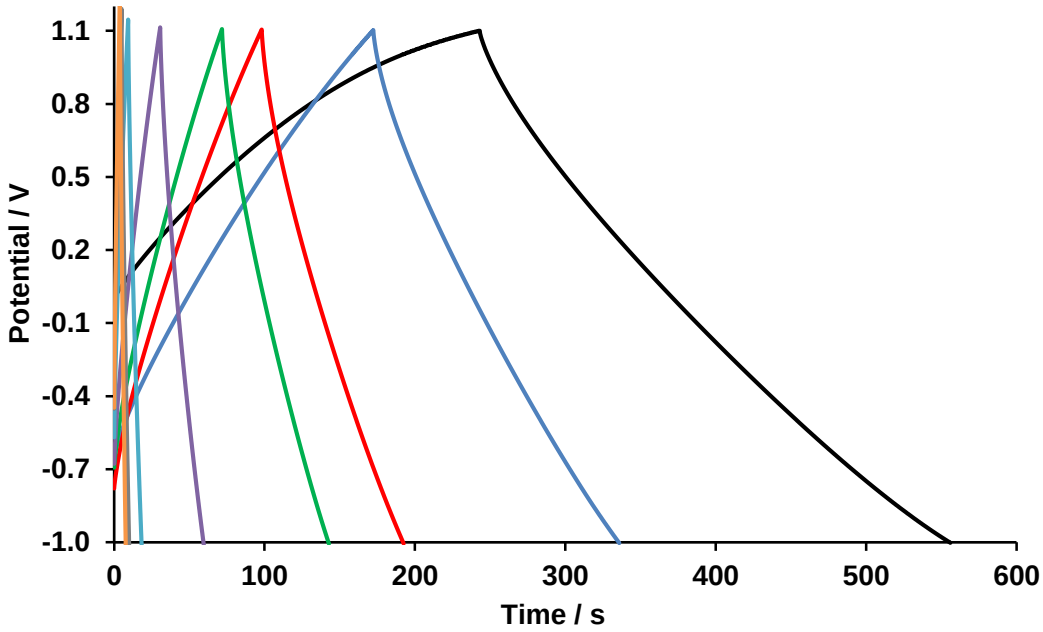

Figure 4.20 GCD curves of one of the EDLS fabricated using [C_2mim][NTf_2] as the electrolyte at different currents densities applied, 0.02 (black), 0.05 (blue), 0.08 (red), 0.1 (green), 0.2 (purple), 0.5 (light blue), 0.8 (grey) and 1 μA cm^{-2} (orange) and at 25 ± 2 ^{o}C

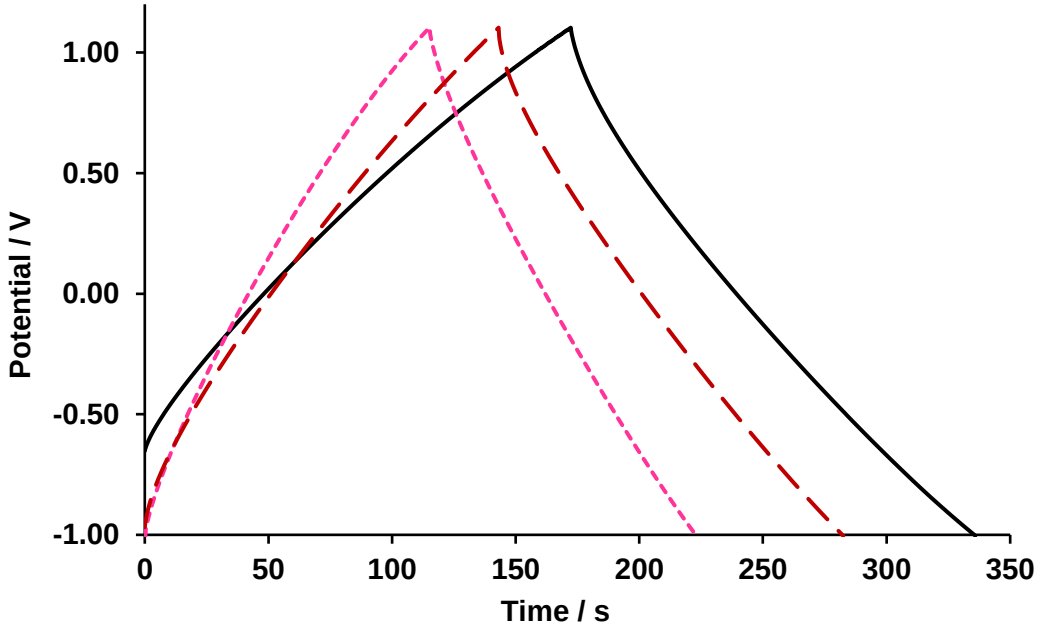

Figure 4.21 GCD curves of the three EDLS fabricated using [C_2mim][NTf_2] as the electrolyte at the current density 0.05 μA cm^{-2} and at 25 ± 2 ^{o}C

The reproducibility of these devices can be demonstrated showing the charge-discharge curve at 0.05 μA cm^{-2} for the three EDLS fabricated. As it can be seen in Figure 4.21, the curves had the same symmetric triangle shape. The total charge-discharge time needed for the three EDLS was 281 ± 56 s, showing the reproducibility of the devices.

From the GCD curves, the equivalent series resistance (ESR) of the device (defined in section 1.4.1) can be calculated using Equation 4.11. The ESR values were calculated from the IR_{drop} (V) that is known as the potential drop at the onset of the discharge current, corresponding to the internal resistance shown in Figure 4.19. In the case of the EDLS, the ESR value was 194 ± 76 kΩ. In general, the supercapacitors fabricated showed high ESR values due to the non-conductive materials used, *e.g.* cellulose as the electrodes' matrix, and aluminium foil as the current collectors. Also, the fabrication of these devices was not carried out with high-pressure sealing, and all, these can be the factors that contributed to the high ESR.

$$ESR = \frac{IR_{drop}}{I_{const.}} \qquad \text{Equation 4.11}$$

The IR_{drop} is an important property in energy storage devices. It is known also, as a voltage drop that occurs when a voltage is applied to a system and current starts to flow through it, and part of the voltage is dropped due to the resistance between the current and the system elements (*e.g.*, electrolyte or electrodes) [330]. Therefore, IR_{drop} determines the electrolyte and the electrolyte-electrode contact resistance. As can be expected, the IR_{drop} values change with the current density applied *i.e.*, the values increased from 9 mV at 0.02 μA cm^{-2} to 200 mV at 1 μA cm^{-2} [331].

The specific and areal capacitances can be calculated also from the GCD curves with Equation 4.12, where $I_{const.}$ (A) is the constant discharge current applied and dEW/dt (V s^{-1}) corresponded to the slope of the discharge current after the correction of the IR_{drop}.

$$C = \frac{I_{const.}}{dEW/dt} \qquad \text{Equation 4.12}$$

The specific and areal capacitance values obtained for these three EDLS were summarised in Table 4.9. As it can be seen, the highest values obtained were lower than the values obtained from the CV experiments (Table 4.6), but if all the values

from GCD, at different current densities are compared to the values from CV, it can be seen that the specific capacitance at the current density of 0.02 μA cm^{-2} (0.67 ± 0.01 mF g^{-1}) corresponded almost to the specific capacitance at the scan rate of 500 mV s^{-1} (0.4 ± 0.2 mF g^{-1}). As Cyclic Voltammetry facilitates the best values of specific and areal capacitance in comparison to GCD, the capacitance values shown from now on will be the ones obtained from CV experiments.

Table 4.9 Specific and areal capacitances average values obtained from the GCD plot at every current density applied to the three EDLS fabricated using [C_2mim][NTf_2] as the electrolyte

Current density / μA cm^{-2}	Slope	C_{Spec} / mF g^{-1}	C_{Areal} / μF cm^{-2}
0.02	0.006 ± 0.001	0.67 ± 0.01	3.6 ± 0.7
0.05	0.015 ± 0.003	0.7 ± 0.2	3.5 ± 0.8
0.08	0.025 ± 0.006	0.6 ± 0.2	3.3 ± 0.7
0.1	0.033 ± 0.007	0.6 ± 0.2	3.1 ± 0.6
0.2	0.078 ± 0.012	0.5 ± 0.1	2.6 ± 0.4
0.5	0.25 ± 0.03	0.4 ± 0.1	2.0 ± 0.3
0.8	0.5 ± 0.1	0.4 ± 0.1	1.8 ± 0.3
1	0.6 ± 0.1	0.3 ± 0.1	1.7 ± 0.3

The complete performance characterisation of an energy storage device is obtained when the energy and power of the device are calculated. The energy is described as the amount of charge that a device can store, and the power density is related to the rate at which the charge is delivered [223]. When a specific potential is applied to a supercapacitor an amount of work (dW) is generated that is able to accumulate charge (dQ) at the electrode/electrolyte interface. Therefore, assuming an insignificant heat loss (dq), as shown in Equation 4.13, and that the small amount of work is the product of the potential and the charge (Equation 4.14), it can be said that the dW is equivalent to the amount of energy (dE) stored in the supercapacitor and it can be integrated to obtain the energy (E), as it is shown in Equation 4.15 where the charge (Q) was related to the capacitance (C) using Equation 1.1 [332,11].

$$dE = dW + dq \xrightarrow{dq=0} dE = dW \qquad \text{Equation 4.13}$$

$$dW = EW \cdot dQ = \frac{Q}{C} dQ \qquad \text{Equation 4.14}$$

$$W = E = \int_0^Q \frac{Q}{C} dQ = \frac{1}{2}\frac{Q^2}{C} = \frac{Q \cdot EW}{2} = \frac{C \cdot EW^2}{2} \qquad \text{Equation 4.15}$$

With the GCD technique the energy, E, (Wh) and power, P, (W) values were obtained using Equation 4.16 and Equation 4.17, respectively, where $I_{const.}$ (A) is the current applied, $t_{dis.}$ (h) is the discharge time and *EW* (V) is the operational potential of the supercapacitor. Both equations were introduced in Chapter 1 as Equation 1.2 and Equation 1.3.

$$E = \frac{C \cdot EW^2}{2} = \frac{1}{2 \cdot 3600} I_{const.} \cdot t_{dis.} \cdot EW \qquad \text{Equation 4.16}$$

$$P = \frac{E}{t} = \frac{C \cdot EW^2}{2 \cdot t} = \frac{1}{2} I_{const.} \cdot EW \qquad \text{Equation 4.17}$$

In order to obtain the specific energy, E_{Spec}, (Wh kg^{-1}) or power, P_{Spec}, (W kg^{-1}), the equations were divided by the weight of the active material in kg and, for the energy density, $E_{Density}$, (Wh cm^{-2}) and power density, $P_{Density}$, (W cm^{-2}) the area of the electrodes was considered in cm^2.

Table 4.10 shows the average energy and power values obtained for the set of three EDLS using GCD. As it was described previously, the time of these EDLS needed for discharging decreases at higher current densities. Comparing the variance of the set of EDLS, it can be said that these three devices needed quite similar times to discharge, obtaining a good reproducibility among the EDLS fabricated. Regarding the specific energy, the highest value obtained was 0.41 ± 0.01 mWh kg^{-1} ($E_{Density}$ = 0.0022 ± 0.0004 μW h cm^{-2}) at a specific power of 4.3 ± 0.9 mW kg^{-1} ($P_{Density}$ = 0.02 μW cm^{-2}); the energy density remained at 0.0010 ± 0.0002 μW h cm^{-2} when the power density increased to 1.16 ± 0.12 μW cm^{-2}, which shows stability in the device. It can be seen that the specific energy decreased from 0.41 ± 0.01 mW h kg^{-1} (P_{Spec} = 4.3 ± 0.9 mW kg^{-1}) to 0.21 ± 0.03 mW h kg^{-1} (P_{Spec} = 222.2 ± 25.6 mW kg^{-1}) showing again a small drop in the energy at high current densities. From the literature

[333,243], the values of energy and power density for this device were found to be similar to graphene-cellulose supercapacitors.

Overall, the maximum power density offered, 1.16 ± 0.12 μW cm^{-2}, could be adequate to power up implantable biomedical devices such as biosensors (< 0.5 μW) [308] which was the target application for this supercapacitor.

Table 4.10 Energy and power average values calculated for the EDLS using $[C_2mim][NTf_2]$ as the electrolyte at different current densities applied and the discharge time obtained using GCD

Current density / μA cm^{-2}	Discharge time / s	E_{Spec} / mW h kg^{-1}	$E_{Density}$ / μW h cm^{-2}	P_{Spec} / mW kg^{-1}	$P_{Density}$ / μW cm^{-2}
0.02	355 ± 74	0.41 ± 0.01	0.0022 ± 0.0004	4.3 ± 0.9	0.0221 ± 0.0001
0.05	136± 28	0.41 ± 0.13	0.0021 ± 0.0005	10.9 ± 2.0	0.057 ± 0.001
0.08	78 ± 16	0.39 ± 0.13	0.0020 ± 0.0005	17.8 ± 3.4	0.092 ± 0.003
0.1	59 ± 11	0.37 ± 0.11	0.0019 ± 0.0004	22.2 ± 3.9	0.115 ± 0.003
0.2	25 ± 4	0.31 ± 0.09	0.0016 ± 0.0002	44.8 ± 7.3	0.23 ± 0.01
0.5	8 ± 1	0.24 ± 0.07	0.0012 ± 0.0002	112.4 ± 15.2	0.59 ± 0.04
0.8	4 ± 1	0.22 ± 0.07	0.0011 ± 0.0002	179.4 ± 20.1	0.94 ± 0.1
1	3 ± 1	0.21 ± 0.07	0.0010 ± 0.0002	222.2 ± 25.6	1.16 ± 0.12

4.2.2.3. Electrochemical Impedance Spectroscopy

Electrochemical impedance spectroscopy is a useful tool to evaluate the charge transfer and ion diffusion properties of an electrode material [334]. These properties can be studied by applying a small amplitude of alternative interrupting potential *e.g.* 10 mV over a wide range of frequencies from 10 mHz to 100 KHz (see Appendix B.5 for the technique theory) [335,39].

The most common representation of the EIS measurements is known as a Nyquist plot (Figure 4.22 (a)) that represents the imaginary impedance (Z'') against the real impedance (Z'). The crossing of the curves at the real impedance axis in the high-frequency region (left part of the plot) reflects the equivalent series resistance (ESR) of the EDLS, which includes: a) the intrinsic resistance of the electrolyte and b) the charge-transfer resistance attributed to the resistance between the electroactive material and electrolyte [285]. At the same point (at which the high and low-frequency

regions in the Nyquist plot met) the frequency found is called "knee frequency" that corresponds to the maximum frequency at which the capacitive behaviour is preserved [336,84a]; therefore, a higher knee frequency corresponds to a better power performance [243], reflecting the diffusion of ions from the electrolyte into the electrode material. The low-frequency region (right part of the graph) should show a line whose inclination indicates the resistivity or capacitive nature of the electrodes, less than 45º inclined line indicates a resistant behaviour and more vertical lines close to 90º reveals an ideal electrical double-layer capacitance behaviour [337].

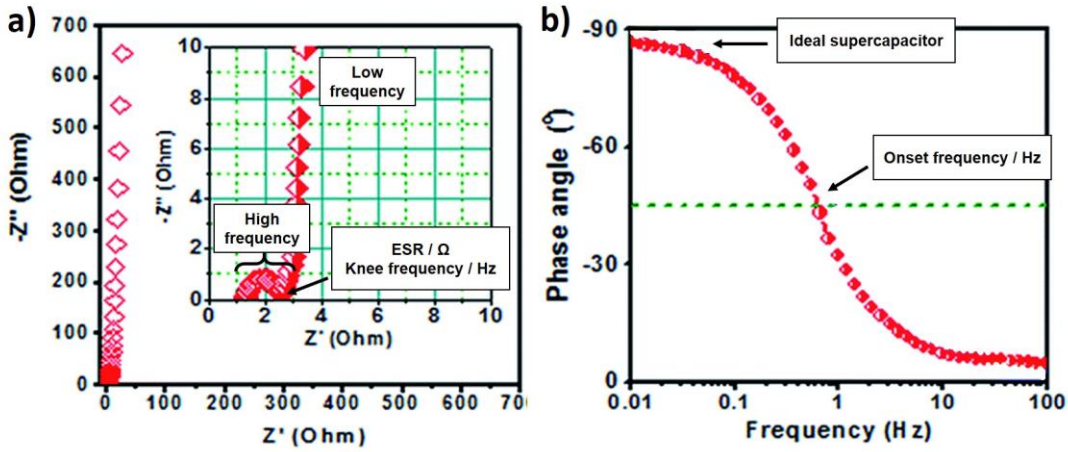

Figure 4.22 Representation of a) Nyquist plot and b) Bode plot of an ideal double-layer supercapacitor. Graphs adapted from reference [338]

Figure 4.23 shows the Nyquist plot obtained for the EDLS using $[C_2mim][NTf_2]$ as the electrolyte at different cycles during the cycle life study of 15000 cycles. Three tails with almost 90º inclination (nearly vertical) were observed, and the capacitance behaviour was proven to be maintained throughout the 15000 cycles of the cycle life studied. In the inset of Figure 4.23, the high-frequency component with the ESR and the knee frequency are shown. In the case of the ESR, the values obtained during cycling increased only slightly from 2.2 kΩ at the OCP (after assembly, therefore, before any other electrochemical technique was used) to 2.9 kΩ after 15000 cycles. This small increase after the cycle life suggests a high ion diffusion into the electrode and demonstrates the good stability of the device. The knee frequency value obtained was 22.2 kHz which suggests that most of its stored energy is accessible at frequencies below this value [336]. The expected knee frequency for a carbon-based supercapacitor found in the literature is 100 Hz [339]; therefore, it can be said that this

supercapacitor could store charge at high and low frequencies from 22.2 kHz to 0.001 Hz.

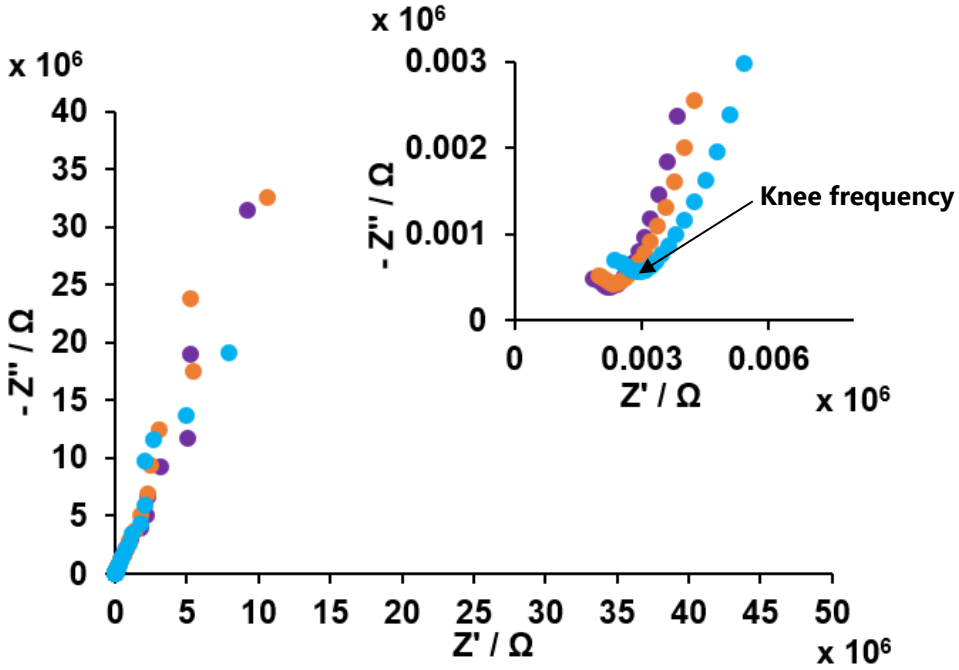

Figure 4.23 Nyquist plot of one of the EDLS using $[C_2mim][NTf_2]$ as the electrolyte during the cycle life (25 ± 2 ^{0}C): at OCP (purple), after 5000 cycles (orange) and after 15000 cycles (light blue). The inset shows the high-frequency part of the Nyquist plot

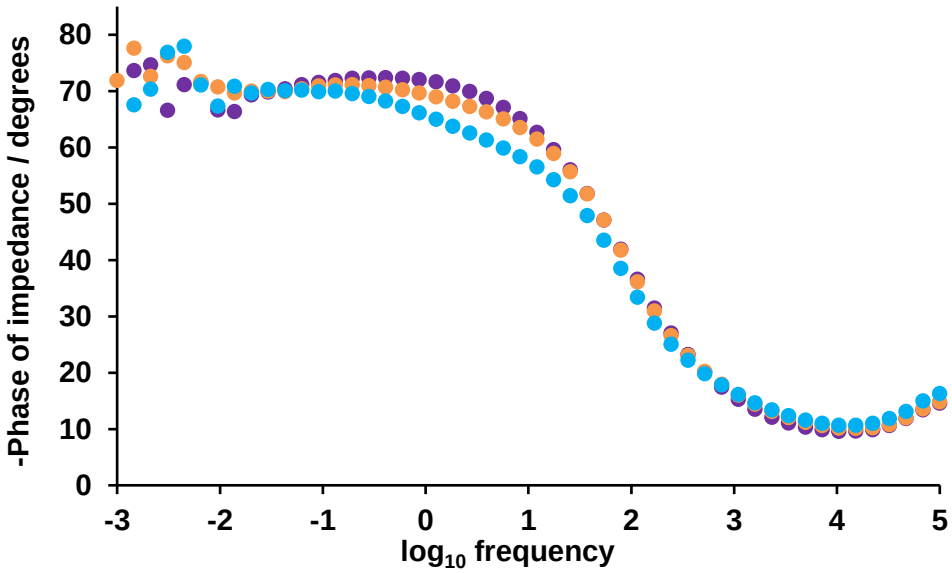

Figure 4.24 Bode plot of one of the EDLS using $[C_2mim][NTf_2]$ as the electrolyte during the cycle life (25 ± 2 ^{0}C): at OCP (purple), after 5000 cycles (orange) and after 15000 cycles (light blue)

The Bode plot is another type of EIS plot that shows the phase angle of impedance *vs.* frequency, as it is shown in Figure 4.22 (b) [340]. From this graph the frequency at which the phase angle reaches -45° is termed as "onset frequency" and

it corresponds to the frequency at which a device changes from exhibiting primarily resistive to primarily capacitive behaviour. In addition, at -90 º phase angle, the ideal capacitor behaviour is obtained [160]. In the case of the EDLS device fabricated (Figure 4.24), the onset frequency changed from 37.2 Hz to 54.3 Hz during the cycle life. For low frequencies, up to 3.9 Hz, the EDLS worked as an ideal capacitor because the phase angle is close to -90 º during the 15000 cycles. It was possible to see that at these low frequencies there is a fluctuation in the values although the phase angle did not suffer a significant drop, keeping an almost ideal capacitor behaviour.

4.2.3. Electrochemical Study of the EDLS Fabricated Using [C_2mim][FAP] as the Electrolyte

An EDLS using [C_2mim][FAP] as the electrolyte was studied electrochemically and compared to the EDLS using [C_2mim][NTf_2]. In this case, one EDLS was fabricated and characterised using the same electrochemical techniques.

The active material in this EDLS was considered to be the graphite from the graphite-cellfib-IL plasticiser composite film, compromising a 33.3 wt % of the total weight at each electrode, and the total mass of the active material was 6.0 mg; the area the electrodes 1 cm^2 and the thickness of the electrodes 130 ± 30 µm.

For the EDLS using [C_2mim][FAP] as the electrolyte, the OCP found was 0.02 V.

4.2.3.1. Cyclic Voltammetry

Cyclic voltammetry measurements showed a symmetrical and nearly rectangular cycle for the EDLS using [C_2mim][FAP] as the electrolyte, as it can be seen in Figure 4.25. The operational voltage found was 3 V showing an increment of 0.9 V in comparison to the EDLS using [C_2mim][NTf_2] as the electrolyte. This increase in the EW was expected because the IL [C_2mim][FAP] is known to be more electrochemically stable as it was shown in section 4.2.1. An electrochemical window of 5.1 V at 25 ± 2 ºC was obtained using glassy carbon as the working electrode.

There are not many articles using [C_2mim][FAP] as the electrolyte in a supercapacitor; Pandey *et al*. [341] published the fabrication and characterisation of an EDLS using multiwall carbon nanotubes as electrodes and a gel polymer using [C_2mim][FAP] as the electrolyte. The operational voltage that they found for their EDLS

was 2 V, being 1 V less electrochemically stable than the EDLS using [C_2mim][FAP] as the electrolyte fabricated for this thesis.

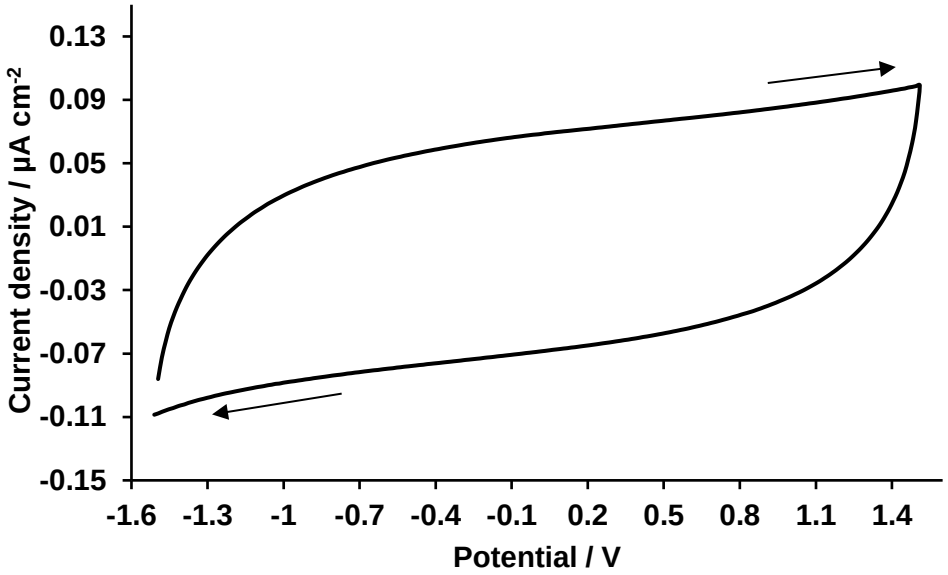

Figure 4.25 Cyclic voltammogram of the EDLS using [C_2mim][FAP] as the electrolyte at 50 mV s^{-1} and at 25 ± 2 ^{0}C. Arrows show the potential direction of the cyclic voltammogram

Using Equation 4.10, the specific capacitance value was found to be 4.1 mF g^{-1}, and the areal capacitance was 24.6 µF cm^{-2}, at the scan rate of 50 mV s^{-1}. These capacitance values were slightly smaller than the ones obtained for the EDLS using [C_2mim][NTf_2] as the electrolyte (section 4.2.2.1). The reason of the smaller capacitance values can be due to transport properties of the electrolyte, *i.e.* the viscosity is higher for [C_2mim][FAP] (60.5 mPa·s) than for [C_2mim][NTf_2] (37 mPa·s) [342].

Figure 4.26 shows the voltammogram of the EDLS at different scan rates to analyse the power capability of the device using [C_2mim][FAP] as the electrolyte. As it was expected, the shape of the cycles showed a slight deviation from the ideal rectangular shape due to an increase of the resistance at high scan rates.

The data from Table 4.11 shows the capacitance values obtained at different scan rates. The capacitance values decreased drastically when higher scan rates were applied. This behaviour was expected because at faster scan rates, minimal time is available to store charge in the electrode/electrolyte interface, as it was explained in section 4.2.2.1 for the EDLS using [C_2mim][NTf_2] as the electrolyte [325].

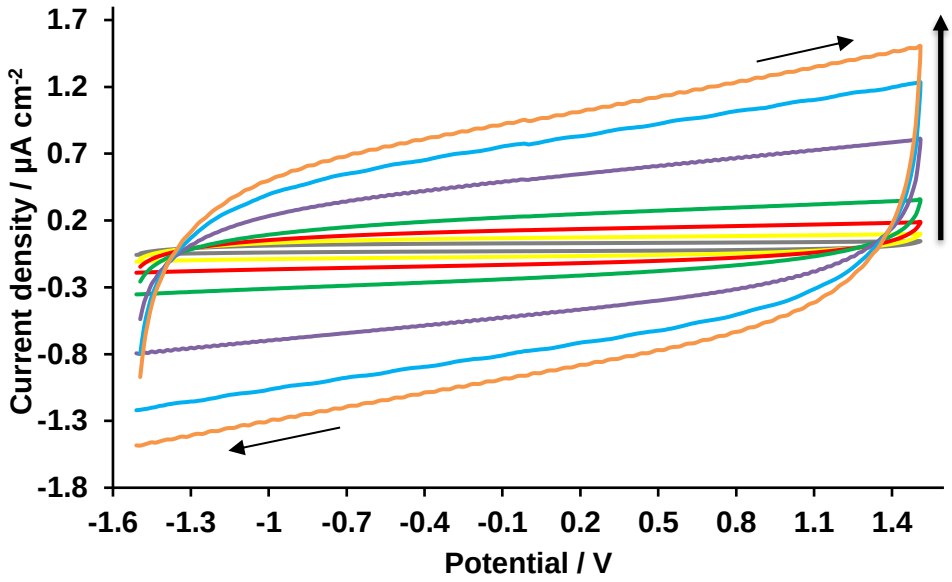

Figure 4.26 Cyclic voltammogram of one of the EDLS using [C_2mim][FAP] as the electrolyte at various scan rates: 1000 (orange), 800 (light blue), 500 (purple), 200 (green), 100 (red), 50 (yellow), 20 (grey) mV s^{-1} and at 25 ± 2 ^{0}C. Arrows show the potential direction of the cyclic voltammogram and the vertical arrow indicates the faster scan rates applied

Table 4.11 Specific and density capacitance values of the EDLS using [C_2mim][FAP] as the electrolyte calculated from the CV at various scan rates

Scan rate / mV s^{-1}	$C_{Spec.}$ / mF g^{-1}	$C_{Density}$/ µF cm^{-2}
20	11.5	69.1
50	4.1	24.6
100	1.8	11.1
200	0.8	5.1
500	0.3	1.8
800	0.2	1.1
1000	0.1	0.9

The bending study was also carried out for this supercapacitor, showing more flexible stability than the previous EDLS, as it can be seen in Figure 4.27. There was an increment in the current density when the supercapacitor was bent (angle of 120 degrees) but the voltammogram returned almost to the normal state after the bending study, thus demonstrating a good flexible stability for this device.

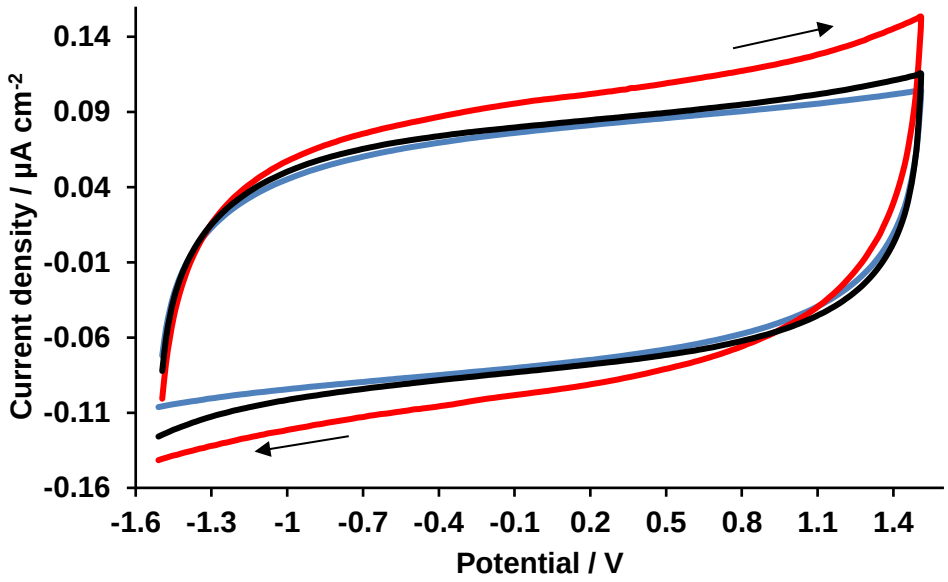

Figure 4.27 Bending study at an angle of 120 degrees of the EDLS using [C_2mim][FAP] as the electrolyte at the scan rate of 50 mV s^{-1} and at 25 ± 2 ^{0}C. Cyclic voltammogram before (blue), during (red) and after (black) bending

The stability of the device on bending was corroborated with the capacitance values obtained before, during and after bending, as it is displayed in Table 4.12. The capacitance increased when the supercapacitor was bent, but the CV was retrieved after the bending study. Therefore, this supercapacitor can be used at different bending angles without damaging the structural integrity of the device.

Table 4.12 Specific and areal capacitance values during the bending

Bending state	$C_{Spec.}$ / mF g^{-1}	C_{Areal} / µF cm^{-2}
Prior to bending	4.7	28.0
120 degrees angle	5.3	32.0
After bending	5.1	30.4

The cycle life of the device was checked using CV and it was measured for 15000 cycles, as the previous EDLS. This supercapacitor showed no obvious change even after 15000 cycles (Figure 4.28), and therefore, has a higher stability than the EDLS using [C_2mim][NTf_2] as the electrolyte. The supercapacitor also showed an excellent cycle life in comparison to EDLS reported in the literature, *e.g.*, ~82 % of capacitance retention during 10000 using multi-walled carbon nanotubes electrodes and [C_2mim][FAP] gel as electrolyte [341].

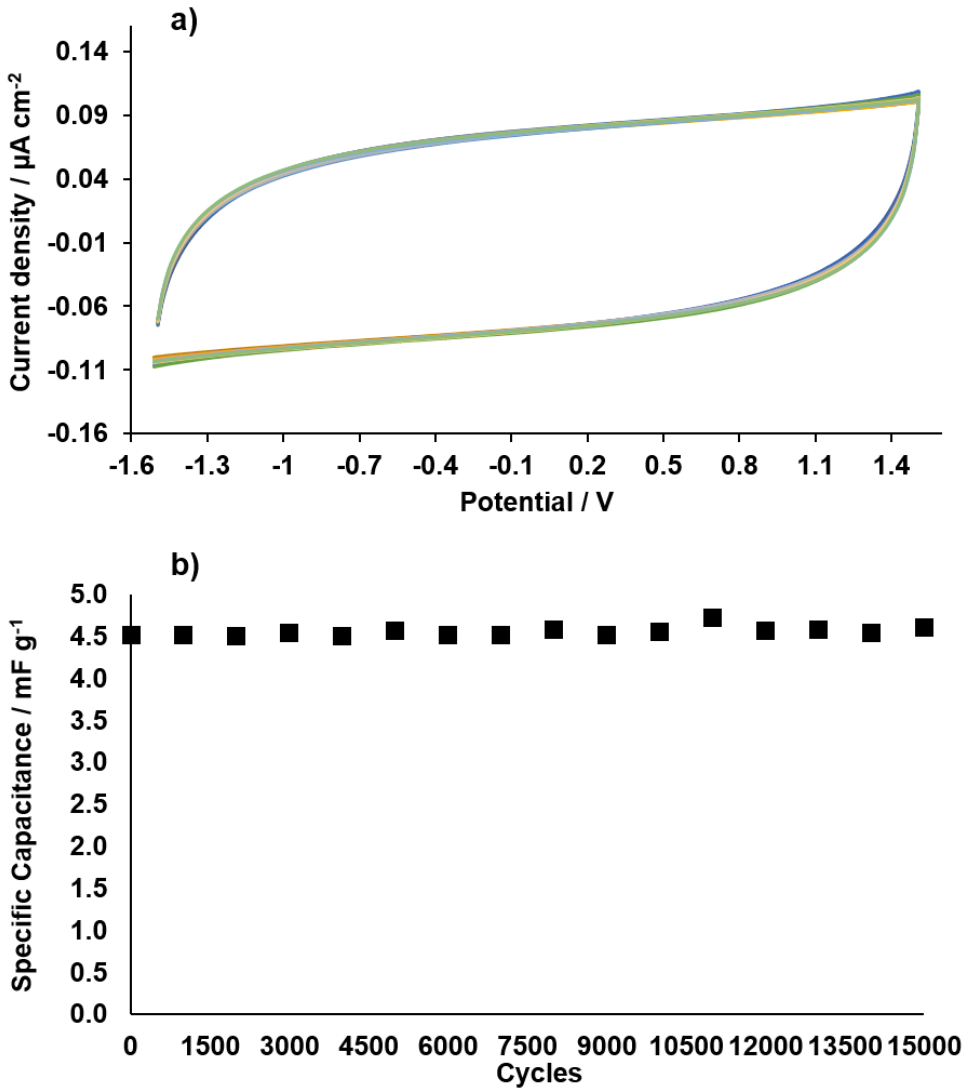

Figure 4.28 a) Cyclic voltammograms of the EDLS using [C_2mim][FAP] as the electrolyte at every 1000th scan from 2 to 15000 cycles at the scan rate of 50 mV s^{-1} and at 25 ± 2 ^{0}C, b) specific capacitance during 15000 cycles

The capacitance values of the 2nd and 15000th cycle are shown in Table 4.13, where it can be seen that the values did not vary significantly after 15000 cycles.

Table 4.13 Specific and areal capacitance of the second cycle and the 15000 cycle

Cycle 2		Cycle 15000	
C_{Spec} / mF g^{-1}	C_{Areal} / µF cm^{-2}	C_{Spec} / mF g^{-1}	C_{Areal} / µF cm^{-2}
4.5	27.1	4.6	27.8

4.2.3.2. Galvanostatic Charge-discharge

Galvanostatic charge-discharge measurements exhibited curves with nearly ideal triangular shape and a small potential drop (IR_{drop}) at the beginning of each discharge curve indicating a low internal resistance for this device, as the Figure 4.29

shows at different current densities applied. Albeit the internal resistance seems low, the ESR for this supercapacitor was higher (249 ± 82 kΩ) than the EDLS using [C_2mim][NTf_2] as the electrolyte, which may be due to the higher viscosity of the [C_2mim][FAP] in comparison to [C_2mim][NTf_2] (section 4.2.3.1).

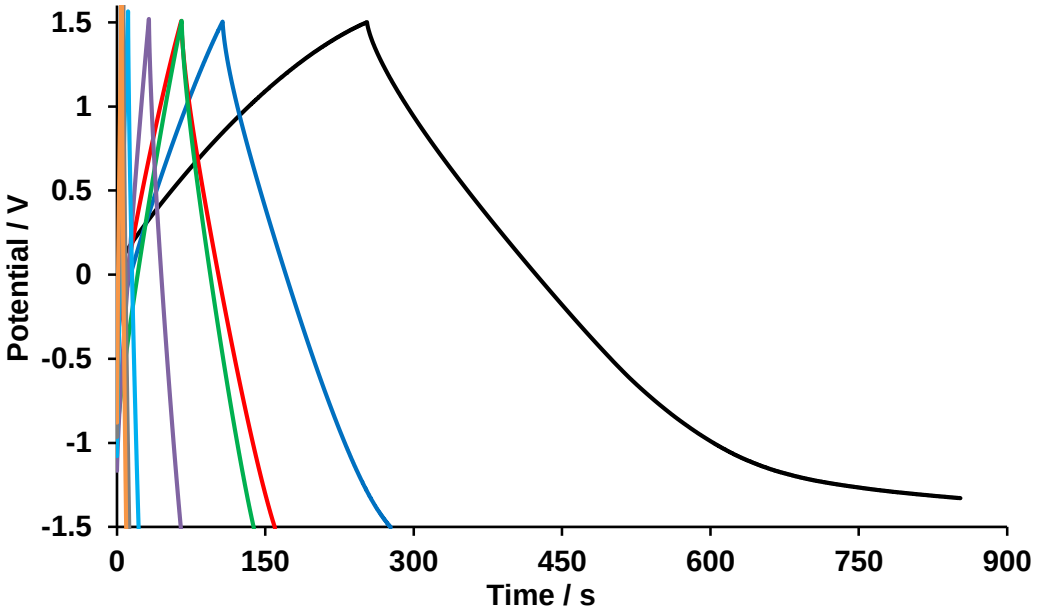

Figure 4.29 GCD curves of the EDLS using [C_2mim][FAP] as the electrolyte fabricated at different currents densities applied, 0.02 (black), 0.05 (blue), 0.08 (red), 0.1 (green), 0.2 (purple), 0.5 (light blue), 0.8 (grey) and 1 μA cm^{-2} (orange) at 25 ± 2 ^{0}C

Table 4.14 Table 4.14 summarises the energy and power values obtained at the different current densities applied and the time needed to discharge the supercapacitor. The discharge time obtained was comparable to the previous EDLS using [C_2mim][NTf_2] as the electrolyte, whereas regarding the lowest current density (0.02 μA cm^{-2}), the supercapacitor needed 600 s to discharge instead of the 355 s observed with the EDLS using [C_2mim][NTf_2] as the electrolyte. The energy and power values were higher for the EDLS using [C_2mim][FAP] than in the case of [C_2mim][NTf_2], showing an improvement in charge storage and delivery using [C_2mim][FAP]. This energy and power increase is related to the larger EW obtained for this IL electrolyte. Equation 4.16 and Equation 4.17 can explain this fact because the power and energy are proportional to the EW.

Table 4.14 Energy and power values calculated for the EDLS using [C_2mim][FAP] as the electrolyte at different current densities applied using GCD as well as the discharge time obtained

Current density / μA cm^{-2}	Discharge time / s	E_{Spec} / mWh kg^{-1}	$E_{Density}$ / μWh cm^{-2}	P_{Spec} / mW kg^{-1}	$P_{Density}$ / μW cm^{-2}
0.02	600	0.93	0.006	5.6	0.03
0.05	170	0.61	0.004	12.9	0.08
0.08	94	0.55	0.003	21.2	0.13
0.1	73	0.54	0.003	26.5	0.16
0.2	32	0.48	0.003	53.7	0.32
0.5	11	0.40	0.002	132.7	0.80
0.8	6	0.36	0.002	207.3	1.24
1	5	0.34	0.002	258.3	1.55

4.2.3.3. Electrochemical Impedance Spectroscopy

The EIS study of this EDLS using [C_2mim][FAP] as the electrolyte showed a more stable device during the cycle life study, albeit it exhibited higher resistance values than in the case of the EDLS using [C_2mim][NTf_2]. This is due to the higher viscosity of [C_2mim][FAP] as it was explained in section 4.2.3.1.

From the Nyquist plot three, almost perpendicular tails corresponding to the different cycles were obtained for this device demonstrating its capacitance behaviour, as it is shown in Figure 4.30. The inset graph shows the ESR obtained at high frequencies, with values from 8.0 kΩ to 9.7 kΩ, which were higher than in the case of the EDLS using [C_2mim][NTf_2] as the electrolyte. Regarding the knee frequency, the values changed from 3.4 kHz to 1.6 kHz during the cycle life. Since the knee frequency value decreased after 15000 cycles, it can be said that the electrolyte access and diffusion into the electrode were more difficult after the cycle life.

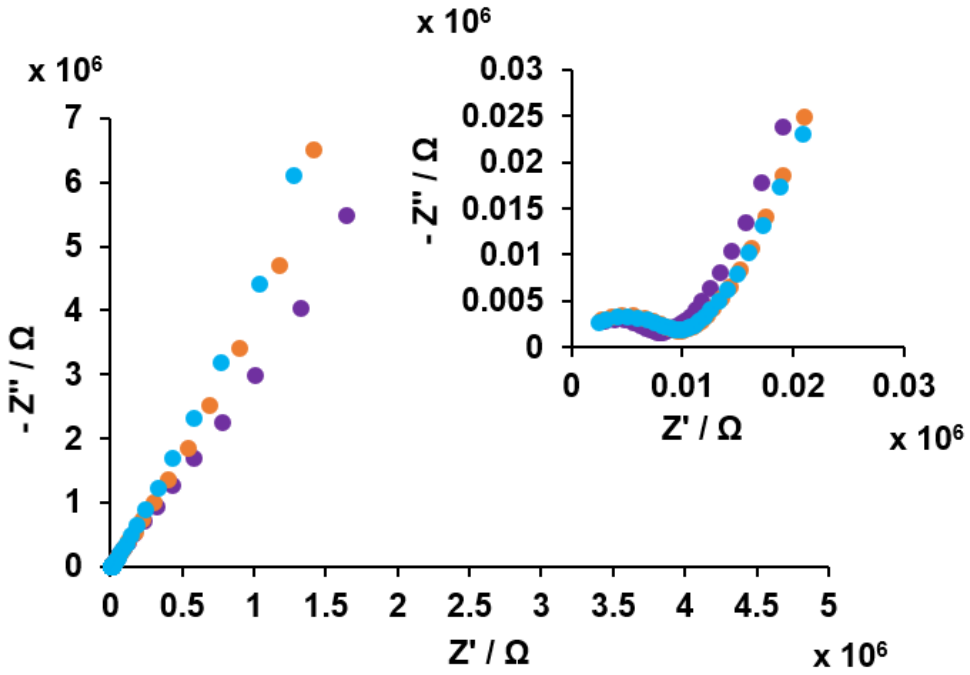

Figure 4.30 Nyquist plot during the cycle life of the EDLS using [C_2mim][FAP] as the electrolyte (25 ± 2 ºC): at OCP (purple), after 5000 cycles (orange) and after 15000 cycles (light blue). The inset shows the high-frequency part of the Nyquist plot

Figure 4.31 shows the Bode plot where the phase of the impedance was plotted *vs.* frequency. From this plot, it can be analysed at what frequency the capacitive behaviour predominates. The frequencies obtained at -45º changed from 17.6 to 8.28 Hz during the 15000 cycles, showing smaller values in comparison to the EDLS using [C_2mim][NTf_2] as the electrolyte. At frequencies of less than ~ 1.26 Hz, this supercapacitor almost worked as an ideal EDLS because the phase angle was almost -90^0 [343].

From all the data obtained from the EIS technique and in comparison to the EDLS using [C_2mim][NTf_2] as the electrolyte, it can be suggested that the ion diffusion from the electrolyte into the porous electrodes was more difficult, resulting in higher resistances, using [C_2mim][FAP] than using [C_2mim][NTf_2]. This agrees with the fact that [C_2mim][FAP] is more viscous than [C_2mim][NTf_2]. Another reason to explain the ion diffusion difficulty may be due to the use of a different anion in comparison to the IL plasticiser that was incorporated on the electrode *i.e.* [$P_{6\,6\,6\,14}$][NTf_2]. This IL was added to impart dual functionality, as a plasticiser and to improve the wettability in the electrodes. Therefore, it can be supposed that if there is a common anion between

the IL plasticiser of the electrode and the IL electrolyte a better performance of the supercapacitor would be obtained.

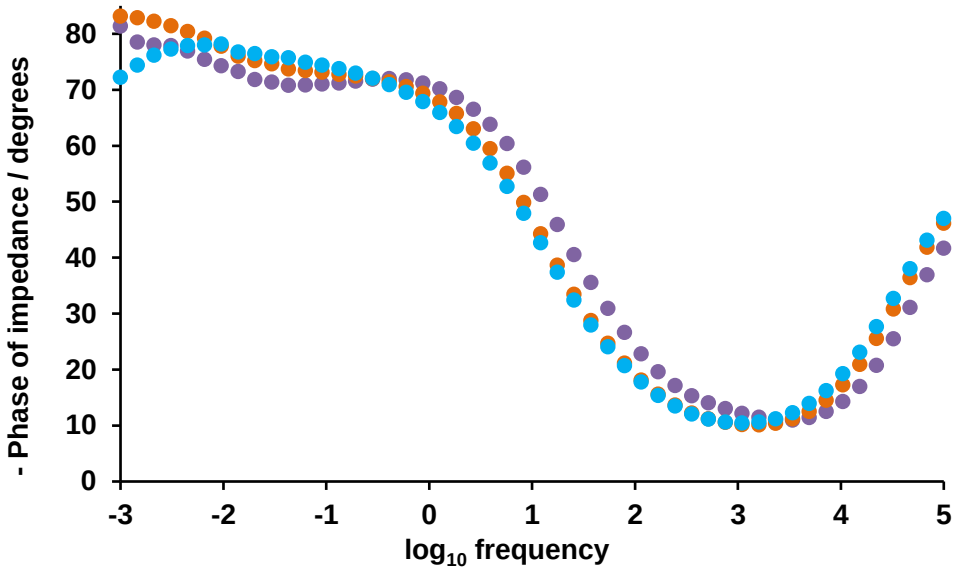

Figure 4.31 Bode plot during the cycle life of the EDLS using [C_2mim][FAP] as the electrolyte (25 ± 2 ^{0}C): at OCP (purple), after 5000 cycles (orange) and after 15000 cycles (light blue)

4.2.4. Chemical and Physical Study of the EDLS Electrodes

The following techniques were used to study any possible differences on the composite electrodes before and after using them in the flexible supercapacitors *i.e.* after 15000 cycles. In this chapter, the graphite-cellfib-IL plasticiser composite film was analysed as a fresh film and after using it as both electrodes in the EDLS using [C_2mim][NTf_2] as the electrolyte for 15000 cycles.

The techniques employed were: Fourier transform-infrared (FT-IR), thermogravimetric analysis (TGA) and scanning electron microscopy (SEM).

The fresh film under study was dried for 48 hours in a vacuum desiccator. In the case of the films used as electrodes after cycling, they were soaked in methanol to remove the ionic liquid electrolyte and by-products and finally dried for 48 hours in a vacuum desiccator.

4.2.4.1. Fourier Transform Infrared (FT-IR)

Fourier transform-infrared spectroscopy was employed to study any possible chemical change in the films before and after the electrochemical characterisation and the cycle life of 15000 cycles.

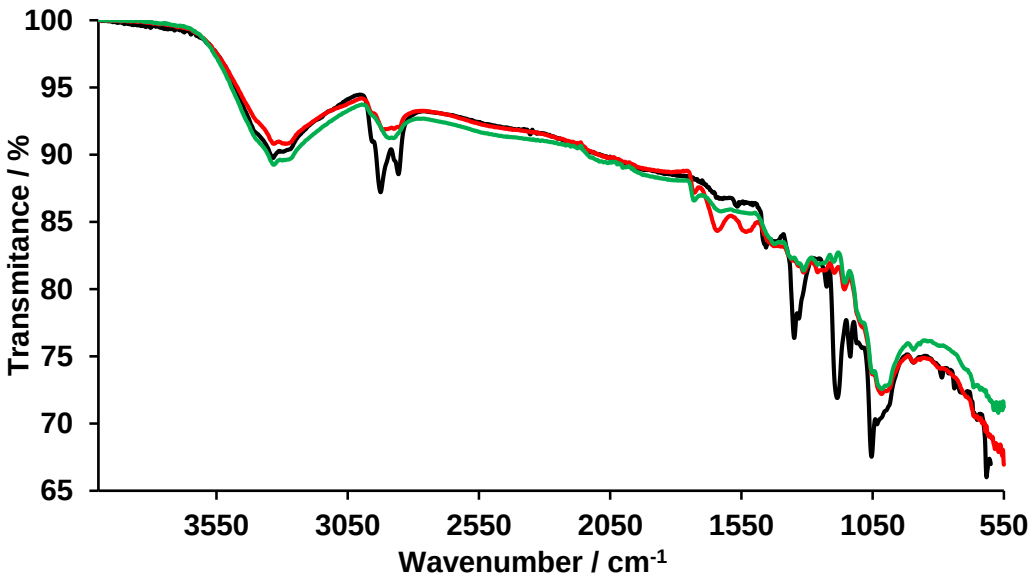

Figure 4.32 Infrared spectra of the graphite-cellfib-IL plasticiser fresh film (black) and after using as both electrodes for 15000 cycles in the EDLS using $[C_2mim][NTf_2]$ as the electrolyte (red and green)

Figure 4.32 shows the infrared spectra of the graphite-cellfib-IL plasticiser film before using it as both electrodes in the symmetric flexible supercapacitor. As it can be seen the fresh film (black plot) shows sharper peaks than the same film after being used as electrodes (red and green plots). It was observed that the peaks at 3000 cm^{-1} and, from 1350 to 1000 cm^{-1} changed in intensity and shape. These peaks belong to the C-H stretching of the $[P_{6\,6\,6\,14}][NTf_2]$ IL, S=O asymmetric /symmetric stretching from the IL plasticiser anion and the C-O, C-OH, C-H and C-O-C ring deformation of cellulose, respectively. In the case of the $[P_{6\,6\,6\,14}][NTf_2]$ peaks, the possible explanation of the reduction of the peak is due to the electromechanical process involved during the charge-discharge cycles. In other words, it is possible that the $[P_{6\,6\,6\,14}][NTf_2]$ in the film was removed from the film surface during the cycling. This may explain the fluctuation showed during the cycle life in section 4.2.2.1.

4.2.4.2. Thermogravimetric Analysis (TGA)

Thermogravimetric analysis was utilised to study the thermal stability of the fresh films and after the cycle life of 15000 cycles.

Figure 4.33 shows the thermogram obtained for the graphite-cellfib-IL plasticiser film before (black plot) and after using it as both electrodes (blue and red plot) in the EDLS. The first decomposition process observed (~ 125 ^0C) is due to loss of water and it was used to estimate the water content of the films. The second weight

loss (~ 5 %) corresponds to the decomposition temperature or onset temperature (T_{onset}) of the composite films. The graph shows a different behaviour for the fresh film than for both electrodes after cycling. This is representative of the change in the film after the charge-discharge process of 15000 cycles.

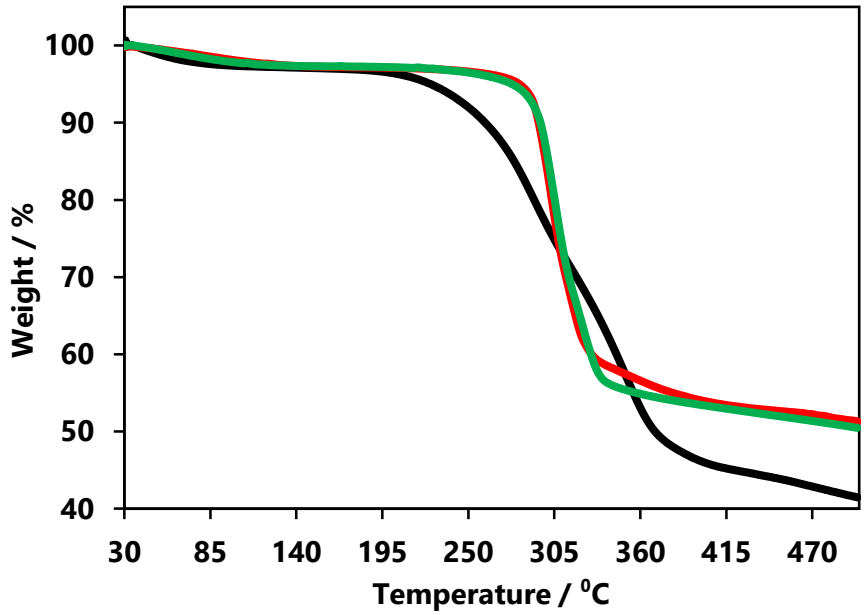

Figure 4.33 Thermogram of the fresh graphite-cellfib-IL plasticiser film (black plot) and the same film used as both electrodes for 15000 cycles in the EDLS using [C_2mim][NTf_2] as the electrolyte (green and red plots)

The values obtained for the EDLS electrodes are reported in Table 4.15. As it can be seen the fresh film (black plot) had a larger amount of water than the same film after being used as electrodes. Taking into account the decomposition temperature, it can be concluded that (i) there was an increment in the thermal stability of the films (from 258 ^{0}C to 291/293 ^{0}C) after using them as electrodes for 15000 cycles and, (ii) the fresh film showed two decompositions temperatures (258 ^{0}C and 335 ^{0}C), whereas the used films just showed one decomposition temperature 291 ^{0}C (red plot) and 293 ^{0}C (green plot). As it was discussed in the previous section on infrared spectroscopy, the changes observed may be related to the electromechanical process during the charge-discharge cycles. The movement of the [$P_{6\,6\,6\,14}$][NTf_2] IL plasticiser from the film surface to the interior of the electrode may contribute to the disappearance of the second decomposition temperature in the thermogram graphs of the used films. As it was explained in section 3.3.2, the increase of the T_{on} when the IL plasticiser is added can be due to a possible IL plasticiser-cellulose interaction [272].

Table 4.15 Water content and decomposition temperature (T_{onset}) values of the graphite-cellfib-IL plasticiser film before and after being used as both electrodes in the EDLS using $[C_2mim][NTf_2]$ as the electrolyte for 15000 cycles

Films	Water content / %	1st T_{onset} / ^{0}C	2nd T_{onset} / ^{0}C
Fresh film (black plot)	3.14	258	335
After 15000 cycles (red plot)	2.61	291	-
After 15000 cycles (green plot)	2.32	293	-

4.2.4.3. Scanning Electron Microscopy (SEM)

Scanning electron microscopy was used to study the morphological changes on the surfaces of the fresh films and after using them as electrodes in the EDLS for 15000 cycles.

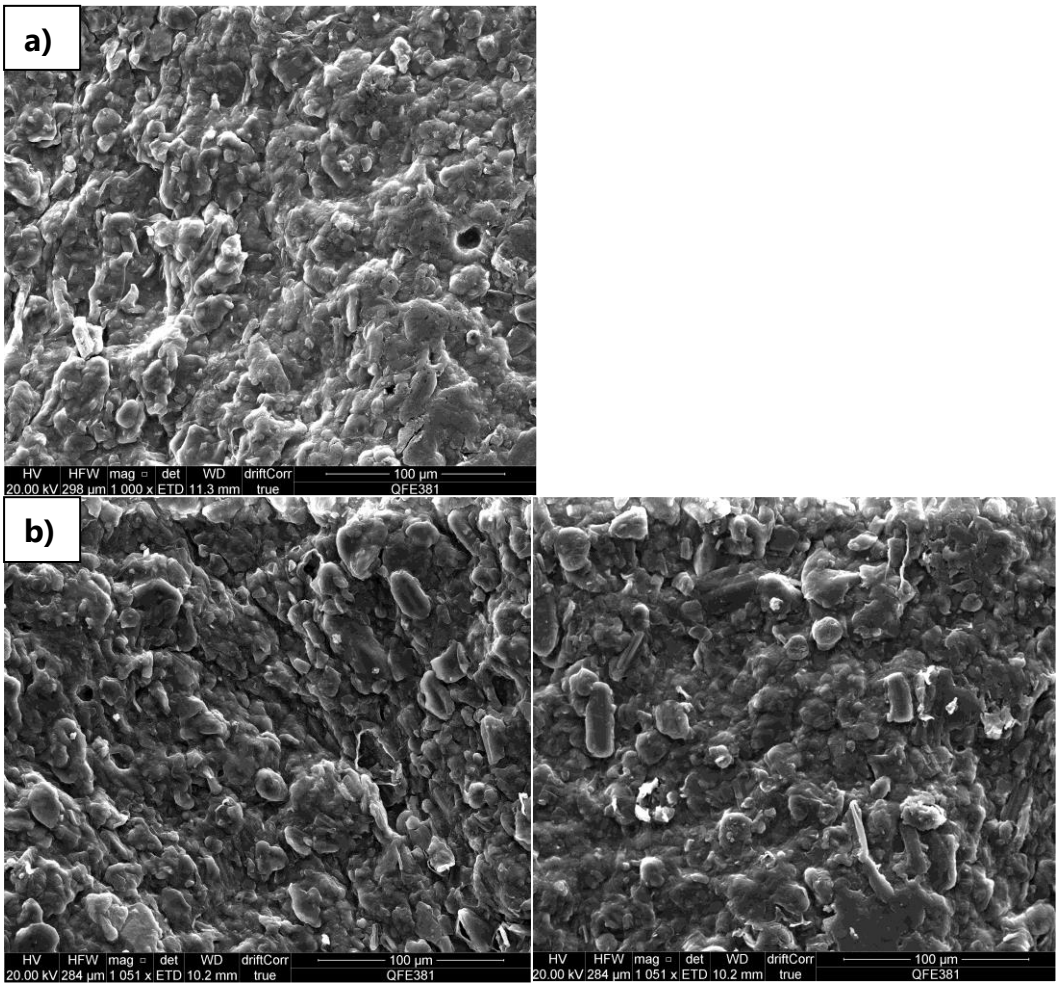

Figure 4.34 SEM pictures with a magnification of 1K of the a) fresh graphite-cellfib-IL plasticiser film and b) the same film after using it as both electrodes in the EDLS using $[C_2mim][NTf_2]$ as electrolyte for 15000 cycles

Figure 4.34 shows three pictures obtained for the same graphite-cellfib-IL plasticiser film (a) as fresh and, (b) after being used in the two electrodes (positive and negative). As it can be seen in the pictures there is no drastic change in the surface of the films. This was the result expected because the charge storage mechanism in this device is electrostatic and consequently, no change in the surface should be developed during the charge-discharge cycles. There are no differences between the two pictures in (b), and therefore, it is not possible to differentiate between positive and negative electrodes.

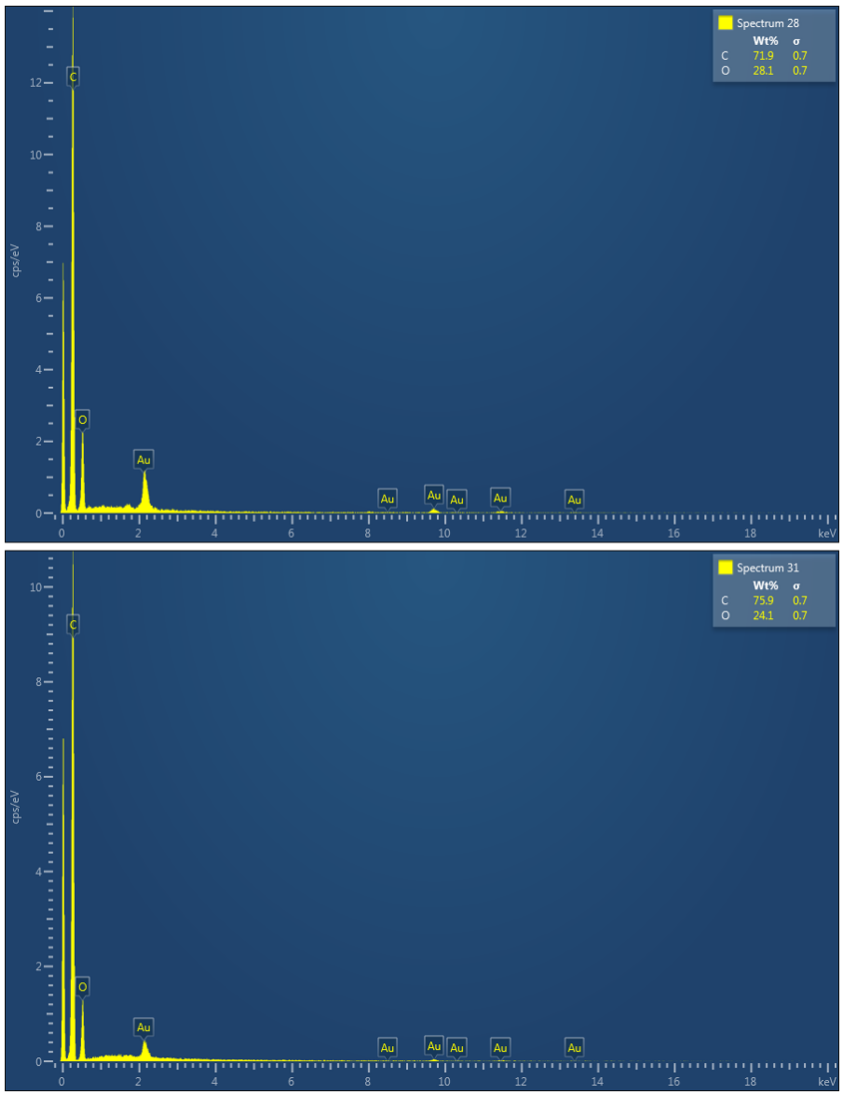

Figure 4.35 EDX spectra of both electrodes of the EDLS using $[C_2mim][NTf_2]$ as the electrolyte for 15000 cycles

Figure 4.35 shows the EDX spectra for both electrodes used in the EDLS after 15000 cycles. The elements seen, carbon and oxygen, are the same elements than in the fresh electrodes (see section 3.8.2). As already observed with the other techniques

(sections 4.2.4.1 and 4.2.4.2), the elements corresponding to the IL plasticiser, $[P_{6\,6\,6\,14}][NTf_2]$, did not appear confirming that the electrode films suffered an electromechanical action during the 15000 cycles that removed the IL plasticiser from the surface of the films.

Elemental analysis of the graphite-cellfib-IL plasticiser as fresh film and both electrodes used in the ES for 15000 cycles

Composite film name	C / wt %	O / wt %	F / wt %	S / wt %	P / wt %	Cl / wt %
Fresh film	63.1	32.9	2.4	0.8	0.3	-
Electrode film 1	71.9	28.1	-	-	-	-
Electrode film 2	75.9	24.1	-	-	-	-

The cross-section of one of the films used as electrodes was checked using SEM, as it is shown in Figure 4.36. The thickness of this film was measured as 31.7 μm. The morphology inside the film showed a layered structure.

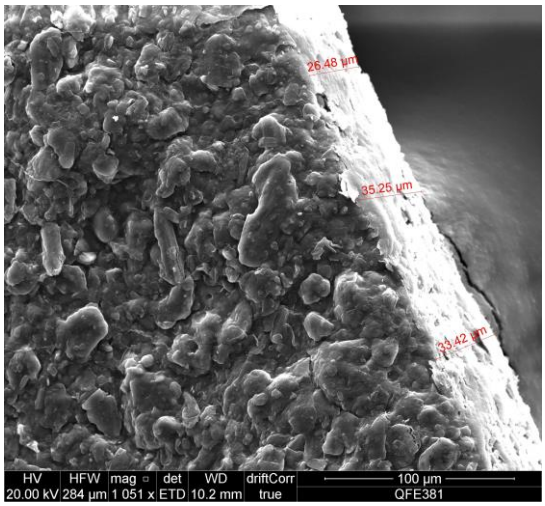

Figure 4.36 Cross-section SEM picture of one of the electrodes of the EDLS using $[C_2mim][NTf_2]$ as electrolyte showing the thickness of this film after 15000 cycles

4.3. Summary and Conclusions

Symmetric flexibles supercapacitors also knew as electrical double-layer supercapacitors (EDLS) using graphite-cellulose fibrous-IL plasticiser films as both electrodes and ILs as electrolytes were fabricated and characterised electrochemically by cyclic voltammetry, galvanostatic charge-discharge and electrochemical impedance spectroscopy. Both EDLS using different electrolytes ($[C_2mim][NTf_2]$ and $[C_2mim][FAP]$) showed long-term stability in the device performance with a cycle life of 15000 cycles and almost 100 % of capacitance retention. Additionally, the chemical nature, morphology and thermal stability of the graphite-cellfib-IL plasticiser-based

electrodes were investigated by infrared spectroscopy, scanning electron microscopy and thermal gravimetric analysis as fresh materials and after 15000 cycles to understand the functional characteristics of the electrical double-layer supercapacitors.

The EDLS fabricated with the IL $[C_2mim][FAP]$ as electrolyte had an operational voltage of 3 V, in contrast, to the EDLS using $[C_2mim][NTf_2]$ as electrolyte with an operational voltage of 2.1 V. The maximum areal capacitance values were obtained using $[C_2mim][NTf_2]$ as electrolyte with a maximum areal capacitance value of 97.8 ± 24.0 μF cm^{-2} and a specific capacitance of 18.8 ± 5.8 mF g^{-1}, at a scan rate of 20 mV s^{-1}.

As the EDLS fabricated with the IL $[C_2mim][FAP]$ as electrolyte had a wider operational voltage (3.0 V) the energy and power characteristics were larger than for the EDLS using $[C_2mim][NTf_2]$ as the electrolyte. In the case of the power density, the maximum value obtained was 1.55 μW cm^{-2} using $[C_2mim][FAP]$ and 1.16 μW cm^{-2} using $[C_2mim][NTf_2]$. The energy density values were much smaller with values of 0.006 μW h cm^{-2} for $[C_2mim][FAP]$ and 0.0022 ± 0.0004 μW h cm^{-2} for $[C_2mim][NTf_2]$. These supercapacitors using graphite-cellulose composite electrodes were comparable to graphene-cellulose based supercapacitors in term of power and energy properties.

The results obtained suggest that the EDLS fabricated have great potential for energy storage applications that need flexible and rechargeable devices such as biomedical implants or portable micropower sources. Also, it was demonstrated that any residual atmospheric moisture does not significantly impact on the device performance.

Chapter 5

Flexible Electrochemical Supercapacitors (ES)

As it was discussed in Chapters 2 and 3, electronically conducting polymer-based electrodes present problems like poor processability due to the electronically conducting polymers (ECPs) insolubility and non-thermoformable nature, making these materials difficult to manage. Currently, to solve these disadvantages the procedure followed in the literature was to coat, graft or deposit the ECP synthesised over flexible substrates such as graphene or paper [252]. However, the electronically conducting polymers when used as electrodes in supercapacitors usually presented a low cycle life and mechanical stability due to the poor adherence to the surface of their host materials leading to degradation of the electrodes [39]. Therefore, the fabrication of a new class of ECP-based electrodes that present durable cycle life and flexibility will be the objective to achieve henceforth.

In this chapter, the discussion of the application of a redox active and flexible material as electrodes in flexible energy storage devices such as supercapacitors is carried out. These composites contained an electronically conducting polymer *e.g.* polypyrrole as the redox active material and a biopolymer *e.g.* cellulose that can be used as electrodes as it was demonstrated in Chapter 3 [184b]. The redox active and flexible composite used in this chapter is a polypyrrole-cellulose fibrous-IL plasticiser film (PPy-cellfib-IL plasticiser film) that it was used as both electrodes (positive and negative) to fabricate a symmetric electrochemical supercapacitor (ES) or pseudocapacitor, exploiting the redox nature of the polypyrrole [84a]. In the case of the electrolyte in the ES, two ionic liquids were chosen as in Chapter 4, *i.e.* $[C_2mim][NTf_2]$ and $[C_2mim][FAP]$ for comparison reasons.

The development of flexible supercapacitors using electronically conducting polymer composites with a biopolymer available in bio-waste to provide a flexible matrix and the ionic liquid technology is the cynosure of this chapter. ECPs provide the smart functionality in these composites, and the ionic liquid plasticiser increases the electro-wettability and plasticity, leading to more durable supercapacitors with the flexible nature needed to adapt to body shapes for their use in biomedical applications.

5.1. Experimental Part

In this section, the experimental part related to the fabrication of a set of electrochemical supercapacitors and their electrochemical characterisation is described.

5.1.1. Fabrication of the Flexible ES

The preparation of the electronically conducting polymer-biopolymer-IL plasticiser (PPy-cellfib-IL plasticiser film) composite electrode used in the ES was carried out using the procedure reported in section 3.8 [184b]. All composite films used as electrodes were dried prior to assembly in a vacuum desiccator for 48 h.

The assembly of the electrochemical supercapacitors was carried out as reported in section 4.1.2 and Figure 4.2.

5.1.2. Electrochemical Study of the ES Fabricated

The electrochemical performance of the electrochemical supercapacitors was carried out as it was explained in section 4.1.3 and Figure 4.3. The techniques used were cyclic voltammetry, galvanostatic charge-discharge and electrochemical impedance spectroscopy.

5.2. Results and Discussion

5.2.1. Electrochemical Study of the ES Fabricated Using $[C_2mim][NTf_2]$ as the Electrolyte

The electrochemical study of a set of three identical electrochemical supercapacitors using $[C_2mim][NTf_2]$ as the electrolyte was carried out to establish their energy storage device capabilities and check their reproducibility. As in the previous chapter, all the electrochemical measurements were performed in a two-electrode system at 25 ± 2 ^{0}C.

An ES is an energy storage device with an electrochemical mechanism, in other words, redox reactions are involved (*i.e.*, the reduction and oxidation of the electronically conducting polymer, polypyrrole). The active material considered was the polypyrrole from the PPy-cellfib-IL plasticiser composite film, comprising a 33.3 wt % of the total weight at each electrode, hence the total mass of the active material was 6.0 ± 1.0 mg, the area of the composite electrodes was 1 cm^2 and the electrode thickness around 300 ± 50 μm.

For the set of ES using $[C_2mim][NTf_2]$ as the electrolyte, the OCP found was 0.029 ± 0.009 V.

5.2.1.1. Cyclic Voltammetry

In the case of the electrochemical supercapacitor, the cyclic voltammogram obtained showed a nearly rectangular and symmetric shape with an operational voltage from -0.9 V to 0.7 V (1.6 V), as it can be seen in Figure 5.1. The EW of the ES was 0.5 V lower in comparison to the EDLS using $[C_2mim][NTf_2]$ as the electrolyte from section 4.2.2.1. The polypyrrole from the composite electrode may reduce the operational voltage, although the EW obtained (1.6 V) is wider than the EW values reported for polypyrrole-based supercapacitors in the literature (*i.e.*, around 0.8 V) [64].

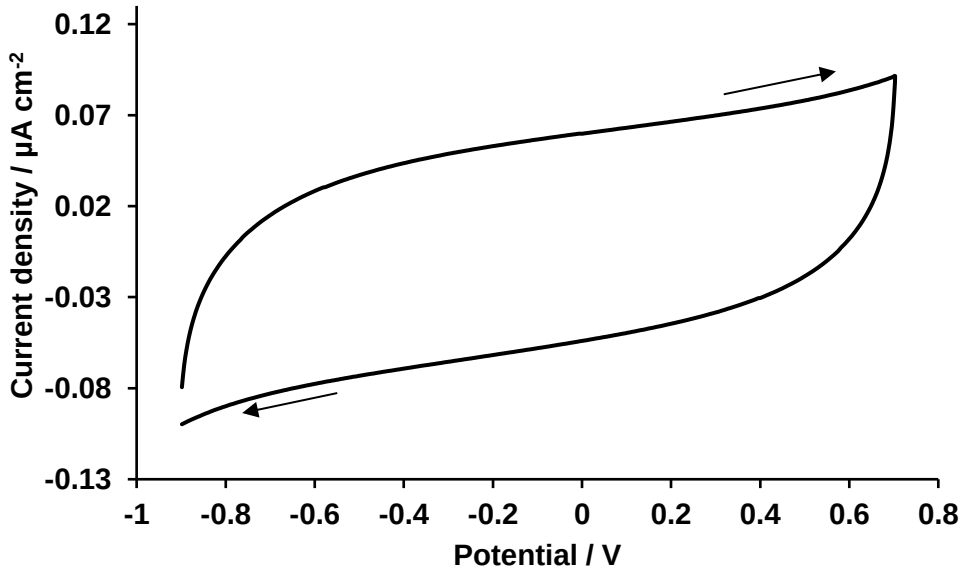

Figure 5.1 Cyclic voltammogram of one of the ES at 50 mV s^{-1} at 25 ± 2 ^{0}C. Arrows show the potential direction of the cyclic voltammogram

The same operational voltage of 1.6 V was found for the three ES fabricated, as shown in Figure 5.2. The specific capacitance, for these three ES at 50 mV s^{-1} and at 25 ± 2 ^{0}C, was 3.8 ± 0.9 mF g^{-1} and the areal capacitance was 23.1 ± 1.5 µF cm^{-2}. As it can be seen the capacitance values were reproducible among the three devices, with a very small variance among the values.

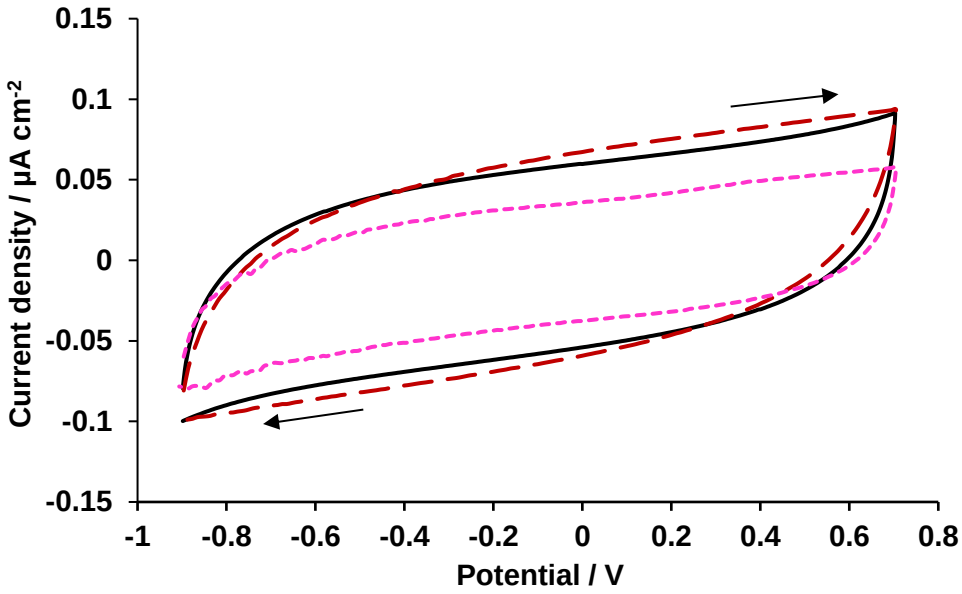

Figure 5.2 Cyclic voltammograms of the three ES fabricated using [C_2mim][NTf_2] as the electrolyte at 50 mV s^{-1} and at 25 ± 2 ^{0}C. Arrows show the potential direction of the cyclic voltammogram

As demonstrated in Figure 5.3, the device can be operated at various scan rates from 20 mV s^{-1} to 1 V s^{-1}; the CVs obtained kept the rectangular shape for all the different scan rates applied. This fact indicates that this supercapacitor can endure fast voltage/current change rates, due to the fast and reversible electrochemical processes carried out by the polypyrrole reduction and oxidation [344].

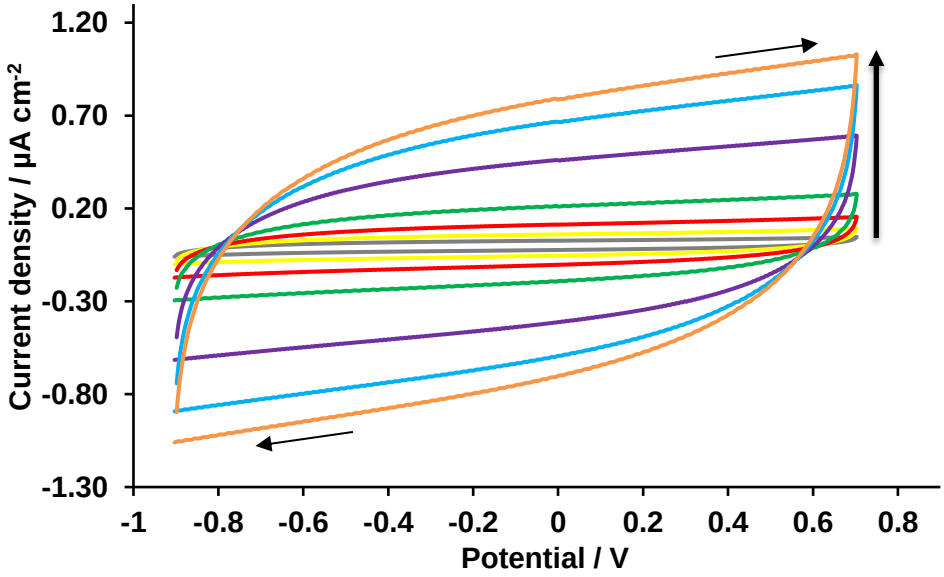

Figure 5.3 Cyclic voltammogram of one of the ES fabricated using [C_2mim][NTf_2] as the electrolyte at various scan rates: 1000 (orange), 800 (light blue), 500 (purple), 200 (green), 100 (red), 50 (yellow), 20 (grey) mV s^{-1} at 25 ± 2 ^{0}C. Arrows show the potential direction of the cyclic voltammogram and the vertical arrow indicates the faster scan rates applied

Regarding the capacitance values at different scan rates (Table 5.1), similar behaviour to the EDLS was found, *i.e.* from 20 to 50 mV s^{-1} there was a quick drop in the capacitance values and then the values decreased slowly. The maximum specific capacitance value obtained was 11.3 ± 2.9 mF g^{-1} at 20 mV s^{-1} (lower than from the EDLS fabricated (section 4.2.2)). The reason for these lower values can be due to the larger thickness of the electrodes (300 ± 50 µm), compared to the EDLS electrodes. It is known that thicker electrodes lead to an increase of the resistance, as well as a decrease in the capacitance per gram (or specific capacitance) due to the limited ion movement. Herein, the dopant ions may have moved to the interior sites of the polypyrrole during the doping and de-doping process [345]. The values of areal capacitance expected would be around 8-15 mF cm^{-2} for a symmetric supercapacitor using the same *p*-doped electronically conducting polymer for both electrodes. In contrast, the maximum value obtained was 66.3 ± 4.4 µF cm^{-2} [64]. This low capacitance values may be due to the low conductivity of the PPy bounded by hydrogen bond to the cellulose matrix [184b]. The conductivity obtained (1450 µS cm^{-1}) is low in comparison to PPy grafted onto fabric or cellulose with a conductivity of 1.2 S cm^{-1} [346].

The standard deviation of the average of the capacitance values, among the three ES fabricated and tested, was very small. This small variance shows the high reproducibility of the fabrication method of electrochemical supercapacitors in this thesis using PPy-cellfib-IL plasticiser composite film as both electrodes in a symmetric supercapacitor.

Table 5.1 Specific and areal capacitance values of the ES using $[C_2mim][NTf_2]$ as the electrolyte calculated from the CV at various scan rates

Scan rate / mV s^{-1}	$C_{Spec.}$ / mF g^{-1}	C_{Areal} / µF cm^{-2}
20	11.3 ± 2.9	66.3 ± 4.4
50	3.8 ± 0.9	22.6± 2.0
100	1.5 ± 0.3	8.8 ± 1.3
200	0.7 ± 0.1	3.9 ± 0.5
500	0.21 ± 0.02	1.3 ± 0.2
800	0.12 ± 0.01	0.7 ± 0.1
1000	0.09 ± 0.01	0.6 ± 0.1

The performance of the three ES fabricated was tested prior to, during and after bending using cyclic voltammetry. Figure 5.4 shows that the CVs from the three stages described above were different, showing a variability in the performance of the device when bent. However, no distortion in the shape of the voltammograms was observed during the bending cycles, showing more stability than in the case of the EDLS displayed in section 4.2.2.1. In all the ES tested, bending caused more resistive behaviour, while the current in the CV increased corresponding to an increase in the capacitance. After bending (blue plot), all of the devices almost recovered the same cycle shape showing in the previous relaxing state (black plot).

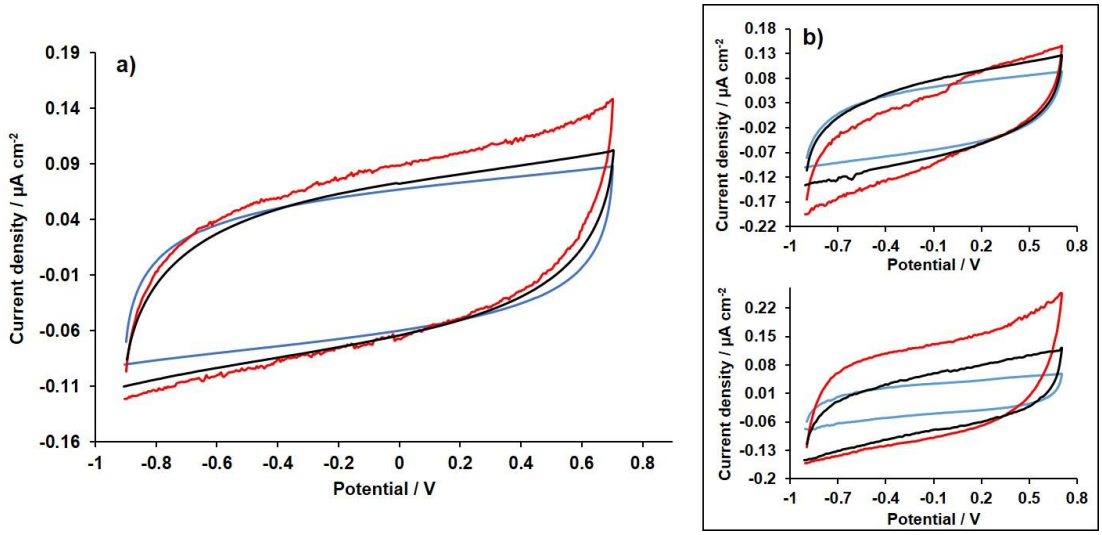

Figure 5.4 Bending study at the angle of 120 degrees of a) one of the ES and b) the other two ES fabricated using $[C_2mim][NTf_2]$ as the electrolyte at the scan rate of 50 mV s^{-1} and at 25 ± 2 ^{0}C. Cyclic voltammogram before (blue), during (red) and after (black) bending

The capacitance values obtained from the bending study (Table 5.2) showed a resistive behaviour during the bending with an increase in the capacitance that was retained after the bending study and could be due to a better contact between the active materials after the bending action. The standard deviation for the capacitance values showed that the three ES fabricated had similar behaviour when they were bent, exhibiting reproducible results.

Table 5.2 Specific and areal capacitance average values of the ES using $[C_2mim][NTf_2]$ as the electrolyte during the bending study

Bending state	$C_{Spec.}$ / mF g^{-1}	C_{Areal} / μF cm^{-2}
Prior to bending	3.9 ± 0.8	23.1 ± 1.5
120 degrees angle	5.1 ± 1.8	29.5 ± 5.4
After bending	4.8 ± 1.5	28.1 ± 4.6

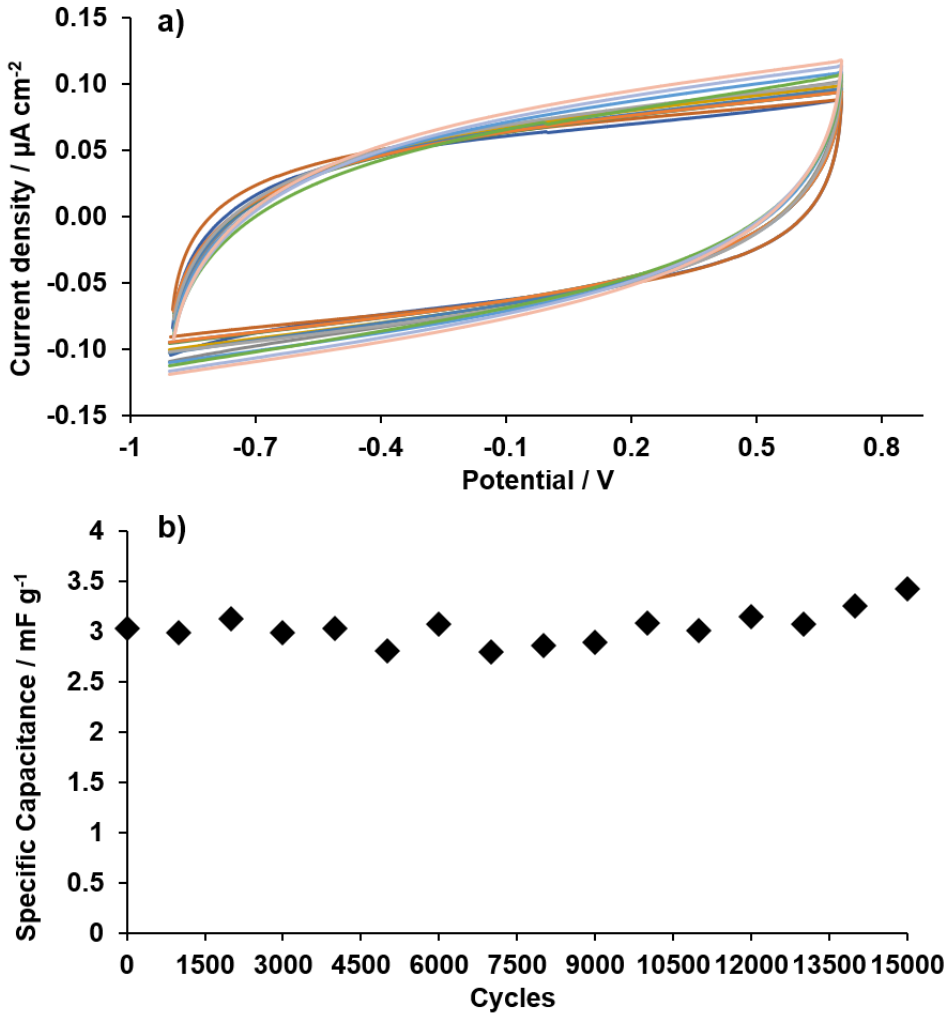

Figure 5.5 a) Cyclic voltammograms of one of the ES fabricated using $[C_2mim][NTf_2]$ as the electrolyte at every 1000th scan from 2 to 15000 cycles at the scan rate of 50 mV s^{-1} and at 25 ± 2 ^{0}C, b) specific capacitance during 15000 cycles

The cycle life, at the scan rate of 50 mV s^{-1} and at 25 ± 2 ^{0}C, was studied for one of the ES fabricated, as shown in Figure 5.5. The cycle life stability for this device was durable and performed for 15000 cycles with an almost 100 % of capacitance retention. Most of the devices using PPy as active materials show a poor cycle life of 10000 cycles maximum due to the structural breakdown of the composite induced by

the large volume increase (doping) and decrease (de-doping) of the polypyrrole during the charge and discharge cycles [344,36]. This supercapacitor utilising polypyrrole bounded to cellulose as composite electrodes showed a considerably improved of the durability compared to systems with deposited polypyrrole on conductive materials such as carbon-shell electrodes [36] or hierarchical structures of functionalised graphene with metal oxide-based electrodes [347,84a].

Table 5.3 shows the capacitance values at the beginning of the cycle life and the last capacitance values from the 15000th cycle. The capacitance showed a little increase in the cycle life study (Figure 5.5 (b)), that may be caused by the thermocapacitance during the charge-discharge process as it was explained in section 4.2.2. The average specific capacitance obtained during 15000 cycles was 3.0 ± 0.2 mF g^{-1}, and the average areal capacitance was 23.0 ± 1.2 μF cm^{-2}, demonstrating an excellent cycle life stability.

Table 5.3 Specific and areal capacitance values of one of the ES using [C_2mim][NTf_2] as the electrolyte at the second cycle and 15000 cycle

Cycle 2		Cycle 15000	
C_{Spec} / mF g^{-1}	C_{Areal} / μF cm^{-2}	C_{Spec} / mF g^{-1}	C_{Areal} / μF cm^{-2}
3.0	22.9	3.4	25.9

5.2.1.2. Galvanostatic Charge-discharge

The electrochemical supercapacitors fabricated were studied also using the galvanostatic charge-discharge technique. Different current densities were applied from 0.02 μA cm^{-2} to 1 μA cm^{-2} using the EW obtained from CV that was 1.6 V (from -0.9 V to 0.7 V). Figure 5.6 shows the graphs obtained with this technique at different current densities applied. As reported in Chapter 4, a nearly symmetric triangle is expected for an ideal double-layer capacitance albeit, for the ES test at small current densities, the triangles obtained had a slight deviation from the ideal behaviour. The reason for this deviation may be due to a not fully reversible polypyrrole reaction [11] (*i.e.*, the doping and de-doping reactions are not totally reversible) [348]. Despite this slight deviation, as it was shown in section 5.2.1.1 the supercapacitor could charge and discharge for 15000 cycles with no drastic capacitance fading observed.

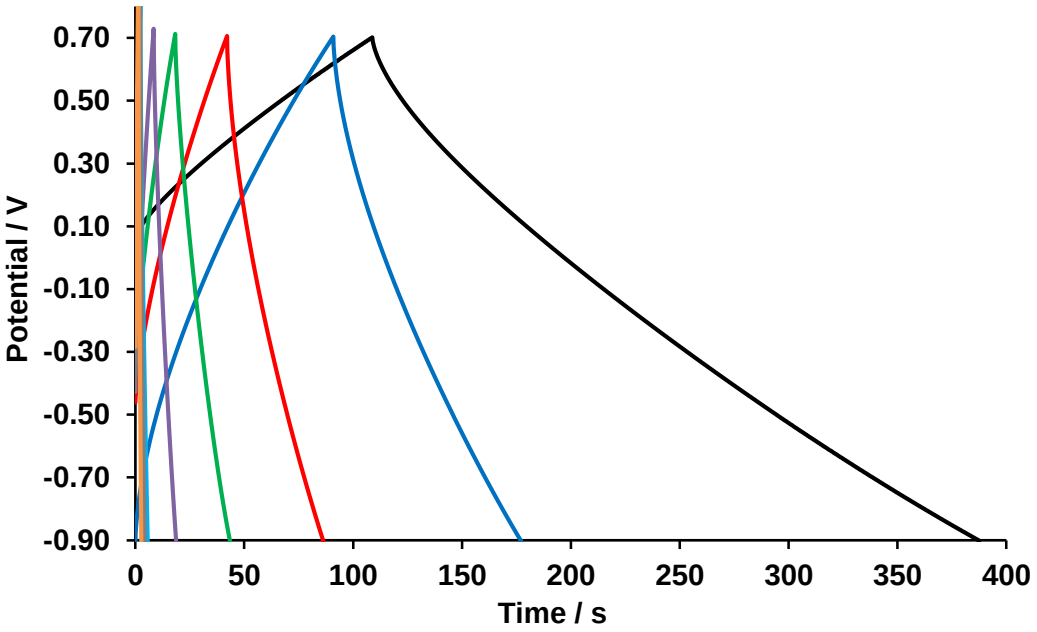

Figure 5.6 GCD curves of one of the ES fabricated using $[C_2mim][NTf_2]$ as the electrolyte at different currents densities applied, 0.02 (black), 0.05 (blue), 0.08 (red), 0.1 (green), 0.2 (purple), 0.5 (light blue), 0.8 (grey) and 1 μA cm^{-2} (orange) and at 25 ± 2 ^{0}C.

The equivalent series resistance of the ES fabricated using $[C_2mim][NTf_2]$ as the electrolyte was calculated using Equation 4.11, giving a value of 325 ± 92 kΩ. This is higher than in the case of the EDLS using $[C_2mim][NTf_2]$ as the electrolyte (section 4.2.2.2), and may be due to the PPy and cellulose hydrogen bond interactions. The potential drop related to the internal resistance was 7.3 mV at the current density of 0.02 μA cm^{-2} and increased to 462 mV at 1 μA cm^{-2}; both values were comparable to the EDLS device.

Figure 5.7 shows the three GCD curves corresponding to the three ES fabricated at the current density of 0.05 μA cm^{-2} and at 25 ± 2 ^{0}C. The shape of the triangle was similar for all the ES fabricated, showing a small deviation to the right in the positive limit of the curve which indicates the existence of redox reactions from the polypyrrole. The average time needed for the total charge-discharge for the three ES was 131 ± 43 s. A non-homogeneous physical nature of the electrodes due to the cellulose-PPy hydrogen bonding could originate the different time needed for charge and discharge the three ES fabricated. Even though cellulose and PPy are chemically connected and not possible to rip-off, they are not controlled in a uniform way physically across the polymer composite surface.

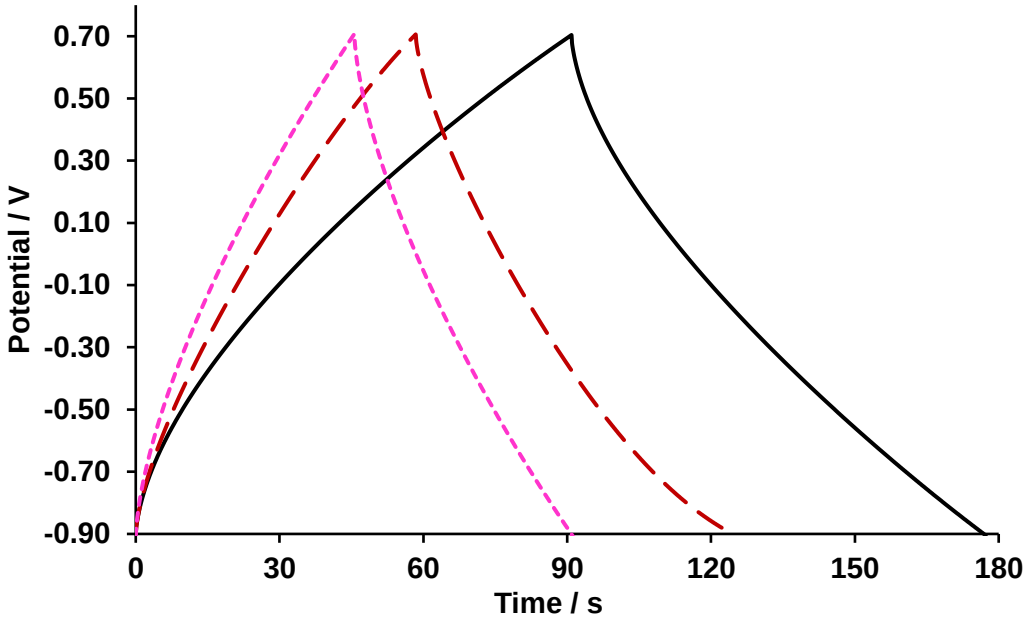

Figure 5.7 GCD curves of the three ES fabricated using $[C_2mim][NTf_2]$ as the electrolyte at the current density 0.05 μA cm^{-2} and at 25 ± 2 ^0C

Table 5.4 Energy and power average values calculated for the ES using $[C_2mim][NTf_2]$ as the electrolyte at different current densities applied and the discharge time obtained using GCD

Current density / μA cm^{-2}	Discharge time / s	E_{Spec} / mW h kg^{-1}	$E_{Density}$ / μW h cm^{-2}	P_{Spec} / mW kg^{-1}	$P_{Density}$ / μW cm^{-2}
0.02	251 ± 47	0.20 ± 0.03	0.0012 ± 0.0002	2.9 ± 0.5	0.0174 ± 0.0002
0.05	66 ± 20	0.13 ± 0.03	0.0008 ± 0.0003	7.4± 1.3	0.044 ± 0.001
0.08	43 ± 3	0.14 ± 0.02	0.0008 ± 0.0001	11.9 ± 2.1	0.071 ± 0.002
0.1	30 ± 4	0.12 ± 0.04	0.0007 ± 0.0001	14.5 ± 3.0	0.086 ± 0.001
0.2	13 ± 2	0.08 ± 0.05	0.0004 ± 0.0002	22.0 ± 12.6	0.13 ± 0.07
0.5	4 ± 1	0.09 ± 0.03	0.0005 ± 0.0001	68.7 ± 12.6	0.41 ± 0.01
0.8	3 ± 0	0.08 ± 0.02	0.0005 ± 0.0001	107.8 ± 19.8	0.64 ± 0.02
1	2 ± 1	0.08 ± 0.03	0.0004 ± 0.0001	128.3 ± 20.4	0.76 ± 0.03

The time that the devices needed to discharge are shown in Table 5.4, the maximum time needed was 251 ± 47 s at the lowest current density applied; and for the highest current density, the ES discharged in 2 ± 1 s, showing that these ES were fast responsive. The maximum energy density was 0.0012 ± 0.0002 μW h cm^{-2} and the maximum power density was 0.76 ± 0.03 μW cm^{-2}. These energy and power values were lower than the ones obtained with the EDLS, which could be related to the lower

EW of the ES, in comparison to the EDLS. The EW is proportional to the energy and power as it was shown in Equation 4.16 and Equation 4.17, respectively.

5.2.1.3. Electrochemical Impedance Spectroscopy

Electrochemical impedance spectroscopy was employed to study the charge transfer and ion diffusion properties of the ES electrode materials during the cycle life.

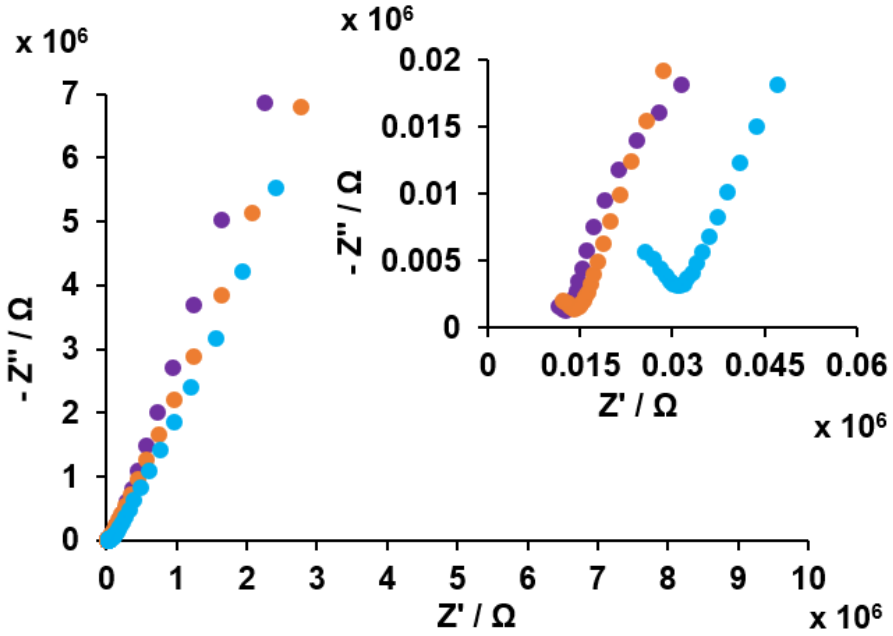

Figure 5.8 Nyquist plot of ES using $[C_2mim][NTf_2]$ as the electrolyte during the cycle life (25 ± 2 ºC): at OCP (purple), after 5000 cycles (orange) and after 15000 cycles (light blue). The inset shows the high-frequency part of the Nyquist plot

Figure 5.8 shows the Nyquist graph of the device, including the results obtained at the OCP of the ES, after 5000 cycles and when it reached 15000 cycles. At low frequencies, the results were similar, showing plots with an angle bigger than 45º. In contrast, changes were observed at high frequencies as it can be seen in the inset of Figure 5.8. The light blue plot corresponding to the 15000-cycle appeared at a lower frequency than the plots at OCP and at 5000-cycle. This fact was reflected in the ESR of the device that increased from 12.7 kΩ to 30.8 kΩ after 15000 cycles. This alteration may be due to thermocapacitance during the charge-discharge process, increasing the resistance in the device [326]. Regarding the knee frequency, values changed from 22.2 KHz to 10.5 kHz, decreasing the range of frequencies at which the energy stored was fully accessible (*i.e.*, at frequencies above the knee frequency the energy stored is not reported to be fully available) [349]. Despite the drop in frequencies, the knee frequency values obtained were still very high in comparison to the literature [339b]

and similar to the ones obtained for the EDLS with [C_2mim][NTf_2] as the electrolyte (section 4.2.2.3).

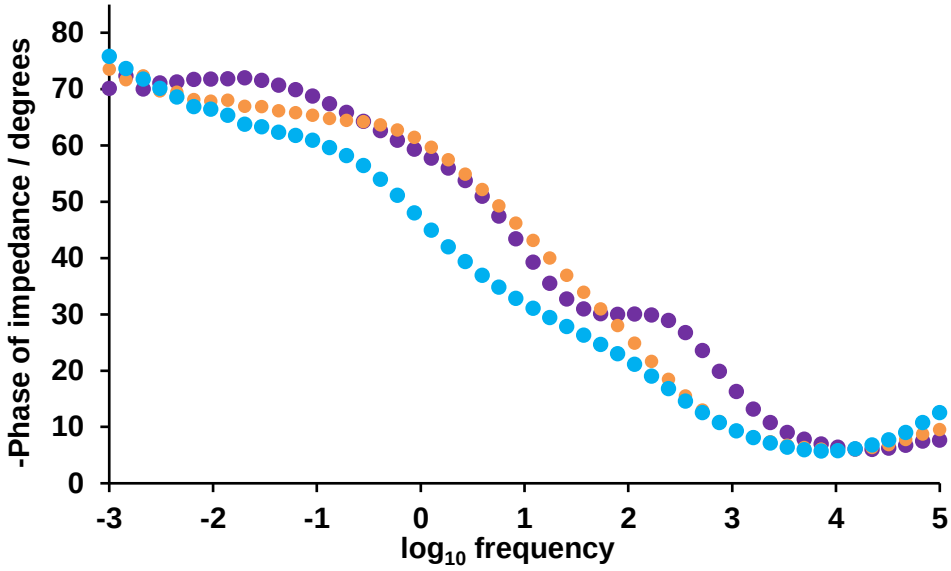

Figure 5.9 Bode plot of ES using [C_2mim][NTf_2] as the electrolyte during the cycle life (25 ± 2 ºC): at OCP (purple), after 5000 cycles (orange) and after 15000 cycles (light blue)

With the Bode plot (Figure 5.9) the frequency at -45^0 (onset frequency) can be studied. This frequency was 5.7 Hz at OCP, a value that increased after 5000 cycles to 8.3 Hz and it dropped to 1.3 Hz after 15000 cycles, *i.e.,* that the range of frequencies at which the device shows primarily capacitive behaviour was reduced after 15000 cycles. As it was explained in section 4.2.2.3, the phase angle of an ideal capacitor should be -90^0 but, as it can be seen in the plot, the phase angle at low frequencies never reached -90^0, being the maximum angle reached -71^0 and up to frequencies of 0.04 Hz.

5.2.2. Electrochemical Study of the ES Fabricated Using [C_2mim][FAP] as the Electrolyte

The study of an electrochemical supercapacitor (pseudocapacitor) using a different electrolyte, in this case, [C_2mim][FAP], was carried out.

The active material in this ES was considered to be the polypyrrole from the PPy-cellfib-IL plasticiser composite film, compromising a 33.3 wt % of the total weight at each electrode; the total mass of the active material was 9.0 mg, the area of the electrodes 1 cm^2 and the thickness of the electrodes 300 ± 50 μm.

For ES using [C_2mim][FAP] as the electrolyte, the OCP found was 0.09 V.

5.2.2.1. Cyclic Voltammetry

The operational voltage for the ES using [C_2mim][FAP] as the electrolyte was found to be much higher than using the [C_2mim][NTf_2] IL as the electrolyte. As it can be seen in Figure 5.10, the EW obtained was 2.3 V, from -1.3 V to 1 V. The voltammogram obtained showed a rectangular and an almost symmetrical shape. The specific capacitance obtained for this device at 50 mV s^{-1} was 3.2 mF g^{-1} and the areal capacitance was 29.1 µF cm^{-2}. Although, the EW for this supercapacitor was 0.7 V higher than in the case of the previous ES using [C_2mim][NTf_2] (section 5.2.1.1) the capacitance values were found to be very similar. The same behaviour was observed in section 4.2.3.1, for the EDLS devices.

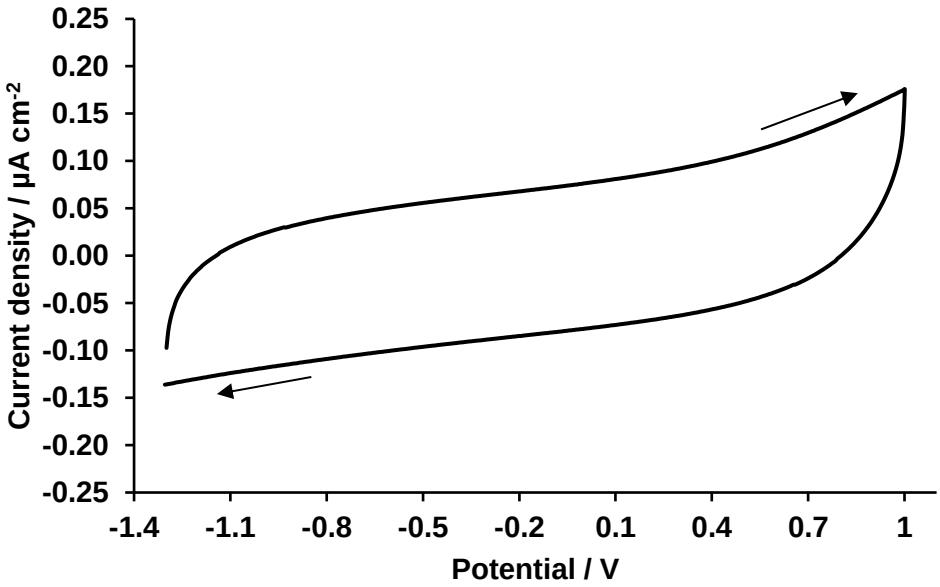

Figure 5.10 Cyclic voltammogram of one of the ES using [C_2mim][FAP] as the electrolyte at 50 mV s^{-1} and at 25 ± 2 ^{0}C. Arrows show the scan potential direction of the cyclic voltammogram

Figure 5.11 shows the rate capability of this device using [C_2mim][FAP] as the electrolyte. The voltammograms obtained at different scan rates kept the symmetrical and rectangular shape even at the highest scan rates and they showed linear enhancement of current with scan rates.

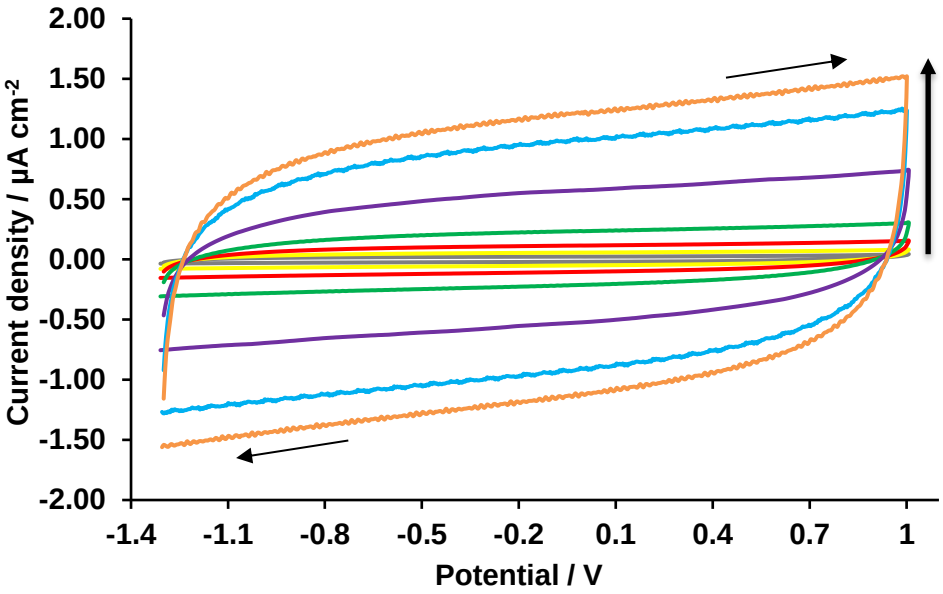

Figure 5.11 Cyclic voltammogram of the ES using [C_2mim][FAP] as the electrolyte at various scan rates: 1000 (orange), 800 (light blue), 500 (purple), 200 (green), 100 (red), 50 (yellow), 20 (grey) mV s^{-1} at 25 ± 2 ^{0}C. Arrows show the potential direction of the cyclic voltammogram and the vertical arrow indicates the faster scan rates applied

The capacitance values obtained decrease when faster scan rates were applied, but in this ES the values decrease smoother than in the case of the previous supercapacitors reported, as it can be seen in Table 5.5. The maximum specific and areal capacitances were 4.96 mF g^{-1} and 45.4 µF cm^{-2}, respectively, both were obtained at the scan rate of 20 mV s^{-1}.

Table 5.5 Specific and areal capacitance values of the ES using [C_2mim][FAP] as the electrolyte calculated from the CV at various scan rates

Scan rate / mV s^{-1}	$C_{Spec.}$ / mF g^{-1}	C_{Areal} / µF cm^{-2}
20	4.96	45.4
50	3.18	29.1
100	1.07	9.8
200	0.55	5.0
500	0.22	2.0
800	0.15	1.4
1000	0.12	1.1

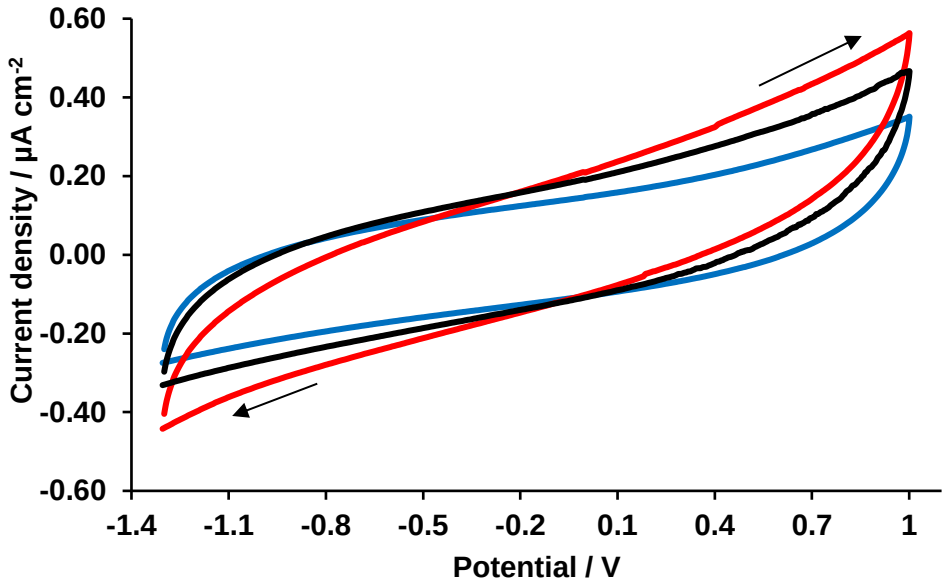

Figure 5.12 Bending study at an angle of 120 degrees of the ES using [C_2mim][FAP] as the electrolyte at the scan rate of 50 mV s^{-1}. Cyclic voltammogram before (blue), during (red) and after (black) bending

During the bending study of this ES using the CV, the voltammogram was altered, with increasing current at both cathodic and anodic limits (resistive behaviour) as shown in Figure 5.12. After bending the voltammogram did not return to the same position of repose condition. From this graph, it can be said that the ES could be used as a flexible supercapacitor but the full recovery after bending was not possible. Although two different electrolytes were used to fabricate the ES, the same behaviour was obtained when the bending study was carried out.

Table 5.6 shows the capacitance values obtained for the bending study and, albeit the voltammograms obtained seemed quite different, the capacitance values were almost the same. The average value for the specific capacitance was 4.5 ± 0.09 mF g^{-1} and for the areal capacitance, the average value was 41.2 ± 0.9 µF cm^{-2}.

Table 5.6 Specific and areal capacitance values of the ES using [C_2mim][FAP] as the electrolyte during the bending study

Bending state	$C_{Spec.}$ / mF g^{-1}	C_{Areal} / µF cm^{-2}
Prior to bending	4.5	40.8
120 degrees angle	4.6	42.4
After bending	4.4	40.2

The cycle life of this electrochemical supercapacitor using [C_2mim][FAP] as the electrolyte was studied using CV. The voltammograms obtained during 15000 cycles

are shown in Figure 5.13 (a), and the capacitance retention during the cycle life can be seen in Figure 5.13 (b). From these graphs, the device showed changes during the study, *i.e.*, the anodic and cathodic limits became more pronounced, incrementing the current of the voltammograms, and showing a more resistive behaviour. These changes resulted in a fluctuation in the capacitance retention which can be due to temperature changes in the supercapacitor during the charge-discharge, as it was explained in section 4.2.2 and/or due to an electromechanical process produced by a volume change in the polypyrrole chains during the charge-discharge process [64]. The graph of the capacitance retention can be separated into two parts, from the 2nd cycle to the 7000th the capacitance retention was maintained around 100 % and, in contrast, from the 8000th cycle to the 15000th cycle the capacitance retention increases to 140 %.

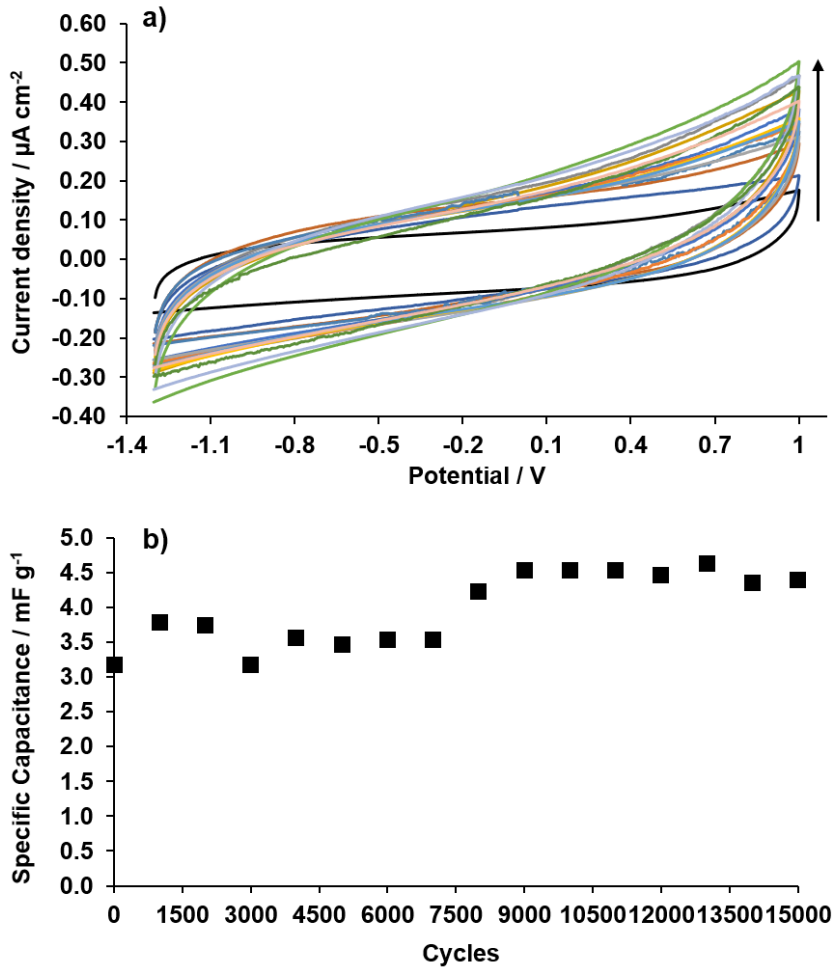

Figure 5.13 a) Cyclic voltammograms of the ES fabricated using [C_2mim][FAP] as the electrolyte at every 1000th scan from 2 to 15000 cycles at scan rate of 50 mV s^{-1} and at 25 ± 2 ^{0}C (arrow shows how the CVs varied during the cycle life) and, b) specific capacitance during 15000 cycles

The values obtained for this device during the cycle life are shown in Table 5.7 where the increase in capacitance values can be observed. During the 15000 cycles, the capacitance values increase in a 37.5 %. The average values of the capacitance during the cycle life were, 4.0 ± 0.5 mF g^{-1} and 36.3 ± 4.3 µF cm^{-2} for the specific and the areal capacitance, respectively.

Table 5.7 Specific and areal capacitance of the ES using [C_2mim][FAP] as the electrolyte at the second cycle and the 15000 cycle

Cycle 2		Cycle 15000	
C_{Spec} / mF g^{-1}	C_{Areal} / µF cm^{-2}	C_{Spec} / mF g^{-1}	C_{Areal} / µF cm^{-2}
3.2	29.1	4.4	40.2

5.2.2.2. Galvanostatic Charge-discharge

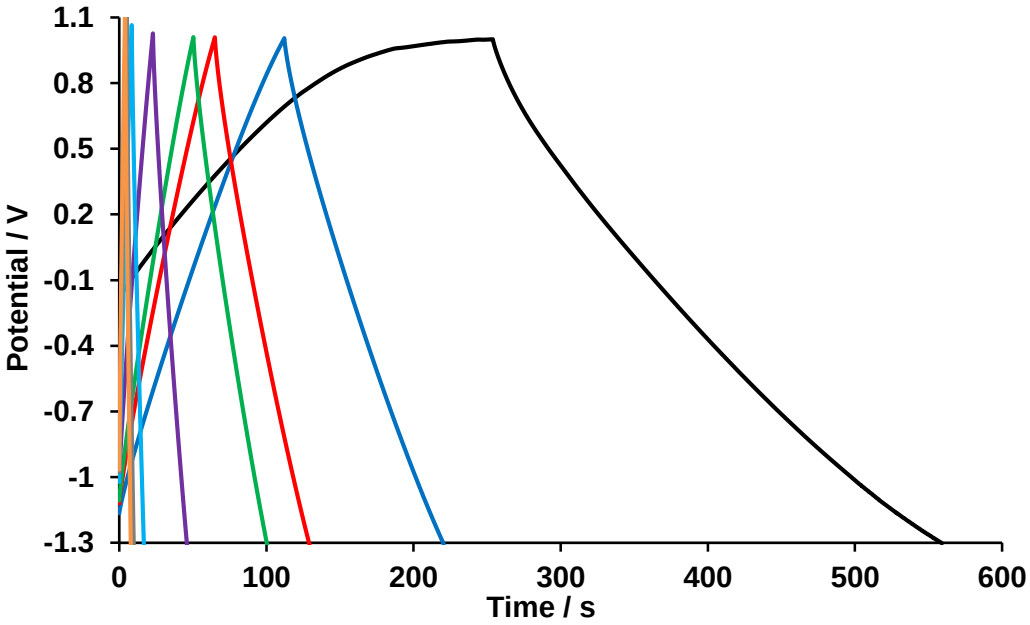

Figure 5.14 GCD curves of the ES fabricated ES using [C_2mim][FAP] as the electrolyte at different currents densities applied, 0.02 (black), 0.05 (blue), 0.08 (red), 0.1 (green), 0.2 (purple), 0.5 (light blue), 0.8 (grey) and 1 µA cm^{-2} (orange) at 25 ± 2 ^{0}C

The electrochemical performance of the symmetric ES using [C_2mim][FAP] as the electrolyte was further investigated with GCD measurements. Typical charge-discharge profiles at different current densities are shown in Figure 5.14., showing a nearly triangular shape for the charge-discharge profile over the operational voltage of the device, from -1.3 V to 1.0 V. From the graph, the time needed for the supercapacitor to charge and discharge can be extracted. As it was expected, at the lowest current densities the device needed more time to charge and discharge with a

total value of 560 s at 0.02 μA cm^{-2}. The ESR value for this ES was 190 ± 72 kΩ showing a similar value than in the case of the EDLS using [C_2mim][FAP] as the electrolyte. This ESR value was much smaller than the ES using [C_2mim][NTf_2] as the electrolyte, which could be due to a better contact between the electrode and this electrolyte or a better contact in the assembly.

The energy and power performance of the device are important factors for practical applications. Hence, the specific energy and power, as well as the energy and power density were calculated using Equation 4.16 and Equation 4.17. The values obtained were summarised in Table 5.8. The discharge time for each current density applied showed shorter times with a maximum of 305 s at the current density of 0.02 μA cm^{-2}, in comparison to the EDLS using the same electrolyte as showed in section 4.2.3.2 which needed 600 s at 0.02 μA cm^{-2}. Regarding the energy, this ES showed a better performance than the previous ES using [C_2mim][NTf_2] as the electrolyte, with a maximum value of specific energy of 0.22 mW h kg^{-1} and energy density of 0.0020 μW h cm^{-2}, due to the larger EW obtained. These values were maintained when bigger current densities were applied, a demonstration that this ES can store almost the same amount of charge at different currents applied. The other important electrochemical properties obtained were the specific and density power, 119.7mW kg^{-1} and 1.10 μW cm^{-2}, respectively, which due to the larger EW, were higher than for the ES using [C_2mim][NTf_2] as the electrolyte.

Table 5.8 Energy and power values calculated at different current densities applied, as well as, the discharge time obtained using GCD

Current density / μA cm^{-2}	Discharge time / s	E_{Spec} / mW h kg^{-1}	$E_{Density}$ / μW h cm^{-2}	P_{Spec} / mW kg^{-1}	$P_{Density}$ / μW cm^{-2}
0.02	305	0.22	0.0020	2.6	0.02
0.05	108	0.20	0.0018	6.5	0.06
0.08	64	0.19	0.0017	10.4	0.10
0.1	50	0.18	0.0017	13.0	0.12
0.2	23	0.17	0.0015	25.9	0.24
0.5	9	0.15	0.0014	63.4	0.58
0.8	5	0.14	0.0013	98.9	0.91
1	4	0.14	0.0012	119.7	1.10

5.2.2.3. Electrochemical Impedance Spectroscopy

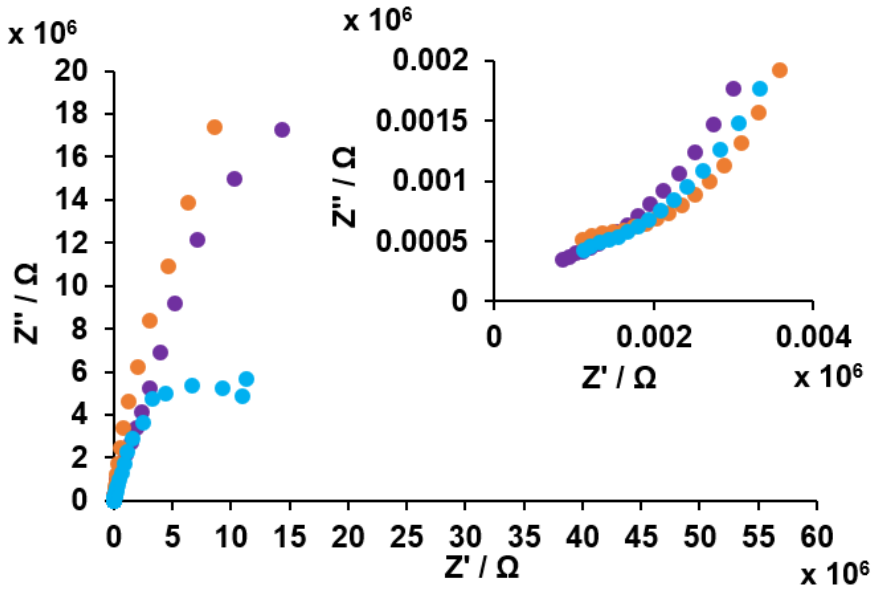

Figure 5.15 Nyquist plot of the ES using [C_2mim][FAP] as the electrolyte during the cycle life (25 ± 2 ^{0}C): at OCP (purple), after 5000 cycles (orange) and after 15000 cycles (light blue). The inset shows the high-frequency part of the Nyquist plot

The EIS results for the ES using [C_2mim][FAP] as the electrolyte were more complex than in the case of the ES using [C_2mim][NTf_2], as it can be seen in Figure 5.15. During the first 5000 cycles, the purple and orange plots showed almost the same tilt at the lower frequencies whilst the plot corresponding to the 15000th cycle (light blue) suffered a decay at the lower frequencies. The angle of all the three plots at various cycle stages were more than 45 ºC showing capacitive behaviour, as it can be seen in the inset of Figure 5.15. The knee frequencies values obtained for this supercapacitor were 15.3 kHz at OCP, 7.2 kHz after 5000 cycles and 15.3 KHz after 15000 cycles. The ESR of this ES was 1.3 kΩ at OCP, reaching 1.7 kΩ after cycling for 15000 cycles. The EIS results support the fact that after 5000 cycles there is a change in the supercapacitor behaviour, as it was shown in section 5.2.2.1 and Figure 5.13 during the cycle life study.

Using the representation known as Bode plot, Figure 5.16, the different behaviour of the ES during the cycle life study can be observed more clearly. At the OCP and after 15000 cycles, the frequency at the phase of impedance -45^0 showed the same value of 79.1 Hz, whilst the frequency at 5000 cycles was 54.3 Hz. In the case of the capacitance behaviour at the lower frequencies, a huge difference can be noticed among the three results presented. The light blue plot corresponding to the

15000th cycle showed a resistive behaviour from frequencies below 4.5 mHz. Hence, this ES with [C_2mim][FAP] as electrolyte exhibited capacitive behaviour and after 15000 cycles started to show resistive behaviour, between frequencies from 4.5 mHz to 79.1 Hz.

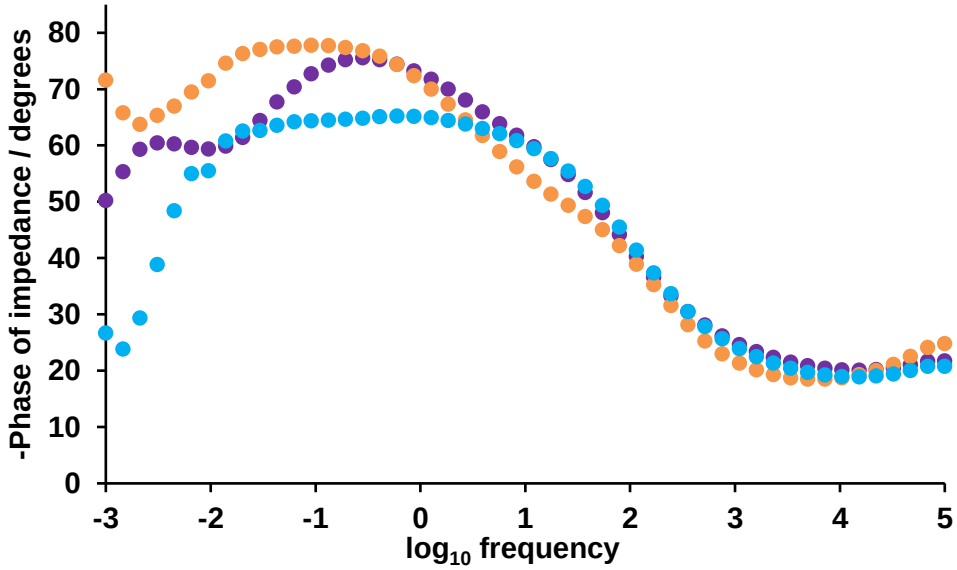

Figure 5.16 Bode plot of the ES using [C_2mim][FAP] as the electrolyte during the cycle life (25 ± 2 ^{0}C): at OCP (purple), after 5000 cycles (orange) and after 15000 cycles (light blue)

5.2.3. Chemical and Physical Study of the ES Electrodes

As in section 4.2.4 several techniques: Fourier transform infrared (FT-IR), thermogravimetric analysis (TGA) and scanning electron microscopy (SEM), were employed to study the fresh films and after the cycling process. In this case, PPy-cellfib-IL plasticiser film before and after being used them as electrodes in the ES using [C_2mim][NTf_2] as electrolyte for a cycle life of 15000 cycles.

5.2.3.1. Fourier Transform Infrared (FT-IR)

Figure 5.17 shows the infrared spectra of the PPy-cellfib-IL plasticiser film before (black plot) and after being used as both electrodes (red and green plots) in the ES for 15000 cycles. In the overlaid spectra (Figure 5.17), the green plot is the one with more changes in comparison with the black plot (fresh film). The main changes found were at: (i) the broad peak at 3300 cm^{-1} corresponding to the N-H stretching of the polypyrrole and the O-H stretching of the cellulose and (ii) the peak at 1050 cm^{-1} corresponding to the C-O, C-OH, C-H and C-O-C ring deformation of the cellulose and the C-H deformation of the polypyrrole. In both cases, the intensity of the peak was reduced substantially. These changes can be due to the oxidation and reduction

of the polypyrrole taking place repeatedly during the 15000 cycles at this electrode (green plot) which, therefore, may be assigned as the positive electrode. The other film (red plot) would then correspond to the negative electrode [64].

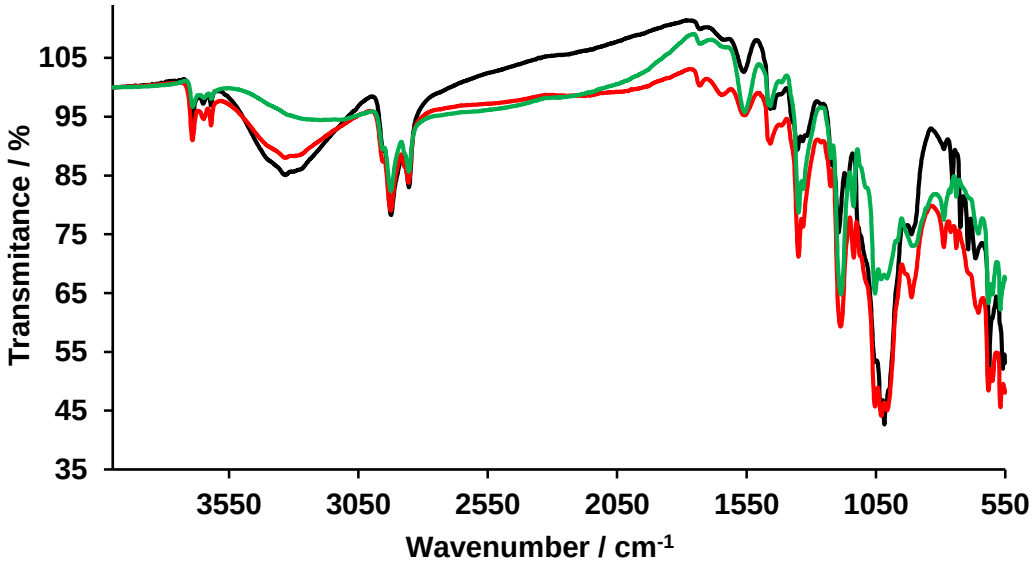

Figure 5.17 Infrared spectra of the PPy-cellfib-IL plasticiser fresh film (black) and after using it as both electrodes for 15000 cycles in the EDLS using $[C_2mim][NTf_2]$ as the electrolyte (red and green)

5.2.3.2. Thermogravimetric Analysis (TGA)

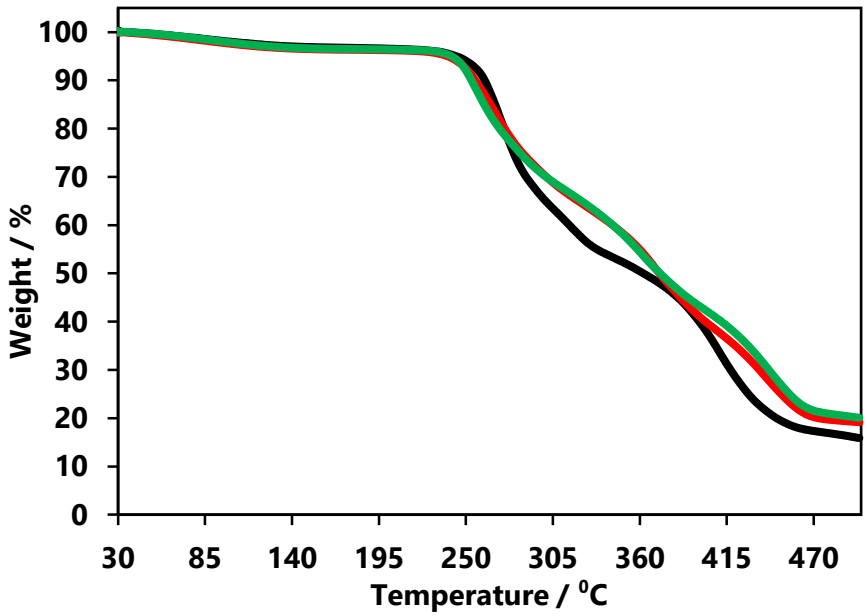

Figure 5.18 Thermogram of the PPy-cellfib-IL plasticiser fresh film (black plot) and the same film used as both electrodes during 15000 cycles in the ES using $[C_2mim][NTf_2]$ as the electrolyte (green and red plots)

Figure 5.18 shows the thermogram obtained for the PPy-cellfib-IL plasticiser fresh film (black plot) and after being used as both electrodes (green and red plots) in the ES. From the graph, the black plot had two decomposition temperatures, and, in contrast, the green and red plots had three decomposition temperatures.

Table 5.9 shows that the water content remained almost the same in the films after using them as electrodes for 15000 cycles. The first decomposition temperature of the films after using them as electrodes decreased around 10 ^{0}C in comparison to the fresh film. The second decomposition temperature may be related to the IL plasticiser, $[P_{6\,6\,6\,14}][NTf_2]$, that was retained inside the film even after the electrochemical study, contrary to what happened when the graphite-cellfib-IL plasticiser was used as electrodes in the EDLS (section 4.2.4.1). This could be related to a better stability of the components due to the polypyrrole-cellulose hydrogen bonding. The appearance of a third decomposition temperature in the used films can be due to the polypyrrole redox reactions involved in the charge-discharge cycles and related to the dopant in the polypyrrole. The amount of residue that remained (~ 20 %), was small in comparison to the electrodes from the EDLS (section 4.2.4.2) which had a residue of ~ 40 %. This may be due to the absence of the graphite component which has a very high decomposition temperature.

Table 5.9 Water content and decomposition temperature (T_{onset}) values of the PPy-cellfib-IL plasticiser film before and after being used as the electrode for 15000 cycles in the ES using $[C_2mim][NTf_2]$ as the electrolyte

Films	Water content / %	1st T_{onset} / ^{0}C	2nd T_{onset} / ^{0}C	3rd T_{onset} / ^{0}C
Before used (black plot)	2.63	256	387	-
After used (red plot)	2.99	244	343	424
After used (green plot)	2.77	246	355	425

5.2.3.3. Scanning Electron Microscopy (SEM)

Figure 5.19 shows three pictures obtained for the same PPy-cellfib-IL plasticiser film (a) before and, (b) after using it as the two electrodes (positive and negative) in the ES. The bottom pictures from (b) revealed that the surface is covered still with the ionic liquid electrolyte, $[C_2mim][NTf_2]$, used in the device, even after washing with methanol. In addition, beneath the electrolyte layer, the picture of the right shows that the surface is much rougher than in the picture on the left. This can be attributed to

the polypyrrole oxidation and reduction during the charge-discharge cycles leading to electroactivation. It is known from the literature [64] that the fast and reversible redox reactions from PPy during the charge-discharge cycling have as a consequence a volume change in the polymer chains. This volume change can explain the surface change observed in the electrode on the right picture. As it was discussed previously in section 5.2.3.1, if there is an indication that polypyrrole has been oxidised and reduced over the film, it can be said that it corresponds to the positive electrode. Therefore, the film on the right can be identified as the positive electrode and the film on the left can be identified as the negative electrode.

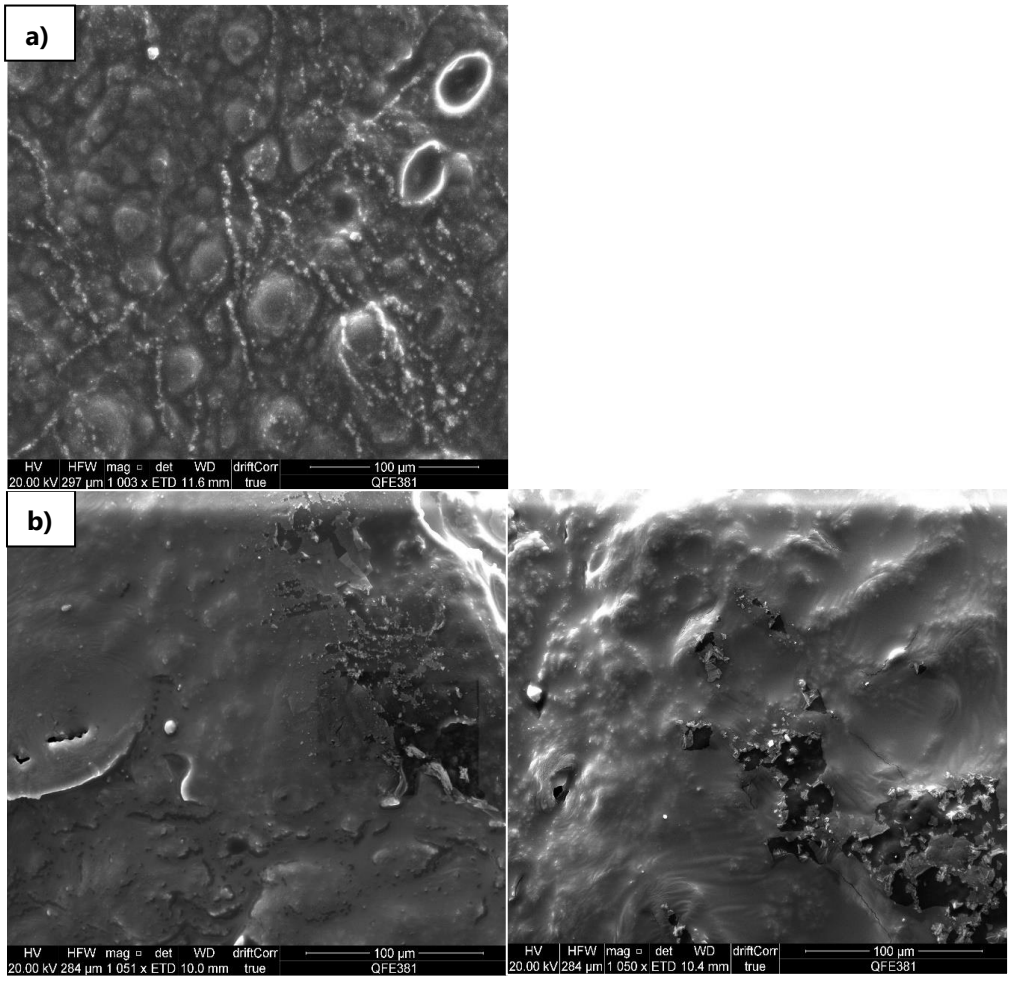

Figure 5.19 SEM pictures with a magnification of 1K of the (a) PPy-cellfib-IL plasticiser fresh film and (b) the same film after using it as both electrodes for 15000 cycles in the ES using $[C_2mim][NTf_2]$ as the electrolyte

In Figure 5.20 the cross-section of one of the electrodes used in the ES is shown. From this picture, the thickness of the film was estimated to be of 90.5 µm. Albeit the surface was covered with electrolyte, distinct layers can be seen inside the film, as it was observed in the EDLS electrode in section 4.2.4.3.

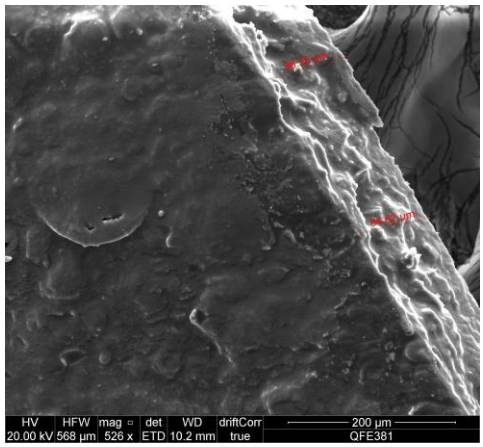

Figure 5.20 Cross-section SEM picture of one of the electrodes of the ES using $[C_2mim][NTf_2]$ as the electrolyte showing the thickness of this film after 15000 cycles

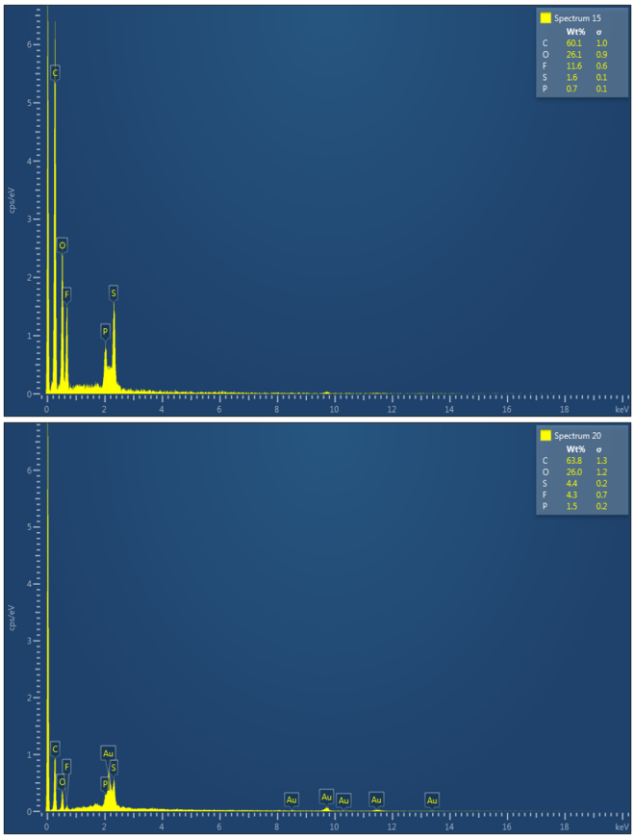

Figure 5.21 EDX spectra of both electrodes after 15000 cycles in the ES using $[C_2mim][NTf_2]$ as the electrolyte

Figure 5.21 shows the EDX obtained for the PPy-cellfib-IL plasticiser composite used as both electrodes in the electrochemical supercapacitor. As it can be seen in Table 5.10, both electrode films showed the same elements (C, O, S, F and P) almost with the same weight percent. The elements found belonged to the polypyrrole, cellulose and IL plasticiser ($[P_{6\,6\,6\,14}][NTf_2]$) as well as the dopant. The higher weight

percent of the elements P, S and F in comparison to the fresh film (data taken from section 3.8.2) could be due to the remaining electrolyte [C_2mim][NTf_2].

Table 5.10 Elemental analysis of the PPy-cellfib-IL plasticiser as fresh film and both electrodes used for 15000 cycles in the ES using [C_2mim][NTf_2] as the electrolyte

Composite film name	C / wt %	O / wt %	F / wt %	S / wt %	P / wt %	Cl / wt %
Fresh film	62.3	35.1	-	1.3	1.0	-
Electrode film 1	60.1	26.1	11.6	1.6	0.7	-
Electrode film 2	63.8	26.0	4.3	4.4	1.5	-

5.3. Summary and Conclusions

The fabrication and characterisation of a set of flexible electrochemical supercapacitors were achieved successfully. A PPy-cellfib-IL plasticiser composite film was used as both electrodes and two ionic liquids were chosen as electrolytes, [C_2mim][NTf_2] and [C_2mim][FAP].

The ES with the wider operational voltage showed a value of 2.3 V, using [C_2mim][FAP] as the electrolyte, and in the case of the ES using [C_2mim][NTf_2] as the electrolyte, the EW found was 1.6 V. It was possible to obtain the same EW in a set of three ES, showing reproducibility. Both devices, with different electrolytes, showed a high cycle life stability, being able to charge and discharge for more than 15000 cycles with an almost 100 % of capacitance retention. During the cycle life, the areal capacitance for the ES using [C_2mim][NTf_2] as the electrolyte was 23.0 ± 1.2 μF cm^{-2} and, for the ES using [C_2mim][FAP] as the electrolyte was 36.3 ± 4.3 μF cm^{-2}.

Regarding the energy and power of these devices, the maximum energy and power values obtained were 0.002 μWh cm^{-2} and 1.10 μW cm^{-2}, respectively, from the ES using [C_2mim][FAP] as the electrolyte.

From the electrochemical impedance spectroscopy experiments, the capacitive behaviour of these devices was studied showing an onset frequency value at OCP of 5.7 Hz in the case of the [C_2mim][NTf_2], and 79.1 Hz for the [C_2mim][FAP]. In other words, the ES using [C_2mim][FAP] as the electrolyte showed capacitive behaviour for a wider range of frequencies than in the case of the other ES using [C_2mim][NTf_2] as the electrolyte.

The PPy-cellfib-IL plasticiser composite film was studied before and after using it as both electrodes in the ES for 15000 cycles. Using infrared-ATR, TGA and SEM/EDX.

This allowed to differentiate between the positive and negative electrodes, due to the changes induced by variations on the polypyrrole volume during the charge-discharge process.

Chapter 6

Flexible Hybrid Supercapacitors (HS)

Chapters 4 and 5 introduced two types of supercapacitors, an electrical double-layer and an electrochemical supercapacitor, respectively. In the case of the EDLS, the graphite-cellfib-IL plasticiser composite was used as both electrodes in the device where the active material was the graphite and in the case of the ES, the PPy-cellfib-IL plasticiser composite film was utilised as both electrodes where the active material was the polypyrrole. Both supercapacitors showed good electrochemical characteristics, therefore, the aim of this chapter is to combine both active materials (graphite and polypyrrole) in one electrode using a PPy-cellfib-IL plasticiser-graphite composite film and its application as both electrodes in a flexible and symmetric supercapacitor.

This new supercapacitor was called symmetric hybrid supercapacitor (HS) because both electrodes contained materials with a different mechanism for storing charge; graphite with an electrical double-layer mechanism and polypyrrole with an electrochemical electron transfer mechanism.

Chapter 6 will show the electrochemical study of the HS as well as, how the combination of both compounds in the same electrode affects the electrochemical characteristics of the supercapacitors. An improvement in the supercapacitors characteristics is expected due to the increase of electronic conductivity of the film with the addition of the graphite in comparison to the ES.

6.1. Experimental Part

In this section, the experimental part related to the fabrication of a set of hybrid supercapacitors and their electrochemical characterisation is described.

6.1.1. Fabrication of the Flexible HS

The preparation of the conducting polymer-biopolymer-ionic liquid-graphite (PPy-cellfib-IL plasticiser-graphite film) composite electrode used in the HS was carried out using the procedure reported in section 3.8.1. All composite films used as electrodes were dried prior to assembly in a vacuum desiccator for 48 h.

The assembly of the hybrid supercapacitors was carried out as reported in section 4.1.2 and Figure 4.2.

6.1.2. Electrochemical Study of the HS Fabricated

The electrochemical performance of the electrochemical supercapacitor was studied as in section 4.1.3 and Figure 4.3. Similarly to that discussed in Chapters 4 and 5 (*re*., EDLS and ES devices, respectively) a set of three HS using [C_2mim][NTf_2] as the electrolyte and one HS using [C_2mim][FAP] as the electrolyte were characterised.

6.2. Results and Discussion

6.2.1. Electrochemical Study of the HS Fabricated Using [C_2mim][NTf_2] as the Electrolyte

The electrochemical study of a set of three hybrid supercapacitors using [C_2mim][NTf_2] as the electrolyte was carried out to established their energy storage and power release capabilities. All the electrochemical measurements were performed in a two-electrode configuration at 25 ± 2 ^{0}C to mimic practical applications.

An HS, described in this thesis, is an energy storage device with electrochemical and electrical double-layer charge storage and release mechanisms. The active materials were considered the polypyrrole and graphite from PPy-cellfib-IL plasticiser-graphite composite film, compromising a 50.0 wt % of the total weight at each electrode; the total mass of the active material was 11.0 ± 1.0 mg. The area of the electrodes was 1 cm^2 and the thickness of the electrodes 210 ± 60 µm.

For the set of HS using [C_2mim][NTf_2] as the electrolyte, the OCP found was 0.013 ± 0.009 V.

6.2.1.1. Cyclic Voltammetry

In this section, the cyclic voltammetry study of the hybrid supercapacitor was carried out. The first characteristic investigated was the operational voltage of the device that resulted to be from -1.1 V to 1.1 V (2.2 V) being the widest operational voltage among the three supercapacitors using [C_2mim][NTf_2] as the electrolyte presented in this thesis. This demonstrates the good stability of the electrodes that combine polypyrrole and graphite in the PPy-cellfib-IL plasticiser-graphite composite film. Besides, the operational voltage of these devices using [C_2mim][NTf_2] as the electrolyte vary between 1.6 and 2.2 V, comparable to IL-based supercapacitors from the literature [310a,350,77].

Figure 6.1 shows the cyclic voltammogram obtained for one of the HS fabricated where a symmetrical and almost rectangular cycle was obtained showing the existence of capacitance for this device.

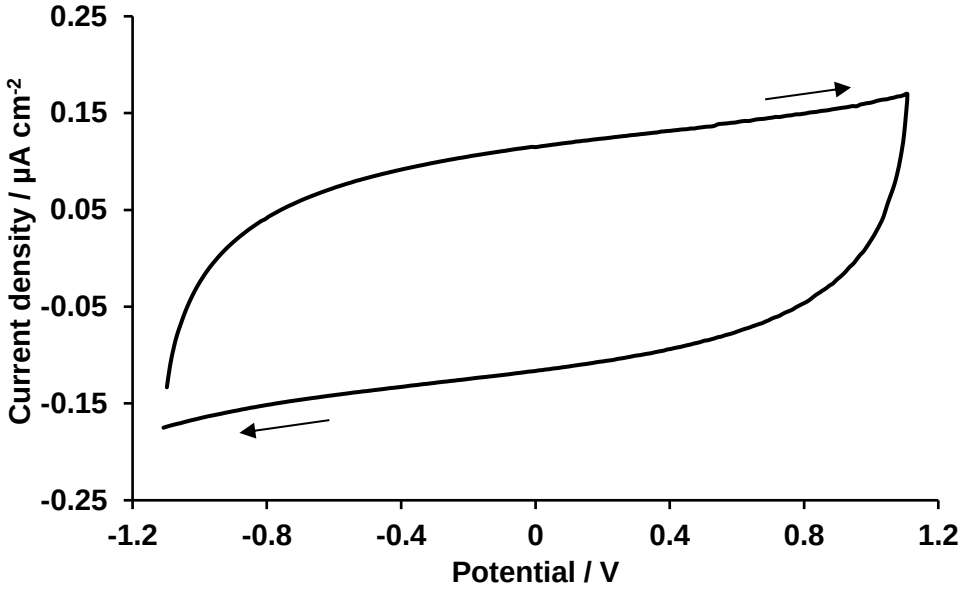

Figure 6.1 Cyclic voltammogram of one of the HS using $[C_2mim][NTf_2]$ as the electrolyte at 50 mV s^{-1} and at 25 ± 2 ^{0}C. Arrows show the potential direction of the cyclic voltammogram

As in the other chapters, the reproducibility of the device was analysed as it is shown in Figure 6.2 by fabricating three identical HS devices and testing them using CV. From the voltammograms obtained it can be seen clearly that two of them showed a similar cycle area whilst, one of them showed a much bigger cycle area. This difference affected the capacitance values obtained and resulted in a bigger variance than in the case of the previous supercapacitors described in section 4.2.2.1 and 5.2.2.1. The capacitance values obtained for these HS were 2.6 ± 1.3 mF g^{-1} and 27.1 ± 11.9 µF cm^{-2} for the specific and areal capacitance, respectively. If the specific capacitance values are compared to the EDLS and ES, the following trend can be seen EDLS > ES > HS in contrast, if the areal capacitance is compared, the trend changed as EDLS > HS > ES. The reason for this discrepancy between specific and areal capacitance was related to the weight % of the active material that was different for each supercapacitor. Therefore, it is more reliable to use the areal capacitance for the comparison among supercapacitors.

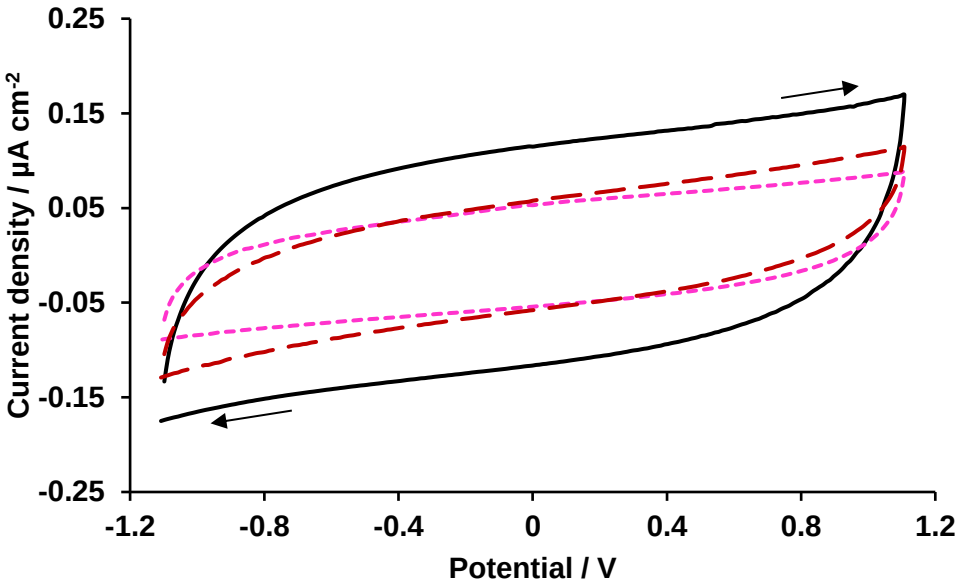

Figure 6.2 Cyclic voltammograms of the three HS fabricated using $[C_2mim][NTf_2]$ as the electrolyte at 50 mV s^{-1} and at 25 ± 2 ^{0}C. Arrows show the potential direction of the cyclic voltammogram

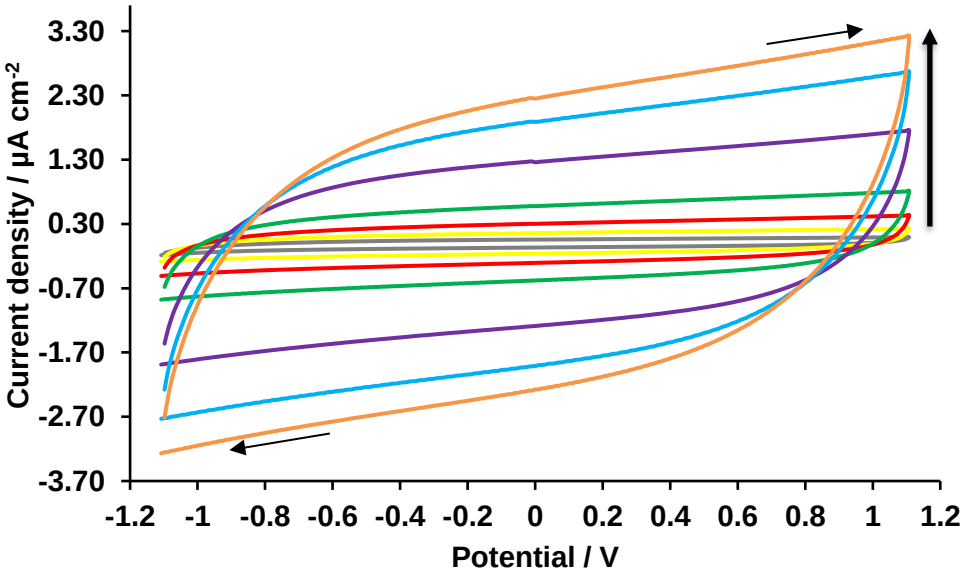

Figure 6.3 Cyclic voltammogram of the one HS using $[C_2mim][NTf_2]$ as the electrolyte at various scan rates: 1000 (orange), 800 (light blue), 500 (purple), 200 (green), 100 (red), 50 (yellow), 20 (grey) mV s^{-1} and at 25 ± 2 ^{0}C. Arrows show the potential direction of the cyclic voltammogram and the vertical arrow shows the faster scan rates applied

The rate capability for this supercapacitor was studied using cyclic voltammetry, as shown in Figure 6.3. The graph shows how the cyclic voltammogram changed when different scan rates were applied. As it was expected the voltammogram was wider by current density when higher scan rates were applied. Consequently, the capacitance decreases at higher scan rates following Equation 4.8. The most relevant fact is that

the nearly rectangular shape and symmetric voltammograms were retained even at the high scan rate of 1 V s^{-1}.

The capacitance values for each scan rate applied were calculated and they are shown in Table 6.1. The capacitance values decreased from 73.3 ± 31.4 µF cm^{-2} at 20 mV s^{-1} to 0.8 ± 0.3 µF cm^{-2} at 1 V s^{-1}, as seen with the other supercapacitors studied (see Table 4.6 and Table 5.1). The capacitance values were reduced more drastically at slow scan rates than at high scan rates, where the values decreased smoothly.

Table 6.1 Specific and areal capacitance average values of the HS using [C_2mim][NTf_2] as the electrolyte calculated from the CV at various scan rates

Scan rate / mV s^{-1}	$C_{Spec.}$ / mF g^{-1}	C_{Areal} / µF cm^{-2}
20	7.0 ± 3.5	73.3 ± 31.4
50	2.7 ± 1.2	28.3± 10.9
100	1.1 ± 0.7	11.3 ± 6.3
200	0.5 ± 0.3	5.1 ± 2.6
500	0.17 ± 0.08	1.8 ± 0.7
800	0.10 ± 0.05	1.0 ± 0.4
1000	0.08 ± 0.03	0.8 ± 0.3

The bending study of the three HS was carried out, and the results are presented in Figure 6.4. The three different voltammograms obtained for each device are displayed showing an excellent electrochemical stability during the bending state. Figure 6.4 (a) shows the bending study of one of the HS which was the device with highest bending stability, since very similar voltammograms were obtained before, during and after bending the device. In the case of the other two, Figure 6.4 (b) and (c), during the bending state (red plot) a different voltammogram was obtained but after the bending study, the voltammogram recovered the same cycle than before the bending state. Therefore, it was demonstrated that the three HS fabricated retained the electrochemical properties under bending.

This superior stability may be attributed to the homogeneity in the composite material and to the chemical stabilisation that was achieved by hydrogen bond and electrostatic forces in the composite among all the components.

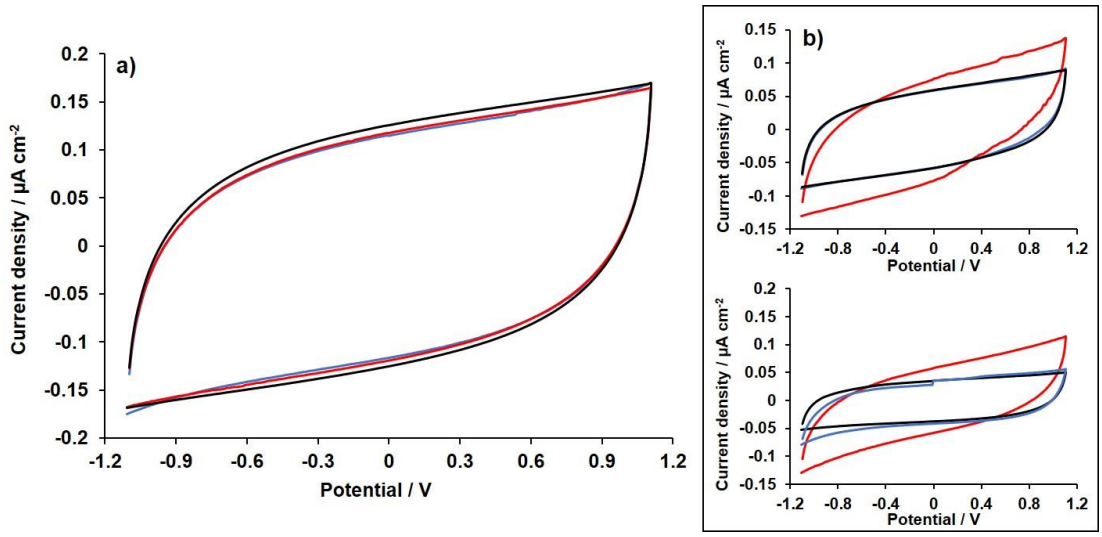

Figure 6.4 Bending study at 120 degrees of a) one of the HS and b) the other two HS using $[C_2mim][NTf_2]$ as the electrolyte at the scan rate of 50 mV $s^{-1}$and at 25 ± 2 ^{0}C. Cyclic voltammogram before (blue), during (red) and after (black) bending

Table 6.2 shows the capacitance values during the bending study. As it was demonstrated by the cyclic voltammograms, the capacitance values reflected also an excellent bending stability, with very similar capacitance values obtained before and after the application of the bending state.

Table 6.2 Specific and areal capacitance average values of the HS using $[C_2mim][NTf_2]$ as the electrolyte during the bending study

Bending state	$C_{Spec.}$ / mF g^{-1}	C_{Areal} / µF cm^{-2}
Prior to bending	2.4 ± 1.5	25.4 ± 13.5
120 degrees angle	2.7 ± 1.2	28.7 ± 10.9
After bending	2.4 ± 1.5	24.7 ± 14.3

The cycle life stability of one of the hybrid supercapacitors was studied using CV for 15000 cycles as it is shown in Figure 6.5 (a); the voltammograms obtained showed an excellent cycle life stability with a little increase in the cycles current that was reflected in the capacitance retention (Figure 6.5 (b)) where an increment of a 30 % in the capacitance was found after 15000 cycles.

The almost 100 % of capacitance retention obtained during 15000 cycles for this HS device demonstrated that the combination of cellulose chemically bound to PPy and the addition of graphite to form the composite electrodes improved considerably the durability of the HS. For example, the mixture of reduced graphene oxide, polypyrrole and cellulose *via* a soak-polymerisation method to obtain supercapacitor

electrodes was published in 2017 by Wan *et al*. [351] showing a maximum capacitance retention of 89.5 % during 5000 cycles.

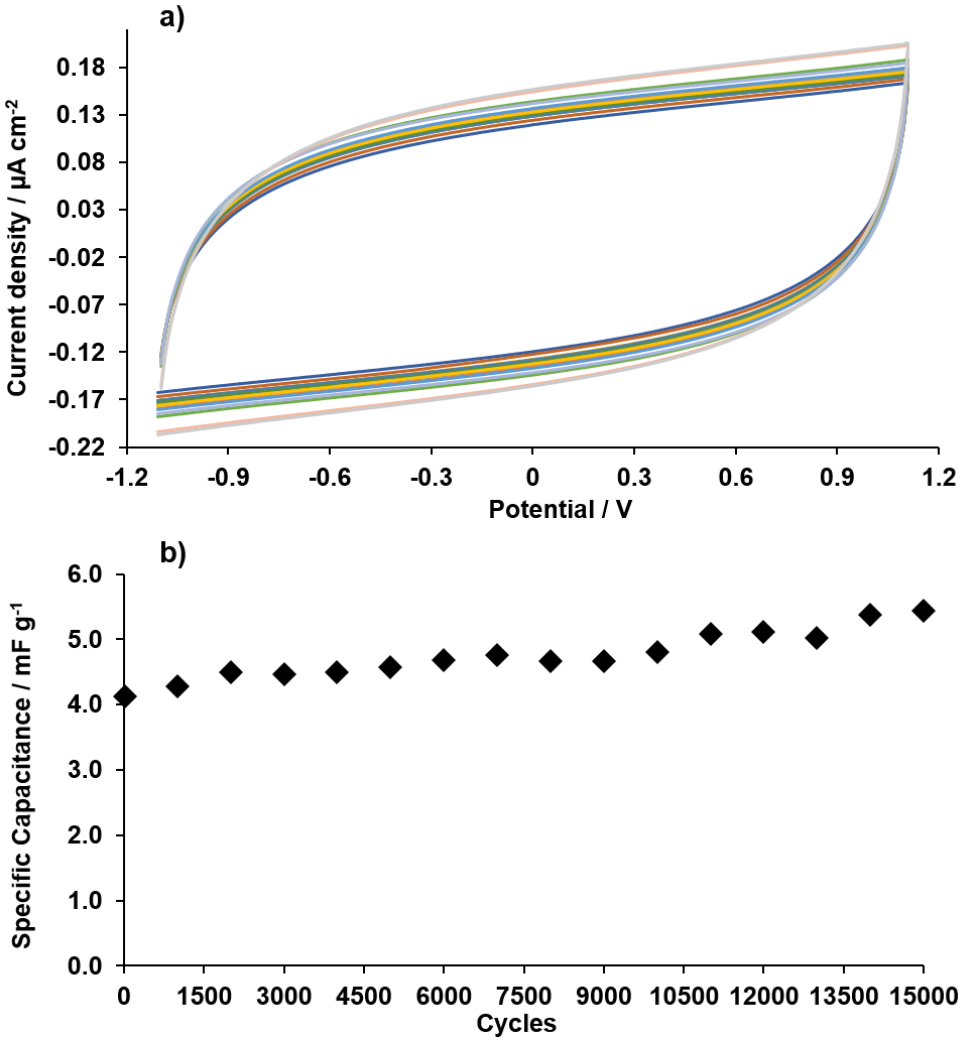

Figure 6.5 a) Cyclic voltammograms of one of the HS fabricated using $[C_2mim][NTf_2]$ as the electrolyte at every 1000th scan from scan 2 to 15000 cycles at the scan rate of 50 mV s^{-1} and at 25 ± 2 ^{0}C, b) specific capacitance during 15000 cycles

The raise in the capacitance during the cycle life can be also seen in Table 6.3, where the capacitance value of the 2nd and 15000 cycles is shown. As the other devices described, the increase in capacitance can be related to the thermocapacitance (see section 4.2.2). The average specific capacitance during the cycle life was 4.8 ± 0.4 mF g^{-1} and for the areal capacitance, the average value was 47.2 ± 3.7 µF cm^{-2}.

Table 6.3 Specific and areal capacitance of one of the HS using $[C_2mim][NTf_2]$ as the electrolyte at the second cycle and at the 15000 cycle

Cycle 2		Cycle 15000	
C_{Spec} / mF g^{-1}	C_{Areal} / µF cm^{-2}	C_{Spec} / mF g^{-1}	C_{Areal} / µF cm^{-2}
4.1	41.0	5.4	54.0

6.2.1.2. Galvanostatic Charge-discharge

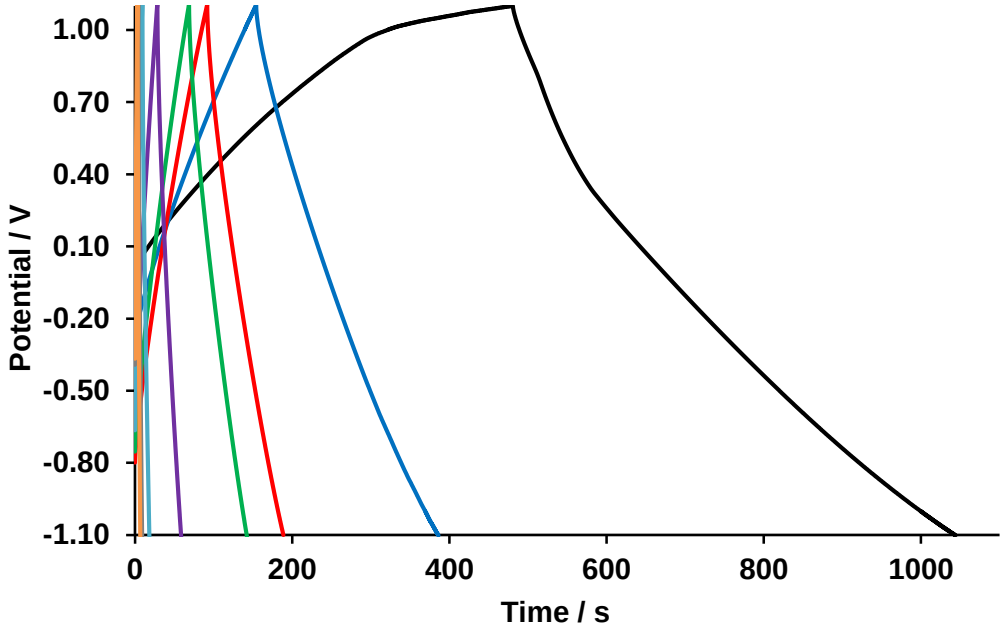

Figure 6.6 GCD curves of one of the HS fabricated using $[C_2mim][NTf_2]$ as the electrolyte at different currents densities applied, 0.02 (black), 0.05 (blue), 0.08 (red), 0.1 (green), 0.2 (purple), 0.5 (light blue), 0.8 (grey) and 1 µA cm^{-2} (orange) at 25 ± 2 ^{0}C

Galvanostatic charge-discharge experiments revealed the rate capability of the device applying different current densities. As with the previous supercapacitors reported, the devices were subjected to current densities from 0.02 to 1 µA cm^{-2} to study their charge-discharge capability and their equivalent series resistance within the operational voltage obtained (2.2 V) from cyclic voltammetry. Hybrid supercapacitor charge-discharge curves are shown in Figure 6.6. At the lowest current density (0.02 µA cm^{-2}) a little plateau at the positive limit is observed, that can correspond to a quasi-reversible redox reaction from the polypyrrole as mentioned in section 5.2.1.2 for the electrochemical supercapacitor [11]. In contrast, from current densities of 0.05 µA cm^{-2}, nearly symmetric triangular curves were obtained, which were closer to the ideal triangle shape than in the case of the EDLS and ES, discussed in sections 4.2.2.1 and 5.2.2.1, respectively.

Therefore, the HS showed better performance than the EDLS and ES devices using current densities higher than 0.05 μA cm^{-2}, further confirming the reinforcement of electrical properties of graphite and the redox properties of PPy.

In terms of total charge-discharge time, the HS needed around 400 s at 0.05 μA cm^{-2} which is comparable to graphene-reinforced polyaniline-based supercapacitors [352].

As it was discussed above a set of three hybrid supercapacitors was fabricated and analysed. The reproducibility was tested by GCD, comparing the charge-discharge curves at 0.05 μA cm^{-2} as shown in Figure 6.7. The three curves looked similar requiring a total charge-discharge time of 347 ± 36, indicating a good reproducibility.

The ESR for the HS, calculated using Equation 4.11, was 323 ± 35 kΩ. A comparison of the ESR among the three types of supercapacitors fabricated shows the following trend from the smallest to the biggest ESR value: EDLS < HS < ES. Therefore, the combination of polypyrrole and graphite decreased the ESR in comparison to the ES.

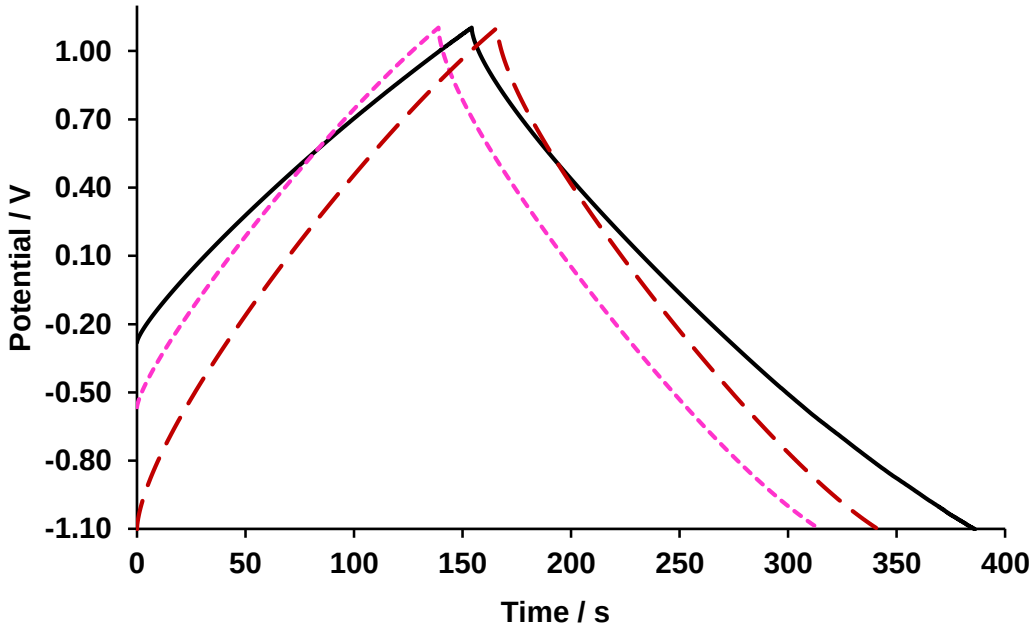

Figure 6.7 GCD curves of the three HS devices fabricated using $[C_2mim][NTf_2]$ as the electrolyte at the current density 0.05 μA cm^{-2} and at 25 ± 2 ^{o}C

From the GCD measurements and using Equation 4.16 and Equation 4.17, the energy and power features of the hybrid supercapacitors were studied. The values obtained are presented in Table 6.4. The maximum energy density obtained (at the current density of 0.05 μA cm^{-2}) was 0.003 ± 0.001 μW h cm^{-2} that corresponded to a

specific energy of 0.30 ± 0.07 mW h kg^{-1}. The energy density for the HS was the highest among the three types of supercapacitors, following the trend: HS > EDLS > ES. In the case of the power density, the maximum value obtained was 1.05 ± 0.21 μW cm^{-2}, and for the specific power, the value was 99.7 ± 28.5 mW kg^{-1}. The comparison of the power density was carried out among the supercapacitors, showing the following trend: EDLS > HS > ES. Therefore, it was possible to improve the energy storage in HS in comparison to the other two supercapacitors, whilst the power density was not reduced. The power density decreased from EDLS to ES, from 1.16 ± 0.12 μW cm^{-2} to 0.76 ± 0.03 μW cm^{-2}.

Table 6.4 Energy and power average values calculated for the HS using $[C_2mim][NTf_2]$ as the electrolyte at different current densities applied and the discharge time obtained using GCD

Current density / μA cm^{-2}	Discharge time / s	E_{Spec} / mW h kg^{-1}	$E_{Density}$ / μW h cm^{-2}	P_{Spec} / mW kg^{-1}	$P_{Density}$ / μW cm^{-2}
0.02	438 ± 129	0.28 ± 0.10	0.003 ± 0.001	2.3 ± 0.1	0.025 ± 0.001
0.05	194 ± 32	0.30 ± 0.07	0.003 ± 0.001	5.4 ± 0.5	0.0583 ± 0.0002
0.08	68 ± 25	0.17 ± 0.08	0.002 ± 0.001	8.8 ± 0.9	0.094 ± 0.002
0.1	53 ± 18	0.17 ± 0.07	0.002 ± 0.001	11.0 ± 1.1	0.117 ± 0.003
0.2	27 ± 6	0.11 ± 0.09	0.0012 ± 0.0009	13.9 ± 9.6	0.15 ± 0.09
0.5	8 ± 1	0.11 ± 0.04	0.0012 ± 0.0003	48.9 ± 16.3	0.52 ± 0.13
0.8	5 ± 0	0.10 ± 0.03	0.0011 ± 0.0002	80.0 ± 24.1	0.84 ± 0.18
1	4 ± 1	0.10 ± 0.03	0.0011 ± 0.0003	99.7 ± 28.5	1.05 ± 0.21

6.2.1.3. Electrochemical Impedance Spectroscopy

From the Nyquist plot showed in Figure 6.8 the ion diffusion and charge transfer properties of the HS fabricated were studied. The graph shows the results obtained during the cycle life of the device during 15000 cycles. At low frequencies, an almost straight line was obtained at the OCP of the device, as well as, after 5000 and 15000 cycles, showing the excellent stability of the device. The inset of Figure 6.8 displays the high frequencies part, showing that the plots, after the knee frequency, had an angle of more than 45 degrees demonstrating that this device showed capacitance. The stability of this device was already established from the ESR obtained during the cycle life which hardly changed, from 5.21 kΩ to 5.98 kΩ. In the case of the knee

frequency, the value did not change during the cycle life showing a constant value of 15.3 kHz.

The comparison of the three types of supercapacitors shows that the ESR increase following the trend EDLS < HS < ES, which agrees with the GCD results showed in section 6.2.1.2. The knee frequency obtained at the OCP of each type of supercapacitor was the same for the EDLS and ES with a value of 22.2 kHz whilst, the HS showed a value of 15.3 kHz. Albeit the value of the knee frequency for the HS at the OCP was smaller than the other supercapacitors, this value did not change during the cycle life.

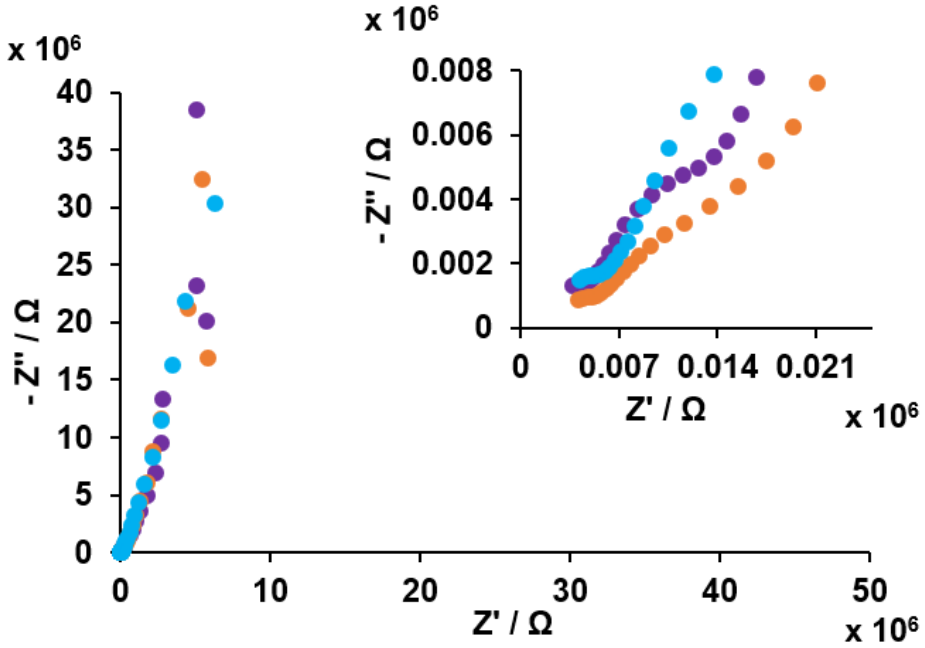

Figure 6.8 Nyquist plot of the HS using [C_2mim][NTf_2] as the electrolyte during the cycle life (25 ± 2 ^{0}C): at OCP (purple), after 5000 cycles (orange) and after 15000 cycles (light blue). The inset shows the high-frequency part of the Nyquist plot

Figure 6.9 shows the Bode plot where the onset frequency at -45º was obtained *e.g.* at OCP this frequency value was 8.3 Hz and after 15000 cycles the frequency decreased to 2.7 Hz, showing a dropping in the range of frequencies at which the HS showed primarily capacitive behaviour. The values obtained were comparable to the electrochemical supercapacitor (section 5.2.1.3).

The maximum phase of impedance reached for this supercapacitor was -82º showing a very close to ideal capacitive behaviour up to frequencies of 0.1 Hz.

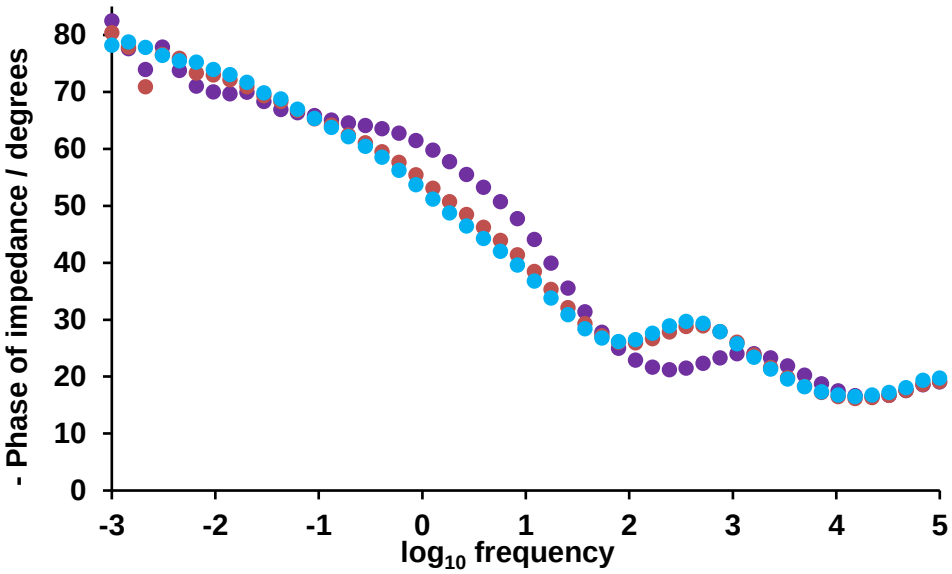

Figure 6.9 Bode plot of the HS using [C_2mim][NTf_2] as the electrolyte during the cycle life(25 ± 2 ^{0}C): at OCP (purple), after 5000 cycles (orange) and after 15000 cycles (light blue)

6.2.2. Electrochemical Study of the HS Fabricated Using [C_2mim][FAP] as the Electrolyte

A hybrid supercapacitor using [C_2mim][FAP] as the electrolyte was studied to analyse how the electrolyte affects the supercapacitor characteristics.

The active materials in this HS were considered the graphite and the polypyrrole from the PPy-cellfib-IL plasticiser-graphite composite film, compromising a 50.0 wt % of the total weight at each electrode; the total mass of the active material was 10.8 mg; the area the electrodes 1 cm^2 and the thickness of the electrodes 210 ± 60 µm.

For the HS using [C_2mim][FAP] as the electrolyte the OCP found was 0.04 V.

6.2.2.1. Cyclic Voltammetry

In the case of the operational voltage of the hybrid supercapacitor using [C_2mim][FAP] as the electrolyte, the value found was 3.2 V. This operational voltage was the widest EW found in this thesis which demonstrates the good combination of the electrode PPy-cellfib-IL plasticiser-graphite composite film and the electrolyte [C_2mim][FAP]. The voltammogram obtained for this device was rectangular and symmetrical demonstrating an ideal capacitive behaviour, as shown in Figure 6.10. The capacitance values calculated with Equation 4.10 at 50 mV s^{-1} and at 25 ± 2 ^{0}C were 2.52 mF g^{-1} and 27.1 µF cm^{-2} for the specific capacitance and the areal capacitance, respectively.

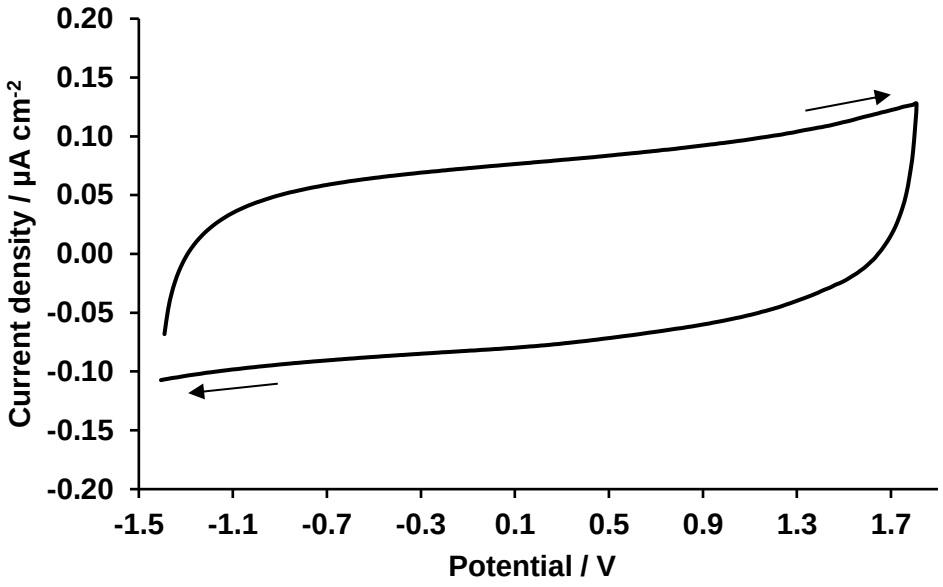

Figure 6.10 Cyclic voltammogram of the HS using [C_2mim][FAP] as the electrolyte at 50 mV s^{-1} and at 25 ± 2 ^{0}C. Arrows show the potential direction of the cyclic voltammogram

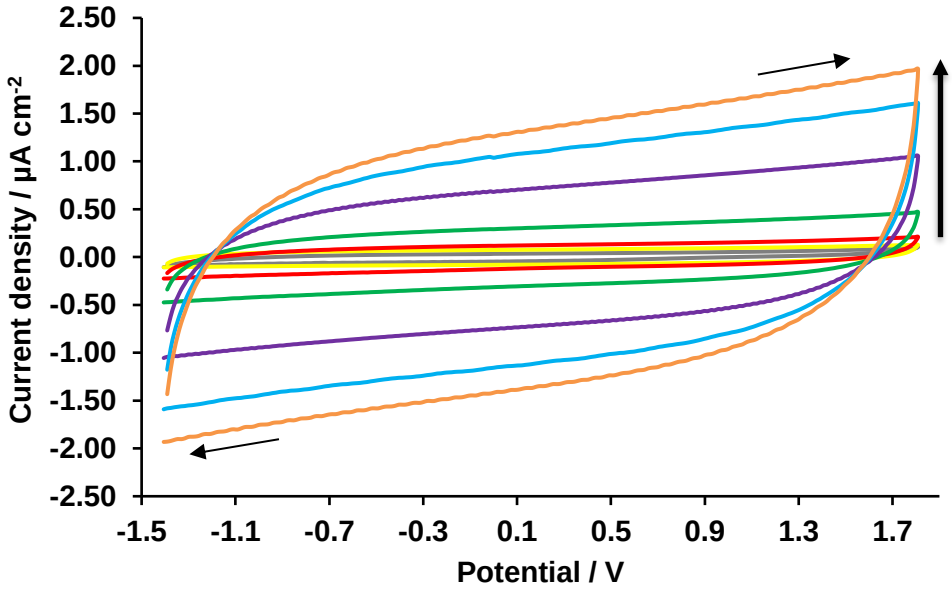

Figure 6.11 Cyclic voltammogram of the HS using [C_2mim][FAP] as the electrolyte at various scan rates: 1000 (orange), 800 (light blue), 500 (purple), 200 (green), 100 (red), 50 (yellow), 20 (grey) mV s^{-1} and at 25 ± 2 ^{0}C. Arrows show the potential direction of the cyclic voltammogram and the vertical arrow shows the faster scan rates applied

The study of the cyclic voltammograms obtained at different scan rates was carried out as shown in Figure 6.11. The symmetrical and rectangular shape was maintained even at the fastest scan rates showing a good rate capability for the HS device using [C_2mim][FAP] as the electrolyte.

Table 6.5 shows the capacitance values obtained at different scan rates with a maximum specific capacitance value of 7.08 mF g^{-1} (76.1 µF cm^{-2}) at the lowest scan

rate. The capacitance calculated showed very similar values for the EDLS using [C_2mim][FAP] as the electrolyte (section 4.2.3.1). In comparison to the ES using [C_2mim][FAP] as the electrolyte (section 5.2.2.1), the capacitance values were higher demonstrating the improvement of combining graphite and polypyrrole in the electrode.

Table 6.5 Specific and areal capacitance values of the HS using [C_2mim][FAP] as the electrolyte calculated from the CV at various scan rates

Scan rate / mV s^{-1}	$C_{Spec.}$ / mF g^{-1}	C_{Areal} / µF cm^{-2}
20	7.08	76.1
50	2.52	27.1
100	1.28	13.8
200	0.64	6.9
500	0.24	2.6
800	0.14	1.5
1000	0.11	1.2

The bending study of this device was carried using cyclic voltammetry (Figure 6.12) prior to, during and after bending the device. The angle chosen was 120 degrees and, as it can be seen when the electrochemical characterisation was carried out in the bending state, the voltammogram increased in current density showing a resistor behaviour. After the bending state, the voltammogram did not recover the previous shape. However, the bending study of this device showed better stability than the ES using [C_2mim][FAP] as the electrolyte (section 5.2.2.1, Figure 5.12).

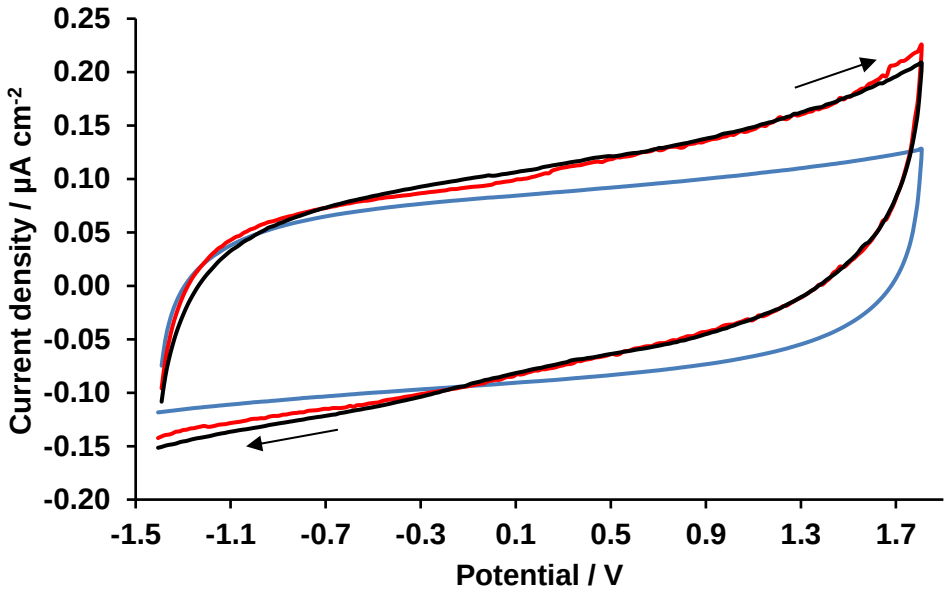

Figure 6.12 Bending study at 120 degrees of the HS using [C_2mim][FAP] as the electrolyte at the scan rate of 50 mV s^{-1} and at 25 ± 2 ^{0}C. Cyclic voltammogram before (blue), during (red) and after (black) bending

The capacitance during the bending study is shown in Table 6.6. The values obtained showed that the capacitance decreased during and after the bending study as it was seen for the ES using [C_2mim][FAP] as the electrolyte (Table 5.6).

Table 6.6 Specific and areal capacitance values of the HS using [C_2mim][FAP] as the electrolyte during the bending study

Bending state	$C_{Spec.}$ / mF g^{-1}	C_{Areal} / µF cm^{-2}
Prior to bending	3.0	31.99
120 degrees angle	2.8	30.61
After bending	2.5	27.08

The cycle life stability of this supercapacitor is shown in Figure 6.13; an excellent stability was achieved for this device. Figure 6.13 (a) shows the voltammograms obtained during 15000 cycles and as it can be seen the cycle just suffered a little change in the positive limit, however, as it is displayed in Figure 6.13 (b) the capacitance retention nearly did not change during these 15000 cycles.

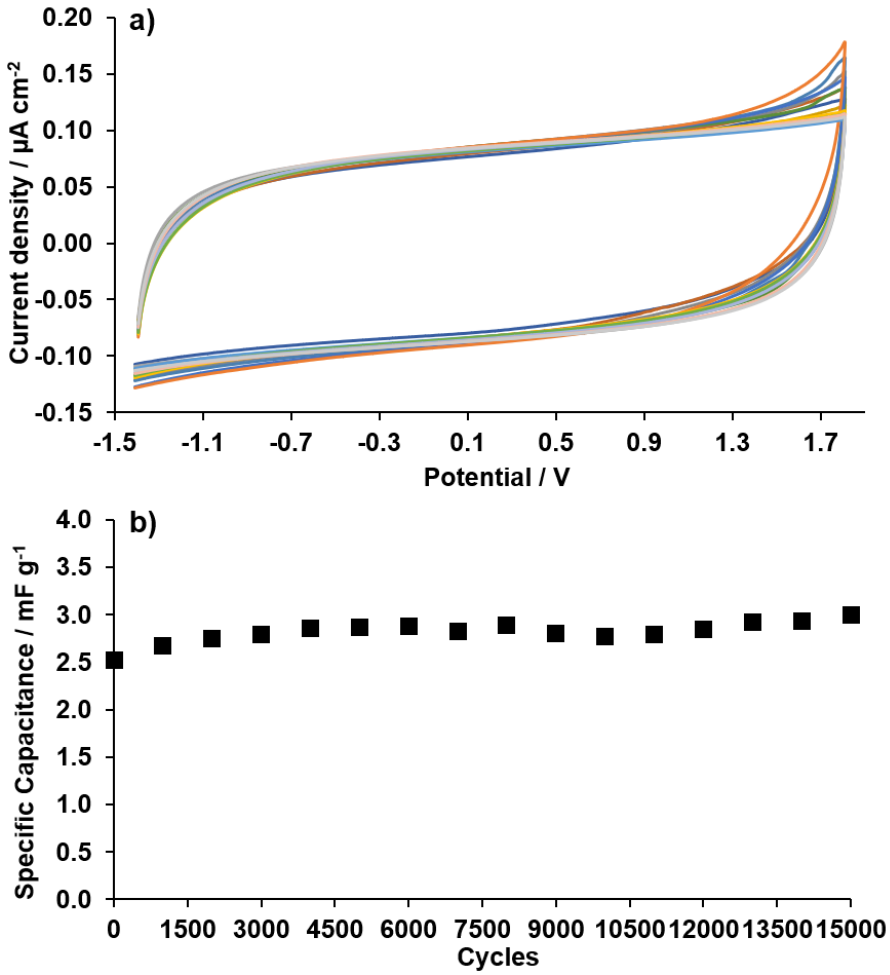

Figure 6.13 (a) Cyclic voltammograms of the HS fabricated using [C_2mim][FAP] as the electrolyte at every 1000th scan from scan 2 to 15000 cycles at the scan rate of 50 mV s^{-1} and at 25 ± 2 ^{0}C, (b) capacitance retention during 15000 cycles

The average capacitance value during the 15000 cycles was 2.8 ± 0.1 mF g^{-1} for the specific capacitance and 30.3 ± 0.9 µF cm^{-2} for areal capacitance, showing only a small variance during the cycle life. The values of the 2nd and 15000th cycles are shown in Table 6.7.

Table 6.7 Specific and areal capacitance of the HS using [C_2mim][FAP] as the electrolyte at the second cycle and 15000 cycles

Cycle 2		Cycle 15000	
C_{Spec} / mF g^{-1}	C_{Areal} / µF cm^{-2}	C_{Spec} / mF g^{-1}	C_{Areal} / µF cm^{-2}
2.5	27.1	3.0	32.2

6.2.2.2. Galvanostatic Charge-discharge

The rate capability of the HS using [C_2mim][FAP] as the electrolyte was studied with the GCD technique. The charge-discharge curves obtained at different current densities applied are shown in Figure 6.14. The curves for this device showed a symmetric triangle demonstrating its ideal capacitive behaviour. The ESR value obtained for this supercapacitor had a value of 269 ± 145 kΩ; similar to that of the EDLS using [C_2mim][FAP] as the electrolyte. The trend of the ESR among the three supercapacitors using [C_2mim][FAP] as the electrolyte was as follows, HS ≈ EDLS > ES.

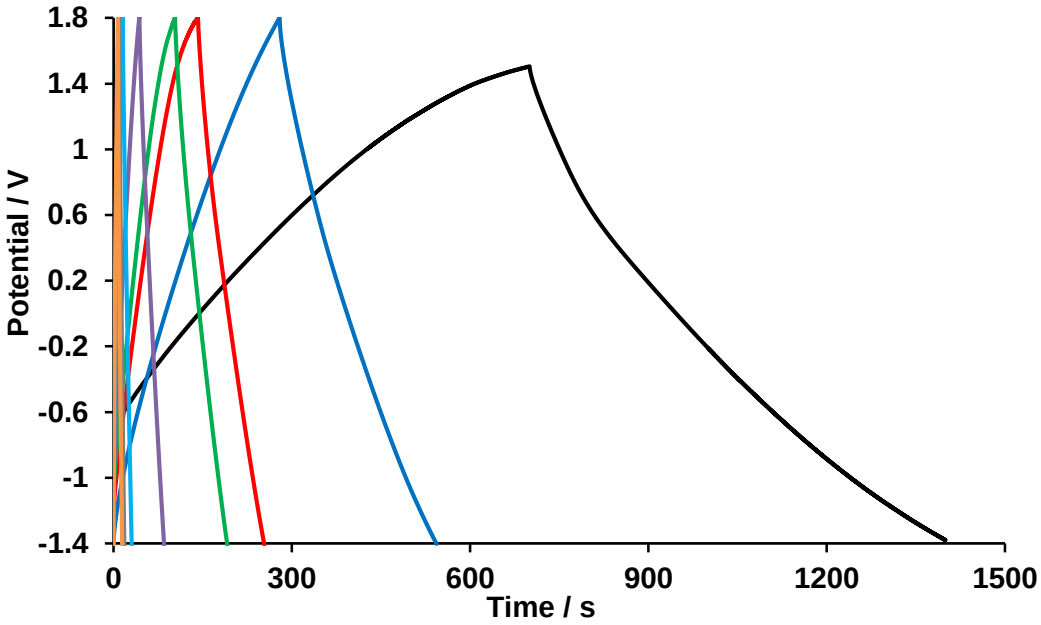

Figure 6.14 GCD curves of the HS fabricated using [C_2mim][FAP] as the electrolyte at different currents densities applied, 0.02 (black), 0.05 (blue), 0.08 (red), 0.1 (green), 0.2 (purple), 0.5 (light blue), 0.8 (grey) and 1 μA cm^{-2} (orange) and at 25 ± 2 ^{o}C

From the charge-discharge curves, this HS needed more than 1000 s to charge and discharge at the lowest current density applied (0.02 μA cm^{-2}), hence it can be said that this supercapacitor was the slowest in comparison to the other two devices using [C_2mim][FAP] as the electrolyte, presented in sections 4.2.3.2 and 5.2.2.2.

The energy and power values at each current density applied are summarised in Table 6.8. The maximum value of specific energy obtained was 0.72 mW h kg^{-1} and for the energy density the value was 0.008 μW h cm^{-2}. These values were very similar to the EDLS and higher than the ES. The maximum specific power value was 165.8 mW kg^{-1} and the power density was found to be 1.78 μW cm^{-2}. The power density for the HS was the highest value among the three devices; however, the value of the specific

power was found to be between those of the EDLS and the ES using [C_2mim][FAP] as the electrolyte, following the trend: EDLS> HS> ES.

Table 6.8 Energy and power values calculated for the HS using [C_2mim][FAP] as the electrolyte at different current densities applied, as well as, the discharge time obtained using GCD

Current density / μA cm^{-2}	Discharge time / s	E_{Spec} / mW h kg^{-1}	$E_{Density}$ / μW h cm^{-2}	P_{Spec} / mW kg^{-1}	$P_{Density}$ / μW cm^{-2}
0.02	710	0.72	0.008	3.6	0.04
0.05	264	0.59	0.006	8.0	0.09
0.08	111	0.39	0.004	12.8	0.14
0.1	88	0.39	0.004	15.9	0.17
0.2	42	0.36	0.004	31.2	0.34
0.5	15	0.33	0.004	77.4	0.83
0.8	9	0.31	0.003	121.6	1.31
1	7	0.33	0.004	165.8	1.78

6.2.2.3. Electrochemical Impedance Spectroscopy

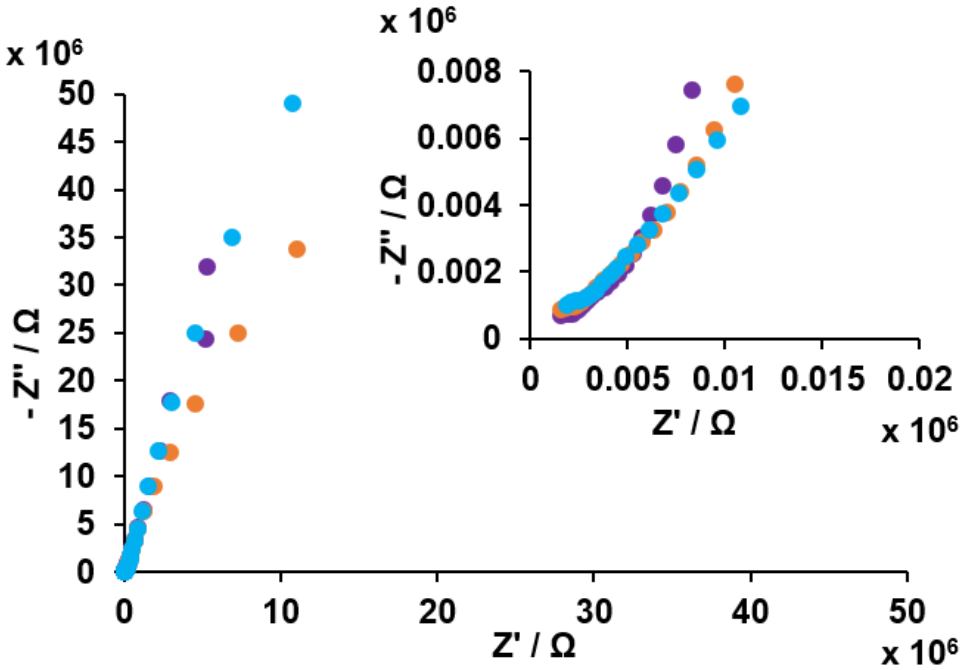

Figure 6.15 Nyquist plot of the HS using [C_2mim][FAP] as the electrolyte during the cycle life (25 ± 2 ^{0}C): at OCP (purple), after 5000 cycles (orange) and after 15000 cycles (light blue). The inset shows the high-frequency part of the Nyquist plot

EIS was used to obtain the Nyquist plot showed in Figure 6.15. The ESR values obtained during the cycle life changed from 2.2 kΩ to 2.8 kΩ at the same "knee

frequency" of 22.2 kHz. The ESR values obtained were very similar to the EDLS and ES devices using [C_2mim][FAP] as the electrolyte. This demonstrates that the devices were well assembled and were reproducible even using different composites as electrodes. In the case of the "knee frequency", the result showed a better access and diffusion of the electrolyte into the electrode than the other two supercapacitors fabricated. The trend obtained for the "knee frequency" at the OCP among the three supercapacitors was the following HS > EDLS ≈ ES.

From the Bode plot, Figure 6.16, the frequency at the phase of the angle of -45º was found to decrease from 37.24 Hz, at the OCP, to 12.08 Hz after 15000 cycles. The comparison of the onset frequencies among the three types of supercapacitors using [C_2mim][FAP] as the electrolyte revealed the following trend: ES > HS > EDLS. Therefore, the ES showed a wider range of frequencies at which the capacitive behaviour was predominant, followed by the HS [160]. This device showed a maximum phase of impedance of -84^0, demonstrating an ideal double-layer capacitance behaviour up to frequencies of 0.41 Hz.

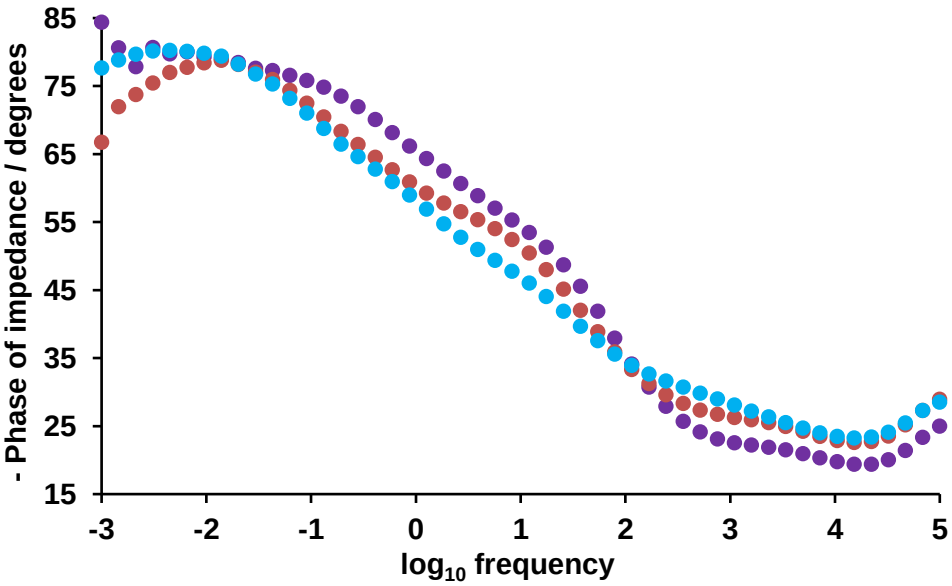

Figure 6.16 Bode plot of the HS using [C_2mim][FAP] as the electrolyte during the cycle life at (25 ± 2 ^{0}C): at OCP (purple), after 5000 cycles (orange) and after 15000 cycles (light blue)

6.2.3. Chemical and Physical Study of the HS Electrodes

Fourier transform infrared (FT-IR) spectroscopy, thermogravimetric analysis (TGA) and scanning electron microscopy (SEM) were employed to study the electrodes (PPy-cellfib-IL plasticiser-graphite film) of the flexible HS using [C_2mim][NTf_2] as the electrolyte before and after using them as electrodes for 15000 cycles.

6.2.3.1. Fourier Transform Infrared (FT-IR)

Figure 6.17 shows the infrared spectra corresponding to the PPy-cellfib-IL plasticiser-graphite fresh film (black plot) and after being using as both electrodes for 15000 cycles in the hybrid supercapacitor (red and green plots). The spectra of this film show the fewest changes in intensity or shape of the peaks, compared to the other devices studied. Therefore, this film used as an electrode appears to be more stable than the other films used in the EDLS and ES. It seems that the polypyrrole-graphite combination was a good choice for storing and releasing charge in a supercapacitor.

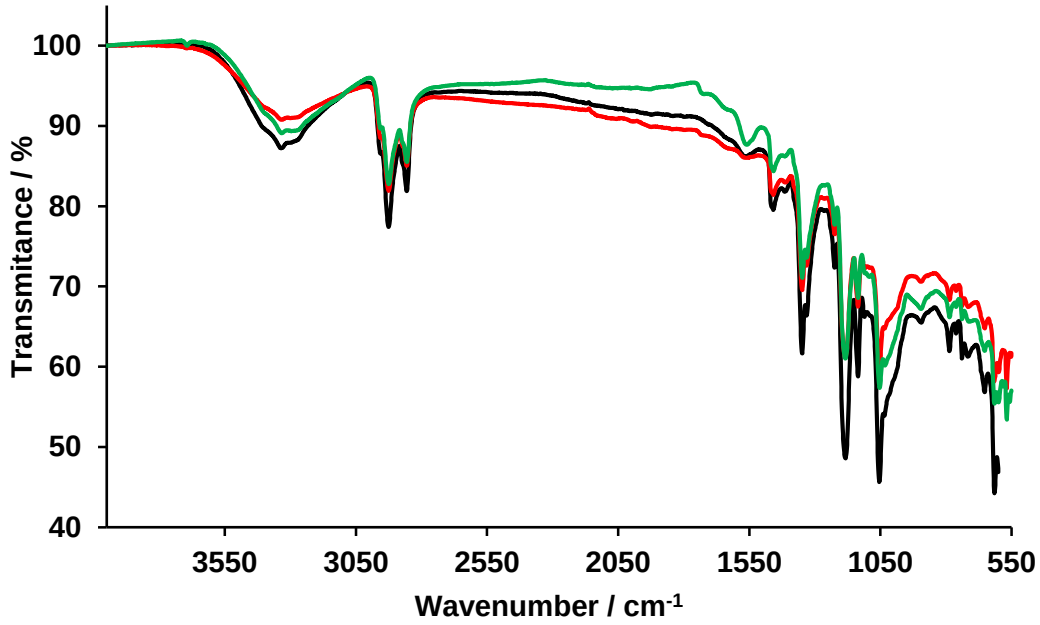

Figure 6.17 Infrared spectra of the PPy-cellfib-IL plasticiser-graphite fresh film (black) and after using it as both electrodes for 15000 cycles in the HS using [C_2mim][NTf_2] as an electrolyte (red and green)

6.2.3.2. Thermogravimetric Analysis (TGA)

Figure 6.18 shows the thermogram graph obtained for the PPy-cellfib-IL plasticiser-graphite as a fresh film (black plot) and after being used as both electrodes (green and red plots) in the hybrid supercapacitor. All the plots looked similar and, therefore, in agreement with the IR results, it was possible to confirm the good stability of the PPy-cellfib-IL plasticiser-graphite film after using it as electrodes for 15000 cycles in the HS using [C_2mim][NTf_2] as the electrolyte.

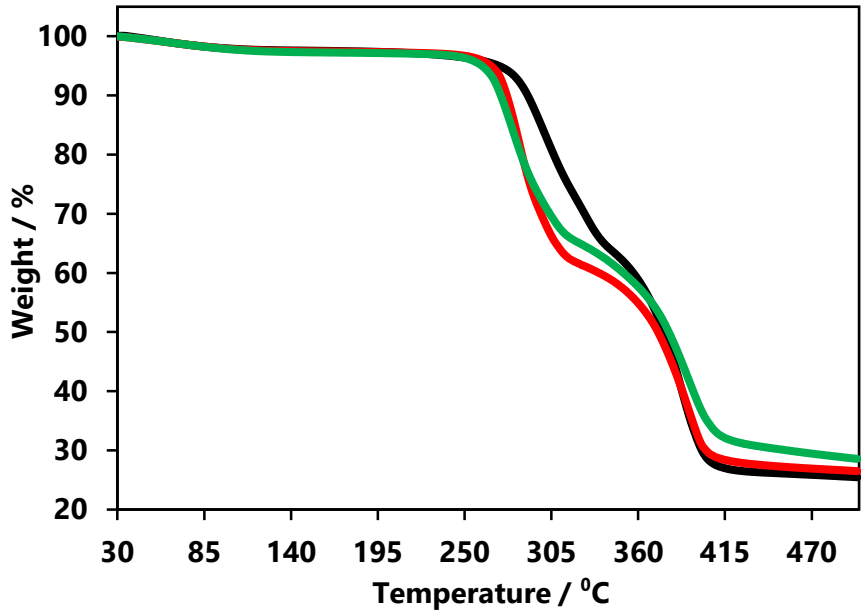

Figure 6.18 Thermogram of the PPy-cellfib-IL plasticiser-graphite fresh film (black plot) and the same film used as both electrodes during 15000 cycles in the HS using $[C_2mim][NTf_2]$ as the electrolyte (green and red plots)

Table 6.9 shows that the water content was almost the same for the three films and in the case of the first decomposition temperature, the value decreased after using the film as electrodes for 15000 cycles. The second decomposition temperature, related to the IL plasticiser, $[P_{6\,6\,6\,14}][NTf_2]$, did not suffer any change.

Table 6.9 Water content and decomposition temperature (T_{onset}) values of the PPy-cellfib-IL plasticiser-graphite film before and after being used as both electrodes for 15000 cycles in the HS HS using $[C_2mim][NTf_2]$ as the electrolyte

Films	Water content / %	1st T_{onset} / ^{0}C	2nd T_{onset} / ^{0}C
Before used (black plot)	2.21	282	369
After used (red plot)	2.36	272	367
After used (green plot)	2.53	265	371

6.2.3.3. Scanning Electron Microscopy (SEM)

Figure 6.19 shows three pictures obtained for the same PPy-cellfib-IL plasticiser-graphite film (a) before and, (b) after being used as the two electrodes (positive and negative) in the hybrid supercapacitor. As it can be seen from (b), the picture on the left was very different in comparison to picture (a). In contrast, the picture on the right was very similar to (a) the fresh film. The picture on the left may, therefore, correspond to the positive electrode, as indicated by the change on the surface, as also suggested

in the case of the ES (section 5.2.3). In the negative electrode (right picture), there was no change on the surface because the graphite is the material that stored the charge electrostatically.

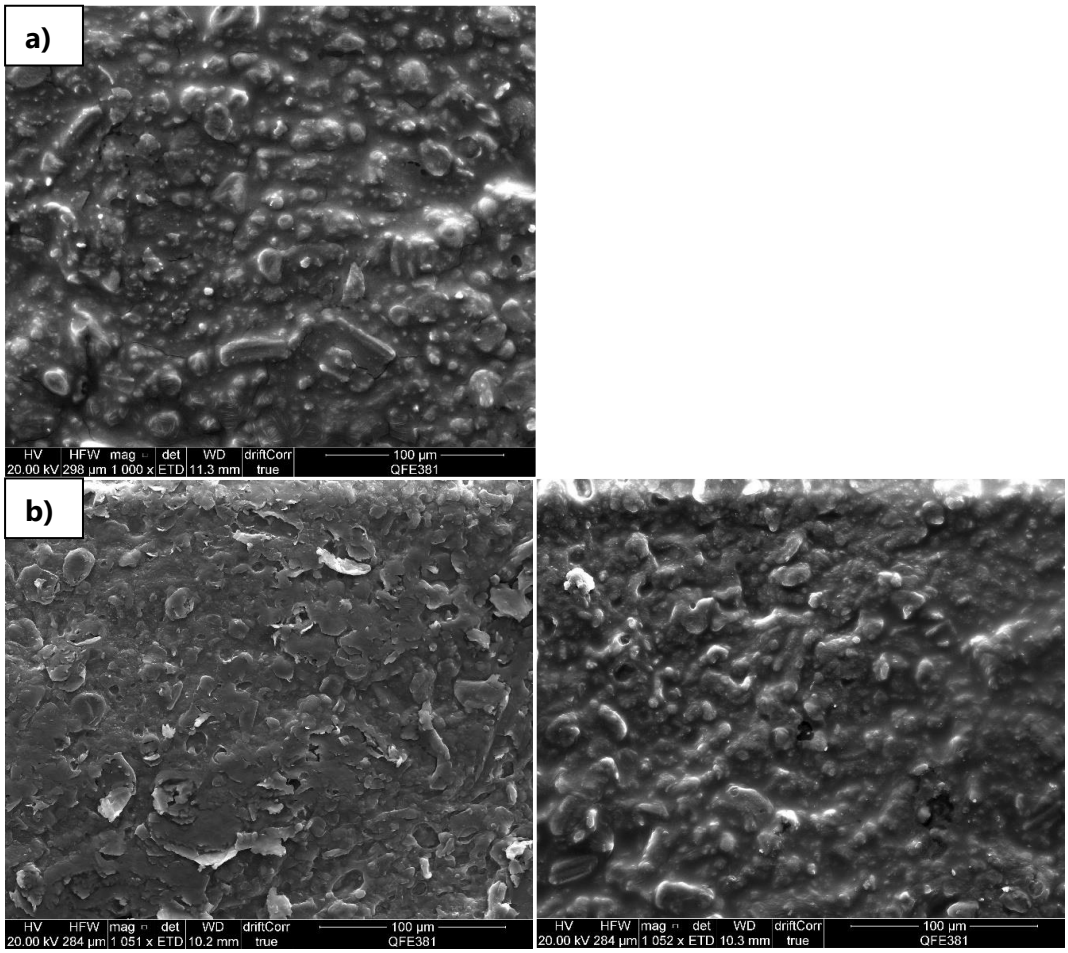

Figure 6.19 SEM pictures with a magnification of 1K of the (a) PPy-cellfib-IL plasticiser-graphite fresh film and (b) the same film after using it as both electrodes for 15000 cycles in the HS using [C_2mim][NTf_2] as the electrolyte

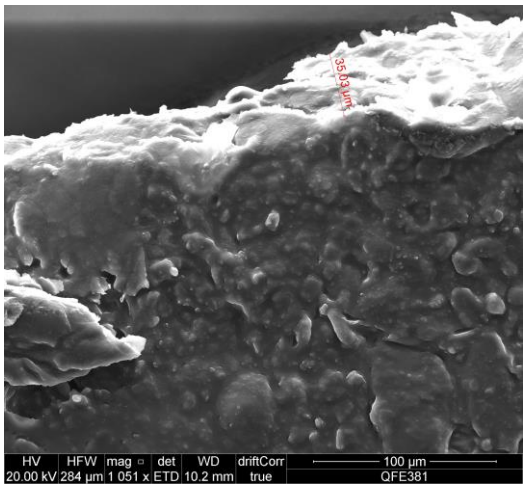

Figure 6.20 Cross-section SEM picture of one of the electrodes of the HS using [C_2mim][NTf_2] as the electrolyte showing the thickness of this film after 15000 cycles

Figure 6.20 shows the cross-section of one of the composites used as an electrode for 15000 in the HS using $[C_2mim][NTf_2]$ as the electrolyte. The thickness of this film was 35.9 µm. As well as with the other two films already studied (section 4.2.4 and 5.2.3), a layered part inside the electrode can be seen from the cross-section.

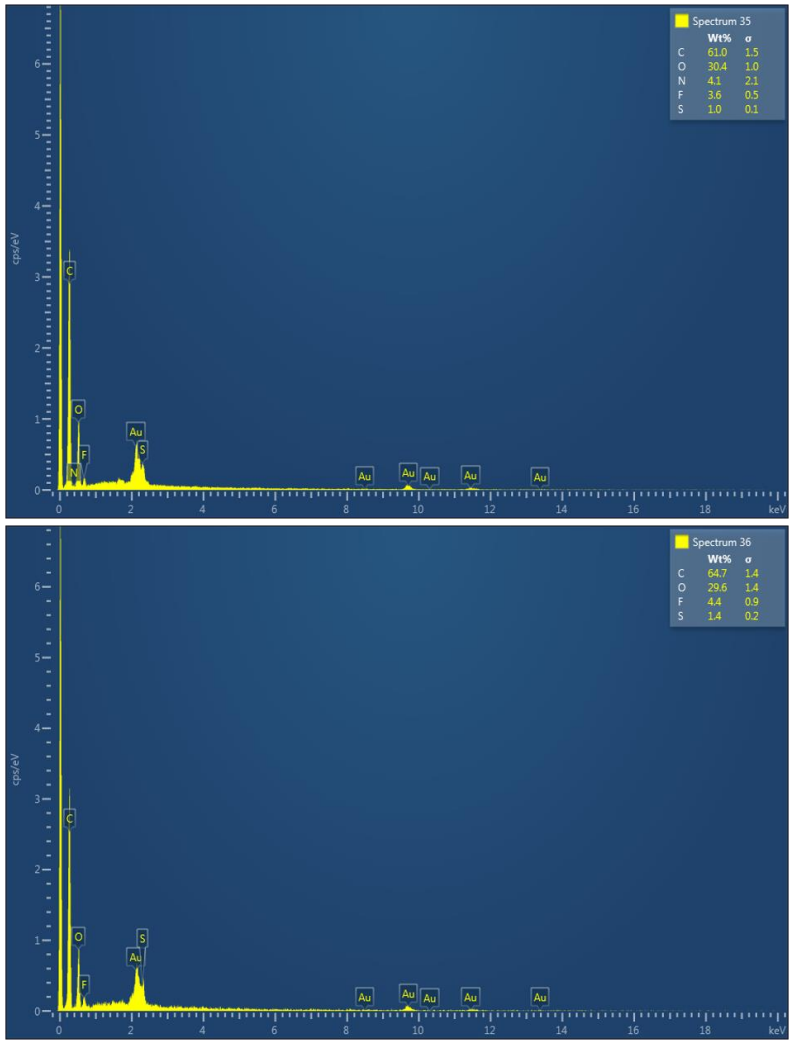

Figure 6.21 EDX spectra of both electrodes used for 15000 cycles in the HS using $[C_2mim][NTf_2]$ as the electrolyte

Figure 6.21 shows the elemental analysis of the composite PPy-cellfib-IL plasticiser-graphite after using it as both electrodes in the hybrid supercapacitor. The elements in each electrode (Table 6.10) were the same but the nitrogen, that appeared in just one of the electrodes, could be due to the volume change of the PPy during the charge and discharge processes (positive electrode). In comparison to the fresh film (section 3.8.2), the amount of C decreased from 70 wt % to ~ 63 wt % and in the case of the O, it increased from 14.4 wt % to ~ 30 wt %.

Table 6.10 Elemental analysis of the PPy-cellfib-IL plasticiser-graphite as fresh film and as both electrodes used for 15000 cycles in the HS using [C_2mim][NTf_2] as the electrolyte

Composite film name	C / wt %	O / wt %	N / wt %	F / wt %	S / wt %	P / wt %	Cl / wt %
Fresh film	70.1	14.4		11.5	2.8	1.2	-
Electrode film 1	61.0	30.4	4.1	3.6	1.0	-	-
Electrode film 2	64.7	29.6	-	4.4	1.4	-	-

6.3. Summary and Conclusions

In this chapter, a study of symmetric and flexible hybrid supercapacitors using as both electrodes a PPy-cellfib-IL plasticiser-graphite composite film was carried out. Both electrostatic and electrochemical mechanisms were involved for the storage of the charge in the supercapacitor. A set of three HS was fabricated using the IL [C_2mim][NTf_2] as the electrolyte and, one HS using [C_2mim][FAP] as the electrolyte.

The HS with [C_2mim][FAP] showed the widest EW (3.2 V) of all the devices in this thesis. The EW of the HS with [C_2mim][NTf_2] was 2.2 V. The maximum areal capacitance values obtained for the HS were 73.3 ± 31.4 μF cm^{-2} and 76.1 μF cm^{-2} for the HS using [C_2mim][NTf_2] and [C_2mim][FAP], respectively. These capacitances were very similar to the EDLS fabricated and much higher than the values for the ES. In addition, the HS showed a better performance under bending conditions than in the case of the ES. These improvements exposed that the combination of graphite and polypyrrole offered better energy storage characteristics than using just polypyrrole in the composite electrode.

The HS using [C_2mim][FAP] as the electrolyte showed the highest specific and density energy among all the devices shown in this thesis. The value of specific energy was 0.72 mWh kg^{-1} and for the energy density the value found was 0.008 μWh cm^{-2}. In the case of the power, it was found that the HS using [C_2mim][FAP] as the electrolyte showed the maximum power density (1.78 μW cm^{-2}) among all the supercapacitors.

From the EIS experiments, the cycle stability could be tested, showing an excellent stability for 15000 cycles in both HS fabricated with different electrolytes. The stability of the composite electrodes was also demonstrated by the chemical characterisation of the electrodes before and after using them in the HS. IR spectroscopy, thermal and SEM/EDX experiments showed that the composites did not suffer any drastic change after the charge-discharge experiments.

Chapter 7

Solid-state Supercapacitors Using Ionic Liquid Gels

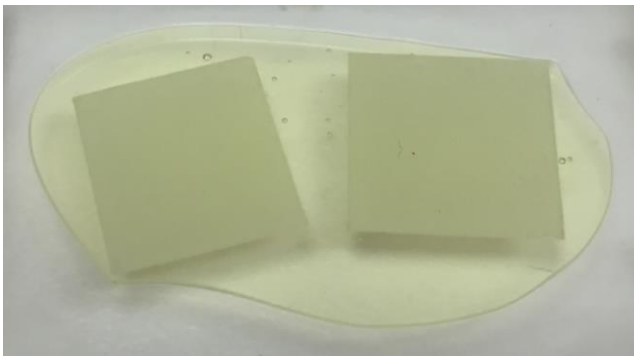

The use of an ionic liquid gel as an electrolyte in solid-state devices relies on the advantages that it offers such as being leakage free, maintenance of the electrochemical properties of the neat ionic liquid electrolyte and possibility of shape modification depending on the application. Hence, they are considered to be safer electrolytes than liquid electrolytes, with large electrochemical windows and good mechanical compliance [22c,348]. As it was described in section 2.1.3.2, an ionic liquid gel is a solid ionic liquid-based composite supported by a structural matrix which offers many benefits of ILs in an immobilised form and it is flexible [33]. Different methods can be used for the formation of the ionic liquid gels *e.g.* sol-gel silica formation, copolymer gelation and thermal-or UV-initiated radical polymerisation [151].

This chapter describes the work carried out for 5 weeks at Tuft's University in Medford (USA). This opportunity was possible due to the Competitive Mobility Scholarship granted by Santander Universities UK in 2016. The group where this work was carried out, is called "Green Energy and Nanostructured Electronics Laboratory" (GENE Lab) under the supervision of Prof Matthew J. Panzer, whose work is focused on the design and characterisation of ionic liquid gel electrolytes [353].

The collaboration with Prof Panzer's group enabled to achieve the fabrication and testing of solid-state flexible supercapacitors by combining the electronically conducting polymer–biopolymer-IL composite electrodes fabricated at QUILL and the ionic liquid gel electrolyte formed at GENE Lab.

Throughout this chapter, the fabrication and characterisation of two electrical double-layer supercapacitors (EDLS) were described. The first EDLS was assembled using an ionic liquid, $[C_4mim][NTf_2]$, as the electrolyte, and the other EDLS was fabricated using an ionic liquid gel, $[C_4mim][NTf_2]$ gel. In both cases, the same electrodes (graphite-cellfib-IL plasticiser composite film) and current collectors (graphene paper, CAS number 7782-42-5) were used.

7.1. Mobility Scholarship Project Objectives

The project aim consisted of fabricating and testing flexible supercapacitors based on ionic liquid gels as electrolytes and conducting biopolymer composites as electrodes. To achieve this goal the following steps were followed:

- Step 1: Supercapacitor fabrication with the cellulose-based composite electrodes fabricated and air-stable ionic liquids
- Step 2: Ionic liquid gels synthesis based on the best performing ionic liquids from step 1
- Step 3: Fabricate and test supercapacitors based on the best selection of candidates from steps 1 and 2

7.2. Experimental Part

All materials used are shown in Appendix A.1, as well as, the instrumental techniques used in this chapter are disclosed in Appendix A.2.

7.2.1. Synthesis of Ionic Liquid Gel Electrolytes

The ionic liquid gel electrolyte was synthesised following the method from Visentin and Panzer [33,354] that form the gel *via* an *in situ* UV-initiated cross-linking of poly(ethylene glycol) diacrylate (PEGDA) inside an ionic liquid, in this case, the ionic liquid chosen was 1-butyl-3-methylimidazolium bis{(trifluoromethyl)sulfonyl}amide, [C_4mim][NTf_2].

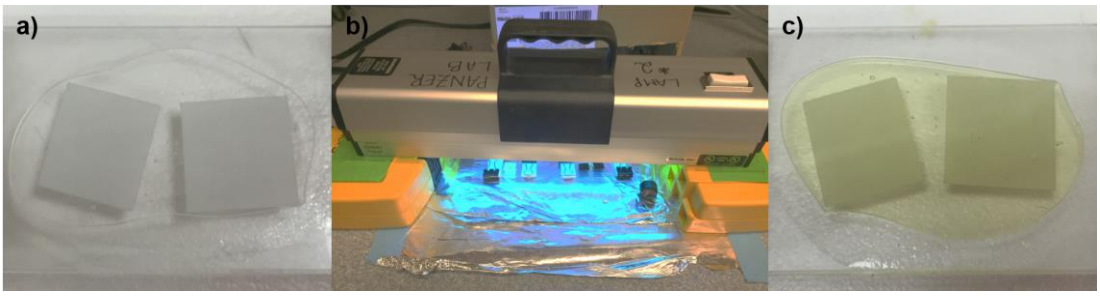

Figure 7.1 UV-cured ionic liquid gel formed using filter paper as a template. The photo a) shows the filter papers soaked in the mixture, b) exposition of this mixture to the UV light and c) the ionic liquid gel formed and integrated to the filter paper

The first step consisted of the synthesis of the ionic liquid gel; in a small glass sample bottle, the IL precursor, [C_4mim][NTf_2], was added and weighed (921 mg). Then, 7 wt % of the polymer, PEGDA (75 mg) and a small amount (13 mg) of the UV-initiator, HOMPP, was added. After all the components were added, the mixture was stirred using a Vortex mixer, and the mixture was impregnated over both sides of a filter paper separator (Figure 7.1 (a)). Finally, the impregnated separator was exposed to a longwave UV radiation at 365 nm for 3 minutes (Figure 7.1 (b)), obtaining the ionic liquid gel as it can be seen in Figure 7.1 (c). The way contemplated to create the

ionic liquid gel over a filter paper (separator) was carried out considering its posterior application as a solid-state electrolyte in a supercapacitor.

7.2.2. Fabrication of the EDLS Using [C_4mim][NTf_2] as the Electrolyte

The procedure for this fabrication took place using the same method as it was explained in section 4.1.2, based on a sandwich shape. Figure 7.2 shows the photo of the symmetric device fabricated. The current collectors were graphene paper, both electrodes were composed of graphite-cellfib-IL plasticiser film, the electrolyte was the IL, [C_4mim][NTf_2], and the separator was a filter paper. This supercapacitor was not sealed using polyester self-adhesive sheets as the previous devices, in this case, the supercapacitor was pressed between two glasses with paper clips to carry out the electrochemical measurements as it can be seen in Figure 7.2.

Figure 7.2 Photo of the EDLS fabricated with graphite-cellfib-IL plasticiser as both electrodes and using [C_4mim][NTf_2] as the electrolyte

7.2.3. Fabrication of the Solid-state EDLS Using [C_4mim][NTf_2] Gel as the Electrolyte

After the paper separator with the ionic liquid gel was ready as explained in section 7.2.1, the assembly of the supercapacitor was carried out using the sandwich model, as explained in section 4.1.2. Graphene paper was used as current collectors and graphite-cellfib-IL plasticiser film as both electrodes obtaining a symmetric solid-state EDLS. Like the previous supercapacitor, the device assembly was sandwiched using two glass plates as it can be seen in Figure 7.3.

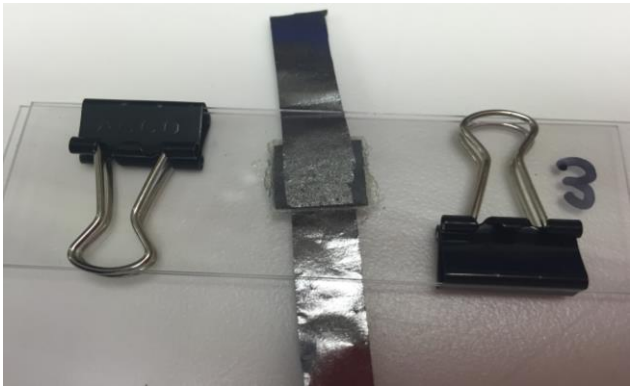

Figure 7.3 Photo of the EDLS fabricated with graphite-cellfib-IL plasticiser as both electrodes and using [C_4mim][NTf_2] gel as the electrolyte

7.3. Results and Discussion

7.3.1. Electrochemical Study of the EDLS Using [C_4mim][NTf_2] as the Electrolyte

The EDLS fabricated used the graphite-cellfib-IL plasticiser composite as both electrodes, considered as the active material the graphite, that corresponded to a 33.3 wt % of the total weight of the electrodes, hence the active material mass was 13.99 mg with an area of 1 cm^2, and thickness of the electrodes was 335 ± 26 µm.

7.3.1.1. Cyclic Voltammetry

The first electrochemical technique employed was cyclic voltammetry which revealed the operational voltage of the device, 2.0 V, as it can be seen in Figure 7.4. The capacitance obtained, using Equation 4.10, for this device at the scan rate of 100 mV s^{-1} was 10.8 mF g^{-1} and 151.4 µF cm^{-2} for the specific and areal capacitance, respectively. The capacitance values were higher in comparison to the EDLS using [C_2mim][NTf_2] as the electrolyte, described in Chapter 4. This raise in the capacitance may be due to the use of more conducting current collectors such as graphene paper instead of aluminium foil, that can reduce the resistance within the electrodes and increase the capacitance [355].

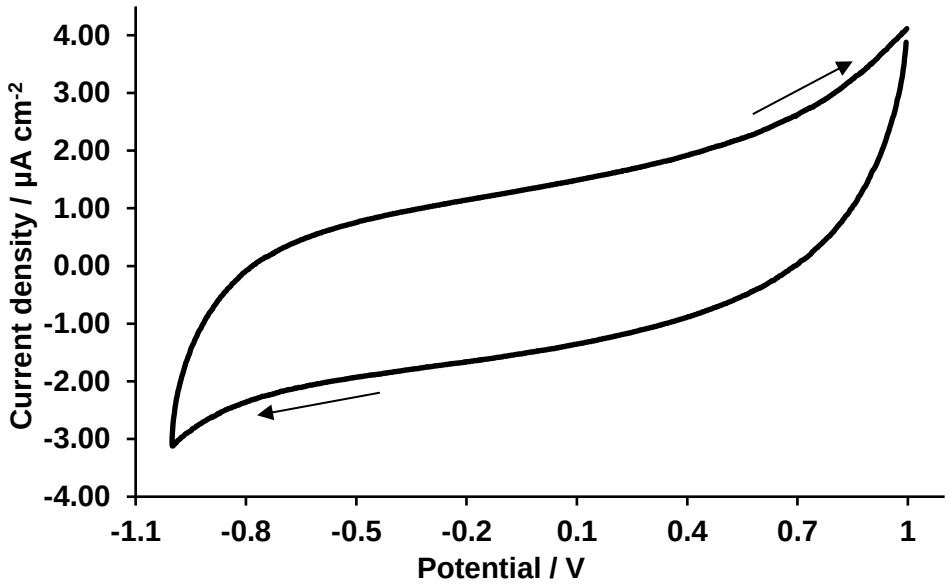

Figure 7.4 Cyclic voltammogram of an EDLS fabricated using [C_4mim][NTf_2] as the electrolyte at 100 mV s^{-1} and at 25 ± 2 ^{0}C. Arrows show the potential direction of the cyclic voltammogram

Different scan rates were applied to test how the capacitance changed. As it can be seen in Figure 7.5, the cycles showed a more resistor behaviour when faster scan rates were applied, as it was expected.

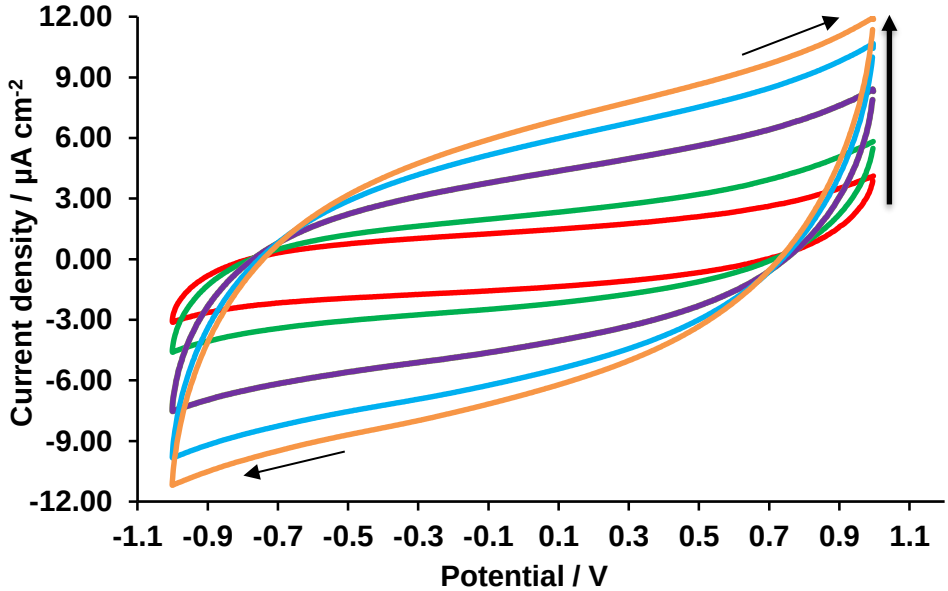

Figure 7.5 Cyclic voltammogram of a EDLS using [C_4mim][NTf_2] as the electrolyte at various scan rates: 1000 (orange), 800 (light blue), 500 (purple), 200 (green), 100 (red) mV s^{-1} and at 25 ± 2 ^{0}C. Arrows show the potential direction of the cyclic voltammogram and the vertical arrow indicates the faster scan rates applied

The capacitance values obtained for this supercapacitor at different scan rates are summarised in Table 7.1. The areal capacitance decreased from 151.4 µF cm^{-2} at

100 mV s^{-1} to 6.5 µF cm^{-2} at 1 V s^{-1}, showing that the resistivity of the device increased considerably when faster scan rates were used.

Table 7.1 Specific and areal capacitance values of a EDLS using [C_4mim][NTf_2] as the electrolyte calculated from the CV at various scan rates

Scan rate / mV s^{-1}	$C_{Spec.}$ / mF g^{-1}	C_{Areal} / µF cm^{-2}
100	10.8	151.4
200	4.2	59.0
500	1.2	16.9
800	0.6	8.8
1000	0.5	6.5

7.3.1.2. Galvanostatic Charge-Discharge

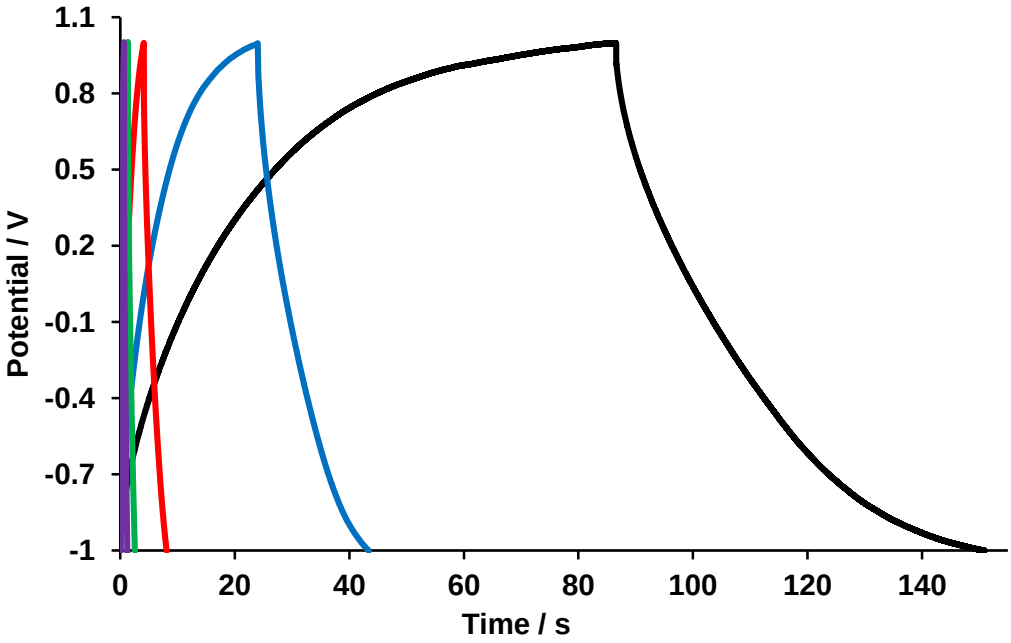

Figure 7.6 GCD curves of the EDLS fabricated using [C_4mim][NTf_2] as the electrolyte at different currents densities applied: 1 (black), 2 (blue), 5 (red), 10 (green) and 15 (purple) µA cm^{-2} and at 25 ± 2 ^{o}C

The next technique employed was galvanostatic charge-discharge using constant currents between 1 and 15 µA cm^{-2}. The charge-discharge curves obtained are shown in Figure 7.6. The triangle curves obtained for 1 and 5 µA cm^{-2} showed a little plateau at the positive limit showing a deviation from the ideal double-layer supercapacitor behaviour. This deviation is sometimes observed in carbon-based SCs, and it could be due to a limitation in the pore accessibility because of a steric effect. If there is a decrease in the pore size, the cation cannot freely access the pores. The

cation in this device, $[C_4mim]^+$, is bigger in comparison to the other devices in this thesis, which used $[C_2mim][NTf_2]$ as the electrolyte [30]. The maximum time needed for this device to charge and discharge was 151 s at the lowest current density of 1 μA cm^{-2}, showing a fast EDLS. The ESR obtained for this device was 52 ± 21 kΩ, lower than in the case of the EDLS using $[C_2mim][NTf_2]$ as the electrolyte, described in Chapter 4. The viscosity of the electrolyte, $[C_4mim][NTf_2]$, is higher (45 mPa·s at 25 ºC) than the electrolyte $[C_2mim][NTf_2]$ used in Chapter 4, with a viscosity of 37 mPa·s at 25 ºC [342b]. Therefore, the decrease in the ESR may be attributed to the nature of electrodes and current collectors, for example, the use of the graphene paper instead of aluminium foil as current collectors reduces the resistance with the electrodes due to its higher conductivity [355], and also pressing the device with a paper clip rather than hand sealing for EDLS in chapter 4. This also provides evidence on tunability.

From the GCD graph, the capacitance values were obtained as it is shown in Table 7.2. The maximum capacitance values for the specific and areal capacitance at the current density of 1 μA cm^{-2} were 2.7 mF g^{-1} and 38.0 μF cm^{-2}, respectively.

Table 7.2 Specific and areal capacitances obtained from the GCD plot at every current density applied to the EDLS using $[C_4mim][NTf_2]$ as the electrolyte

Current density / μA cm^{-2}	C_{Spec} / mF g^{-1}	C_{Areal} / μF cm^{-2}
1	2.7	38.0
2	1.6	22.6
5	0.9	12.1
10	0.6	8.0
15	0.5	6.6

The energy and power values were determined using the GCD graph and Equation 4.16 and Equation 4.17. Table 7.3 shows the values obtained. The maximum value obtained for the specific energy was 1.39 mW h kg^{-1}, and for the energy density was 0.0194 μW h cm^{-2}, at the smallest current density (1 μA cm^{-2}). The energy values decreased when higher current densities were applied. In contrast, the power values increased at higher current densities showing a maximum value of 913.07 mW kg^{-1} for the specific power and 12.77 μW cm^{-2} for the power density. In comparison to the EDLS from Chapter 4, the energy and power values obtained here were higher than the ones obtained in Chapter 4; the increase in the energy and power can be due to

several factors: (i) the higher capacitance values obtained for this EDLS, (ii) the discharge time needed for this EDLS that was five times faster than in the case of the previous EDLS (Chapter 4) and (iii) the smaller ESR obtained for this device.

Table 7.3 Energy and power values calculated from the GCD plot at the different current densities applied, as well as, the discharge time obtained for the EDLS using $[C_4mim][NTf_2]$ as the electrolyte

Current density / μA cm^{-2}	Discharge time / s	E_{Spec} / mW h kg^{-1}	$E_{Density}$ / μW h cm^{-2}	P_{Spec} / mW kg^{-1}	$P_{Density}$ / μW cm^{-2}
1	64.3	1.39	0.0194	77.51	1.08
2	19.3	0.79	0.0111	147.99	2.07
5	3.4	0.38	0.0053	345.99	4.84
10	1.2	0.21	0.0029	617.73	8.64
15	0.6	0.15	0.0021	913.07	12.77

7.3.1.3. Electrochemical Impedance Spectroscopy

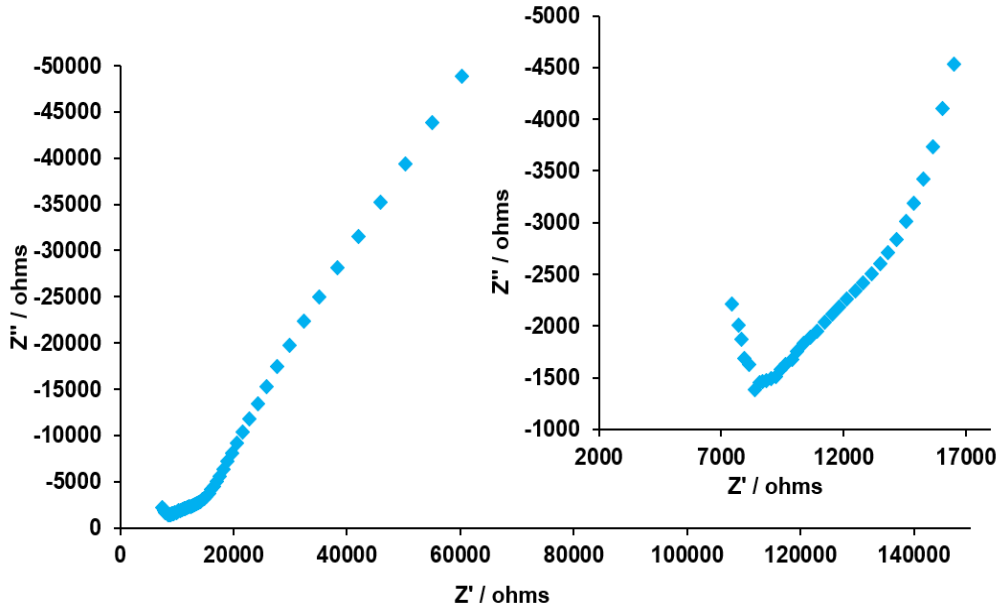

Figure 7.7 Nyquist plot of the EDLS using $[C_4mim][NTf_2]$ as the electrolyte at OCP and at 25 ± 2 ^{0}C

EIS was used to confirm the capacitive behaviour of this device. Figure 7.7 shows the Nyquist plot of the EDLS using $[C_4mim][NTf_2]$ as the electrolyte at the OCP and at 25 ± 2 ^{0}C. The knee frequency obtained from the Nyquist plot was 31.6 kHz and the ESR value 8.4 kΩ. Both values obtained were similar to the ones obtained for the EDLS using $[C_2mim][NTf_2]$ as the electrolyte showed in section 4.2.2.3. This knee frequency

showed a high value, demonstrating that this device had a higher maximum frequency at which capacitive behaviour is dominant in comparison to a few solid-state EDLS found in the literature [230,356].

From the Bode plot, Figure 7.8, the onset frequency at -45 degrees showed a value of 0.15 mHz and the maximum phase of impedance obtained was -64 degrees, demonstrating, as well as in the GCD curves, a deviation from the ideal double-layer supercapacitor behaviour. The onset frequency obtained was lower in comparison to the EDLS from Chapter 4, therefore, this device shows capacitive behaviour for a lower range of frequencies.

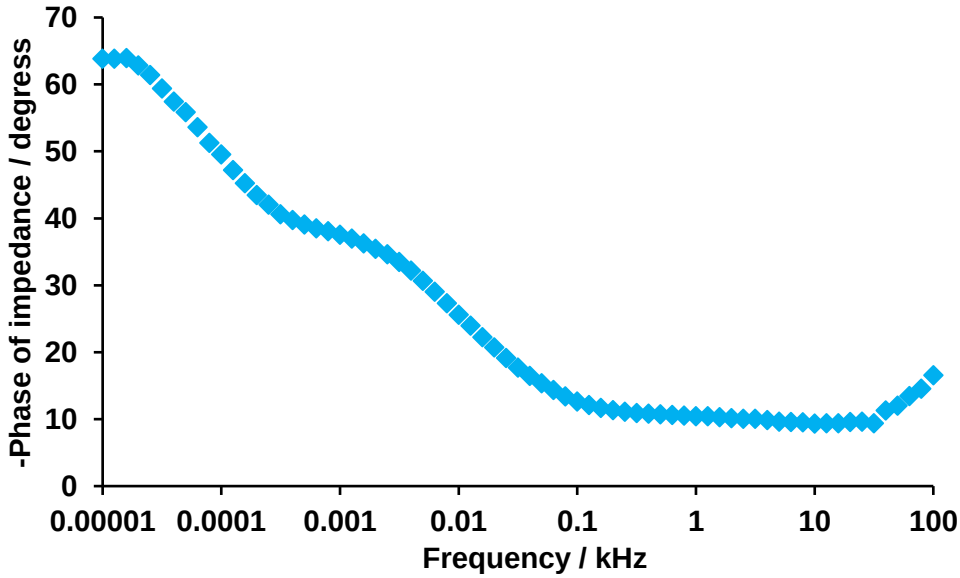

Figure 7.8 Bode plot of the EDLS using [C_4mim][NTf_2] as the electrolyte at OCP and at 25 ± 2 ^{o}C

7.3.2. Electrochemical Study of the Solid-state EDLS Using [C_4mim][NTf_2] Gel as the Electrolyte

In this section, the electrochemical characterisation of an EDLS using [C_4mim][NTf_2] gel as the electrolyte is described. A solid-state EDLS was assembled and characterised using the graphite-cellfib-IL plasticiser composite film as both electrodes, considering graphite as the active material that corresponded to 33.3 wt % of the total weight of the electrodes hence, the active material mass was 10.82 mg with an area of 0.81 cm^2 and thickness of 320 µm. The current collectors were graphene paper and the separator filter paper.

7.3.2.1. Cyclic Voltammetry

The cyclic voltammogram obtained for this solid-state EDLS is shown in Figure 7.9 where the operational voltage found was 1.5 V. In comparison to the EW of the EDLS using $[C_4mim][NTf_2]$ as the electrolyte, the EW decreased 0.5 V in the new device. However, a better symmetric and rectangular cycle for this device at 200 mV s^{-1} with a specific capacitance of 13.0 mF g^{-1} and areal capacitance of 173.4 µF cm^{-2} was obtained. The capacitance values for the solid-state EDLS were larger than for the EDLS using $[C_4mim][NTf_2]$ as the electrolyte.

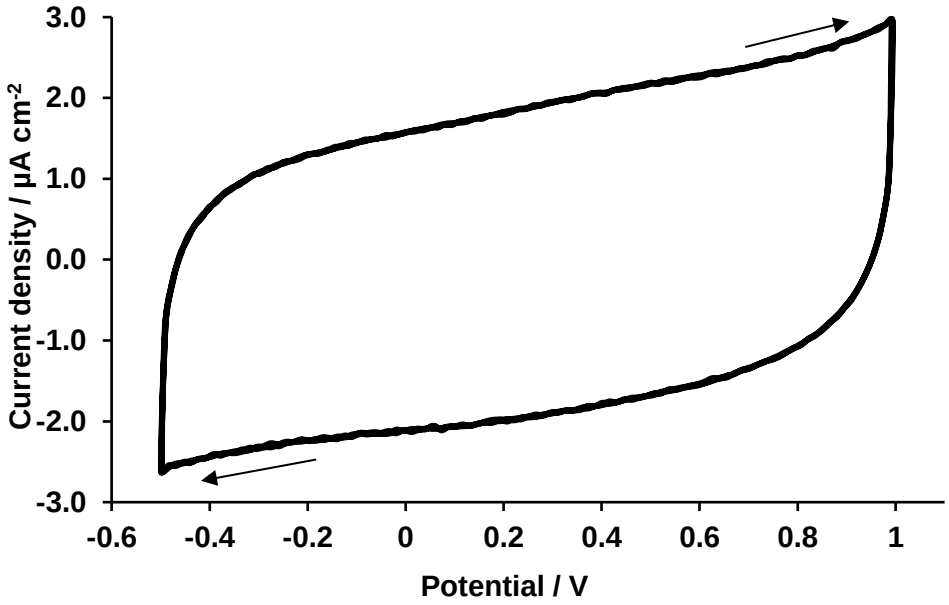

Figure 7.9 Cyclic voltammogram of the EDLS fabricated using $[C_4mim][NTf_2]$ gel as the electrolyte at 200 mV s^{-1} and at 25 ± 2 ^{0}C. Arrows show the potential direction of the cyclic voltammogram

The areal capacitance of this EDLS is higher than a solid-state supercapacitor based on graphene electrodes developed by Gao *et al.* [357] in 2013. The authors fabricated a transparent and flexible solid-state EDLS using graphene sheets as electrodes and poly(vinyl alcohol)/phosphoric acid gel as the electrolyte which showed an areal capacitance of 12.4 µF cm^{-2} at 10 mV s^{-1}.

The rate capability was studied using CV. Different scan rates were applied as shown Figure 7.10 and the symmetric and rectangular shape of the cycle was maintained even at the highest scan rate of 1 V s^{-1}, in contrast to the previous EDLS (section 7.3.1), which showed resistance behaviour at faster scan rates. Therefore, the use of the IL gel as the electrolyte has improved the rate capability of the device.

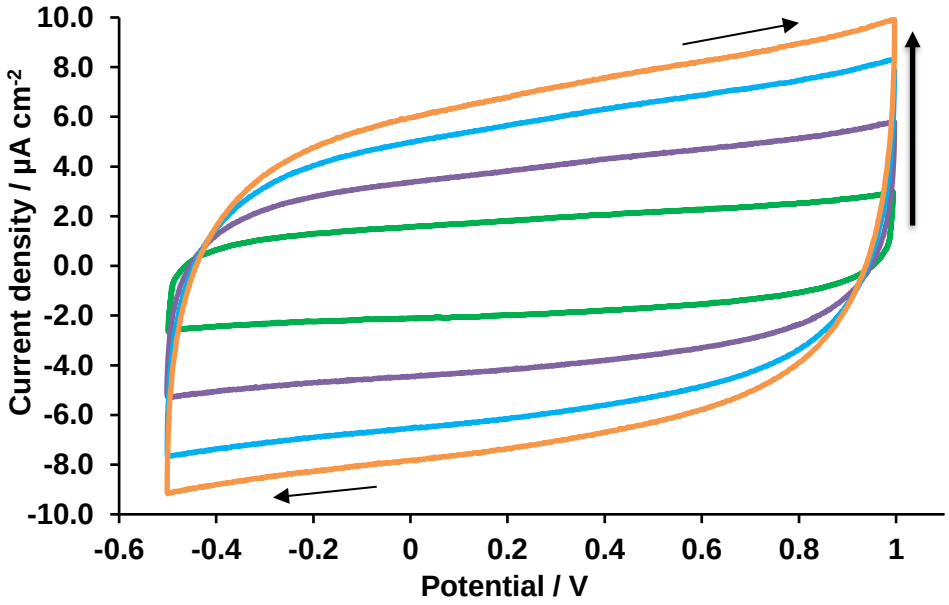

Figure 7.10 Cyclic voltammogram of the EDLS using [C_4mim][NTf_2] gel as the electrolyte at various scan rates: 1000 (orange), 800 (light blue), 500 (purple), and 200 (green) mV s^{-1} and at 25 ± 2 ^{0}C. Arrows show the potential direction of the cyclic voltammogram and the vertical arrow indicates the faster scan rates applied

The high rate capability can be confirmed by the capacitance results obtained (Table 7.4) that showed high values even at high scan rates. The maximum values obtained were 13.0 mF g^{-1} and 173.4 µF cm^{-2} at the scan rate of 200 mV s^{-1} for the specific and areal capacitance, respectively.

Table 7.4 Specific and areal capacitance values of the EDLS using [C_4mim][NTf_2] gel as the electrolyte calculated from the CV at various scan rates

Scan rate / mV s^{-1}	$C_{Spec.}$ / mF g^{-1}	C_{Areal} / µF cm^{-2}
200	13.0	173.4
500	5.6	74.6
800	1.6	21.2
1000	1.2	16.3

7.3.2.2. Galvanostatic Charge-Discharge

The galvanostatic charge-discharge experiments showed symmetric and triangular curves demonstrating an almost ideal double-layer capacitance behaviour. Also, a drastic IR_{drop} during the onset of the discharge process was observed (Figure 7.11). The maximum time needed for charge and discharge the device was 34 s at the current density of 1 µA cm^{-2}, and the minimum time was 1 s at the current density of 15 µA cm^{-2}; half of the time needed in comparison to the EDLS using [C_4mim][NTf_2] as

the electrolyte (section 7.3.1.2). The ESR obtained from this device was found to be 44 ± 31 kΩ, which is similar to the ESR obtained for the EDLS using [C_4mim][NTf_2] as the electrolyte, demonstrating that the solid nature of the electrolyte did not increase the resistance in the device.

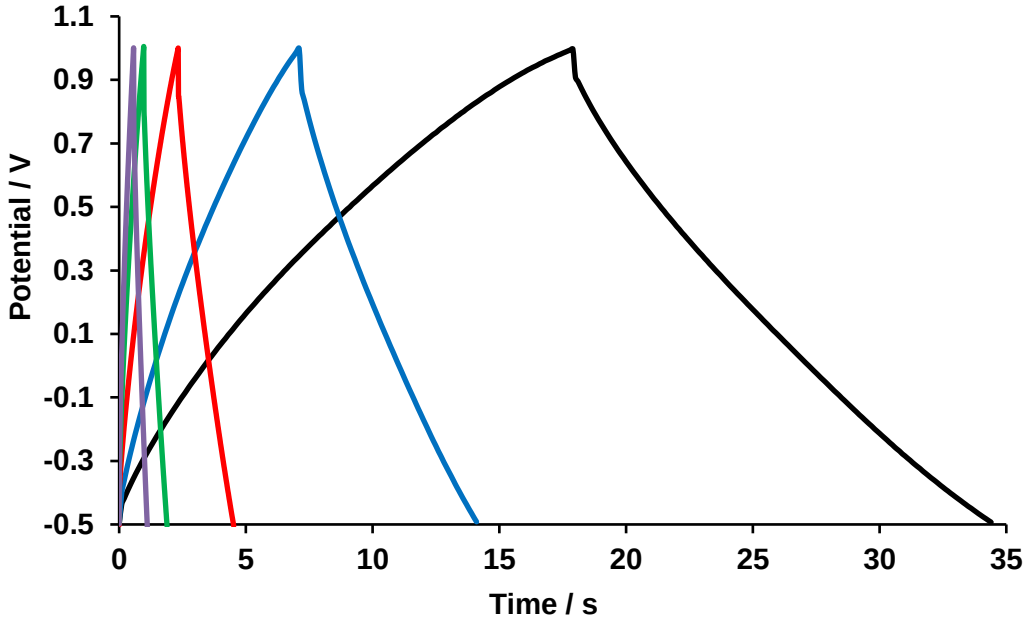

Figure 7.11 GCD curves of the EDLS fabricated using [C_4mim][NTf_2] gel as the electrolyte at different currents densities applied, 1 (black), 2 (blue), 5 (red), 10 (green) and 15 (purple) μA cm^{-2} and at 25 ± 2 ^{o}C

The capacitance values obtained from the GCD experiments were lower than in the case of the CV technique as it is shown in Table 7.5. The maximum values for the specific capacitance were found to be 1.0 mF g^{-1} and 12.1 μF cm^{-2}, respectively.

Table 7.5 Specific and areal capacitances obtained from the GCD plot at every current density applied to the EDLS using [C_4mim][NTf_2] gel as the electrolyte

Current density / μA cm^{-2}	C_{Spec} / mF g^{-1}	C_{Areal} / μF cm^{-2}
1	1.0	12.1
2	0.8	10.4
5	0.7	8.2
10	0.6	7.1
15	0.5	6.5

The final evaluation of the EDLS performance was carried out through the calculation of the energy and power at each current density applied. As it can be seen in Table 7.6, the maximum specific energy and energy density found was 0.31 mW h

kg^{-1} and 0.0038 μW h cm^{-2}, respectively. The specific power and power density had values of 1123.9 mW kg^{-1} and 13.85 μW cm^{-2}, respectively. These power values were higher than in the case of the previous EDLS using $[C_4mim][NTf_2]$ as the electrolyte, as it was expected due to the good rate capabilities showed with the cyclic voltammetry and galvanostatic charge-discharge techniques. In the case of the energy, the solid-state EDLS showed lower values than the previous EDLS (section 7.3.1.2)

Table 7.6 Energy and power values calculated at different current densities applied using GCD as well as the discharge time obtained of the EDLS using $[C_4mim][NTf_2]$ gel as the electrolyte

Current density / μA cm^{-2}	Discharge time / s	E_{Spec} / mW h kg^{-1}	$E_{Density}$ / μW h cm^{-2}	P_{Spec} / mW kg^{-1}	$P_{Density}$ / μW cm^{-2}
1	16.4	0.31	0.0038	67.3	0.83
2	6.9	0.26	0.0033	137.9	1.70
5	2.18	0.21	0.0026	343.9	4.24
10	0.91	0.18	0.0022	716.4	8.83
15	0.53	0.17	0.0020	1123.9	13.85

7.3.2.3. Electrochemical Impedance Spectroscopy

EIS was employed to understand the capacitive behaviour of the solid-state supercapacitor which revealed a low ESR with a value of 0.3 kΩ (taken from the Nyquist plot showed in Figure 7.12). In the inset of this graph hardly a semi-circular loop corresponding to the charge-transfer resistance was found in the high-frequency region producing, as a result, a decrease in the ESR of the device. The knee frequency is known as the separation frequency among the high frequencies and low frequencies but, as well as in the case of the ESR, there was no inflexion point where to do the separation; therefore, the knee frequency was considered to be the first frequency recorded, in this case, 100 kHz. These results indicated that this system is kinetically fast, which agrees with the galvanostatic charge-discharge results.

In comparison to the EDLS shown in Chapter 4, the knee frequency revealed that this device can store energy at a larger range of frequencies and showed a lower value of ESR. Therefore, it can be said that the combination of the electrodes (graphite-cellfib-IL plasticiser composite film) and the $[C_4mim][NTf_2]$ gel as the electrolyte showed good supercapacitor characteristics with the advantage that the materials to fabricate the device were in the solid-state.

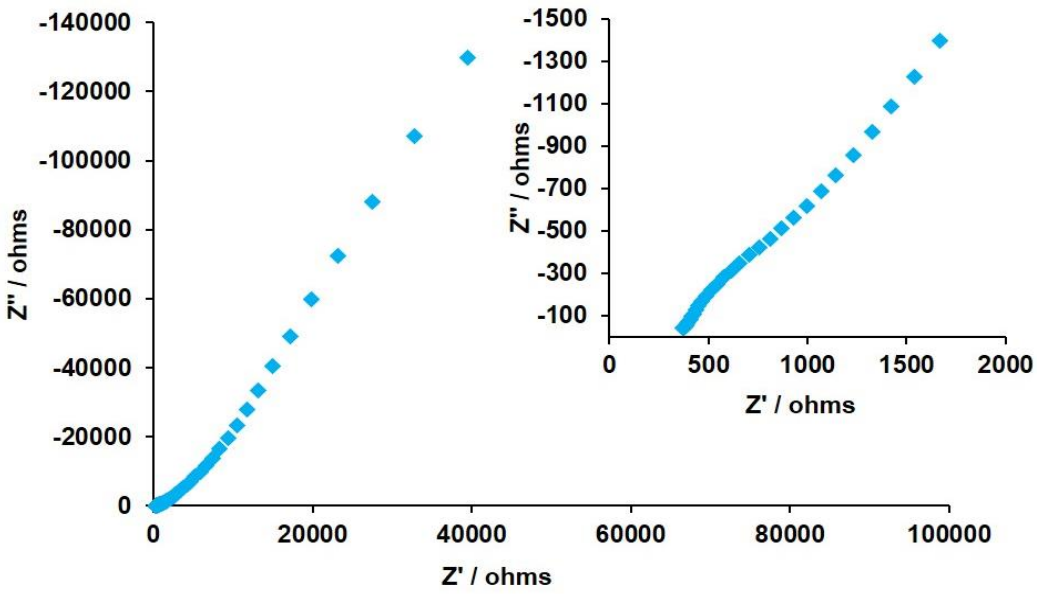

Figure 7.12 Nyquist plot of the EDLS using [C_4mim][NTf_2] gel as the electrolyte at OCP (light blue) and at 25 ± 2 ^{0}C

In Figure 7.13 the Bode plot of the solid-state EDLS is displayed, showing the dependency of the phase of the impedance with the frequencies. The onset frequency was found to be 39.8 Hz which means that this supercapacitor showed primarily capacitance behaviour for a higher range of frequencies than the previous EDLS using [C_4mim][NTf_2] as the electrolyte. The maximum phase of impedance obtained for this EDLS was around -72 degrees showing an almost ideal double-layer capacitive behaviour that was accessible for frequencies below 1 Hz.

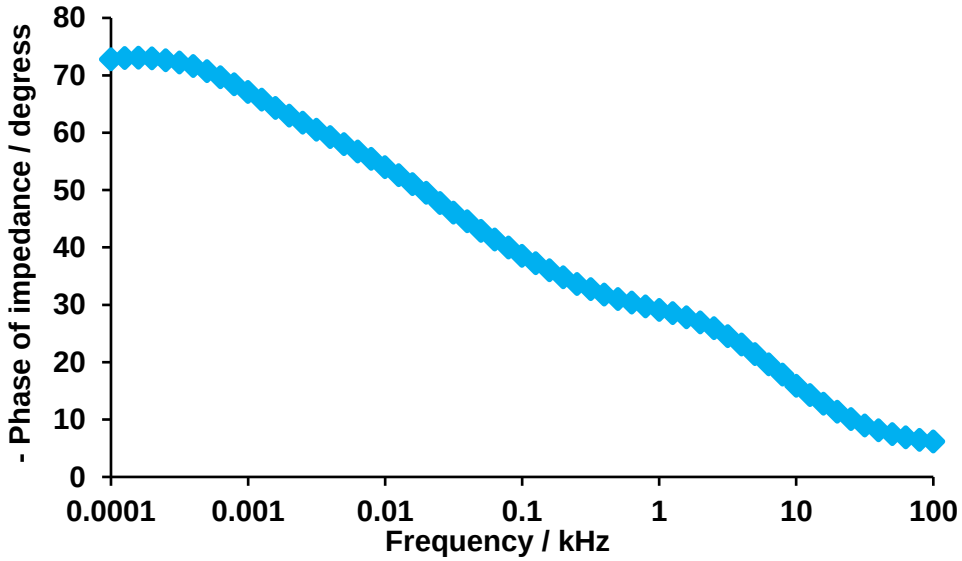

Figure 7.13 Bode plot of the EDLS using [C_4mim][NTf_2] gel as the electrolyte at OCP (light blue) and at 25 ± 2 ^{0}C

7.4. Summary and Conclusions

In this chapter, the work developed for 5 weeks at Tuft's University was described, starting with the synthesis of ionic liquid gels over both sides of a filter paper to obtain a filter paper impregnated with an electrolyte gel. The ionic liquid gel fabricated was composed of the ionic liquid $[C_4mim][NTf_2]$ and a polymer known as PEGDA. The polymerisation process to obtain the gel electrolyte was carried out using a UV-initiator called HOMPP and UV radiation, obtaining the $[C_4mim][NTf_2]$ gel electrolyte.

Two EDLS were fabricated and electrochemically characterised. One had an IL gel as the electrolyte, and therefore, it was a solid-state EDLS. The other device was assembled with the same IL but in a liquid state for comparison.

The solid-state EDLS fabricated showed a maximum EW of 1.5 V with maximum specific and areal capacitance values of 13.0 mF g^{-1} and 173.4 μF cm^{-2}, respectively. In the case of the energy, the maximum values obtained were 0.31 mWh kg^{-1} and 0.0038 μWh cm^{-2} for the specific and energy density, respectively. The maximum specific power value obtained was 1123.9 mW kg^{-1}, and 13.85 μW cm^{-2} for the power density. The results obtained for the solid-state EDLS were quite similar to the results obtained when the electrolyte was the IL $[C_4mim][NTf_2]$ in the liquid state. However, there were some differences such as the EW obtained that was 2.0 V, the specific energy with a value of 1.42 mWh kg^{-1} and the energy density was 0.0198 μWh cm^{-2}.

Therefore, the fabrication of a solid-state supercapacitor was achieved showing good energy storage characteristics that can be compared to the neat IL as the electrolyte.

It was not possible to carry out bending studies and a further cycle life the for the supercapacitors fabricated in this period, due to time restrictions. Additional studies can be done using the composite films obtained (Chapter 3) and the IL gel electrolytes described in this chapter.

Chapter 8

Summary & Way Forward

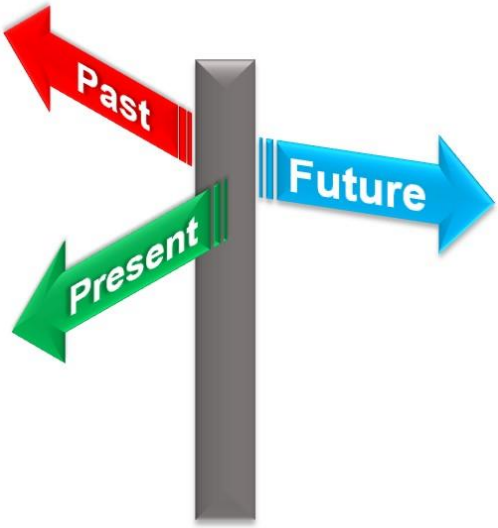

The aim of this thesis consisted of fabricating a flexible supercapacitor (FSC) by developing new flexible cellulose-based electrodes and ionic liquids as the electrolyte. Therefore, the fabrication of flexible electrodes and their characterisation was the first part of the project. After the flexible electrodes synthesis was optimised, their assembly as electrodes in a sandwich shape and symmetric supercapacitor was carried out. Finally, the supercapacitor was characterised electrochemically.

A novel strategy for producing a new class of electronically active materials comprising electronically conducting polymer-biopolymer composites that are chemically blended was reported in Chapter 3. A one-pot synthesis method was proposed (Figure 8.1) in which the use of the ionic liquids technology to dissolve biomass, in this case, a biopolymer such as cellulose was exploited. Afterwards, within the cellulose-IL solvent mixture an *in situ* polymerisation of an electronically conducting polymer, specifically, polypyrrole which provided electronic conductivity was carried out. An IL plasticiser, $[P_{6\,6\,6\,14}][NTf_2]$, and graphite were added to the mixture to enhance the flexibility and conductivity of the resulting composite films obtained, respectively. This one-pot mixture of components was used to cast electrode films using a simple coating machine resulting in a free-standing film.

The cellulose-based composite films obtained were characterised using different techniques such as infrared spectroscopy and thermal stability which revealed, for example, the hydrogen bond interaction between the PPy and cellulose in the composite films. The uniform morphology and the elemental compositions of the PPy-cellulose films *etc*. were analysed using characterisation techniques such as IR, Raman, TGA and SEM/EDX. From the thermal analysis using TGA, the decomposition temperatures of the flexible composite films were found to be between 238 ºC and 283 ºC which means that these materials can be used in most of the real world electronic devices with operational temperatures around 200 ºC [184b]. The flexibility of the composite films was measured using a tensile strength test. The Young's Moduli of these films were obtained showing values around 45 MPa, similar to literature values of polypyrrole composite films [302]. The electroactivity of the composite films was studied using cyclic voltammetry. The three films showed an electrochemical response which indicates that they could be applied as electrodes in electrochemical devices such as supercapacitors.

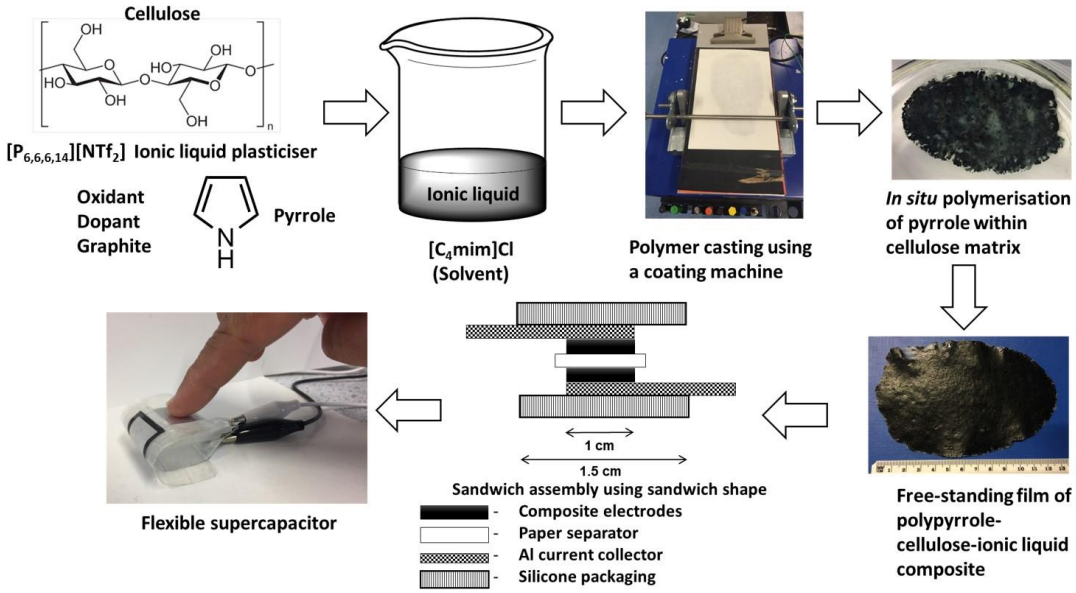

Figure 8.1 Procedure developed for the synthesis of free-standing cellulose-based electrodes and their application of electrodes in a flexible supercapacitor [84a]

Using this facile fabrication method, three types of composites electrodes were prepared *viz*. PPy-cellfib-IL plasticiser, PPy-cellfib-IL plasticiser-graphite and graphite-cellfib-IL plasticiser composite films, and they were used as flexible electrodes in supercapacitors. The flexible supercapacitors using PPy-cellfib-IL plasticiser and PPy-cellfib-IL plasticiser-graphite composite electrodes showed inherent stability, which could be attributed to the hydrogen bond between polypyrrole and cellulose as reported from FT-IR studies in Chapter 3. Three types of SCs were constructed *viz*. electrical double-layer (EDLS), electrochemical (ES) and hybrid supercapacitor (HS) based on the chemical composition of the comprising electrodes. They differ in the charge storage and release mechanisms *i.e*. the graphite-cellfib-IL plasticiser film by electrical double-layer mechanism, PPy-cellfib-IL plasticiser film by electrochemical mechanism and PPy-cellfib-IL plasticiser-graphite by the hybrid mechanism. Each device was characterised electrochemically by cyclic voltammetry, galvanostatic charge-discharge studies and electrochemical impedance spectroscopy, as shown in Chapter 4 for the EDLS, Chapter 5 for the ES and Chapter 6 for the HS. From the opportunity to visit and work at Tuft's University with a Mobility Scholarship, the fabrication and characterisation of a solid-state flexible electrical double-layer supercapacitor using graphite-cellfib-IL plasticiser film as the electrodes and $[C_4mim][NTf_2]$ IL gel as the electrolyte (EDLS $[C_4mim][NTf_2]$ gel) was carried out (see

Chapter 7); also, an EDLS with the same electrodes using the $[C_4mim][NTf_2]$ IL as liquid electrolyte was studied for comparison.

Overall, the devices fabricated showed excellent stability in their cycle life performance of 15000 cycles with almost 100 % of capacitance retention as shown in Table 8.1. The cycle life of the EDLS using $[C_4mim][NTf_2]$ and $[C_4mim][NTf_2]$ gel were not studied due to the limited time spent at Tufts University. Chapter 7 includes only a feasibility study to show the possibility of using ionic liquid gels as electrolytes for solid-state systems. Therefore, from the comparison among the devices studied in Chapter 4, 5 and 6, the best EW was obtained for the HS using $[C_2mim][FAP]$ IL as the electrolyte with a value of 3.2 V. In the case of the specific and areal capacitance, the EDLS using $[C_2mim][NTf_2]$ as electrolyte showed the highest capacitance values in comparison to the other SCs reported in this thesis, hence, this device exhibited a low ESR with a value of 194 ± 76 kΩ. The time needed for charging and discharging the supercapacitor showed that the lowest charge-discharge time was obtained for the ES using $[C_2mim][NTf_2]$ as the electrolyte with a value of 44 s for an EW of 1.6 V. Nevertheless, all the supercapacitors obtained in this thesis showed fast charge and discharge times *e.g.* for the HS using $[C_2mim][FAP]$ as the electrolyte with the largest EW (3.2 V) the time needed for charging and discharging was 161 s, demonstrating the good rate capability of these devices. With the EIS technique, an interesting property called knee frequency was calculated; this value gives the maximum frequency at which the supercapacitor shows capacitive behaviour. As it can be seen (Table 8.1) the knee frequencies obtained had values between 3.4 kHz and 100 kHz; these values were much higher than those of carbon-based supercapacitors found in the literature with knee frequencies around 100 Hz [339b]. As one of the objectives of this PhD was to obtain a supercapacitor that can retain their electrochemical performance while different bending states were applied to the device, a bending study was carried out using cyclic voltammetry to analyse the electrochemical performance and the devices' stability prior to, during and after bending. All the devices from Chapter 4, 5 and 6 were able to function while a bending angle of 120 degrees was applied.

Table 8.1 Summary of the electrochemical results obtained for each device fabricated in this thesis

	Chapter 4		Chapter 5		Chapter 6		Chapter 7	
Electrochemical properties	EDLS [C_2mim] [NTf_2]	EDLS [C_2mim] [FAP]	ES [C_2mim] [NTf_2]	ES [C_2mim] [FAP]	HS [C_2mim] [NTf_2]	HS [C_2mim] [FAP]	EDLS [C_4mim] [NTf_2]	EDLS [C_4mim] [NTf_2] gel
EW / V	2.1	3.0	1.6	2.3	2.2	3.2	2.0	1.5
C_{Spec} / mF g^{-1} (100 mV s^{-1})	3.0 ± 0.6	1.8	1.5 ± 0.3	1.07	1.1 ± 0.7	1.28	10.8	13.0 (200 mV s^{-1})
C_{Areal} / µF cm^{-2} (100 mV s^{-1})	15.4 ± 0.2	11.1	8.8 ± 1.3	9.8	11.3 ± 6.3	13.8	151.4	173.4 (200 mV s^{-1})
ESR/ kΩ	194 ± 76	249 ± 82	325 ± 92	190 ± 72	323 ± 35	269 ± 145	52 ± 21	44 ± 31
Time charge-discharge / s (1µA cm^{-2})	143	138	44	100	142	191	151	34
Cycle life / cycles	15000	15000	15000	15000	15000	15000	-	-
Bending study	Yes	Yes	Yes	Yes	Yes	Yes	-	-
Knee frequency at OCP / kHz	22.2	3.4	22.2	15.3	15.3	22.2	31.6	100

In the electrochemical characterisation of supercapacitors, the energy and power density calculation is a requirement because these properties describe the performance of the devices in real life conditions. The Ragone plot, as it was explained in section 1.1, is a comparative performance evaluation of the energy density *vs.* the power density of the supercapacitors at different current densities applied with the GCD technique. Figure 8.2 shows the Ragone plots obtained for the flexible supercapacitors fabricated in this PhD. As it can be seen in Figure 8.2 (a) the three type of SCs (EDLS, ES and HS) using two different IL as electrolytes ([C_2mim][NTf_2] and [C_2mim][FAP]) are displayed in which, the HS using [C_2mim][FAP] as the electrolyte (pink line) showed the maximum energy density (0.008 μW h cm^{-2}) and power density (1.78 μW cm^{-2}) in comparison to the other supercapacitors developed from this research work.

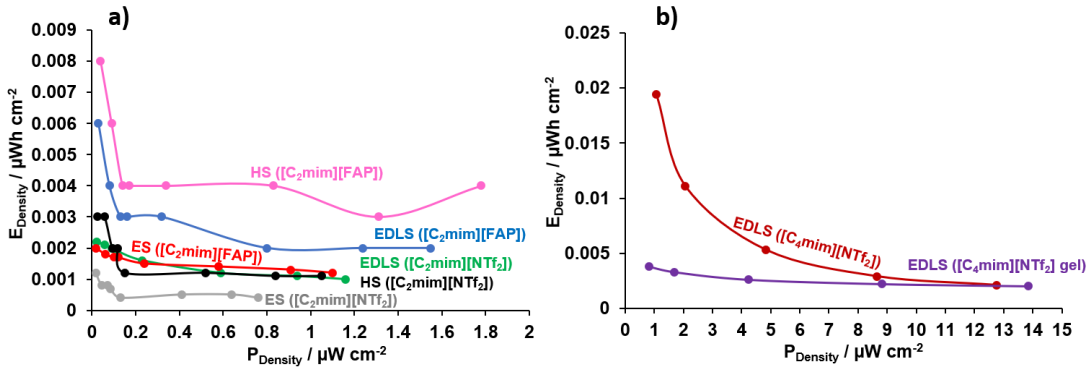

Figure 8.2 Ragone plot of the flexible supercapacitors fabricated in this PhD: a) EDLS, ES and HS using [C_2mim][NTf_2] and [C_2mim][FAP] as the electrolytes and, b) EDLS fabricated using [C_4mim][NTf_2] and [C_4mim][NTf_2] gel as the electrolytes.

Figure 8.2 (b) shows the Ragone plot corresponding to the two devices from Chapter 7 and as it can be seen, the maximum energy density (0.0194 μW h cm^{-2}) was obtained with the EDLS using [C_4mim][NTf_2] in comparison to the EDLS using a gel as the electrolyte. In contrast, the maximum power density (13.85 μW cm^{-2}) obtained was from the EDLS using [C_4mim][NTf_2] gel as the electrolyte. From all the data obtained, displayed in Figure 8.2, it can be said that these flexible supercapacitors showed a power density range that is expected to be sufficient to power up *e.g.* biosensors in medical implants [358].

The chemical composition, morphology and thermal stability of the composite cellulose-based electrodes were investigated by infrared spectroscopy, scanning electron microscopy and thermal gravimetric analysis as fresh materials and after

being used as electrodes for 15000 cycles in the SCs using $[C_2mim][NTf_2]$ as the electrolyte to understand the functional characteristics of the devices. The HS based on PPy-cellfib-IL plasticiser-graphite composite films as the electrode materials showed the highest chemical, physical and thermal stability after the cycle life of 15000 cycles.

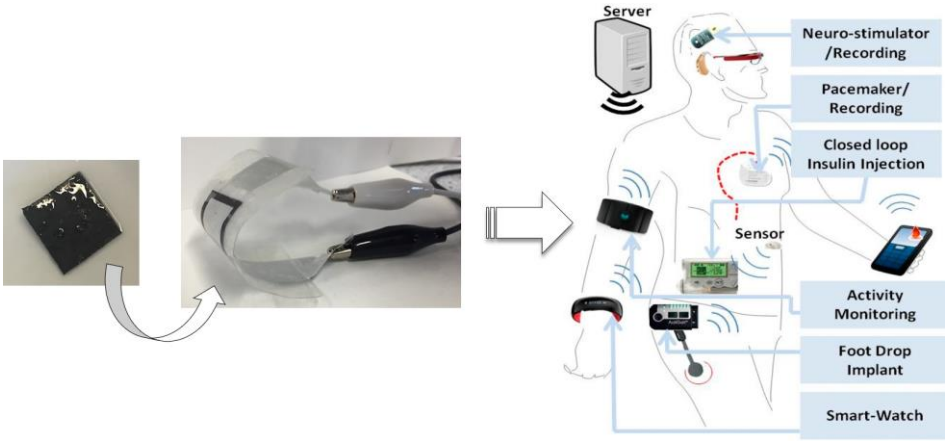

Figure 8.3 Summary of the project achievements: fabrication and characterisation of flexible supercapacitors using the flexible cellulose-based electrodes developed for a possible application in medical devices which need a source of power

To summarise, the synthesis procedure proposed to develop a set of new flexible cellulose-based composite materials which could be applied as electrodes in a flexible energy storage device such as a supercapacitor was accomplished successfully. Moreover, the multifunctional *rôle* of ionic liquids was demonstrated as solvent, plasticiser and electrolyte.

A one-pot facile method was developed by processing biomass using the ionic liquid technology which demonstrates the possibility of recycling biowaste, and the use of conventional inexpensive materials such as cellulose for the flexible supercapacitors assembly offers a cost-effective system. For all these reasons, and due to the use of biocompatible chemicals such as cellulose [359], polypyrrole [360] or the IL plasticiser $[P_{6\,6\,6\,14}][NTf_2]$ [265], these devices can be suitable for medical applications such as pacemakers, stimulators, biosensors, *etc.* as it is shown in Figure 8.3 [70]. Bench-top testing demonstrated that these power devices are stable under ambient conditions without the need for sophisticated sealing. In addition, the hydrophobic nature of the composites is favourable for *in vivo* applications [361]. The tunable nature of various composites, electrolytes and their combinations could lead to the development of novel SCs for task-specific applications in the future.

Appendix

Appendix A: Materials and Techniques

A.1. Starting Materials

Table A. 1 Material Sources

Chemical	Source	Purity / %
ammonium persulfate	Sigma-Aldrich	98
benzenesulfonic acid	Sigma-Aldrich	97
(+)-camphor-10-sulfonic acid (ß)	Fluka	98
cellulose (fibrous, CAS 9004-34-6)	Sigma-Aldrich	
cellulose (powder, ca. ~20 µm)	Sigma-Aldrich	
1-ethyl-3-methylimidazolium ethanoate ($[C_2mim][C_1COO]$)	Sigma-Aldrich	
ferrocene	Sigma-Aldrich	98
graphite powder (1-2 micron)	Sigma-Aldrich	
2-hydroxy-2-methylpropiophenone (HOMPP)	Sigma-Aldrich	97
iron (III) chloride anhydrous	Sigma-Aldrich	97
poly(ethylene glycol) diacrylate (PEGDA)	Sigma-Aldrich	Average M_n 700
potassium chloride	Sigma-Aldrich	99
pyrrole	Sigma-Aldrich	98
sodium chloride	Sigma-Aldrich	
trihexyl(tetradecyl)phosphonium chloride ($[P_{6\,6\,6\,14}]Cl$)	Sigma-Aldrich	
trimethylphosphate	Sigma-Aldrich	97

NMR solvents

- D_2O-*d*$_2$ (99.9 atom %D) from Sigma-Aldrich
- $CDCl_3$-*d* (99.9 atom %D) from Sigma-Aldrich
- MeOD-*d* (99.9 atom %D) from Sigma-Aldrich
- $(CD_3)_2SO$-*d*$_6$ (99.9 atom %D) from Sigma-Aldrich

Donated ionic liquids from Merck

- 1-ethyl-3-methylimidazolium bis{(trifluoromethyl)sulfonyl}amide, [C_2mim][NTf_2].

  ^{1}H NMR (400 MHz, MeOD, δ): 8.82 (s, 1H), 7.59 (s, 1H), 7.52 (s, 1H), 4.24 (q, *J* = 7.3 Hz, 2H), 3.91 (s, 3H), 1.52 (t, *J* = 7.3 Hz, 3H). ^{13}C NMR (101 MHz, MeOD): δ 136.06 (s), 123.56 (s), 121.88 (s), 119.81 (q, *J* = 322.4 Hz), 44.64 (s), 35.05 (s), 14.07 (s).

- 1-ethyl-3-methylimidazolium tris(pentafluoroethyl)trifluoro phosphate, [C_2mim][FAP] [362].

  ^{1}H NMR (300 MHz, $(CD_3)_2SO$, *δ*): 9.57 (s, 1H), 7.91 (s, 1H), 7.81 (s, 1H), 4.23 (q, *J* = 7.3 Hz, 2H), 3.87 (s, 3H), 1.40 (t, *J* = 7.3 Hz, 3H). ^{19}F NMR (377 MHz, $(CD_3)_2SO$, *δ*): -118.8 (m, CF_2), -85.3 (m, CF_2), -79.3 (m, CF_3), -40.2 (m, PF_3).

Materials used

- Supercapacitor current collectors: aluminium kitchen foil (Chapter 4, 5 and 6) and Graphene paper size 11.5 in.×23.5 in., thickness 120 µm. CAS Number 7782-42-5, https://www.sigmaaldrich.com/catalog/product/aldrich/900451?lang=en&region=US&cm_sp=Insite-_-prodRecCold_xviews-_-prodRecCold10-1 (Chapter 7)
- Supercapacitor separator: lab tissue paper WW 18 14E, white 2 PLY; thickness: 10 µm from Centre Pull (Chapter 4,5 and 6) and filter paper Fisherbrand QL100 from Fisher Scientific (Chapter 7)
- Sealer: waterproof polyester self-adhesive film from Labelplanet (Chapter 4, 5 and 6)

A.2. Instrumental Techniques

Chapter 3

To cast the films a coating machine was used (K control coater model 101 from RK Printcoat Instruments), the components necessary for casting the films were: proofing paper (gloss/matt) using the gloss part to cast the films and bar No. 8 (wet film thickness 100 µM).

ASTM D3359 test method with slight modification was used. A piece of Scotch brand transparent tape was placed firmly on the casted polymer film and pressed gently to achieve even contact between tape and film, then gently peeled off. Any

visible quantity of the composite material on the tape from the surface of the cellulose-polypyrrole material was used to determine the adhesive nature of the material.

The solid-state characterisation was carried out with a Fourier transform infrared (FTIR) spectrometer (Spectrum 100 from PerkinElmer) equipped with an attenuated total reflectance (ATR) accessory in the range of 4000-550 cm^{-1} by the accumulation of 16 scans at a resolution of 4 cm^{-1}. In the case of Raman Spectroscopy, a RamanStation™ 400F Raman Spectrophotometer from Perkin Elmer® was used with an Echelle spectrograph and CCD detector using a 785 nm laser and a spectral range of 200-1950 cm^{-1} Raman shift. All the films were analysed using the same time of acquisition and the same number of cycles (2s x 80). Further processing of Raman spectra was conducted using Spectragryph optical spectroscopy software 1.2.8 (https://www.effemm2.de/ spectragryph/index.html). Both infrared and Raman spectra were normalised for their comparison.

Thermogravimetric analysis (TGA) was used to determine the thermal stability of the films using a thermogravimetric analyser Q5000 V3.17 build 265 from TA Instruments. Experiments were carried out with a heating rate of 10 °C min^{-1} ranging from 30 to 500 °C under dinitrogen flow at 25 mL min^{-1}. A platinum pan was used as the sample holder. Analysis performed by A. Brownlie or Dr S. Huq.

The ^{35}Cl NMR spectra of the cellulose-ILs mixtures were acquired on a Bruker Ascend™ 600 spectrometer with a frequency of 59 MHz and the ^{31}P NMR spectra were acquired on a Bruker Spectrospin 400 Ultrashield spectrometer with a frequency of 162 MHz. Both measurements were carried out at room temperature. Measurements carried out by R. Murphy.

Topography and morphology characteristics were studied using a FEI Quanta FEG Scanning Electron Microscopy (SEM) attached with Energy Dispersive X-Ray (EDX) spectrometer and Everhart Thorley Detector (ETD) or Backscattered electrons detector (BSED). The composite films were sputtered 40 s with gold using a sputtering machine prior to the examination.

The tensile strength of dried films with a thickness between 0.3 and 0.4 mm was performed using a tensile analyser (Instron 5564). The analysis was performed at room

temperature at a speed of 5 mm min^{-1} using a sample with a rectangular shape and size of 10 x 15 mm.

Potentiostat Autolab PGSTAT302N from Eco Chemie with GPES software was used to conduct the cyclic voltammetry (CV) technique. CV studies were performed using three electrodes cell, using platinum wires as reference and counter electrodes and the composite films as the working electrode. The potential range chosen was from – 1.0 V to + 0.5 V *vs.* platinum at a scan rate of 20 mV s^{-1} in 0.1 M KCl solution.

Chapter 4, 5 and 6

- Electrochemical Study of Ionic Liquids as Electrolytes

The water content of the ILs was determined by Karl Fischer titration method, by the well-known Bunsen reaction which is used to determine sulphur dioxide in aqueous solutions. After a few modifications, the reaction used for this titration is displayed as Equation A. 1, where the alcohol (*e.g* methanol), as the solvent of the sample analysed, reacts with SO_2 and a base (*e.g.* imidazole) to form an intermediate alkylsulfite salt, which is then oxidised by iodine to an alkylsulfate salt in the presence of water. The quantity of water present in the sample is calculated based on the amount of iodine consumed in the titration by an electrode [363,314]. Analysis carried out by A. Brownlie or Dr S. Huq.

$$H_2O + I_2 + BaseH^+SO_3^- + Base \rightarrow 2BaseH^+I^- + BaseH^+SO_4^-$$ Equation A. 1

Potentiostat Autolab PGSTAT302N from Eco Chemie with GPES software was used to conduct the cyclic voltammetry (CV) technique for the electrochemical characterisation of the ILs ($[C_2mim][NTf_2]$ and $[C_2mim][FAP]$) as the electrolytes. CV studies were performed using a three-electrode cell *i.e.* platinum wire as the counter electrode, a non-aqueous $Ag|Ag^+$ as the reference electrode and platinum. (Pt, 99.95% purity), gold (Au, 99.95% purity) and glassy carbon (GC) as the working electrodes. The diameter for each electrode was: Pt = 1.6 mm, Au = 1.6 mm and GC = 3.0 mm. All the measurements were carried out passing through the cell an Argon current. Neat and ferrocene ILs mixtures were analysed; the electrolytes were stirred for 1 minute and then, they were settled down for 2 minutes before each electrochemical measurement. After every CV measurement, the working electrodes

were polished using alumina-polishing micro cloth (tan, velvet) with an alumina slurry and rinsed with acetonitrile. In the case of the Pt wire (counter electrode), it was cleaned at a red-hot flame using a Bunsen torch until it was incandescent. The reference electrode ($Ag|AgNTf_2$ in $[C_2mim][NTf_2]$) was washed with acetonitrile and kept in contact with $[C_2mim][NTf_2]$ while it was stored.

- Electrochemical Study of the Supercapacitors Fabricated

Potentiostat Autolab PGSTAT302N from Eco Chemie with GPES software was used to conduct the cyclic voltammetry and galvanostatic charge-discharge experiments. CV (potentiodynamic mode) and GCD (galvanostat mode) were performed using a two-electrode system of the flexible supercapacitors fabricated. The same instrument was used for electrochemical impedance spectroscopy measurements with a built-in frequency response analyser (FRA), the frequency was logarithmically swept from 100 kHz to 10 mHz with an AC perturbation of 10 mV at OCP. All electrochemical characterisations were carried out at 25 ± 2 ºC and three sets of each device (EDLS, ES and HS) were fabricated identically and tested to study reproducibility.

Chapter 7 (Measurements carried out at Tuft's University)

- Synthesis of Ionic Liquid Gels

UV radiator Spectronic Corp., 8 W, applying a longwave UV radiation at 365 nm was utilised for the polymerisation of the polymer to obtain an ionic liquid gel.

- Electrochemical Study of the Supercapacitors Fabricated

Cyclic voltammetry (CV), galvanostatic charge-discharge (GCD) and electrical impedance spectroscopy (EIS) were performed using a potentiostat with a built-in frequency response analyser (VersaSTAT 3, Princeton Applied Research).

Appendix B: Theory of the Characterisation Techniques

B.1. Vibrational Spectroscopy: FTIR and Raman

Vibrational spectroscopy is a valuable tool for the elucidation of molecular structures which studies the interaction of the electromagnetic radiation with matter [364]. There are three principal methods by which the molecular vibrations may be

studied namely infrared, Raman and inelastic neutron scattering spectroscopies (in this thesis the technique infrared and Raman were utilised).

Depending on the energy of the radiation and its mechanism of interaction with the matter, a molecule containing *N* atoms (Cartesian coordinate system as reference) has 3*N* degrees of freedom or motions which excluding rotational and translational motions of zero frequency, is 3*N*-6 in general and 3*N*-5 for linear molecules (the third rotation is the molecular axis itself) which represent the internal vibration of the molecule [269]. Vibrational spectroscopy selection rules can be based on the group theory which will reveal the molecular symmetry and can predict if a molecule is active in infrared and/or Raman spectroscopy [365].

Infrared Spectroscopy

Infrared spectroscopy is based on an absorption process, detecting vibrations involving a change in the dipole moment of the molecule [366], in other words, for a molecular motion to be detected by infrared spectroscopy, an oscillating dipole moment should be producing during the vibration.

The technique consists of passing through a sample an electromagnetic radiation which interacts with the matter; this radiation is absorbed only for the specific frequencies corresponding to the vibrational modes of the molecule and which fulfil the infrared selection rules (IR-active modes); therefore, the radiation absorbed by the sample is attenuated and by measuring the intensity of the transmitted radiation at each frequency, the IR-active modes can be determined [367].

Originally infrared was obtained by a standard IR spectrometer (dispersive scanning spectrophotometer) but, currently, an interferometer is used which can measure all the frequencies simultaneously, resulting in an interferogram that is resolved by Fourier transformation and a spectrum can be obtained. Furthermore, a sampling technique called attenuated total reflection (ATR) can be attached to the IR and the direct examination of the solid and liquid sample can be carried out without further preparation. ATR is based on a total internal reflection after the infrared radiation is introduced into a crystal of high refractive index, resulting in an evanescent wave that reflects the internal surface in contact with the sample; the distortion of the evanescent wave by the sample is measured producing a spectrum [368].

Raman Spectroscopy

Raman spectroscopy is based on an inelastic scattering process, detecting vibrations involving a change in the molecule polarisability *i.e.* a change in the volume occupied by the molecule must happen [366]. A sample is illuminated with a monochromatic laser beam which interacts with the molecules of the sample and originated a scattered light; when light is scattered from a molecule most photons are elastically scattered (scattered photons with the same energy than the incident photons) and a small fraction of light is scattered at different energy (frequencies), inelastic scattering, which can be lower or higher than the energy of the incident photons, this process of inelastic scattering is known as Raman effect and can originate a change in vibrational energy of the molecule [369]. The difference in energy between the Raman scattered (Stokes (low energy) or Anti-Stokes Raman scattering (high energy)) and the incident photon is equal to the energy of a vibration of the scattering molecule which will be plot as Raman shift in wavenumbers *vs.* the intensity of scattered light to obtain a Raman spectrum.

The selections rules for Raman spectroscopy differ from the infrared selection rules, in contrast to IR, a variation in molecular polarisability is the requirement of Raman scattering, for example, homonuclear diatomic molecules show a Raman spectrum since the stretching vibration change the polarisability of the molecule, on the contrary, in the IR spectrum will not appear any vibration mode as they do not have a dipole moment. It is known that for highly symmetric molecules (with a centre of inversion) the molecular vibrations are active in IR but not in Raman and *vice versa*. Also, vibrational modes of molecules of low symmetry are likely to be active in both IR and Raman spectroscopy [364].

B.2. Morphology and Elemental Analysis: SEM and EDX

Scanning electron microscopy (SEM) is a powerful technique for the examination of the morphology and topography of a sample which proportionates a surface image with high magnification and with good depth that can be also analysed. The basis of this technique is that a suitable source shoots a high-energy electron beam which is converted in a thin beam of electrons (after passing through a high voltage accelerator (*e.g.* 20 kV), electromagnetic lenses and a system of apertures) that

scans the surface of the sample and with a detector the outcoming electrons emitted [370]. The electrons emitted can be: (i) secondary electrons which are the low energy electrons (close to the surface of the atom) detected by an Everhart-Thornley detector (ETD) or, (ii) backscattered electrons which are the high energy electrons (elastic scattering, internal electrons) detected by a Backscatter electron detector (BSD) [371].

A complementary technique to SEM is the energy dispersive X-Ray (EDX) which can determine the composition of the sample shown in the SEM image. The principle is based on the generation of X-Rays within the specimen by the electron beam, therefore, the elemental composition of the sample can be identified because each element has a characteristic X-Ray line(s) [372].

As it was explained in section 3.2.2, the need for sputtering the polymeric matrix composite films with an electrically conducting material such as gold relies on preventing the charging effect during measurement. The sputtering method consists of introducing a controlled gas, *e.g* argon, into a vacuum chamber where there is an electrically energising cathode to establish a self-sustaining plasma with the material to be deposited *e.g.* gold and the sample which is placed previously. The gas atoms lose electrons inside the plasma to become positively charged ions which are accelerated into the gold and strike with enough kinetic energy to dislocate atoms of the gold which constitutes a vapour stream that traverses the chamber and hits the sample, sticking to it as a coating [373].

B.3. Cyclic Voltammetry

Cyclic voltammetry is one of the most powerful and popular electroanalytical voltammetry techniques, commonly it is used to investigate the oxidation and reduction processes of molecular species in the working electrode-electrolyte interface [318].

In the cyclic voltammetry technique, a varying potential is applied to the working electrode/device and the instantaneous current obtained between the two designated potential values (switching potentials) is recorded to characterise the type of electrical or electrochemical reactions involved and, the data obtained are plotted as current (A) *vs*. potential as Figure B. 1 shows [323]. Usually, the potential scan is terminated at

the end of the first cycle, but it can be continued for any number of cycles, hence the terminology of cyclic voltammetry.

In the case of an energy storage device, the cycles obtained can differ according to the charge storage mechanism *i.e.* supercapacitors (electrical double-layer or pseudocapacitance) and batteries (faraday reactions). Figure B. 1 shows the theoretical graphs obtained when the characterisation of supercapacitors and batteries are carried out using CV. Figure B. 1 (a) shows the expected rectangular shape voltammogram of a supercapacitor due to the capacitance existence in the device (behaviour governed by Equation 1.1) that shows that the current, i, flowing through a supercapacitor is proportional to the linear variation of the scan rate, v, but independent of the potential of the device itself. Therefore, this rectangular shape of the cyclic voltammogram is an experimental criterion for qualitatively characterised the capacitive behaviour of the active material used as electrodes in the supercapacitor [11].

In contrast, a battery shows the typical oxidation and reduction current peaks on the CV which are dependent on the potential (Figure B. 1 (b)) because the battery stores charge by reduction and oxidation and/or intercalation of an ion from the electrolyte into the electrode matrix [19c].

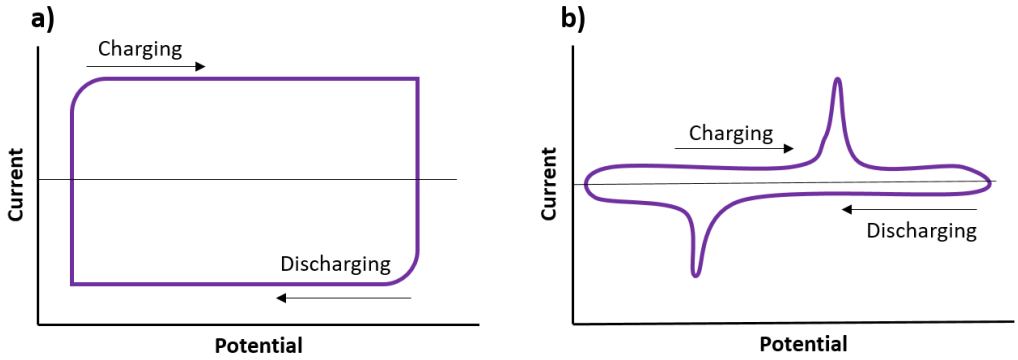

Figure B. 1 Cyclic voltammogram of (a) supercapacitor and (b) battery

B.4. Galvanostatic Charge-Discharge

In galvanostatic charge-discharge (GCD), the current is the electrical variable that is controlled by means of a galvanostat while the variation of the working electrode/device potential with the time is monitored as Figure B. 2 shows [374].

In the case of the supercapacitor and battery GCD graphs, a constant current is applied to charge (positive current) and to discharge (negative current) the energy storage device. Figure B. 2 (a) shows the GCD graph of a supercapacitor that is plotted as the operational voltage *vs.* the time during a cycle of constant charging and discharging currents; as it can be seen for a supercapacitor a triangle curve is expected (see section 4.2.2.2), in contrast, to what is obtained for a battery (Figure B. 2 (b)) which shows charge and discharge potential plateaux due to the strong dependence between the electrode reaction and the potential applied.

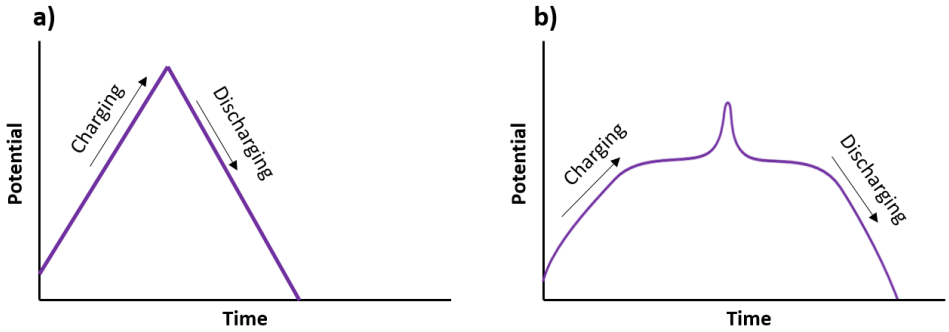

Figure B. 2 GCD plot obtained for (a) supercapacitor and (b) battery

B.5. Electrochemical Impedance Spectroscopy

Electrochemical impedance spectroscopy is a widely used technique to investigate electrochemical systems that consist in applying a sinusoidal AC excitation signal varying the frequency to the system under study and measure the AC response at each frequency [375]. The result obtained is the impedance (Z) of the system at different frequencies, expressed in ohms (Ω) and phase of impedance degrees (º).

Impedance measures the ability of a circuit to resist the flow of electrical current but, unlike resistance, impedance refers to the frequency dependent resistance to current flow of a circuit element such as resistor, capacitor or inductor. Equation B. 1 and Equation B. 2 show the impedance and resistance equations, which are based on Ohm's Law Equation B. 2 where R is the resistance at the zero frequency and as it can be seen in Equation B. 1 all the elements are frequency dependant (ω).

$$Z = {}^{E_\omega}/_{I_\omega} \qquad \text{Equation B. 1}$$

$$R = {}^{E}/_{I} \qquad \text{Equation B. 2}$$

With impedance data a complete description of an electrochemical system can be carried out, *i.e.* resistor, capacitor, inductor or any combination of these behaviours

can be analysed using EIS. As it was introduced in section 4.2.2.3 this technique is analysed by the Nyquist and Bode plot and the different behaviour in the system will be interpreted depending on the phase shift and magnitude of the AC current originated as Figure B. 3 shows [340]. In the case of a resistor (Figure B. 3 (a)), the impedance is independent of the frequency therefore the phase shift does not vary (phase shift = 0º) and, for a capacitor the current through is phase shifted by -90^0 with respect to the voltage as Figure B. 3 (b) shows [376].

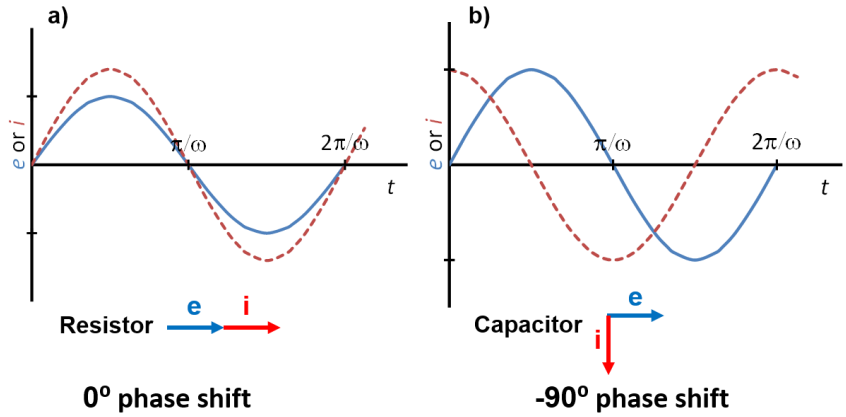

Figure B. 3 Impedance phase shift corresponded to (a) resistor and (b) capacitance behaviour

Appendix C: Synthesis and Characterisation of Ionic Liquids

C.1. Synthesis Ionic Liquids

1-butyl-3-methylimidazolium chloride [C$_4$mim]Cl

Figure C. 1 shows the synthesis of [C$_4$mim]Cl, which was carried out by the quaternisation reaction as described in the literature [377].

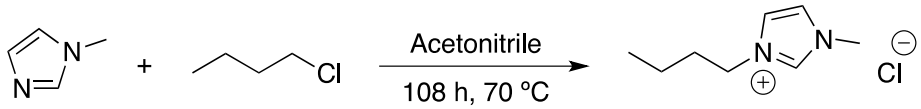

Figure C. 1 [C$_4$mim]Cl synthetic route

In a 100 mL round bottom flask equipped with a reflux condenser, and previously purged with dinitrogen, 1-methylimidazole (102.6 g, 1.2 mol) was added and dissolved in 100 mL of acetonitrile. After that, the addition of 1-chlorobutane (127.2 g, 1.3 mol) was carried out and the mixture was stirred and heated at 70 ºC for 108 hours. After the reaction was completed, the acetonitrile was removed by evaporation under reduced pressure on a heating bath at 40 ºC. Remaining yellow and viscous liquid was washed with ethyl ethanoate (3 x 160 mL) and with diethyl

ether (3 x 60 mL). The solvents were removed by evaporation under reduced pressure on a heating bath at 40 ºC and then, the product was dried under vacuum at 60 ºC during 72 hours to yield the pure ionic liquid [C_4mim]Cl (198.7 g, 93%) as a pale yellow solid.

1-butyl-3-methylimidazolium ethanoate [C_4mim][C_1COO]

Figure C. 2 shows the synthesis of [C_4mim][C_1COO], which was carried out by two metathesis reactions where the anion was exchanged as was described in the literature [378].

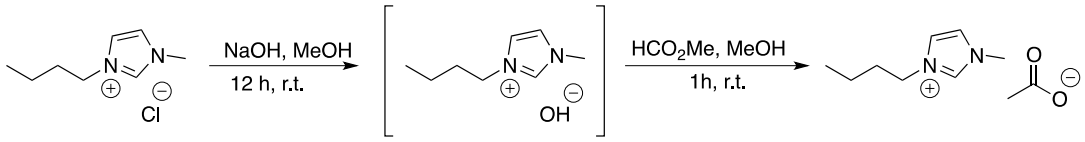

Figure C. 2 [C_4mim][C_1COO] synthetic route

Firstly, 1-butyl-3-methylimidazolium chloride was dried under vacuum at 70 ºC for 24 hours. In a 2-neck round bottom flask equipped with a reflux condenser, on the upper part, and previously purged, 1-butyl-3-methylimidazolium chloride (7.05 g, 40.36 mmol) was dissolved in 15 mL of methanol. A solution of sodium hydroxide (1.66 g, 41.45 mmol) in 5 mL of methanol was added to the previous solution and was stirred and heated at 40 ºC for 12 hours. After 12 hours, the white precipitate was removed by filtration and to the filtrate solution, an acetic acid (2.35 mL, 41.45 mmol) was added and the mixture was stirred for 1 hour. The solvent was removed by evaporation under reduced pressure on a heating bath at 50-60 ºC remaining a lightning yellow and viscous liquid. To purify the ionic liquid, dichloromethane was added (4x10 mL) and the white precipitate formed was filtrated three times until the precipitate was not seen when the dichloromethane was added. The solvent was removed by evaporation under reduced pressure on a heating bath at 30-60 ºC and then was dried under vacuum at 60 ºC during 24 hours to yield the pure ionic liquid [C_4mim][C_1COO] (7.39 g, 92%) as a pale yellow and viscous liquid.

Trihexyl(tetradecyl)phosphonium bis{(trifluoromethyl)sulfonyl}amide [$P_{6\,6\,6\,14}$][NTf_2]

Figure C. 3 shows the synthesis method for [$P_{6\,6\,6\,14}$][NTf_2], which was carried out by the quaternisation reaction as described in the literature [379].

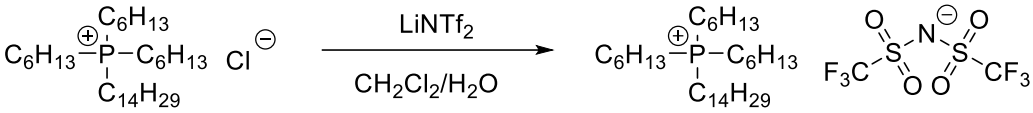

Figure C. 3 [$P_{6\,6\,6\,14}$][NTf_2] synthetic route

Lithium bis{(trifluoromethyl)sulfonyl}amide (9.12 g, 31.77 mmol) dissolved in the minimum quantity of water was added to a flask containing a solution of tetradecyltrihexylphosphonium chloride (15.00 g, 28.88 mmol) in dichloromethane (40 mL). The reaction mixture was stirred for 24 h at room temperature. Volatiles were removed in vacuum and the resulting oil was dissolved in dichloromethane (50 mL) and washed with aliquots of distilled water (5 x 15 mL). The organic layer was dried over anhydrous Na_2SO_4 and the volatiles were removed in vacuum to afford tetradecyltrihexylphosphonium bis{(trifluoromethyl)sulfonyl}amide (20.40 g, 84%) as a pale-yellow oil.

C.2. Characterisation of the Ionic Liquids Synthesised

Characterisation of [C_4mim]Cl

The ionic liquid [C_4mim]Cl was characterised by ^{1}H NMR and ^{13}C NMR using chloroform-*d* as a solvent on a spectrometer (Bruker 300 MHz) for the determination of molecular structures.

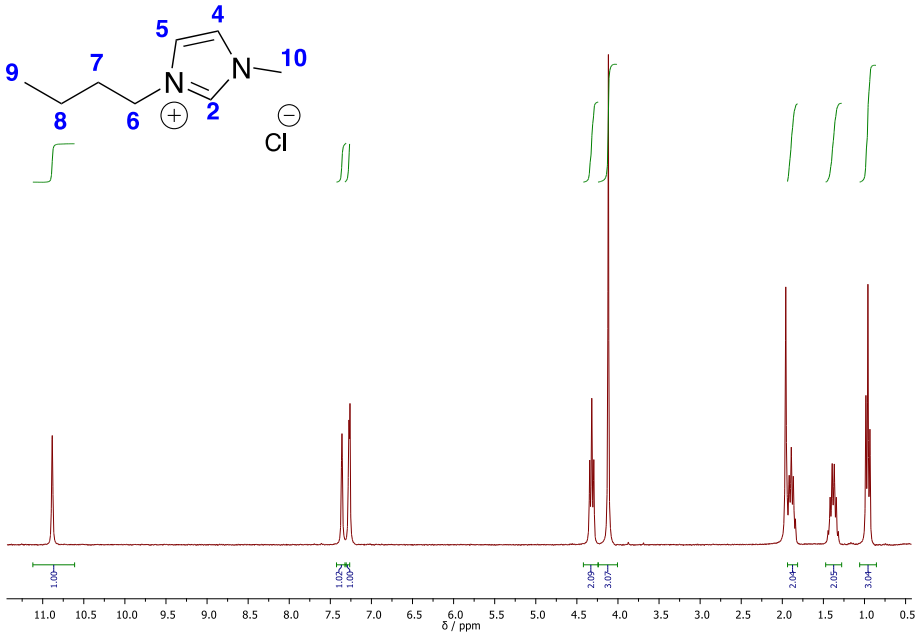

Figure C. 4 ^{1}H NMR of [C_4mim]Cl

The proton assignation for the [C_4mim]Cl from Figure C. 4 was as follows, ^{1}H NMR ($CDCl_3$): δ 10.83 (H2, s, 1H), 7.30 (H5, s, 1H), 7.22 (H4, s, 1H), 4.26 (H6, t, J=7.3 Hz, 2H), 4.06 (H10, s, 3H), 1.88-1.76 (H7, m, 2H), 1.42-1.22 (H8, m, 2H), 0.90 (H9, t, *J*=7.3 Hz, 3H).

In the case of the Figure C. 5 the carbon assignation for the [C_4mim]Cl was ^{13}C NMR ($CDCl_3$): δ 137.82 (C2), 124.11 (C4), 122.44 (C5), 49.89 (C6), 36.70 (C10), 32.37 (C7), 19.63 (C8), 13.64 (C9).

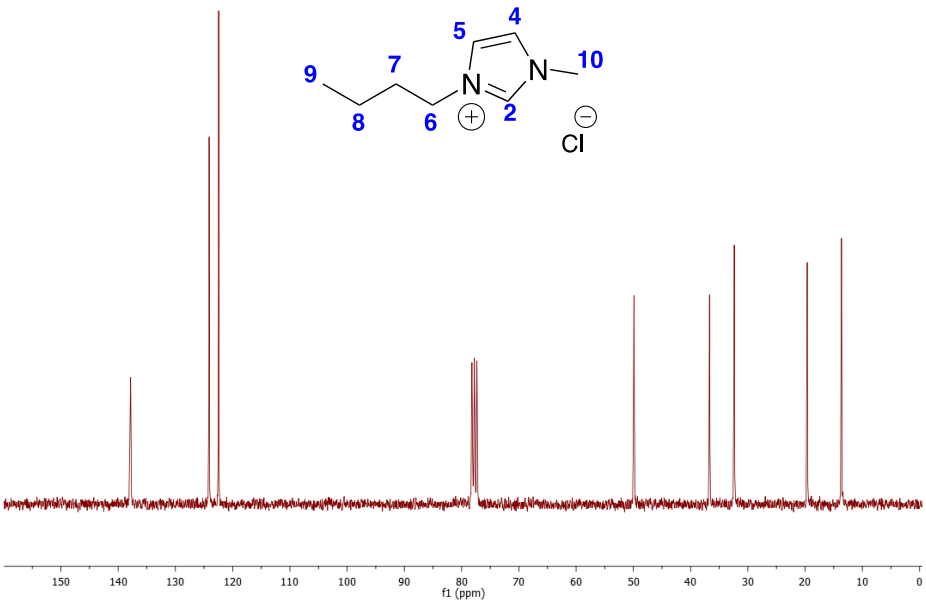

Figure C. 5 ^{13}C NMR of [C_4mim]Cl

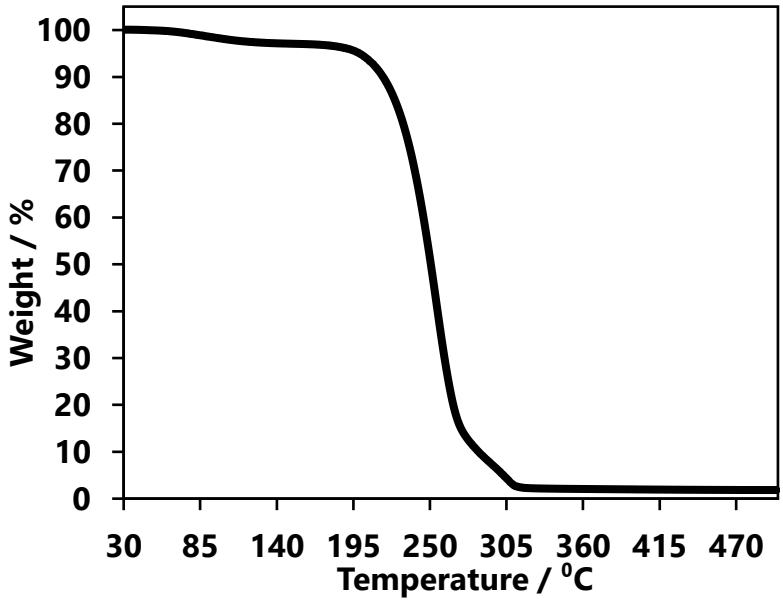

Figure C. 6 TGA thermogram of [C_4mim]Cl

In the case of the TGA graph for this IL, Figure C. 6, the decomposition temperature obtained was 224.81 ^{0}C. Figure C. 7 shows the DSC thermogram of the ionic liquid [C_4mim]Cl with a melting point of 67.73 ^{0}C and the glass transition temperature -49.17 ^{0}C. The thermal analysis was in agreement with the literature [260a].

All the DSC thermograms for the characterisation of the ILs synthesised were obtained with a differential scanning calorimeter to get the thermal behaviour of the ionic liquid using a DSC Q2000 model FC100 from TA Instruments. The experiment was carried out with a cooling/heating rate of 5 ºC min^{-1} ranging from -90 ºC to 50 º, 100 ºC or 150 ºC (depending on the thermal stability of the IL) under nitrogen flow at 50 mL min^{-1}. An aluminium hermetic pan was used as the sample holder.

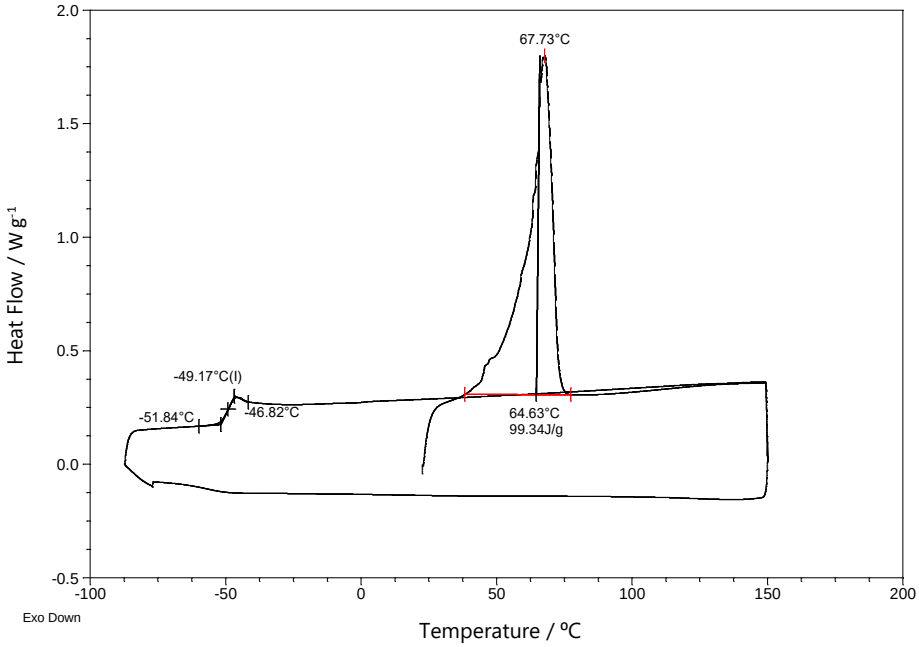

Figure C. 7 DSC thermogram of [C_4mim]Cl

Characterisation of [C_4mim][C_1COO]

The ionic liquid [C_4mim][C_1COO] was characterised by ^{1}H NMR and ^{13}C NMR using chloroform-*d* as a solvent on a spectrometer (Bruker 300 MHz) for the determination of molecular structures.

Figure C. 8 shows the ^{1}H NMR spectrum of the [C_4mim][C_1COO] with the following assignation ^{1}H NMR ($CDCl_3$): δ 10.68 (H2, s, 1H), 7.44 (H5, s, 1H), 7.31 (H4, s, 1H), 4.05 (H6, t, *J*=7.3 Hz, 2H), 3.83 (H10, s, 3H), 1.71 (H1', s, 3H), 1.68-1.58 (H7, m, 2H), 1.17-1.05 (H8, m, 2H), 0.69 (H9, t, *J*=7.3 Hz, 3H).

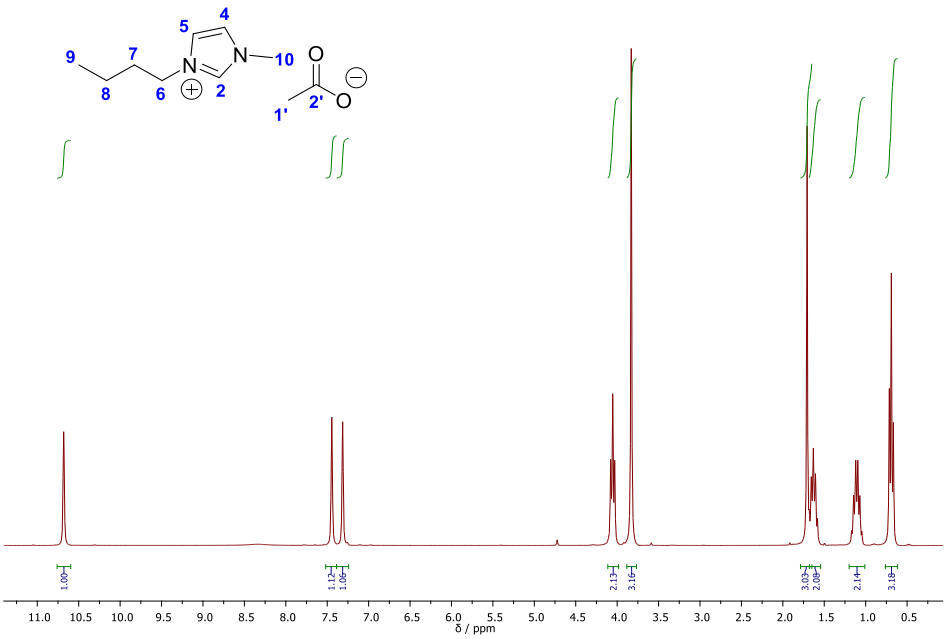

Figure C. 8 ^{1}H NMR of [C_4mim][C_1COO]

For the ^{13}C NMR spectrum from Figure C. 9 the assignation was, ^{13}C NMR ($CDCl_3$): δ 177.23 (C2'), 139.16 (C2), 123.67 (C4), 122.05 (C5), 49.55 (C6), 36.24 (C10), 32.20 (C7), 25.52 (C1'), 19.44 (C8), 13.46 (C9).

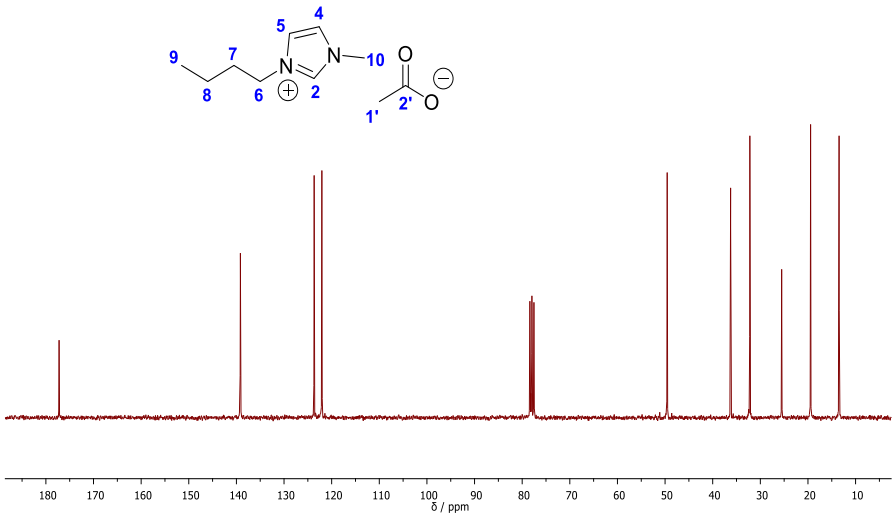

Figure C. 9 ^{13}C NMR of [C_4mim][C_1COO]

Thermal analysis was carried out by thermogravimetric analysis (TGA) and differential scanning calorimetry (DSC). The decomposition temperature of [C_4mim][C_1COO] was obtained from the thermogravimetric analysis. As it can be seen in Figure C. 10 there are like two curves, the first curve, over 100 °C, corresponds to the water entrapped in the ionic liquid and, the second curve corresponds to the decomposition of the ionic liquid, 206.45 °C.

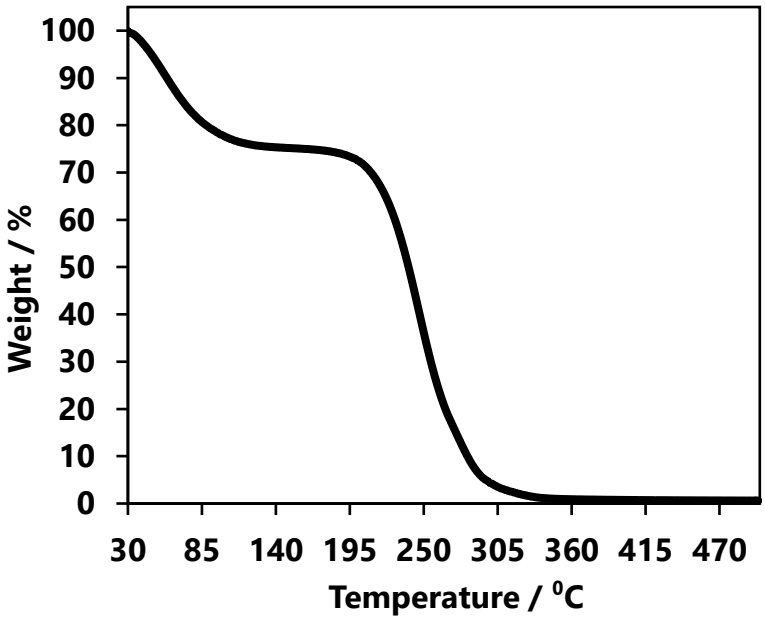

Figure C. 10 TGA thermogram of [C_4mim][C_1COO]

Figure C. 11 shows the DSC thermogram of [C_4mim][C_1COO]. It can be seen in the spectrum one peak, -74-59 ºC, corresponding to the glass transition of the IL that is liquid at room temperature. From the literature [380], it is known that the peak of crystallization for acetic acid appears at -16.63 ºC, which was absent in this thermogram, therefore, the ionic liquid did not contain an excess of acetic acid.

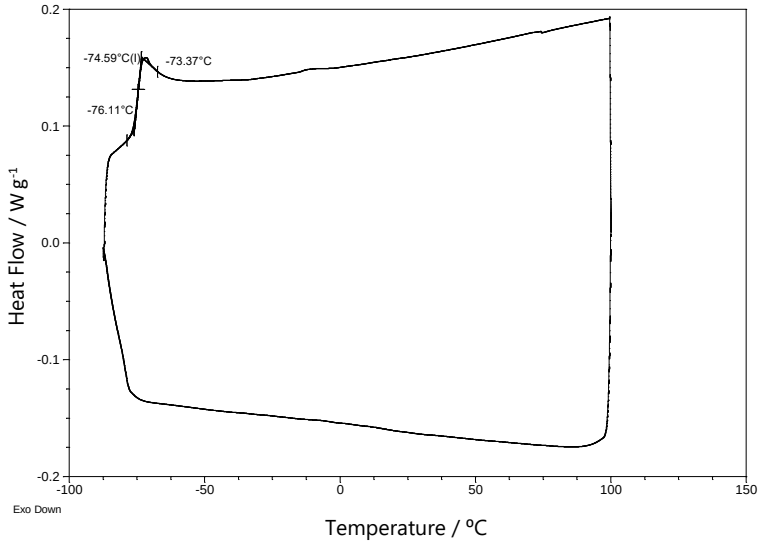

Figure C. 11 DSC thermogram of [C_4mim][C_1COO]

To know the number of impurities that may have retained in the ionic liquid [C_4mim][C_1COO], in terms of salts (NaCl) a metal analysis were carried out. Inductive Coupled Plasma (ICP) was used to quantify the Na content in the ionic liquid. The result was 870 ppm of Na. This impurity is due to the metathesis reaction where the

Cl^- anion is changed for HO^- anion forming NaCl as a byproduct and is challenging to remove completely. This sodium content may have an impact on the various processes carried out using this ionic liquid. Alternate methods will be employed to synthesise ILs pure from NaCl impurities

Characterisation of $[P_{6\,6\,6\,14}][NTf_2]$

The ionic liquid $[P_{6\,6\,6\,14}][NTf_2]$ was characterised by ^1H NMR and ^{13}C NMR using chloroform-*d* as a solvent for the determination of molecular structure.

NMR spectra (Figure C. 12 and Figure C. 13) were compared with the data found in the literature confirming that the anion exchange was carried out and $[P_{6\,6\,6\,14}][NTf_2]$ was obtained [381]. The peak that identifies the structure desired is shown in the ^{13}C NMR, this peculiar peak is a quartet at 120.32 ppm corresponded to the group $–CF_3$ in the anion NTf_2.

^1H NMR ($CDCl_3$): δ 2.10-2.06 (H2, m, 8H), 1.48-1.19 (H3, m, 48H), 0.89 (H4, q, *J*=6.7 Hz, 12H).

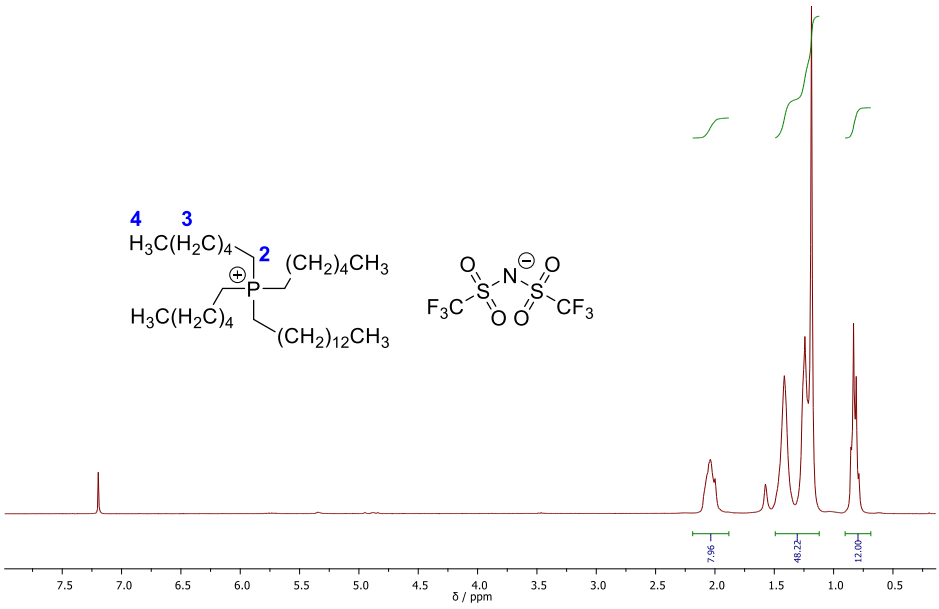

Figure C. 12 ^1H NMR spectrum of $[P_{6\,6\,6\,14}][NTf_2]$

^{13}C NMR ($CDCl_3$): δ 120.32 (C3, q, *J*=321.8 Hz, 12H), 32.31, 31.63-30.41 (m), 30.41-29.44 (m), 29.17, 23.07, 22.65, 21.84 (d, *J*=4.4 Hz), 19.34, 18.71, 14.48, 14.19.

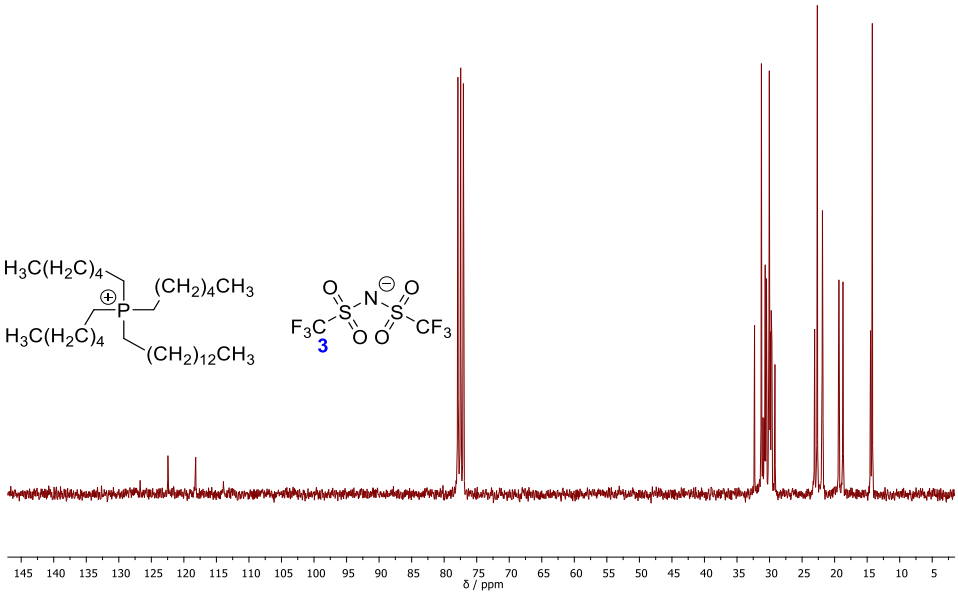

Figure C. 13 ^{13}C NMR of $[P_{6\,6\,6\,14}][NTf_2]$

Table C. 1 shows the data obtained from the elemental analysis. The experimental values correspond with the theoretical values confirming that the structure corresponds to $[P_{6\,6\,6\,14}][NTf_2]$. Halogens analysis were summit (F and Cl) to have all the data corresponded to this ionic liquid but the analysis was not done because of the high fluorine quantity in the sample that can damage the oxygen flask.

Table C. 1 Elemental analysis obtained from the ionic liquid $[P_{6\,6\,6\,14}][NTf_2]$

$[P_{6\,6\,6\,14}][NTf_2]$	C	H	N	S
Theoretical / %	53.45	8.97	1.83	8.39
Experimental / %	53.52	9.43	1.66	8.29

The decomposition temperature of $[P_{6\,6\,6\,14}][NTf_2]$ was obtained using a thermogravimetric analyser. As it can be seen in Figure C. 14 there is just one curve corresponded to the decomposition of the ionic liquid, 314.86 ºC [265].

Figure C. 15 shows the DSC thermogram of $[P_{6\,6\,6\,14}][NTf_2]$. The cycle consisted of firstly cooling and then heating and was possible to see the freezing point (exothermic peak, cooling part) at -76.71 ºC and the melting point (endothermic peak, heating part) at -71.91 ºC [267].

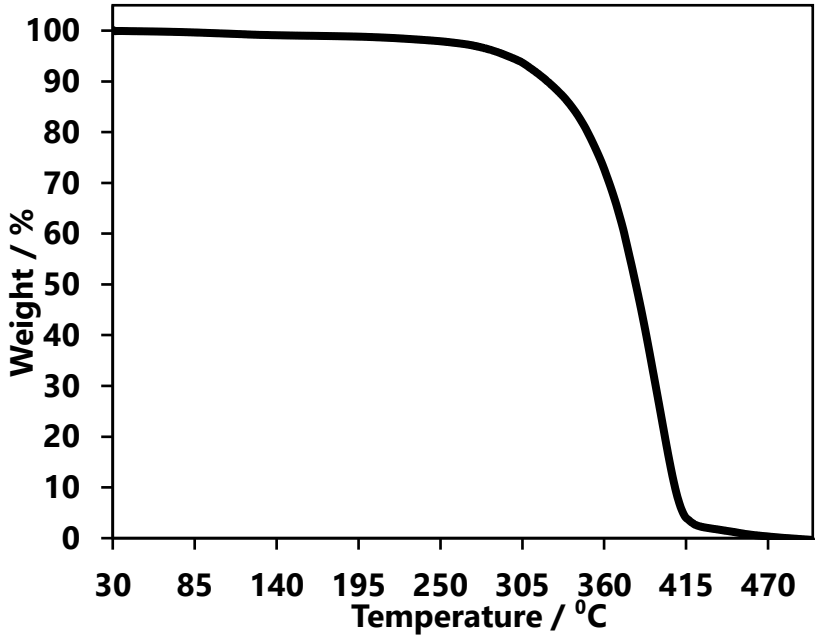

Figure C. 14 TGA thermogram of $[P_{6\,6\,6\,14}][NTf_2]$

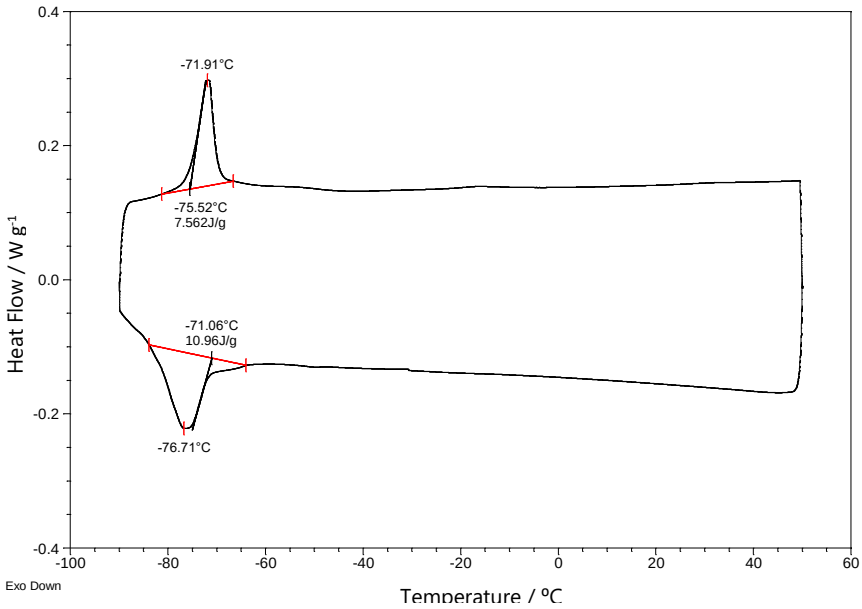

Figure C. 15 DSC thermogram of $[P_{6\,6\,6\,14}][NTf_2]$.

Appendix D: Fabrication and Calibration of an Ionic Liquid Reference Electrode

D.1. Fabrication of an IL Reference Electrode

The fabrication of an IL reference electrode was carried out based on the procedure found in the literature [307,382]. The non-aqueous reference electrode kit was purchased by BAS Bioanalytical Systems Inc.

The assembly of the reference electrode was carried out in the Glovebox under N_2 atmosphere. The non-aqueous solution chosen was 10mM of $AgNTf_2$ in $[C_2mim][NTf_2]$. Previous the assembly the Ag wire was polished with sandpaper and washed with methanol three times. The reference electrode fabricated was soaked in the IL $[C_2mim][NTf_2]$ for storing purposes.

D.2. Calibration of an IL Reference Electrode

The electrochemical experiments carried out for the calibration of the reference electrode were undertaken with a Potentiostat Autolab PGSTAT302N from Eco Chemie with GPES software, using a three electrodes cell with a Pt wire as working electrode, a large area (wire wound) counter electrode and the reference electrode prepared. The electrolyte prepared was 0.1 M of tetrabutylammonium perchlorate (TBAP) in acetonitrile and as the internal standard 10mM of Ferrocene was added to the electrolyte.

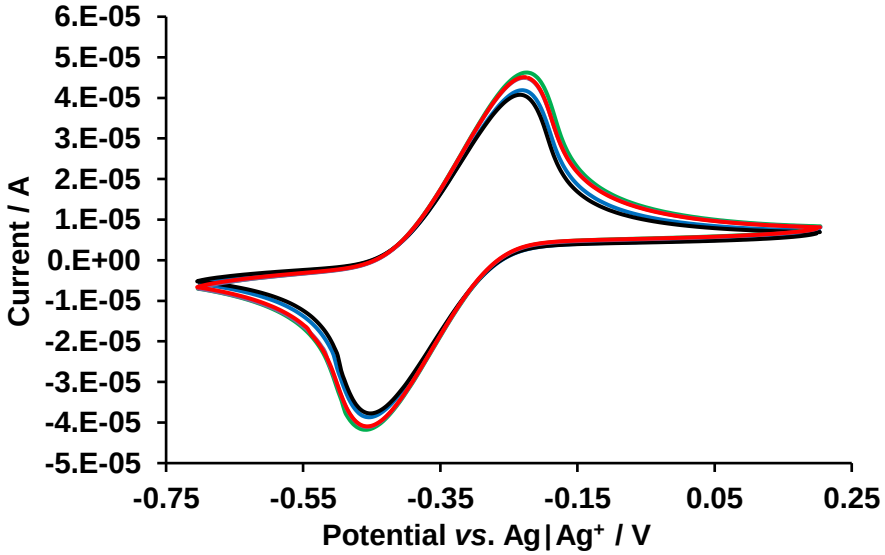

Figure D. 1 Cyclic voltammograms of $Fc|Fc^+$ (10 mM) in a solution of 0.1 M of TBAP in acetonitrile. Calibration test using the $Ag|Ag^+$ reference electrode 5 times each 15 min

The cyclic voltammetry was the technique utilised for the calibration of the reference electrode, the electrode was tested by recording cyclic voltammograms every 15 min for 5 times as Figure D. 1 shows. The measurements were carried out under an Argon blanket and at 25 ± 2 ºC.

Table D. 1 includes the $Fc|Fc^+$ cathodic and anodic peak potentials, the ferrocene peaks separation ($\Delta E_{Fc|Fc+}$) calculated using Equation 4.4 and the formal electrode potential ($E^{\circ\prime}_{Fc|Fc+}$) or also known as the half-wave potential between peaks was

calculated using Equation D. 1. The values obtained for the formal electrode potential were reproducibled (-0.343 ± 0.002 V) and they agree with the values found in the literature for the same system [307,382].

$$E^{\circ\prime}_{Fc|Fc+} = {}^{1}/_{2}\,(E_{AP} + E_{CP}) \qquad \text{Equation D. 1}$$

Table D. 1 Formal electrode potential of $Fc|Fc^{+}$ (10 mM) in 0.1 M TBAP in acetonitrile. Platinum WE vs. $Ag|Ag^{+}$ (10mM of $AgNTf_2$ in $[C_2mim][NTf_2]$) at the scan rate of 0.05 V s^{-1}

Test	E_{CP} / V	E_{AP} / V	$\Delta E_{Fc\|Fc+}$ /V	$E^{\circ\prime}_{Fc\|Fc+}$ / V
1	-0.452	-0.239	-0.691	-0.346
2	-0.455	-0.225	-0.680	-0.340
3	-0.451	-0.236	-0.687	-0.344
4	-0.455	-0.23	-0.685	-0.343
5	-0.456	-0.231	-0.687	-0.344

Appendix E: Mathematical Data Treatment

In chapters 4, 5, 6 and 7 a series of statistic equations were used for the supercapacitors characterisation results as well as the integration and derivation of a curve needed for the capacitance calculation from the cyclic voltammetry and galvanostatic charge-discharge measurements, respectively.

E.1. Statistics: The Mean and the Standard Deviation

The mean and standard deviation reported in this Thesis were calculated using Microsoft Office Excel.

The following rules can be applied when all the uncertainties are random and small, for N measurements/quantities, x_i,..., x_N of the same x, performed with the same method [383].

The mean (arithmetic average) can be defined using Equation E. 1 and it is considered the best estimation for x.

$$\bar{x} = \frac{1}{N}\sum\sum_{i=1}^{i=N} x_i \qquad \text{Equation E. 1}$$

The standard deviation is defined by Equation E. 2 and is related to the variance of a set of data values, x.

$$\sigma_x = \sqrt{\frac{1}{N-1}\sum_{i=1}^{i=N}(x_i - \bar{x})^2}$$ Equation E. 2

E.2. Integral under the Curve

The integral ($\int_{V_i}^{V_f} I(V)dV$) under the discharge curve between two selected points in a cyclic voltammetry graph needed for the Equation 4.8 was performed by the GPES program.

E.3. Derivation of a Curve

The derivation ($^{dV}/_{dt}$) needed for Equation 4.9 was obtained from the slope of the discharge curve from a galvanostatic charge-discharge using Microsoft Excel

References

[1] Mendes, T.C., Zhou, F., Barlow, A.J., Forsyth, M., Howlett, P.C. and MacFarlane, D.R., "An ionic liquid based sodium metal-hybrid supercapacitor-battery", *Sustainable Energy & Fuels* **2** (4), 763-771 (2018).

[2] Wang, Z.L., "Triboelectric Nanogenerators as New Energy Technology for Self-Powered Systems and as Active Mechanical and Chemical Sensors", *ACS Nano* **7** (11), 9533-9557 (2013).

[3] Simon, P. and Gogotsi, Y., "Materials for electrochemical capacitors", *Nat. Mater.* **7** (11), 845-854 (2008).

[4] Sakai, M. and Amano, M., *Energy Storage Devices and Systems*, Hitachi Chemical Technical Report (2013).

[5] Winter, M. and Brodd, R.J., "What Are Batteries, Fuel Cells, and Supercapacitors?", *Chem. Rev.* **104** (10), 4245-4270 (2004).

[6] Whittingham, M.S., "Lithium Batteries and Cathode Materials", *Chem. Rev.* **104** (10), 4271-4301 (2004).

[7] Hiroshi, K., Youichi, M. and Hirokazu, C., "Base-Metal Electrode-Multilayer Ceramic Capacitors: Past, Present and Future Perspectives", *Jpn. J. Appl. Phys.* **42** (1R), 1 (2003).

[8] Frackowiak, E. and Beguin, F., "Carbon materials for the electrochemical storage of energy in capacitors", *Carbon* **39** (6), 937-950 (2001).

[9] Zhang, Y., Feng, H., Wu, X., Wang, L., Zhang, A., Xia, T., Dong, H., Li, X. and Zhang, L., "Progress of electrochemical capacitor electrode materials: A review", *Int. J. Hydrogen Energy* **34** (11), 4889-4899 (2009).

[10] Srinivasan, A., Sharan, S. and Sandhu, G.S., *Methods of forming a silicon nitride film, a capacitor dielectric layer and a capacitor*, US Pat. 5882978A (1999).

[11] Chen, G.Z., "Understanding supercapacitors based on nano-hybrid materials with interfacial conjugation", *Prog. Nat. Sci.: Mater. Int.* **23** (3), 245-255 (2013).

[12] Goodenough, J.B. and Park, K.-S., "The Li-Ion Rechargeable Battery: A Perspective", *J. Am. Chem. Soc.* **135** (4), 1167-1176 (2013).

[13] Li, X. and Wei, B., "Supercapacitors based on nanostructured carbon", *Nano Energy* **2** (2), 159-173 (2013).

[14] Ragone, D.V., in 'Review of Battery Systems for Electrically Powered Vehicles' (1968).

[15] (a) Helmholtz, H., "Studien über electrische Grenzschichten", *Annalen der Physik* **243** (7), 337-382 (1879); (b) Trasatti, S. and Kurzweil, P., "Electrochemical supercapacitors as versatile energy stores", *Platin. Met. Rev.* **38** (2), 46-56 (1994).

[16] Ray, S., Garain, S., Das, S., Jana, S., De, D. and Gangopadhyay, U., "State of Art of Supercapacitor", *IJRCEE* **3** (5) (2014).

[17] Becker, H.I., *Low voltage electrolytic capacitor*, US Pat. 2800616A (1957).

[18] Rightmire, R.A., *Electrical energy storage apparatus*, US Pat. 3288641 (1966).

[19] (a) Angerstein-Kozlowska, H., Conway, B.E., Barnett, B. and Mozota, J., "The role of ion adsorption in surface oxide formation and reduction at noble metals: general features of the surface process", *J. Electroanal. Chem. Interfacial Electrochem.* **100**, 417-446 (1979); (b) Conway, B.E., "The evaluation and use of

properties of individual ions in solution", *J. Solution Chem.* **7** (10), 721-770 (1978); (c) Conway, B.E., "Transition from "supercapacitor" to "battery" behavior in electrochemical energy storage", *J. Electrochem. Soc.* **138** (6), 1539-1548 (1991); (d) Conway, B.E., Angerstein-Kozlowska, H., Sattar, M.A. and Tilak, B.V., "Study of a decomposing hydride phase at nickel cathodes by measurement of open-circuit potential decay", *J. Electrochem. Soc.* **130** (9), 1825-1836 (1983); (e) Hadži-Jordanov, S., Angerstein-Kozlowska, H. and Conway, B.E., "Surface oxidation and H deposition at ruthenium electrodes: Resolution of component processes in potential-sweep experiments", *J. Electroanal. Chem. Interfacial Electrochem.* **60** (3), 359-362 (1975).

[20] (a) Bullard, G.L., Sierra-Alcazar, H.B., Lee, H.L. and Morris, J.L., "Operating principles of the ultracapacitor", *Magnetics, IEEE Transactions on* **25** (1), 102-106 (1989); (b) Sharma, P. and Bhatti, T.S., "A review on electrochemical double-layer capacitors", *Energy Convers. Manage.* **51** (12), 2901-2912 (2010).

[21] Wu, Z.-S., Feng, X. and Cheng, H.-M., "Recent advances in graphene-based planar micro-supercapacitors for on-chip energy storage", *National Science Review* **1** (2), 277–292 (2014).

[22] (a) Balducci, A., Bardi, U., Caporali, S., Mastragostino, M. and Soavi, F., "Ionic liquids for hybrid supercapacitors", *Electrochem. Commun.* **6** (6), 566-570 (2004); (b) Conway, B.E. and Pell, W.G., "Double-layer and pseudocapacitance types of electrochemical capacitors and their applications to the development of hybrid devices", *J. Solid State Electrochem.* **7** (9), 637-644 (2003); (c) Lu, X., Yu, M., Wang, G., Tong, Y. and Li, Y., "Flexible solid-state supercapacitors: Design, fabrication and applications", *Energy Environ. Sci.* **7** (7), 2160-2181 (2014); (d) Pandolfo, A.G. and Hollenkamp, A.F., "Carbon properties and their role in supercapacitors", *J. Power Sources* **157** (1), 11-27 (2006).

[23] Long, J.W., Bélanger, D., Brousse, T., Sugimoto, W., Sassin, M.B. and Crosnier, O., "Asymmetric electrochemical capacitors—Stretching the limits of aqueous electrolytes", *MRS Bull.* **36** (7), 513-522 (2011).

[24] Choudhary, N., Li, C., Moore, J., Nagaiah, N., Zhai, L., Jung, Y. and Thomas, J., "Asymmetric Supercapacitor Electrodes and Devices", *Adv. Mater.* **29** (21), 1605336-n/a, Article ID 1605336 (2017).

[25] Tasaki, S., Ando, N., Nagai, M., Shirakami, A., Matsui, K. and Hato, Y., *Lithium ion capacitor*, US Pat. 7697264B2 (2010).

[26] Amatucci, G., Badway, F. and DuPasquier, A., "Novel asymmetric hybrid cells and the use of pseudo-reference electrodes in three electrode cell characterization", in *Intercalation compounds for battery materials*, Eds. G.A. Nazri, M. Thackeray and T. Ohzuku (2000), pp. 344-359.

[27] Ohno, H., "Electrochemical Aspects of Ionic Liquids", (John Wiley & Sons, Inc., 2005), pp. 1-392.

[28] Parsons, R., "The electrical double layer: recent experimental and theoretical developments", *Chem. Rev.* **90** (5), 813-826 (1990).

[29] (a) Bockris, J.O.M., "The structure of water in the double layer", *Inorg. Chim. Acta* **40**, X14 (1980); (b) Stojek, Z., "The Electrical Double Layer and Its Structure", in *Electroanalytical Methods: Guide to Experiments and Applications*, Eds. F. Scholz, A.M. Bond, R.G. Compton, D.A. Fiedler, G. Inzelt, H. Kahlert, Š. Komorsky-Lovrić, H. Lohse, M. Lovrić, F. Marken, A. Neudeck, U. Retter, F.

Scholz and Z. Stojek (Springer Berlin Heidelberg, Berlin, Heidelberg, 2010), pp. 3-9.

[30] Simon, P., Taberna, P.-L. and Béguin, F., "Electrical Double-Layer Capacitors and Carbons for EDLCs", in *Supercapacitors* (Wiley-VCH Verlag GmbH & Co. KGaA, 2013), pp. 131-165.

[31] Chen, T. and Dai, L., "Flexible supercapacitors based on carbon nanomaterials", *J. Mater. Chem. A* **2** (28), 10756-10775 (2014).

[32] Beguin, F., Presser, V., Balducci, A. and Frackowiak, E., "Carbons and electrolytes for advanced supercapacitors", *Adv. Mater.* **26** (14), 2219-2251, 2283 (2014).

[33] Visentin, A.F. and Panzer, M.J., "Poly(Ethylene Glycol) Diacrylate-Supported Ionogels with Consistent Capacitive Behavior and Tunable Elastic Response", *ACS Appl. Mater. Interfaces* **4** (6), 2836-2839 (2012).

[34] Frackowiak, E., "Electrode Materials with Pseudocapacitive Properties", in *Supercapacitors* (Wiley-VCH Verlag GmbH & Co. KGaA, 2013), pp. 207-237.

[35] Ning, W., Xingxiang, Z., Haihui, L. and Benqiao, H., "1-Allyl-3-methylimidazolium chloride plasticized-corn starch as solid biopolymer electrolytes", *Carbohydr. Polym.* **76** (3), 482-484 (2009).

[36] Liu, T., Finn, L., Yu, M., Wang, H., Zhai, T., Lu, X., Tong, Y. and Li, Y., "Polyaniline and Polypyrrole Pseudocapacitor Electrodes with Excellent Cycling Stability", *Nano Lett.* **14** (5), 2522-2527 (2014).

[37] Conway, B.E., Birss, V. and Wojtowicz, J., "The role and utilization of pseudocapacitance for energy storage by supercapacitors", *J. Power Sources* **66** (1), 1-14 (1997).

[38] Deng, W., Ji, X., Chen, Q. and Banks, C.E., "Electrochemical capacitors utilising transition metal oxides: an update of recent developments", *RSC Adv.* **1** (7), 1171-1178 (2011).

[39] Wang, G., Zhang, L. and Zhang, J., "A review of electrode materials for electrochemical supercapacitors", *Chem. Soc. Rev.* **41** (2), 797-828 (2012).

[40] Wu, Z., Li, L., Yan, J.M. and Zhang, X.B., "Materials Design and System Construction for Conventional and New-Concept Supercapacitors", *Adv. Sci.* **4** (6), 1600382 (2017).

[41] Wang, Y., Shi, Z., Huang, Y., Ma, Y., Wang, C., Chen, M. and Chen, Y., "Supercapacitor Devices Based on Graphene Materials", *J. Phys. Chem. C* **113** (30), 13103-13107 (2009).

[42] Frackowiak, E., "Carbon materials for supercapacitor application", *Phys. Chem. Chem. Phys.* **9** (15), 1774-1785 (2007).

[43] Miloslav, N., Jiri, J. and Bedrich, K., 'IUPAC. Compendium of Chemical Terminology (the "Gold Book")', http://goldbook.iupac.org/index.html, (2005).

[44] Wang, Q., Yan, J. and Fan, Z., "Carbon materials for high volumetric performance supercapacitors: design, progress, challenges and opportunities", *Energy Environ. Sci.* **9** (3), 729-762 (2016).

[45] Wang, G.-X., Zhang, B.-L., Yu, Z.-L. and Qu, M.-Z., "Manganese oxide/MWNTs composite electrodes for supercapacitors", *Solid State Ion.* **176** (11–12), 1169-1174 (2005).

[46] Shi, F., Li, L., Wang, X.-l., Gu, C.-d. and Tu, J.-p., "Metal oxide/hydroxide-based materials for supercapacitors", *RSC Adv.* **4** (79), 41910-41921 (2014).

[47] MacDiarmid, A.G., ""Synthetic metals": A novel role for organic polymers (Nobel Lecture)", *Angew. Chem., Int. Ed.* **40** (14), 2581-2590 (2001).

[48] Shirakawa, H., Louis, E.J., MacDiarmid, A.G., Chiang, C.K. and Heeger, A.J., "Synthesis of electrically conducting organic polymers: halogen derivatives of polyacetylene, $(CH)_x$", *J. Chem. Soc., Chem. Commun.* (16), 578-580 (1977).

[49] Prize, N., 'The Nobel Prize in Chemistry 2000', http://www.nobelprize.org/nobel_prizes/chemistry/laureates/2000/index.html , (January, 2018).

[50] Dai, L., "Conducting Polymers", in *Intelligent Macromolecules for Smart Devices: From Materials Synthesis to Device Applications* (Springer London, London, 2004), pp. 41-80.

[51] Diaz, A.F., Kanazawa, K.K. and Gardini, G.P., "Electrochemical polymerization of pyrrole", *J. Chem. Soc., Chem. Commun.* (14), 635-636 (1979).

[52] Diaz, A.F. and Logan, J.A., "Electroactive polyaniline films", *J. Electroanal. Chem. Interfacial Electrochem.* **111** (1), 111-114 (1980).

[53] Koßmehl, G. and Chatzitheodorou, G., "Electrical conductivity of poly(2,5-thiophenediyl)-AsF5-complexes", *Die Makromolekulare Chemie, Rapid Communications* **2** (9-10), 551-555 (1981).

[54] Skotheim, T.A., *Handbook of conducting polymers* (CRC press, 1997).

[55] Guimard, N.K., Gomez, N. and Schmidt, C.E., "Conducting polymers in biomedical engineering", *Prog. Polym. Sci.* **32** (8–9), 876-921 (2007).

[56] Pringle, J.M., Ngamna, O., Chen, J., Wallace, G.G., Forsyth, M. and MacFarlane, D.R., "Conducting polymer nanoparticles synthesized in an ionic liquid by chemical polymerization", *Synth. Met.* **156** (14-15), 979-983 (2006).

[57] Gurunathan, K., Murugan, A.V., Marimuthu, R., Mulik, U.P. and Amalnerkar, D.P., "Electrochemically synthesised conducting polymeric materials for applications towards technology in electronics, optoelectronics and energy storage devices", *Mater. Chem. Phys.* **61** (3), 173-191 (1999).

[58] Ateh, D.D., Navsaria, H.A. and Vadgama, P., "Polypyrrole-based conducting polymers and interactions with biological tissues", *J. R. Soc., Interface* **3** (11), 741-752 (2006).

[59] Bredas, J.L. and Street, G.B., "Polarons, bipolarons, and solitons in conducting polymers", *Acc. Chem. Res.* **18** (10), 309-315 (1985).

[60] (a) Håkansson, E., Lin, T., Wang, H. and Kaynak, A., "The effects of dye dopants on the conductivity and optical absorption properties of polypyrrole", *Synth. Met.* **156** (18), 1194-1202 (2006); (b) Shen, Y. and Wan, M., "In situ doping polymerization of pyrrole with sulfonic acid as a dopant", *Synth. Met.* **96** (2), 127-132 (1998).

[61] Harrison, W.A., *Solid state theory* (Dover Publications, New York, 1979).

[62] (a) Heeger, A.J., "Semiconducting and Metallic Polymers: The Fourth Generation of Polymeric Materials (Nobel Lecture)", *Angew. Chem. Int. Ed.* **40** (14), 2591-2611 (2001); (b) Inzelt, G., *Conducting polymers: a new era in electrochemistry* (Springer Science & Business Media, 2012).

[63] (a) Chen, X.B., Issi, J.P., Devaux, J. and Billaud, D., "The stability of polypyrrole and its composites", *J. Mater. Sci.* **32** (6), 1515-1518 (1997); (b) Pud, A.A., "Stability and degradation of conducting polymers in electrochemical systems", *Synth. Met.* **66** (1), 1-18 (1994).

[64] Snook, G.A., Kao, P. and Best, A.S., "Conducting-polymer-based supercapacitor devices and electrodes", *J. Power Sources* **196** (1), 1-12 (2011).

[65] Shown, I., Ganguly, A., Chen, L.-C. and Chen, K.-H., "Conducting polymer-based flexible supercapacitor", *Energy Sci. Eng.* **3** (1), 2-26 (2015).

[66] Zhong, C., Deng, Y., Hu, W., Qiao, J., Zhang, L. and Zhang, J., "A review of electrolyte materials and compositions for electrochemical supercapacitors", *Chem. Soc. Rev.* **44** (21), 7484-7539 (2015).

[67] Dyatkin, B., Presser, V., Heon, M., Lukatskaya, M.R., Beidaghi, M. and Gogotsi, Y., "Development of a Green Supercapacitor Composed Entirely of Environmentally Friendly Materials", *Chem. Sus. Chem.* **6** (12), 2269-2280 (2013).

[68] Costa, R., Pereira, C.M. and Silva, F., "Double layer in room temperature ionic liquids: influence of temperature and ionic size on the differential capacitance and electrocapillary curves", *Phys. Chem. Chem. Phys.* **12** (36), 11125-11132 (2010).

[69] Seddon, K.R., "Ionic liquids for clean technology", *J. Chem. Technol. Biotechnol.* **68** (4), 351-356 (1997).

[70] Ghafar-Zadeh, E., "Wireless Integrated Biosensors for Point-of-Care Diagnostic Applications", *Sensors* **15** (2), 3236 (2015).

[71] Belhocine, T., Forsyth, S.A., Gunaratne, H.Q.N., Nieuwenhuyzen, M., Nockemann, P., Puga, A.V., Seddon, K.R., Srinivasan, G. and Whiston, K., "Azepanium ionic liquids", *Green Chem.* **13** (11), 3137-3155 (2011).

[72] Armand, M., Endres, F., MacFarlane, D.R., Ohno, H. and Scrosati, B., "Ionic-liquid materials for the electrochemical challenges of the future", *Nat. Mater.* **8** (8), 621-629 (2009).

[73] Earle, M.J., Esperança, J.M.S.S., Gilea, M.A., Canongia Lopes, J.N., Rebelo, L.P.N., Magee, J.W., Seddon, K.R. and Widegren, J.A., "The distillation and volatility of ionic liquids", *Nature* **439**, 831 (2006).

[74] Smiglak, M., Reichert, W.M., Holbrey, J.D., Wilkes, J.S., Sun, L., Thrasher, J.S., Kirichenko, K., Singh, S., Katritzky, A.R. and Rogers, R.D., "Combustible ionic liquids by design: is laboratory safety another ionic liquid myth?", *Chem. Commun.* (24), 2554-2556 (2006).

[75] Sheldon, R., "Catalytic reactions in ionic liquids", *Chem. Commun.* (23), 2399-2407 (2001).

[76] Schneuwly, A. and Gallay, R., "Properties and applications of supercapacitors: From the state-of-the-art to future trends", *Rossens, Switzerland* (2000).

[77] Perez-Madrigal, M.M., Edo, M.G. and Aleman, C., "Powering the future: application of cellulose-based materials for supercapacitors", *Green Chem.* **18** (22), 5930-5956 (2016).

[78] Jost, K., Dion, G. and Gogotsi, Y., "Textile energy storage in perspective", *J. Mater. Chem. A* **2** (28), 10776-10787 (2014).

[79] (a) Coenen, P., Leemans, F. and Mulder, G., "Applying large electric double layer capacitor systems", *J. Appl. Electrochem.* **44** (4), 533-542 (2014); (b) Technologies, M., 'Maxwell Ultracapacitors: Enabling Energy's Future', http://www.maxwell.com/products/ultracapacitors, (2018).

[80] Zhang, X., Xue, H., Xu, Y., Chen, H. and Tan, C., "An investigation of an uninterruptible power supply (UPS) based on supercapacitor and liquid nitrogen hybridization system", *Energy Convers. Manage.* **85**, 784-792 (2014).

[81] Andrieu, X. and Poignant, P., in 'Electrical power supply circuit, in particular for portable appliances' (2000).

[82] Elliman, R., Gould, C. and Al-Tai, M., "Review of current and future electrical energy storage devices", in *2015 50th International Universities Power Engineering Conference (UPEC)* (2015), pp. 1-5.

[83] Mond, H.G. and Freitag, G., "The Cardiac Implantable Electronic Device Power Source: Evolution and Revolution", *PACE* **37** (12), 1728-1745 (2014).

[84] (a) Lorenzo, M. and Srinivasan, G., "Durable Flexible Supercapacitors Utilizing the Multifunctional Role of Ionic Liquids", *Energy Technology* **6** (1), 196-204 (2018); (b) Market Research Store, S.M.A., 'Global Market Outlook (2015-2022)', http://www.marketresearchstore.com/report/smart-materials-applications-global-market-outlook-46838, (October, 2016).

[85] Agency, U.S.E.P., 'Advancing Sustainable Materials Management: Facts and Figures', https://www.epa.gov/smm/advancing-sustainable-materials-management-facts-and-figures, (October, 2016).

[86] Pushparaj, V.L., Shaijumon, M.M., Kumar, A., Murugesan, S., Ci, L., Vajtai, R., Linhardt, R.J., Nalamasu, O. and Ajayan, P.M., "Flexible energy storage devices based on nanocomposite paper", *Proc. Natl. Acad. Sci. U. S. A.* **104** (34), 13574-13577 (2007).

[87] Jost, K., Perez, C.R., McDonough, J.K., Presser, V., Heon, M., Dion, G. and Gogotsi, Y., "Carbon coated textiles for flexible energy storage", *Energy Environ. Sci.* **4** (12), 5060-5067 (2011).

[88] Gwon, H., Kim, H.-S., Lee, K.U., Seo, D.-H., Park, Y.C., Lee, Y.-S., Ahn, B.T. and Kang, K., "Flexible energy storage devices based on graphene paper", *Energy Environ. Sci.* **4** (4), 1277-1283 (2011).

[89] Lee, K.-S., Spendelow, J.S., Choe, Y.-K., Fujimoto, C. and Kim, Y.S., "An operationally flexible fuel cell based on quaternary ammonium-biphosphate ion pairs", *Nature Energy* **1**, 16120 (2016).

[90] (a) Gao, H., Xiao, F., Ching, C.B. and Duan, H., "Flexible All-Solid-State Asymmetric Supercapacitors Based on Free-Standing Carbon Nanotube/Graphene and Mn_3O_4 Nanoparticle/Graphene Paper Electrodes", *ACS Appl. Mater. Interfaces* **4** (12), 7020-7026 (2012); (b) Karthika, P., Rajalakshmi, N. and Dhathathreyan, K.S., "Flexible Polyester Cellulose Paper Supercapacitor with a Gel Electrolyte", *Chem. Phys. Chem.* **14** (16), 3822-3826 (2013).

[91] Dong, L., Xu, C., Li, Y., Huang, Z.-H., Kang, F., Yang, Q.-H. and Zhao, X., "Flexible electrodes and supercapacitors for wearable energy storage: a review by category", *J. Mater. Chem. A* **4** (13), 4659-4685 (2016).

[92] Shi, S., Xu, C., Yang, C., Li, J., Du, H., Li, B. and Kang, F., "Flexible supercapacitors", *Particuology* **11** (4), 371-377 (2013).

[93] Gabriel, S. and Weiner, J., "Ueber einige Abkömmlinge des Propylamins", *Berichte der deutschen chemischen Gesellschaft* **21** (2), 2669-2679 (1888).

[94] (a) P., W., "Über die Molekulargrösse und elektrische Leifähigkeit einiger gesehmolzenen Salze", *Bull. Acad. Imp. Sci. Saint-Pétersbourg* **8**, 405-422

(1914); (b) Sugden, S. and Wilkins, H., "CLXVII.—The parachor and chemical constitution. Part XII. Fused metals and salts", *J. Chem. Soc.*, 1291-1298 (1929).

[95] Hurley, F., "US Pat. 4,446,331 ", *TP Wier Jr, US Pat* **4** (1948).

[96] (a) Chum, H.L., Koch, V., Miller, L. and Osteryoung, R., "Electrochemical scrutiny of organometallic iron complexes and hexamethylbenzene in a room temperature molten salt", *J. Am. Chem. Soc.* **97** (11), 3264-3265 (1975); (b) Robinson, J. and Osteryoung, R.A., "An electrochemical and spectroscopic study of some aromatic hydrocarbons in the room temperature molten salt system aluminum chloride-*n*-butylpyridinium chloride", *J. Am. Chem. Soc.* **101** (2), 323-327 (1979).

[97] Wilkes, J.S., Levisky, J.A., Wilson, R.A. and Hussey, C.L., "Dialkylimidazolium chloroaluminate melts: a new class of room-temperature ionic liquids for electrochemistry, spectroscopy and synthesis", *Inorg. Chem.* **21** (3), 1263-1264 (1982).

[98] Wilkes, J.S. and Zaworotko, M.J., "Air and water stable 1-ethyl-3-methylimidazolium based ionic liquids", *J. Chem. Soc., Chem. Commun.* (13), 965-967 (1992).

[99] Deetlefs, M., Fanselow, M. and Seddon, K.R., "Ionic liquids: the view from Mount Improbable", *RSC Adv.* **6** (6), 4280-4288 (2016).

[100] (a) Hallett, J.P. and Welton, T., "Room-temperature ionic liquids: solvents for synthesis and catalysis. 2", *Chem. Rev.* **111** (5), 3508-3576 (2011); (b) Ho, T.D., Zhang, C., Hantao, L.W. and Anderson, J.L., "Ionic Liquids in Analytical Chemistry: Fundamentals, Advances, and Perspectives", *Anal. Chem.* **86** (1), 262-285 (2014).

[101] Brandt, A., Grasvik, J., Hallett, J.P. and Welton, T., "Deconstruction of lignocellulosic biomass with ionic liquids", *Green Chem.* **15** (3), 550-583 (2013).

[102] Welton, T., "Room-Temperature Ionic Liquids. Solvents for Synthesis and Catalysis", *Chem. Rev.* **99** (8), 2071-2084 (1999).

[103] (a) M. Gordon, C., D. Holbrey, J., R. Kennedy, A. and R. Seddon, K., "Ionic liquid crystals: hexafluorophosphate salts", *J. Mater. Chem.* **8** (12), 2627-2636 (1998); (b) MacFarlane, D.R., Meakin, P., Sun, J., Amini, N. and Forsyth, M., "Pyrrolidinium Imides: A New Family of Molten Salts and Conductive Plastic Crystal Phases", *J. Phys. Chem. B* **103** (20), 4164-4170 (1999); (c) Verdia, P., Gonzalez, E.J., Rodriguez-Cabo, B. and Tojo, E., "Synthesis and characterization of new polysubstituted pyridinium-based ionic liquids: application as solvents on desulfurization of fuel oils", *Green Chem.* **13** (10), 2768-2776 (2011).

[104] Cammarata, L., Kazarian, S.G., Salter, P.A. and Welton, T., "Molecular states of water in room temperature ionic liquids", *Phys. Chem. Chem. Phys.* **3** (23), 5192-5200 (2001).

[105] Giernoth, R., "Task-Specific Ionic Liquids", *Angew. Chem. Int. Ed.* **49** (16), 2834-2839 (2010).

[106] Kasahara, S., Kamio, E., Otani, A. and Matsuyama, H., "Fundamental Investigation of the Factors Controlling the CO_2 Permeability of Facilitated Transport Membranes Containing Amine-Functionalized Task-Specific Ionic Liquids", *Ind. Eng. Chem. Res.* **53** (6), 2422-2431 (2014).

[107] Lu, W., Fadeev, A.G., Qi, B., Smela, E., Mattes, B.R., Ding, J., Spinks, G.M., Mazurkiewicz, J., Zhou, D., Wallace, G.G., MacFarlane, D.R., Forsyth, S.A. and

Forsyth, M., "Use of Ionic Liquids for π-Conjugated Polymer Electrochemical Devices", *Science* **297** (5583), 983-987 (2002).

[108] Leveque, J.M., Aminuddin, N.F., Kermanioryani, M., Mutalib, M.I.A., Lethesh, K.C. and Mazlan, F.A., "An easy, green and ultra-fast synthesis of dicationic ionic liquids: From days to minutes", *AIP Conference Proceedings* **1787** (1), 040006 (2016).

[109] Visser, A.E., Swatloski, R.P., Reichert, W.M., Mayton, R., Sheff, S., Wierzbicki, A., Davis, J.J.H. and Rogers, R.D., "Task-specific ionic liquids for the extraction of metal ions from aqueous solutions", *Chem. Commun.* (1), 135-136 (2001).

[110] Yue, C., Fang, D., Liu, L. and Yi, T.-F., "Synthesis and application of task-specific ionic liquids used as catalysts and/or solvents in organic unit reactions", *J. Mol. Liq.* **163** (3), 99-121 (2011).

[111] Cole, A.C., Jensen, J.L., Ntai, I., Tran, K.L.T., Weaver, K.J., Forbes, D.C. and Davis, J.H., "Novel Brønsted Acidic Ionic Liquids and Their Use as Dual Solvent−Catalysts", *J. Am. Chem. Soc.* **124** (21), 5962-5963 (2002).

[112] Devarajan, T., Higashiya, S., Dangler, C., Rane-Fondacaro, M., Snyder, J. and Haldar, P., "Novel ionic liquid electrolyte for electrochemical double layer capacitors", *Electrochem. Commun.* **11** (3), 680-683 (2009).

[113] Padua, A.A.H., Costa Gomes, M.F. and Canongia Lopes, J.N.A., "Molecular Solutes in Ionic Liquids: A Structural Perspective", *Acc. Chem. Res.* **40** (11), 1087-1096 (2007).

[114] Canongia Lopes, J.N., Costa Gomes, M.F. and Pádua, A.A.H., "Nonpolar, Polar, and Associating Solutes in Ionic Liquids", *J. Phys. Chem. B* **110** (34), 16816-16818 (2006).

[115] Zhang, S., Sun, N., He, X., Lu, X. and Zhang, X., "Physical Properties of Ionic Liquids: Database and Evaluation", *J. Phys. Chem. Ref. Data* **35** (4), 1475-1517 (2006).

[116] Aparicio, S., Atilhan, M. and Karadas, F., "Thermophysical Properties of Pure Ionic Liquids: Review of Present Situation", *Ind. Eng. Chem. Res.* **49** (20), 9580-9595 (2010).

[117] Dean, P.M., Pringle, J.M. and MacFarlane, D.R., "Structural analysis of low melting organic salts: perspectives on ionic liquids", *Phys. Chem. Chem. Phys.* **12** (32), 9144-9153 (2010).

[118] Hiroyuki, O., "Functional Design of Ionic Liquids", *Bull. Chem. Soc. Jpn.* **79** (11), 1665-1680 (2006).

[119] Huddleston, J.G., Visser, A.E., Reichert, W.M., Willauer, H.D., Broker, G.A. and Rogers, R.D., "Characterization and comparison of hydrophilic and hydrophobic room temperature ionic liquids incorporating the imidazolium cation", *Green Chem.* **3** (4), 156-164 (2001).

[120] Forsyth, S.A., Batten, S.R., Dai, Q. and MacFarlane, D.R., "Ionic Liquids Based on Imidazolium and Pyrrolidinium Salts of the Tricyanomethanide Anion", *Aust. J. Chem.* **57** (2), 121-124 (2004).

[121] Plechkova, N.V. and Seddon, K.R., "Applications of ionic liquids in the chemical industry", *Chem. Soc. Rev.* **37** (1), 123-150 (2008).

[122] Liaw, H.-J., Huang, S.-K., Chen, H.-Y. and Liu, S.-N., "Reason for Ionic Liquids to be Combustible", *Procedia Engineering* **45**, 502-506 (2012).

[123] Kroon, M.C., Buijs, W., Peters, C.J. and Witkamp, G.-J., "Quantum chemical aided prediction of the thermal decomposition mechanisms and temperatures of ionic liquids", *Thermochim. Acta* **465** (1), 40-47 (2007).

[124] Fernández, A., Torrecilla, J.S., García, J. and Rodríguez, F., "Thermophysical Properties of 1-Ethyl-3-methylimidazolium Ethylsulfate and 1-Butyl-3-methylimidazolium Methylsulfate Ionic Liquids", *J. Chem. Eng. Data* **52** (5), 1979-1983 (2007).

[125] Greaves, T.L. and Drummond, C.J., "Protic Ionic Liquids: Properties and Applications", *Chem. Rev.* **108** (1), 206-237 (2008).

[126] Wang, X., Chi, Y. and Mu, T., "A review on the transport properties of ionic liquids", *J. Mol. Liq.* **193**, 262-266 (2014).

[127] Gardas, R.L. and Coutinho, J.A.P., "A group contribution method for viscosity estimation of ionic liquids", *Fluid Phase Equilib.* **266** (1), 195-201 (2008).

[128] Fredlake, C.P., Crosthwaite, J.M., Hert, D.G., Aki, S.N.V.K. and Brennecke, J.F., "Thermophysical Properties of Imidazolium-Based Ionic Liquids", *J. Chem. Eng. Data* **49** (4), 954-964 (2004).

[129] (a) O'Mahony, A.M., Silvester, D.S., Aldous, L., Hardacre, C. and Compton, R.G., "Effect of Water on the Electrochemical Window and Potential Limits of Room-Temperature Ionic Liquids", *J. Chem. Eng. Data* **53** (12), 2884-2891 (2008); (b) Zhao, H., "Review: Current studies on some physical properties of ionic liquids", *Phys. Chem. Liq.* **41** (6), 545-557 (2003).

[130] Bonhôte, P., Dias, A.-P., Papageorgiou, N., Kalyanasundaram, K. and Grätzel, M., "Hydrophobic, Highly Conductive Ambient-Temperature Molten Salts", *Inorg. Chem.* **35** (5), 1168-1178 (1996).

[131] McEwen, A.B., Ngo, H.L., LeCompte, K. and Goldman, J.L., "Electrochemical properties of imidazolium salt electrolytes for electrochemical capacitor applications", *J. Electrochem. Soc.* **146** (5), 1687-1695 (1999).

[132] Ueno, K., Tokuda, H. and Watanabe, M., "Ionicity in ionic liquids: correlation with ionic structure and physicochemical properties", *Phys. Chem. Chem. Phys.* **12** (8), 1649-1658 (2010).

[133] MacFarlane, D.R., Forsyth, M., Izgorodina, E.I., Abbott, A.P., Annat, G. and Fraser, K., "On the concept of ionicity in ionic liquids", *Phys. Chem. Chem. Phys.* **11** (25), 4962-4967 (2009).

[134] Chiappe, C. and Pieraccini, D., "Ionic liquids: solvent properties and organic reactivity", *J. Phys. Org. Chem.* **18** (4), 275-297 (2005).

[135] Maton, C., De Vos, N. and Stevens, C.V., "Ionic liquid thermal stabilities: decomposition mechanisms and analysis tools", *Chem. Soc. Rev.* **42** (13), 5963-5977 (2013).

[136] (a) MacFarlane, D.R., Tachikawa, N., Forsyth, M., Pringle, J.M., Howlett, P.C., Elliott, G.D., Davis, J.H., Watanabe, M., Simon, P. and Angell, C.A., "Energy applications of ionic liquids", *Energy Environ. Sci.* **7** (1), 232-250 (2014); (b) Zarrougui, R., Raouafi, N. and Lemordant, D., "New Series of Green Cyclic Ammonium-Based Room Temperature Ionic Liquids with Alkylphosphite-Containing Anion: Synthesis and Physicochemical Characterization", *J. Chem. Eng. Data* **59** (4), 1193-1201 (2014).

[137] (a) Earle, M.J. and Seddon, K.R., "Ionic liquids. Green solvents for the future", *Pure Appl. Chem.* **72** (7), 1391-1398 (2000); (b) Wang, H., Gurau, G. and Rogers,

R.D., "Ionic liquid processing of cellulose", *Chem. Soc. Rev.* **41** (4), 1519-1537 (2012); (c) Welton, T., "Ionic liquids in catalysis", *Coord. Chem. Rev.* **248** (21), 2459-2477 (2004).

[138] (a) Scott, M.P., Rahman, M. and Brazel, C.S., "Application of ionic liquids as low-volatility plasticizers for PMMA", *Eur. Polym. J.* **39** (10), 1947-1953 (2003); (b) Zhou, Y. and Qu, J., "Ionic Liquids as Lubricant Additives: A Review", *ACS Appl. Mater. Interfaces* **9** (4), 3209-3222 (2017).

[139] Egorova, K.S., Gordeev, E.G. and Ananikov, V.P., "Biological Activity of Ionic Liquids and Their Application in Pharmaceutics and Medicine", *Chem. Rev.* (2017).

[140] Doe, W.K., Narendra, B., Eric, M.H., Shawn, C.K., Darrel, F.U. and Mortimer, J.T., "Electron transfer processes occurring on platinum neural stimulating electrodes: a tutorial on the i (V e) profile", *Journal of Neural Engineering* **13** (5), 052001 (2016).

[141] Galinski, M., Lewandowski, A. and Stepniak, I., "Ionic liquids as electrolytes", *Electrochim. Acta* **51** (26), 5567-5580 (2006).

[142] Tooming, T., Thomberg, T., Siinor, L., Tonurist, K., Janes, A. and Lust, E., "A type high capacitance supercapacitor based on mixed room temperature ionic liquids containing specifically adsorbed iodide anions", *J. Electrochem. Soc.* **161** (3), A222-A227 (2014).

[143] (a) Dias, A.M.A., Marceneiro, S., Johansen, H.D., Barsan, M.M., Brett, C.M.A. and de Sousa, H.C., "Phosphonium ionic liquids as greener electrolytes for poly(vinyl chloride)-based ionic conducting polymers", *RSC Adv.* **6** (92), 88979-88990 (2016); (b) Eftekhari, A., Liu, Y. and Chen, P., "Different roles of ionic liquids in lithium batteries", *J. Power Sources* **334**, 221-239 (2016); (c) Timperman, L., Beguin, F., Frackowiak, E. and Anouti, M., "Comparative study of two protic ionic liquids as electrolyte for electrical double-layer capacitors", *J. Electrochem. Soc.* **161** (3), A228-A238 (2014).

[144] Kuehnel, R.-S., Reiter, J., Jeong, S., Passerini, S. and Balducci, A., "Anodic stability of aluminum current collectors in an ionic liquid based on the (fluorosulfonyl)(trifluoromethanesulfonyl)imide anion and its implication on high voltage supercapacitors", *Electrochem. Commun.* **38**, 117-119 (2014).

[145] Bhatt, A.I., May, I., Volkovich, V.A., Hetherington, M.E., Lewin, B., Thied, R.C. and Ertok, N., "Group 15 quaternary alkyl bistriflimides: ionic liquids with potential application in electropositive metal deposition and as supporting electrolytes", *J. Chem. Soc., Dalton Trans.* (24), 4532-4534 (2002).

[146] Howlett, P.C., MacFarlane, D.R. and Hollenkamp, A.F., "High lithium metal cycling efficiency in a room-temperature ionic liquid", *Electrochem. Solid-State Lett.* **7** (5), A97-A101 (2004).

[147] Balducci, A., Dugas, R., Taberna, P.L., Simon, P., Plée, D., Mastragostino, M. and Passerini, S., "High temperature carbon–carbon supercapacitor using ionic liquid as electrolyte", *J. Power Sources* **165** (2), 922-927 (2007).

[148] Kurig, H., Vestli, M., Jänes, A. and Lust, E., "Electrical Double Layer Capacitors Based on Two 1-Ethyl-3-Methylimidazolium Ionic Liquids with Different Anions", *Electrochem. Solid-State Lett.* **14** (8), A120-A122 (2011).

[149] Brandt, A., Pohlmann, S., Varzi, A., Balducci, A. and Passerini, S., "Ionic liquids in supercapacitors", *MRS Bull.* **38** (7), 554-559 (2013).

[150] Almdal, K., Dyre, J., Hvidt, S. and Kramer, O., "Towards a phenomenological definition of the term 'gel'", *Polym. Gels Networks* **1** (1), 5-17 (1993).
[151] Marr, P.C. and Marr, A.C., "Ionic liquid gel materials: applications in green and sustainable chemistry", *Green Chem.* **18** (1), 105-128 (2016).
[152] Ueki, T. and Watanabe, M., "Macromolecules in Ionic Liquids: Progress, Challenges, and Opportunities", *Macromolecules* **41** (11), 3739-3749 (2008).
[153] Fuller, J., Breda, A.C. and Carlin, R.T., "Ionic Liquid‐Polymer Gel Electrolytes", *J. Electrochem. Soc.* **144** (4), L67-L70 (1997).
[154] Fukushima, T., Kosaka, A., Ishimura, Y., Yamamoto, T., Takigawa, T., Ishii, N. and Aida, T., "Molecular Ordering of Organic Molten Salts Triggered by Single-Walled Carbon Nanotubes", *Science* **300** (5628), 2072-2074 (2003).
[155] Hanabusa, K., Tange, J., Taguchi, Y., Koyama, T. and Shirai, H., "Small molecular gelling agents to harden organic liquids: alkylamide of N-benzyloxycarbonyl-L-valyl-L-valine", *J. Chem. Soc., Chem. Commun.* (4), 390-392 (1993).
[156] Yu, P., Yan, J., Zhao, H., Su, L., Zhang, J. and Mao, L., "Rational Functionalization of Carbon Nanotube/Ionic Liquid Bucky Gel with Dual Tailor-Made Electrocatalysts for Four-Electron Reduction of Oxygen", *J. Phys. Chem. C* **112** (6), 2177-2182 (2008).
[157] Zhao, Y., Liu, H., Kou, Y., Li, M., Zhu, Z. and Zhuang, Q., "Structural and characteristic analysis of carbon nanotubes-ionic liquid gel biosensor", *Electrochem. Commun.* **9** (10), 2457-2462 (2007).
[158] Wang, P., Zakeeruddin, S.M., Comte, P., Exnar, I. and Grätzel, M., "Gelation of Ionic Liquid-Based Electrolytes with Silica Nanoparticles for Quasi-Solid-State Dye-Sensitized Solar Cells", *J. Am. Chem. Soc.* **125** (5), 1166-1167 (2003).
[159] Díaz, M., Ortiz, A. and Ortiz, I., "Progress in the use of ionic liquids as electrolyte membranes in fuel cells", *J. Membr. Sci.* **469**, 379-396 (2014).
[160] Horowitz, A.I. and Panzer, M.J., "High-performance, mechanically compliant silica-based ionogels for electrical energy storage applications", *J. Mater. Chem.* **22** (32), 16534-16539 (2012).
[161] Yu Jin, K., Haegeun, C., Chi-Hwan, H. and Woong, K., "All-solid-state flexible supercapacitors based on papers coated with carbon nanotubes and ionic-liquid-based gel electrolytes", *Nanotechnology* **23** (28), 289501 (2012).
[162] Pandey, G.P., Liu, T., Hancock, C., Li, Y., Sun, X.S. and Li, J., "Thermostable gel polymer electrolyte based on succinonitrile and ionic liquid for high-performance solid-state supercapacitors", *J. Power Sources* **328**, 510-519 (2016).
[163] Rabek, C.L., Stelle, R.V., Dziubla, T.D. and Puleo, D.A., "The Effect of Plasticizers on the Erosion and Mechanical Properties of Polymeric Films", *J. Biomater. Appl.* **28** (5), 10.1177/0885328213480979 (2014).
[164] Rösler, J., Harders, H. and Baeker, M., *Mechanical behaviour of engineering materials: metals, ceramics, polymers, and composites* (Springer Science & Business Media, 2007).
[165] Vieira, M.G.A., da Silva, M.A., dos Santos, L.O. and Beppu, M.M., "Natural-based plasticizers and biopolymer films: A review", *Eur. Polym. J.* **47** (3), 254-263 (2011).

[166] Scott, M.P., Brazel, C.S., Benton, M.G., Mays, J.W., Holbrey, J.D. and Rogers, R.D., "Application of ionic liquids as plasticizers for poly(methyl methacrylate)", *Chem. Commun.* (13), 1370-1371 (2002).

[167] Sankri, A., Arhaliass, A., Dez, I., Gaumont, A.C., Grohens, Y., Lourdin, D., Pillin, I., Rolland-Sabaté, A. and Leroy, E., "Thermoplastic starch plasticized by an ionic liquid", *Carbohydr. Polym.* **82** (2), 256-263 (2010).

[168] Lunstroot, K., Driesen, K., Nockemann, P., Viau, L., Mutin, P.H., Vioux, A. and Binnemans, K., "Ionic liquid as plasticizer for europium(iii)-doped luminescent poly(methyl methacrylate) films", *Phys. Chem. Chem. Phys.* **12** (8), 1879-1885 (2010).

[169] (a) Desai, S., Shepherd, R.L., Innis, P.C., Murphy, P., Hall, C., Fabretto, R. and Wallace, G.G., "Gel electrolytes with ionic liquid plasticiser for electrochromic devices", *Electrochim. Acta* **56** (11), 4408-4413 (2011); (b) Ito, A., Yasuda, T., Ma, X. and Watanabe, M., "Sulfonated polyimide/ionic liquid composite membranes for carbon dioxide separation", *Polym J* **49**, 671 (2017); (c) Mizuta, T., Sueyoshi, K., Endo, T. and Hisamoto, H., "Ionic liquid-based dye: A "Dyed plasticizer" for rapid and highly sensitive anion optodes based on a plasticized PVC membrane", *Sensors and Actuators B: Chemical* **258**, 1125-1130 (2018).

[170] Colomines, G., Decaen, P., Lourdin, D. and Leroy, E., "Biofriendly ionic liquids for starch plasticization: a screening approach", *RSC Adv.* **6** (93), 90331-90337 (2016).

[171] Plechkova, N.V. and Seddon, K.R., "Ionic Liquids: "Designer" Solvents for Green Chemistry", in *Methods and Reagents for Green Chemistry* (John Wiley & Sons, Inc., 2007), pp. 103-130.

[172] (a) Crowhurst, L., Mawdsley, P.R., Perez-Arlandis, J.M., Salter, P.A. and Welton, T., "Solvent-solute interactions in ionic liquids", *Phys. Chem. Chem. Phys.* **5** (13), 2790-2794 (2003); (b) Forsyth, S.A., Pringle, J.M. and MacFarlane, D.R., "Ionic Liquids-An Overview", *Aust. J. Chem.* **57** (2), 113-119 (2004).

[173] (a) Ribeiro, B.D., Santos, A.G. and Marrucho, I.M., "Biocatalysis in ionic liquids", in *RSC Green Chem. Ser.*, Vol. 45 (Royal Society of Chemistry, 2016), pp. 136-177; (b) Rosa, C.D., Ormachea, C., Kneeteman, M.N., Adam, C. and Mancini, P.M., "Diels–Alder reactions of< i> N</i>-tosylpirroles developed in protic ionic liquids. Theoretical studies using DFT methods", *Tetrahedron Lett.* **52** (50), 6754-6757 (2011); (c) Van Rantwijk, F. and Sheldon, R.A., "Biocatalysis in Ionic Liquids", *Chem. Rev.* **107** (6), 2757-2785 (2007); (d) Wilkes, J.S., "Properties of ionic liquid solvents for catalysis", *J. Mol. Catal. A: Chem.* **214** (1), 11-17 (2004); (e) Xu, H., Zhang, C., Chen, G., Shen, R. and Ying, A., "Application of task-specific ionic liquids to organic synthesis", *Youji Huaxue* **36** (10), 2353-2367 (2016).

[174] Swatloski, R.P., Spear, S.K., Holbrey, J.D. and Rogers, R.D., "Dissolution of Cellulose with Ionic Liquids", *J. Am. Chem. Soc.* **124** (18), 4974-4975 (2002).

[175] Hulsbosch, J., De Vos, D.E., Binnemans, K. and Ameloot, R., "Biobased Ionic Liquids: Solvents for a Green Processing Industry?", *ACS Sustainable Chem. Eng.* **4** (6), 2917-2931 (2016).

[176] (a) Administration, I.S.A.U.S.E.I., 'Trends in Renewable Energy Consumption and Electricity ', https://www.eia.gov/renewable/annual/trends/, (2012); (b) Liu, Z., Sun, X., Hao, M., Huang, C., Xue, Z. and Mu, T., "Preparation and

characterization of regenerated cellulose from ionic liquid using different methods", *Carbohydr. Polym.* **117** (0), 99-105 (2015).

[177] Gupta, K.M. and Jiang, J., "Cellulose dissolution and regeneration in ionic liquids: A computational perspective", *Chem. Eng. Sci.* **121**, 180-189 (2015).

[178] Payen, A., "Mémoire sur la composition du tissu propre des plantes et du ligneux", *Comptes rendus* **7**, 1052-1056 (1838).

[179] Kim, J., Yun, S. and Ounaies, Z., "Discovery of Cellulose as a Smart Material", *Macromolecules* **39** (12), 4202-4206 (2006).

[180] (a) Mahadeva, S.K. and Kim, J., "Enhanced electrical properties of regenerated cellulose by polypyrrole and ionic liquid nanocoating", *Proc. Inst. Mech. Eng., Part N* **225** (1), 33-39 (2011); (b) Yun, S., Jang, S.-D., Yun, G.-Y., Kim, J.-H. and Kim, J., "Paper transistor made with covalently bonded multiwalled carbon nanotube and cellulose", *Appl. Phys. Lett.* **95** (10), 104102 (2009).

[181] Clough, M.T., Geyer, K., Hunt, P.A., Son, S., Vagt, U. and Welton, T., "Ionic liquids: not always innocent solvents for cellulose", *Green Chem.* **17** (1), 231-243 (2015).

[182] Xu, A., Wang, J. and Wang, H., "Effects of anionic structure and lithium salts addition on the dissolution of cellulose in 1-butyl-3-methylimidazolium-based ionic liquid solvent systems", *Green Chem.* **12** (2), 268-275 (2010).

[183] Medronho, B. and Lindman, B., "Brief overview on cellulose dissolution/regeneration interactions and mechanisms", *Adv. Colloid Interface Sci.* **222**, 502-508 (2015).

[184] (a) Chiellini, E. and Solaro, R., "Biodegradable Polymeric Materials", *Adv. Mater.* **8** (4), 305-313 (1996); (b) Lorenzo, M., Zhu, B. and Srinivasan, G., "Intrinsically flexible electronic materials for smart device applications", *Green Chem.* **18** (12), 3513-3517 (2016).

[185] El-Saied, H., Basta, A.H. and Gobran, R.H., "Research Progress in Friendly Environmental Technology for the Production of Cellulose Products (Bacterial Cellulose and Its Application)", *Polymer-Plastics Technology and Engineering* **43** (3), 797-820 (2004).

[186] (a) Leschine, S.B., "Cellulose Degradation in Anaerobic Environments", *Annu. Rev. Microbiol.* **49** (1), 399-426 (1995); (b) Shafizadeh, F. and Bradbury, A., "Thermal degradation of cellulose in air and nitrogen at low temperatures", *J. Appl. Polym. Sci.* **23** (5), 1431-1442 (1979).

[187] Cross, C.F., Bevan, E.J. and B'eadle, C., *Plastic Compound of Cellulose*, US Pat. 20770A (1894).

[188] Tim, L., "Cellulose Solvents? Remarkable History, Bright Future", in *Cellulose Solvents: For Analysis, Shaping and Chemical Modification*, ACS Symposium Series, Vol. 1033 (American Chemical Society, 2010), pp. 3-54.

[189] Mäki-Arvela, P., Anugwom, I., Virtanen, P., Sjöholm, R. and Mikkola, J.P., "Dissolution of lignocellulosic materials and its constituents using ionic liquids—A review", *Ind. Crops. Prod.* **32** (3), 175-201 (2010).

[190] Graenacher, C., *Cellulose solution*, US Pat. 1943176A (1934).

[191] (a) Kilpeläinen, I., Xie, H., King, A., Granstrom, M., Heikkinen, S. and Argyropoulos, D.S., "Dissolution of Wood in Ionic Liquids", *J. Agric. Food Chem.* **55** (22), 9142-9148 (2007); (b) Stefanescu, C., Daly, W.H. and Negulescu, I.I., "Biocomposite films prepared from ionic liquid solutions of chitosan and

cellulose", *Carbohydr. Polym.* **87** (1), 435-443 (2012); (c) Tadesse, H. and Luque, R., "Advances on biomass pretreatment using ionic liquids: an overview", *Energy Environ. Sci.* **4** (10), 3913-3929 (2011).

[192] (a) El Seoud, O.A., Koschella, A., Fidale, L.C., Dorn, S. and Heinze, T., "Applications of Ionic Liquids in Carbohydrate Chemistry: A Window of Opportunities", *Biomacromolecules* **8** (9), 2629-2647 (2007); (b) Miyata, A. and Miyafuji, H., "Reaction behavior of cellulose in various pyridinium-based ionic liquids", *J. Wood Sci.* **60** (6), 438-445 (2014); (c) Zhu, S., Wu, Y., Chen, Q., Yu, Z., Wang, C., Jin, S., Ding, Y. and Wu, G., "Dissolution of cellulose with ionic liquids and its application: a mini-review", *Green Chem.* **8** (4), 325-327 (2006).

[193] Zhang, H., Wu, J., Zhang, J. and He, J., "1-Allyl-3-methylimidazolium Chloride Room Temperature Ionic Liquid: A New and Powerful Nonderivatizing Solvent for Cellulose", *Macromolecules* **38** (20), 8272-8277 (2005).

[194] Fukaya, Y., Hayashi, K., Wada, M. and Ohno, H., "Cellulose dissolution with polar ionic liquids under mild conditions: required factors for anions", *Green Chem.* **10** (1), 44-46 (2008).

[195] Zhang, S., Sun, J., Zhang, X., Xin, J., Miao, Q. and Wang, J., "Ionic liquid-based green processes for energy production", *Chem. Soc. Rev.* **43** (22), 7838-7869 (2014).

[196] (a) Andanson, J.-M., Padua, A.A.H. and Gomes, M.C., "Thermodynamics of Cellulose Dissolution in an Imidazolium Acetate Ionic Liquid", *Chem. Commun.* (2015); (b) Ding, Z.-D., Chi, Z., Gu, W.-X., Gu, S.-M., Liu, J.-H. and Wang, H.-J., "Theoretical and experimental investigation on dissolution and regeneration of cellulose in ionic liquid", *Carbohydr. Polym.* **89** (1), 7-16 (2012).

[197] Yang, Y.-J., Shin, J.-M., Kang, T.H., Kimura, S., Wada, M. and Kim, U.-J., "Cellulose dissolution in aqueous lithium bromide solutions", *Cellulose* **21** (3), 1175-1181 (2014).

[198] Yu, C., Ma, P., Zhou, X., Wang, A., Qian, T., Wu, S. and Chen, Q., "All-Solid-State Flexible Supercapacitors Based on Highly Dispersed Polypyrrole Nanowire and Reduced Graphene Oxide Composites", *ACS Appl. Mater. Interfaces* **6** (20), 17937-17943 (2014).

[199] Crowhurst, L., Falcone, R., Lancaster, N.L., Llopis-Mestre, V. and Welton, T., "Using Kamlet−Taft Solvent Descriptors To Explain the Reactivity of Anionic Nucleophiles in Ionic Liquids", *J. Org. Chem.* **71** (23), 8847-8853 (2006).

[200] Remsing, R.C., Swatloski, R.P., Rogers, R.D. and Moyna, G., "Mechanism of cellulose dissolution in the ionic liquid 1-*n*-butyl-3-methylimidazolium chloride: a ^{13}C and $^{35}/^{37}Cl$ NMR relaxation study on model systems", *Chem. Commun.* (12), 1271-1273 (2006).

[201] Liu, H., Sale, K.L., Holmes, B.M., Simmons, B.A. and Singh, S., "Understanding the interactions of cellulose with ionic liquids: a molecular dynamics study", *J Phys Chem B* **114** (12), 4293-4301 (2010).

[202] (a) Pinkert, A., Marsh, K.N., Pang, S. and Staiger, M.P., "Ionic liquids and their interaction with cellulose", *Chem. Rev.* **109** (12), 6712-6728 (2009); (b) Zhang, J., Zhang, H., Wu, J., Zhang, J., He, J. and Xiang, J., "NMR spectroscopic studies of cellobiose solvation in EmimAc aimed to understand the dissolution mechanism of cellulose in ionic liquids", *Phys. Chem. Chem. Phys.* **12** (8), 1941-1947 (2010).

[203] Isik, M., Sardon, H. and Mecerreyes, D., "Ionic Liquids and Cellulose: Dissolution, Chemical Modification and Preparation of New Cellulosic Materials", *Int. J. Mol. Sci.* **15** (7), 11922 (2014).

[204] Zhao, H., Jones, C.L., Baker, G.A., Xia, S., Olubajo, O. and Person, V.N., "Regenerating cellulose from ionic liquids for an accelerated enzymatic hydrolysis", *J. Biotechnol.* **139** (1), 47-54 (2009).

[205] Pang, J.-H., Liu, X., Wu, M., Wu, Y.-Y., Zhang, X.-M. and Sun, R.-C., "Fabrication and Characterization of Regenerated Cellulose Films Using Different Ionic Liquids", *J. Spectrosc.* **2014**, 8, Article ID 214057 (2014).

[206] Kaur, G., Adhikari, R., Cass, P., Bown, M. and Gunatillake, P., "Electrically conductive polymers and composites for biomedical applications", *RSC Adv.* **5** (47), 37553-37567 (2015).

[207] Goel, S., Mazumdar, N.A. and Gupta, A., "Synthesis and characterization of polypyrrole nanofibers with different dopants", *Polym Advan Technol* **21** (3), 205-210 (2010).

[208] (a) Pickup, P.G. and Osteryoung, R.A., "Electrochemical polymerization of pyrrole and electrochemistry of polypyrrole films in ambient temperature molten salts", *J. Am. Chem. Soc.* **106** (8), 2294-2299 (1984); (b) Pickup, P.G. and Osteryoung, R.A., "Charging and discharging rate studies of polypyrrole films in $AlCl_3$: 1-methyl-(3-ethyl)-imidazolium chloride molten salts and in CH_3CN", *J. Electroanal. Chem. Interfacial Electrochem.* **195** (2), 271-288 (1985).

[209] Sekiguchi, K., Atobe, M. and Fuchigami, T., "Electropolymerization of pyrrole in 1-ethyl-3-methylimidazolium trifluoromethanesulfonate room temperature ionic liquid", *Electrochem. Commun.* **4** (11), 881-885 (2002).

[210] Angeli, A. and Alessandri, L., "Pyrrole Black", *Gazz. Chim. Ital.* **46** (II), 279 (1916).

[211] Gardini, G.P., "The Oxidation of Monocyclic Pyrroles", in *Adv. Heterocycl. Chem.*, Eds. A.R. Katritzky and A.J. Boulton, Vol. 15 (Academic Press, 1973), pp. 67-98.

[212] Tan, Y. and Ghandi, K., "Kinetics and mechanism of pyrrole chemical polymerization", *Synth. Met.* **175**, 183-191 (2013).

[213] Jeon, I.-Y., Choi, H.-J., Tan, L.-S. and Baek, J.-B., "Nanocomposite prepared from in situ grafting of polypyrrole to aminobenzoyl-functionalized multiwalled carbon nanotube and its electrochemical properties", *J. Polym. Sci., Part A: Polym. Chem.* **49** (12), 2529-2537 (2011).

[214] (a) Huang, L., Li, C. and Shi, G., "High-performance and flexible electrochemical capacitors based on graphene/polymer composite films", *J. Mater. Chem. A* **2** (4), 968-974 (2014); (b) Malinauskas, A., "Chemical deposition of conducting polymers", *Polymer* **42** (9), 3957-3972 (2001).

[215] Yosomiya, R., Hirata, M., Haga, Y., An, H. and Seki, M., "Electrical properties of polypyrrole-polymer composite films", *Die Makromolekulare Chemie, Rapid Communications* **7** (11), 697-701 (1986).

[216] Ramasubramaniam, R., Chen, J. and Liu, H., "Homogeneous carbon nanotube/polymer composites for electrical applications", *Appl. Phys. Lett.* **83** (14), 2928-2930 (2003).

[217] Zadorecki, P. and Michell, A.J., "Future prospects for wood cellulose as reinforcement in organic polymer composites", *Polym. Compos.* **10** (2), 69-77 (1989).

[218] Wellinghoff, S.T., *Metal oxide-polymer composites*, US Pat. 5670583A (1994).

[219] Lee, K.I. and Jopson, H., "Electrically conductive thermoplastic elastomer/polyacetylene blends", *Polym. Bull.* **10** (1), 105-108 (1983).

[220] Ojio, T. and Miyata, S., "Highly Transparent and Conducting Polypyrrole–Poly(vinyl alcohol) Composite Films Prepared by Gas State Polymerization", *Polym J* **18**, 95 (1986).

[221] (a) Gindl, W. and Keckes, J., "All-cellulose nanocomposite", *Polymer* **46** (23), 10221-10225 (2005); (b) Zhang, Y.-Z., Wang, Y., Cheng, T., Lai, W.-Y., Pang, H. and Huang, W., "Flexible supercapacitors based on paper substrates: a new paradigm for low-cost energy storage", *Chem. Soc. Rev.* **44** (15), 5181-5199 (2015).

[222] He, Y., Chen, W., Li, X., Zhang, Z., Fu, J., Zhao, C. and Xie, E., "Freestanding Three-Dimensional Graphene/MnO_2 Composite Networks As Ultralight and Flexible Supercapacitor Electrodes", *ACS Nano* **7** (1), 174-182 (2013).

[223] Chee, W.K., Lim, H.N., Zainal, Z., Huang, N.M., Harrison, I. and Andou, Y., "Flexible Graphene-Based Supercapacitors: A Review", *J. Phys. Chem. C* **120** (8), 4153-4172 (2016).

[224] Sugimoto, W., Yokoshima, K., Ohuchi, K., Murakami, Y. and Takasu, Y., "Fabrication of Thin-Film, Flexible, and Transparent Electrodes Composed of Ruthenic Acid Nanosheets by Electrophoretic Deposition and Application to Electrochemical Capacitors", *J. Electrochem. Soc.* **153** (2), A255-A260 (2006).

[225] Peng, S., Fan, L., Rao, W., Bai, Z., Xu, W. and Xu, J., "Bacterial cellulose membranes coated by polypyrrole/copper oxide as flexible supercapacitor electrodes", *J. Mater. Sci.*, 1-13 (2016).

[226] He, Y., Chen, W., Gao, C., Zhou, J., Li, X. and Xie, E., "An overview of carbon materials for flexible electrochemical capacitors", *Nanoscale* **5** (19), 8799-8820 (2013).

[227] Borenstein, A., Hanna, O., Attias, R., Luski, S., Brousse, T. and Aurbach, D., "Carbon-based composite materials for supercapacitor electrodes: a review", *J. Mater. Chem. A* **5** (25), 12653-12672 (2017).

[228] Yu, C., Masarapu, C., Rong, J., Wei, B. and Jiang, H., "Stretchable Supercapacitors Based on Buckled Single-Walled Carbon-Nanotube Macrofilms", *Adv. Mater.* **21** (47), 4793-4797 (2009).

[229] Chen, Y.-C., Hsu, Y.-K., Lin, Y.-G., Lin, Y.-K., Horng, Y.-Y., Chen, L.-C. and Chen, K.-H., "Highly flexible supercapacitors with manganese oxide nanosheet/carbon cloth electrode", *Electrochim. Acta* **56** (20), 7124-7130 (2011).

[230] Kang, Y.J., Chung, H., Han, C.H. and Kim, W., "All-solid-state flexible supercapacitors based on papers coated with carbon nanotubes and ionic-liquid-based gel electrolytes", *Nanotechnology* **23** (6), 65401 (2012).

[231] Yoo, J.J., Balakrishnan, K., Huang, J., Meunier, V., Sumpter, B.G., Srivastava, A., Conway, M., Mohana Reddy, A.L., Yu, J., Vajtai, R. and Ajayan, P.M., "Ultrathin Planar Graphene Supercapacitors", *Nano Lett.* **11** (4), 1423-1427 (2011).

[232] Jiang, Y., Ling, X., Jiao, Z., Li, L., Ma, Q., Wu, M., Chu, Y. and Zhao, B., "Flexible of multiwalled carbon nanotubes/manganese dioxide nanoflake textiles for high-performance electrochemical capacitors", *Electrochim. Acta* **153**, 246-253 (2015).

[233] Amitha, F.E., Reddy, A.L.M. and Ramaprabhu, S., "A non-aqueous electrolyte-based asymmetric supercapacitor with polymer and metal oxide/multi-walled carbon nanotube electrodes", *J. Nanopart. Res.* **11** (3), 725-729 (2009).

[234] Chen, P.-C., Shen, G., Shi, Y., Chen, H. and Zhou, C., "Preparation and characterization of flexible asymmetric supercapacitors based on transition-metal-oxide nanowire/single-walled carbon nanotube hybrid thin-film electrodes", *ACS Nano* **4** (8), 4403-4411 (2010).

[235] (a) Bay, L., Jacobsen, T., Skaarup, S. and West, K., "Mechanism of Actuation in Conducting Polymers: Osmotic Expansion", *J. Phys. Chem. B* **105** (36), 8492-8497 (2001); (b) Le, T.-H., Kim, Y. and Yoon, H., "Electrical and Electrochemical Properties of Conducting Polymers", *Polymers* **9** (4), 150 (2017).

[236] Horng, Y.-Y., Lu, Y.-C., Hsu, Y.-K., Chen, C.-C., Chen, L.-C. and Chen, K.-H., "Flexible supercapacitor based on polyaniline nanowires/carbon cloth with both high gravimetric and area-normalized capacitance", *J. Power Sources* **195** (13), 4418-4422 (2010).

[237] Zhu, C., Zhai, J., Wen, D. and Dong, S., "Graphene oxide/polypyrrole nanocomposites: one-step electrochemical doping, coating and synergistic effect for energy storage", *J. Mater. Chem.* **22** (13), 6300-6306 (2012).

[238] Zhang, J., Chen, P., Oh, B.H.L. and Chan-Park, M.B., "High capacitive performance of flexible and binder-free graphene-polypyrrole composite membrane based on in situ reduction of graphene oxide and self-assembly", *Nanoscale* **5** (20), 9860-9866 (2013).

[239] Peng, S., Fan, L., Wei, C., Liu, X., Zhang, H., Xu, W. and Xu, J., "Flexible polypyrrole/copper sulfide/bacterial cellulose nanofibrous composite membranes as supercapacitor electrodes", *Carbohydr. Polym.* **157**, 344-352 (2017).

[240] Nyholm, L., Nyström, G., Mihranyan, A. and Strømme, M., "Toward Flexible Polymer and Paper‐Based Energy Storage Devices", *Adv. Mater.* **23** (33), 3751-3769 (2011).

[241] Lay, M., González, I., Tarrés, J.A., Pellicer, N., Bun, K.N. and Vilaseca, F., "High electrical and electrochemical properties in bacterial cellulose/polypyrrole membranes", *Eur. Polym. J.* **91** (Supplement C), 1-9 (2017).

[242] Gui, Z., Zhu, H., Gillette, E., Han, X., Rubloff, G.W., Hu, L. and Lee, S.B., "Natural Cellulose Fiber as Substrate for Supercapacitor", *ACS Nano* **7** (7), 6037-6046 (2013).

[243] Weng, Z., Su, Y., Wang, D.-W., Li, F., Du, J. and Cheng, H.-M., "Graphene–Cellulose Paper Flexible Supercapacitors", *Adv. Energy Mater.* **1** (5), 917-922 (2011).

[244] Tao, J., Ma, W., Liu, N., Ren, X., Shi, Y., Su, J. and Gao, Y., "High-Performance Solid-State Supercapacitors Fabricated by Pencil Drawing and Polypyrrole Depositing on Paper Substrate", *Nano-Micro Letters* **7** (3), 276-281 (2015).

[245] Chen, J., Minett, A.I., Liu, Y., Lynam, C., Sherrell, P., Wang, C. and Wallace, G.G., "Direct Growth of Flexible Carbon Nanotube Electrodes", *Adv. Mater.* **20** (3), 566-570 (2008).

[246] Li, S., Huang, D., Zhang, B., Xu, X., Wang, M., Yang, G. and Shen, Y., "Flexible Supercapacitors Based on Bacterial Cellulose Paper Electrodes", *Adv. Energy Mater.* **4** (10), 1301655 (2014).

[247] Gates, B.D., Xu, Q., Stewart, M., Ryan, D., Willson, C.G. and Whitesides, G.M., "New Approaches to Nanofabrication: Molding, Printing, and Other Techniques", *Chem. Rev.* **105** (4), 1171-1196 (2005).

[248] Liu, S., Yu, T., Wu, Y., Li, W. and Li, B., "Evolution of cellulose into flexible conductive green electronics: a smart strategy to fabricate sustainable electrodes for supercapacitors", *RSC Adv.* **4** (64), 34134-34143 (2014).

[249] Bock, D.C., Marschilok, A.C., Takeuchi, K.J. and Takeuchi, E.S., "Batteries used to Power Implantable Biomedical Devices", *Electrochim. Acta* **84**, 155-164 (2012).

[250] Chen, J., Xu, J., Wang, K., Qian, X. and Sun, R., "Highly Thermostable, Flexible, and Conductive Films Prepared from Cellulose, Graphite, and Polypyrrole Nanoparticles", *ACS Appl. Mater. Interfaces* **7** (28), 15641-15648 (2015).

[251] Romero, I.S., Schurr, M.L., Lally, J.V., Kotlik, M.Z. and Murphy, A.R., "Enhancing the Interface in Silk–Polypyrrole Composites through Chemical Modification of Silk Fibroin", *ACS Appl. Mater. Interfaces* **5** (3), 553-564 (2013).

[252] Kim, J., Deshpande, S.D., Yun, S. and Li, Q., "A Comparative Study of Conductive Polypyrrole and Polyaniline Coatings on Electro-Active Papers", *Polym J* **38** (7), 659-668 (2006).

[253] Cruz, H., Fanselow, M., Holbrey, J.D. and Seddon, K.R., "Determining relative rates of cellulose dissolution in ionic liquids through in situ viscosity measurement", *Chem. Commun.* **48** (45), 5620-5622 (2012).

[254] Cao, Y., Wu, J., Zhang, J., Li, H., Zhang, Y. and He, J., "Room temperature ionic liquids (RTILs): A new and versatile platform for cellulose processing and derivatization", *Chem. Eng. J.* **147** (1), 13-21 (2009).

[255] Mazza, M., Catana, D.-A., Vaca-Garcia, C. and Cecutti, C., "Influence of water on the dissolution of cellulose in selected ionic liquids", *Cellulose* **16** (2), 207-215 (2009).

[256] (a) Fort, D.A., Remsing, R.C., Swatloski, R.P., Moyna, P., Moyna, G. and Rogers, R.D., "Can ionic liquids dissolve wood? Processing and analysis of lignocellulosic materials with 1-n-butyl-3-methylimidazolium chloride", *Green Chem.* **9** (1), 63-69 (2007); (b) Kosan, B., Michels, C. and Meister, F., "Dissolution and forming of cellulose with ionic liquids", *Cellulose (Dordrecht, Neth.)* **15** (1), 59-66 (2008).

[257] Freemantle, M., *An introduction to ionic liquids* (Royal Society of chemistry, 2010).

[258] (a) Aloui, H., Khwaldia, K., Slama, M.B. and Hamdi, M., "Effect of glycerol and coating weight on functional properties of biopolymer-coated paper", *Carbohydr. Polym.* **86** (2), 1063-1072 (2011); (b) Khwaldia, K., Basta, A.H., Aloui, H. and El-Saied, H., "Chitosan–caseinate bilayer coatings for paper packaging materials", *Carbohydr. Polym.* **99**, 508-516 (2014).

[259] (a) Ciolacu, D., Ciolacu, F. and Popa, V.I., "Amorphous cellulose - structure and characterization", *Cellul. Chem. Technol.* **45** (1-2), 13-21 (2011); (b) Fan, M., Dai, D. and Huang, B., *Fourier transform infrared spectroscopy for natural fibres*, Fourier Transform-Materials Analysis (InTech, 2012).

[260] (a) Dharaskar, S.A., Varma, M.N., Shende, D.Z., Yoo, C.K. and Wasewar, K.L., "Synthesis, characterization and application of 1-butyl-3-methylimidazolium chloride as green material for extractive desulfurization of liquid fuel", *Sci. World J.*, 395274-395274 (2013); (b) Jeon, Y., Sung, J., Kim, D., Seo, C., Cheong,

H., Ouchi, Y., Ozawa, R. and Hamaguchi, H.-o., "Structural Change of 1-Butyl-3-methylimidazolium Tetrafluoroborate + Water Mixtures Studied by Infrared Vibrational Spectroscopy", *J. Phys. Chem. B* **112** (3), 923-928 (2008).

[261] Wiley, J.H. and Atalla, R.H., "Band assignments in the raman spectra of celluloses", *Carbohydr. Res.* **160**, 113-129 (1987).

[262] Atalla, R.H., "Raman spectral studies of polymorphy in cellulose. Part 1, Celluloses I and II" (1975).

[263] (a) Agarwal, U.P., Reiner, R.S. and Ralph, S.A., "Cellulose I crystallinity determination using FT–Raman spectroscopy: univariate and multivariate methods", *Cellulose* **17** (4), 721-733 (2010); (b) Dumitriu, S., *Polysaccharides: structural diversity and functional versatility*, 2nd Edit., Series Ed. L. Taylor & Francis Group (CRC press, New York, 2004); (c) Edwards, H.G.M., Farwell, D.W. and Webster, D., "FT Raman microscopy of untreated natural plant fibres", *Spectrochim. Acta, Part A* **53** (13), 2383-2392 (1997); (d) Schenzel, K., Fischer, S. and Brendler, E., "New Method for Determining the Degree of Cellulose I Crystallinity by Means of FT Raman Spectroscopy", *Cellulose* **12** (3), 223-231 (2005).

[264] Coats, A.W. and Redfern, J.P., "Thermogravimetric analysis. A review", *Analyst* **88** (1053), 906-924 (1963).

[265] Dias, A.M.A., Marceneiro, S., Braga, M.E.M., Coelho, J.F.J., Ferreira, A.G.M., Simões, P.N., Veiga, H.I.M., Tomé, L.C., Marrucho, I.M., Esperança, J.M.S.S., Matias, A.A., Duarte, C.M.M., Rebelo, L.P.N. and de Sousa, H.C., "Phosphonium-based ionic liquids as modifiers for biomedical grade poly(vinyl chloride)", *Acta Biomaterialia* **8** (3), 1366-1379 (2012).

[266] Adamova, G., Gardas, R.L., Nieuwenhuyzen, M., Puga, A.V., Rebelo, L.P.N., Robertson, A.J. and Seddon, K.R., "Alkyltributylphosphonium chloride ionic liquids: synthesis, physicochemical properties and crystal structure", *Dalton Trans.* **41** (27), 8316-8332 (2012).

[267] Del Sesto, R.E., Corley, C., Robertson, A. and Wilkes, J.S., "Tetraalkylphosphonium-based ionic liquids", *J. Organomet. Chem.* **690** (10), 2536-2542 (2005).

[268] Stockmann, T.J. and Ding, Z., "Hydrophobicity of room temperature ionic liquids assessed by the Galvani potential difference established at micro liquid/liquid interfaces", *J. Electroanal. Chem.* **649** (1), 23-31 (2010).

[269] Paschoal, V.H., Faria, L.F.O. and Ribeiro, M.C.C., "Vibrational Spectroscopy of Ionic Liquids", *Chem. Rev.* **117** (10), 7053-7112 (2017).

[270] (a) Berg, R.W., "Raman Spectroscopy and Ab-Initio Model Calculations on Ionic Liquids", *Monatshefte für Chemie - Chemical Monthly* **138** (11), 1045-1075 (2007); (b) Furer, V.L., Vandyukov, A.E., Fuchs, S., Majoral, J.P., Caminade, A.M. and Kovalenko, V.I., "DFT study of Raman spectra of phosphorus-containing dendrons built from cyclotriphosphazene core with terminal carbamate and ester groups", *Spectrochim. Acta, Part A* **120**, 195-200 (2014).

[271] Hernández Battez, A., Bartolomé, M., Blanco, D., Viesca, J.L., Fernández-González, A. and González, R., "Phosphonium cation-based ionic liquids as neat lubricants: Physicochemical and tribological performance", *Tribol. Int.* **95**, 118-131 (2016).

[272] Shalu, Chaurasia, S.K., Singh, R.K. and Chandra, S., "Thermal Stability, Complexing Behavior, and Ionic Transport of Polymeric Gel Membranes Based on Polymer PVdF-HFP and Ionic Liquid, [BMIM][BF_4]", *J. Phys. Chem. B* **117** (3), 897-906 (2013).

[273] Fedotov, M.A., Malkina, O.L. and Malkin, V.G., "35/37Cl NMR chemical shifts and nuclear quadrupole couplings for some small chlorine compounds: experimental and theoretical study", *Chem. Phys. Lett.* **258** (3), 330-335 (1996).

[274] Bradaric, C.J., Downard, A., Kennedy, C., Robertson, A.J. and Zhou, Y., "Industrial preparation of phosphonium ionic liquids", *Green Chem.* **5** (2), 143-152 (2003).

[275] (a) Avent, A.G., Chaloner, P.A., Day, M.P., Seddon, K.R. and Welton, T., "Evidence for hydrogen bonding in solutions of 1-ethyl-3-methylimidazolium halides, and its implications for room-temperature halogenoaluminate(III) ionic liquids", *J. Chem. Soc., Dalton Trans.* (23), 3405-3413 (1994); (b) Hall, C., Haller, G.L. and Richards, R.E., "N.M.R. studies of lithium chloride and lithium bromide solutions in methanol-water mixtures", *Mol. Phys.* **16** (4), 377-394 (1969).

[276] Neves, C.M.S.S., Carvalho, P.J., Freire, M.G. and Coutinho, J.A.P., "Thermophysical properties of pure and water-saturated tetradecyltrihexylphosphonium-based ionic liquids", *J. Chem. Therm.* **43** (6), 948-957 (2011).

[277] McAtee, Z.P. and Heitz, M.P., "Density, viscosity and excess properties in the trihexyltetradecylphosphonium chloride ionic liquid/methanol cosolvent system", *J. Chem. Therm.* **93**, 34-44 (2016).

[278] Tat'yana, V.V. and Oleg, N.E., "Polypyrrole: a conducting polymer; its synthesis, properties and applications", *Russ. Chem. Rev.* **66** (5), 443 (1997).

[279] Stanke, D., Hallensleben, M.L. and Toppare, L., "Oxidative polymerization of pyrrole with iron chloride in nitromethane", *Synth. Met.* **72** (2), 159-165 (1995).

[280] (a) Ajjan, F.N., Jafari, M.J., Rebis, T., Ederth, T. and Inganas, O., "Spectroelectrochemical investigation of redox states in a polypyrrole/lignin composite electrode material", *J. Mater. Chem. A* **3** (24), 12927-12937 (2015); (b) Kaynak, A., Rintoul, L. and George, G.A., "Change of mechanical and electrical properties of polypyrrole films with dopant concentration and oxidative aging", *Mater. Res. Bull.* **35** (6), 813-824 (2000).

[281] (a) Liu, Y.-C., Hwang, B.-J., Jian, W.-J. and Santhanam, R., "*In situ* cyclic voltammetry-surface-enhanced Raman spectroscopy: studies on the doping–undoping of polypyrrole film", *Thin Solid Films* **374** (1), 85-91 (2000); (b) Nguyen Thi Le, H., Bernard, M.C., Garcia-Renaud, B. and Deslouis, C., "Raman spectroscopy analysis of polypyrrole films as protective coatings on iron", *Synth. Met.* **140** (2), 287-293 (2004).

[282] Yan, F., Xue, G. and Zhou, M., "Preparation of electrically conducting polypyrrole in oil/water microemulsion", *J. Appl. Polym. Sci.* **77** (1), 135-140 (2000).

[283] Chang, J.H., Aleman de Leon, C.R. and Hunter, I.W., "Self-Assembled, Nanostructured Polypyrrole Films Grown in a High-Gravity Environment", *Langmuir* **28** (10), 4805-4810 (2012).

[284] Muller, D., Rambo, C.R., Porto, L.M., Schreiner, W.H. and Barra, G.M.O., "Structure and properties of polypyrrole/bacterial cellulose nanocomposites", *Carbohydr. Polym.* **94** (1), 655-662 (2013).

[285] Sk, M.M. and Yue, C.Y., "Layer-by-layer (LBL) assembly of graphene with p-phenylenediamine (PPD) spacer for high performance supercapacitor applications", *RSC Adv.* **4** (38), 19908-19915 (2014).

[286] Shishlov, N.M. and Khursan, S.L., "Effect of ion interactions on the IR spectrum of benzenesulfonate ion. Restoration of sulfonate ion symmetry in sodium benzenesulfonate dimer", *J Mol Struct* **1123**, 360-366 (2016).

[287] Byl, O., Liu, J.-C., Wang, Y., Yim, W.-L., Johnson, J.K. and Yates, J.T., "Unusual Hydrogen Bonding in Water-Filled Carbon Nanotubes", *J. Am. Chem. Soc.* **128** (37), 12090-12097 (2006).

[288] Edwards, H.G.M., Brown, D.R., Dale, J.A. and Plant, S., "Raman spectroscopy of sulfonated polystyrene resins", *Vib. Spectrosc* **24** (2), 213-224 (2000).

[289] Mavinakuli, P., Wei, S., Wang, Q., Karki, A.B., Dhage, S., Wang, Z., Young, D.P. and Guo, Z., "Polypyrrole/Silicon Carbide Nanocomposites with Tunable Electrical Conductivity", *J. Phys. Chem. C* **114** (9), 3874-3882 (2010).

[290] Wissler, M., "Graphite and carbon powders for electrochemical applications", *J. Power Sources* **156** (2), 142-150 (2006).

[291] Sengupta, R., Bhattacharya, M., Bandyopadhyay, S. and Bhowmick, A.K., "A review on the mechanical and electrical properties of graphite and modified graphite reinforced polymer composites", *Prog. Polym. Sci.* **36** (5), 638-670 (2011).

[292] Ţucureanu, V., Matei, A. and Avram, A.M., "FTIR Spectroscopy for Carbon Family Study", *Crit. Rev. Anal. Chem.* **46** (6), 502-520 (2016).

[293] Friedel, R.A. and Carlson, G.L., "Infrared spectra of ground graphite", *J. Phys. Chem.* **75** (8), 1149-1151 (1971).

[294] Ferrari, A.C., "Raman spectroscopy of graphene and graphite: Disorder, electron–phonon coupling, doping and nonadiabatic effects", *Solid State Commun.* **143** (1), 47-57 (2007).

[295] (a) Cho, N.H., Krishnan, K.M., Veirs, D.K., Rubin, M.D., Hopper, C.B., Bhushan, B. and Bogy, D.B., "Chemical structure and physical properties of diamond-like amorphous carbon films prepared by magnetron sputtering", *J. Mater. Res.* **5** (11), 2543-2554 (2011); (b) Wei, J., Chen, W., Chen, D. and Yang, K., "An amorphous carbon-graphite composite cathode for long cycle life rechargeable aluminum ion batteries", *J. Mater. Sci. Technol.* (2017).

[296] Crumpton, D.M., Laitinen, R.A., Smieja, J. and Cleary, D.A., "Thermal Analysis of Carbon Allotropes: An Experiment for Advanced Undergraduates", *J. Chem. Educ.* **73** (6), 590 (1996).

[297] (a) Ahmad, F. and Sheha, E., "Preparation and physical properties of (PVA)0.7(NaBr)0.3(H_3PO_4)$_x$M solid acid membrane for phosphoric acid – Fuel cells", *J. Adv. Res.* **4** (2), 155-161 (2013); (b) Zhao, C., Wang, C., Yue, Z., Shu, K. and Wallace, G.G., "Intrinsically Stretchable Supercapacitors Composed of Polypyrrole Electrodes and Highly Stretchable Gel Electrolyte", *ACS Appl. Mater. Interfaces* **5** (18), 9008-9014 (2013).

[298] Intertek, 'Plastics Tensile Testing for ASTM D638', http://www.intertek.com/polymers/tensile-testing/astm-d638-iso-527/.

[299] International, A., in 'Standard Test Method for Tensile Properties of Thin Plastic Sheeting', United States (2002).

[300] Davis, J.R., *Tensile testing*, 2nd Edit. (ASM international, United States of America, 2004).

[301] Sundberg, J., Toriz, G. and Gatenholm, P., "Effect of xylan content on mechanical properties in regenerated cellulose/xylan blend films from ionic liquid", *Cellulose* **22** (3), 1943-1953 (2015).

[302] Yin, W., Liu, H., Li, J., Li, Y. and Gu, T., "Conducting composite films based on polypyrrole and crosslinked poly(styrene - butyl acrylate - hydroxyethyl acrylate)", *J. Appl. Polym. Sci.* **64** (12), 2293-2298 (1997).

[303] Anderson, C., *Mechanical Properties of Conducting Polymer Composites for Triggered Drug Delivery Applications,* Final Project Report MEE 4040, School of Mechanical and Aerospace Engineering, Queen's University Belfast (2017).

[304] Harnisch, F. and Freguia, S., "A Basic Tutorial on Cyclic Voltammetry for the Investigation of Electroactive Microbial Biofilms", *Chem. - Asian J.* **7** (3), 466-475 (2012).

[305] (a) Foroughi, J., Spinks, G.M., Wallace, G.G. and Whitten, P.G., "Production of polypyrrole fibres by wet spinning", *Synth. Met.* **158** (3), 104-107 (2008); (b) Tallman, D.E., Spinks, G., Dominis, A. and Wallace, G.G., "Electroactive conducting polymers for corrosion control", *J. Solid State Electrochem.* **6** (2), 73-84 (2002).

[306] Kim, J.-H., Shim, B., Kim, H., Lee, Y.-J., Min, S.-K., Jang, D., Abas, Z. and Kim, J., "Review of nanocellulose for sustainable future materials", *Int. J. of Precis. Eng. and Manuf.-Green Tech.* **2** (2), 197-213 (2015).

[307] Huber, B. and Roling, B., "Development of a Ag/Ag^+ micro-reference electrode for electrochemical measurements in ionic liquids", *Electrochim. Acta* **56** (19), 6569-6572 (2011).

[308] Jia, X., Wang, C., Ranganathan, V., Napier, B., Yu, C., Chao, Y., Forsyth, M., Omenetto, F.G., MacFarlane, D.R. and Wallace, G.G., "A Biodegradable Thin-Film Magnesium Primary Battery Using Silk Fibroin–Ionic Liquid Polymer Electrolyte", *ACS Energy Letters* **2** (4), 831-836 (2017).

[309] (a) Dai, Z., Peng, C., Chae, J.H., Ng, K.C. and Chen, G.Z., "Cell voltage versus electrode potential range in aqueous supercapacitors", *Scientific Reports* **5**, 9854 (2015); (b) Garche, J., Dyer, C.K., Moseley, P.T., Ogumi, Z., Rand, D.A. and Scrosati, B., *Encyclopedia of electrochemical power sources* (Newnes, 2013).

[310] (a) Lewandowski, A. and Galinski, M., "Carbon-ionic liquid double-layer capacitors", *J. Phys. Chem. Solids* **65** (2-3), 281-286 (2004); (b) Mousavi, M.P.S., Dittmer, A.J., Wilson, B.E., Hu, J., Stein, A. and Bühlmann, P., "Unbiased Quantification of the Electrochemical Stability Limits of Electrolytes and Ionic Liquids", *J. Electrochem. Soc.* **162** (12), A2250-A2258 (2015).

[311] (a) Buzzeo, M.C., Evans, R.G. and Compton, R.G., "Non-haloaluminate room-temperature ionic liquids in electrochemistry-a review", *Chem. Phys. Chem.* **5** (8), 1106-1120 (2004); (b) McEwen, A.B., Ngo, E.L., LeCompte, K. and Goldman, J.L., "Electrochemical properties of imidazolium salt electrolytes for electrochemical capacitor applications", *J. Electrochem. Soc.* **146** (5), 1687-1695 (1999).

[312] Gorodetsky, B., Ramnial, T., Branda, N.R. and Clyburne, J.A.C., "Electrochemical reduction of an imidazolium cation: a convenient preparation of imidazol-2-

ylidenes and their observation in an ionic liquid", *Chem. Commun.* (17), 1972-1973 (2004).

[313] (a) Koch, V.R., Dominey, L.A., Nanjundiah, C. and Ondrechen, M.J., "The Intrinsic Anodic Stability of Several Anions Comprising Solvent‐Free Ionic Liquids", *J. Electrochem. Soc.* **143** (3), 798-803 (1996); (b) Rogers, E.I., Šljukić, B., Hardacre, C. and Compton, R.G., "Electrochemistry in Room-Temperature Ionic Liquids: Potential Windows at Mercury Electrodes", *J. Chem. Eng. Data* **54** (7), 2049-2053 (2009).

[314] Zhao, C., Bond, A.M. and Lu, X., "Determination of Water in Room Temperature Ionic Liquids by Cathodic Stripping Voltammetry at a Gold Electrode", *Anal. Chem.* **84** (6), 2784-2791 (2012).

[315] (a) Hayyan, M., Mjalli, F.S., Hashim, M.A., AlNashef, I.M. and Mei, T.X., "Investigating the electrochemical windows of ionic liquids", *J. Ind. Eng. Chem.* **19** (1), 106-112 (2013); (b) Kazemiabnavi, S., Zhang, Z., Thornton, K. and Banerjee, S., "Electrochemical Stability Window of Imidazolium-Based Ionic Liquids as Electrolytes for Lithium Batteries", *J. Phys. Chem. B* **120** (25), 5691-5702 (2016).

[316] Gagne, R.R., Koval, C.A. and Lisensky, G.C., "Ferrocene as an internal standard for electrochemical measurements", *Inorg. Chem.* **19** (9), 2854-2855 (1980).

[317] Lewandowski, A., Waligora, L. and Galinski, M., "Electrochemical Behavior of Cobaltocene in Ionic Liquids", *J. Solut. Chem.* **42** (2), 251-262 (2013).

[318] Kissinger, P.T. and Heineman, W.R., "Cyclic voltammetry", *J. Chem. Educ.* **60** (9), 702 (1983).

[319] (a) Lewandowski, A., Waligora, L. and Galinski, M., "Ferrocene as a Reference Redox Couple for Aprotic Ionic Liquids", *Electroanalysis* **21** (20), 2221-2227 (2009); (b) Nagy, L., Gyetvai, G., Kollár, L. and Nagy, G., "Electrochemical behavior of ferrocene in ionic liquid media", *J. Biochem. Bioph. Methods* **69** (1), 121-132 (2006).

[320] Villagrán, C., Banks, C.E., Hardacre, C. and Compton, R.G., "Electroanalytical Determination of Trace Chloride in Room-Temperature Ionic Liquids", *Anal. Chem.* **76** (7), 1998-2003 (2004).

[321] (a) Ignat'ev, N.V., Welz-Biermann, U., Kucheryna, A., Bissky, G. and Willner, H., "New ionic liquids with tris(perfluoroalkyl)trifluorophosphate (FAP) anions", *J. Fluor. Chem.* **126** (8), 1150-1159 (2005); (b) Salgado, J., Villanueva, M., Parajó, J.J. and Fernández, J., "Long-term thermal stability of five imidazolium ionic liquids", *J. Chem. Therm.* **65** (Supplement C), 184-190 (2013).

[322] Seki, S., Serizawa, N., Hayamizu, K., Tsuzuki, S., Umebayashi, Y., Takei, K. and Miyashiro, H., "Physicochemical and Electrochemical Properties of 1-Ethyl-3-Methylimidazolium Tris(pentafluoroethyl)trifluorophosphate and 1-Ethyl-3-Methylimidazolium Tetracyanoborate", *J. Electrochem. Soc.* **159** (7), A967-A971 (2012).

[323] Zhang, S. and Pan, N., "Supercapacitors Performance Evaluation", *Adv. Energy Mater.* **5** (6), 1401401 (2015).

[324] Instruments, G., 'Two, Three and Four Electrode Experiments', https://www.gamry.com/application-notes/electrodes-cells/two-three-and-four-electrode-experiments/, (2018).

[325] (a) Sezgin, S., Ates, M., Parlak, E.A. and Sarac, A.S., "Scan rate effect of 1-(4-methoxyphenyl)-1H-pyrrole electro-coated on carbon fiber: characterization via cyclic voltammetry, FTIR-ATR and electrochemical impedance spectroscopy", *Int. J. Electrochem. Sci* **7**, 1093-1106 (2012); (b) Singh, S., Supriya, n., Rakib, S.K.A., Chavhan, M.P. and Ganguly, S., "Double layer capacitance for different thicknesses of carbon overlay and types of electrolytes: a circuit analogue approach", *Asia-Pac. J. Chem. Eng.* **11** (2), 296-304 (2016).

[326] Schiffer, J., Linzen, D. and Sauer, D.U., "Heat generation in double layer capacitors", *J. Power Sources* **160** (1), 765-772 (2006).

[327] d'Entremont, A.L. and Pilon, L., "Thermal effects of asymmetric electrolytes in electric double layer capacitors", *J. Power Sources* **273**, 196-209 (2015).

[328] Xiong, G., Kundu, A. and Fisher, T.S., "Thermal Considerations for Supercapacitors", in *Thermal Effects in Supercapacitors*, Ed. S. Briefs (Springer, Cham, 2015), pp. 11-26.

[329] Zequine, C., Ranaweera, C.K., Wang, Z., Dvornic, P.R., Kahol, P.K., Singh, S., Tripathi, P., Srivastava, O.N., Singh, S., Gupta, B.K., Gupta, G. and Gupta, R.K., "High-Performance Flexible Supercapacitors obtained via Recycled Jute: Bio-Waste to Energy Storage Approach", *Scientific Reports* **7**, 1174 (2017).

[330] Paulis, F.d., Raimondo, L. and Orlandi, A., "IR-DROP Analysis and Thermal Assessment of Planar Electromagnetic Bandgap Structures for Power Integrity Applications", *IEEE Transactions on Advanced Packaging* **33** (3), 617-622 (2010).

[331] Wang, K., Wu, H., Meng, Y., Zhang, Y. and Wei, Z., "Integrated energy storage and electrochromic function in one flexible device: an energy storage smart window", *Energy Environ. Sci.* **5** (8), 8384-8389 (2012).

[332] Atkins, P. and De Paula, J., *Physical Chemistry*, 8th Edit. (W H Freeman & Co (Sd), 2006).

[333] Gao, K., Shao, Z., Li, J., Wang, X., Peng, X., Wang, W. and Wang, F., "Cellulose nanofiber-graphene all solid-state flexible supercapacitors", *J. Mater. Chem. A* **1** (1), 63-67 (2013).

[334] Balducci, A., Dugas, R., Taberna, P.L., Simon, P., Plee, D., Mastragostino, M. and Passerini, S., "High temperature carbon-carbon supercapacitor using ionic liquid as electrolyte", *J. Power Sources* **165** (2), 922-927 (2007).

[335] Albery, W.J., Chen, Z., Horrocks, B.R., Mount, A.R., Wilson, P.J., Bloor, D., Monkman, A.T. and Elliott, C.M., "Spectroscopic and electrochemical studies of charge transfer in modified electrodes", *Faraday Discuss. Chem. Soc.* **88**, 247-259 (1989).

[336] Hughes, M., Chen, G.Z., Shaffer, M.S.P., Fray, D.J. and Windle, A.H., "Electrochemical Capacitance of a Nanoporous Composite of Carbon Nanotubes and Polypyrrole", *Chem. Mat.* **14** (4), 1610-1613 (2002).

[337] (a) Senthilkumar, S.T., Selvan, R.K., Lee, Y.S. and Melo, J.S., "Electric double layer capacitor and its improved specific capacitance using redox additive electrolyte", *J. Mater. Chem. A* **1** (4), 1086-1095 (2013); (b) Taberna, P.L., Simon, P. and Fauvarque , J.F., "Electrochemical Characteristics and Impedance Spectroscopy Studies of Carbon-Carbon Supercapacitors", *J. Electrochem. Soc.* **150** (3), A292-A300 (2003).

[338] Tian, W., Gao, Q., Tan, Y., Yang, K., Zhu, L., Yang, C. and Zhang, H., "Bio-inspired beehive-like hierarchical nanoporous carbon derived from bamboo-based industrial by-product as a high performance supercapacitor electrode material", *J. Mater. Chem. A* **3** (10), 5656-5664 (2015).

[339] (a) Basiricò, L. and Lanzara, G., "Moving towards high-power, high-frequency and low-resistance CNT supercapacitors by tuning the CNT length, axial deformation and contact resistance", *Nanotechnology* **23** (30), 305401 (2012); (b) Niu, C., Sichel, E.K., Hoch, R., Moy, D. and Tennent, H., "High power electrochemical capacitors based on carbon nanotube electrodes", *Appl. Phys. Lett.* **70** (11), 1480-1482 (1997).

[340] Macdonald, J.R. and Barsoukov, E., "Impedance spectroscopy: theory, experiment, and applications", *History* **1** (8) (2005).

[341] Pandey, G.P. and Hashmi, S.A., "Performance of solid-state supercapacitors with ionic liquid 1-ethyl-3-methylimidazolium tris(pentafluoroethyl) trifluorophosphate based gel polymer electrolyte and modified MWCNT electrodes", *Electrochim. Acta* **105** (Supplement C), 333-341 (2013).

[342] (a) Nazet, A., Sokolov, S., Sonnleitner, T., Makino, T., Kanakubo, M. and Buchner, R., "Densities, Viscosities, and Conductivities of the Imidazolium Ionic Liquids [Emim][Ac], [Emim][FAP], [Bmim][BETI], [Bmim][FSI], [Hmim][TFSI], and [Omim][TFSI]", *J. Chem. Eng. Data* **60** (8), 2400-2411 (2015); (b) Yu, G., Zhao, D., Wen, L., Yang, S. and Chen, X., "Viscosity of ionic liquids: Database, observation, and quantitative structure‐property relationship analysis", *Aiche J.* **58** (9), 2885-2899 (2012).

[343] Lajnef, W., Vinassa, J.M., Briat, O., Azzopardi, S. and Woirgard, E., "Characterization methods and modelling of ultracapacitors for use as peak power sources", *J. Power Sources* **168** (2), 553-560 (2007).

[344] Huang, Y., Tao, J., Meng, W., Zhu, M., Huang, Y., Fu, Y., Gao, Y. and Zhi, C., "Super-high rate stretchable polypyrrole-based supercapacitors with excellent cycling stability", *Nano Energy* **11** (Supplement C), 518-525 (2015).

[345] Liu, X., Dai, X., Wei, G., Xi, Y., Pang, M., Izotov, V., Klyui, N., Havrykov, D., Ji, Y., Guo, Q. and Han, W., "Experimental and theoretical studies of nonlinear dependence of the internal resistance and electrode thickness for high performance supercapacitor", *Scientific Reports* **7**, 45934 (2017).

[346] Xu, J., Wang, D., Yuan, Y., Wei, W., Gu, S., Liu, R., Wang, X., Liu, L. and Xu, W., "Polypyrrole-coated cotton fabrics for flexible supercapacitor electrodes prepared using CuO nanoparticles as template", *Cellulose* **22** (2), 1355-1363 (2015).

[347] Choi, B.G., Huh, Y.S., Hong, W.H., Erickson, D. and Park, H.S., "Electroactive nanoparticle directed assembly of functionalized graphene nanosheets into hierarchical structures with hybrid compositions for flexible supercapacitors", *Nanoscale* **5** (9), 3976-3981 (2013).

[348] Wang, S., Hsia, B., Carraro, C. and Maboudian, R., "High-performance all solid-state micro-supercapacitor based on patterned photoresist-derived porous carbon electrodes and an ionogel electrolyte", *J. Mater. Chem. A* **2** (21), 7997-8002 (2014).

[349] Zhang, S., Peng, C., Ng, K.C. and Chen, G.Z., "Nanocomposites of manganese oxides and carbon nanotubes for aqueous supercapacitor stacks", *Electrochim. Acta* **55** (25), 7447-7453 (2010).

[350] Pandey, G.P. and Rastogi, A.C., "Solid-State Supercapacitors Based on Pulse Polymerized Poly(3,4-ethylenedioxythiophene) Electrodes and Ionic Liquid Gel Polymer Electrolyte", *J. Electrochem. Soc.* **159** (10), A1664-A1671 (2012).

[351] Wan, C., Jiao, Y. and Li, J., "Flexible, highly conductive, and free-standing reduced graphene oxide/polypyrrole/cellulose hybrid papers for supercapacitor electrodes", *J. Mater. Chem. A* **5** (8), 3819-3831 (2017).

[352] Yu, P., Zhao, X., Huang, Z., Li, Y. and Zhang, Q., "Free-standing three-dimensional graphene and polyaniline nanowire arrays hybrid foams for high-performance flexible and lightweight supercapacitors", *J. Mater. Chem. A* **2** (35), 14413-14420 (2014).

[353] Horowitz, A.I. and Panzer, M.J., "Poly(dimethylsiloxane)-Supported Ionogels with a High Ionic Liquid Loading", *Angewandte Chemie International Edition* **53** (37), 9780-9783 (2014).

[354] Zopf, S.F. and Panzer, M.J., "Integration of UV-cured Ionogel Electrolyte with Carbon Paper Electrodes", *AIMS Mater. Sci.* **1** (1), 59-69 (2014).

[355] Zhang, M., Hou, C., Halder, A., Wang, H. and Chi, Q., "Graphene papers: smart architecture and specific functionalization for biomimetics, electrocatalytic sensing and energy storage", *Mater. Chem. Front.* **1** (1), 37-60 (2017).

[356] Kim, D., Shin, G., Kang, Y.J., Kim, W. and Ha, J.S., "Fabrication of a Stretchable Solid-State Micro-Supercapacitor Array", *ACS Nano* **7** (9), 7975-7982 (2013).

[357] Gao, Y., Zhou, Y.S., Xiong, W., Jiang, L.J., Mahjouri-samani, M., Thirugnanam, P., Huang, X., Wang, M.M., Jiang, L. and Lu, Y.F., "Transparent, flexible, and solid-state supercapacitors based on graphene electrodes", *APL Materials* **1** (1), 012101 (2013).

[358] Patel, P., 'Dissolvable batteries made of silk', http://cen.acs.org/articles/95/web/2017/04/Dissolvable-batteries-made-silk.html?+Engineering+News%3A+Latest+News%29, (2017).

[359] Miyamoto, T., Takahashi, S.i., Ito, H., Inagaki, H. and Noishiki, Y., "Tissue biocompatibility of cellulose and its derivatives", *J. Biomed. Mater. Res.* **23** (1), 125-133 (1989).

[360] Geetha, S., Rao, C.R.K., Vijayan, M. and Trivedi, D.C., "Biosensing and drug delivery by polypyrrole", *Anal. Chim. Acta* **568** (1), 119-125 (2006).

[361] Ulery, B.D., Nair, L.S. and Laurencin, C.T., "Biomedical Applications of Biodegradable Polymers", *J. Polym. Sci., Part B: Polym. Phys.* **49** (12), 832-864 (2011).

[362] Guleria, A., Singh, A.K., Adhikari, S. and Sarkar, S.K., "Radiation induced physicochemical changes in FAP (fluoro alkyl phosphate) based imidazolium ionic liquids and their mechanistic pathways: influence of hydroxyl group functionalization of the cation", *Dalton Trans.* **43** (2), 609-625 (2014).

[363] Scholz, E., *Karl Fischer titration: Determination of water*, Chemical Laboratory Practice (Springer Berlin Heidelberg, Riedel-de Haën AG, Seelze/Hannover, 1984).

[364] Sathyanarayana, D.N., *Vibrational spectroscopy: theory and applications*, 2nd Edit. (New Age International, 2005).

[365] (a) Cotton, F.A., *Chemical applications of group theory*, 3rd Edit. (John Wiley & Sons, New York, 1990); (b) Herman, M. and Lievin, J., "Group theory. From common objects to molecules", *J. Chem. Educ.* **54** (10), 596 (1977).

[366] Le Pevelen, D.D., "NIR FT-Raman ", in *Encyclopedia of Spectroscopy and Spectrometry*, 3rd Edit., Eds. J. Lindon, G.E. Tranter and D.W. Koppenaal (Academic Press, Oxford, 2017), pp. 98-109.

[367] Gonze, X., Rignanese, G.-M. and Caracas, R., "First-principle studies of the lattice dynamics of crystals, and related properties", *Z. Krist.* **220** (5/6/2005), 458-472 (2005).

[368] Ramer, G. and Lendl, B., "Attenuated Total Reflection Fourier Transform Infrared Spectroscopy", in *Encyclopedia of Analytical Chemistry* (John Wiley & Sons, Ltd, 2013).

[369] (a) Bumbrah, G.S. and Sharma, R.M., "Raman spectroscopy – Basic principle, instrumentation and selected applications for the characterization of drugs of abuse", *Egypt. J. Forensic Sci.* **6** (3), 209-215 (2016); (b) Clark, R.J.H., *Applied Laser Spectroscopy: Techniques, Instrumentation and Applications*, Vol. 6, Book Ed. D.L. Andrews (VCH, Weinheim 1992).

[370] Joy, D.C., "Scanning electron microscopy", in *Mater. Sci. Technol.*, Eds. R.W. Cahn, P. Haasen and E.J. Kramer (Wiley Online Library, University of Tennessee, Knowville, TN, US, 2006).

[371] Goldstein, J.I., Newbury, D.E., Michael, J.R., Ritchie, N.W., Scott, J.H.J. and Joy, D.C., *Scanning electron microscopy and X-ray microanalysis* (Springer, 2017).

[372] Kanda, K., *Energy dispersive X-ray spectrometer*, US Pat. 5065020A (1991).

[373] Wasa, K., "Sputtering Phenomena", in *Handbook of Sputtering Technology* 2nd Edit. (William Andrew Publishing, Oxford, 2012), pp. 41-75.

[374] Thomas, F.G. and Henze, G., *Introduction to voltammetric analysis: theory and practice* (Csiro Publishing, 2001).

[375] Park, S.-M. and Yoo, J.-S., "Peer reviewed: electrochemical impedance spectroscopy for better electrochemical measurements", *Anal. Chem.* **75** (21), 455 A–461 A (2003).

[376] Cesiulis, H., Tsyntsaru, N., Ramanavicius, A. and Ragoisha, G., "The Study of Thin Films by Electrochemical Impedance Spectroscopy", in *Nanostructures and Thin Films for Multifunctional Applications: Technology, Properties and Devices*, Eds. I. Tiginyanu, P. Topala and V. Ursaki (Springer International Publishing, Cham, 2016), pp. 3-42.

[377] Earle, M.J., Gordon, C.M., Plechkova, N.V., Seddon, K.R. and Welton, T., "Decolorization of Ionic Liquids for Spectroscopy", *Anal. Chem.* **79** (2), 758-764 (2007).

[378] Ko, D.H., Lee, S.G., Kwon, O.H., Moon, J.J., Kim, D.C., Choi, J.H., Hong, B.K. and Eom, S.S., *Method of preparing organic acids from aldehyde compounds by means of liquid phase oxidation reaction*, EP Pat. 1784376B1 (2012).

[379] Keith, A.J., Kosik, S.D., Tillekeratne, L.M.V. and Mason, M.R., "Ion-Tagged Phosphines as Ligands for Suzuki Coupling of Aryl Halides in a Phosphonium Ionic Liquid", *Synlett* **25** (07), 977-982 (2014).

[380] Troshenkova, S.V., Sashina, E.S., Novoselov, N.P., Arndt, K.F. and Jankowsky, S., "Structure of ionic liquids on the basis of imidazole and their mixtures with water", *Russ. J. Gen. Chem.* **80** (1), 106-111 (2010).

[381] Blundell, R.K. and Licence, P., "Quaternary ammonium and phosphonium based ionic liquids: a comparison of common anions", *Phys. Chem. Chem. Phys.* **16** (29), 15278-15288 (2014).

[382] Snook, G.A., Best, A.S., Pandolfo, A.G. and Hollenkamp, A.F., "Evaluation of a $Ag|Ag^+$ reference electrode for use in room temperature ionic liquids", *Electrochem. Commun.* **8** (9), 1405-1411 (2006).

[383] Taylor, J.R., *An Introduction to Error Analysis, The Study of Uncertainties in Physical Measurements*, 2nd. Edit. (University Science Books, Sausalito, California, 1982).